ATMÓSFERA

Revista trimestral publicada por el
Instituto de Ciencias de la Atmósfera y Cambio Climático
de la Universidad Nacional Autónoma de México

Volumen 35
Número 2
1 de abril de 2022

CONTENTS

MÉXICO 2022

INFORMATION FOR CONTRIBUTORS

ATMOSFERA seeks contributions on theoretical, empirical and applied research in all the areas of atmospheric sciences, with emphasis on meteorology, climatology, aeronomy, physics, chemistry, and aerobiology. Interdisciplinary contributions are also accepted; especially those related with oceanography, hydrology, ecology, forestry, glaciology, agriculture, environmental pollution, and other topics related to economy and society as they are affected by climate variability and change, and atmospheric hazards.

ATMOSFERA publishes articles, short contributions and correspondence in English. The submission of a contribution to be considered an article is assumed to indicate that no similar paper, other than an abstract or preliminary report, has been or will be submitted for publication elsewhere. Short contributions should not exceed 1000 words. Correspondence is intended for discussion of papers published in the journal and should not exceed 250 words.

Manuscripts. Please submit an electronic copy of your final version of the manuscript, preferably prepared with MS Word or compatible software, through the journal's webpage at http://www.revistascca.unam.mx/atm/index.php/atm/about/submissions#onlineSubmissions. It should be formatted with wide margins, double-spacing and all pages numbered. Footnotes to the text should be avoided. When symbols in mathematical work could be in doubt, the authors should submit a list identifying typographically the symbols used. Equations will be numbered in parentheses to the right.

Title, name, address. Provide the title in full and suggest a short title for headers on odd-numbered pages. Author's name, affiliation, e-mail and present postal address will not be included in the document, but they should be captured in the "Submission Metadata" section.

Abstract. All articles shall include an abstract, both in Spanish and in English. Abstracts are not required for short contributions.

Text. The text should be divided into sections, each with a separate heading.

Acknowledgements. Brief.

Appendices. Supplementary materials and lengthy mathematical analyses, whose details are subordinate to the main theme of the paper, should normally appear in an appendix. Each appendix should have a title.

Units, abbreviations and symbols. The International System of Units (m, kg, s, K) should be used. Only standardized terms that have been generally accepted should be used. Unfamiliar abbreviations must be defined when first used. Particular care should be taken to ensure that all symbols are clearly identified. The minus sign should be –.

References. Articles should be fully documented with references in the text and a reference listing ordered alphabetically by author's names at the end of the paper. Digital object identifiers (DOIs) should be provided whenever possible for each reference. Authors are encouraged to adjust to the citation system. Examples:

Articles in journals: Hoerling M.P. and Kumar A., 2002. Atmosphere response patterns associated with tropical forcing. J. Climate 15, 2184-2203.

Chapters in books: Magaña V. and Conde C., 2003. Climate variability and climate change and their impacts on the freshwater resources in the border region: A case study for Sonora, México. In: Climate and water-transboundary challenges in the Americas (Díaz H.F. and Morehouse B.S., Eds.). Kluwer Academic Publishers, Dordrecht, 373-393.

Articles in proceedings: Gallardo L., Córdova A.M., Rojas M., Quintana J., Alcafuz R. and Ramos I., 2004. Stratosphere-troposphere exchange (STE) over Easter Island and Cerro Tololo stations in South America: analysis and simulation of an intensive sounding campaign. 8th International Global Atmospheric Chemistry Conference, Christchurch, New Zealand, September 2004.

Books: Thompson R.D., 1998. *Atmospheric processes and systems.* Routledge, New York, 194 pp.

References cited in the text should indicate, within parenthesis, the last name of each author and the year of publication. If there are more than two authors, the last name of the first author should be followed by et al. When the name forms part of the content of the article, and does not appear solely as a reference, the year of publication is parenthesized. For example:

...a weekly cycle has been observed in surface temperature (Gordon, 1994).

...Gordon (1994) has observed a weekly cycle in surface temperature.

Illustrations and tables. Vector graphics should be supplied in a vector format (eps, ps, ai, etc.) or as pdfs. Photographs should be provided as tiff or jpeg images (with at least 300 dpi); the same applies to line drawings (with at least 1000 dpi). Graphics created in Microsoft Office applications should be supplied in their original format. Figure captions should be self-explanatory and printed on a separate sheet of paper. All figures should be numbered and specifically mentioned in the text by number. Please number all tables with Roman numerals and include a short title.

Proofs. Copies of the proofs will be sent to the author. Revised proofs should be returned to the publisher without delay. The only changes that could be accepted in proofs are on grammar or related to printing errors.

Authors can print copies of their articles from: http://www.revistascca.unam.mx/atm/index.php/atm.

ATMÓSFERA

Revista trimestral publicada por el
Instituto de Ciencias de la Atmósfera y Cambio Climático
de la Universidad Nacional Autónoma de México

MÉXICO 2022

Atmósfera is included in: Web of Science (WoS), SCOPUS, SCISEARCH, Research Alert, GeoBase, Current Contents Connect, and Aquatic Sciences and Fisheries Abstracts (ASFA).

Registrada en el Sistema de Clasificación de Revistas Mexicanas de Investigación Científica y Tecnológica del Consejo Nacional de Ciencia y Tecnología (CONACyT), e indizada en PERIÓDICA.

Manuscripts should be submitted through our website at: https://www.revistascca.unam.mx/atm/.

Subscriptions and all correspondence should be sent to:
Editor of *Atmósfera*, Instituto de Ciencias de la Atmósfera y Cambio Climático, UNAM, Circuito Exterior, Ciudad Universitaria, 04510 Coyoacán, Ciudad de México. Tel.: 52 (55) 5622-4240 Ext. 81888; fax: 52 (55) 5616-0789; e-mail: editorial@atmosfera.unam.mx

Subscription information: Institutional rate: US $90.00 per volume (4 issues); Private rate: US $70.00 per volume (4 issues).

The complete texts of Atmósfera are available in digital format at:
https://www.revistascca.unam.mx/atm/;   Redalyc: https://redalyc.org;   SciELO: https://www.scielo.org.mx/.

Atmósfera, vol. 35, núm. 2, abril-junio de 2022, es una publicación trimestral editada por la Universidad Nacional Autónoma de México, Ciudad Universitaria, 04510 Coyoacán, Ciudad de México, teléfono (55) 5622-4240, ext.81888, https://www.revistascca.unam.mx/atm/. Editor responsable: Graciela B. Raga. Reserva de derechos al uso exclusivo del título núm. 001559/94 otorgado por el Instituto Nacional del Derecho de Autor. ISSN: 0187-6236. Certificado de licitud de título y contenido 7719 y 5464 otorgados por la Comisión Calificadora de Publicaciones y Revistas Ilustradas de la Secretaría de Gobernación. Las opiniones expresadas por los autores no necesariamente reflejan la postura del editor de la publicación.

Printed in Mexico.

Atmósfera 35(2), 197-220 (2022)
https://doi.org/10.20937/ATM.52899

CONTENTS

A momentum-balance theory for the updraft structure in density currents analogous to squall lines

Diego A. ALFARO and Fernando LEZANA*

Instituto de Ciencias de la Atmósfera y Cambio Climático, Universidad Nacional Autónoma de México, Circuito Exterior s/n, Ciudad Universitaria, 04510 Mexico City, Mexico.
*Corresponding author; email: music.is.math@ciencias.unam.mx

Received: August 02, 2020, accepted: October 23, 2020

RESUMEN

Se desarrolla una teoría de balance de momento para la orientación de corrientes ascendentes en corrientes de densidad con el fin de entender las interacciones entre cizalla y líneas de turbonada. La motivación surge de estudios mostrando las limitaciones diagnósticas de la teoría de balance de vorticidad de Rotunno et al. (1988) (teoría RKW) al variar los perfiles de cizalla, aunado a la restricción de balance de flujo-fuerza sobre la profundidad de ela capa de cizalla en corrientes de densidad óptimas. Considerando que el balance de flujo-fuerza se deriva de la ecuación de momento horizontal, conceptos de balance de momento son explorados como alternativa a la teoría RKW, donde la pendiente de la corriente ascendente está determinada por el balance entre tendencias advectivas del aire entrante y el trabajo hecho por perturbaciones de presión dentro del fluido más denso. Se simularon corrientes de densidad bajo diversos perfiles de cizalla y flotabilidad. Los resultados muestran que el balance de momento diagnostica acertadamente la pendiente de la corriente ascendente en los niveles bajos y medios en experimentos que contemplan tanto variaciones c-ΔU «clásicas», así como cambios en los perfiles verticales de cizalla y flotabilidad. También se encuentra que casos con flujo relativo al sistema más intenso tienden a producir ascenso más profundo de aire ambiental cercano a la superficie, sin importar la pendiente de la corriente ascendente. El criterio cuantitativo de la teoría RKW ($c/\Delta U$) no es tan efectivo para diagnosticar la pendiente de la corriente ascendente, ni la profundidad alcanzada por parcelas originadas cerca de la superficie, aunque $c/\Delta U$ provee una idea de la pendiente en niveles altos. Este resultado justifica la reinterpretación de $c/\Delta U$ como una medida del impacto de velocidades de viento en lo alto de la corriente ascendente.

ABSTRACT

A momentum-balance theory for the orientation of updrafts in density currents is developed for understanding squall-line–shear interactions. The motivation arises from studies showing the diagnostic limitations of the vorticity-balance theory by Rotunno et al. (1988) (RKW theory) under varying shear profiles, together with the flow-force balance constraint (FFB) which determines the shear-layer depth in optimal density currents. Considering that the FFB is derived from the horizontal momentum equation, momentum-balance concepts are explored as an alternative to RKW theory, by assuming that the updraft's slope is determined by the balance between advective tendencies of inflowing air and the work done by pressure perturbations within the denser fluid. Density currents were simulated under diverse shear and buoyancy profiles. Results show that momentum-balance effectively diagnoses the updraft's slope at low and mid-levels in experiments contemplating both "classic" c-ΔU variations, as well as changes to the shear and buoyancy vertical profiles. It is also found that cases with stronger system-relative inflow tend to produce deeper lifting of near-surface environmental air, notwithstanding the updraft's slope. RKW theory's quantitative criterion ($c/\Delta U$) is not as effective at diagnosing the updraft's slope nor the depth reached by near-surface parcels, although $c/\Delta U$ provides guidance for the updraft's slope at upper levels. This result justifies a reinterpretation of $c/\Delta U$ as a measure of the impacts of wind velocities aloft on the updraft.

Keywords: Rotunno-Klemp-Weisman (RKW) theory, linear squall lines, updraft vertical orientation.

1. Introduction

It is well-known that the organization of squall lines (SLs) is strongly dependent on the environmental vertical wind-shear throughout the low and mid-troposphere (Thorpe et al., 1982; Barnes and Sieckman, 1984; Bluestein and Jain, 1985; Rotunno et al., 1988, hereafter RKW88; Fovell and Ogura, 1989; Alfaro, 2017). The magnitude of the shear can affect a SLs maintenance (Coniglio et al., 2007; Alfaro and Coniglio, 2018), its precipitation rate (Rotunno et al., 1990; Weisman and Rotunno, 2004, hereafter WR04; Bryan et al., 2006; Alfaro, 2017), mesoscale circulations within the stratiform region (Lafore and Moncrieff, 1989; Weisman, 1992; Parker and Johnson, 2004a), and the intensity of surface wind speeds (Weisman, 1993; Bryan et al., 2006; Cohen et al., 2007). But consensus about the physical mechanisms governing the interactions between SLs and the low-to-mid-tropospheric shear is lacking within the community of mesoscale meteorologists, as reflected by decades of vigorous scientific debate continuing to this date (e.g. WR04; Stensrud et al., 2005; Bryan et al., 2012; Coniglio et al., 2012; Alfaro, 2017). Thus, further research on storm-shear interactions is warranted, especially because better understanding of such processes might lead to improved forecasts (e.g. Coniglio et al., 2007; Alfaro and Coniglio, 2018) and parameterizations (e.g. Dai, 2006; Moncrieff, 2010).

The leading paradigm for explaining how the low-to-mid-tropospheric shear affects SLs with well-defined cold pools (e.g. Bryan et al., 2005; Engerer et al., 2008; Bryan and Parker, 2010; Provod et al., 2016) is RKW88's theory of vorticity-balance (hereafter RKW theory). RKW theory contends that the orientation and intensity of the deep convective updraft, a fundamental structural element of SLs, is primarily determined by the amount of baroclinically generated vorticity at the edge of the cold pool relative to the inflowing environmental vorticity due to the shear. Specifically, RKW88 refer to the horizontal vorticity equation to argue that the shear's vorticity, which favors downshear updraft tilting (Asai, 1964), can counter the cold pool's tendency to "sweep" parcels over the denser air when both vorticity sources have opposite signs and similar magnitude. Per RKW theory, a SL's updraft leans downshear (upshear) if the shear's vorticity inflow is greater (less) than the baroclinically generated vorticity, with updraft verticality depending directly on the degree of vorticity-balance. And given that slanted updrafts tend to be weaker than vertically oriented ones (Asai, 1964; Lilly, 1979; Parker, 2010), RKW theory also ostensibly explains the intensity and depth of ascending motions.

To evaluate their theory, RKW88 derived a quantitative diagnostic from the vorticity equation in density currents, where the denser fluid represents a SL's cold pool. They found that in steady systems with strictly vertical updrafts, referred to as "optimal" (Bryan and Rotunno, 2014, hereafter BR14), the density current's theoretical propagation speed (c) (Benjamin, 1968), which measures the rate of baroclinic vorticity generation, must equal the change in wind speed within the shear-layer (ΔU), which measures the shear's vorticity inflow. This result led to the conclusion that upshear (downshear) leaning updrafts arise when c is greater (less) than ΔU, a matter substantiated in RKW88 by density current simulations. Thereafter $c/\Delta U$ has been the focus of many numerical studies which find that simulated density currents (e.g. WR04; BR14) and SLs (e.g. Weisman et al., 1988; Rotunno et al., 1990; Weisman, 1992; WR04; Bryan et al., 2006) behave as predicted by RKW theory, leading WR04 to state that cold-pool–shear relationships "*represent the most fundamental internal control on squall-line structure and evolution*".

For all its apparent success, there is ample evidence that RKW theory is not as restrictive on the structure of SLs (e.g. Parker and Johnson, 2004b) and density currents as suggested by the studies mentioned above. For instance, Alfaro (2017) showed that ΔU affects the intensity of SL's primarily through its impact on layer-lifting convective instability, rather than vorticity-balance effects, perhaps explaining the lack of robust observational evidence for RKW theory (Evans and Doswell, 2001; Gale et al., 2002; Stensrud et al., 2005; Coniglio et al., 2012). More relevant to this study is the fact that RKW theory does not provide a strict criterion for determining the depth over which ΔU should be computed. This is important because SLs organize in a variety of kinematic environments (Evans and Doswell, 2001; Gale et al., 2002; Cohen et al., 2007; Coniglio et al., 2007; Coniglio et al., 2012), and these systems are known to be sensitive to the shear-layer depth, for a given $c/\Delta U$ (e.g. WR04). Furthermore, BR14 found that density currents with $c \approx \Delta U$ can develop shallow, tilted updrafts, both in the downshear and upshear directions, depending on the depth of the shear-layer; conversely, highly vorticity-unbalanced flows can develop vertical updrafts if a suitable shear-layer depth is chosen (see BR14, Fig. 18). These findings challenge the commonly held notion that $c/\Delta U$ provides a strong constraint on an updraft's orientation and depth, both in SLs and density currents.

The objective of this research is to develop a theory of storm-shear interactions that accounts for the impacts of the shear profile, especially the shear-layer depth, on an updraft's structure. For simplicity, only adiabatic density current simulations will be considered, as described in subsection 2.1. Subsection 2.2 reviews the theoretical foundations of RKW theory, where we argue that $c/\Delta U$ is not a robust measure of vorticity-balance for non-optimal flows, being better suited for measuring the strength of system-relative wind velocities aloft, whose relevance was noted by Thorpe et al. (1982). Per this interpretation, $c/\Delta U$ is pertinent to the updraft's structure aloft, so we seek a framework for diagnosing the updraft's structure throughout low-to-mid-levels. Motivated by BR14's results showing that the flow-force balance constraint of Benjamin (1968) is a necessary condition for optimal density currents, subsection 2.3 explores the application of momentum-balance concepts for defining a metric (MB) to diagnose the updraft's orientation at low and mid-levels. In order to validate our interpretation of $c/\Delta U$ and the momentum-balance framework, 2D adiabatic density currents are simulated following the methodology of BR14, as described in section 3. Section 4 analyzes the results by contrasting the diagnostic skill of MB to that of $c/\Delta U$. Results are discussed in Section 5, while a summary and future work around applications to SLs are presented in Section 6.

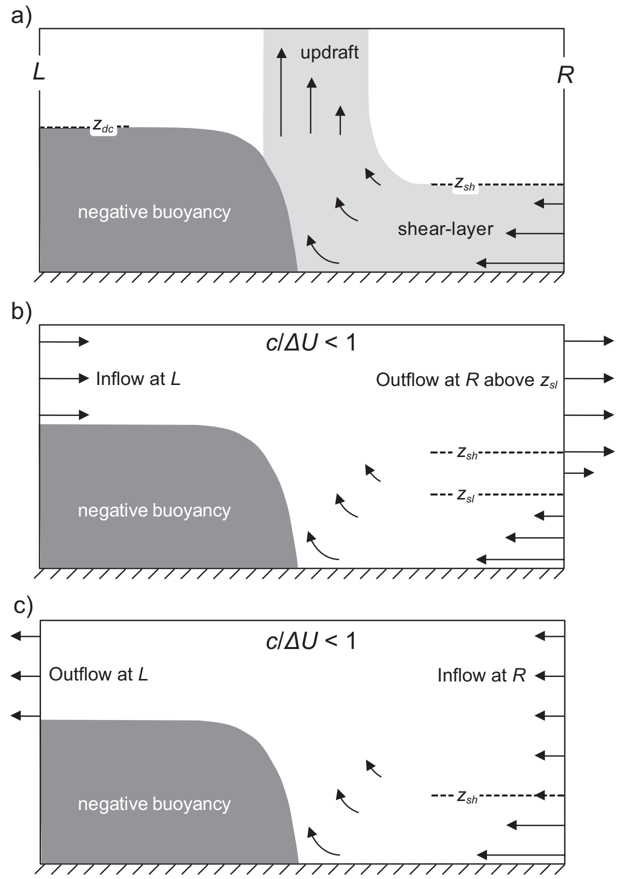

Fig. 1. Schematic depiction of density currents. The dark-gray area corresponds to the denser fluid, while arrows indicate the flow at lateral boundaries and near the density current's edge. The flow in a) has a vertical updraft, with static air outside the region in light-gray. Cases in b) and c) have $c/\Delta U < 1$ and $c/\Delta U > 1$, respectively.

2. Vorticity-balance and momentum-balance in density currents

2.1 Adiabatic, inviscid, incompressible, and steady density currents

This subsection considers density currents, as those depicted in Figure 1. Density currents are frequently used to study storm-shear interactions (RKW88; Liu and Moncrieff, 1996; WR04; Alfaro, 2017), as they have many features in common with cold pools (Charba, 1974; Wakimoto, 1982), while being much simpler than SLs.

The density current analysis is based on the 2D, incompressible, adiabatic, and inviscid Boussinesq equations in a neutrally stratified fluid:

$$\frac{du}{dt} = -\frac{\partial \rho'}{\rho_0 \partial x} \tag{1}$$

$$\frac{dw}{dt} = -\frac{\partial \rho'}{\rho_0 \partial z} + b \tag{2}$$

$$\frac{db}{dt} = 0 \tag{3}$$

$$\frac{\partial u}{\partial x} = -\frac{\partial w}{\partial z}, \tag{4}$$

where u and w are the horizontal and vertical components of the wind velocity, respectively, ρ_0 is (constant) density, p is pressure, $b = -g\rho'/\rho_0$ is buoyancy, and g is the constant of gravitational acceleration. The naught symbol indicates constants that characterize the light fluid, while primed variables are perturbations with respect to the environment, i.e. the flow at R in Figure 1a.

To delimit the problem, consider a steady density current (Fig. 1; the frame of reference is such that air is static within the density current). The fluid is infinitely deep, with open lateral boundaries and a rigid, flat, and free slip lower boundary. Pressure is assumed to be constant at the upper boundary and the flow at both lateral boundaries is hydrostatically balanced, i.e. the rhs of (2) is equal to zero. With these assumptions, the conservation of Bernoulli energy can be applied to the inflow streamline from R to the density current edge to determine the environmental surface wind speed (Xu, 1992):

$$u_{R,0} = -[2p'_{L,0}/\rho_0]^{1/2}, \tag{5}$$

where the first subscript specifies lateral boundaries L or R (Fig. 1) and the second subscript specifies height (z). Applying hydrostatic balance, while considering $\rho'_L = 0$ for $z > z_{dc}$, where z_{dc} is the density current depth, (5) can be expressed as

$$u_{R,0} = -[2\int_0^{z_{dc}} - b_L\, dz]^{1/2} \equiv -c. \tag{6}$$

Note that c in (6) equals the density current's theoretical propagation speed, as defined by RKW88, and that $u_{R,0} = c$ is a consequence of the assumptions made. In addition, mass conservation in an infinitely deep fluid requires $u_L \approx u_R$ some distance above $z_{max} = max(z_{sh}, z_{dc}) < \infty$, where z_{sh} is the environmental shear-layer height, which is consistent with density current simulations analyzed in RKW88 and BR14. In other words, if one considers a fluid of depth z^* with a given u_R profile, then mass conservation requires that the inflow/outflow at L satisfies $\int_0^{z^*} u_L\, dz / \int_0^{z^*} u_R\, dz = 1$; this condition is satisfied in the limit $z^* \to \infty$ when winds aloft at L equal winds aloft at R (this is a consequence of the intuitive fact that winds above z_{max} dominate the mass flux at lateral boundaries as $z^* \to \infty$). These are the working assumptions for all subsequent analyses.

2.2 $c/\Delta U$ as a measure of wind velocities aloft

This subsection argues for an interpretation of $c/\Delta U$ that differs from the vorticity-balance espoused by RKW theory. To justify our interpretation, we follow RKW88's derivation. Consider the horizontal vorticity equation for a steady incompressible density current:

$$-\frac{\partial}{\partial x}(u\eta) - \frac{\partial}{\partial z}(w\eta) - \frac{\partial b}{\partial x} = 0, \tag{7}$$

where $\eta = \partial u / \partial z - \partial w / \partial x$. Rearranging terms and integrating (7) in the control volume framed by $L < x < R$ and $0 < z < d$, where d is some height $d > z_{max}$ above which $u_L = u_R$ (required for mass conservation), gives

$$\int_L^R (w\eta)_d\, dx = \int_0^d (u\eta)_L\, dz - \int_0^d (u\eta)_R\, dz + \int_0^d b_L\, dz. \tag{8}$$

Note that $b_R = 0$ by definition. The first and second terms on the rhs of (8) are the flux of vorticity at L and R, respectively, while the third term represents the rate of baroclinic vorticity generation at the density current's edge. Hydrostatic balance at lateral boundaries implies $\eta = \partial u / \partial z$ at L and R, so (8) can be expressed as

$$\int_L^R (w\eta)_d\, dx = \left(\frac{u_{L,d}^2}{2}\right) - \left(\frac{u_{R,d}^2}{2} - \frac{u_{R,0}^2}{2}\right) + \int_0^{z_{dc}} b_L\, dz, \tag{9}$$

where $u_{L,0} = 0$ and $b_L = 0$ above z_{dc} were used.

Following RKW88 and BR14, we consider an optimal density current as the one depicted in Figure 1a, where winds aloft are assumed to be static, i.e. $u_{L,d} = u_{R,d} = 0$; furthermore, the vertical updraft implies $\eta = -\partial w / \partial x$ at d, which in turns implies that the lhs of (9) vanishes since $w = 0$ in L and R, hence (9) gives

$$\Delta U = u_{R,d} - u_{R,0} = -u_{R,0} = (2\int_0^{z_{dc}} - b_L\, dz)^{1/2} = c, \tag{10}$$

where the third equality in (10) results from applying the optimal state assumptions to (9), while the first and last equalities are the definitions of ΔU and c. Note that (6) and (10) are equivalent but pertain to different aspects of the flow. RKW theory's interpretation of (10) is that "*the import of the positive vorticity associated with the low-level shear [measured by* ΔU*] just balances the net buoyant generation of negative vorticity by the cold pool in the volume [measured by* c*]*" (RKW88), leading to a vertical updraft that exports equal amounts of positive and negative vorticity through d. This interpretation led to the widespread use of $c/\Delta U$ as a vorticity-balance explanation to the updrafts' structure in SLs.

RKW88 derived (10) assuming an optimal density current (Bryan et al., 2012), so care must be exercised when dealing with non-optimal cases, i.e. $c/\Delta U \neq 1$. For instance, consider a case with $c/\Delta U < 1$ (Fig. 1b) where (6) implies $u_{R,d} > 0$, so there is outflow of vorticity at R between z_{sh} and the steering level (z_{sl}), the latter being the level of vanishing environmental wind speed. Mass conservation and (6) require $u_{L,d} = u_{R,d} = \Delta U - c$, so the outflow of vorticity at R is balanced by inflowing vorticity at L (Fig. 1b), implying that only the environmental shear below z_{sl} needs to be considered when using (9) to analyze the vorticity budget. Formally, setting $u_{L,d} = u_{R,d}$ in (9) results in

$$\int_0^R (w\eta)_d \, dx = \frac{u_{R,0}^2}{2} + \int_0^{z_{dc}} b_L \, dz. \tag{11}$$

Equation (6) implies that lateral vorticity fluxes, given by the first term on the rhs of (11), must balance baroclinic sources of vorticity, i.e. the lhs of (11) equals zero regardless of the value of $c/\Delta U$. This observation also applies to cases with $c/\Delta U > 1$, as long as $u_{L,d} = u_{R,d}$. It is not clear from (11) that $c/\Delta U$ represents a measure of vorticity-balance, even though that the derivation was performed under the working assumptions of RKW88. One could still argue that $c/\Delta U$ is related to the vorticity structure near the SLs leading edge (WR04; BR14), which determines the flow via the stream function (Batchelor, 2000); however, this interpretation of $c/\Delta U$ warrants caution, not only because the vorticity over the denser air required for mass conservation is ignored, but also because that metric is insensitive to varying shear and buoyancy profiles, for given values of c and ΔU. Wesiman (1992) contemplated vorticity sources at L in SLs, but such effects were not explicitly acknowledged by BR14 in simulations with $c \neq \Delta U$.

A more natural interpretation for $c/\Delta U$ can be found in (6), given that cases with $c/\Delta U > 1$ have downshear directed flow at R,d, while cases with $c/\Delta U > 1$ have upshear directed flow, as noted by Alfaro (2017). Therefore, under the present assumptions, the quantitative criterion of RKW theory unequivocally measures the wind velocity aloft, which is consistent with the wind fields in RKW88's Figure 20 and the movement of the density current's edge in BR14's Figures 15-16. For cases where shear is confined to low and mid-levels, such impacts are measured by $c/\Delta U$, as exemplified by the density current in Figure 1b (1c), which is likely to develop a downshear (upshear) tilted updraft following the wind direction aloft. This matter is the essence of the interpretation given by Thorpe et al. (1982), who hypothesize that the organization of SLs is favored by weak system-relative environmental inflow aloft.

2.3 Momentum-balance

To expose the importance of the momentum fluxes at lateral boundaries, we incorporate the impacts of momentum structure at low levels, including the pressure field associated with the denser air, to the concepts argued in the previous section. We expect a close relationship between momentum-balance and density current's updraft slope throughout low and mid-levels, while $c/\Delta U$ is expected to be more relevant aloft.

To illustrate momentum-balance, we follow BR14's derivation of the flow-force balance condition for the optimal state, applied to Figure 1a, which has static environmental winds aloft. First, we integrate (1) for a steady flow within the control volume framed by $L < x < R$ and $0 < z < z_{max}$:

$$-\iint \left[u\frac{\partial u}{\partial x} + w\frac{\partial u}{\partial z} + \frac{\partial p'}{\rho_0 \partial x} \right] dxdz = 0. \tag{12}$$

It is straightforward to show that (4) and vanishing vertical velocities at $z = 0$ can be used to express (12) as

$$\int (uw)z_{max} \, dx = -\int (u_R^2 - u_L^2) \, dz + \int \frac{p_L'}{\rho_0} \, dz. \tag{13}$$

Note that the flux of horizontal momentum through the control volume's upper boundary on the lhs of (13) is related to the updraft's tilt, such that positive (negative) values might be expected in cases with upwind[1] (downwind) tilted updrafts, while vertical updrafts have $(uw)_{z_{max}} = 0$. Given that the updraft is assumed to be vertical, that the flow is static outside the shear-layer (implying $u_L = 0$), and that $p'_L = 0$ for $z \geq z_{dc}$, from (13) it follows that

$$\int_0^{z_{sh}} u_R^2 \, dz = \int_0^{z_{dc}} \frac{p'_L}{\rho_0} \, dz, \tag{14}$$

where the term on the lhs of (14) measures the lateral flux of momentum (LFM), while the term on the rhs is the motive force (MF). The interpretation of (14) is that the work done by horizontal pressure gradients due to negatively buoyant air at *L*—measured by MF—balances the advective tendency due to inflowing momentum at *R*—measured by LFM. Per this interpretation, the MF accounts for the denser air's tendency to accelerate the flow upwind, while LFM measures the tendency of the environmental air to accelerate the flow downwind. In words of BR14, (14) represents a condition for "*the incoming horizontal momentum [being] 'stopped' by the cold pool*". This reasoning leads us to expect that the inflowing air will not be completely stopped in cases where LFM is greater than MF, in which case the updraft tilts downwind, consistent with the lhs of (13) being negative; conversely, in cases with MF greater than LFM the work done by horizontal pressure gradients overwhelm advective tendencies of horizontal momentum, turning the flow away from the denser air through an upwind tilted updraft, consistent with the lhs of (13) being positive. Motivated by this interpretation, and in analogy to RKW theory's quantitative criterion, we focus on terms associated with lateral boundaries to define a dimensionless momentum-balance index,

$$\mathrm{MB} = \frac{\mathrm{LFM}}{\mathrm{MF}}, \tag{15}$$

where MB = 1 corresponds to vertical updrafts, while MB > (<) 1 indicates a downwind (upwind) tilt. The more MB differs from 1, the greater the tendency of the flow to produce slanted updrafts.

It is important to note that the LFM derived from (14) applies only to cases with static winds aloft. An LFM applicable to cases with $c/\Delta U \neq 1$ could be defined as the first term on the rhs of (13). But care must be taken to guarantee conceptual consistency between the impacts of momentum fluxes on the updraft's orientation and the mathematical expressions derived herein, as the latter represent global constraints on horizontal momentum within the control volume. This is crucial because we are interested in the impacts of momentum fluxes at *L* and *R* on the updraft's slope, rather than simply keeping track of sources/sinks of horizontal momentum through direct application of (13).

To motivate the more general definition of the LFM, consider the density current in Figure 1b, which has $c/\Delta U < 1$ and $z_{zh} < z_{dc}$. There is inflowing momentum below z_{sl}, contributing to tilt the updraft in the downwind direction, in agreement with our interpretation of (14). On the other hand, there is no obvious reason why outflowing momentum above z_{sl} should also contribute to downwind updraft tilting; if anything, our arguments on the transfer of momentum from winds aloft onto ascending near-surface air (subsection 2.2) suggest that environmental outflow at *R* favors upwind updraft tilting above z_{max}. This would not be a problem if u_R did not appeared squared in (13), and thus implying that outflowing (positive) momentum is treated the same way as inflowing (negative) momentum, as expected from a momentum budget in the control volume. This leads to conceptual inconsistencies when applying (13) to the updraft slope. Given that such inconsistencies are associated to outflow at lateral boundaries, we define the first term on the rhs of (13) as

$$\mathrm{LFM} = \int_{I_R} u_R^2 \, dz - \int_{I_L} u_L^2 \, dz, \tag{16}$$

where $I_R = \{z \mid 0 < z < z_{max};\ u_{R(z)} < 0\}$ and $I_L = \{z \mid 0 < z < z_{max};\ u_{L(z)} > 0\}$ specify the levels of inflow at *R* and *L*, respectively. The upper limit at z_{max} avoids ambiguity about the layer over which momentum-balance effects are computed, and it is considered reasonable to account for near-surface interactions between the denser air and inflowing air at low levels. The neglect of outflow at lateral

[1]Hereafter the upwind (downwind) direction is toward the right (left) as per configuration in Figure 1, whereby the low-level inflow serves as a reference.

boundaries implies that our indices are not consistent with total momentum fluxes, which is why momentum budget analyses are not considered.

2.4 A comparison between MB and c/ΔU

Herein we analyze the implications of considering MB to diagnose the updraft's orientation.

First, we want to show that MB correctly predicts the updraft's behavior for "classic" c-ΔU variations around an optimal case. On one hand, if c is modified by adding a constant to b_L, while holding ΔU fixed, as illustrated in Figure 2a, then (6) implies that both MF and LFM vary in concert with c. The change in MF due to varying $p_{L,0}$ is half as large as the change in LFM through $u^2_{R,0}$ (while hydrostaticity at L implies that the magnitude of pressure changes decreases continuously to zero from the surface to z_{dc}, environmental winds change by the same amount at all levels). Therefore, although both LFM and MF vary in concert with c, LFM changes more than MF, implying that an increase (decrease) in c around the optimal case leads to MB > (<) 1, consistent with downwind (upwind) updraft tilting. On the other hand, if ΔU is increased, everything else being equal,

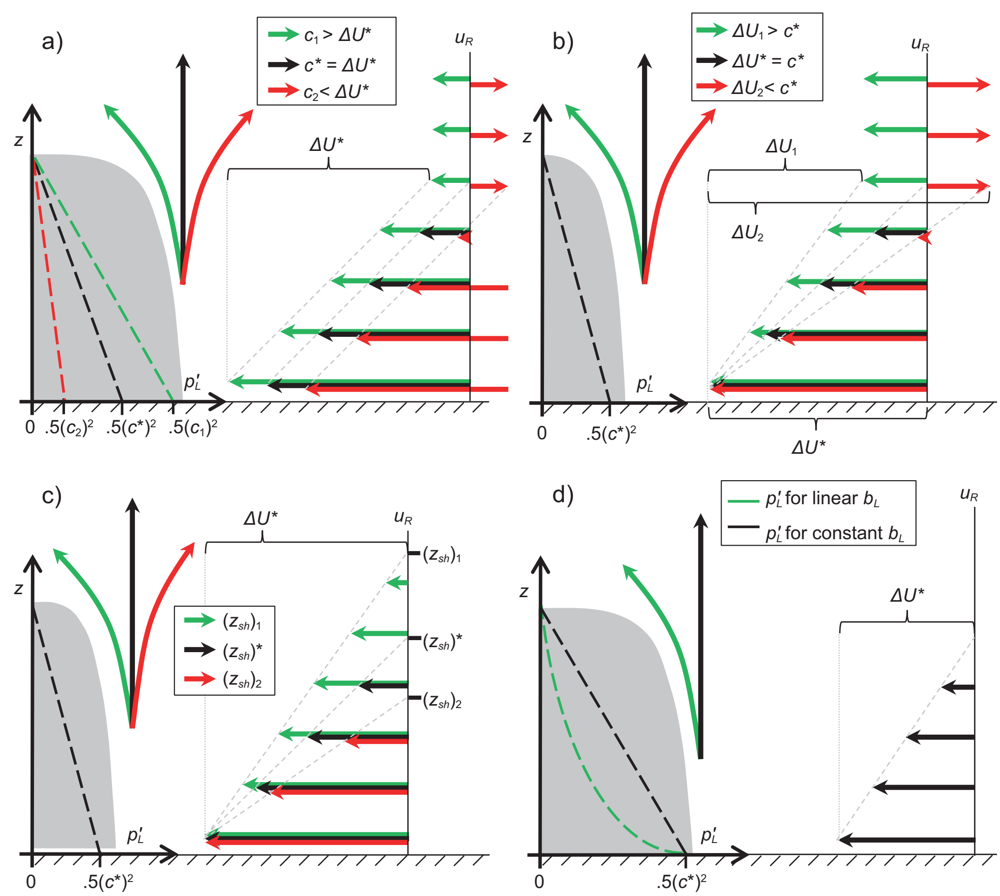

Fig. 2. Schematic illustration of density currents under different environmental conditions and buoyancy profiles: environmental winds are displayed on the right (horizontal arrows), the gray area on the left represents the denser air, on top of which pressure perturbation profiles at L are overlaid (thick dashed lines), and next to which the updrafts diagnosed by MB are displayed (arrows pointing upwards). Each figure represents specific variations of the airflow at L or R around an "optimal" baseline case with $c^* = \Delta U^*$ and MB = 1 (the asterisk indicates baseline parameter values). Baseline profiles are shown in black, while profiles corresponding to LFM > MF (LFM < MF) are in green (red). The effects of performing "classic" c and ΔU variations are displayed in a) and b), respectively, c) shows the impacts of modifying z_{sh} while holding ΔU fixed, and d) depicts a case with a linear buoyancy profile which gives c^*.

as illustrated in Figure 2b, then a reduction in height of inflowing system-relative winds takes place. This reduction lowers the value of LFM, which is favorable for the development of upwind tilted updrafts. It follows that momentum-balance correctly diagnoses the orientation of updrafts in density currents under classic c-ΔU variations.

An important difference between MB and $c/\Delta U$ is that the former depends on the specific distributions of hydrostatic pressure perturbations at L and environmental winds, while the latter is completely specified by the limit values determining environmental winds aloft: $u_{R,0}$, $u_{R,z_{sh}}$, $p'_{L,0}$ and p'_L (z_{dc}), although the latter is zero in all cases considered herein. Consequently, MB can differ significantly from $c/\Delta U$.

For instance, consider an environment with constant shear below z_{sh}, that is, $u_R = u_{R,0}$ $(1 - z/z_{sh})$ for $0 < z < z_{sh}$, constant wind velocity aloft, $u_L = 0$, and $c/\Delta U = 1$. In this case, solving the integrals in (16) gives LFM = $(\Delta U^2/3)$ z_{sh}, i.e. LFM is directly proportional to the shear-layer depth. Given that greater LFM is associated with downwind updraft tilting, as illustrated in Figure 2c, it is possible that MB can account for BR14's results revealing the updraft's sensitivity to the environmental shear-layer depth for cases with $c/\Delta U = 1$. Similarly, for given c and z_{dc}, it can be shown that the MF corresponding to a linear b distribution below z_{dc} is lower than the MF for constant b, implying that the former case is more favorable for the development of downwind tilted updrafts (Fig. 2d). This suggests that momentum-balance might also explain updraft sensitivities to the buoyancy distribution within denser air, as documented for density currents (Droegemeier and Wilhelmson, 1987) and MCSs (Alfaro and Khairoutdinov, 2015).

3. Methodology

3.1 Numerical framework

The 2D density current simulations closely follow BR14's approach to enable us to compare our results to theirs. Numerical experiments are performed with the non-hydrostatic cloud model CM1 version 18 (code and documentation available at http://www2.mmm.ucar.edu/people/bryan/cm1/). The dynamical core is based on the viscous compressible Boussinesq equations. The model is run as a direct numerical simulation (DNS), with Prandtl and Reynolds numbers set to 1 and 10^4, respectively. The viscous stress and conductivity terms are calculated as in BR14. Upper and lower boundaries are flat, rigid and free-slip, while lateral boundaries are open. The domain is 100 km wide and 20 km deep, with $\Delta x = \Delta z = 50$ m grid spacing.

The initial conditions are not entirely consistent with a steady flow in equilibrium. It takes some time for the dense fluid to accelerate and reach a quasi-steady state. Consequently, the simulations are run for 3 h to allow the updrafts to reach quasi-steadiness. This strategy, whereby the dense fluid is initially static, is common practice in time-evolving simulations of density currents (e.g. RKW88, WR04 and BR14).

Initial conditions are prescribed through the buoyancy and vorticity profiles at L and R, respectively, which are extended to the interior of the domain as follows:

$$b(x, z) = \begin{cases} b_L(z) & \text{if } x < x^* \text{ and } 0 \le z \le z_{dc} \\ 0 & \text{otherwise} \end{cases} \tag{17}$$

$$\eta(x, z) = \begin{cases} \partial u_R(z) / \partial z & \text{if } x > x^* \text{ and } \\ & 0 \le z \le z_{sh} \\ -(2 \int_0^z b_L(z')\, dz')^{1/2} / (6\Delta x) & \text{if } (x^* - 6\Delta x) \le x \le x^* \\ & \text{and } 0 \le z \le z_{dc} \\ (\Delta U - c)/(6\Delta z) & \text{if } x < x^* \text{ and } \\ & z_{dc} < z \le (z_{dc} + 6\Delta z) \\ 0 & \text{otherwise} \end{cases} \tag{18}$$

where $\eta = \partial u / \partial z - \partial w / \partial x$ is the horizontal vorticity and x^* is the center of the domain. Equations (17) and (18) were chosen based on results by BR14 showing that they produce initial conditions lacking a well-defined updraft and with nearly static denser air (Fig. 3a). The second equality in (18) is determined by the theoretical speed of parcels that follow the density current's interface under the assumption of strictly vertical pressure gradients therein and Bernoulli energy conservation (the layer of baroclinically generated shear extends 6 grid points, roughly corresponding to the minimum resolvable scale). The third equality in (18), which was not considered in BR14, is included to guarantee that (6) is satisfied at initiation, helping maintain z_{dc} nearly constant throughout the simulation. BR14's Figures 15-16 show that density currents

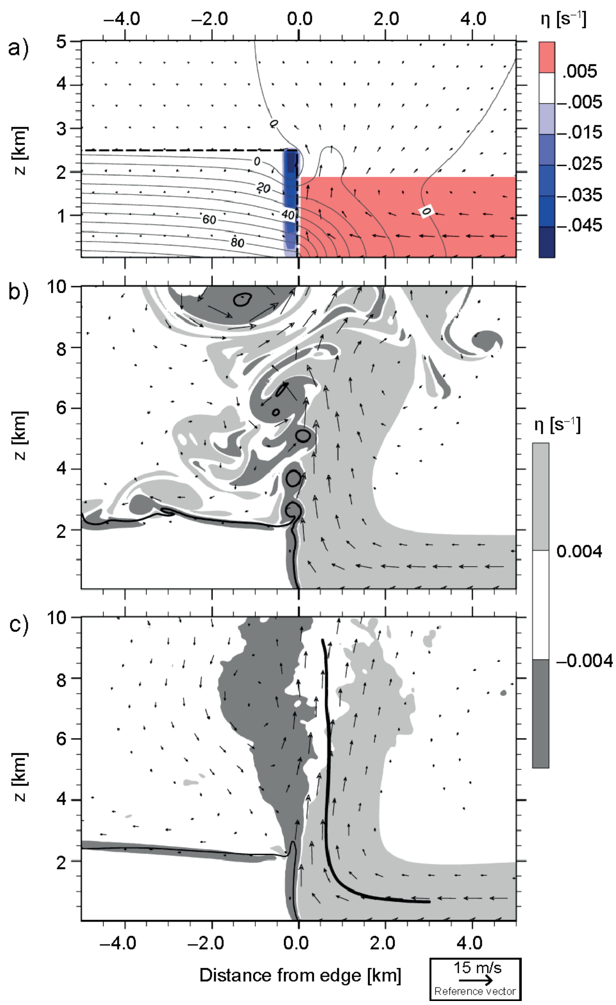

Fig. 3. Fields produced by the baseline simulation. Initial conditions are shown in a), where the vorticity field is indicated by colored contours, thin gray lines contour the pressure perturbation field (every 10 Pa), the thick dashed line outlines the denser fluid, and arrows represent velocity vectors (compare to Fig. 3 in BR14). Instantaneous fields at $t = 60$ min are displayed in b), with filled contours contrasting regions of positive and negative vorticity, solid contours indicating the -0.015 m s^{-2} buoyancy level, and wind velocities with magnitude greater than 1 m s^{-1} depicted by arrows (compare to Fig. 5a in BR14). c) is as b), but with fields corresponding to time-averages of snapshots taken every 2.5 min between 60 min and 180 min, with the mean parcel trajectory indicated by the thick solid line.

eventually develop thin layers with vorticity of the same sign as $\Delta U - c$ immediately above the denser air. This vorticity is mainly produced baroclinically as z_{dc} changes near the density current's edge, and it manifests as the flow seeks to satisfy (6) with $u_L = u_R$ above z_{max}.

The initial wind field is obtained from (18) by solving

$$\nabla^2 \psi = \eta, \tag{19}$$

where $\nabla^2 = \partial^2/\partial x^2 + \partial^2/\partial z^2$ and ψ is the stream-function of the flow, through which the velocity field is determined by $u = \partial\psi / \partial z$ and $w = -\partial\psi / \partial x$. Boundary conditions for (19) are $\psi = 0$ at the upper and lower boundaries, and $\partial\psi / \partial x = 0$ at lateral boundaries, the latter implying that $w_L = w_R = 0$. After the wind field is retrieved via (18) and (19), the initial pressure perturbation field is found by solving the diagnostic pressure perturbation equation for inviscid and incompressible 2D fluids (Markowski and Richardson, 2010):

$$\frac{1}{\rho_0}\nabla^2 p' = -\nabla \cdot (\mathbf{v} \cdot \nabla \mathbf{v}) + \frac{\partial b}{\partial z}, \tag{20}$$

where $\mathbf{v} = (u, w)$. Boundary conditions for (20) are $\partial p' / \partial z = -b$ at the lower boundary, which guarantees zero vertical acceleration per (2); $p' = 0$ at the upper boundary, and $\partial p' / \partial x = 0$ at lateral boundaries. Equation (20) is satisfied by inviscid flows governed by (1)-(4), so it provides reasonable guidance for specifying initial conditions in the present context. Figure 3a shows the initial wind, vorticity and pressure perturbation fields of a density current simulation which develops a vertical updraft by 60 min, as revealed by Figures 3b and 3c.

3.2 Experimental design and the baseline simulation

The experimental design consists of modifications to initial b_L and η_R profiles (Eqs. 12-13) around a baseline case studied in detail by BR14. The baseline simulation is specified by $z_{sh} = 1900$ m and $\Delta U = 15$ m s^{-1}, such that $\eta_R = \Delta U / z_{sh}$ below z_{sh}, while $\eta_R = 0$ aloft; also, $b_L = -0.045$ m s^{-2} below $z_{dc} = 2533$ m, giving $c = 15$ m s^{-1}. The resulting initial conditions and simulated fields at 60 min are displayed in Figures 3a-3b. Figure 3b shows that the baseline density current develops a vertical updraft, which is consistent with it having MB = 1 and $c / \Delta U = 1$. Given that our simulations are not strictly steady, subsequent analyses focus on time averaged wind fields, as those presented in Figure 3c (the horizontal frame of reference has the origin anchored at the density current's edge).

To further characterize updrafts, we consider the mean Lagrangian trajectories traced by parcels originating near the surface, as depicted by the solid line in Figure 3c. The mean trajectory is defined as in Alfaro (2017):

$$\overline{[x(s), z(s)]} = N^{-1} \sum_{i=1}^{N} [x(s), z(s)]_i, \quad (21)$$

where $[x(s), z(s)]_i$ is the i-th trajectory parameterized by s, the trajectory length, and N is the number of different parcels used for averaging. Parcels are initialized ahead of the density current edge 60 min into the simulation, when the updraft appears to be well developed (Fig. 3b), being uniformly distributed in space every 2500 m in the horizontal, with heights at 425 m, 625 m, and 825 m. Each trajectory in (21) is initialized by the condition $s = 0$ when the parcel first arrives at 3 km ahead of the density current edge. Only trajectories that reach $s > 10$ km at the end of the simulation are used for averaging; however, to evaluate MB we focus on the layer between 1.5 km and 5.5 km height, the lower limit being near the level where the trajectory in Figure 3c first appears vertical, while the upper limit is slightly above the deepest shear-layer considered herein. We consider this layer to be appropriate for characterizing how updrafts are affected by interactions between the negatively buoyant air and the surface-based shear.

4. Results

We analyze the updrafts developed by several simulated density currents, considering the impact of systematically changing one specific characteristic of the flow, everything else being equal. Several parameters describing the simulations are presented in Table I in dimensional form to facilitate comparisons with SLs and their environments. The parameters α and β determine the shear and buoyancy profiles, respectively (subsection 4.2, Eqs. 22-23), with baseline values of $\alpha = 1$ (constant η_R below z_{sh}) and $\beta = 0$ (constant b_L below z_{dc}). As in BR14, values reported in Table I were computed from initial b_L and η_R profiles, where it is assumed that (6) holds and that $u_R = u_L$ above z_{max}. We held z_{dc} constant among all experiments, guaranteeing that our simulations are dynamically distinct from each other.

Table I. Relevant parameters, determined by initial conditions, of simulated density currents.

Fig.	3	4a	4b	4c	4d	4e	4f	6a	6b	6c	6d
$c/\Delta U$	1.00	1.50	1.30	1.20	0.60	0.70	0.80	1.00	1.00	1.00	1.00
MB	1.00	1.56	1.33	1.22	0.60	0.70	0.80	2.60	2.00	0.66	0.83
z_{sh}	1900	1900	1900	1900	1900	1900	1900	5050	3800	1250	1580
α	1	1	1	1	1	1	1	1	1	1	1
β	0.0	0.0	0.0	0.0	0.0	0.0	0.0	0.0	0.0	0.0	0.0
Fig.	7a	7b	7c	7d	9a	9b	9c	10a	10b	10c	11a
$c/\Delta U$	1.00	1.00	1.00	1.00	1.00	1.00	1.00	1.00	1.00	1.00	1.00
MB	1.50	1.20	0.60	0.75	2.00	1.50	1.25	1.00	0.75	0.63	3.60
z_{sh}	1900	1900	1900	1900	1900	1900	1900	950	950	950	3800
α	0.5	0.75	2	1.5	1	1	1	1	1	1	0.75
β	0.0	0.0	0.0	0.0	2.0	1.0	0.5	2.0	1.0	0.5	1.0
Fig.	11b	12a	12b	12c	12d	12e	12f	13a	13b	13c	13d
$c/\Delta U$	1.00	0.70	1.33	0.80	1.35	0.67	1.20	0.60	1.50	0.75	1.20
MB	0.50	1.00	1.00	1.00	1.00	1.00	1.00	1.00	1.00	2.40	0.70
z_{sh}	1250	5050	1250	1900	1900	1900	950	3800	1250	3800	1250
α	1.5	1	1	0.75	2	1	1	0.75	1.5	0.75	1.5
β	0.0	0.0	0.0	0.0	0.0	1.0	1.0	1.0	0.0	1.0	0.0

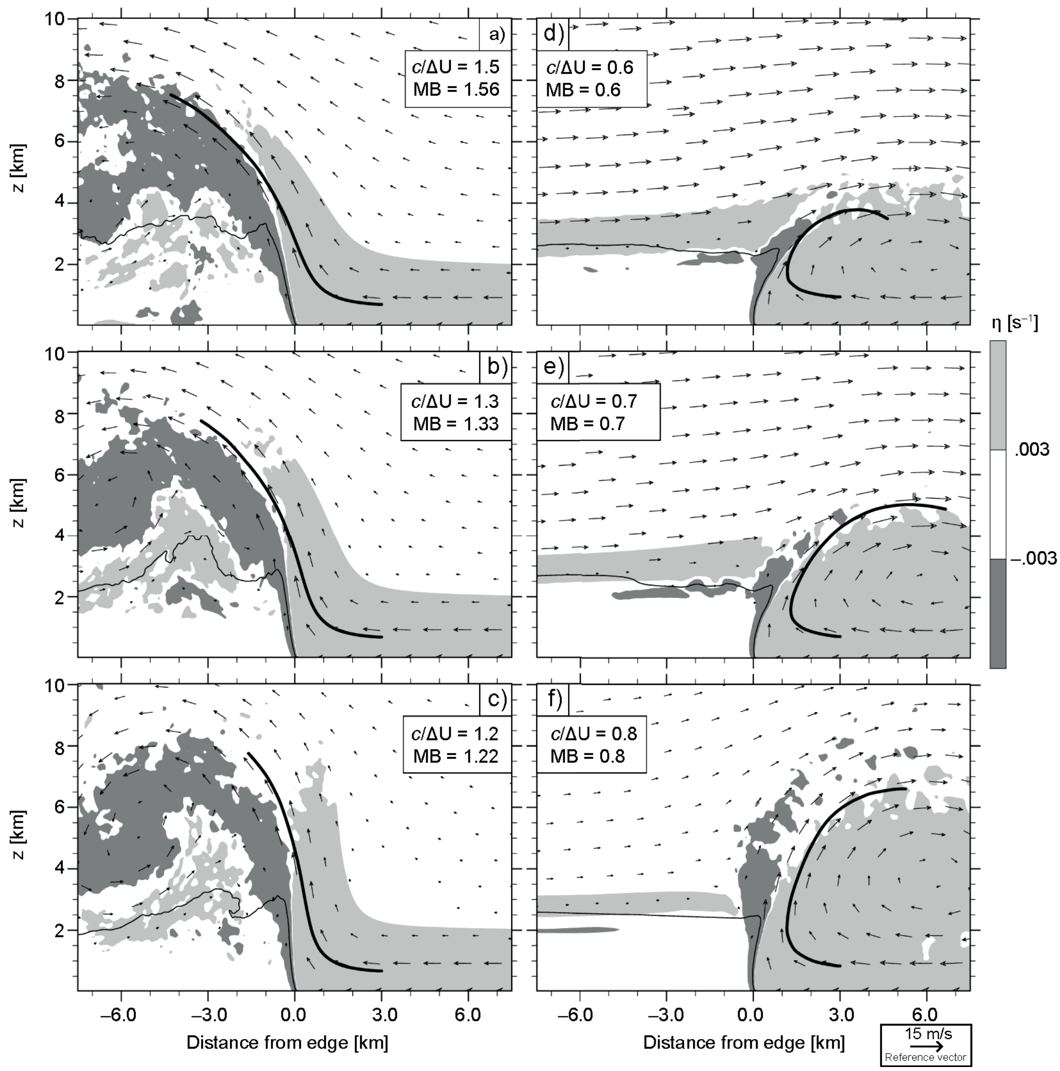

Fig. 4. As Figure 3c, depicting cases with varying ΔU (subsection 4.1). For reference, each figure displays the corresponding $c/\Delta U$ and MB (see Table I).

4.1 "Classic" ΔU variations

This subsection considers the effect of varying the constant determining η_R below z_{sh}, everything else being equal (Fig. 2b). These classic inter-case variations are analogous to those contemplated by RKW88, WR04, and BR14. We do not show cases where c is varied, as we find that updrafts respond in analogy to ΔU variations as a function of $c/\Delta U$, in agreement with BR14.

Figure 4 shows results corresponding to six simulations, three with $1 < c/\Delta U \leq 1.5$ (Figs. 4a-4c) and three having $0.6 \leq c/\Delta U < 1$ (Figs. 4d-4f). As in previous investigations, flows with $1 < (>)\ c/\Delta U$ develop downwind (upwind) slanted updrafts, following the direction of environmental winds aloft. That $c/\Delta U \approx MB$ in each simulation implies that both metrics vary in concert under classic ΔU variations, which explains the large sensitivity of the updraft slope to changes in the shear's strength (the same is true for c variations; not shown). Also note that simulations with downwind (upwind) tilted updrafts develop vortices on the downwind (upwind) side of the density current's edge, a feature that is common to many simulations considered in latter subsections. These circulations complicate the interpretation of the rhs of (13) as a measure of the updraft's orientation, while the fact that they induce non-hydrostatic pressure perturbations and

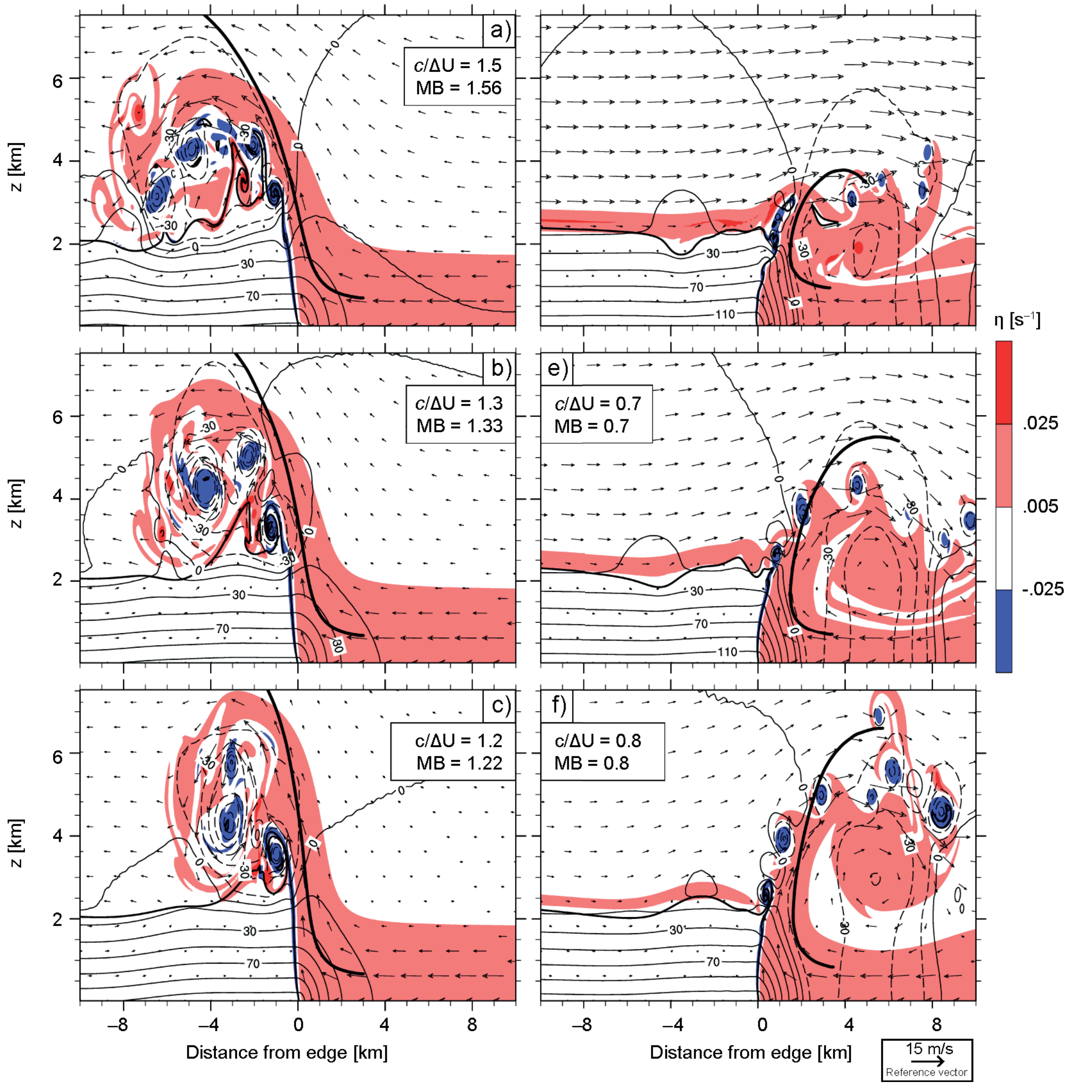

Fig. 5. Instantaneous pressure perturbations (contour lines; dashed for negative values), wind velocities (arrows), and vorticity field (colors) at 30 min corresponding to the simulations in Figure 4. Mean trajectories are included for reference.

alter wind velocities suggests that caution must be exercised when defining the control volume to compute MB.

Instantaneous fields at 30 min are shown in Figure 5, revealing the association between the aforementioned circulations and non-hydrostatic pressure perturbations. As expected from (20), vortices are centered on $p' < 0$, while flow deformations occur within $p' > 0$ (Markowski and Richardson, 2010, pp. 27-28), e.g. at the rightmost edge of Figs. 5e, where air that previously exited the updraft encounters inflowing environmental air. It is worth noting that these features reach lateral boundaries late in the simulations, affecting the instantaneous computation of MB. This, however, does not undermine our results, as we found little sensitivity in time averaged fields and mean trajectories when the simulations with $c/\Delta U = 1.5$ (Fig. 4a) and $c/\Delta U = 0.6$ (Fig. 4f) were performed in a domain twice as large (not shown). In fact, the case-by-case similarity between updrafts at 30 min (Fig. 5) and the time averaged updrafts (Fig. 4) suggests that the flow's structure near the density current's edge is established early in the simulation, remaining quasi-steady thereafter. These considerations, which

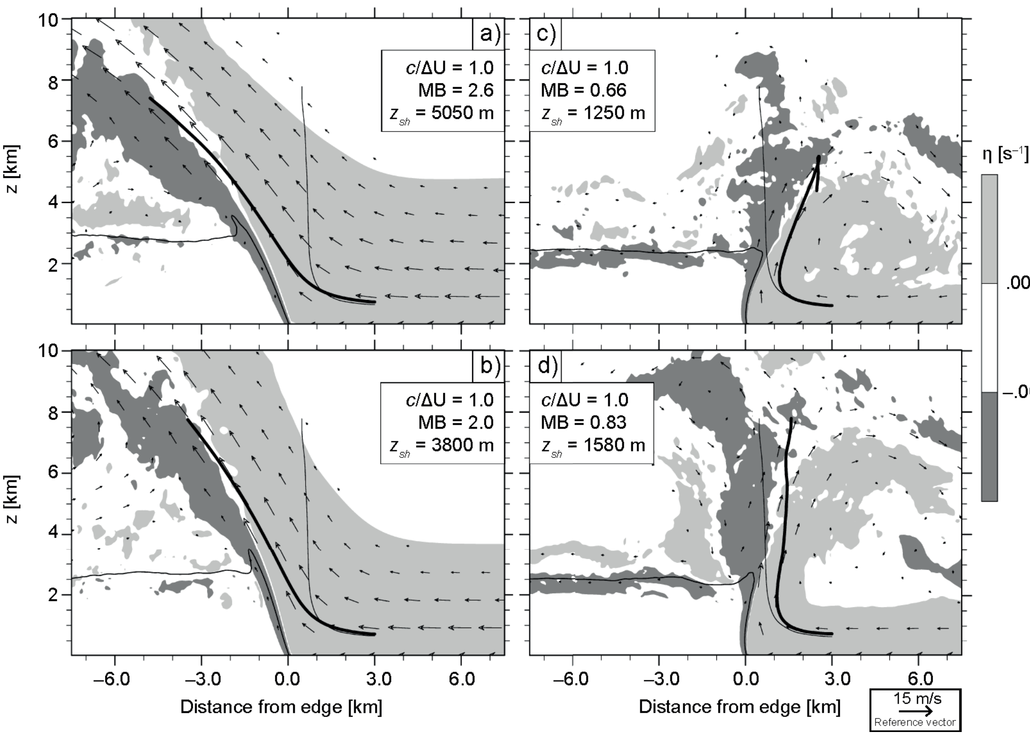

Fig. 6. As Figure 4, depicting cases with varying z_{sh} (subsection 4.2). The thin line indicates baseline's mean trajectory.

apply to all simulations considered herein, justify our interpretation of time averaged fields and mean trajectories through the MB computed from initial conditions.

4.2 Simulations with c/ΔU=1

First, we consider the effects of varying z_{sh} in cases with baseline's ΔU satisfying $c/\Delta U = 1$. Simulations in Figure 6 have z_{sh} varying between $2(z_{dc})$=5050 m (Fig. 6a) and $0.5(z_{dc})$ = 1,250 m (Fig. 6c), showing that shallow (deep) shear layers favor upwind (downwind) updraft tilting. The variety of updraft structures in Figure 6 demonstrate that $c/\Delta U$ does not provide accurate guidance on the density-current–shear interactions that modulate the ascent of near-surface air. On the other hand, updraft slopes vary systematically as a function of MB, in agreement with Figure 2c, suggesting that momentum-balance captures relevant features to which $c/\Delta U$ is insensitive. Also note that vortices resembling those in Figure 4 appear on the updraft's flank determined by its slope, showing that these circulations arise independently of the value of $c/\Delta U$.

Figure 7 shows results from density currents in environments with non-constant shear below a fixed baseline's z_{sh}. The u_R profiles used for these simulations are displayed in Figure 8a, which were determined by

$$u_R(z) = \Delta U\,[1 - (1 - z/z_{sh})^{\alpha}\,] - c \quad \text{for} \quad z < z_{sh}, \qquad (22)$$

where α = 0.5 (Fig. 7a), 0.75 (Fig. 7b), 2 (Fig. 7c), and 1.5 (Fig. 7d). Note that (22) can produce different LFM for given ΔU and z_{sh} (Eq. 16). It is readily seen in Figure 8a that environmental wind speeds within the shear-layer are a decreasing function of α, such that greater α is associated with lower LFM and MB. Consistent with the value of MB, and notwithstanding $c/\Delta U = 1$, greater momentum inflow at R favors downwind updraft tilting (Figs. 7a-7b), while weak inflow leads to upwind sloping updrafts (Figs. 7c-7d).

Simulations depicted in Figure 9 have varying b_L profiles with baseline's c and u_R. From hydrostaticity at L, buoyancies are expected to affect MB via the MF (rhs of Eq. 14). The buoyancy profiles considered herein, shown in Figure 8b, were specified as follows:

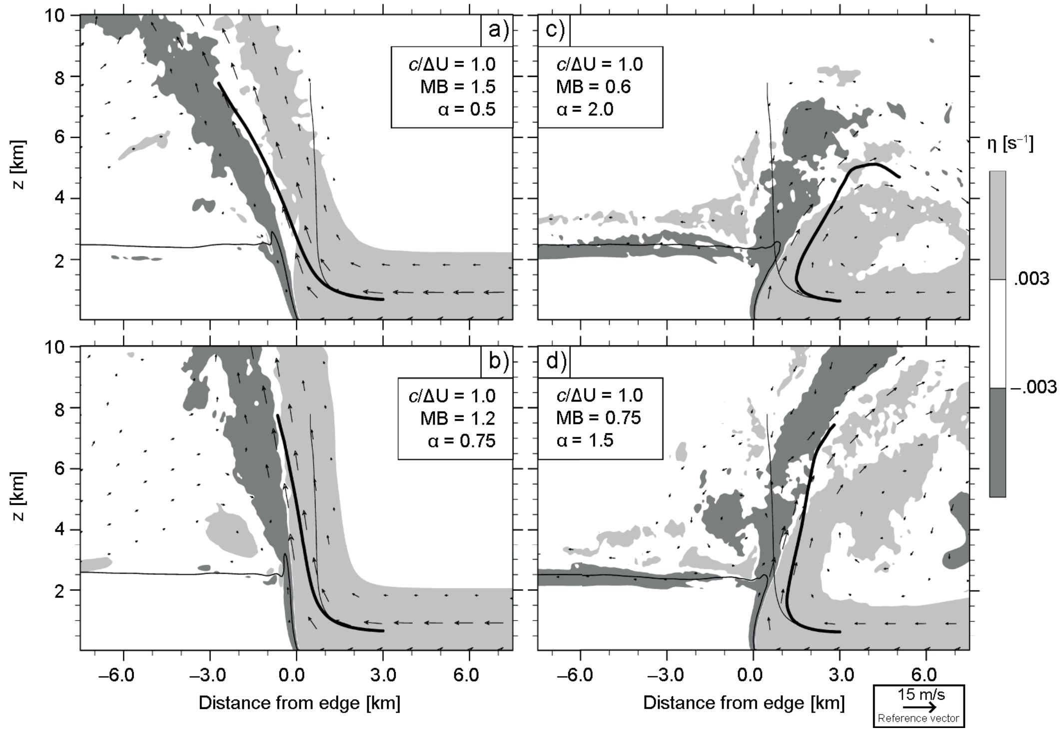

Fig. 7. As Figure 6, depicting cases with varying u_R (z) profiles (subsection 4.2).

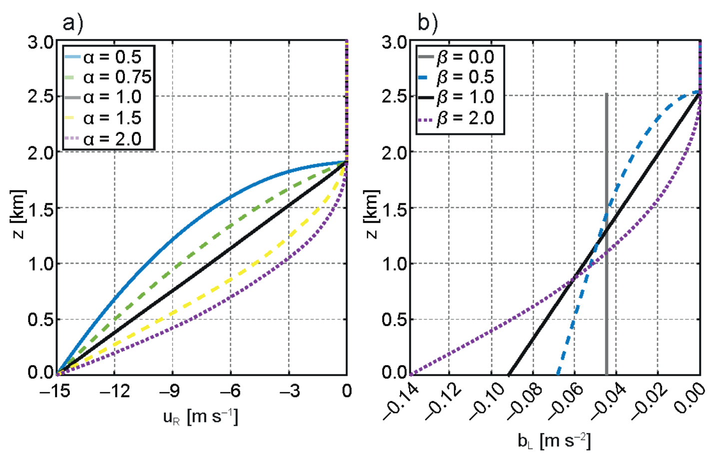

Fig. 8. In a) environmental wind profiles with baseline's z_{sh} and ΔU derived from (22). In b) varying buoyancy profiles as determined by (23). The gray line denotes the constant b_0 corresponding to the baseline case.

$$b_L(z) = b_0 \,(1 - z / z_{dc})^{\beta} \quad \text{for} \quad z < z_{dc}, \tag{23}$$

where $\beta = 2$ (Fig. 9a), 1 (Fig. 9b), and 0.5 (Fig. 9c); and b_0 is the surface buoyancy required for baseline's c. It is easy to show that MF (MB) is a decreasing (increasing) function of β, in agreement with the downwind tilted updrafts in Figure 9 ($\beta = 0$ in baseline), with greater slopes corresponding to larger β. Analogously, fields in Figure 10 demonstrate that, for given c and u_R, updrafts can tilt upwind in response

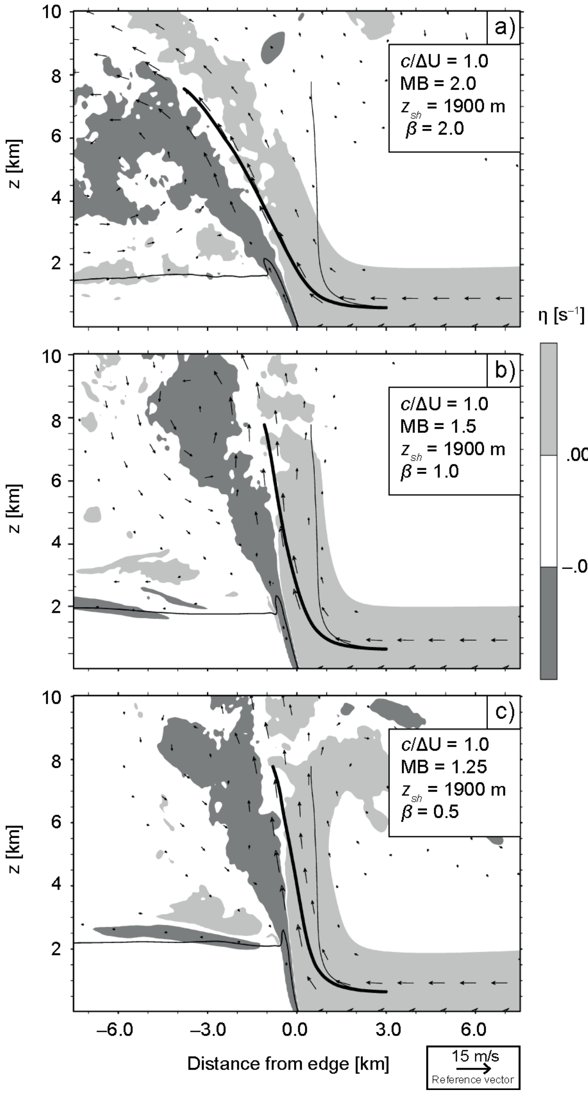

Fig. 9. As Figure 6, depicting cases with varying b_L (z) profiles (subsection 4.2).

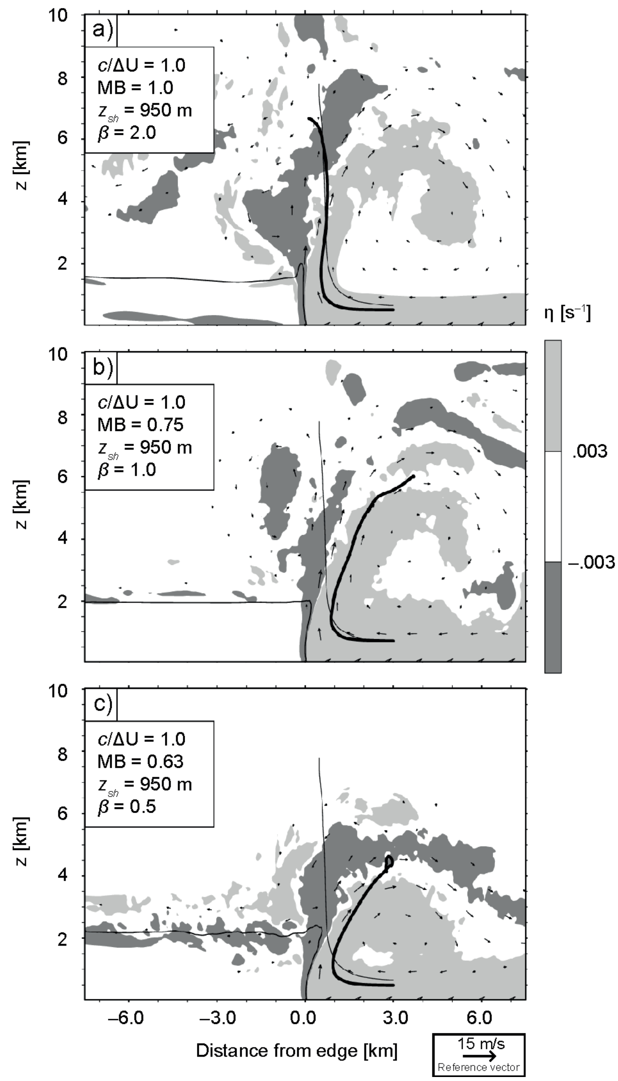

Fig. 10. As Figure 6, depicting cases with varying b_L (z) profiles and small z_{sh} (subsection 4.2).

to changes in b_L. Simulations in Figure 10 have z_{sh} = 950 m, which gives MB = 1 in the case where $\beta = 2$. Thus, the density current in Figure 10a is momentum-balanced, consistent with its vertical updraft, while cases in Figures 10b-10c have lower MB (higher MF), in agreement with their upwind tilted updrafts.

Finally, we consider the combined effects of varying u_R and b_L to produce MB that differs significantly from 1 for $c/\Delta U = 1$. Results in Figure 11a correspond to a case with baseline's c and ΔU, but with z_{sh} = 3800 m, α = 0.75, and β = 0.75, giving MB = 3.6. Fields in Figure 11b were produced by a simulation with z_{sh} =1266 m, α = 1.5, and β = 0, giving MB = 0.5. These two density currents have the most pronounced updraft slopes among all cases considered, consistent with their contrasting MB, and notwithstanding both having $c\ /\Delta U = 1$. This result highlights the importance of processes ignored by $c/\Delta U$ but measured by MB. This, and the fact that vertical updrafts arise when z_{sh} is adjusted to satisfy MB = 1, as revealed by Figure 10a and shown by BR14 for varying shear profiles (see their Fig. 19), supports the momentum-balance concepts discussed in subsection 2.3 and illustrated in Figure 2.

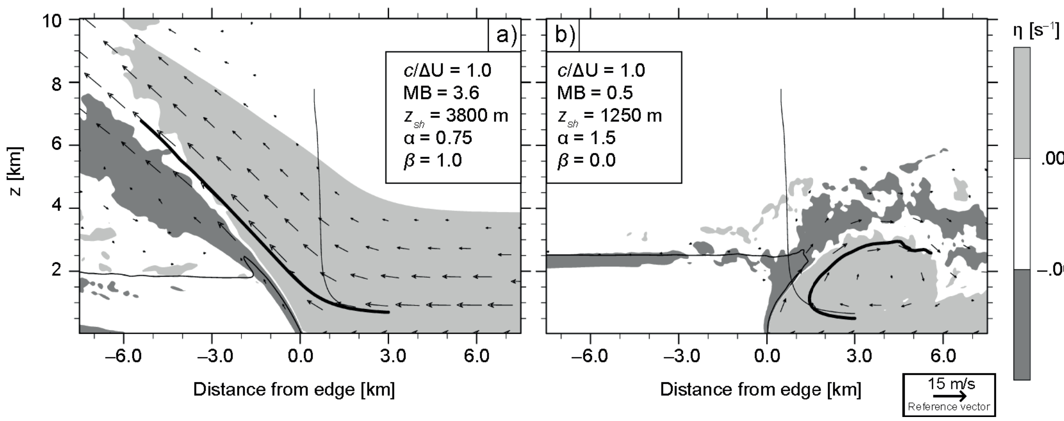

Fig. 11. As Figure 6, depicting cases with combined z_{sh}, u_R (z) and b_L (z) profile variations (subsection 4.2).

4.3 Simulations with MB=1 and c/ΔU≠1

This subsection analyzes momentum-balanced density currents based on cases analyzed in the previous subsection. Specifically, ΔU is varied to satisfy MB = 1, while holding c, z_{sh}, α, and β fixed. We consider the following simulations: cases with z_{sh} values of 5050 m (Fig. 12a; compare to Fig. 6a) and 1250 m (Fig. 12b; compare to Fig. 6b); with α equal to 0.75 (Fig. 12c; compare to Fig. 7b) and 2 (Fig. 12d; compare to Fig. 7c; α = 0.5 is not shown because it developed vortices due to Kelvin-Helmholtz instability); the two cases with β = 1 (Figs. 12e-12f; compare to Figs. 9b and 10b), as linear b profiles are relevant to SLs (RKW88; WR04); and the two cases with combined effects (Figs. 13a and 13b, compare to Figs. 11a and 11b, respectively).

Figure 12 shows that most updrafts are nearly vertical throughout low and mid-levels, especially if a case-by-case comparison is made with the mean trajectory of the simulation having the most similar $c/\Delta U$ among the density currents described in subsection 4.1 and illustrated in Figure 4 (e.g. Fig. 4e and Fig. 12a both have $c/\Delta U = 0.7$). In other words, at low levels, updrafts tend to become vertical for MB $\approx$ 1, despite $c/\Delta U \neq 1$; at upper-levels, updrafts tilt in the direction of environmental winds aloft, as diagnosed by $c/\Delta U$. Note that the tilt at upper levels determines the updraft's flank where noticeable vortices develop, which in turn could have minor effects on the updraft's slope at low and mid-levels, e.g. the modest upwind slopes at low levels in Figures 12d-12e.

Figure 13 further exemplifies the behavior described above, wherein the case with MB = 1 in Figure 13a (13b) should be contrasted with its counterpart in Figure 13c (13d), the latter having MB > (<) 1 and $c/\Delta U$ < (>) 1, i.e. opposing MB and $c/\Delta U$: the updraft of the former is nearly vertical at low levels, tilting aloft in the direction determined by $c/\Delta U$; in the latter, the updraft tilts downwind (upwind) at low levels, as determined by MB, changing its direction aloft in accordance with $c/\Delta U$. We consider these results and those presented in the previous subsection to be strongly indicative of the fact that $c/\Delta U$ is more appropriate as a measure of the tendency of the updraft to tilt in the direction of environmental winds aloft, rather than near-surface density-current–shear interactions, for which MB seems to be better suited.

4.4 Updraft orientation and lifting of environmental air for all simulated density currents

Results presented above consistently indicate that MB can account for the impacts of the shear and buoyancy profiles on the updraft's orientation throughout low and mid-levels. To get a broader perspective of this result, the mean trajectories of all previously described simulations are shown in Figures 14a-14b. Each trajectory is translated horizontally such that $x(s) = 0$ for s satisfying $z(s) = 1.5$ km (Eq. 16), which facilitates comparing among different updraft slopes between 1.5 km and 5.5 km height. Curves are colored per MB^{-1} in Figure 14a, and per $\Delta U/c$ in Figure 14b, where the reciprocal is used because it provides greater symmetry of index

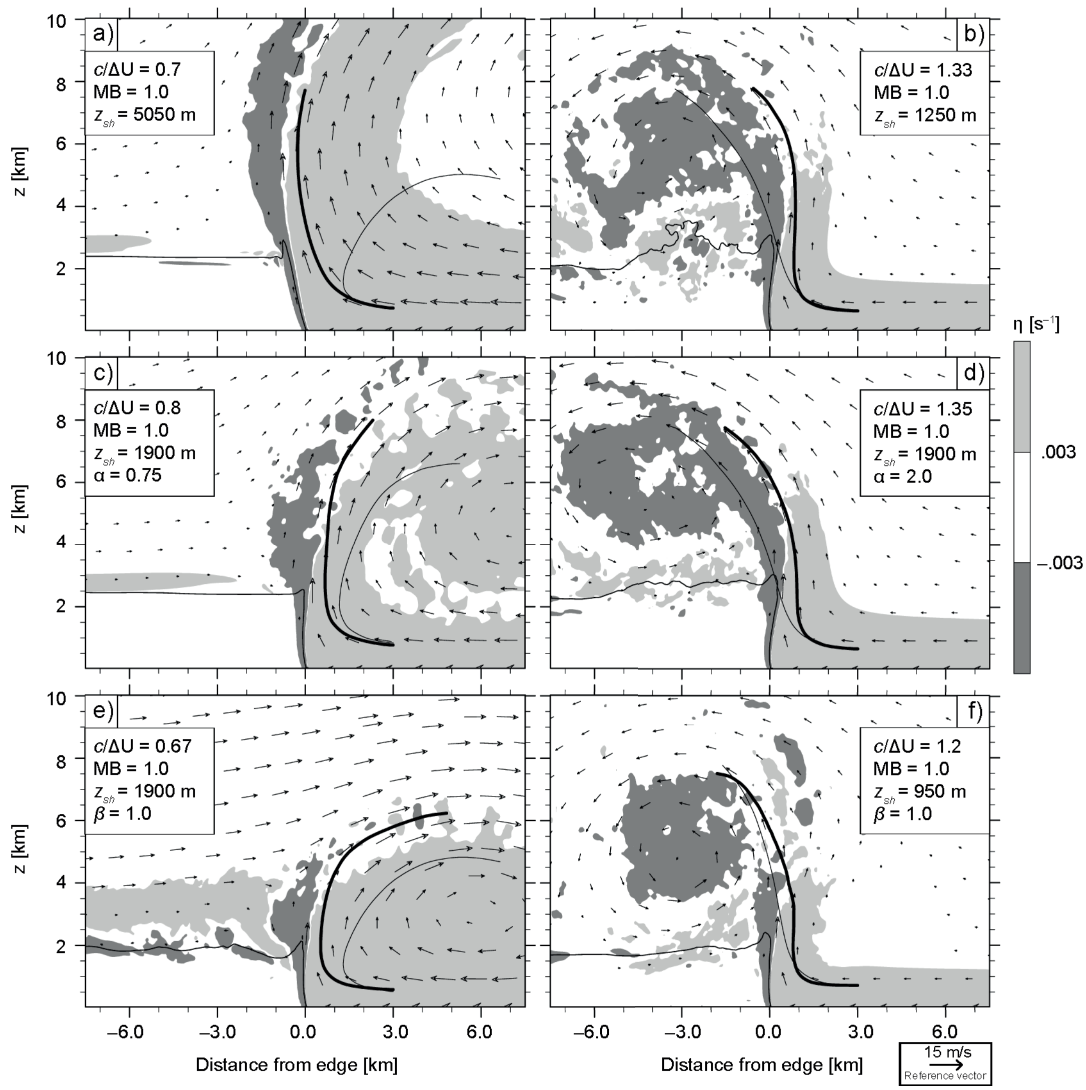

Fig. 12. As Figure 4, depicting cases with MB = 1 and varying $c/\Delta U$ (subsection 4.3). The thin line indicates the mean trajectory produced by the case in Figure 4 with the closest corresponding value of $c/\Delta U$.

values around 1. Updraft slopes appear to be in close correspondence with MB, but there is no indication of such a relation with $c/\Delta U$. Another way to visualize this result is by looking at scatterplots where the ordinate axis indicates the horizontal position of the trajectory at 5.5 km height, denoted by $x_{5.5}$, and either MB^{-1} or $\Delta U/c$ in the abscissa axis (Figs. 14c-14d). An extrapolation is made to compute $x_{5.5}$ in cases where the updraft does not reach 5.5 km height, assuming the slope between 1.5 km and the trajectory's maximum height is constant up to 5.5 km.

In Figure 14c there appears to be a linear correspondence between MB^{-1} and $x_{5.5}$, with momentum-balanced simulations ($\mathrm{MB}^{-1} = 1$) spanning a relatively narrow range of slopes around $x_{5.5} = 0$. On the other hand, Figure 14d does not reveal any obvious functional relation between $\Delta U/c$ and the updraft slope, with simulations having static environmental winds aloft spanning the entire range of simulated $x_{5.5}$.

In addition to the updraft slope, we are interested in analyzing the depth reached by near-surface environmental air, a matter that is central to RKW theory (Bryan et al., 2012), for which WR04 and BR14 found $\Delta U/c$ to be an effective diagnostic. We follow WR04 and BR14 by specifying a passive tracer, tr, initialized as $tr(x, z, t_0) = z$ at $t_0 = 60$ min; its

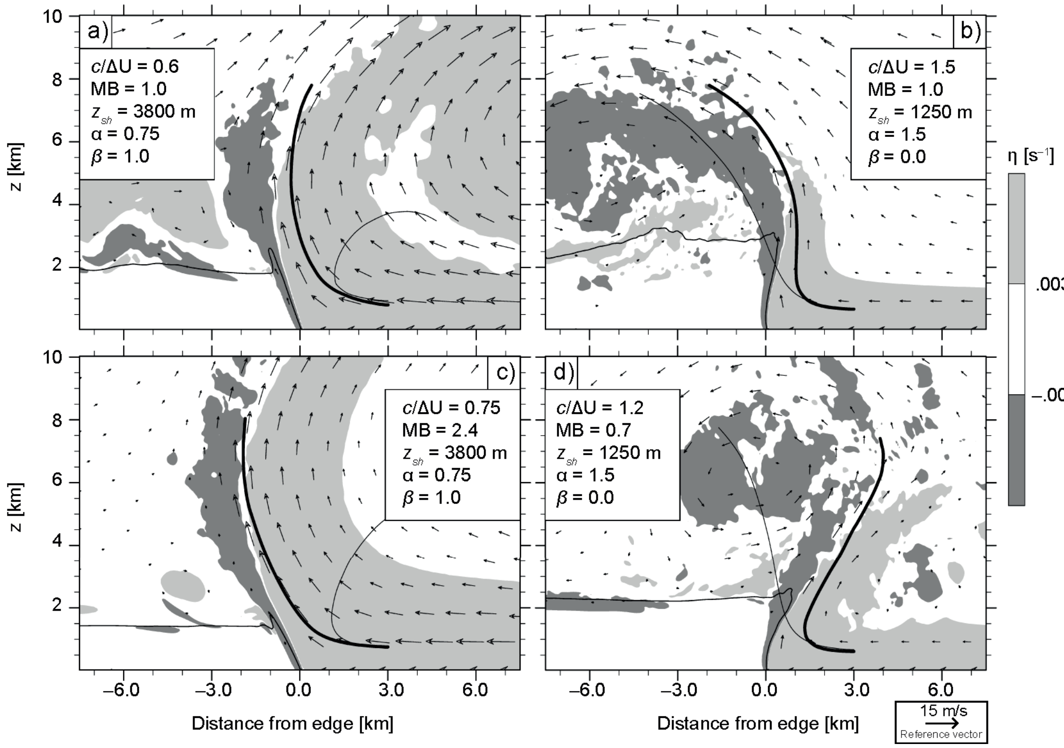

Fig. 13. As Figure 12, depicting cases with combined z_{sh}, u_R (z) and b_L (z) profile variations (subsection 4.3).

maximum displacement at $t_1 = 90$ min being defined as $\delta_{max} = \max\{z - tr(x, z, \mathrm{t}_1) \,|\, tr < 1 \text{ km}\}$. Results are presented in Figure 15, wherein the ordinate axis specifies δ_{max}, while the abscissa corresponds to either MB^{-1} or $\Delta U/c$ (Figs. 15a-15b).

Figure 15a shows that cases with MB = 1, which have the most vertical updrafts (Figs. 14a and 14c), do not necessarily produce the deepest lifting of environmental air. Yet, near-surface air tends to reach deeper in cases with large MB, implying that systems with downwind tilted updrafts are the most effective at lifting environmental air. It appears that greater momentum inflow at R is associated with deeper updrafts (e.g. Figs. 6a, 6b, 7a, 7b, 11a, which have large z_{sh} or $\alpha < 1$, or both), perhaps because greater system-relative mass inflow enables broader circulations near the density current's edge than when the inflow is weak. This behavior is consistent with the notion that deep shear-layers favor the lifting of near-surface environmental air high into the upper-troposphere, as suggested by Coniglio et al. (2006). However, a more detailed analysis of the relationship between inflowing air and of the depth of the updraft is beyond the scope of this work.

Figure 15b does not reveal a close relation between the depth reached by near-surface environmental air and $\Delta U/c$. In order to validate this finding, we performed additional simulations with varying c to create Figure 15c, which shows results consistent with those in BR14's Figure 17, wherein near-surface parcels reach deeper in cases with $c/\Delta U$ closer to 1. Therefore, *while c/ΔU seems to be an effective diagnostic under classic c variations, under more general conditions the environmental wind speed aloft is not an effective diagnostic of a density current's ability to lift near-surface air*.

5. Discussion

5.1 Merits and limitations of momentum-balance in density currents

Our results show that momentum-balance can be effective for diagnosing the orientation of updrafts in density currents, accounting for "classic" c-ΔU

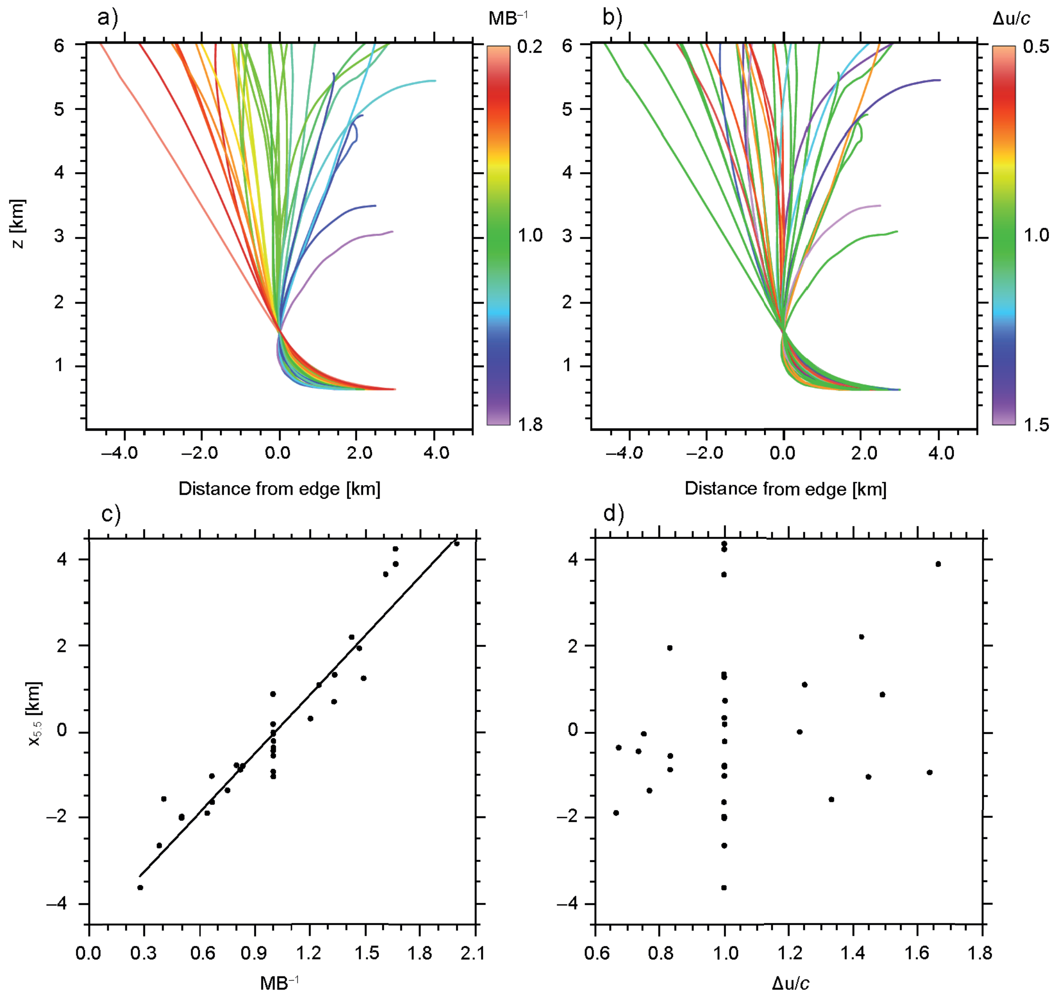

Fig. 14. In a) and b) the mean trajectories of all simulations are displayed up to their maximum height. Trajectories are colored by the simulation's MB^{-1} in a) and $\Delta U/c$ in b). The scatter plots in c) and d) show all simulations per their MB^{-1} and $\Delta U/c$ in the abscissa axis, and $x_{5.5}$ in the ordinate axis. The line in c) corresponds to the best linear fit to the data.

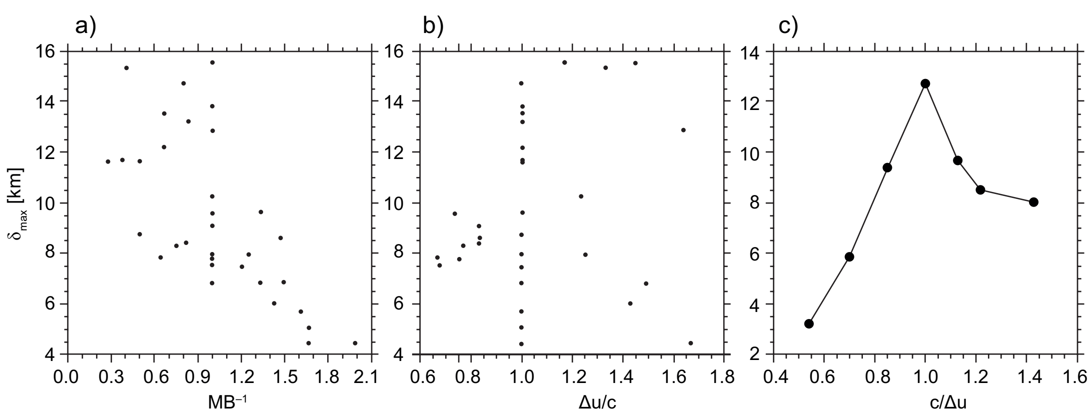

Fig. 15. Scatter plots showing δ_{max} (ordinate). All simulations are displayed in a) and b), where the abscissa indicates MB^{-1} and $\Delta U/c$, respectively. The scatter plot in c) displays $c/\Delta U$- δ_{max} for "classic" variations (compare to BR14's Fig. 17).

variations, the shear-layer depth, the shear profile, and buoyancies within the denser air. It is true that the experiments considered herein include a limited set of initial conditions, so generalizations could warrant caution, especially in no-shear environments, which were not contemplated since they are not very relevant to SLs' organization. Yet, the robustness of our results is substantiated by the fact that the numerical experiments considered herein mirror those contemplated by BR14 (except for buoyancy profile variations, which were not included in that study), guaranteeing that our methodology was not designed to favor MB over $c/\Delta U$. Furthermore, this study considers more diverse variations to environmental winds and buoyancy profiles than previous analyses of density currents aimed at understanding SL-shear interactions (RKW88; WR04; BR14). We are thus led to the conclusion that *momentum-balance represents an effective conceptual framework for characterizing the slope of a density current's updraft throughout low and mid-levels, which is advantageous over RKW's quantitative criterion for its greater ability to account for varying shear and buoyancy profiles*.

It is important to mention that only modest changes around $c/\Delta U = 1$ were contemplated in this study. This is so because cases of relevance to SL environments where $c/\Delta U$ differs significantly from 1 produce updrafts with pronounced slopes in the direction of winds aloft. This is due to the underlying relationship between MB and $c/\Delta U$, as exemplified by considering classic ΔU variations: both MB and $c/\Delta U$ vary in concert in response to changes in ΔU (Fig. 2b; subsection 4.1), implying that the airflow aloft and momentum-balance interactions between the denser air and inflowing winds tend to tilt the updraft in the same direction. However, it does not follow that MB only provides relevant information in cases with $c/\Delta U \approx 1$, especially in SLs, which develop significant within-storm pressure perturbations above the cold pool (Fovell and Ogura, 1988; Lafore and Moncrieff, 1989), directly affecting the MF. Such features, together with non-stagnant air within the cold pool, can strongly affect the system-relative inflow through the propagation speed (Trier et al., 2006; Mahoney et al., 2009), suggesting that $c/\Delta U$ might not provide reasonable guidance for system-relative winds aloft.

There are two issues that deserve further note: circulations affecting the momentum structure near the updraft and the neglect of outflowing momentum at lateral boundaries of the control volume. Regarding the former, vortices flanking the updraft are likely to have an impact on ascending motions, even though in cases considered herein they do not significantly affect the diagnostic skill of MB. Perhaps more relevant are the circulations associated with non-hydrostatic pressure perturbations that reach lateral boundaries, complicating the definition of L and R. However, as mentioned in subsection 4.1, relevant characteristics of the updrafts seem to be established early in the simulations, justifying the use of initial conditions to compute MB. On the other hand, such features are not likely to be relevant to SLs, the phenomenon motivating this study, wherein stably stratified environmental and within-storm conditions should damp those circulations, guaranteeing nearly hydrostatically balanced flow at lateral boundaries.

The neglect of outflowing momentum at lateral boundaries might seem ad-hoc for the density currents considered herein, as there is no formal argument based on the momentum theorem (Batchelor, 2000) for defining LFM as in (16). The problem arises because the momentum theorem does not represent an equation for the updraft's slope, although there clearly exists a close relationship between the momentum structure at lateral boundaries and updraft characteristics. We believe that the physical plausibility of our arguments, wherein inconsistencies arise between the foreseen effects of outflowing air and the mathematical expressions derived from the momentum theorem (subsection 2.3), substantiate our definition of the LFM, while results presented throughout section 4 provide strong support for this choice. It is worth noting that WR04 and BR14 proceeded in this way (see Bryan et al., 2012), i.e. first providing plausible qualitative arguments relating the updraft's structure to the quantitative criterion derived from a single "optimal" density current, and then validating numerically the applicability of $c/\Delta U$ to non-optimal cases. Therefore, considering that this is not a study about the momentum theorem in diverse density currents, we think that the momentum-balance concepts discussed are appropriate means for diagnosing the updraft's orientation throughout low and mid-levels, as long as physical arguments and numerical evidence support this interpretation.

5.2 RKW theory and the reinterpretation of the quantitative criterion

One of the most surprising findings of this investigation is the lack of correspondence between the quantitative criterion of RKW theory and both the updraft's slope and the depth reached by near-surface environmental air. We believe that the close correspondence between MB and $c/\Delta U$ under classic c-ΔU variations led previous studies to misidentify $c/\Delta U$ as an accurate measure of near-surface density-current–shear interactions. This is further substantiated by the fact that the vorticity-balance relation in (11) does not show a clear relationship with $c/\Delta U$ for non-optimal configurations.

In addition, results presented in section 4 lend weight to our reinterpretation of $c/\Delta U$ as a measure of the impacts of winds aloft on the updraft's structure. Such effects are akin to those contemplated by Thorpe et al. (1982) in the context of SLs, wherein the movement of the cold pool edge relative to previously triggered deep convective cells is of primary importance to the organization and maintenance of storms. The importance of system-relative winds aloft lies in their ability to tilt the top of the updraft, which may be the result of the airflow impinging on ascending parcels with near-surface origins. This effect was recognized by Shapiro (1992) and Coniglio et al. (2006) in flows with deep shear-layers. Thus, we are inclined to interpret $c/\Delta U$ as a measure of an updraft's tendency to slope in the direction of the wind velocity aloft, instead of the near-surface interactions between the density current and inflowing winds, as originally intended by RKW88. For clarity, we do not deny that $c/\Delta U$ is related to the near-surface vorticity field in the updraft's vicinity, but these theoretical considerations and results presented lead us to conclude that *$c/\Delta U$ does not provide an accurate measure of the near-surface density-current–shear interactions considered by Rotunno et al. (1988), Weisman and Rotunno (2004), and Bryan and Rotunno (2014)*.

It is worth mentioning that this interpretation of $c/\Delta U$ fits within the momentum framework, with winds aloft "pushing" the updraft in the direction determined by $c/\Delta U$. Therefore, we interpret MB as a momentum-balance metric for near-surface interactions between the density current and inflowing air, while $c/\Delta U$ provides information on the impact of wind velocity aloft on the updraft.

6. Summary and future work

This study presents a momentum-balance framework for diagnosing the slope of a density current's updraft in sheared environments, pursuing a theory of storm-shear interactions that can bridge gaps in the RKW theory of vorticity-balance. The motivation arose from results by BR14 showing that the quantitative criterion of RKW theory, $c/\Delta U$, cannot account for the impacts of shear-layer depth variations on a density current's updraft, while also demonstrating the importance of the flow-force balance constraint (Benjamin, 1968) for the development of the optimal state. Given that the flow-force balance represents a condition on the horizontal momentum equation determining the shear-layer depth for the optimal state, momentum-balance concepts are explored as an alternative to RKW theory.

We derived a non-dimensional quantitative diagnostic concerning the degree of momentum-balance (MB) for density currents, which depends on both the shear and buoyancy profiles. MB measures the extent to which hydrostatic pressure perturbations within the denser air—which favor upwind tilted updrafts—can counter advective tendencies due to inflowing environmental air—which favor downwind tilted updrafts. We evaluate the diagnostic skill of MB by comparing the updrafts produced by several numerically simulated density currents, wherein profiles of environmental winds and buoyancies within the denser fluid were varied systematically from case to case. Results show that MB can effectively diagnose the updraft's slope throughout low and mid-levels, accounting for classic c-ΔU variations, changes to the shear-layer depth, and varying buoyancy and shear profiles.

Regarding RKW theory, our results show that $c/\Delta U$ is not as restrictive on a density current's updraft as suggested by previous investigations (RKW88; WR04). In particular, we do not find a clear relationship between $c/\Delta U$ and either the low-to-mid level updraft slope or the lifting of near-surface air. This could be due to $c/\Delta U$ not being an accurate measure of vorticity-balance in non-optimal density currents. On the other hand, the close correspondence between $c/\Delta U$ and environmental wind velocities at upper levels lead us to reinterpret $c/\Delta U$ as a measure of the impacts of the airflow aloft on the updraft. Consistent with this interpretation, updraft slopes at upper levels follow the direction of the environmental winds aloft, as determined by $c/\Delta U$.

It is early to guarantee the application of MB concepts to observed SLs, but lateral flux of momentum (LFM) can be computed from data analysis by estimating the system's propagation velocity, e.g. by using Corfidi vectors (Corfidi, 2003) to provide additional information in understanding SLs organization. The motive force (MF) term is more difficult to estimate because it requires knowledge about characteristics within the storm, which are hard to measure. However, the layer lifting model of convection by Alfaro (2017) produces indices, that could be used to approximate within-storm characteristics.

Future research will focus on the validation of momentum-balance concepts in numerically simulated SLs. First, by diagnosing a SL's evolution throughout early stages, and second, by comparing the updraft structures developed by mature storms in diverse environmental conditions. It is expected that momentum-balance will provide a useful framework for incorporating the circulations within the cold pool in SLs with trailing-stratiform precipitation.

Acknowledgements

We thank Jorge García Franco, Mike Coniglio, and David Adams for their constructive suggestions. We also thank George Bryan for making CM1 publicly available. This study was funded by the PAPIIT program at UNAM under grant IA101418. Computational resources of DGTIC-UNAM at Miztli are acknowledged.

References

Alfaro DA, Khairoutdinov M. 2015. Thermodynamic constraints on the morphology of simulated midlatitude squall lines. Journal of the Atmospheric Sciences 72: 3116-3137. https://doi.org/10.1175/JAS-D-14-0295.1

Alfaro DA. 2017. Low-tropospheric shear in the structure of squall lines: Impacts on latent heating under layer-lifting ascent. Journal of the Atmospheric Sciences 74: 229-248. https://doi.org/10.1175/JAS-D-16-0168.1

Alfaro DA, Coniglio MC. 2018. Discrimination of mature and dissipating severe-wind-producing MCSs with layer-lifting indices. Weather and Forecasting 33: 3-21. https://doi.org/10.1175/WAF-D-17-0088.1

Asai T. 1964. Cumulus convection in the atmosphere with vertical wind shear: Numerical experiment. Journal of the Meteorological Society of Japan 42: 245-259. https://doi.org/10.2151/jmsj1923.42.4_245

Barnes GM, Sieckman K. 1984. The environment of fast- and slow-moving tropical mesoscale convective cloud lines. Monthly Weather Review 112: 1782-1794. https://doi.org/10.1175/1520-0493(1984)112<1782:TEOFAS>2.0.CO;2

Batchelor GK. 2000. An introduction to fluid dynamics. Cambridge: Cambridge University Press. https://doi.org/10.1017/CBO9780511800955

Benjamin T. 1968. Gravity currents and related phenomena. Journal of Fluid Mechanics 31: 209-248. https://doi.org/10.1017/S0022112068000133

Bluestein HB, Jain MH. 1985. Formation of mesoscale lines of precipitation: Severe squall lines in Oklahoma during the spring. Journal of the Atmospheric Sciences 42: 1711-1732. https://doi.org/10.1175/1520-0469(1985)042<1711:FOMLOP>2.0.CO;2

Bryan GH, Ahijevych D, Davis C, Trier S, Weisman M. 2005. Observations of cold pool properties in mesoscale convective systems during BAMEX. Preprints. 11th Conference on Mesoscale Processes. Albuquerque: American Meteorological Society, JP5J.12. Available at https://ams.confex.com/ams/32Rad11Meso/techprogram/paper_96718.htm (accessed on August 1, 2020).

Bryan GH, Knievel JC, Parker MD. 2006. A multimodel assessment of RKW theory's relevance to squall-line characteristics. Monthly Weather Review 134: 2772-2792. https://doi.org/10.1175/MWR3226.1

Bryan GH, Parker MD. 2010. Observations of a squall line and its near environment using high-frequency rawinsonde launches during VORTEX2. Monthly Weather Review 138: 4076-4097. https://doi.org/10.1175/2010MWR3359.1

Bryan GH, Rotunno R, Weisman M. 2012. What is RKW theory. Preprints. 26th Conference on Severe Local Storms. Nashville: American Meteorological Society, 4B.6. Available at https://ams.confex.com/ams/26SLS/webprogram/Paper211731.html (accessed on August 1, 2020).

Bryan GH, Rotunno R. 2014. The optimal state for gravity currents in shear. Journal of the Atmospheric Sciences 71: 448-468. https://doi.org/10.1175/JAS-D-13-0156.1

Charba J. 1974. Application of gravity current model to analysis of squall-line gust front. Monthly Weather Review 102: 140-156. https://doi.org/10.1175/1520-0493(1974)102<0140:AOGCMT>2.0.CO;2

Cohen AE, Coniglio MC, Corfidi SF, Corfidi SJ. 2007. Discrimination of mesoscale convective system environments using sounding observations. Weather and Forecasting 22: 1045-1062. https://doi.org/10.1175/WAF1040.1

Coniglio MC, Stensrud DJ, Wicker LJ. 2006. Effects of upper-level shear on the structure and maintenance of strong quasi-linear mesoscale convective systems. Journal of the Atmospheric Sciences 63: 1231-1252. https://doi.org/10.1175/JAS3681.1

Coniglio MC, Brooks HE, Weiss SJ, Corfidi SF. 2007. Forecasting the maintenance of quasi-linear mesoscale convective systems. Weather and Forecasting 22: 556-570. https://doi.org/10.1175/WAF1006.1

Coniglio MC, Corfidi SF, Kain JS. 2012. Views on applying RKW theory: An illustration using the 8 May 2009 derecho-producing convective system. Monthly Weather Review 140: 1023-1043. https://doi.org/10.1175/MWR-D-11-00026.1

Corfidi SF. 2003. Cold pools and MCS propagation: Forecasting the motion of downwind-developing MCSs. Weather and Forecasting 18: 997-1017. https://doi.org/10.1175/1520-0434(2003)018<0997:CPAMP-F>2.0.CO;2

Dai A. 2006. Precipitation characteristics in eighteen coupled climate models. Journal of Climate 19: 4605-4630. https://doi.org/10.1175/JCLI3884.1

Droegemeier KK, Wilhelmson RB. 1987. Numerical simulation of thunderstorm outflow dynamics. Part I: Outflow sensitivity experiments and turbulence dynamics. Journal of the Atmospheric Sciences 44: 1180-1210. https://doi.org/10.1175/1520-0469(1987)044<1180:N-SOTOD>2.0.CO;2

Engerer NA, Stensrud DJ, Coniglio MC. 2008. Surface characteristics of observed cold pools. Monthly Weather Review 136: 4839-4849. https://doi.org/10.1175/2008MWR2528.1

Evans JS, Doswell III CA. 2001. Examination of derecho environments using proximity soundings. Weather and Forecasting 16: 329-342. https://doi.org/10.1175/1520-0434(2001)016<0329:EODEUP>2.0.CO;2

Fovell RG, Ogura Y. 1988. Numerical simulation of a midlatitude squall line in two dimensions. Journal of the Atmospheric Sciences 45: 3846-3879. https://doi.org/10.1175/1520-0469(1988)045<3846:NSO-AMS>2.0.CO;2

Fovell RG, Ogura Y. 1989. Effect of vertical wind shear on numerically simulated multicell storm structure. Journal of the Atmospheric Sciences 46: 3144-3176. https://doi.org/10.1175/1520-0469(1989)046<3144:E-OVWSO>2.0.CO;2

Gale JJ, Gallus WA, Jungbluth KA. 2002. Toward improved prediction of mesoscale convective system dissipation. Weather and Forecasting 17: 856-872. https://doi.org/10.1175/1520-0434(2002)017<0856:TIPOMC>2.0.CO;2

Lafore JP, Moncrieff MW. 1989. A numerical investigation of the organization and interaction of the convective and stratiform regions of tropical squall lines. Journal of the Atmospheric Sciences 46: 521-544. https://doi.org/10.1175/1520-0469(1989)046<0521:ANI-OTO>2.0.CO;2

Lilly DK. 1979. The dynamical structure and evolution of thunderstorms and squall lines. Annual Review of Earth and Planetary Sciences 7: 117-161. https://doi.org/10.1146/annurev.ea.07.050179.001001

Liu C, Moncrieff MW. 1996. A numerical study of the effects of ambient flow and shear on density currents. Monthly Weather Review 124: 2282-2303. https://doi.org/10.1175/1520-0493(1996)124<2282:AN-SOTE>2.0.CO;2

Mahoney KM, Lackmann GM, Parker MD. 2009. The role of momentum transport in the motion of a quasi-idealized mesoscale convective system. Monthly Weather Review 137: 3316-3338. https://doi.org/10.1175/2009MWR2895.1

Markowski P, Richardson Y. 2010. Mesoscale Meteorology in Midlatitudes. Chichester: Wiley-Blackwell. https://doi.org/10.1002/9780470682104

Moncrieff MW. 2010. The multiscale organization of moist convection and the intersection of weather and climate. In: Sun D-Z, Bryan F, eds. Climate Dynamics: Why Does Climate Vary? Washington: American Geophysical Union, 3-26. https://doi.org/10.1029/2008GM000838

Parker MD, Johnson RH. 2004a. Structures and dynamics of quasi-2D mesoscale convective systems. Journal of the Atmospheric Sciences 61: 545-567. https://doi.org/10.1175/1520-0469(2004)061<0545:SADO-QM>2.0.CO;2

Parker MD, Johnson RH. 2004b. Simulated convective lines with leading precipitation. Part II:

evolution and maintenance. Journal of the Atmospheric Sciences 61: 1656-1673. https://doi.org/10.1175/1520-0469(2004)061<1656:SCLWLP>2.0.CO;2

Parker MD. 2010. Relationship between system slope and updraft intensity in squall lines. Monthly Weather Review 138: 3572-3578. https://doi.org/10.1175/2010MWR3441.1

Provod M, Marsham JH, Parker DJ, Birch CE. 2016. A characterization of cold pools in the West African Sahel. Monthly Weather Review 144: 1923-1934. https://doi.org/10.1175/MWR-D-15-0023.1

Rotunno R, Klemp JB, Weisman ML. 1988. A theory for strong, long-lived squall lines. Journal of the Atmospheric Sciences 45: 463-485. https://doi.org/10.1175/1520-0469(1988)045<0463:ATFSLL>2.0.CO;2

Rotunno R, Klemp JB, Weisman ML. 1990. Comments on “A numerical investigation of the organization and interaction of the convective and stratiform regions of tropical squall lines”. Journal of the Atmospheric Sciences 47: 1031-1033. https://doi.org/10.1175/1520-0469(1990)047<1031:CONIOT>2.0.CO;2

Shapiro A. 1992. A hydrodynamical model of shear flow over semi-infinite barriers with application to density currents. Journal of the Atmospheric Sciences 49: 2293-2305. https://doi.org/10.1175/1520-0469(1992)049<2293:AHMOSF>2.0.CO;2

Stensrud DJ, Coniglio MC, Davies-Jones RP, Evans JS. 2005. Comments on “‘A theory for strong long-lived squall lines’ revisited”. Journal of the Atmospheric Sciences 62: 2989-2996. https://doi.org/10.1175/JAS3514.1

Thorpe AJ, Miller MJ, Moncrieff MW. 1982. Two-dimensional convection in non-constant shear: A model of mid-latitude squall lines. Quarterly Journal of the Royal Meteorological Society 108: 739-762. https://doi.org/10.1002/qj.49710845802

Trier SB, Davis CA, Ahijevych DA, Weisman ML, Bryan GH. 2006. Mechanisms supporting long-lived episodes of propagating nocturnal convection within a 7-day WRF model simulation. Journal of the Atmospheric Sciences 63: 2437-2461. https://doi.org/10.1175/JAS3768.1

Wakimoto RM. 1982. The life cycle of thunderstorm gust fronts as viewed with Doppler radar and rawinsonde data. Monthly Weather Review 110: 1060-1082. https://doi.org/10.1175/1520-0493(1982)110<1060:TLCOTG>2.0.CO;2

Weisman ML, Klemp JB, Rotunno R. 1988. Structure and evolution of numerically simulated squall lines. Journal of the Atmospheric Sciences 45: 1990-2013. https://doi.org/10.1175/1520-0469(1988)045<1990:SAEONS>2.0.CO;2

Weisman ML. 1992. The role of convectively generated rear-inflow jets in the evolution of long-lived mesoconvective systems. Journal of the Atmospheric Sciences 49: 1826-1847. https://doi.org/10.1175/1520-0469(1992)049<1826:TROCGR>2.0.CO;2

Weisman ML. 1993. The genesis of severe, long-lived bow echoes. Journal of the Atmospheric Sciences 50: 645-670. https://doi.org/10.1175/1520-0469(1993)050<0645:TGOSLL>2.0.CO;2

Weisman ML, Rotunno R. 2004. “A theory for strong long-lived squall lines” revisited. Journal of the Atmospheric Sciences 61: 361-382. https://doi.org/10.1175/1520-0469(2004)061<0361:ATFSLS>2.0.CO;2

Xu Q. 1992. Density currents in shear flows—A two-fluid model. Journal of the Atmospheric Sciences 49: 511-524. https://doi.org/10.1175/1520-0469(1992)049<0511:DCISFA>2.0.CO;2

Atmósfera 35(2), 221-235 (2022)
https://doi.org/10.20937/ATM.52910

CONTENTS

Statistical analysis of the relationship between Quasi-Biennial Oscillation and Southern Annular Mode

Fernanda Cerqueira VASCONCELLOS[1], Maria Lívia Lins MATTOS-GAVA[2] and Clovis Angeli SANSIGOLO[2]

[1] *Department of Meteorology, Geosciences Institute, Federal University of Rio de Janeiro (UFRJ), Rio de Janeiro, RJ 21941-916, Brazil.*
[2] *National Institute for Space Research (INPE), São José dos Campos-SP, Brazil.*
*Correspondence author; fernandavasconcellos@igeo.ufrj.br

Received: May 22, 2020, acepted: October 26, 2020

RESUMEN

El Modo Anular del Sur (SAM) es un patrón extratropical que influye en el clima de todo el hemisferio sur. Sin embargo, la variabilidad de este modo es un área de investigación activa. La influencia de los modos de frecuencia más baja en SAM es un camino hacia un mejor conocimiento sobre este patrón. La relación entre la Oscilación Cuasi-Bienal (QBO) y la contraparte de SAM en el Hemisferio Norte (Modo Anular del Norte) se ha abordado en trabajos anteriores. Aún así, pocos estudios se centran en la asociación entre QBO y SAM. El objetivo de este trabajo fue evaluar la posible relación QBO-SAM mediante análisis estadísticos. Esta asociación se investigó comparando los índices QBO y SAM, este último en diferentes niveles de la tropósfera y la estratósfera, para el período 1981-2010. El análisis de ondeletas mostró que los índices SAM para la tropósfera y la estratósfera presentaban variabilidad en muchas escalas, incluida una banda de dos años. La técnica de ondeletas cruzadas ("*cross-wavelets*") entre QBO y SAM identificó que dicha relación tiene una interacción compleja. Hubo una alta potencia común significativa alrededor de la banda de dos años, con rezagos que variaron durante el período analizado, incluido sin rezago. Un análisis adicional sin rezago confirmó estudios previos, lo que indica que la fase SAM negativa (positiva) es más frecuente para QBO del este (oeste). Sin embargo, esto no fue válido para todos los meses. Algunos análisis adicionales sugirieron que la propagación de ondas ascendentes a la estratósfera para cada fase de QBO cambia el chorro estratosférico y, en consecuencia, la fase de SAM.

ABSTRACT

The Southern Annular Mode (SAM) is an extratropical pattern that influences the climate of all Southern Hemisphere. However, the variability of this mode is an active area of research. The influence of lower frequency modes on SAM is a path to better knowledge about this pattern. The relationship between Quasi-Biennial Oscillation (QBO) and SAM's counterpart in the Northern Hemisphere (Northern Annular Mode) has been addressed by previous work. Still, few studies focus on the association between QBO and SAM. The goal of this work was to evaluate the possible QBO-SAM relationship through statistical analyses. This association was investigated by comparing QBO and SAM indices, the latter on different levels of the troposphere and stratosphere, for the 1981-2010 period. The wavelet analysis showed that the SAM indices for troposphere and stratosphere presented variability in many scales, including a two-year band. Cross-wavelets techniques between QBO and SAM ratified that this relation has a complex interaction. There was a significant common high power around the two-year band, with lags varying over the analyzed period, including no lag. Further analysis without lag confirmed previous studies, indicating that the negative (positive) SAM phase is more frequent for easterly (westerly) QBO. However, this was not valid for all months. Some additional analysis suggested that the upward wave propagation to the stratosphere for each QBO phase changes the stratospheric jet and, consequently, the SAM phase.

Keywords: Teleconnection patterns, wavelets, wave propagation.

1. Introduction

The atmosphere is a complex system with interactions at different temporal and spatial scales. Studies of these interactions are necessary since their influen ces on atmospheric circulation can explain abnormal events in various regions of the globe. Teleconnection patterns, in which local anomalies influence remote areas, are a great example of this mechanism.

The Quasi-Biennial Oscillation (QBO) is a tele connection pattern that occurs in the tropical stratosphere. It is characterized by the almost periodic alternation between easterly and westerly winds, called, respectively, the easterly and westerly QBO phases (Ebdon, 1960, 1975; Reed et al., 1961). The cycle of zonal wind oscillation varies from 22 to 34 months, with an average of around 28 months (Baldwin et al., 2001). Naujokat (1986) described the main characteristics of QBO: the signal propagates downward to the lower stratosphere with time; the wind speed decreases at lower levels; the amplitude and the period of this oscillation change reasonably from cycle to cycle; the transition between easterly and westerly phases occurs between 30 and 50 hPa; the easterly QBO phase is, in general, more intense than the westerly one, and during the westerly phase, the winds propagate downwards faster, favoring the prevalence of this phase for a longer time in lower levels of the stratosphere. Although QBO is not literally a biennial oscillation, there is a preferential season for phase reversal. Considering the 50 hPa level, the onset of both the easterly and westerly phases occurs mainly in the late austral autumn (Dunkerton, 1990).

In the extratropics, the Annular Modes stand out as the leading mode of climate variability. This teleconnection pattern describes north-south "seesaws" of atmospheric mass between the high latitudes and parts of the midlatitudes in both hemispheres. In the Northern Hemisphere (NH), it is known as Arctic Oscillation (AO) or Northern Annular Mode (NAM), while it the Southern Hemisphere (SH), is named Antarctic Oscillation (AAO) or Southern Annular Mode (SAM). This pattern's structure is very similar for both hemispheres, occurring all months in the troposphere. The SAM reaches its "active phase" - maximum intensity in the stratosphere - at the end of austral spring, whereas for the NAM this stage occurs during the boreal winter. The positive (negative) Annular Mode phase is characterized by negative (positive) anomalies of geopotential height over polar regions and positive (negative) anomalies at mid-latitudes (Gong and Wang, 1999; Thompson and Wallace, 2000). This mode of variability is an active research area (Schenzinger and Osprey, 2015; Fogt and Marshall, 2020). The influence of lower frequency modes on SAM is a path to better knowledge about this pattern. Kodera and Koide (1997) and Baldwin and Dunkerton (1999) indicate that the typical NAM signal first appears in the stratosphere and then propagates downwards, suggesting that the NAM phase could be influenced by stratospheric circulation.

Although it is a tropical phenomenon, the QBO influence on the extratropical regions has been investigated by several authors, mainly in HN (e.g., Holton and Tan, 1980, 1982; Baldwin and Tung, 1994; Coughlin and Tung, 2001; Naoe and Shibata, 2010; Kuroda and Yamazaki, 2010; Roy and Haigh, 2011; Anstey and Shepherd, 2014; Li et al., 2020). Holton and Tan (1980) showed that the geopotential height at high latitudes is significantly lower during the westerly QBO phase. They suggested that the QBO may act either to focus planetary wave activity toward high latitudes or to allow its passage into the Tropics, through modulation of the latitudinal extent of the winter westerlies. The easterly QBO increases extratropical confinement of wave activity, weakening the vortex. The opposite situation during the westerly QBO, strengthens it (known as the Holton-Tan effect).

Studies relating QBO and Annular Modes have been carried out before, but they are generally focused on HN. Holton and Tan (1980), when examining 50 hPa geopotential composites in the NH, generated from the QBO phases, found a similar pattern to NAM. Coughlin and Tung (2001) showed a statistically significant relationship between the QBO signal and each level of the NAM, from 10 mb to 1000 mb, in which they all peak with the same frequency as the QBO. Other studies reveal that the positive (negative) NAM phase is associated with the westerly (easterly) QBO phase (e.g., Ruzmaikin et al., 2005; Scaife et al., 2014; Anstey and Shepherd, 2014). Kuroda and Yamazaki (2010) investigated the influence of the 11-year solar cycle and the QBO on the SAM in late winter/spring. They found that the SAM signal is strongly affected by both the solar cycle and the QBO. The SAM signal was restricted to the troposphere and disappeared very quickly in years with low solar activity.

Several studies have indicated the separate influence of QBO (e.g., Gray, 1984; Mukherjee et al., 1985; Jury et al., 1994; Peings et al., 2013; Gray et al., 2018) and SAM (e.g., Gillett et al., 2006; Silvestri and Vera, 2003, 2009; Carvalho et al., 2005; Reboita et al., 2009; Vasconcellos and Cavalcanti, 2010; Blázquez and Solman, 2017; Rosso et al., 2018; Vasconcellos et al., 2019) around the globe. As discussed above, the QBO-NAM relationship has been addressed by previous studies, indicating an association between them. However, few studies show the association between QBO and SAM (e.g., Roy and Haigh, 2011; Anstey and Shepherd, 2014). It is, therefore, necessary to verify whether this relationship also occurs in the SH and investigate its variability, to better understand the variability of SAM.

In this study, we specifically focused on evaluating the possible relationship between QBO and SAM patterns through statistical analysis. As part of this investigation, the following questions were addressed:

1. Is there a relationship between QBO and SAM?
2. Does this relationship occur on all months?
3. Are there lags between them?

These questions were investigated by comparing QBO and SAM indices, the latter on different levels of the troposphere and stratosphere. The Continuous Wavelet Transform (CWT) and Cross Wavelet Transform (XWT) techniques were applied to identify significant common power and phase difference between the QBO and SAM. Contingency tables and composite analyses were also used to complement the study.

This paper is outlined as follows. Section 2 introduces the datasets and describes the methodology used to investigate the association between QBO and SAM. Section 3 presents and discusses the main findings. Summary and conclusions are presented in Section 4.

2. Dataset and Methods

Monthly datasets of ERA-Interim reanalysis from the European Centre for Medium Range Weather Forecasts (ECMWF) were used for the following variables: geopotential height at 700, 200, and 30 hPa, and zonal wind at 30 hPa. The daily ERA-Interim dataset was also used for air temperature and meridional wind at 30 hPa. ERA-Interim features a global spatial coverage, with a horizontal resolution of 0.5º x 0.5º latitude/longitude and 60 vertical levels from the surface to 0.1 hPa. Details on the data assimilation system of ERA-Interim can be found in Dee et al. (2011). The 1981-2010 period was evaluated. Monthly anomalies were constructed for each month by subtracting the corresponding 1981-2010 climatological monthly mean.

The QBO index was calculated based on Naujokat (1986): zonal mean (0º –360º) of 30 hPa zonal wind at 0º latitude. The index has negative values in the easterly QBO phase and positive values in the westerly QBO phase. The SAM indices were calculated for three different levels (troposphere and stratosphere): 700, 200, and 30 hPa. The index (for each level) was obtained from the principal component time series of geopotential height monthly anomaly polewards of 30ºS, using Empirical Orthogonal Function (EOF) (Vasconcellos et al., 2019). Positive (negative) values of the SAM index are associated with negative (positive) geopotential height anomalies over Antarctica and positive (negative) geopotential height anomalies at midlatitudes.

The wavelet transform can be used to analyze time series that contain nonstationary power at many different frequencies (Daubechies, 1990). Torrence and Compo (1998) indicate that the wavelet transform allows the identification of the dominant modes of variability with a more significant contribution to the signal observed in a given period. In time or space, the CWT has movable windows, which expand or compress to capture low and high-frequency signals, respectively. Thus, it becomes a useful tool to capture the contribution of each frequency to the time series, even if that contribution varies throughout the series (Labat, 2005). CWT was applied to the SAM index time series (for each level), to find the different scales that contribute to the SAM's large variability. The CWT figures display the time series on the X-axis and the frequency on the Y-axis. The cold colors represent less contribution to the series, and the warm colors are the frequencies that most contribute to the signal variability (high power). The CWT has edge artifacts because the wavelet is not entirely localized in time. It is, therefore, useful to introduce a Cone of Influence (COI) in which edge effects cannot be ignored. Here, the region outside of COI is in blurred shade. The Monte Carlo test wats applied to find a 90% confidence level of the signal.

The XWT displays the regions in which the two time series vary together and reveals information about the relationship between their phases through phase vectors. It means that even if the relationship between the two signals does not occur simultaneously, the XWT can identify it. The XWT allows to identify the similarity between two signals, quantifying the degree of the relationship between them over time (Labat, 2005). The XWT was calculated using QBO and SAM indices (for each level). The figures obtained from the XWT are similar to those obtained with CWT. Peak power locations correspond to regions where the time series are related. The XWT figures also have arrows, the phase angles that indicate the lag between the two time series. To analyze the phase angles, it is necessary to know which time series was processed first, and in this case, QBO was the first. The phase relationship is shown as arrows, with in-phase pointing right, anti-phase point ing left, the QBO leading SAM by 90º (270º) pointing straight down (up). The toolbox based on the methodology described in Grinsted et al. (2004) was used to calculate both CWT and XWT (available in http://grinsted.github.io/wavelet-coherence/).

Further analysis was performed comparing QBO and SAM with no lag. The SAM is a result of the sum of influences at diverse time scale (Schenzinger and Osprey, 2015; Fogt and Marshall, 2020). As QBO is a low-frequency pattern, to compare these two series, the SAM index for each level was filtered to exclude high-frequency variability, using a moving average filter. The moving average is a simple linear filter that converts a series X_t, into another series Y_t, by the linear operation (Equation 1):

$$Y_t = \sum_{r=-q}^{s} a_r X_{t+r} \tag{1}$$

where q and s represent the limits of the sum, and for this study q = s. X_t represents the series to be filtered, Y_t the resulting series, and a_r are the weights used in the moving average. In this study a_r is given by the expansion of the term $(1/2+1/2)^{2q}$. In this way, the weight of the terms closest to the center is higher, giving them greater importance. For the 24-month (2-year) filter, the corresponding q is 12. However, for larger q values, the terms farther from the center get smaller and become negligible for the calculation. Therefore, when filtering the series, q = 4 was used, a sufficiently large value. This methodology was based on Chatfield (2004). Because of this q value, applying this filter to the first and last four months of the analyzed period is impossible. Thus, the filtered SAM index for the 1981 to 2010 period started in May 1981 and ended in August 2010.

Monthly contingency tables between the QBO and SAM (filtered) indices were created (without lag). The 2x2 tables were used. The upper-left square corresponds to the negative SAM phase events during the easterly QBO phase; the upper-right square corresponds to the negative SAM phase cases during the westerly QBO; the bottom-left square corresponds to the positive SAM phase along easterly QBO; and the bottom-right square corresponds to occurrences of a positive SAM phase along westerly QBO. These tables were created for each SAM index (700, 200, and 30 hPa). Because of the moving average filter, the contingency tables of January-April and September-December had 29 observations. The other months had 30 observations.

The correlation between the SAM index and zonal mean, both filtered using the moving average filter described above, was calculated to complement the results. The latitude versus pressure profile of this correlation was built. A t-student test (Wilks, 2006) was applied to composites at a 90% confidence level.

Geopotential height anomaly at 30 hPa and zonal wind were also filtered using the moving average filter described above. These were used to generate composite analyses for each QBO phase (without lag). The zonal wind was taken to create a latitude versus pressure profile (zonal mean). The geopotential height anomaly at 30 hPa was shown on a polar stereographic map. Also, we calculated the meridional heat flux ($v'T'$) at 30 hPa from the daily dataset and built composites for easterly and westerly QBO. Trenberth (1991) showed that the meridional heat flux ($v'T'$) is proportional to the Eliassen-Palm vertical component. Edmon et al. (1980) suggested the Eliassen-Palm flux components denote the direction and magnitude of the planetary wave propagation, so

30 hPa could be used as a measure of the activity of the waves entering the stratosphere. As for the other composites, the flux was also filtered.

Since November is the active period of SAM (Thompson and Wallace, 2000), we choose this month to analyze the correlation and composites described above. The periods used for these composites were identified with the CWT of the SAM index at 30 hPa (1987-1990 and 2000-2004, see Section 3 - Results). A t-student test (Wilks, 2006) was applied to composites and correlations at a 90% confidence level.

3. Results

As mentioned, the CWT technique was applied to SAM indices at 700, 200, and 30 hPa, and results are shown in Figure 1. Warm colors in Fig. 1 have higher power, corresponding to where most of the energy in the series is concentrated, and the black line represents the 95% significance level. The analysis of the 700 hPa SAM index (Fig. 1a) shows peak power in the 1-6 months band in several tyears of the time series, ceasing around 2007. It also presents high power regions in the 1-2 year band, for the periods: 1985-1990, 2000-2003 and 2007; a peak is also seen in the 4-6 year band, between 1993 and 2001. The CWT for the 500 hPa SAM index was quite similar to Figure 1a (not shown). In the upper troposphere (200hPa - Fig. 1b), the SAM index exhibited similar power peaks as in the lower troposphere, but generally for shorter periods. Peaks were observed in the 1-2 year band around 1989, 2000-2004 (this peak extended longer than 2-year band) and 2007. Significantly higher power in the 4-6 year band extended from approximately 1995 to 2001. The CWT obtained for the stratospheric SAM index (30 hPa) presented differences compared to tropospheric ones, as shown in Figure 1c. First, the significant peaks in power in the band up to 3 months were less frequent. Significant high power was observed in the bands around 6 months-1 year, 1-2 years (this peak also extended longer than 2 years), while the 4-6 years band had no significant power. Significant high power in the 1-2 year band was observed in periods 1987-1990 and 2000-2004. Fogt and Marshal (2019) discuss the variability in the SAM and show that this variability stems from changes in the extratropical atmospheric circulation from the surface up through the stratosphere. Phenomena with several timescales can cause these changes, from synoptic (e.g., positive feedback between transient eddies and polar jet) to low-frequency modes (e.g., QBO and El Niño-Southern Oscillation), consistent with our CWT results.

Figure 1 revealed that the SAM index had several bands of high power, indicating many sources of variability. Schenzinger and Osprey (2015) and Fogt and Marshall (2020) also suggested sources with various timescales influencing the SAM. In addition, the SAM indices showed variability near the 2-year band for both the troposphere and stratosphere, suggesting that the QBO pattern could influence SAM variability in this band.

To verify this possibility, the XWT was applied between QBO and SAM indices (for 700, 200, and 30 hPa SAM indices). Figure 2a, corresponding to the XWT between QBO index and SAM index at 700 hPa, shows intense power peaks in the 2-year band around 1984-1985, 1988-1995, and from 1999 to the end of the time series. This result indicates an association between these two patterns in this band (approximately two years). When analyzing the phase vectors, lag phases can be seen between the QBO and SAM index time series. In the 2-year band (red rectangle) for the 1984-1985 period, the vectors are inclined approximately 90º (6 months lag) and 0º (in-phase), respectively. In the period 1988-1991, the phase vectors changed from 180º (anti-phase) to 90º (6 months lag). The 1992-1995 period had vectors in-phase (around 0º). In 1999, the patterns had 6 months lag (~90º) and, in 2000 became again in-phase (around 0º). The 2001-2004 period presented a higher phase difference, approximately 270º (18 months lag). From after 2004 until the end of the time series, the patterns were in phase (around 0º). The corresponding analysis with SAM index at 500 hPa (not shown) and 200 hPa (Fig. 2b) were similar to 700 hPa.

Some differences were observed in the stratospheric XWT (30 hPa - Fig. 2c) compared to the tropospheric ones (Fig. 2a-b). The high power observed in the stratosphere (around 2-year band) was more intense than in the troposphere. As in the troposphere, 1984 had about 6 months lag in the stratosphere. While in the stratosphere the period 1985-1987 was in phase, only 1985 was significant

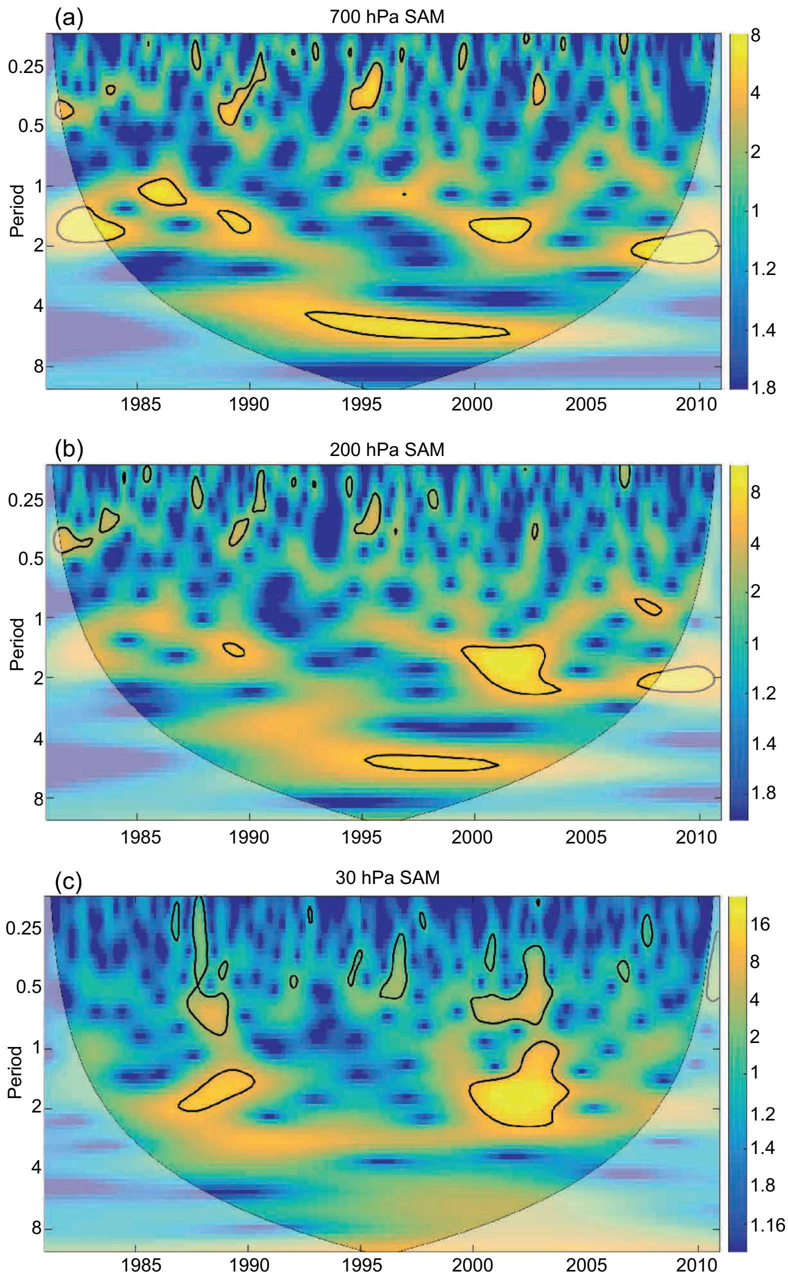

Fig. 1. Power spectrum of the continuous wavelet transform (CWT) of SAM index at: (a) 700 hPa, (b) 200 hPa, and (c) 30 hPa. The thick black contour designates the 5% significance level and the cone of influence (COI) where edge effects might distort the picture is shown as a blurred shade.

in the troposphere. In the 1988-1989 period, the vectors inclined approximately 270° (18 months lag) and 180° (anti-phase), respectively. Although the 2-year band had no significance in 1990-1992, there was a significant area right below 2-year (still within the QBO period) in which the arrows were in phase. The 1993-1996 and 1999 periods presented a 6-month lag (around 90º). In the 2000-2005 period, the vectors had a counterclockwise rotation, starting at 0º (in-phase), passing through the 270º (18-month

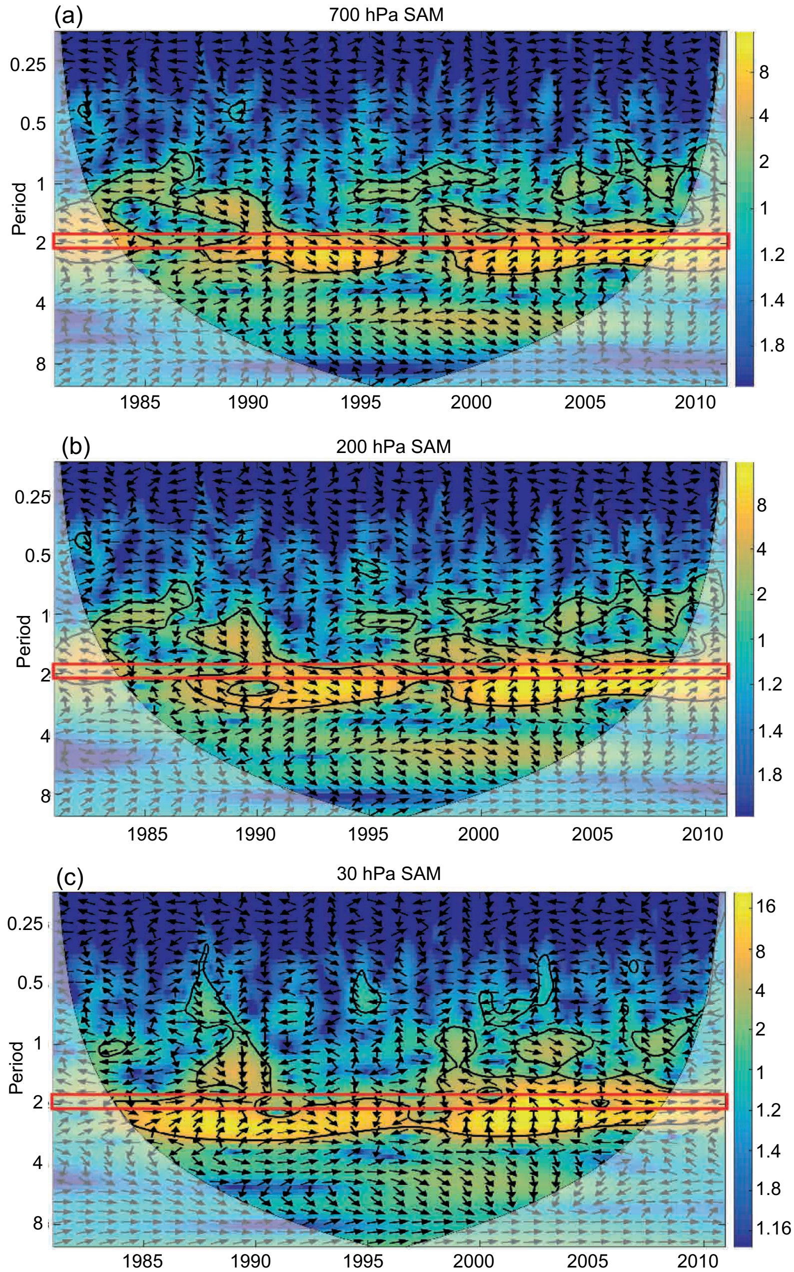

Fig. 2. Cross-wavelet transform (XWT) of the QBO and SAM index time series. The thick black contour designates the 5% significance level. The relative phase relationship is shown as arrows, with in-phase pointing right, anti-phase pointing left, the QBO leading SAM by 90º (270º) pointing straight down (up). The red rectangle displays the 2-year band.

lag) in 2001-20002, and 180º (anti-phase) in 2003-2004, finishing at 90º (6-month lag) in 2005. From 2006 onwards, the patterns were in phase (around 0º) as in the troposphere.

Figure 2 shows that there are different lags between QBO and SAM, including no lag; thus, we complement these results focusing on no lag. Monthly contingency tables counting the occurrences of simultaneous cases (no lag) of QBO and SAM phases (filtered) are shown in Figures 3-5 (700, 200, and 30 hPa SAM index, respectively). It is noteworthy that the frequency of the SAM phases related to QBO phases varied slightly through the atmosphere. Perhaps this behavior occurred because the Annular Mode signal first appears in the stratosphere and propagates downwards with time (Kodera and Koide, 1997; Baldwin and Dunkerton, 1999), but that in the same month the propagation may not have yet reached the lowest levels. Additionally, Kuroda and Yamasaki (2010) indicate that the SAM signal stays restricted to the troposphere in years with low solar activity, which could also explain troposphere-stratosphere differences. It is necessary to observe the behavior of the SAM relative to the phases of QBO

	SAM	QBO E	QBO W
JANUARY	NEG	13	5
	POS	5	6
FEBRUARY	NEG	8	8
	POS	7	6
MARCH	NEG	6	8
	POS	6	9
APRIL	NEG	5	8
	POS	8	8
MAY	NEG	10	6
	POS	7	7
JUNE	NEG	14	3
	POS	6	7
JULY	NEG	12	4
	POS	9	5
AUGUST	NEG	8	6
	POS	10	6
SEPTEMBER	NEG	10	4
	POS	7	8
OCTOBER	NEG	12	5
	POS	6	6
NOVEMBER	NEG	10	5
	POS	8	6
DECEMBER	NEG	12	3
	POS	6	8

Fig. 3. Monthly contingency tables between the QBO and SAM indices. SAM index (filtered) calculated for 700 hPa. The upper-left square corresponds to the events of the negative SAM phase during the easterly QBO phase (E); the upper-right square corresponds to the cases of negative SAM phase during the westerly QBO (W); the bottom-left square corresponds to events of positive SAM phase along easterly QBO (E); and the bottom-right square corresponds to occurrences of a positive SAM phase along westerly QBO (W).

	SAM	QBO E	QBO W
JANUARY	NEG	14	5
	POS	4	6
FEBRUARY	NEG	10	8
	POS	5	6
MARCH	NEG	6	10
	POS	6	7
APRIL	NEG	4	9
	POS	9	7
MAY	NEG	10	7
	POS	7	6
JUNE	NEG	13	3
	POS	7	7
JULY	NEG	12	4
	POS	9	5
AUGUST	NEG	10	5
	POS	8	7
SEPTEMBER	NEG	10	3
	POS	7	9
OCTOBER	NEG	12	4
	POS	6	7
NOVEMBER	NEG	10	5
	POS	8	6
DECEMBER	NEG	13	2
	POS	5	9

Fig. 4. Same as Figure 3, but for SAM index calculated at 200 hPa.

JANUARY

SAM \ QBO	E	W
NEG	13	3
POS	4	8

FEBRUARY

SAM \ QBO	E	W
NEG	10	8
POS	5	6

MARCH

SAM \ QBO	E	W
NEG	3	12
POS	9	5

APRIL

SAM \ QBO	E	W
NEG	4	9
POS	9	7

MAY

SAM \ QBO	E	W
NEG	9	6
POS	87	7

JUNE

SAM \ QBO	E	W
NEG	11	5
POS	9	5

JULY

SAM \ QBO	E	W
NEG	11	4
POS	10	5

AUGUST

SAM \ QBO	E	W
NEG	12	3
POS	6	9

SEPTEMBER

SAM \ QBO	E	W
NEG	12	4
POS	5	8

OCTOBER

SAM \ QBO	E	W
NEG	12	4
POS	6	7

NOVEMBER

SAM \ QBO	E	W
NEG	12	4
POS	6	7

DECEMBER

SAM \ QBO	E	W
NEG	13	3
POS	5	8

Fig. 5. Same as Figure 3, but for SAM index calculated at 30 hPa.

to analyze the contingency tables since the QBO is the longer-lasting phenomenon. Inspection of the columns in each table identified which SAM phase was more frequent in each QBO phase, to establish a relationship among them. When a SAM phase occurred more frequently during the easterly QBO and, during the westerly phase, the opposite SAM phase was more frequent ("oblique behavior" in the contingency tables), a relationship between the phenomena is suggested. Table I summarizes the results from the contingency tables (Figs. 3-5). The most frequent pattern presented the negative SAM phase related to the easterly QBO phase and the positive SAM phase associated with the westerly QBO phase. Months not included in the table did not present the "oblique behavior".

Table II – Classification of easterly and westerly QBO years (November) used for composite analysis (Figure 6). The period analyzed is 1987-1990 and 2000-2004.

Easterly QBO	Westerly QBO
1988, 1989, 2000, 2001, 2002, 2003	1987, 1990, 2004

November is the active SAM period (Thompson and Wallace, 2000), so we choose this month to ana lyze the latitude versus pressure profile of correlation between the SAM index and zonal wind (both filtered) (Figure 6). The most significant correlations were found in the extratropics. This result was expected since the SAM is the leading mode of the extra-tropical region (Thompson and Wallace, 2000). The correlation map highlighted the relationship between SAM phase and the polar stratospheric vortex and polar night jet, showing a significant strengthening (weakening) of the stratospheric jet during positive (negative) SAM phase, as discussed in previous work (e.g., Thompson and Wallace, 2000; Fogt and Mar-

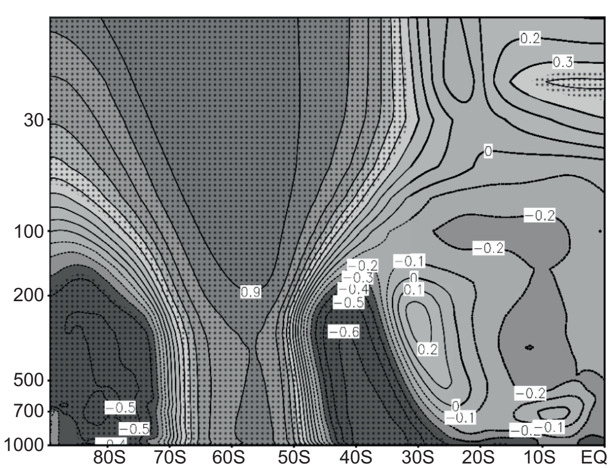

Fig. 6. Latitude versus pressure profile of correlation between the SAM index at 700 hPa and zonal wind (both filtered) for November. Areas with 90% significance are dotted (t-student test).

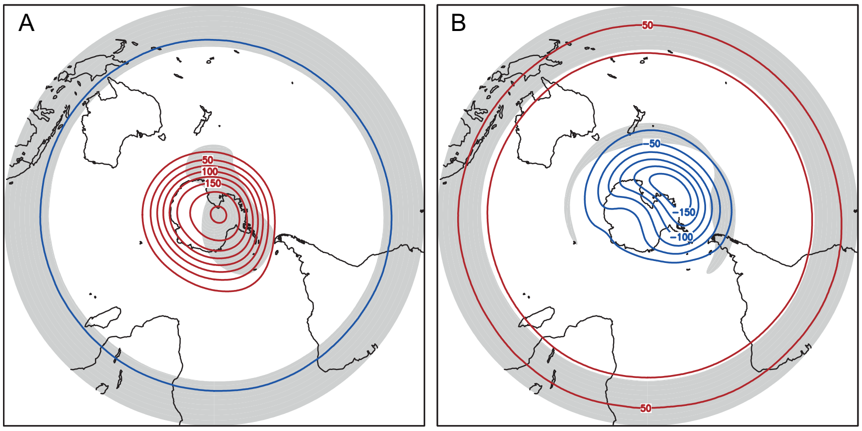

Fig. 7. Composite of geopotential height anomaly (m - filtered) for 30 hPa: (a) easterly QBO, and (b) westerly QBO. Contour interval of 25 m. Areas with 90% significance are shown in shaded (t-student test).

shall, 2019). There was also a significant positive correlation in the tropical stratosphere, i.e., positive (negative) SAM phase related to westerly (easterly) wind, although, at levels higher than 30hPa, this tropical region is dominated by the QBO. This result agreed with the contingency tables, indicating a relationship between positive (negative) SAM phase and westerly (easterly) QBO phase.

We also analyzed composites of geopotential height anomaly at 30 hPa for each QBO phase (Fig. 7). The period of these composites was identified from the CWT of the 30 hPa SAM index as no lag (1987-1990 and 2000-2004 - Fig. 2c). Table II shows the years used for each composite. Although there were few areas with statistical significance, the geopotential height anomaly composites displayed positive (negative) anomalies at polar (middle) latitudes for easterly QBO phase, indicating negative SAM phase. The westerly QBO composite presented the opposite pattern, suggesting a positive SAM phase. These composites confirmed the results from the contingency tables.

Although the scope of this work was not to investigate the mechanisms of the QBO-SAM relationship, a possible cause of this link is wave propagation to the stratosphere, which affects the QBO and the polar stratospheric vortex (e.g., Baldwin and Tung, 1994; Thompson and Wallace, 2000; Fogt and Marshall, 2019; Li et al., 2020). The maximum of this wave propagation from the troposphere to the stratosphere in the SH occurs in late spring (Charney and Drazin, 1961; Randel and Newman, 1998). To corroborate

Table I – Summary of results presented in the monthly contingency tables (Fig. 3-5). Months not included in the table are those that do not present the “oblique behavior”.

	Easterly QBO/negative SAM Westerly QBO/positive SAM	Easterly QBO/positive SAM Westerly QBO/negative SAM
700 hPa SAM index	January, May, June, July, September, October, November, December	-
200 hPa SAM index	January, June, July, August, September, October, November, December	April
30 hPa SAM index	January, May, July, August, September, October, November, December	March, April

this hypothesis, we analyzed the composites of meridional heat flux at 30 hPa for November (Fig. 8). The composites were built for the period described in Table II. Edmon et al. (1980) discussed the role Eliassen-Palm flux components to identify the direction and magnitude of the planetary wave propagation. The meridional heat flux is proportional to the Eliassen-Palm vertical component (Trenberth, 1991), and it can be used to measure the activity of the waves entering the stratosphere. Maximum negative values occurred at 60ºS, and there was almost no difference between QBO phases at this latitude (Fig. 8). However, at higher latitudes where the polar stratospheric vortex was located, the easterly QBO displayed stronger values, which suggested there was more wave propagation to the stratosphere in this phase, compared to westerly QBO. Li et al. (2020) also indicated stronger (weaker) upward wave propagation to the stratosphere with easterly (westerly) QBO and linked this to the polar stratospheric vortex. The wave develops in the troposphere and propagates vertically into the stratosphere along the jet core axis. The wave decelerates the stratospheric polar jet by depositing easterly momentum into the westerly stratospheric jet (Charney and Drazin, 1961; Edmon et al., 1980; Randel and Newman, 1998; Kuroda and Yamazaki, 2010). Figure 9 confirmed the stratospheric jet weakening in the easterly QBO composite. A weak (strong) stratospheric jet is associated with a negative (positive) SAM phase (Thomson and Wallace, 2000; Fogt and Marshall 2020). The results presented above confirmed the relationship between QBO and SAM and indicated upward wave propagation to the stratosphere at high latitudes as a possible mechanism.

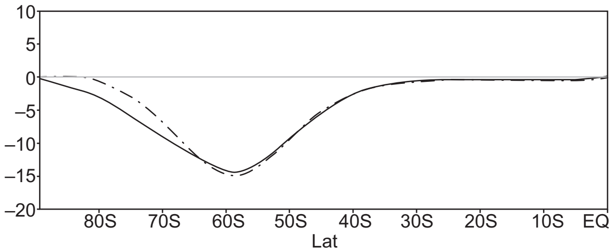

Fig. 8. Composite of zonal mean meridional heat flux (K ms^{-1}) for 30 hPa. Solid line: easterly QBO, and dot dashed line: westerly QBO.

4. Summary and conclusions

The SAM pattern influences climate over the SH (e.g., Gillett et al., 2006; Silvestri and Vera, 2003, 2009; Vasconcellos et al., 2019). However, the varia-

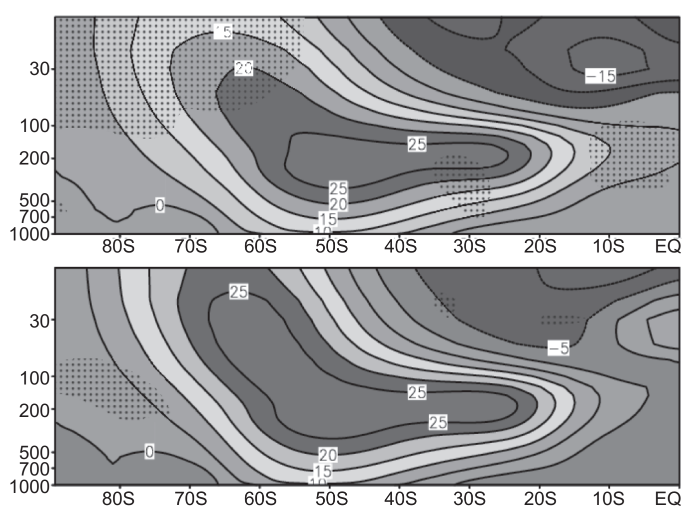

Fig. 9. Latitude versus pressure profile of composite of zonal mean zonal wind (ms^{-1} - filtered): (top) easterly QBO, and (bottom) westerly QBO. Areas with 90% significance are dotted (t-student test).

bility of this mode is an active area of research. The influence of lower frequency modes on SAM is a path to better knowledge about its variability. While prior works have studied the relationship between QBO and NAM, few studies showed an association between QBO and SAM. This study confirmed that this relationship also occurs in the SH and investigated the variability associated with this relation.

CWT applied to SAM indices in the troposphere and stratosphere, showed power peaks for different bands, including around 2 years. In the stratosphere (30 hPa), the significantly higher power around the 2-year band was seen for the periods 1987-1990 and 2000-2004. This result indicated SAM index had variability at various scales, including two-years, possibly because of the QBO influence. The XWTs analysis between the QBO and SAM indices revealed significant common high power around the 2-year band for all the results obtained. However, this band showed lag variations between the QBO and SAM series over the analyzed period, including no lag., suggesting that the influence of the QBO on the SAM could happen simultaneously and several months later.

Focusing on the QBO influence on the SAM with no lag, we built monthly contingency tables between the QBO index and the SAM indices at different levels (30, 200, and 700 hPa - filtered, without lags). These results showed that, for most of the months, during the QBO easterly phase, there was a higher occurrence of the negative SAM phase. Alternatively, during the QBO westerly phase, there was a higher occurrence of the positive SAM phase. This relationship between QBO and SAM is consistent with previous results (e.g., Roy and Haigh, 2011; Anstey and Shepherd, 2014). Nevertheless, this study showed that this relationship is not valid for all months. Composite analyses for each QBO phase (period described at 30 hPa SAM`s CWT) were performed for the SAM active period (November), confirming the results from the contingency tables. More (less) upward wave propagation into the stratosphere at high latitudes for easterly (westerly) QBO phase, weakening (strengthens) the stratospheric polar vortex, leading to negative SAM phase. These results agree with results by Fogt and Marshall (2020) and Li et al. (2020).

This study confirmed that there is a relationship between the QBO and the SAM. It also showed various lags between these two patterns, suggesting that this relation has a complex interaction. Nevertheless, analyses without lag indicated that the negative (positive) SAM phase was more frequent for easterly (westerly) QBO in most (but not all) months, including the SAM active period (November). It lies beyond the scope of this study to determine the physical mechanisms associated with the influence of QBO on SAM. However, some additional analysis indicated that the upward wave propagation to the stratosphere for each QBO phase modifies the stratospheric jet and, consequently, the SAM phase. This study provides insight on SAM variability and its predictability. Further research is ongoing and will be presented in future publications.

Acknowledgments

This work has been supported by Universal Project (420731/2018-0) and by Institutional Scientific Initiation Scholarship Program of National Institute of Space Research (PIBIC/INPE), both funding by National Council for Scientific and Technological Development (CNPq).

References

Anstey JA, Shepherd TG. 2014. High-latitude influence of the quasi-biennial oscillation. Quarterly Journal of the Royal Meteorological Society 140: 1-21. https://doi.org/10.1002/qj.2132

Baldwin MP, Dunkerton TJ. 1999. Propagation of the Arctic Oscillation from the stratosphere to the troposphere. Journal of Geophysical Research 104: 30937-30946. https://doi.org/10.1029/1999JD900445

Baldwin MP, Gray LJ, Dunkerton TJ, Hamilton K, Haynes PH, Randel WJ, Holton JR, Alexander MJ, Hirota I, Horinouchi T, Jones DBA, Kinnersley JS, Marquardt C, Sato K, Takahashi M. 2001. The quasi-biennial oscillation. Reviews of Geophysics 39: 179- 229. https://doi.org/10.1029/1999RG000073

Baldwin MP, Tung KK. 1994. Extra-tropical QBO signals in angular momentum and wave forcing. Geophysical research letters 21: 2717-2720. https://doi.org/10.1029/94GL02119

Blázquez J, Solman SA. 2017. Interannual variability of the frontal activity in the Southern Hemisphere: relationship with atmospheric circulation and precipitation over southern South America. Climate Dynamics 48: 2569-2579. https://doi.org/10.1007/s00382-016-3223-3

Carvalho LMV, Jones C, Ambrizzi T. 2005. Opposite phases of the Antarctic Oscillation and relationships with intraseasonal to interannual activity in the tropics during the austral summer. Journal of Climate 18: 702-718. https://doi.org/10.1175/JCLI-3284.1

Charney JG, Drazin PG. 1961. Propagation of planetary-scale disturbances from the lower into the upper atmosphere. Journal of Geophysical Research 66: 83-109. https://doi.org/10.1029/JZ066i001p00083

Chatfield C. 2004. The Analysis of Time Series: An introduction. Boca Raton, FL: Chapman and Hall/CRC.

Coughlin K, Tung, KK. 2001. QBO signal found at the extratropical surface through northern annular modes. Geophysical Research Letters 28: 4563-4566. https://doi.org/10.1029/2001GL013565

Dee DP, Uppala SM, Simmons AJ, Berrisford P, Poli P, Kobayashi S, Andrae U, Balmaseda MA, Balsamo G, Bauer P, Bechtold P, Beljaars ACM, van de Berg L, Bidlot J, Bormann N, Delsol C, Dragani R, Fuentes M, Geer AJ, Haimberger L, Healy SB, Hersbach H, Hólm EV, Isaksen L, Kållberg P, Köhler M, Matricardi M, McNally AP, Monge-Sanz BM, Morcrette JJ, Park BK, Peubey C, de Rosnay P, Tavolato C, Thépaut JN, Vitart F. 2011. The ERA-Interim reanalysis: configuration and performance of the data assimilation system. Quarterly Journal of the Royal Meteorological Society 137: 553-597. https://doi.org/10.1002/qj.828

Daubechies I. 1990. The wavelet transform time-frequency localization and signal analysis. IEEE Transactions on Information Theory 36: 961-1004. https://doi.org/10.1109/18.57199

Dunkerton TJ. 1990. Annual variation of deseasonalized mean flow acceleration in the equatorial lower stratosphere. Journal of the Meteorological Society of Japan 68: 499-508. https://doi.org/10.2151/jmsj1965.68.4_499

Ebdon RA. 1975. The quasi-biennial oscillation and its association with tropospheric circulation patterns. Meteorological Magazine 104: 282-297.

Edmon HJ, Hoskins BJ, Mcintyre ME. 1980. Eliassen-palm cross section for the troposphere. Journal of Atmospheric Sciences 37: 2600-2616. https://doi.org/10.1175/1520-0469(1980)037<2600:EPCSFT>2.0.CO;2

Fogt RL, Marshall, GJ. 2020. The Southern Annular Mode: Variability, trends, and climate impacts across the Southern Hemisphere. WIREs Climate Change 11: e652. https://doi.org/10.1002/wcc.652

Gillett NP, Kell TD, Jones PD. 2006. Regional climate impacts of the Southern Annular Mode. Geophysical Research Letters 33: L23704. https://doi.org/10.1029/2006GL027721

Gong D, Wang S. 1999. Definition of Antarctic Oscillation index. Geophysical Research Letters 26: 459–462. https://doi.org/10.1029/1999GL900003

Gray WM. 1984. Atlantic seasonal hurricane frequency. Part I: El Niño and 30 mb Quasi Biennial Oscillation influences. Monthly Weather Review 112: 1649-1668. https://doi.org/10.1175/1520-0493(1984)112<1649:ASHFPI>2.0.CO;2

Gray LJ, Anstey JA, Kawatani Y, Lu H, Osprey S, Schenzinger V. 2018. Surface impacts of the Quasi Biennial Oscillation. Atmospheric Chemistry and Physics 18: 8227-8247. https://doi.org/10.5194/acp-18-8227-2018

Grinsted A, Moore JC, Jevrejeva S. 2004. Application of the cross wavelet transform and wavelet coherence to geophysical time series. Nonlinear Processes in Geophysics 11: 561-566. https://doi.org/10.5194/npg-11-561-2004

Holton JR, Tan H. 1980. The influence of the equatorial Quasi-Biennial Oscillation on the global circulation at 50 mb. Journal of the Atmospheric Sciences 37: 2200-2208. https://doi.org/10.1175/1520-0469(1980)037<2200:-TIOTEQ>2.0.CO;2

Holton JR, Tan H. 1982. The Quasi-Biennial Oscillation in the Northern Hemisphere lower stratosphere. Journal of the Meteorological Society of Japan 60: 140-148. https://doi.org/10.2151/jmsj1965.60.1_140

Jury MR, Mc Queen C, Levey K. 1994. SOI and QBO signals in the African region. Theoretical and Applied Climatology 50: 103-115. https://doi.org/10.1007/BF00864907

Kodera K, Koide H. 1997. Spatial and seasonal characteristics of recent decadal trends in the northern hemispheric troposphere and stratosphere. Journal of Geophysical Research 102: 19443-19447. https://doi.org/10.1029/97JD01270

Kuroda Y, Yamazaki K. 2010. Influence of the solar cycle and QBO modulation on the Southern Annular Mode. Geophysical Research Letters 37: L12703. https://doi.org/10.1029/2010GL043252

Labat, D. 2005. Recent advances in wavelet analyses: Part 1. A review of concepts. Journal of Hydrology

314: 275 – 288, 2005. https://doi.org/10.1016/j.jhydrol.2005.04.003

Li Z., Chu X, Harvey VL, Jandreau J, Lu X, Yu Z, Zhao J, Fong W. 2020. First lidar observations of Quasi-Biennial Oscillation-induced interannual variations of gravity wave potential energy density at McMurdo via a modulation of the Antarctic polar vortex. Journal of Geophysical Research 125: 22p. https://doi.org/10.1029/2020JD032866

Mukherjee BK, Indira K, Reddy RS, Murty BVR. 1985. Quasi-Biennial Oscillation in Stratospheric Zonal Wind and Indian Summer Monsoon. Monthly weather review 113: 1421-1424. https://doi.org/10.1175/1520-0493(1985)113<1421:QBOISZ>2.0.CO;2

Naoe H, Shibata K. 2010. Equatorial quasi-biennial oscillation influence on northern winter extratropical circulation. Journal of Geophysical Research 115: D19102. https://doi.org/10.1029/2009JD012952

Naujokat B. 1986. An update of the observed quasi-biennial oscillation of the stratospheric winds over the tropics. Journal of the Atmospheric Sciences 43: 1873-1877. https://doi.org/10.1175/1520-0469(1986)043<1873:AUOTOQ>2.0.CO;2

Peings Y, Brun E, Mauvais V, Douville H. 2013. How stationary is the relationship between Siberian snow and Arctic Oscillation over the 20th century? Geophysical Research Letters 40: 183-188. https://doi.org/10.1029/2012GL054083

Reboita MS, Ambrizzi T, Rocha RP. 2009. Relationship between the southern annular mode and southern hemisphere atmospheric systems. Revista Brasileira de Meteorologia 24: 48-55. https://dx.doi.org/10.1590/S0102-77862009000100005

Reed RJ, Campbell WJ, Rasmussen LA, Rogers DG. 1961. Evidence of a downward-propagating, annual wind reversal in the equatorial stratosphere. Journal of Geophysical Research 66: 813-818. https://doi.org/10.1029/JZ066i003p00813

Randel WJ, Newman PA. 1998. The stratosphere in the southern hemisphere. In: Karoly DJ, Vincent DG (eds) Meteorology of the Southern Hemisphere. Meteorological Monographs, American Meteorological Society, Boston, MA. https://doi.org/10.1007/978-1-935704-10-2_9

Rosso FV, Boiaski NT, Ferraz SET, Robles TC. 2018. Influence of the Antarctic Oscillation on the South Atlantic Convergence Zone. Atmosphere 9: 431. https://doi.org/10.3390/atmos9110431

Roy I, Haigh JD. 2011. The influence of solar variability and the quasi-biennial oscillation on sea level pressure. Atmospheric Chemistry and Physics 11: 11679-11687. https://doi.org/10.5194/acp-11-11679-2011

Ruzmaikin A, Feynman J, Jiang X, Yung YL. 2005. Extratropical signature of the quasi-biennial oscillation. Journal of Geophysical Research 110: D11111. https://doi.org/10.1029/2004JD005382

Scaife AA, Athanassiadou M, Andrews M, Arribas A, Baldwin M, Dunstone N, Knight J, MacLachlan C, Manzini E, Müller WA, Pohlmann H, Smith D, Stockdale T, Williams A. 2014. Predictability of the quasi-biennial oscillation and its northern winter teleconnection on seasonal to decadal timescales. Geophysical Research Letters 41: 1752 - 1758. https://doi.org/10.1002/2013GL059160

Schenzinger V, Osprey SM. 2015. Interpreting the nature of Northern and Southern Annular Mode variability in CMIP5 Models. Journal of Geophysical Research 120: 11,203-11,214. https://doi.org/10.1002/2014JD022989

Silvestri GE, Vera CS. 2003. Antarctic oscillation signal on precipitation anomalies over southeastern South America. Geophysical Research Letters 30: 2115-2118. https://doi.org/10.1029/2003GL018277

Silvestri GE, Vera CS. 2009. Nonstationary impacts of the southern annular mode on southern hemisphere climate. Journal of Climate 22: 6142-6148. https://doi.org/10.1175/2009JCLI3036.1

Thompson DW, Wallace JM. 2000. Annular modes in the extratropical circulation. Part I: Month-to-month variability. Journal of climate 13: 1000-1016. https://doi.org/10.1175/1520-0442(2000)013<1000:AMITEC>2.0.CO;2

Trenberth KE. 1991. Storm Track in the Southern Hemisphere. Journal of the Atmospheric Sciences 48: 2159-2178. https://doi.org/10.1175/1520-0469(1991)048<2159:STITSH>2.0.CO;2

Torrence C, Compo GP. 1998. A practical guide to wavelet analysis. Bulletin of American Meteorological Society 79: 61-78. https://doi.org/10.1175/1520-0477(1998)079<0061:APGTWA>2.0.CO;2

Vasconcellos FC, Cavalcanti IFA. 2010. Extreme precipitation over Southeastern Brazil in the austral summer and relations with the Southern Hemisphere annular mode. Atmospheric Science Letters 11: 21-26. https://doi.org/10.1002/asl.247

Vasconcellos FC, Pizzochero RM, Cavalcanti IFA. 2019. Month-to-month impacts of Southern Annular Mode over South America climate. Anuário de Instituto de Geociências da UFRJ 42: 783-792. http://dx.doi.org/10.11137/2019_1_783_792

Wilks DS. 2006. Statistical Methods in the Atmospheric Sciences. San Diego, CA: Academic Press (International Geophysics Series, v. 91).

Atmósfera 35(2), 237-271 (2022)
https://doi.org/10.20937/ATM.52890

CONTENTS

Wavelet coherence between ENSO indices and two precipitation databases for the Andes region of Colombia

Diana DÍAZ[1]* and Nancy VILLEGAS[2]

[1] *Departamento de Ciencias Básicas y Modelado, Facultad de Ciencias e Ingeniería, Universidad Jorge Tadeo Lozano, Carrera 4 # 22–61, Bogotá, Colombia.*
[2] *Departamento de Geociencias, Facultad de Ciencias, Universidad Nacional de Colombia, Carrera 30 Calle 45–03, Bogotá, Colombia.*
*Corresponding author: dianac.diaz@utadeo.edu.co

Received: April 21, 2020, accepted: November 20, 2020

RESUMEN

La influencia de El Niño Oscilación del Sur (ENOS) en las variables hidrológicas de Colombia ha sido demostrada en diferentes estudios. La mayoría de las metodologías implementadas han identificado relaciones lineales y han asociado la fase cálida (fría) llamada El Niño (La Niña) con anomalías negativas (positivas) de precipitación y flujo en ríos. Uno de los impactos más adversos es la reducción del suministro de agua durante la fase cálida. El primer objetivo de este estudio es explorar las correlaciones no lineales entre ENOS y la precipitación y el segundo es identificar qué índices permitirían mejorar la predictibilidad de las variables hidroclimatológicas. El análisis de coherencia de ondeletas se realiza para series de tiempo de precipitación mensual e índices ENOS de 1981 a 2016. Los resultados muestran que los eventos ENOS influyen en la precipitación como períodos de déficit o exceso de lluvia. Además, la precipitación está organizada en bandas y las escalas de 2 a 8 años explican la mayor parte de su varianza. Los sectores más significativos son los que cubren los eventos de El Niño cuando los impactos sobre las precipitaciones tienden a ser mayores. En contraste, los sectores son más pequeños cuando ocurren episodios de La Niña. Los resultados también permitieron identificar que los índices Niño 3, Niño 3.4, ONI y BEST pueden ser buenos predictores para regiones específicas. La intercomparación de dos conjuntos de datos permite establecer la viabilidad de utilizar datos satelitales en regiones con escasa información, pero se reportan menos anomalías a partir de los datos satelitales. Si bien la estructura de coherencia es similar en ambos conjuntos de datos, para períodos entre 36 y 48 meses, hubo discrepancias de $\pi / 4$ en la diferencia de fase, es decir, entre 3 y 6 meses de diferencia en los rezagos calculados con cada base de datos.

ABSTRACT

The influence of El Niño Southern Oscillation (ENSO) on Colombia's hydrological variables has been shown in different studies. Most of the methodologies implemented have identified linear relationships and have associated the warm (cold) phase called El Niño (La Niña) with negative (positive) rainfall and streamflow anomalies. One of the most adverse impacts is the reduction in water supply during the warm phase. One aim of this study is to explore nonlinear correlations between ENSO and precipitation and the second is to identify which indices will enable improving the predictability of hydro-climatological variables. Wavelet coherence analysis is performed for monthly precipitation time series and ENSO indices from 1981–2016. Results show that ENSO events influence precipitation as periods of rainfall deficit or excess. Also, precipitation organized in the 2-8-year scales explain most of their variance. The most significant sectors are those that cover El Niño events when impacts on precipitation tend to be greater. In contrast, sectors are smaller when La Niña episodes occur. Results also allowed to identify that Niño 3, Niño 3.4, ONI, and BEST indices can be good predictors for specific regions. Intercomparison of two datasets allows to establish the feasibility of using satellite data in regions with scarce information, but fewer anomalies are reported from the satellite data. While the coherence structure is similar in both datasets, for periods between 36 and 48 months, there were discrepancies of π /4 in the phase difference, that is, between 3 and 6 months of difference in lags calculated with each database.

Keywords: Precipitation variability, climate ENSO indices, continuous wavelet transform, CHIRPS.

1. Introduction

The influence of large-scale climate oscillations on hydrological variables affects the natural water supply of a specific region (Ouachani et al., 2013; Nalley et al., 2016). A leading pattern of weather and inter-annual climate variability over Colombia is El Niño Southern Oscillation (ENSO) (Poveda and Mesa,1997). ENSO results from the ocean-atmosphere interaction that causes positive and negative anomalies of the sea surface temperature (SST) in the central and eastern tropical Pacific. The warm phase is known as El Niño, and the cold phase as La Niña and its effects are not universal in their timing, sign, or magnitude (Tedeschi et al., 2015).

For the case of Colombia, several studies through linear correlation have shown that ENSO strongly influences its hydroclimatology. El Niño has been related to negative rainfall and streamflow anomalies and La Niña to the opposite behavior. The strongest relation occurs from December to February and the weakest from March to May. Studies have also shown that the impact of ENSO on hydrological variables propagates from west to east and that north and central regions experience the most significant impact, while east and southeast regions are less affected (Poveda et al., 1997; 2006; 2011; Córdoba-Machado et al., 2015a; Córdoba-Machado et al., 2015b). El Niño is also associated with extreme events such as droughts, frosts, forest fires, and La Niña with torrential rains, floods, and landslides (Hoyos et al., 2013; Córdoba-Machado et al., 2015a). One of the most serious consequences of ENSO events is the shortage of drinking water, which causes human health problems and affects food production.

Although linear correlation methods revealed the connection between ENSO and climate variables, the linear coefficients obtained are usually low, a fact that requires the use of other methodologies such as spectral analysis to explore more characteristics of each of the series and its relationship with another series (Fu et al., 2012; Jiang et al., 2019).

Several studies have explored spectral analysis based on Fourier Transform (FT), Wavelet Transform (WT), or Hilbert-Huang transform (HHT), to improve knowledge of climate variability in Colombia at different time scales. For example, Poveda et al. (2002a) used FT and WT and found that El Niño diminished the diurnal rainfall cycle while La Niña intensifies it. Poveda et al. (2002b) implemented WT to identify changes in average monthly river flow during warm events. Arias and Poveda (2005) studied the space-time variability of rainfall in Colombia through Empirical Orthogonal Functions (EOF) and WT for monthly records; they found that the first EOF explains 90% of the variance associated with annual and semi-annual periodicities resulting from the meridional oscillation of the Intertropical Convergence Zone (ITCZ). The WT of this first EOF exhibits significant variance at 4-8 months and 8–16 months, whose relative importance varies with time. Rueda and Poveda (2006) found a significant coupling between ENSO and the annual advection cycle of low-level winds known as "Chocó Jet." Carmona and Poveda (2012 and 2014) explored FT, WC, and HHT to detect principal modes of hydroclimatic variability in Colombia; they also identified links between ENSO and precipitation, temperature, and river discharge. More recently, Restrepo et al. (2019) implemented HHT and WT to identify the contribution of low-frequency climatic–oceanic oscillations to streamflow variability in coastal rivers of the Sierra Nevada de Santa Marta (Colombia). All these studies have detected evidence of the ENSO–precipitation relation; however, they have also established that ENSO teleconnections have substantial heterogeneity at different spatio-temporal scales over Colombia. This heterogeneity has been attributed to several factors, such as the country's orography, geographical aspects like the proximity to the Pacific Ocean, the Caribbean Sea, and Amazonia. More specifically, links to the dynamics of the three main low-level jets (LLJ), the Caribbean LLJ, the Chocó LLJ, and

Orinoco LLJ, and also the Cross-Equatorial Flow (CEF). All of them co-occur and mutually influence one another, generating moisture advection anomalies during ENSO phases that are different for each region of the country (Poveda et al., 1997, 2006, Salas et al., 2020). Therefore, there is still a need to carry out studies to determine local ENSO influences in more detail (Sun et al., 2017; Restrepo et al., 2019).

Another method used to assess links between large-scale climate oscillations and local climate variability is coherence analysis (CA). CA applied the idea of time-varying coherence using time-frequency analysis methods like FT, HHT, or WT (Torrence and Compo, 2011; Massei and Fournier, 2012; Schulte et al., 2016; Restrepo et al., 2019). The Wavelet-based coherence (WC) and the HHT coherence (HHTC) are the most widely used time-varying coherence methods (Restrepo et al., 2019). WC was selected because previous results have shown that even though HHTC has higher time resolution and frequency resolution than WC under ideal conditions, the WC is more stable; further, it has been implemented and explored for climate teleconnection analysis with a proven performance (Zhang et al., 2004; Ouachani et al., 2013; Araghi et al., 2016; Nalley et al., 2016; Schulte et al., 2016, Restrepo et al., 2019).

WC can be used to identify the influence of large-scale climate indices on hydroclimatic variables in different regions. For example, Ouachani et al. (2013) applied WC to examine ENSO's influence on precipitation and streamflow variability in the Mediterranean region. Kenner et al. (2010), and Sharma and Srivastava (2016) analyzed the same variables for southeastern United States. Fu et al. (2012) and Nalley et al. (2016) implemented WC to analyze the combined influence of solar activity and other dominant large-scale oscillations on streamflow across southern Canada, and Araghi et al. (2016) utilized WC to study the influence of ENSO on precipitation variability in Iran. More recently WC has also been implemented to assess extreme precipitation events and their spatiotemporal variability (Jiang et al., 2019), to study the simultaneous influence of climate teleconnections at differing time-frequency scales on precipitation and streamflow (Nalley et al., 2019; Das et al., 2020).

Studies provide evidence of ENSO's influence on hydroclimatic variables in Colombia; the purpose now is to know in greater detail the nonlinear dynamics of this relationship and to improve forecasts, particularly in zones where impacts are significant and imply economic and life losses. Data from the Unidad Nacional para la Gestión del Riesgo de Desastres (National Unit for Disaster Risk Management -UNGRD) indicate that the economic losses of the last strong La Niña event (2010–2011) reached 6500 million dollars, equivalent to 5.7% of the gross domestic product during that time, and that an El Niño event of low to moderate intensity would cost more than 288 million dollars. The latest Estudio Nacional del Agua (National Water Study -ENA) also identified zones with increased risk of water shortage associated with climate variability (ENA 2018); between 300,000 and 500,000 people affected in those zones during El Niño 2015–2016 (UNGRD, 2016).

Moreover, around 70 % of the electric energy in Colombia is generated by hydropower plants, which depend on precipitation. Studies by Marengo and Espinoza, 2016 and Weng et al. (2020) indicate how El Niño linked with other anthropogenic causes, like deforestation, have magnified droughts and reduced river flows resulting in an energy crisis (Weng et al., 2020; Alves et al., 2017; Erfanian et al., 2017). For example, the 2015−2016 drought exceeded the severity of those associated with strong El Niño events 1982/1983 and 1997/1998 (Jiménez-Muñoz et al., 2016; Marengo et al., 2016). Research to understand these teleconnections can contribute to better energy planning. The methodology can also be applied to study other variables that support energy transition towards sustainability under climate change, offering security in the power supply.

Based on all the previous studies, the present paper evaluates nonlinear correlations of the ENSO-precipitation relationship, mainly over six regions where freshwater resources have been significantly reduced during the last El Niño events. Moreover, an attempt is made to identify which indices will enable improved predictability of hydroclimatological variables.

2. Methodology

2.1. Study area

The study area are six places in Colombia were the freshwater resources have been significantly reduced during the last El Niño events. Figure 1 displays the stations' location. Wavelet transform (WT) and the wavelet coherence (CW) was performed with data from the indices that represent the ENSO and with monthly precipitation series for the period 1981–2016.

2.2. ENSO Data

Nine climate indices were selected to represent ENSO and obtained from the National Oceanic and Atmospheric Administration (NOAA) Climate Prediction Center (CPC) and the NOAA Earth System Research Laboratory's Physical Sciences Division (PSD). The indices were Niño 1+2, Niño 3, Niño 3.4, Niño 4, ONI, SOI, BEST, ESPI, MEI. Table I presents a short description of these indices; a more detailed explanation of each index can be found in https://www.esrl.noaa.gov/psd/data/climateindices/list/.

The precipitation data were taken from two databases to compare results, the first from the Institute of Hydrology, Meteorology and Environmental Studies (IDEAM), and the second from the Climate Hazards Group InfraRed Precipitation (CHIRPS), which combines satellite with station data.

2.3. IDEAM Data

The Institute of Hydrology, Meteorology and Environmental Studies of Colombia (IDEAM) supplied the time series used for first analysis. This information corresponds to monthly precipitation series from six stations where there is a high probability of shortage during El Niño events (ENA 2019). Table II presents the rainfall stations' characteristics and Figures 2 and 3 show the time series used. Figure 2 also presents the ENSO events with the most signifi cant consequences registered, red box for El Niño,

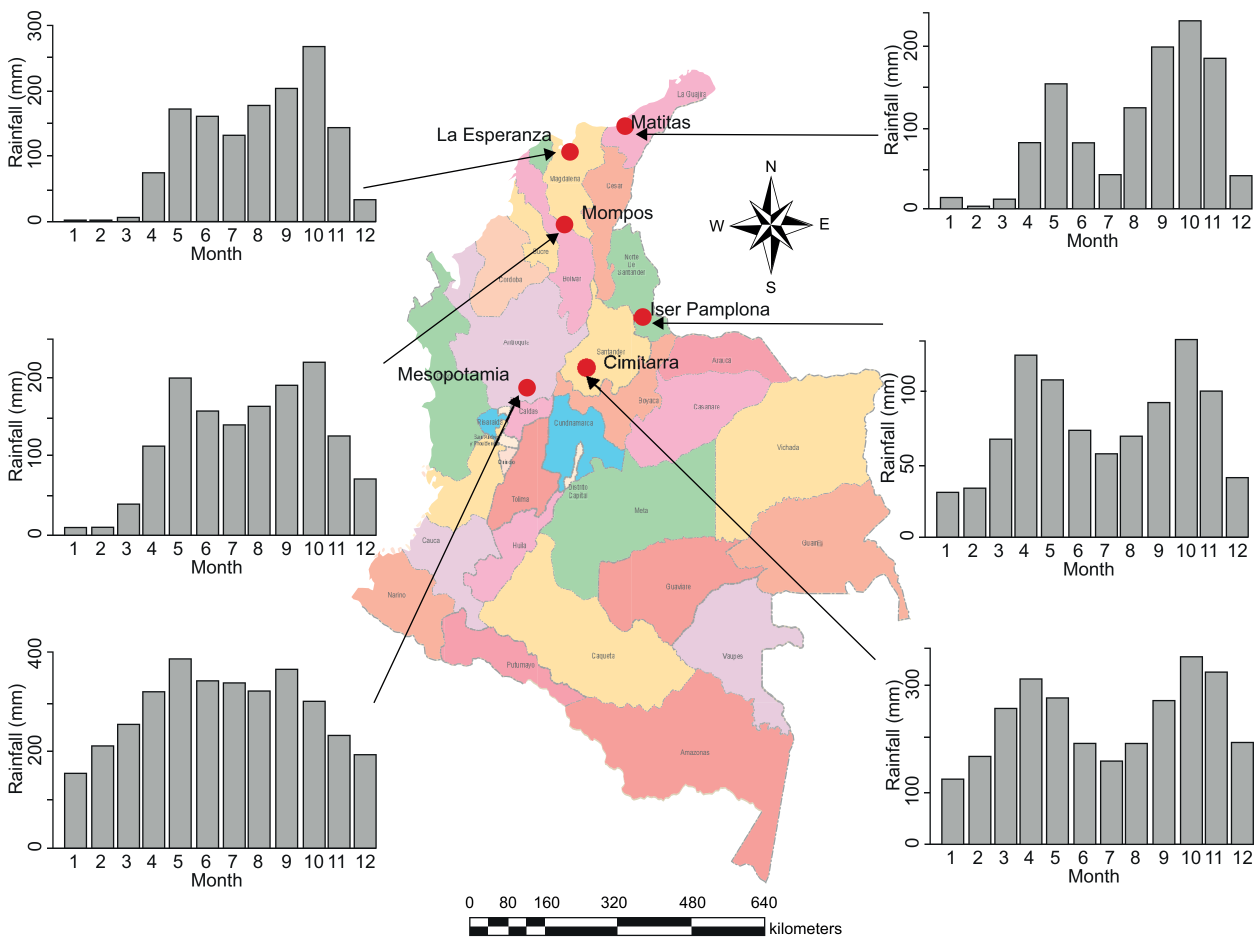

Fig. 1. Map of the location of rainfall stations used in the study, and their monthly climatology.

Table I. Indices used to represent ENSO

Niño 1+2	Extreme Eastern Tropical Pacific SST *(0-10S, 90W-80W). Data from CPC.
Niño 3	Eastern Tropical Pacific SST (5N-5S,150W-90W). Data from CPC.
Niño 3.4	East Central Tropical Pacific SST* (5N-5S)(170-120W). Data from CPC.
Niño 4	Central Tropical Pacific SST *(5N-5S) (160E-150W). Data from CPC.
ONI	Oceanic El Niño Index calculated as the three-month running mean of SST anomalies in the Niño 3.4 region. Climatology used for the anomaly was 1986-2015. Data from CPC.
SOI	Southern Oscillation Index calculated as the pressure difference between Tahiti and Darwin. Data from CPC.
BEST	Bivariate ENSO Timeseries Calculated from combining a standardized SOI and a standardized Niño 3.4 SST timeseries. The values are averaged for each month and then, 3-month running mean is applied to both time series. Data from PSD.
ESPI	ENSO precipitation index estimates the gradient of rainfall anomalies across the Pacific basin and ensures a good relationship with SST- and pressure-based indices. Data from Curtis and Adler (2000).
MEI	Multivariate ENSO Index Version 2, MEI is the time series of the leading combined Empirical Orthogonal Function (EOF) of five different variables (sea level pressure (SLP), sea surface temperature (SST), zonal and meridional components of the surface wind, and outgoing longwave radiation (OLR)) over the tropical Pacific basin (30 ºS-30 ºN and 100 ºE-70 ºW). Data from PSD.

Table II. Rainfall stations characteristics (Data from IDEAM)

Station Name	Region	Longitude (º)	Latitude (º)	Altitude (m)	Mean annual rainfall (mm)	Standard Deviation (mm)	Coefficient of variation
La Esperanza	Caribe	–74,30	10,74	25	1378	921.88	0.67
Matitas	Sierra Nevada de Santa Marta	–73,03	11,26	20	1171	468	0.39
Mompós	Sinú San Jorge–Nechi	–74,43	9,26	20	1461	361	0.24
Mesopotamia	Cuenca del alto Cauca	–75,31	5,88	2314	3445	651	0.19
Cimitarra	Cuenca Medio Cauca y Alto Nechi	–73,95	6,30	300	2805	671	0.24
Iser Pamplona	Cuenca del Catatumbo	–72,64	7,37	2340	925	243	0.26

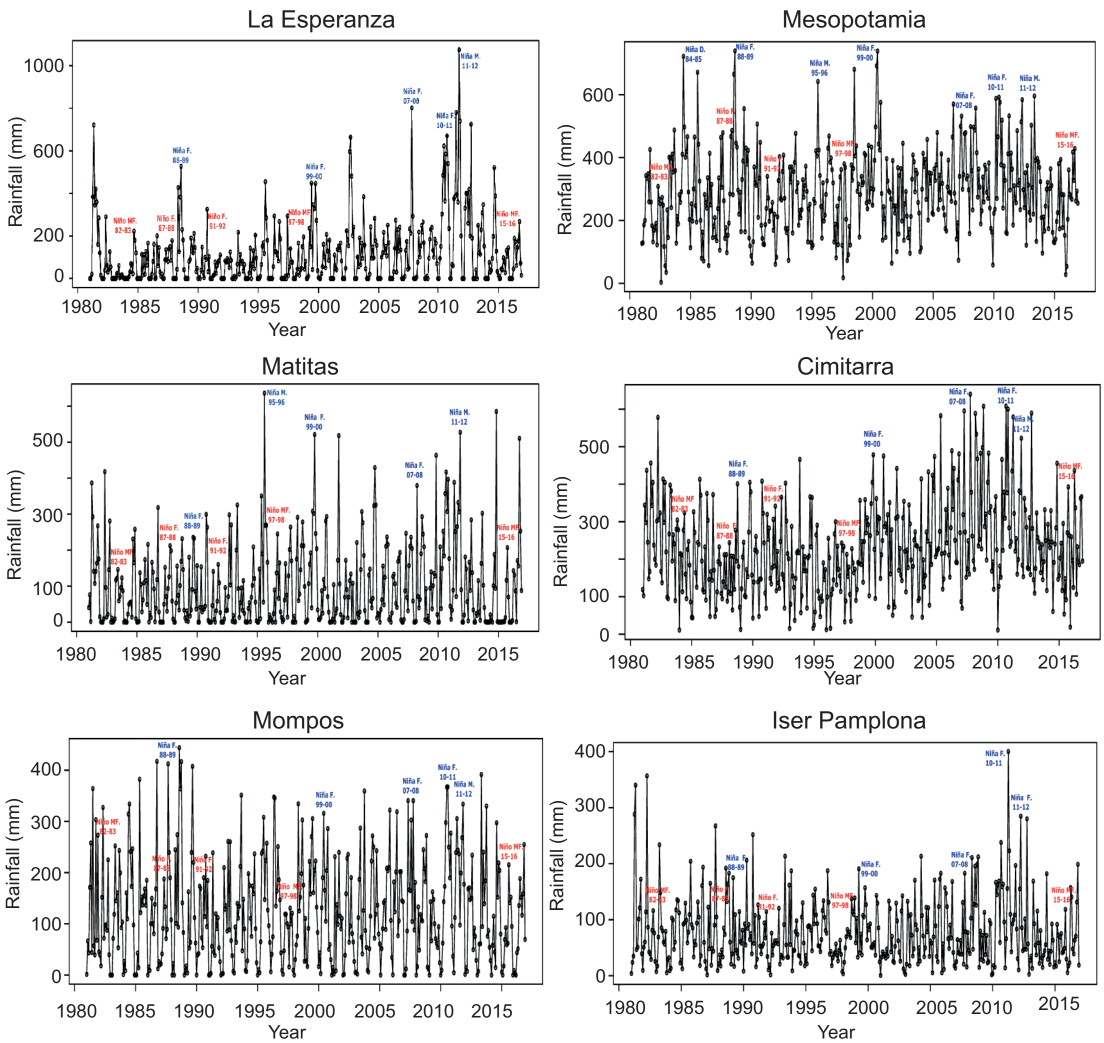

Fig. 2. Time series of the mean monthly rainfall data from IDEAM. The graphs indicate El Niño and La Niña events that have most affected precipitation levels. Red box for El Niño, and blue for La Niña episodes.

and blue for La Niña episodes. Figure 3 presents the series of standardized anomalies for each station, which were calculated by dividing anomalies by the climatological standard deviation, and anomalies were determined by subtracting climatological values from data. Figure 3 provides more information about the magnitude of the anomalies without the influence of dispersion and helps to identify variability in recent years.

The methodology to calculate the anomalies can affect the results, as mentioned by Salas et al. (2020). However, other methods for calculating anomalies such as the F-filtering of the annual cycle by moving average, the annual cycle extracted by the singular spectrum, were explored, and the spectra obtained were not pretty different. However, this affirmation is qualitative and could be contrasted with a sensitivity analysis in further work.

2.4 CHIRPS Data

The U.S. Geological Survey (USGS) and the University of California, Santa Barbara (UCSB) created and supplied a public precipitation database called Climate Hazards Group InfraRed Precipitation (CHIRPS) available since 2014. CHIRPS data is available over land from 1981 to the present, with spatial resolution

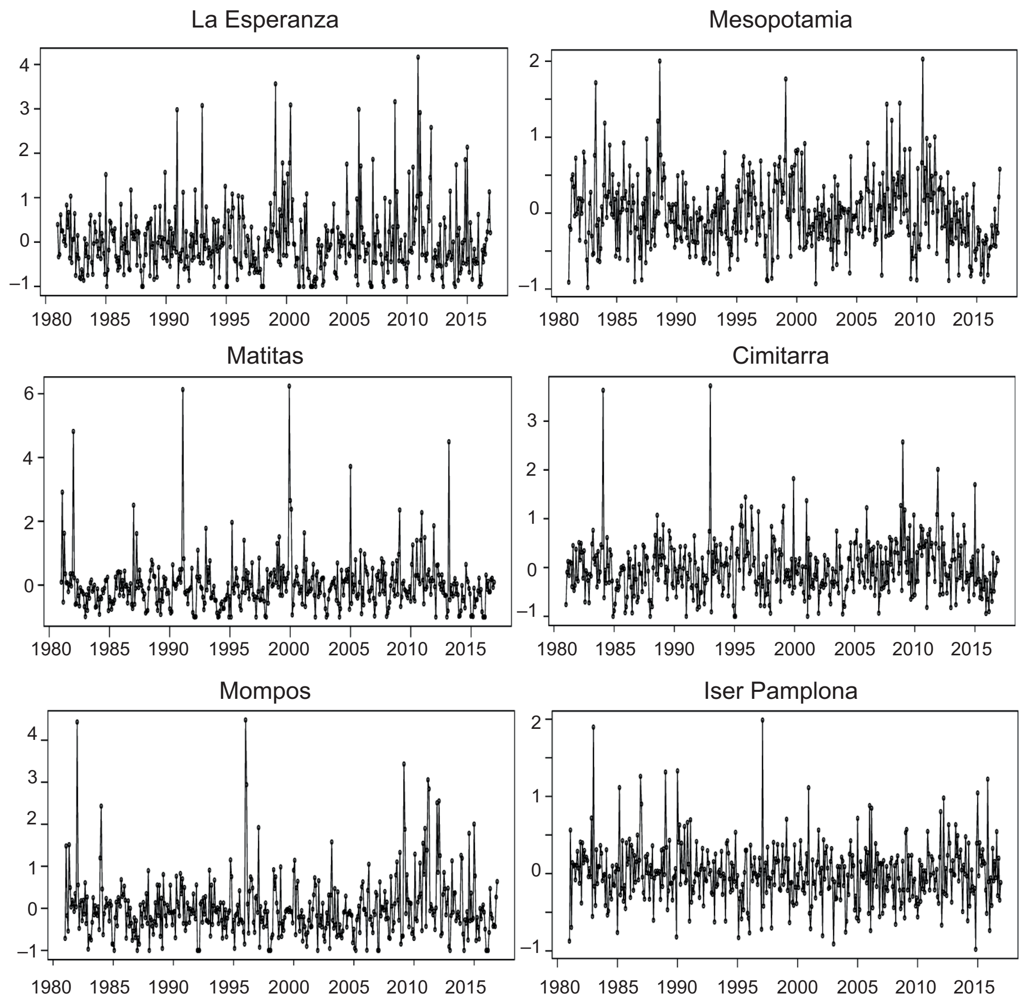

Fig. 3. Rainfall standardized anomalies from IDEAM data.

of 0.05º, from 50 ºS to 50 ºN for all longitudes. The temporal resolution provided is days, pentads, months, decades, and years. Monthly information was selected for the present case. CHIRPS was created with data from CHPClim (Climate Hazards Precipitation Climatology), Geostationary thermal infrared (IR), TRMM (Tropical Rainfall Measuring Mission, NOAA Climate Prediction System (CFSv2) atmospheric model of precipitation fields; and in situ observations of precipitation obtained from various meteorological services (Funk et al., 2015; Salas et al., 2020). In situ data for Colombia was provided by IDEAM and therefore, IDEAM and CHIRPS datasets are not so different, in fact CHIRPS has been validated for Colombia and this allows it to be use in places where there is no information (Urrea et al., 2016; Pedraza and Serna, 2018). The purpose of using both datasets (IDEAM and CHIRPS) is to compare whether the results obtained are similar and to verify if, for studies evaluating non-linear relationships, it may also be appropriate to use CHIRPS in those places without in-situ data. The precipitation time series from CHIRPS were taken from coordinates close to those of the six IDEAM stations. Table III presents the rainfall data from CHIRPS close to the in-situ stations, and Figures 4 y 5 show the time series anomalies created in the same way as with IDEAM data.

Tables II and III and Figures 2 to 5 show that although the coordinates used with both databases were as close as possible, there are several differences

Table III. Rainfall stations characteristics (Data from CHIRPS)

Station Name	Region	Longitude (º)	Latitude (º)	Mean annual rainfall (mm)	Standard Deviation (mm)	Coefficient of variation
CHIRPS 1	Caribe	–74,25	10,72	1095	200	0.18
CHIRPS 2	Sierra Nevada de Santa Marta	–73,1	11,32	994	326	0.34
CHIRPS 3	Sinú San Jorge–Nechi	–74,45	9,22	1452	325	0.22
CHIRPS 4	Cuenca del alto Cauca	–75,5	5,82	2376	378	0.16
CHIRPS 5	Cuenca Medio Cauca y Alto Nechi	–73,7	6,22	2933	252	0.085
CHIRPS 6	Cuenca del Catatumbo	–72,75	7,32	966	141	0.14

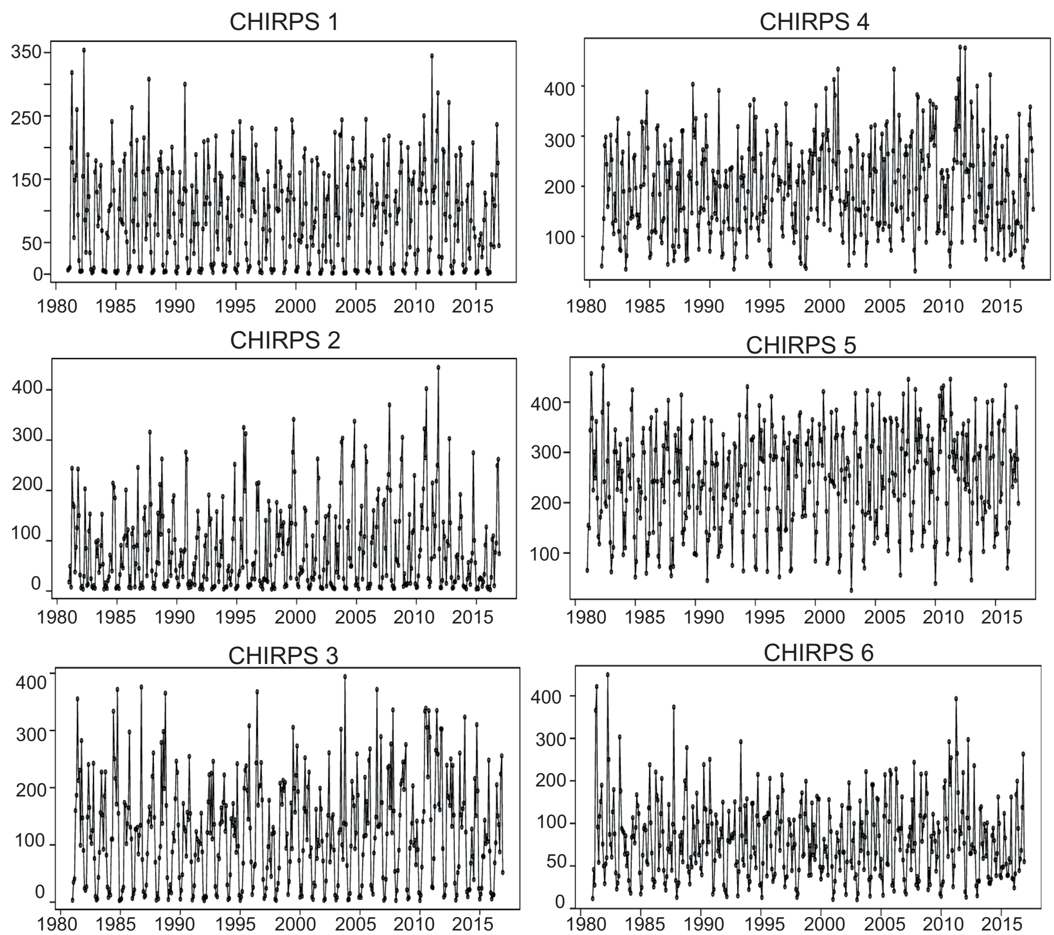

Fig. 4. Time series of the mean monthly rainfall data from CHIRPS.

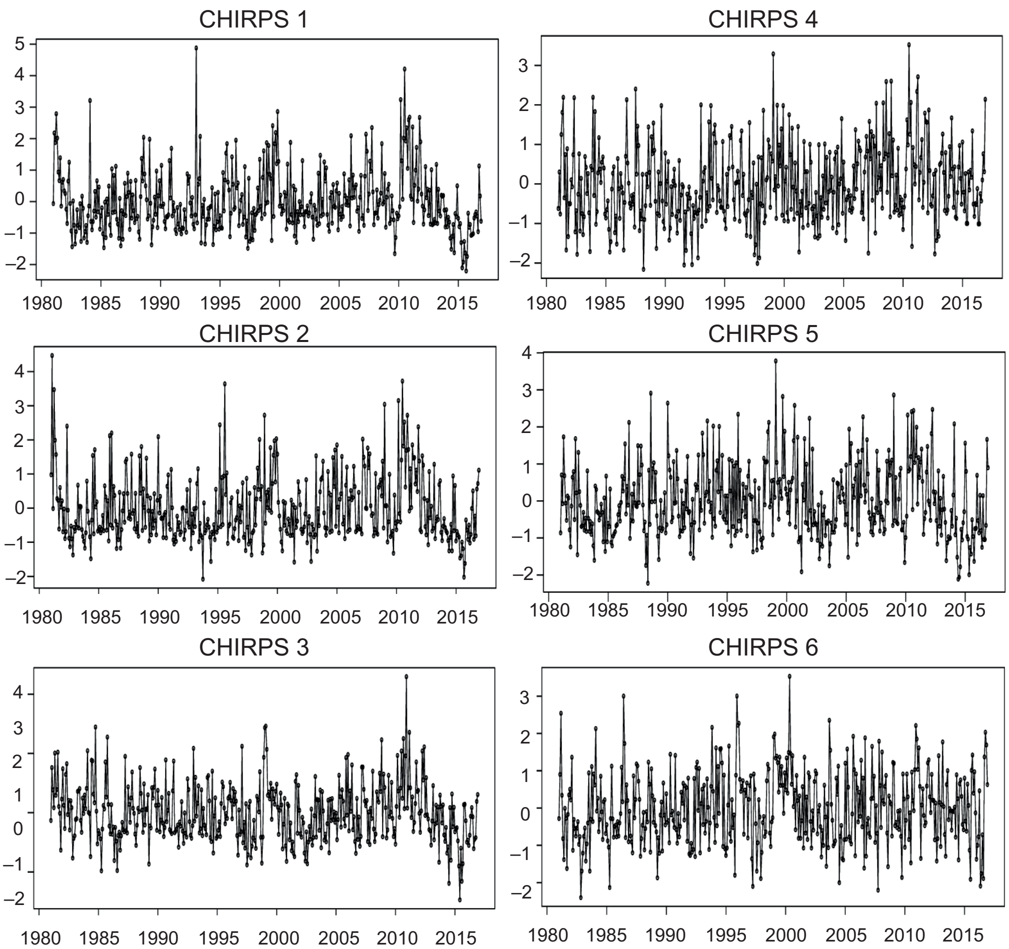

Fig. 5. Time series of standardized rainfall anomalies from CH.

between them; for example, the values of the mean annual rainfall vary, the standard deviation, the coefficient of variation, as well as the number of highs and lows associated with El Niño or La Niña events, respectively. In general, in the selected stations, the CHIRPS series tend to present fewer local minima or maxima; this implies that ENSO's influence may be more difficult to detect in these series, which is important to consider for this analysis.

2.5 Methods

2.5.1 Background of Wavelet transform (WT) computation

Continuous wavelet transform (WT) is a method to analyze the frequency and phase variations across time in a signal at several scales simultaneously (Torrence and Compo, 2011; Massei and Fournier, 2012; Schulte et al., 2016; Restrepo et al., 2019). The transform is defined as the convolution of the time series x_t with a set of "daughter" wavelets Ψ $(t - \tau/s)$ which are generated by the "mother" wavelet $\Psi(t)$ by translation in time by τ and scaling by s:

$$T_x(\tau, s) = \sum_t x_t \frac{1}{\sqrt{s}} \Psi^* \left(\frac{t-\tau}{s}\right) \quad (1)$$

The symbol * represents the complex conjugate. The "mother" wave Ψ implemented in this case is a Morlet wavelet:

$$\Psi(\mathrm{t}) = \pi^{-1/4} e^{i\omega t}\, e^{-t^{2}/2} \quad (2)$$

The angular frequency is set to six to make the Morlet wavelet approximately analytic; therefore, the period is 2π/6. The position of Ψ $(t - \tau/s)$ in the time domain is given by being shifted a dt. The value of s determines wavelet coverage of x_t in the time-frequency (or time-scale) domain, the minimum ($s_{mín}$) and maximun (s_{max}) scale are the minimum and maximum values of s respectively (Torrence and Compo, 2011; Nalley et al., 2016, 2019).

There are multiple options to select the mother wave however, previous research about the time–frequency evolutions of hydroclimatic series have shown that Morlet is better than others (e.g. Mexican Hat, Haar and others). The reasons for preferring Morlet are: 1. Frequency resolution is better; 2. Detection and localization of scale is improved; 3. Morlet detects peaks and valleys like the others and splits the wavelet into its real and imaginary parts. The real part describes oscillatory time series characteristics. The imaginary part conserves the phase information that is requisite when calculating the coherence wavelet with another time series, which is the main purpose of this work (Biswas and Si, 2011; Kravchenko et al., 2011).

The amplitude A of each periodic component found in x_t and how it evolves with time is obtained by calculating:

$$A_x(\tau, s) = \frac{1}{s^{1/2}} |T_x(\tau, s)| \tag{3}$$

This rectified version avoids the underestimate of high-frequency events. The square of the amplitude gives information about time-frequency wavelet energy density $P_x(\tau, s)$ or wavelet power spectrum:

$$P_x(\tau, s) = \frac{1}{s} |T_x(\tau, s)|^2 \tag{4}$$

More detailed information of Eqns. (1) to (4) is presented in Torrence and Compo (2011), Nalley et al. (2016), and Restrepo et al. (2019).

The wavelet power spectrum is what allows the visualization of the frequency variation across time at different scales simultaneously. To calculate the wavelet transform it is necessary to consider the edge effect, which appears because the wavelet used to compute the CWT on non-cyclic data is not fully localized in time and frequency. Edge effects are overcome by padding the data with zeros; the prurpose is to complete the length of the time series up to the next scale. The edge effect is shown in the wavelet power spectrum as a concave-up shaped area called the cone of influence COI. The analysis of the wavelet transform power spectra must be limited to areas outside the COI.

The CWT also allows analyzing its phase changes. These variations in the displacements concerning a particular origin are given by the instantaneous wavelet phase, represented as:

$$\Phi(\tau, s) = Arg(T_x(\tau, s)) = \tan^{-1} \frac{\mathrm{Im}(Tx(\tau, s))}{\mathrm{Re}(Tx(\tau, s))} \tag{5}$$

Equation (5) is essential to study the nonlinear ENSO-precipitation relationship, which will be explored through the wavelet-based-coherence explained below.

2.5.2. Wavelet Coherence

The wavelet-based coherence (WC) is the method selected to compare the ENSO indices with the monthly precipitation time series. WC evaluates the frequency and phase synchronization among signals (Nalley et al., 2019; Das et al., 2020). WC is based on cross-wavelet analysis concepts; according to Veleda et al. (2012), the cross-wavelet transform is:

$$T_{x,y}(\tau, s) = \frac{1}{s} T_x(\tau, s) \cdot T_y^*(\tau, s) \tag{6}$$

where $T_x(\tau, s)$ and $T_y(\tau, s)$ acording with equation (1), are:

$$T_x(\tau, s) = \sum_t x_t \frac{1}{\sqrt{s}} \Psi * \left(\frac{t-\tau}{s}\right) \tag{7}$$

$$T_y(\tau, s) = \sum_t y_t \frac{1}{\sqrt{s}} \Psi * \left(\frac{t-\tau}{s}\right) \tag{8}$$

The module of (6) is the cross-wavelet energy density and produces the cross-wavelet power spectrum useful to compare the two series:

$$P_{x,y}(\tau, s) = |T_{x,y}(\tau, s)| \tag{9}$$

The cross-wavelet is the covariance analog, but it depends on the unit of measurement of the series, defining wavelet coherency avoids an erroneous interpretation of the results (Torrence and Compo, 2011, Nalley et al., 2019; Das et al., 2020) and is defined as:

$$C(x_t, y_t) = \frac{sT_{x,y}}{\sqrt{sP_x sP_y}} \tag{10}$$

P_x and P_y are the wavelet power of each series defined as:

$$P_x(\tau, s) = \frac{1}{s}\,|T_x(\tau, s)|^2 \tag{11}$$

$$P_y(\tau, s) = \frac{1}{s}\,|T_y(\tau, s)|^2 \tag{12}$$

The letter s that precedes each amount indicates that these values should be smoothed. The wavelet coherency is an analogous concept to the classical correlation (Torrence and Compo, 2011, Nalley et al., 2019; Das et al., 2020); then, in this context the wavelet coherence is defined as the analogous to the correlation coefficient:

$$C^2_{x,y}(x_t, y_t) = \frac{|sT_{x,y}|^2}{sP_x sP_y} \tag{13}$$

The value of the coefficient $C^2_{x,y}$ (x_t, y_t) varies between 0 and 1, where 1 would indicate that the covariance between the series compared is maximum and 0 that there is no relationship.

To obtain information about the phase synchronization in terms of the instantaneous or local phase, we use the phase difference:

$$\Phi_x(\tau, s) - \Phi_y(\tau, s) = Arg\,(T_{x,y}(\tau, s)) = \tan^{-1}\left(\frac{\mathrm{Im}(T_{x,y}(\tau, s))}{\mathrm{Re}(T_{x,y}(\tau, s))}\right) \tag{14}$$

where ϕ_x (τ,s) and ϕ_y (τ,s), following Eqn. (5), are the individual phases of each signal. If phase difference has an absolute value less (greater) than $\pi/2$ it means that series move in phase (anti-phase), the sign of the phase difference indicates which signal leads the other.

The wavelet coherence and phase difference results are displayed in a spectrum in a similar way to wavelet power spectrum. Here $C^2_{x,y}$ (x_t,y_t) is represented by colors and $\phi_x(\tau, s) - \phi_y(\tau, s)$ by arrows . An in-phase relationship is indicated by arrows that point straight to the right, and anti-phase relation is indicated by arrows pointing straight to the left. Other cases show a lead/lag relationship, when a ENSO index led the precipitation response (Nalley et al., 2016). Arrows are only plotted if $C^2_{x,y}$ (x_t,y_t) >0.5, Table AI in Apendix A helps to better interpretate the direction of the arrows.

To interpret the phase difference between two signals, it helps to express the resulting angle, given in radians, in terms of units of time. The phase difference $\phi_x(\tau, s) - \phi_y(\tau, s)$ varies between $-\pi$ to $+\pi$; therefore, for a given period, the correspondence is made so that the duration of the entire period is equivalent to traversing all radians between $-\pi$ to $+\pi$. For example, for a 12-month scale or period, a difference of phase of $+\pi$ is equal to 6 months, one of $+\pi/2$ to 3 months; for a scale of 48 months, a phase difference of $+\pi$. would correspond to 24 months, one of $+\pi/2$ would be equivalent to 12 months and so on. Let us remember that the sign only refers to which signal is ahead of the other, as indicated in Table AI.

2.5.3. Statistical test of significance

The statistical significance was tested through simulation algorithms. The null hypothesis of "no periodicity" (for WT) or of "no joint periodicity" (for WC) can be assessed with a variety of alternatives to test against, for example, white or red noise, shuffling the time series, time series with a similar spectrum, AR, and ARIMA (Rösch and Schmidbauer, 2018). To determine the significance levels for wavelet spectra or wavelet coherence spectra it is necessary to choose a background spectrum to compare against. The theoretical white noise wavelet power spectra were chosen to derive and compare via Monte Carlo using 1000 simulations. A complete explanation is provided in Rösch and Schmidbauer (2018) and Torrence and Compo (2011).

All spectra obtained contain the cone of influence and contour lines that delimit the areas where results are statistically significant at the confidence interval > 95%, i.e., at 5% significance level.

The Waveletcomp library of R (Rösch and Schmidbauer, 2018) was used to compute the wavelet transforms and the coherence wavelet power spectra; Table AII in apendix A presents parameters used in the script.

2.6 Procedures

The wavelet coherence analysis, carried out with each database (IDEAM and CHIRPS), proceeded as follows:

1. The WT procedures were computed on monthly precipitation data from IDEAM to evaluate their time-frequency variability. Results are shown in Figure 6.

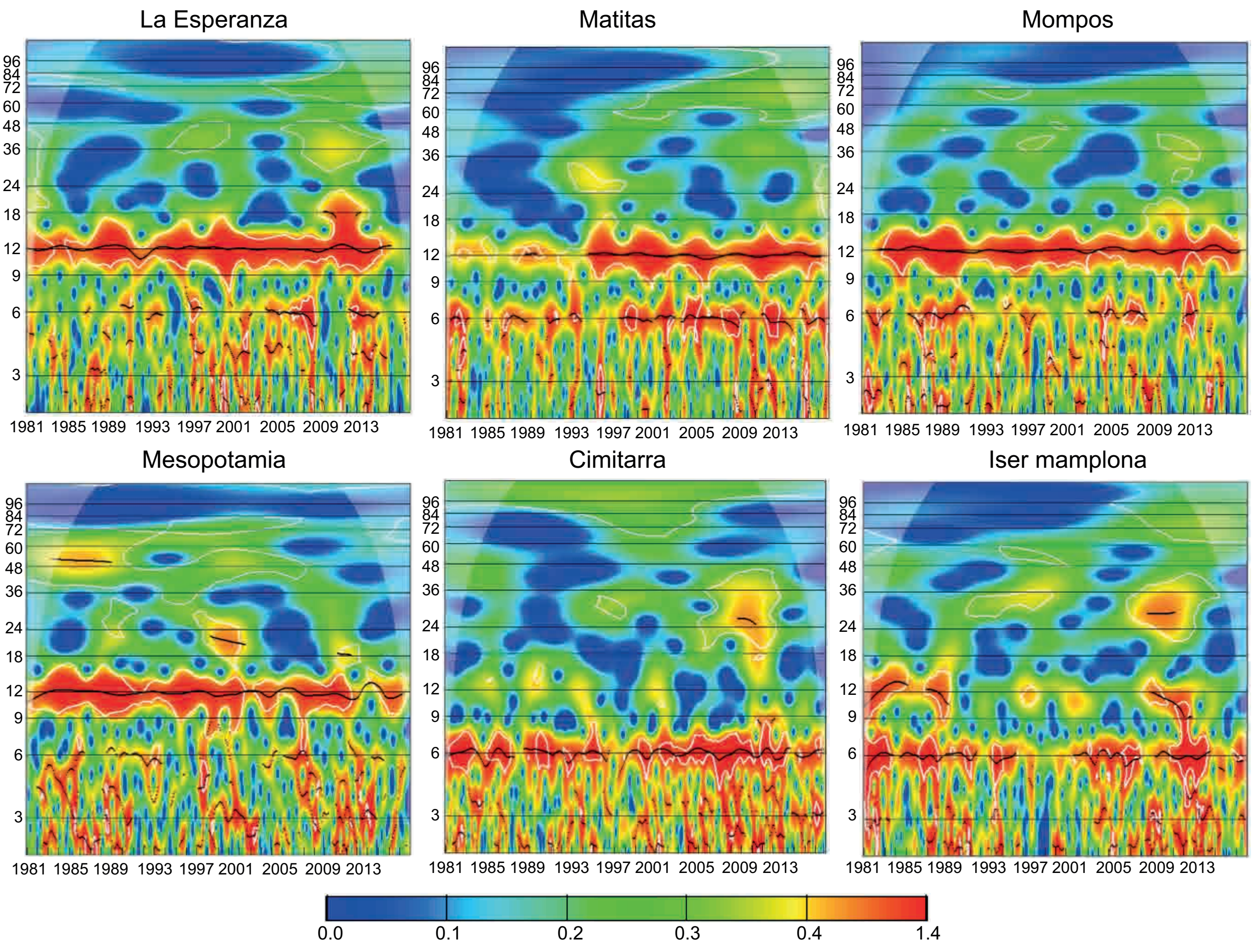

Fig. 6. Continuous wavelet spectra of the monthly precipitation data. Colors represent power $P_x(\tau,s)$. The cone of influence is located outside of the lines with a concave-down shape, and the thick white lines enclose regions of significant periodicities at 5%. Data from IDEAM.

2. Step 1. is repeated but with the CHIRPS precipitation data. Results are shown in Figure 7.
3. The WT procedures were computed on ENSO indices to evaluate their time-frequency variability. Results are shown in Figure 8.
4. The WC procedures were computed between the monthly precipitation from IDEAM and indices: Niño 1+2, Niño 3, Niño 3.4 and Niño 4, i. e. the SST of these regions (Table I). Results are shown in the first four panels in Figures 9 to 14.
5. The WC procedures were computed between the monthly precipitation anomalies from IDEAM data and ONI, MEI, SOI, BEST, ESPI, and MEI data. Results are shown in in the last five panels in Figures 9 to 14.
6. Step 4 is repeated but with the CHIRPS precipitation data. Results are shown in the first four panels in Figures A1 to A6.
7. Step 5 is repeated but with the CHIRPS precipitation data. Results are shown in the last five panels in Figures A1 to A6.

3. Results and Discussion

Figures 6 and 7 show the continuous wavelet spectra of the monthly precipitation data from IDEAM and CHIRPS respectively. Figure 6 displays the intraseasonal, seasonal, and interannual components in the signals. The spectra of the stations show a different precipitation variability at each location. Esperanza

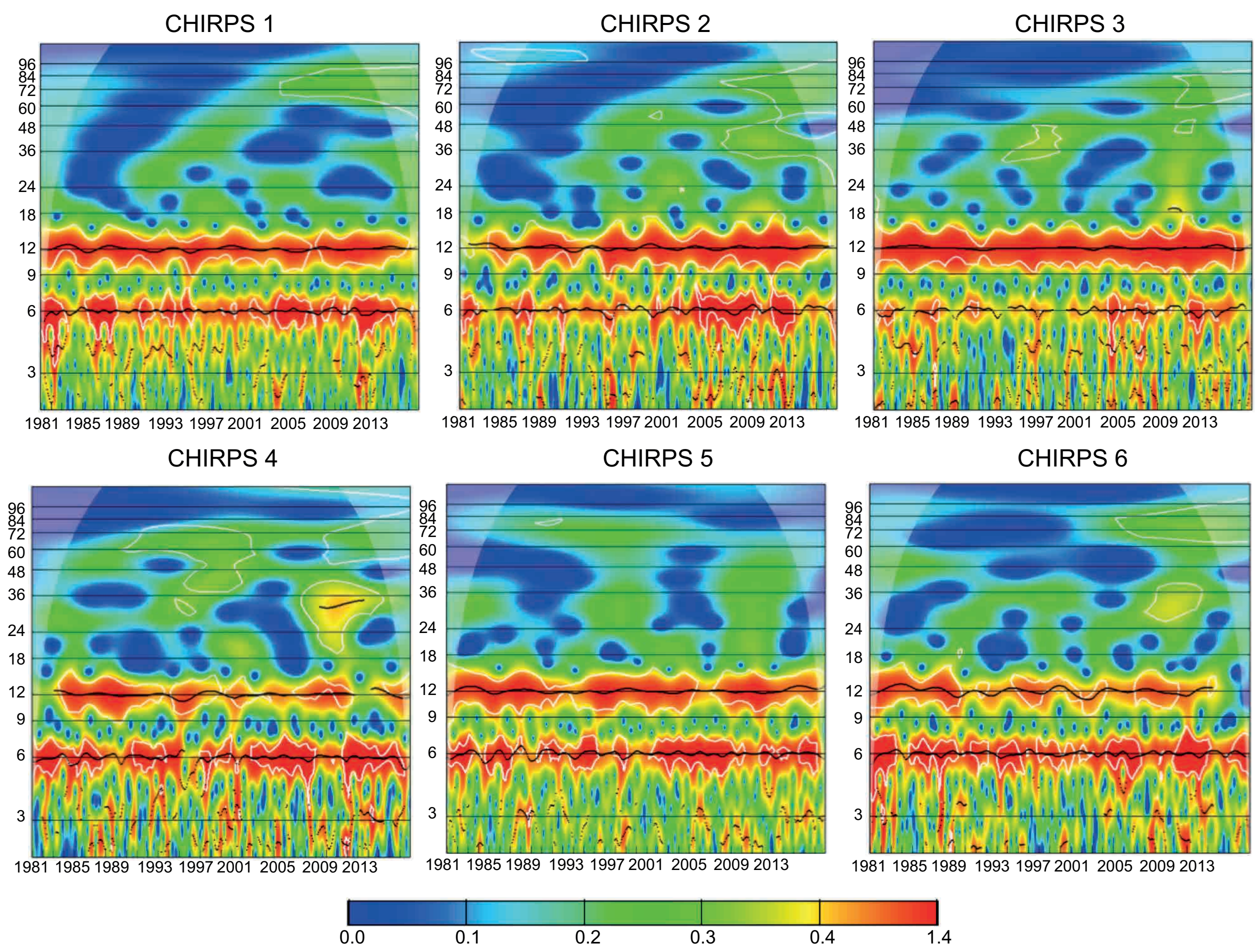

Fig 7. Continuous wavelet spectra of the monthly precipitation data. Colors represent power $P_x(\tau,s)$. The cone of influence is located outside of the lines with a concave-down shape, and the thick white lines enclose regions of significant periodicities at 5%. Data from CHIRPS

and Matitas have clear annual, and semi-annual cycles, the power on these scales stands out more than the others. Mompos and Mesopotamia also have an annual cycle, but the semi-annual cycle decreases its power. In contrast, in Cimitarra and Iser Pamplona, the semi-annual cycle's power exceeds the annual.

On the inter-annual scale, the period is different for a different station. For example, La Esperanza has a significant area between 2000 and 2015 above the 32-months, and another between 1985 and 1995 above 64 months. Matitas has an area of maximum power around 1985. Mompos have homogeneous areas at interannual scales; no particular periodicity stands out. In contrast, Mesopotamia has three distinguishable areas, one between 32 and 64 months before 2000, and two between 16 and 32 months after 2000. Finally, Cimitarra and Iser Pamplona have only one great area on scales between 16 and 32 months after 2005. From Figures 2 and 3, it is appreciated that the location of significant areas coincides with strong or very strong ENSO events. However, not all stations indicate the same degree of influence. For example, La Esperanza, Cimitrarra, and Iser Pamplona correspond more with strong La Niña events in their precipitation signals, while Matitas and Mesopotamia reveal a greater coincidence with El Niño, and Mompos, has a homogeneous response.

These results are in line with previous findings about ENSO effects across Colombia (Díaz and Villegas, 2015; Beltrán and Díaz, 2020; Navarro-Monterroza

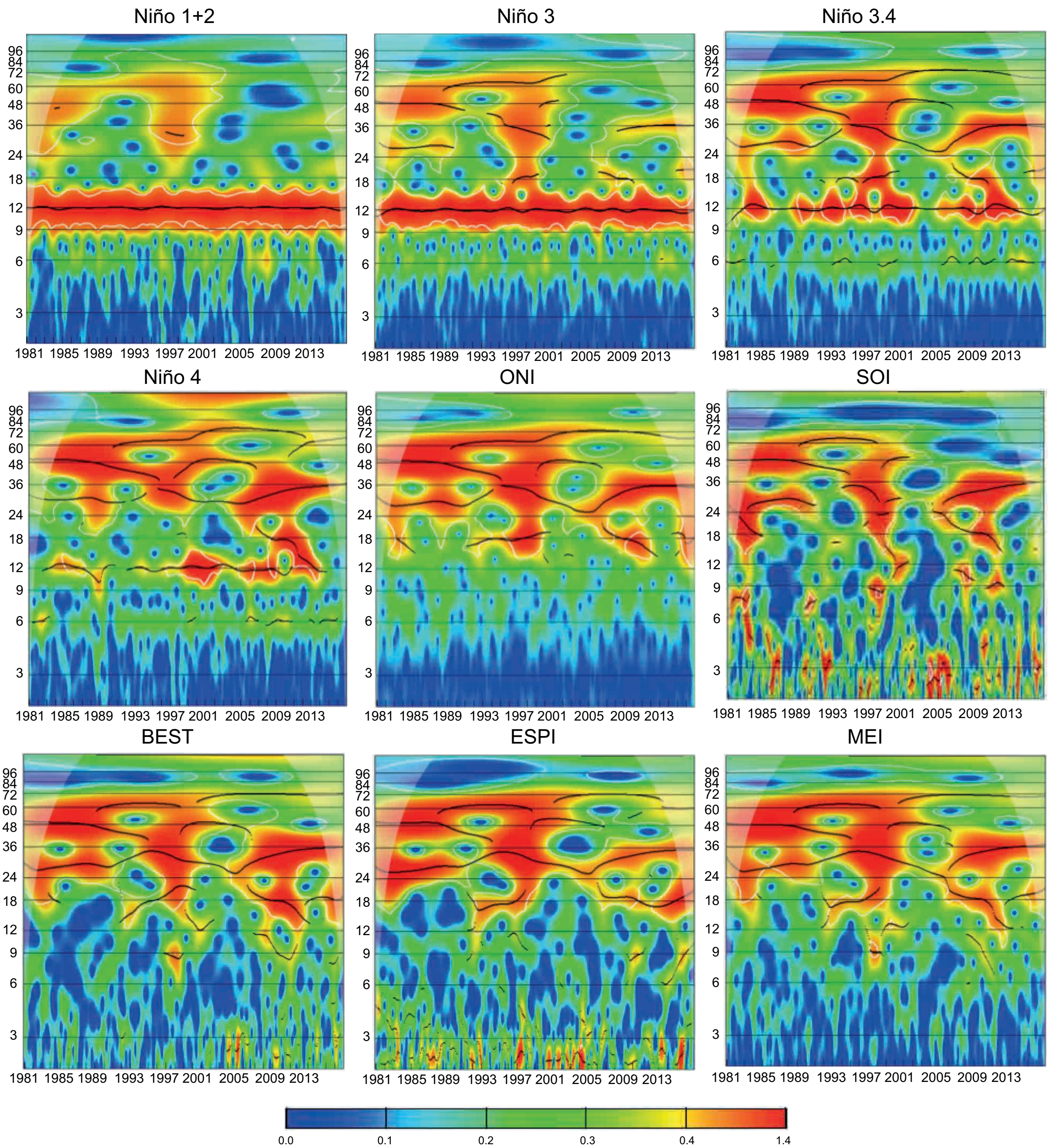

Fig 8. Continuous wavelet spectra of the ENSO indices. Colors represent power $P_x(\tau,s)$. The cone of influence is located outside of the lines with a concave-down shape, and the thick white lines enclose regions of significant periodicities at 5%.

et al. (2019) Poveda et al., 2020; Salas et al., 2020). These studies all affirm that ENSO's influence depends on the intensity and the longitudinal location of the maximum SST anomaly over the Pacific and the region of Colombia that is analyzed, even stations with similar geographic coordinates and elevation can be influenced differently. The effects are not always homogeneous (Díaz and Villegas, 2015; ENA, 2018;

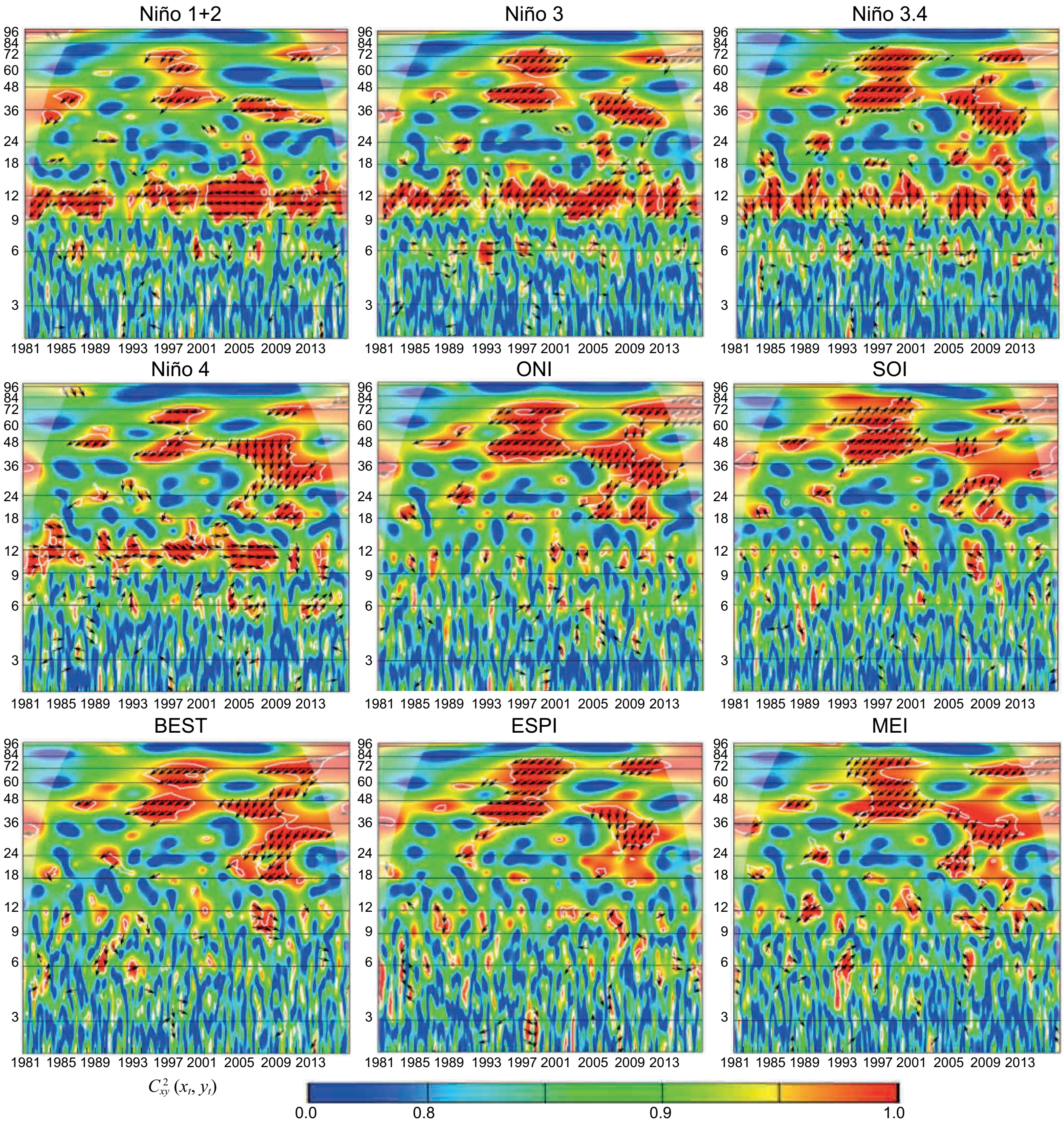

Fig 9. Wavelet coherence $C^2_{x,y}(x_t, y_t)$ and phase difference $Arg(T_{x,y}(\tau,s))$ between ENSO indices and precipitation of La esperanza station. The cone of influence is the area outside of the with a concave-down shape, and sectors of significant periodicities at 5% are enclosed by the thick white lines. (Anti-phase: ← ; In-phase: →)

Beltrán and Díaz, 2020). Those findings that have been verified first through linear correlations are clearer with the wavelet spectra of Figure 3 because it is appreciated over time and at different periodicity scales how annual and semi-annual variability are similar. However, at interannual and longer scales, each station has its power distribution for each frequency component. The reason is that for each site, the effects of orography,

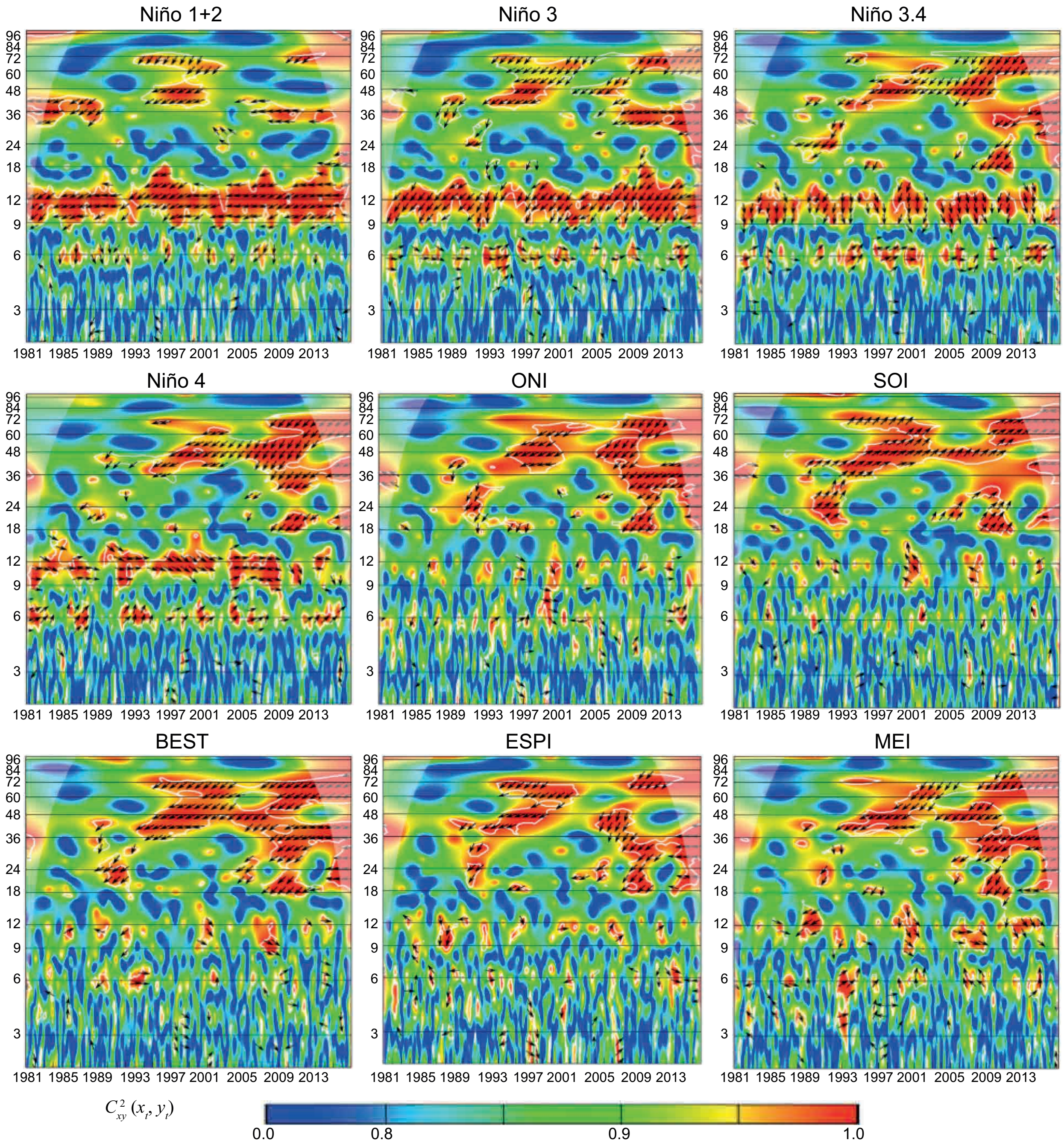

Fig. 10. Wavelet coherence $C^2_{x,y}(x_t, y_t)$ and phase difference $Arg\,(T_{x,y}(\tau,s))$ between ENSO indices and precipitation of Matitas station. The cone of influence is the area outside of the with a concave-down shape, and sectors of significant periodicities at 5% are enclosed by the thick white lines. Data from IDEAM. (Anti-phase: ←; In-phase: →).

proximity to the Caribbean, to the Amazon, local circulation systems are combined and added with ENSO to generate varied responses. Efforts to describe these effects in greater detail can be found, for example, in the recent works by Navarro-Monterroza et al. (2019) and Poveda et al. (2020)

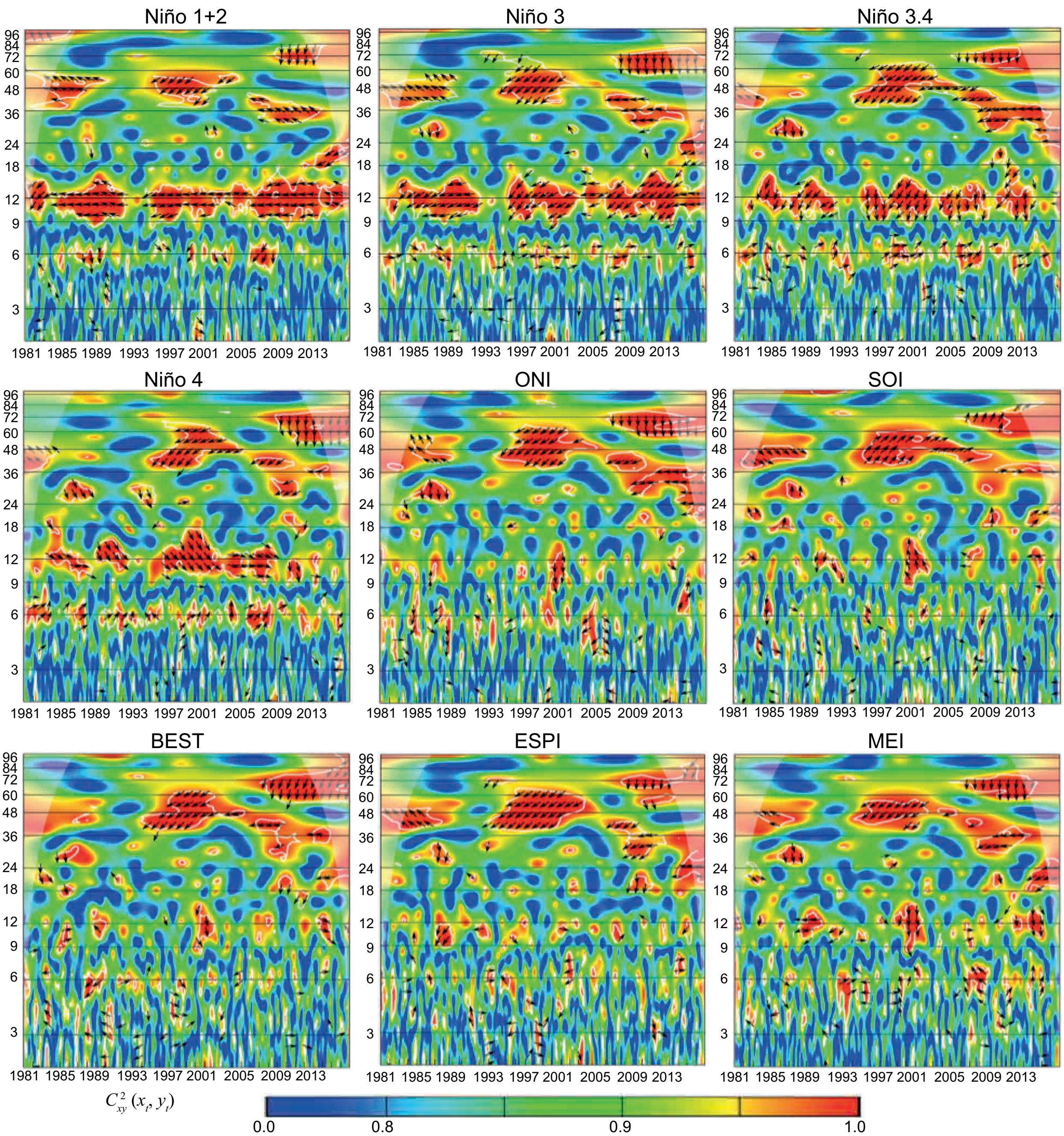

Fig. 11. Wavelet coherence $C^2_{x,y}(x_t, y_t)$ and phase difference $Arg\,(T_{x,y}(\tau,s))$ between ENSO indices and precipitation of Mompos station. The cone of influence is the area outside of the with a concave-down shape, and sectors of significant periodicities at 5% are enclosed by the thick white lines. Data from IDEAM. (Anti-phase: ←; In-phase: →).

In Figure 7, we can see periodicities of 6 and 12 months in all cases using CHIRPS data, different for results using the IDEAM data, where such periodicities are not always visible. In contrast, the zones with significant periodicity greater than 12 months have less power than that revealed with the IDEAM data.

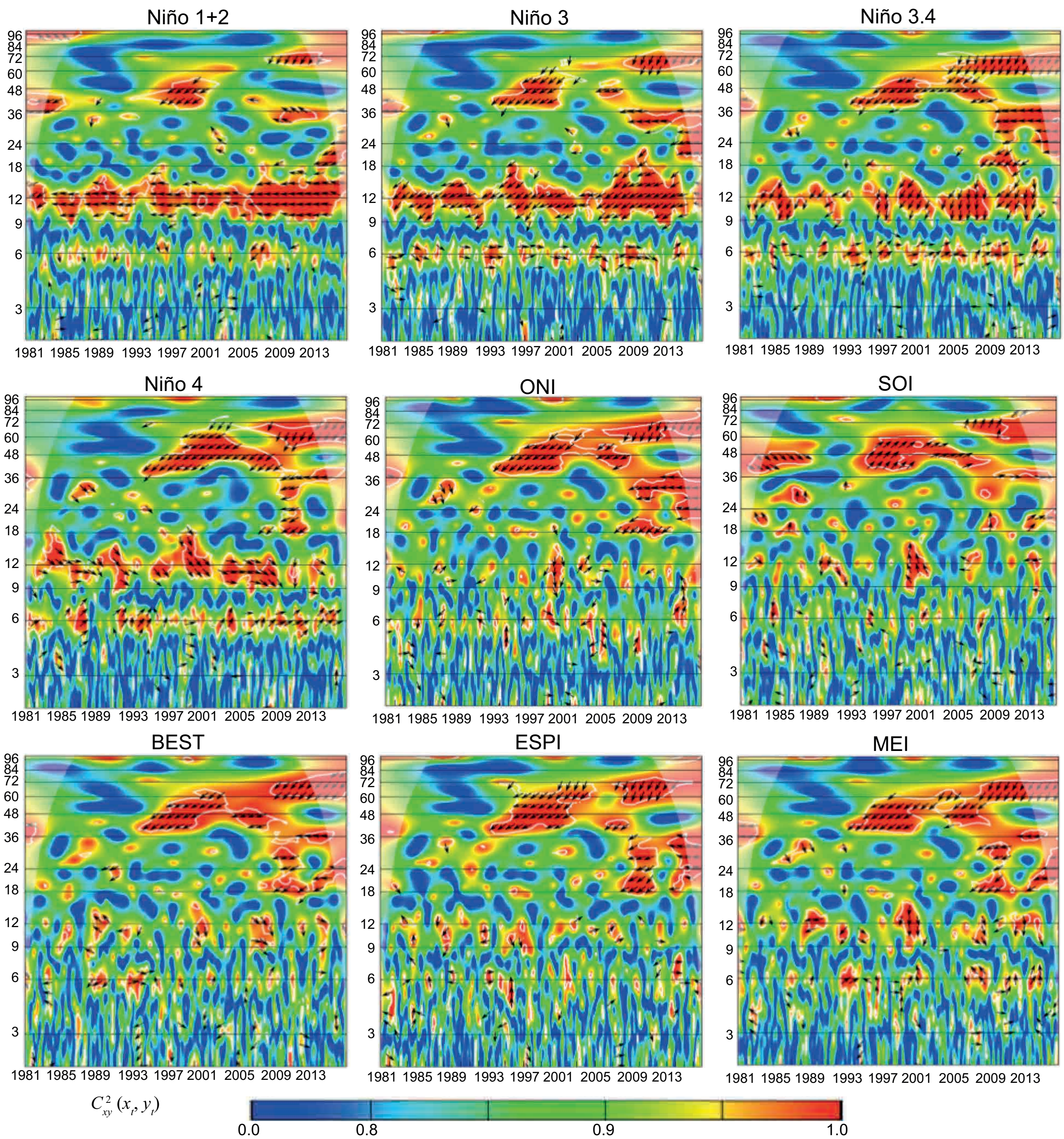

FIg. 12. Wavelet coherence $C^2_{x,y}\ (x_t, y_t)$ and phase difference $Arg\ (T_{x,y}(\tau,s))$ between ENSO indices and precipitation of Mesopotamia station. The cone of influence is the area outside of the with a concave-down shape, and sectors of significant periodicities at 5% are enclosed by the thick white lines. Data from IDEAM. (Anti-phase: ←; In-phase: →).

Figure 8 shows the continuous wavelet spectra of the ENSO indices. The first four spectra are for the SST of the different regions Niño 1+2, Niño 3, Ñino 3.4, and Niño 4. The annual cycle stands out with greater power, the semi-annual cycle is more evident with Niño 3.4 and Niño 4 compared to Niño 1+2 and

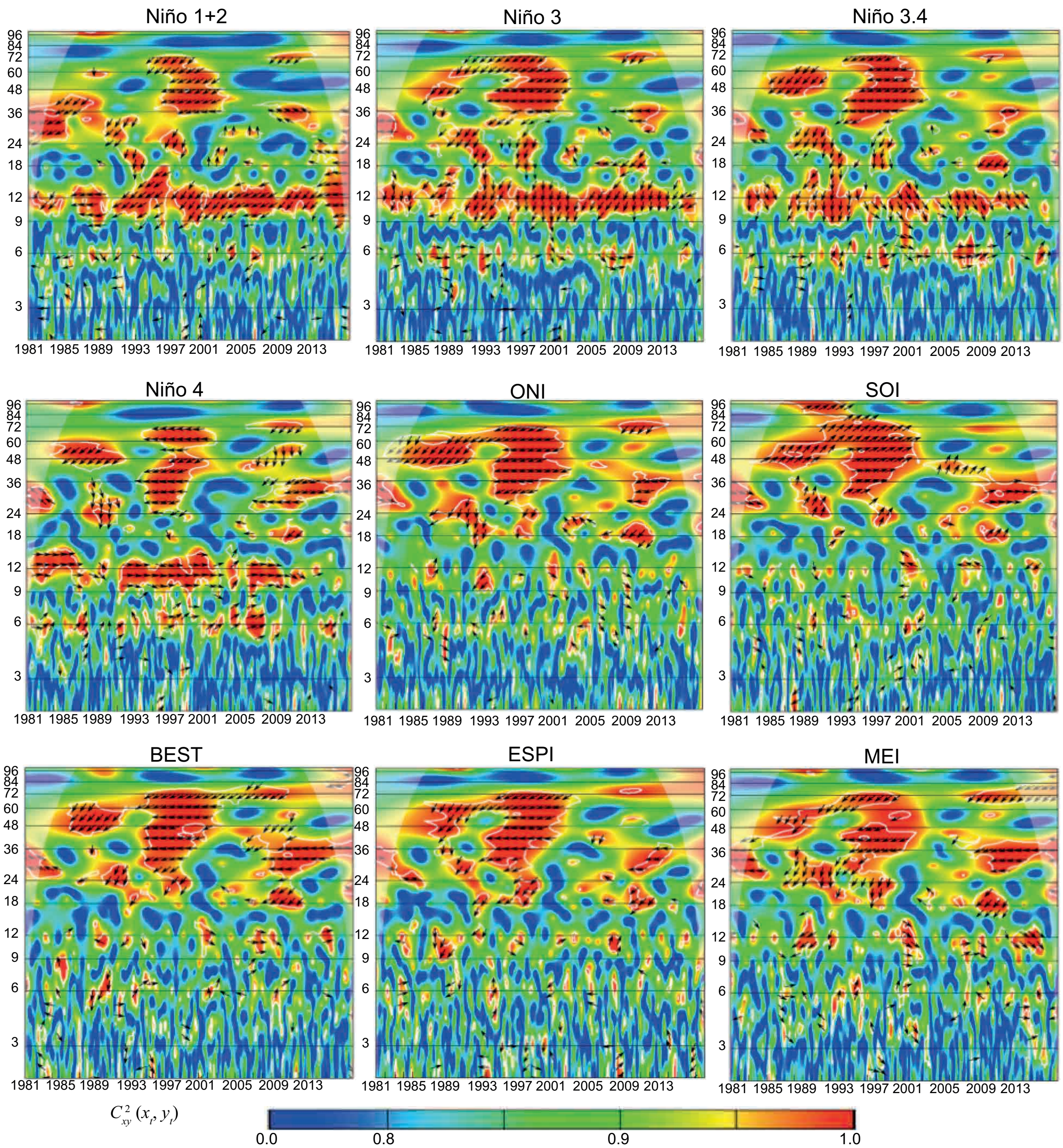

Fig. 13. Wavelet coherence $C^2_{x,y}(x_t, y_t)$ and phase difference $Arg(T_{x,y}(\tau,s))$ between ENSO indices and precipitation of Cimitarra station. The cone of influence is the area outside of the with a concave-down shape, and sectors of significant periodicities at 5% are enclosed by the thick white lines. Data from IDEAM. (Anti-phase: ←; In-phase: →).

Niño 3. The last four spectra correspond to ONI, SOI, BEST, and MEI indices, based on anomalies as described in Table I, therefore, they do not present an annual or semi-annual component. In higher scales, the power distribution reveals that each index has a greater sensitivity to warm or cold events, compared

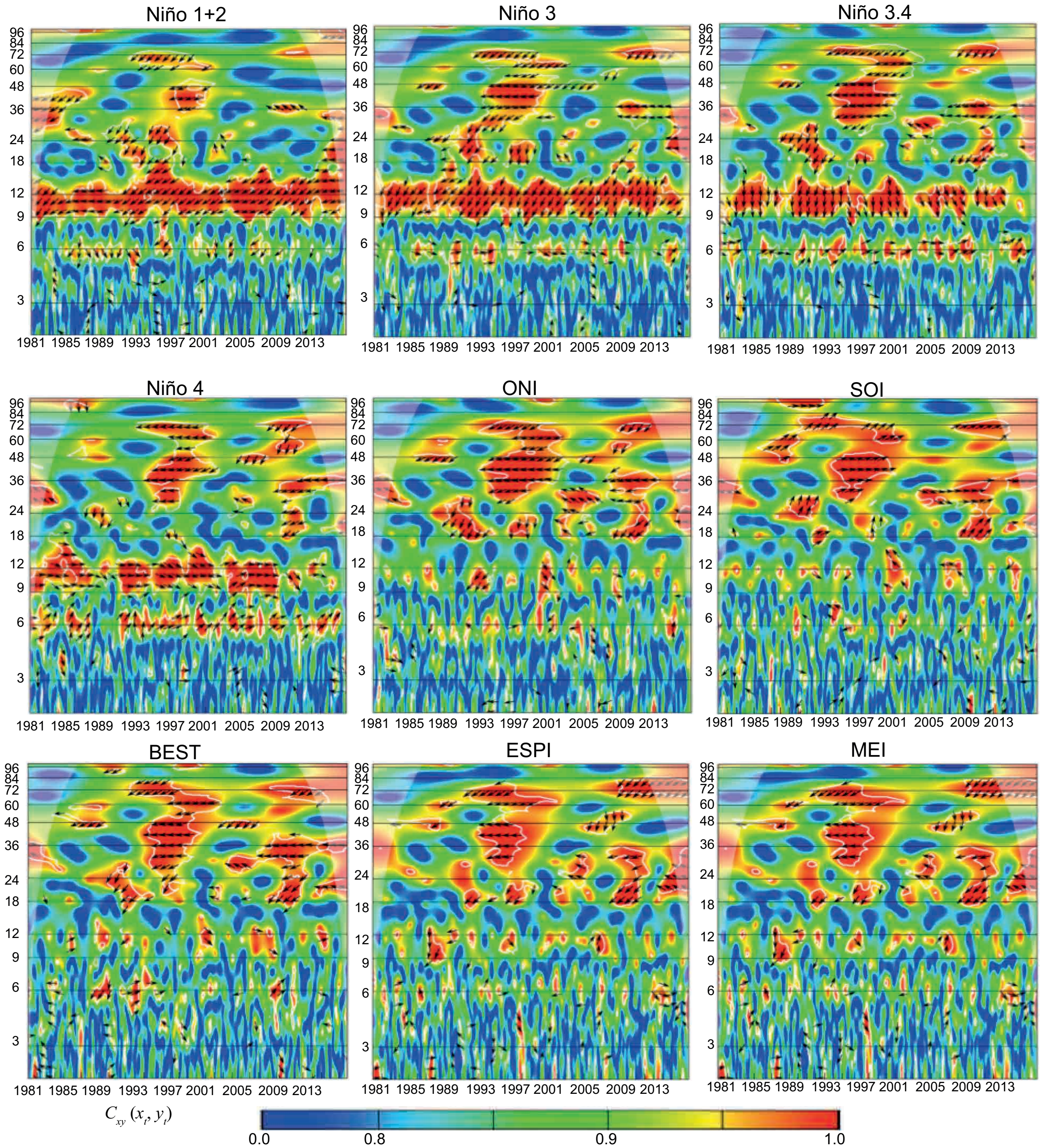

Fig. 14. Wavelet coherence $C^2_{x,y}(x_t, y_t)$ and phase difference $Arg(T_{x,y}(\tau,s))$ between ENSO indices and precipitation of Iser Pamplona station. The cone of influence is the area outside of the with a concave-down shape, and sectors of significant periodicities at 5% are enclosed by the thick white lines. Data from IDEAM. (Anti-phase: ←; In-phase: →).

with Figure 2, the indices with greater power for El Niño events are ONI, ESPI, and MEI, and for La Niña is BEST. Studies carried out to compare the indices using linear techniques revealed that each index tends to represent better warm or cold events. For example, it has been found that El Niño 1 + 2 is more sensitive to contributing positive anomalies and Niño 4 to negative ones (Hanley et al., 2003; Yu et al., 2015; Nikreftar and Sam-Khaniani, 2018; Ballari et al., 2020). Therefore, to analyze ENSO's impact at a specific site, it is highly recommended to identify which indices show a better relationship with the local interannual climate variability (Nikreftar and Sam-Khaniani, 2018; Ballari et al., 2020).

Figures 9 to 14 show the wavelet coherence and phase difference obtained with data from IDEAM at the six stations described in Table II. Figures A1 to A6, included in Appendix A, show the results computed with CHIRPS data. Note that the general coherence structure with both databases is very similar, but the phase difference is not always coincident; the description that follows is for Figures 9 to 14.

For Esperanza station, the coherence spectra show periodicities of 6–12 along the time, but it is particularly evident with the Niño 1+2, Niño 3, Niño 3.4 and Niño 4. The direction of the arrows changes for each index and periodicities; for example, around 12 months, arrows indicate anti-phase relationships with El Niño 1+2 and El Niño 3, then show a phase difference reduction for El Niño 3.4 and finally an in-phase with El Niño 4. For the remaining four indices, as expected, the annual and semiannual cycles are not evident. The significant sector located for the 24–36 month periodicities is present between 1985 and 1995; for most cases, the direction of the arrows implies that the index leads the precipitation. The next significant sector located between periodicities of 24–36 months occurs around 2008–2010 and is especially apparent with Niño 4, ONI, and SOI indices; the direction of the arrows also implies that the index leads the precipitation.

For Matitas station, the coherence spectra show the annual cycle of Niño 1+2, Niño 3, Niño 3.4 and Niño 4 indices. The direction of the arrows is the same as for Esperanza station. The second significant sector, located at periodicities of 36–60 months, and between 1995–2005, is most noticeable with ONI, SOI, BEST, and ESPI indices, and arrows indicate an anti-phase relationship where indices lead precipitation signal. The third sector, with periodicities of 36–48 months and between 2006–2010, is especially apparent with Niño 3.4 and Niño 4, and the direction of the arrows is the same as in the previous cases. Finally, the fourth sector with periodicities of 48–64 months, and between 2009–2015, is evident for all spectra, arrows indicate an anti-phase relationship, but the lag is reduced.

For Mompós station, spectra show the annual cycle of Niño 1+2, Niño 3, Niño 3.4 and Niño 4, but the directions of the arrows are different, in this case, the arrows indicate anti-phase relation with Niño 1+2, Niño 3, and the opposite with Niño 3.4 and Niño 4. The second and third sectors are located at periodicities of 36–60 months between 1993–2002, and exceeding 48 months between 1983–198. Both sectors are observed for most of the spectra, and arrows indicate predominant anti-phase relation.

For Mesopotamia station, similar to Mompos, the spectra show the annual cycle with Niño 1+2, Niño 3, Niño 3.4 and Niño 4, and arrows change directions in each case. The second and third sectors are located at periodicities of 32–72 months between 1981–2016, and 24–36 months between 2008–2012 respectively; and are present for all indices; arrows correspond to an anti-phase relationship between signals.

For Cimitarra station, the spectra do not show a clear relationship between annual components. Spectra show small significant sectors located at periodicities of 24–48 months between 2009–2012 and another of 48–72 months between 1997–2008. In general, this station presents smaller significant areas with all indices, and the arrows have directions less consistent with each other.

Finally, for Iser Pamplona station, the spectra do not show significant coherence between annual components either. The significant sectors are located at periodicities of 36–48 months between 1995–2002, at 24–48 months between 2006–2012, and 60–72 months between 2008–2015, especially with Niño 4, ONI, SOI, MEI and BEST. Arrows suggest a negative correlation but the lag changes for each index.

As stated in the Introduction, the first objective of this work is to explore nonlinear correlations of the ENSO-precipitation relationship, particularly for specific regions where the freshwater resources have been significantly reduced during El Niño events. And the second one is to identify which indices will improve the predictability of hydro-climatological variables. Regarding the first objective, the spectra visualize the non-linear character of the ENSO-precipitation relationship; that is, ENSO events with similar characteristics generate different responses in precipitation. Moreover, the influence also changes depending on the site. The differences between the spectra in Figures 9 to 14 show that this teleconnection is much more complicated than simple linear correlation, as it has also been mentioned in studies such as those of Carmona and Poveda (2012), Restrepo et al. (2019), Navarro-Monterroza et al. (2019), Das et al., (2020), Salas et al. (2020).

For example, all stations have a bimodal precipitation regime but have particular characteristics. The three most northern ones have two dry seasons, but the first one (December-February) is more marked than the second one (June-August); also, these stations have two wet seasons, but the second one (September-November) is more intense. The other three stations have both dry and wet seasons with similar rainfall levels on average. Despite their differences in altitude, mean annual rainfall, and coefficient of variation, all of them record significant impacts during ENSO events.

The nonlinear behavior of this relationship can be attributed to several factors, such as, the nexus of ENSO with other large-scale climate oscillations, the phase combinations of the oscillatory processes are multiple, and for each one, the resulting atmospheric state is quite different (Massei et al., 2012; Nalley et al., 2016; Araghi et al., 2016; Das et al., 2020). Another aspect is that two previously classified events in the same category may not be as similar as previously thought; several studies have revealed that ENSO's influence on the climate variability of other remote regions depends on the longitudinal position of the maximum SST anomaly over the Pacific (Zhang et al., 2015 and 2019). For example, it has been documented that El Niño events with the highest development in the central Pacific generally have linear responses on the atmospheric-ocean dynamics over the Atlantic and the American continent, but in contrast, La Niña events located especially over eastern Pacific generate nonlinear responses in these regions (Li and Lau, 2012; Zhang et al., 2015 and 2019; Whan and Zwiers, 2017). Other methodologies, such as complex networks or deep learning techniques, are being explored to understand the behavior and complexity of the ENSO teleconnections around the planet (Donges et al., 2009, Feldhoff et al., 2015).

Regarding the second objective, which was to compare the wavelet coherence spectra with different indices, the results show that the significant areas are located in time-scales that correspond to ENSO periodicities, as has also been obtained by Poveda et al. (2011), Carmona and Poveda (2014), or Restrepo et al. (2019). The quantity and size of the significant areas varies for each case considered, therefore, to study the ENSO-precipitation relation with a single index can yield partial results, as has been shown in other investigations (Ballari et al., 2020).

Other areas that are at low-frequency bands are also visible in the spectra, which could correspond to ENSO with other quasi-decadal oscillatory processes. Several studies have tried to establish connections of other climate oscillations on variables such as precipitation or flow rates. However, the cause of these significant regions has not yet been established, neither in the power spectra of the wavelet transform nor in those of coherence (Nalley et al., 2019). Something similar happens to high-frequency bands, where a combination of the ENSO signal with others such as the Madden Julian Oscillation can also be found (Torres and Pabón, 2017, Beltrán and Díaz, 2020).

Table IV and Figure A10 show sectors that are especially evident and significant at the 95% confidence

Table IV. Periods during which observed significant joint periodicities occurred as shown in the wavelet coherence spectra of the monthly precipitation and climate index data.

Sector	1	2	3	4	5	6	7
Periodicities (months)	6	12	24-36	24-36	36-48	36-60	60-72
Periods (years)	1981-2016	1981-2016	1983-1992	2008-2012	1983-1992	1995-2005	2008-2012
El Niño events	3VS,2S, 4M	3VS,2S, 4M	1VS,2S, 1M	1M	1VS,2S, 1M	1VS,2M	1M
La Niña events	5S, 2M	5S, 2M	-	2S,1M	-	2S,1M	2S,1M

interval. Also, it presents for each case the number of ENSO events with categories: very strong (VS), strong (S), or moderate (M) according to ONI index classification (https://ggweather.com/enso/oni.htm). Table IV shows that during the period considered (1981–2016), nine El Niño events occurred, which according to the classification based on the ONI index, three were very strong, two strong and four moderate. On the other hand, seven La Niña events occurred in this same period, five strong and two moderate. In total, eight of nine El Niño events occurred precisely during the periods for which joint periodicities were observed between precipitation and ENSO indices. In contrast, only three of the seven La Niña events coincided with these periods of occurrence.

These results are coherent with the descriptions made by Navarro-Monterroza et al. (2019), Poveda et al. (2020), Salas at al. (2020), Beltrán and Díaz (2020). Those studies affirm that the influence of warm events on precipitation seems to be greater than of the cold events, and for this reason, the coherence of the two signals increases during El Niño events. Response to La Niña events seems to be more complex to identify. Similar results have also been obtained in studies carried out in other regions of the planet (Li and Lau, 2012; Zhang et al., 2015 and 2019; Whan and Zwiers, 2017). As it was mentioned before, authors suggest that when there is a decrease in SST in the Pacific, the processes of ocean-atmosphere interaction that are generated depend on the area where the maximum cooling is located; in the central Pacific, the atmospheric response takes less time than in the eastern Pacific, because SST is colder in this zone and the reaction of the atmosphere take longer. In contrast, when there SST increases in any area of the Pacific, deep convection processes that are released in the atmosphere become evident much faster in both the central or eastern Pacific. This difference in the mechanisms of ocean-atmosphere interaction could be the key to understanding why in most of the studies, the influence of El Niño on the variability of precipitation is more evident than of La Niña (Zhang et al., 2015 and 2019; Whan and Zwiers, 2017, Navarro-Monterroza et al. (2019).

Sectors 1 and 2, that correspond to coherence in the annual and semiannual cycles are present in four of the six stations, especially with the indices Niño 1+2, Niño 3, Niño 3.4 and Niño 4, and are almost continuous over time. Sectors 3 and 5 seem to be just a single band. For the Mompos and Mesopotamia spectra, these areas are more significant than for the Cimitarra or Iser Pamplona spectra. During the periods corresponding to the sectors 3 and 5, there were four El Niño events: 1982–1983 (VS), 1987–1988(S), 1991–1992(S), and 1986–1987(M). Sectors 4 and 7 are present in the Cimitarra and Iser Pamplona spectra with all the indices, but in the case of Mompos and Mesopotamia stations, they are less distinguishable. During the periods for sectors 4 and 7, there were three events La Niña: 2007–2008(S), 2010–2011(S), and 2011–2012(M), and just one El Niño: 2009–2010(M). Finally, sector 6 is present in all spectra. There were three El Niño: 1997–1998(VS), 1994–1995(M), and 2002–2003(M), and three La Niña: 1998–1999(S), 1999–2000(S) and 1995–1996(M).

The spectra obtained with precipitation data from IDEAM and CHIRPS show that Esperanza and Matitas are the stations with the largest number of sectors with significant coherence with ENSO. In those analyzing CHIRPS data, the area and definition are greater, for example, the sectors 5, 6 and 7 appear to be a single wide band located at periodicities greater than 48 months. Mesopotamia and Cimitarra also have significant sectors, although with less area and more discontinuities. Mompos and Iser Pamplona are the ones that are less consistent with the ENSO indices.

Note that the directions of the arrows are slightly different depending on the index. For sectors 1 and 2, the phase difference varies in particular for the first four indices. Figure 15 shows how most of the arrows obtained in these sectors indicate a negative correlation between precipitation and Niño 1+2, Niño 3, and Niño 3.4 with a predominant phase shift between $-\pi/2$ and π; in contrast, correlation is positive with Niño 4 and the lag interval is $-\pi/2$ to 0. These changes in direction are interesting to understand because it reveals not just that local climate is related to the sea surface temperature but also the changes in the lag depending on each region in the equatorial Pacific Ocean. Related issues are explored in Navarro-Monterroza et al. (2019). For sectors 3 to 7, directions are more similar among all the spectra.

The direction of the arrows of spectra in Figures 9–14 and A1–A6 are coincident except in the range from 36 to 48. Figures 9–14 indicate anti-phase signals with a lag of π /4, while those of A1–A6 show

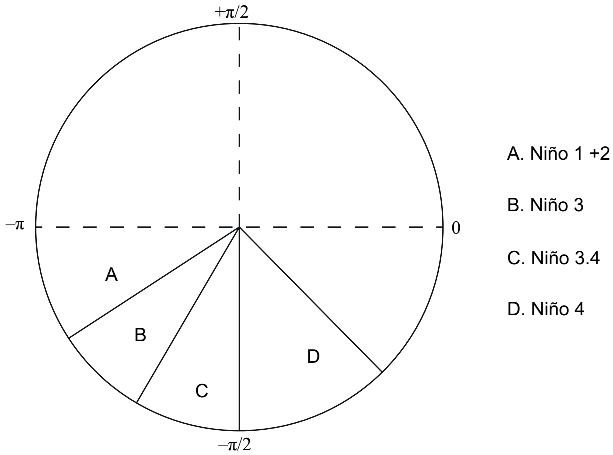

Fig. 15. Predominant phase shifts for periodicities of 12 months. Negative correlation with indices: Niño 1+2, Niño 3, Niño 3.4, and Positive with indices Niño 4.

anti-phase signals without lag. That is, between 3 and 6 months of difference in lags calculated with each database. One possibility to understand this result is the reduced presence of anomalies in the CHIRPS series associated with ENSO events, which can modify the calculation of the phase difference. This reduction in recorded anomalies is due to the effect of combining in-situ observations and satellite data. However, the CHIRPS database also includes in-situ information, but there are large regions where there is no information, and the imputation of the data in these areas becomes difficult.

This difference occurs in all stations, and the only index that shows a minor discrepancy is ESPI, which is precisely also calculated from satellite precipitation data (Table I). To date only Urrea et al. (2016) have validated the CHIRPS data for Colombia, so it is the first time that is evident that the phase difference calculated between ENSO and precipitation changes depending on the database used, particularly on the scale of 36 to 48 months. Other validation studies have found that CHIRPS presents difficulties in estimating data from places located above 1000 m.a.s.l (Rivera et al., 2018); however, the six stations had lower and higher elevations and the discrepancy remained. This aspect should surely be the object of a more extensive and detailed investigation in future work.

Although all the indices could be used to feed statistical forecast models according to the results obtained, each station has one or more with which significant sectors of maximum coherence with greater area and definition of the phase difference were obtained. In Esperanza, ONI, Matitas with BEST, Mesopotamia with ONI or BEST and for Mompos, Cimitarra, and Iser Pamplona an option would be Niño 3 ONI and BEST.

The unique aspect of the present work is applying a non-linear method to explore relationships between ENSO and precipitation anomalies using two databases that are of different origin, although not completely independent. The results allow us to affirm that the exploration of non-linear connections obtained with each database is consistent. In other words, it was possible to identify synchronicity of the precipitation series of both databases with ENSO indices. This represents an opportunity to evaluate regional climate anomalies on the national territory where there is not enough in-situ information.

The most innovative contribution was to identify that for periods from 36 to 48 months, there is a distinction between the phase differences recorded with the IDEAM data and those of CHIRPS, and that this does not exist when both the precipitation and indices data contains satellite information.

Considering that there are two more extensive databases, more wavelet coherence between the ENSO indices was computed, the graphs in Figure 16 count the percent of spectra with each of the seven sectors chosen concerning the total of stations, which were 300 with IDEAM data and 1250 with CHIRPS. Figure 16 helps to visualize that the structure of wavelet coherence at the national level is similar both with the Pacific SST series and with the other indices. The main differences lie in the phase difference between the signals, which varies according to the database. Future work consists of expanding the scope to the whole country, finding an explanation for the change in the phase difference with the satellite data, and performing a wavelet analysis filtering bands of specific periods related to ENSO and for particular seasons where the influence is maximum like December-February.

4. Conclusions

The purpose of exploring non-linear aspects of the ENSO-precipitation relationship is achieved by

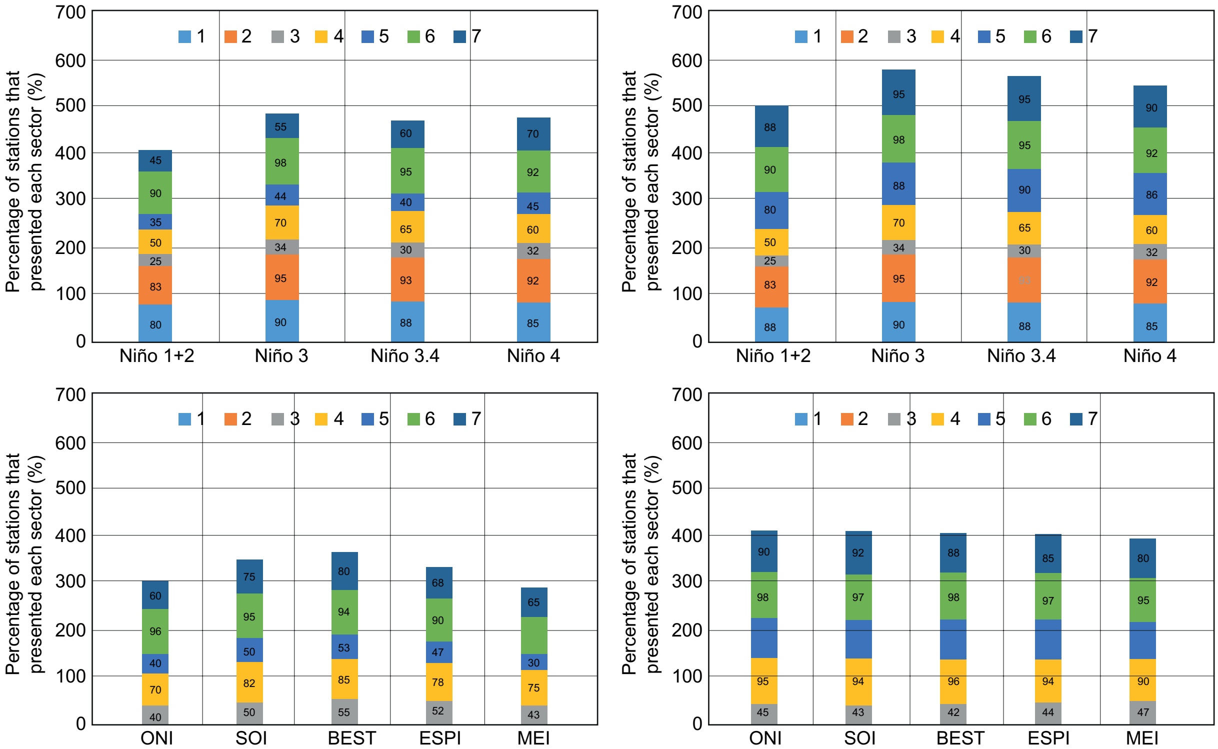

Fig. 16. Percentage of stations that presented the seven sectors described in Table IV with significant periodicities at 5%. Left: Data from IDEAM, Right: CHIR.

wavelet coherence analysis. The reasons for the non-linear character of the influence of ENSO on the climate variability of different regions have been attributed to the superposition of the ENSO signal with other large-scale oscillations and the influence of the longitudinal position of ENSO on the type of ocean-atmospheric response. The spectra obtained show the ENSO-precipitation relationship and also that wavelet coherence and phase difference change from one index to another. Results also indicate that the ENSO-precipitation relationship is diferent for each estation.

In the spectra, sectors of lower and higher frequency than those associated with ENSO are also visible and can be related to other climate oscillations not yet explored. The results show that ENSO years are reflected in the precipitation as periods of rainfall deficit or excess, also that precipitation is organized in bands and that most of their variance is explained by the 2–8-year scales. The most significant sectors are those that cover El Niño events, while sectors are smaller during La Niña, implying that impacts on precipitation tend to persist longer during warm events. The location of the seven most recurring sectors coincides with times in which the greatest rainfall anomalies in Colombia have occurred, and which have been associated respectively with El Niño event of 1997–1998, La Niña of 2010–2011, El Niño of 1982–1983, and La Niña of 1988–1989. Spectra also diplay, for the annual cycle, changes in the phase difference between SST of different regions and precipitation. The most influenced site have been La Esperanza y Matitas, followed by Mesopotamia y Mompos, while Cimitarra and Iser Pamplona have less influence. The indices with which significant coherence was maxima were Niño 3, ONI and BEST. The comparation of results using two different datasets (IDEAM and CHIRPS) showed that the coherence structure was similar but found discrepancies of in the phase difference in particular between 36 and 48 months.

Acknowledgement

Authors would like to thanks to Luz Edith Ortega because your participation in data review and map elaboration, also to the editor and anonymous reviewers for their comments to improve the manuscript significantly.

References

Alves LM, Marengo JA, Fu R, Bombardi RJ. 2017. Sensitivity of Amazon regional climate to deforestation. Am. J. Clim. Chang 6, 75–98. https://doi.org/10.4236/ajcc.2017.61005

Arias PA, Poveda G. 2005. Efecto de la desagregación temporal sobre la coherencia espacial de la precipitación en Colombia. Avances en Recursos Hidráulicos 12, 135–147.

Araghi A, Mousavi-Baygi M, Adamowski J, Martinez C. 2016. Association between three prominent climatic teleconnections and precipitation in Iran using wavelet coherence. International Journal of Climatology 37, 2809–2830. https://doi.org/10.1002/joc.4881

Ballari D, Campozano L, Samaniego E, Orellana, D. 2020. Spatial Association to Characterize The Climate Teleconnection Patterns In Ecuador Based On Satellite Precipitation Estimates. In 2020 IEEE Latin American GRSS ISPRS Remote Sensing Conference (LAGIRS) (pp. 219–224). IEEE. https://doi.org/10.1109/LAGIRS48042.2020.9165647

Beltrán L, Díaz DC. 2020. Oscilaciones Macroclimáticas que Afectan la Oferta Hídrica en la Cuenca del Río Gachaneca; Boyacá-Colombia. Revista Brasileira de Meteorologia 35, 171-185. https://doi.org/10.1590/0102-7786351012

Biswas A, Si BC. 2011. Application of continuous wavelet transform in examining soil spatial variation: a review. Mathematical Geosciences 43, 379-396. https://doi.org/10.1007/s11004-011-9318-9

Carmona AM, Poveda G. 2012. Application of Hilbert-Huang transform to detect hydroclimatic variability modes in Colombia. Dyna, 79, 72-80.

Carmona AM, Poveda G. 2014. Detection of long-term trends in monthly hydro-climatic series of Colombia through Empirical Mode Decomposition. Climatic change 123, 301-313. https://doi.org/10.1007/s10584-013-1046-3

Córdoba-Machado S, Palomino-Lemus R, Goamiz-Fortis S, Castro-Diez, Y, Esteban-Parra M. 2015a. Influence of tropical Pacic sst on seasonal precipitation in Colombia: prediction using el Niño and el Niño Modoki. Climate Dynamics, 44,1293-1310. https://doi.org/10.1007/s00382-014-2232-3

Córdoba-Machado S, Palomino-Lemus R, Goamiz-Fortis S, Castro-Diez, Y, Esteban-Parra M. 2015b. Assessing the impact of el Niño Modoki on seasonal precipitation in Colombia. Global and Planetary Change 124, 41-61. https://doi.org/10.1016/j.gloplacha.2014.11.003

Curtis S, Adler R. 2000. ENSO indices based on patterns of satellite-derived precipitation. Journal of Climate, 13, 2786-2793. https://doi.org/10.1175/1520-0442(2000)013<2786:EIBOPO>2.0.CO;2

Das J, Jha S, Goyal MK. 2020. On the relationship of climatic and monsoon teleconnections with monthly precipitation over meteorologically homogenous regions in India: Wavelet global coherence approaches. Atmospheric Research 238, 104889. https://doi.org/10.1016/j.atmosres.2020.104889

Díaz D, Villegas N. 2015. Canonical correlation between large scale climate oscillations and surface meteorological variables in Colombia. Revista UDCA Actualidad Divulgación Científica 18, 543-552.

Donges JF, Zou Y, Marwan N, Kurths J. 2009. Complex networks in climate dynamics. The European Physical Journal Special Topics 174, 157-179. https://doi.org/10.1140/epjst/e2009-01098-2

Erfanian A, Wang G, Fomenko L. 2017. Unprecedented drought over tropical South America in 2016: significantly under-predicted by tropical SST. Scientific Reports 7, 5811. https://doi.org/10.1038/s41598-017-05373-2

Feldhoff, J. H., Lange, S., Volkholz, J., Donges, J. F., Kurths, J., & Gerstengarbe, F. W. 2015. Complex networks for climate model evaluation with application to statistical versus dynamical modeling of South American climate. Climate Dynamics 44, 1567-1581. https://doi.org/10.1007/s00382-014-2182-9

Fu C, James AL, Wachowiak MP. 2012. Analyzing the combined influence of solar activity and El-Niño on streamflow across southern Canada. Water Resources Reserach 48, W05507. https://doi.org/10.1029/2011WR011507

Funk C, Peterson P, Landsfeld M, Pedreros D, Verdin J, Shukla S, Michaelsen J. 2015. The climate hazards infrared precipitation with stations a new environmental record for monitoring extremes. Scientific Data, 2, 150066. https://doi.org/10.1038/sdata.2015.66

Hanley DE, Bourassa MA, O'Brien JJ, Smith SR, Spade ER. 2003. A quantitative evaluation of ENSO indices. Journal of Climate 16, 1249-1258. https://doi.org/10.1175/1520-0442(2003)16%3C1249:AQEOEI%3E2.0.CO;2

Hoyos N, Escobar J, Restrepo JC, Arango AM, Ortiz JC. 2013. Impact of the 2010-2011 La Niña phenomenon in Colombia, South America: The human toll of an extreme weather event. Applied Geography 39,16-25. https://doi.org/10.1016/j.apgeog.2012.11.018

IDEAM, Estudio Nacional del Agua 2019. Bogotá, D. C., 2015. 496 páginas.

Jiang R, Wang Y, Xie J, Zhao Y, Li F, Wang X. 2019. Assessment of extreme precipitation events and their teleconnections to El Niño Southern Oscillation, a case study in the Wei River Basin of China. Atmospheric Research 218, 372-384. https://doi.org/10.1016/j.atmosres.2018.12.015

Jiménez-Muñoz JC, Mattar C, Barichivich J, Santamaría-Artigas A, Takahashi K, Malhi Y, Sobrino JA, Schrier G. 2016. Record-breaking warming and extreme drought in the Amazon rainforest during the course of El Niño 2015-2016. Scientific Reports 6, 33130. https://doi.org/10.1038/srep33130

Kravchenko VO, Evtushevsky OM, Grytsai AV, Milinevsky GP. 2011. Decadal variability of winter temperatures in the Antarctic Peninsula region. Antarctic Science 23, 614. https://doi.org/10.1017/S0954102011000423

Li Y, Lau NC. 2012. Impact of ENSO on the atmospheric variability over the North Atlantic in late Winter-Role of transient eddies. Journal of Climate 25, 320–342. https://doi.org/10.1175/JCLI-D-11-00037.1

Marengo JA, Espinoza JC, 2016. Extreme seasonal droughts and floods in Amazonia: causes, trends and impacts. International Journal of Climatolology 36, 1033–1050. https://doi.org/10.1002/joc.4420

Massei N, Fournier M. 2012. Assessing the expression of large-scale climatic fluctuations in the hydrological variability of daily Seine river flow (France) between 1950 and 2008 using Hilbert–Huang Transform. Journal of Hydrology 448, 119-128. https://doi.org/10.1016/j.jhydrol.2012.04.052

Nalley D, Adamowski J, Khalil B, Biswas A. 2016. Inter-annual to inter-decadal streamflow variability in Quebec and Ontario in relation to dominant large-scale climate indices. Journal of Hydrology 536, 426-446. https://doi.org/10.1016/j.jhydrol.2016.02.049

Nalley D, Adamowski J, Biswas A, Gharabaghi B, Hu W. 2019. A multiscale and multivariate analysis of precipitation and streamflow variability in relation to ENSO, NAO and PDO. Journal of Hydrology 574, 288-307. https://doi.org/10.1016/j.jhydrol.2019.04.024

Navarro-Monterroza E, Arias PA, Vieira SC. 2019. El Niño-Oscilación del Sur, fase Modoki, y sus efectos en la variabilidad espacio-temporal de la precipitación en Colombia. Revista de la Academia Colombiana de Ciencias Exactas, Físicas y Naturales, 43, 120-132. https://doi.org/10.18257/raccefyn.704

Ouachani R, Bargaoui Z, Ouarda T. 2013. Power of teleconnection patterns on precipitation and streamflow variability of upper Medjerda Basin. International Journal of Climatology 33, 58-76. https://doi.org/10.1002/joc.3407

Pedraza AM, Serna J. 2018. Validación de las estimaciones de precipitación con CHIRPS e IRE/IDEAM. Nota Técnica IDEAM-METEO/002-2018. http://bart.ideam.gov.co/wrfideam/new_modelo/DOCUMENTOS/2018/NT_IDEAM-002-2018.pdf

Poveda G, Mesa O. 1997. Feedbacks between hydrological processes in tropical south America and large-scale ocean-atmospheric phenomena. Journal of Climate, 10, 2690-2702. https://doi.org/10.1175/1520-0442(1997)010<2690:FBHPIT>2.0.CO;2

Poveda G, Vélez J, Mesa O. Hoyos C, Mejía J, Barco O, Correa P. 2002a. Influencia de fenómenos macroclimáticos sobre el ciclo anual de la hidrología colombiana: Cuantificación lineal, no lineal y percentiles probabilísticos. Meteorología Colombiana 6. 121-130.

Poveda G, Mesa O, Agudelo P, Álvarez J, Arias P, Moreno H, Vieira S. 2002b. Influencia de ENSO, oscilación Madden-Julian, ondas del Este, huracanes y fases de la Luna en el ciclo diurno de la precipitación en los Andes Tropicales de Colombia. Meteorología Colombiana 5, 3-12.

Poveda G, Waylen P, y Pulwarty R. 2006. Annual and inter-annual variability of the present climate in northern south America and southern Mesoamerica. Palaeogeography, Palaeoclimatology, Palaeoecology 234, 3-27. https://doi.org/10.1016/j.palaeo.2005.10.031

Poveda G, Álverez DM, Rueda OA. 2011. Hydro-climatic variability over the Andes of Colombia associated with ENSO: A review of climatic processes and their impact on one of the Earth's most important biodiversity hotspots. Climate Dynamics 36, 2233-2249. https://doi.org/10.1007/s00382-010-0931-y

Poveda G, Espinoza JC, Zuluaga MD, Solman SA, Garreaud R, van Oevelen PJ. 2020. High Impact Weather Events in the Andes. Frontiers in Earth Science 8, 162. https://doi.org/10.3389/feart.2020.00162

Restrepo JC, Higgins A, Escobar J, Ospino S, Hoyos N. 2019. Contribution of low-frequency climatic–oceanic oscillations to streamflow variability in small, coastal rivers of the Sierra Nevada de Santa Marta (Colombia). Hydrology and Earth System Sciences 23, 2379-2400.

Hydrology and Earth System Science 23, 2379–2400, 2019.

https://doi.org/10.5194/hess-23-2379-2019

Rivera JA, Marianetti G, Hinrichs S. 2018. Validation of CHIRPS precipitation dataset along the Central Andes of Argentina. Atmospheric Research 213, 437-449. https://doi.org/10.1016/j.atmosres.2018.06.023

Rösch A, Schmidbauer H. 2018. WaveletComp: Computational Wavelet Analysis. R package version 1.1. https://CRAN.R-project.org/package=WaveletComp

Rueda OA, Poveda G. 2006. Spatial and temporal variabillty of the Choco jet stream and its effect on the hydrocllmatology of the Colombian Pacific. Meteorología Colombiana 10, 132-145

Salas HD, Poveda G, Mesa ÓJ, Marwan, N. 2020. Generalized Synchronization Between ENSO and Hydrological Variables in Colombia: A Recurrence Quantification Approach. Frontiers in Applied Mathematics and Statistics 6, 3. https://doi.org/10.3389/fams.2020.00003

Sharma S, Srivastava P. 2016. Teleconnection of Instream Total Organic Carbon Loads with

El Niño Southern Oscillation (ENSO), North Atlantic Oscillation (NAO), and Pacific Decadal

Oscillation (PDO). Transactions of the ASABE, 59, 81-95. https://doi.org/10.13031/trans.59.10980

Schulte JA. 2016. Wavelet analysis for non-stationary, nonlinear time series. Nonlinear Processes in Geophysics 23, 257–267. https://doi.org/10.5194/npg-23-257-2016

Tedeschi RG, Grimm AM, Cavalcanti IF. 2015. Influence of Central and East ENSO on extreme events of precipitation in South America during austral spring and summer. International Journal of Climatology, 35(8), 2045-2064.

Torrence C, and Compo GP. 2011. A Practical Guide to Wavelet Analysis: With significance and confidence testing. University of Colorado at Boulder, Program in Atmospheric and Oceanic Sciences. https://atoc.colorado.edu/research/wavelets/

UNGRD. 2016. Informe técnico de avance y ejecución de Plan Nacional de Contingencia y

Posible fenómeno de “El Niño” 2014-2015. Bogotá, Colombia.

Urrea V, Ochoa A, Mesa O. 2016. Validación de la base de datos de precipitación CHIRPS para Colombia a escala diaria, mensual y anual en el periodo 1981-2014. In XXVII Congreso Latinoamericano de Hidráulica, IAHS, Lima, Perú, URL http://ladhi2016. org

Veleda D, Montagne R, Araujo M. 2012. Cross-wavelet bias corrected by normalizing scales. Journal of Atmospheric and Oceanic Technology 29, 1401-1408. https://doi.org/10.1175/JTECH-D-11-00140.1

Whan K, and Zwiers F. 2017. The impact of ENSO and the NAO on extreme winter precipitation in North America in observations and regional climate models. Climate Dynamics 48, 1401–1411. https://doi.org/10.1007/s00382-016-3148-x

Weng W, Becker SL, Lüdeke, M. K., Lakes, T. 2020. Landscape matters: Insights from the impact of mega-droughts on Colombia’s energy transition. Environmental Innovation and Societal Transitions 36, 1-16. https://doi.org/10.1016/j.eist.2020.04.003

Yu B, Zhang X, Lin H, Yu JY. 2015. Comparison of wintertime North American climate impacts associated with multiple ENSO indices. Atmosphere-ocean 53, 426-445. https://doi.org/10.1080/07055900.2015.1079697

Zhang Z, Leng Y, Yang Y, Xiao X, Ge S. 2014. Comparative study on wavelet coherence and HHT coherence. In 2014 7th International Congress on Image and Signal Processing (pp. 867-872). IEEE. https://doi.org/10.1109/CISP.2014.7003899

Zhang W, Wang L, Xiang B, Qi L, He J. 2015. Impacts of two types of La Nina on the NAO during boreal winter. Climate Dynamics 44, 1351–1366. https://doi.org/10.1007/s00382-014-2155-z

Zhang W, Wang Z, Stuecker MF, Turner AG, Jin FF, Geng X. 2019. Impact of ENSO longitudinal position on teleconnections to the NAO. Climate Dynamics 52, 257-274. https://doi.org/10.1007/s00382-018-4135-1

APPENDIX

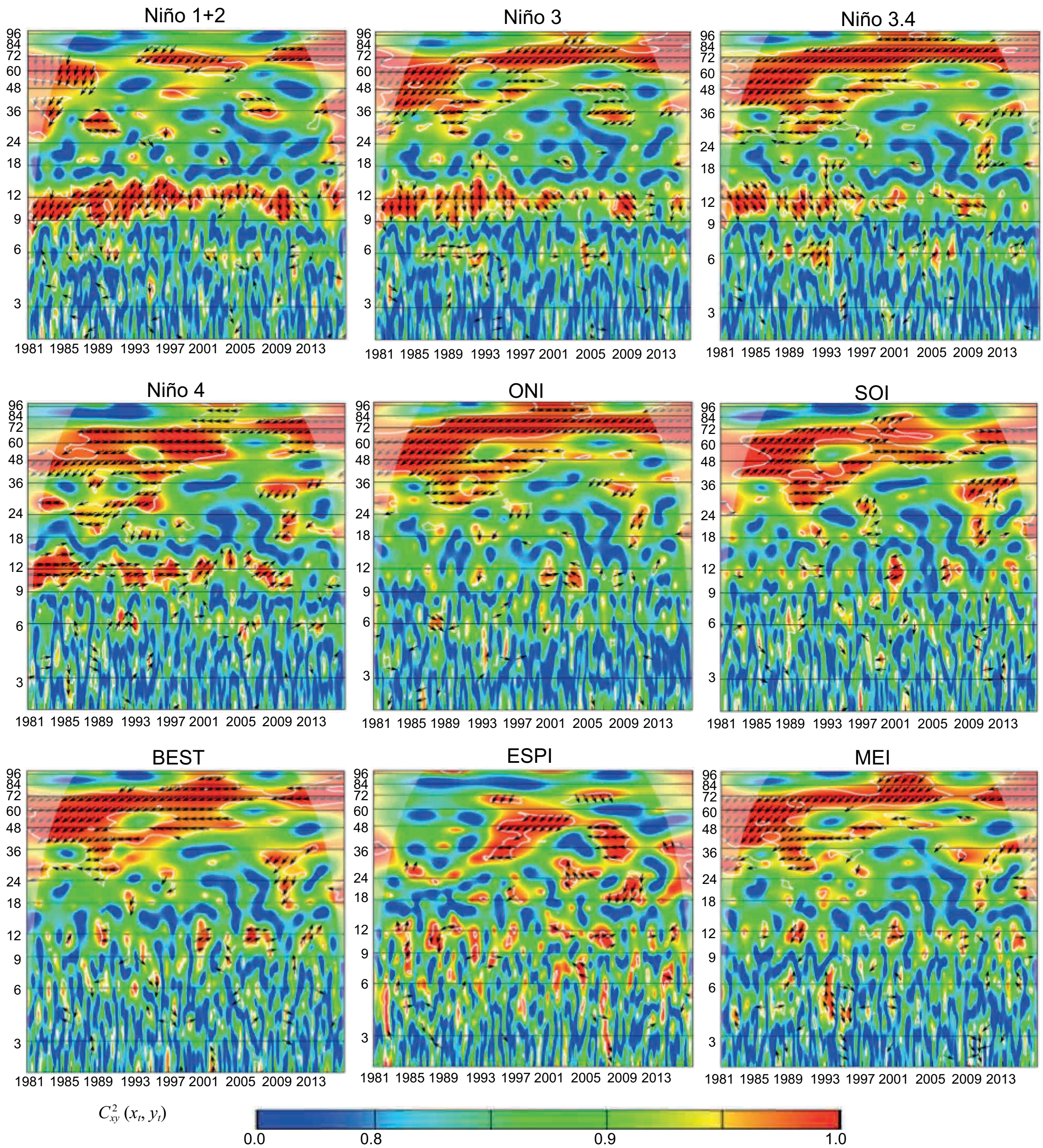

Fig. A1. Wavelet coherence $C^2_{x,y}(x_t, y_t)$, and phase difference $Arg(T_{x,y}(\tau, s))$ between ENSO indices and precipitation of La esperanza station. The cone of influence is the area outside of the with a concave-down shape, and regions of significant periodicities at a 5% are enclosed by the thick white lines. Data from CHIRPS. Anti-phase: ← In-phase: →

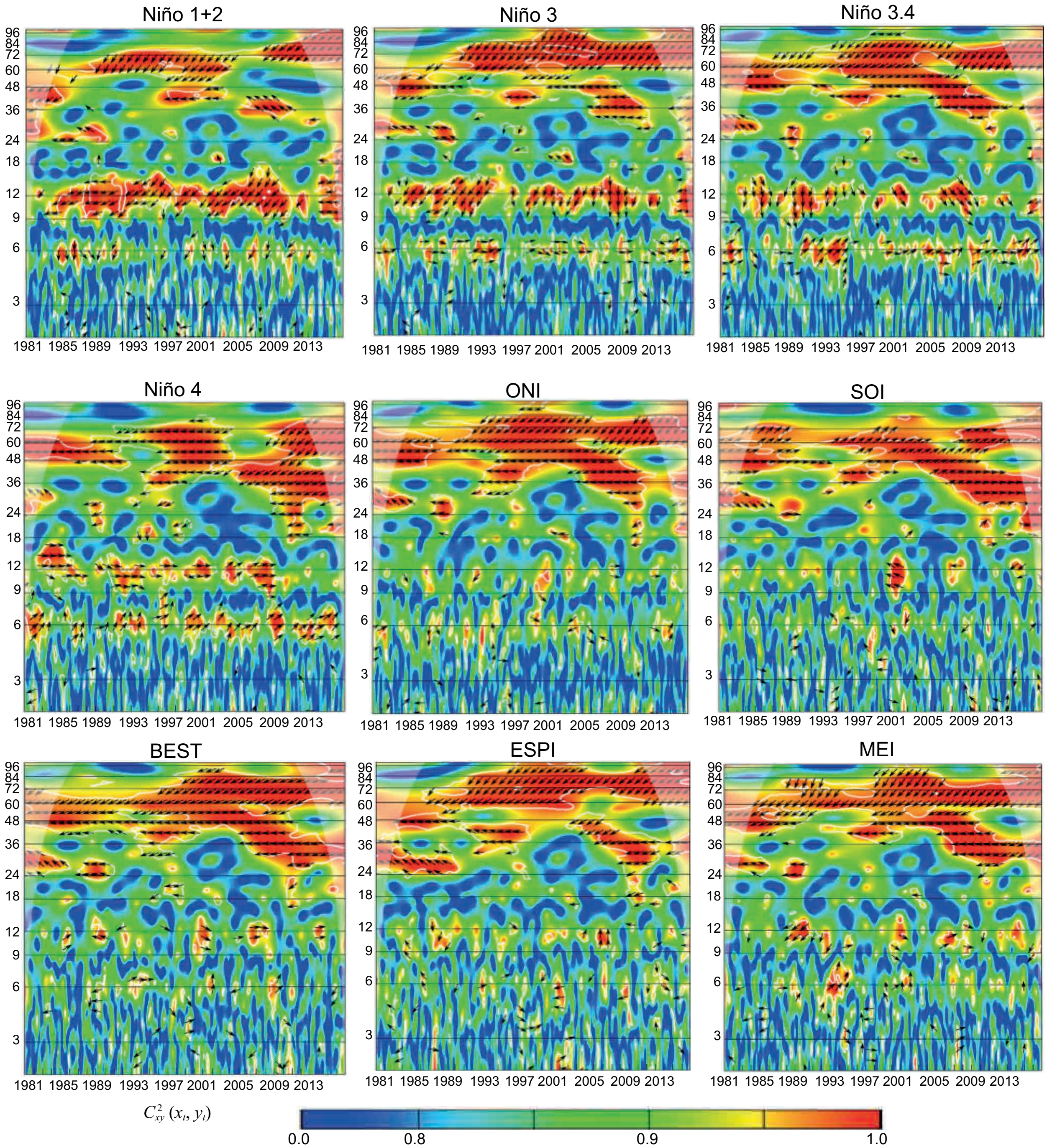

Fig. A2. Wavelet coherence $C^2_{x,y}(x_t, y_t)$, and phase difference $Arg(T_{x,y}(\tau, s))$ between ENSO indices and precipitation of Matitas station. The cone of influence is the area outside of the with a concave-down shape, and regions of significant periodicities at a 5% are enclosed by the thick white lines. Data from CHIRPS. Anti-phase:← In-phase: →

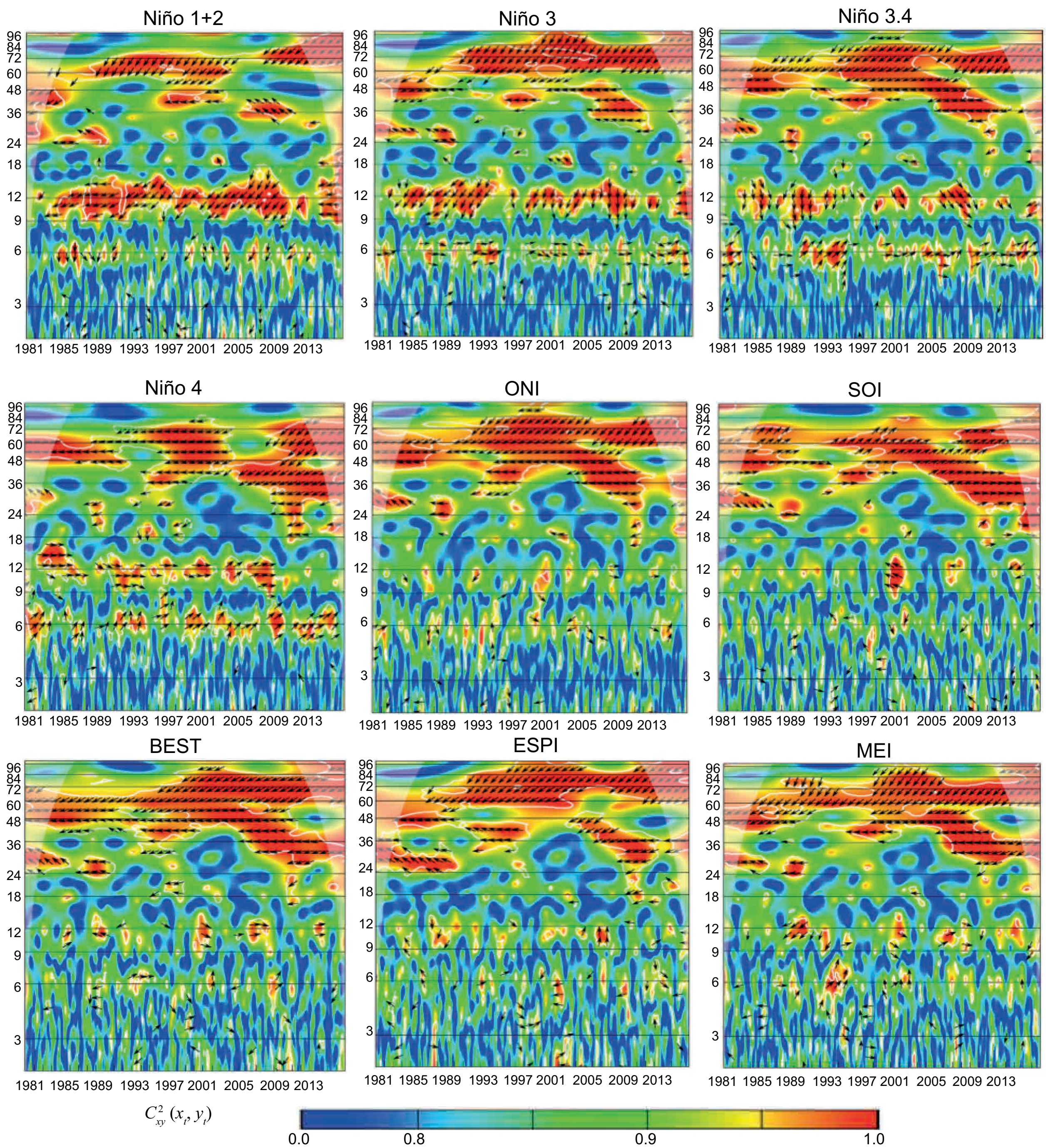

Fig. A3. Wavelet coherence $C^2_{x,y}(x_t, y^t)$, and phase difference $Arg(T_{x,y}(\tau, s))$ between ENSO indices and precipitation of Mompos station. The cone of influence is the area outside of the with a concave-down shape, and regions of significant periodicities at a 5% are enclosed by the thick white lines. Data from CHIRPS. Anti-phase: ← In-phase: →

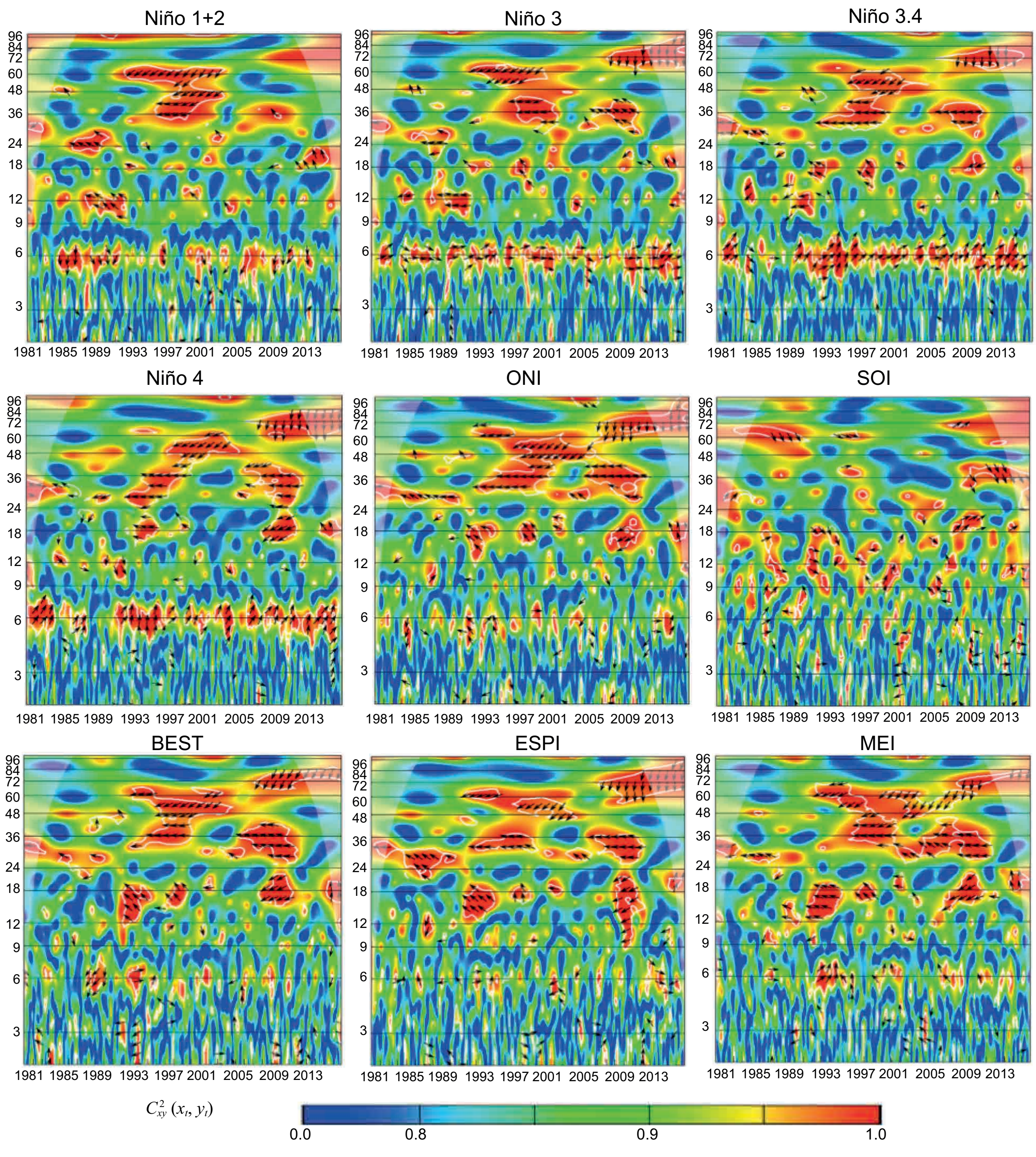

Fig. A4. Wavelet coherence $C^2_{x,y}\,(x_t, y^t)$, and phase difference $Arg(T_{x,y}\,(\tau, s))$ between ENSO indices and precipitation of Mesopotamia station. The cone of influence is the area outside of the with a concave-down shape, and regions of significant periodicities at a 5% are enclosed by the thick white lines. Data from CHIRPS. Anti-phase: ← In-phase: →

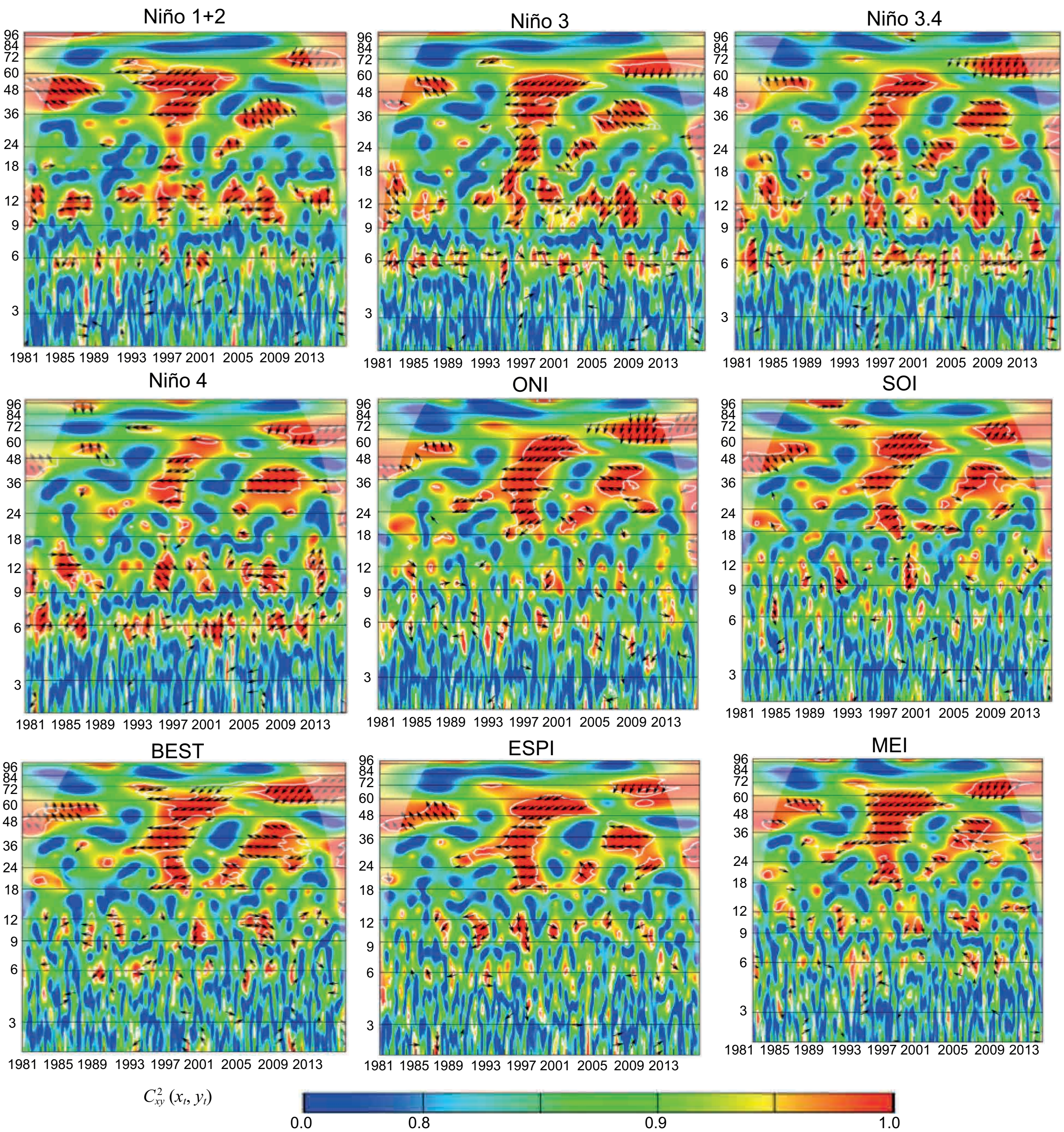

Fig. A5. Wavelet coherence $C^2_{x,y}(x_t, y^t)$, and phase difference $Arg(T_{x,y}(\tau, s))$ between ENSO indices and precipitation of Cimitarra station. The cone of influence is the area outside of the with a concave-down shape, and regions of significant periodicities at a 5% are enclosed by the thick white lines. Data from CHIRPS. Anti-phase: ← In-phase: →

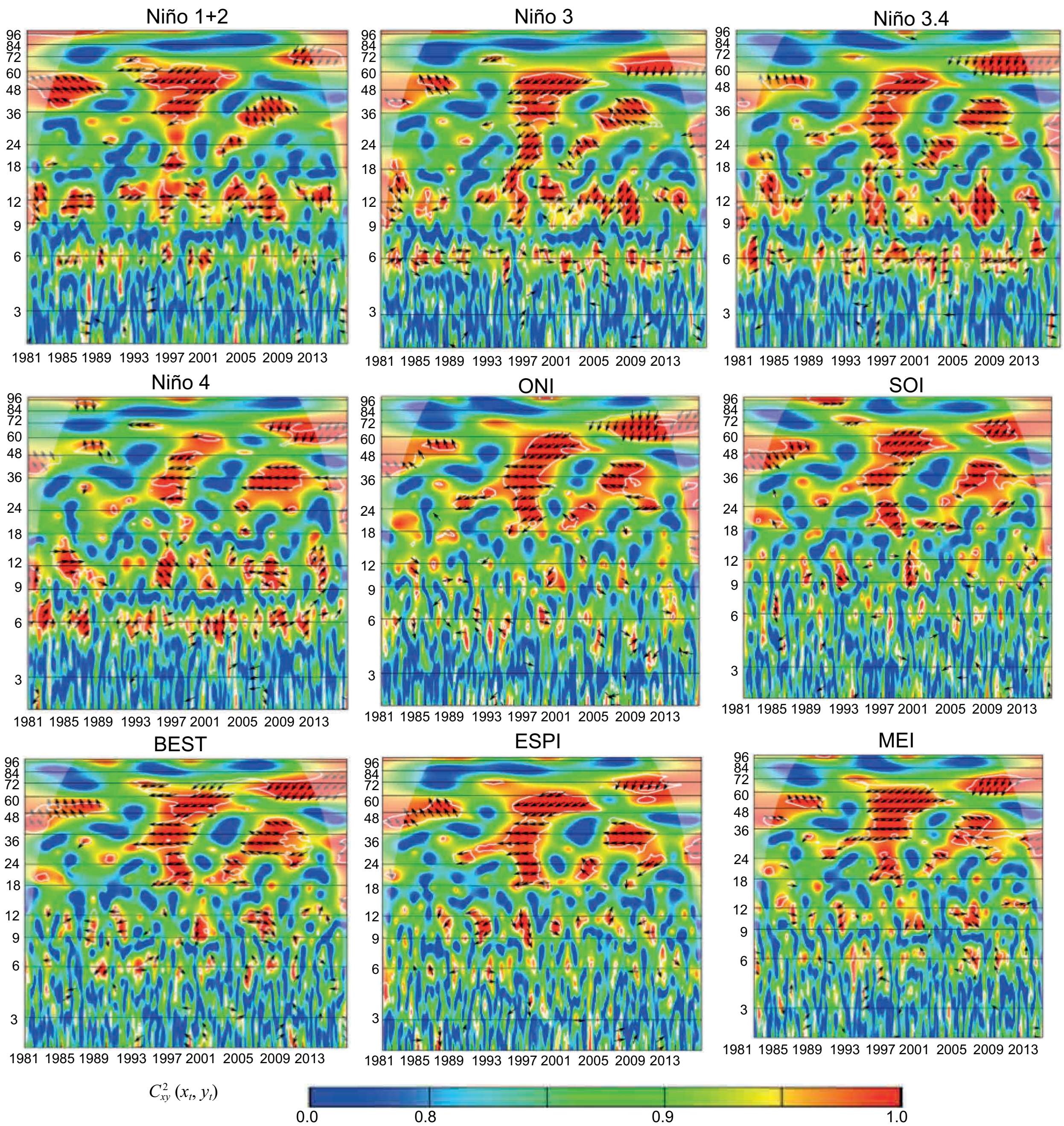

Fig A6. Wavelet coherence $C^2_{x,y}(x_t, y^t)$, and phase difference $Arg(T_{x,y}(\tau, s))$ between ENSO indices and precipitation of Iser Pamplona station. The cone of influence is the area outside of the with a concave-down shape, and regions of significant periodicities at a 5% are enclosed by the thick white lines. Data from CHIRPS. Anti-phase: ← In-phase: →

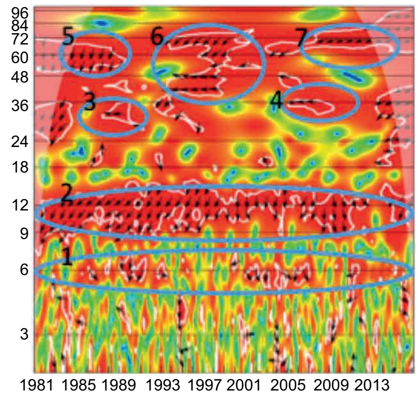

Fig. A7. Location of the most recurrent significant areas in wavelet coherence spectra.

Table AI. Phase differences and their interpretation. Based in Torrence and Compo (2011).

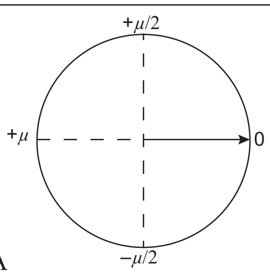 A In phase	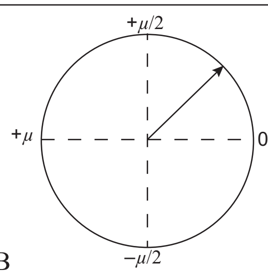 B In phase. *Leading: x, lagging: y.*	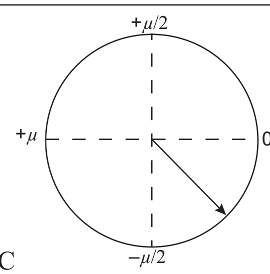 C In phase. *Leading: y, lagging: x*
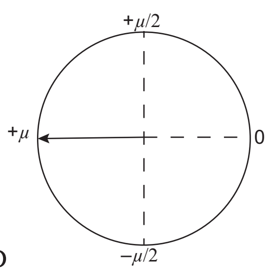 D Anti-phase	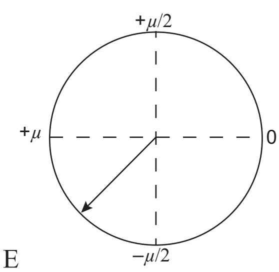 E Anti-phase. *Leading: x, lagging: y*	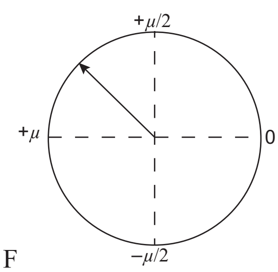 F Anti-phase. *Leading: y, lagging: x*

Table AII: Paramenters for the WT and WC procedures

Paramenter	Value
Time resolution (*dt*):	1 month
Frequency resolution (*dj*):	1/20
Lower Period ($s_{mín}$):	2
Upper Period (s_{max}):	120
Method to make contour lines	Red noise
Numero de simulaciones	1000

Atmósfera 35(2), 273-286 (2022)
https://doi.org/10.20937/ATM.52901

CONTENTS

Vorticity and Thermodynamics in a Gulf of Mexico Atmospheric River

José MARTÍNEZ-CLAROS[1]*, David J. RAYMOND[1,2] and Željka FUCHS-STONE[1,2]

[1] *Physics Department, New Mexico Tech, Socorro, NM, US.*
[2] *Climate and Water Consortium, New Mexico Tech, Socorro, NM, USA.*
*Corresponding author: jose.martinezclaros@student.nmt.edu

Received: May 11, 2020, acepted: August 19, 2020

RESUMEN

Este artículo examina la interacción de la humedad tropical con un río atmosférico. El análisis de este trabajo se centra principalmente en los datos de sondas lanzadas desde aviones ("*dropsondes*") recopilados durante el quinto día del Experimento de Procesos Convectivos (CPEX). Se elige un área de interés en el centro del Golfo de México, hasta donde la humedad remanente del sistema tropical Beatriz penetró desde el Pacífico Oriental después de tocar tierra en la costa occidental de México. Los resultados de este estudio muestran un patrón de vorticidad a nivel medio con inclinación hacia el este, junto con una alta fracción de saturación y un bajo índice de inestabilidad en el régimen predominantemente estratiforme presente en la región. Una relación inversa entre la fracción de saturación y el índice de inestabilidad, como lo indica el cuasi-equilibrio de humedad (MQE), se encuentra en un régimen previamente dominado por convección. El fuerte cizallamiento vertical indica que el patrón de vorticidad dentro de este sistema estratiforme está siendo advectado hacia latitudes medias. En este caso de estudio se observan canales estrechos de humedad, denominados ríos atmosféricos (AR), moviéndose hacia el polo. Proporcionamos información sobre la vorticidad y MQE como herramientas conceptuales para caracterizar el mecanismo de humedad de los ríos atmosféricos en los trópicos, donde los procesos físicos detrás de estas estructuras similares a los ríos son menos conocidos.

ABSTRACT

This paper examines the interaction of tropical moisture with an atmospheric river. The analysis of this paper is focused mainly on dropsonde data collected during the fifth day of the Convective Processes Experiment (CPEX). An area of interest is chosen over the central Gulf of Mexico, where the remnant moisture of the tropical system Beatriz penetrated from the Eastern Pacific after making landfall in the western coast of Mexico. Results in this study show an eastward-tilting pattern of enhanced mid-level vorticity, coupled with high saturation fraction and low instability index in the predominantly stratiform regime present in the region. An inverse relation between saturation fraction and instability index, as indicated by moisture quasi-equilibrium (MQE), is found in a previously-dominant convective regime. Strong vertical shear signals that the vorticity pattern within this stratiform system is being advected poleward into mid-latitudes. Poleward-moving moisture plumes in narrow channels called atmospheric rivers (ARs) are observed during the mission. We provide insights into vorticity and MQE as conceptual tools to characterize the moisture mechanism of atmospheric rivers near the tropics, where the physical processes behind these river-like structures are less well-understood.

Keywords: Moisture quasi-equilibrium, vorticity, atmospheric rivers, moisture transport.

1. Introduction

The study of the large-scale water vapor fluxes in the atmosphere has gained increasing level of interest from scientists of diverse fields in the past three decades. A commonly-known structure by which moisture transport is accomplished at planetary scales is the atmospheric river (AR). The usage of this term has transcended the scientific community into the public lexicon (Ralph et al., 2018), in great part due to associated flooding hazards, as well as drought-relief benefits related to this phenomenon (Ralph et al., 2018, 2019).

ARs are defined as “long, narrow and transient” channels of “strong, horizontal” transport of water vapor, commonly associated a “low-level jet stream ahead of the cold front of an extratropical cyclone” (Zhu and Newell. 1998; Ralph et al., 2004, 2006, 2017; Bao et al., 2006; Stohl et al., 2008; Warner et al., 2012; Cordeira et al., 2013; Sodeman and Stohl, 2013; Dacre et al., 2015). Consistent with this definition, AR transport, also known as integrated vapor transport (IVT) (Ralph et al., 2017) is defined as the vertically-integrated horizontal flux of water vapor, and this transport is expected to be mostly at low levels (see e.g., Ralph et al., 2006, 2017).

Early AR studies depended on satellite-based observations of integrated water vapor (IWV), the vertically-integrated water vapor, using Special Sensor Microwave/Imager (SSM/I) satellite data (e.g., Ralph et al., 2004; Wick et al., 2013), or on reanalyses and model-derived analyses (e.g., Neiman et al., 2008; Lavers et al., 2011; Cordeira et al., 2013). Several studies exist at the present time that are based on analysis of in-situ dropsondes deployed over a region of interest for atmospheric rivers (e.g., Ralph et al., 2004, 2005, 2017). These measurements serve as validations to the estimates of horizontal waterr vapor transport provided by satellite, reanalysis, and model-derived calculations. According to Ralph et al. (2017), the accuracy of the estimate of the amount of water vapor transported by ARs is, however, still questionable.

The current characterization of the behavior of atmospheric rivers near tropical regions remains poorly-understood and has been subject of extensive debate. According to Ralph et al. (2017), IWV measurements identify AR signatures in locations with weak horizontal vapor transport, often in what is defined as the equatorward tail of these elongated corridors. Ralph et al. (2019) establishes a distinction between ARs detected in subtropical latitudes and those detected in mid-latitudes, based on observations on the relative importance of the wind field in producing the ARs. Additionally, upward forcing of water vapor leading to heavy precipitation, is not an intrinsic feature of atmospheric rivers, based on the two-dimensional definition of AR transport. This definition on its own limits the ability to elucidate the impact of tropical dynamics in the physical processes of ARs.

The tropical troposphere is characterized by the absence of baroclinic instability, mainly due to the weak nature of horizontal temperature gradients (Charney, 1963; Sobel and Bretherton, 2000). MQE is a convective feedback mechanism identified by strong anti-correlation between tropospheric column moisture and moist convective instability, which indicates a link between the environmental moisture and the temperature structure. This mechanism was first observed empirically in TCS08 and PREDICT, and has since been documented in numerous observations (e.g., Raymond et al., 2011; Gjorgjievska and Raymond, 2014; Raymond et al., 2014) and cloud-resolving models (e.g., Singh and O’Gorman, 2013; Raymond and Flores, 2016; Raymond and Kilroy, 2019.

IWV and IVT, measurements based on precipitable water have historically been used to characterize atmospheric rivers (e.g., Ralph et al., 2004, 2006, 2011, 2017; Neiman et al., 2008; Dettinger et al., 2011). Recent studies indicate that the rainfall rate is strongly linked with saturation fraction (Bretherton et al., 2004; Raymond et al., 2011; Gjorgjievska and Raymond, 2013; Raymond et al., 2014). Raymond (2000) defines saturation fraction as

$$S = \frac{\int r dp}{\int r^* dp} \tag{1}$$

where the numerator corresponds to the pressure integral of the water-vapor mixing ratio r, and the denominator corresponds to the pressure integral of water-vapor saturation mixing ratio r^*. In simple terms, saturation fraction is the ratio between precipitable water and saturated precipitable water.

According to Raymond and Sessions (2007) and Raymond and Flores (2016), decreasing instability index corresponds to higher saturation fraction and more precipitation. Instability index is defined as (Raymond et al., 2011).

$$I = s^{*}_{low} - s^{*}_{mid} \tag{2}$$

where s^{*}_{low} is the vertically-averaged water-vapor saturated moist entropy for the low troposphere (1-3 *km* altitude), and s^{*}_{mid} is the vertically-averaged water-vapor saturated moist entropy for a portion of the mid-troposphere (5-7 *km*). Saturated moist entropy is a function of pressure and temperature; thus, at a given pressure, it depends solely on the temperature profile. Tropical temperature profiles associated with deep convection frequently exhibit a vertical dipole pattern, with a relative cooling in the lower troposphere and relative warming in the upper troposphere. Near-zero instability index values indicate a sharp temperature anomaly dipole between low and middle levels in the troposphere, whereas high instability index values indicate a temperature anomaly dipole of the opposite sign.

MQE plus the relationship between saturation fraction and precipitation set two thermodynamic constraints that are hypothesized to control the average behavior of convection in the tropical troposphere, discounting the behavior of the boundary layer. The upper bound, or set point, in column moisture as a function of instability index is a key concept behind MQE. Singh and O'Gorman (2013) present a similar argument by identifying a set point of Convective Available Potential Energy (CAPE) as a function of saturation deficit in the near-zero buoyancy limit.

The causality of MQE is associated with vorticity and instability index. Hoskins et al. (1985) show how vertical temperature perturbations are related to the potential vorticity distribution. Raymond (1992) shows that over tropical oceans, where horizontal temperature gradients are generally weak, absolute vorticity, specifically its vertical component, is the part of potential vorticity that matters the most. Raymond et al. (2011) and Gjorgjievska and Raymond (2014) explain that the presence of a mid-level vortex induces a temperature anomaly dipole - with cooling below and warming above - by virtue of the thermal wind balance. As the adjusted thermodynamic environment reduces the instability index, convection responds to this temperature anomaly by modifying the vertical mass flux profile to relatively more bottom-heavy (Raymond and Sessions, 2007; Gjorgjievska and Raymond, 2014; Sessions et al., 2015, 2016, 2019). As a result, low-level convergence is favored, which in turn increases column moisture.

This paper explores how the deformation of a pre-existing mid-level vorticity pattern in the Gulf of Mexico, caused by strong vertical shear, influences the moisture profile in the resulting river-like structure. We use data from CPEX and expand it with NCEP FNL analysis. Section 2 presents data and methods; in section 3, we describe results from CPEX and FNL; in section 4, we discuss these results.

2. Data and Methods

The NASA Convective Processes Experiment (CPEX) was a one-month aircraft field campaign that took place in the North Atlantic - Gulf of Mexico - Caribbean oceanic region during May and June of 2017. The aircraft instruments used were: dropsondes, a downward pointing K-band radar (APR-2), a wind profile lidar (DAWN), and 3 microwave instruments (MTHP, MASC, HAMSR). The data used in this paper were obtained from the 16 research flights that occurred in May and June of 2017.

For our particular research flight, 19 dropsondes were launched from the NASA DC-8 aircraft from an altitude of 12.5 km. This provided vertical profiles of dynamic and thermodynamic variables, such as wind velocity, air and dew point temperature of all vertical levels of the tropical troposphere. For the case study of this paper, we used only dropsonde vertical profiles to develop further analysis.

A three-dimensional variational scheme (3DVar) described in López Carrillo and Raymond (2011) was used as a tool to visualize the dynamic and thermodynamic structure within the bounds of the experimental box, by constructing an interpolated volume grid using only vertical profile data obtained from the dropsondes. For our case study, the experiment was designed assuming a stationary system, during the time window from the first to the last dropsonde launch.

The output of the 3DVar analysis in the chosen regular grid includes fields from measured variables, such as pressure, air and dew point temperatures, and wind velocity, as well as derived field calculations, such as moist entropy, saturated moist entropy, vorticity and divergence.

Every research flight required us to understand large-scale conditions for a region of interest over the tropical ocean basins of the field campaign. At the beginning of June 2017, the remnant outflow of tropical system Beatriz had transported overcast cloudiness from the eastern Pacific into the Gulf of Mexico. As a result of this outflow combining with other sources of moisture, a large system centered around (24º N, 93º W) covered a significant portion of the Gulf of Mexico on June 2, 2017, as shown in the satellite image of Figure 1. The mission concerning this case study occurred on this date, and it was the fifth one in the sequence.

The mission consisted of making two cross-sections of the moisture flowing to the NE over the central Gulf of Mexico, originating from the remnants of eastern Pacific tropical storm Beatriz. The first, westbound cross section went from (23º N, 87º W) to (23º N, 96º W). The second cross section went from (24º N, 96º W) to (24º N, 87º W). A total of 19 sondes were dropped in a box-shaped E-W cross sectional area; due to partial sonde malfunction, more sondes were dropped in the eastern half of the box. Figure 2 shows a total of 15 sondes that were considered useful after quality control, for further gridded analysis. The box we chose for the experiment covers a large longitude range, compared to the range in latitude.

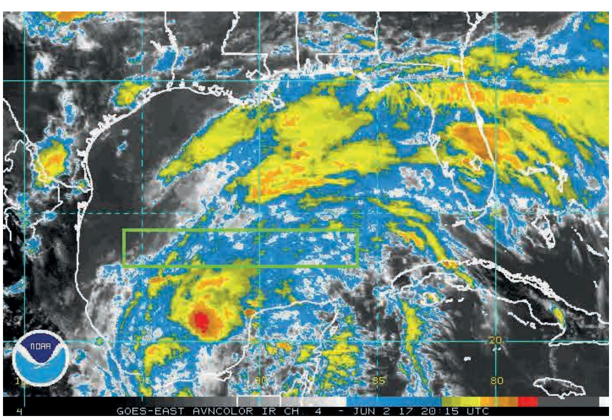

Fig. 1. GOES-13 infrared (IR) satellite image for June 2, 2017, centered on the Gulf of Mexico. The green rectangle represents the domain of the research flight for that day. Credit: Adapted from NOAA/NHC.

Therefore, all the cross-sections plotted after 3DVar analysis are averaged with respect to latitude.

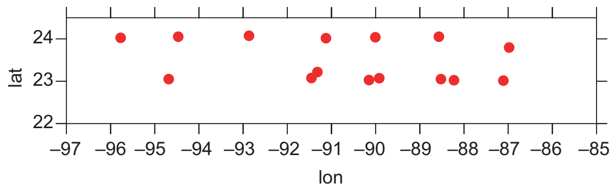

Fig. 2. Location of 15 quality-controlled dropsondes used for 3DVar analysis

As an ancillary tool to our observations we used data from the Airborne Precipitation Radar (APR-2). APR-2 is a downward pointing K-band radar that operates on dual frequency bands, namely 13.4 GHz (Ku-band) and 35.6 GHz (Ka-band). It was deployed on the NASA DC-8, as part of every mission flight. For our case study, we used APR-2 to classify environmental cloudiness as stratiform or convective, for the duration of the flight. We used Ku-band radar reflectivity data to visualize east-west vertical cross-sections of the disturbance within the experimental box.

Figure 3 shows APR-2 radar-indicated Ku-band reflectivity cross-sections with respect to longitude. Every longitude in the flight path of our domain of interest was crossed at least once. The cross-sections at the top of Figure 3 correspond to regions of predominantly stratiform cloudiness, as indicated by the presence of bright bands at a height of 4 km. These bright bands between 92.5º W and 88.5º W indicate the presence of melting snow, in addition to weak updrafts aloft (Houze, 1997). Conversely, isolated large vertical, towering portions of strong reflectivity (Figure 3, bottom) from the surface to levels of 8 km (left) and 4 km (right) indicate strong updrafts associated with active convection near 96º W and 93º W, respectively.

3. Results

3.1 Along-system and across-system winds

In an effort to better understand the predominant direction of the flow at different vertical levels within the system we studied, it was convenient to

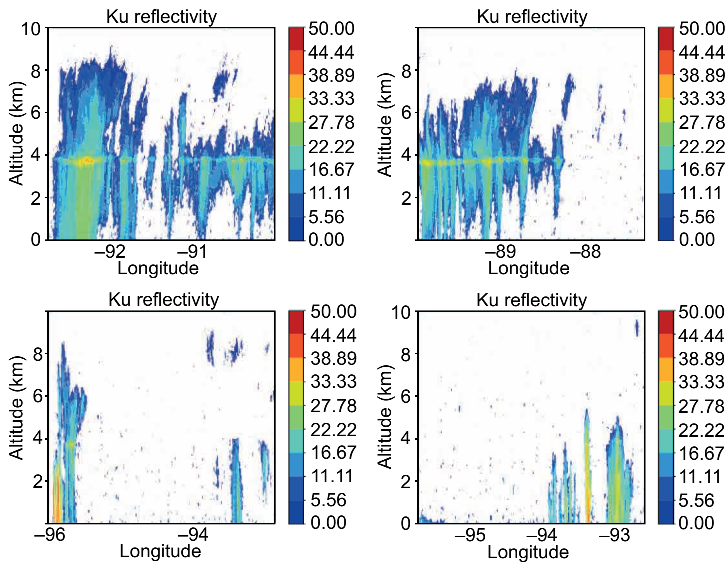

Fig. 3. APR-2 Ku-band reflectivity vertical cross-sections, showing different stages of convection during different parts of the mission.

rotate the coordinate system of the experimental box counterclockwise by 45 degrees. This technique was useful to define two main coordinate axes for the wind velocities, which were along (northeastward) and across (northwestward) system, separately displayed as the left and right plots of Figure 4, respectively. The system is defined as the extensive region of cloud coverage over the Gulf of Mexico, as indicated by the satellite image of Figure 1.

Figure 4 (left) shows a vertically-sheared structure, most prominently on the western part of the cross section. A northeastward jet tilts upward between altitude. Figure 4 (right) shows a strong northwestward jet at low levels on the east side of the box, leading to apparent low-level convergence around 93º W.

The horizontal structure of the winds at 5-km altitude (Figure 4, left) indicates there is horizontal

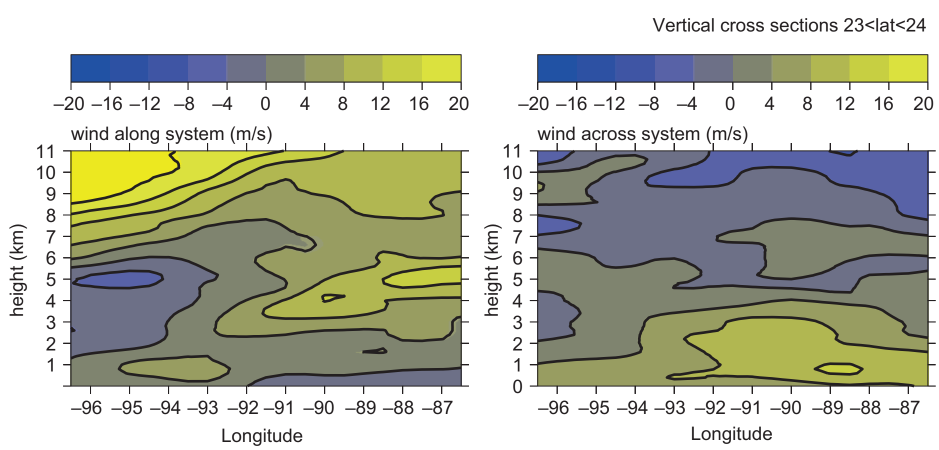

Fig. 4. Northeastward (along system) and northwestward (across system) winds. The system is defined as the extensive region of cloud coverage over the Gulf of Mexico, as indicated by the satellite image of Figure 1.

shear corresponding to cyclonic vorticity, as the direction of the winds shifts from southwestward (west) to northeastward (east). This is consistent with the strong mid-level vorticity shown in Figure 10, peaking roughly at 5-km altitude.

3.2 Air temperature anomalies

Figure 5 shows air temperature anomaly cross-sections for the experimental region. A close look at Figure 5 shows warm anomalies above cold anomalies with eastward tilt, from low levels to mid-levels. This temperature anomaly structure is indicative of a more stable environment. Additionally, Figure 5 shows sharp cold anomalies near the surface within a small sub-region of the experimental box, between 93º W and 91º W. This smaller sub-region of much colder air than that of the surroundings at either direction can be identified as a cold pool.

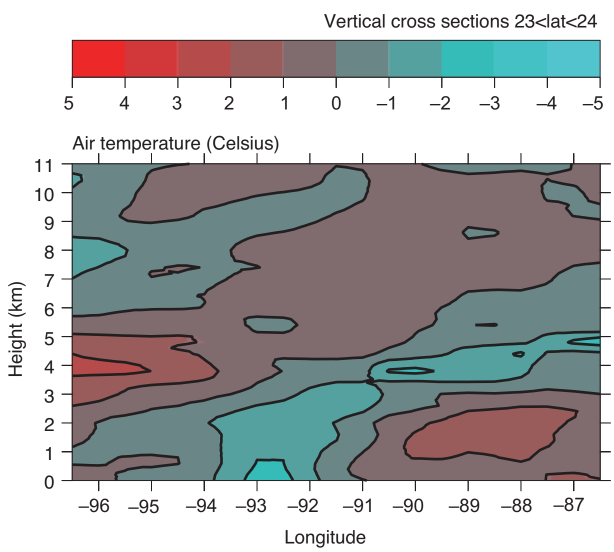

Fig. 5. Air temperature anomaly cross sections.

3.3 Entropy

Figure 6 shows cross-sections for moist entropy and saturated moist entropy, at the left and center plot boxes, respectively. Moist entropy is a variable similar to equivalent potential temperature, which is conserved under phase transitions. Saturated moist entropy is a variable like saturated equivalent potential temperature, and is a function of only pressure and temperature. A constant saturated moist entropy value with respect to height corresponds to moist neutral instability (Raymond, 2013).

Boundary-layer values of moist entropy and saturated moist entropy are low at a small sub-region, located between 93º W and 91º W longitude (red ellipses in Figure 6). Therefore, both temperature and moisture are lower near surface in this small sub-region, a manifestation of the cold pool discussed in Figure 5. Red vertical lines in Figure 6 point out the locations where convective updrafts were observed in APR-2 radar reflectivity (Figure 3, bottom). The length of these vertical lines represents the approximate vertical extent of the observed updrafts. We note that both updrafts are seen to the west of the observed cold pool. Both moist entropy and saturated moist entropy values are high between the locations of the updrafts. Relative humidity cross-sections are shown for comparison (Figure 6, right). We note that the highest values of relative humidity correspond to the regions of melting snow at the freezing level, consistent with the observed bright bands seen in the APR-2 radar reflectivity cross-sections. Conversely, the cold pool at 93º W is barely a distinctive feature seen in relative humidity cross-sections.

3.4 Saturation fraction and instability index

Figure 7 shows plots of saturation fraction and instability index as a function of longitude, indicating that saturation fraction is anti-correlated to instability index within the region of our study. Close to 92º W, a relative maximum in saturation fraction corresponds to a relative minimum in instability index. We note that this is a fairly extreme case, as the instability index actually becomes negative between 91º W and 93º W, i.e., nearly co-located with the cold pool. However, the maximum value of saturation fraction does not increase indefinitely, even in this extreme case. This result is consistent with the constraint of MQE. i.e., an apparent upper bound in moisture as function of instability.

To test the validity of the results obtained through 3DVar analysis of dropsonde profiles in Figure 7 within the bounds of the experimental domain, we compare with analysis data from the FNL, a spectral analysis system created by NCEP. Figure 8 shows the same plots as Figure 7 but based only on FNL analysis data. Figure 8 shows remarkable agreement with

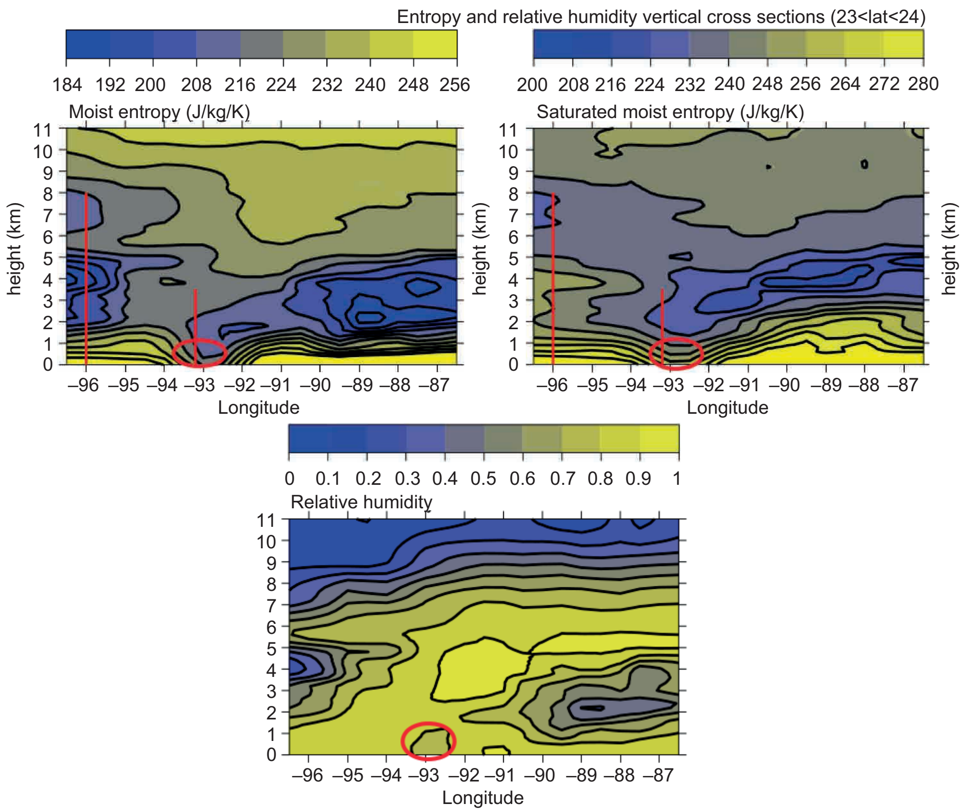

Fig. 6. Moist entropy (left) and saturated moist entropy (center) cross sections. Red ellipses indicate approximate location of cold pool; red vertical lines indicate regions of APR-2 reflectivity-indicated vertical updrafts, and the vertical depth of the updraft. Relative humidity (right) cross sections are shown for comparison.

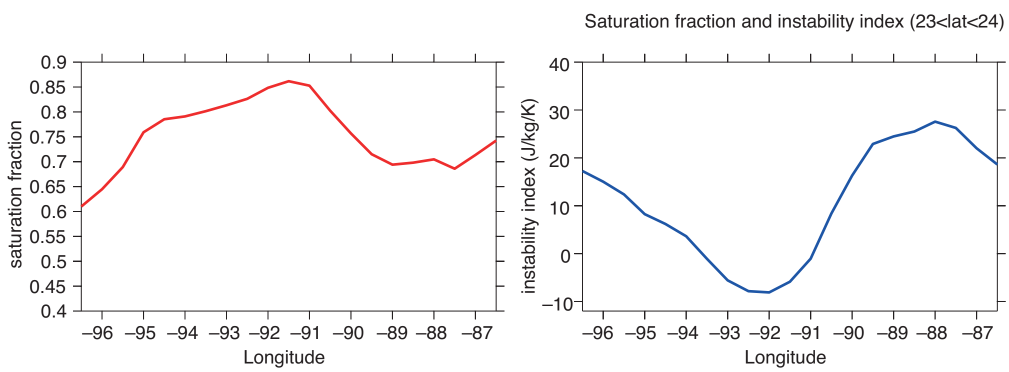

Fig. 7. Saturation fraction (left) and instability index (right) cross sections.

Figure 7, in terms of showing a relative maximum of saturation around 92º W. For instability index, the profiles are similar to an acceptable degree; however, we note that instability index does not become negative in Figure 8, as it does in Figure 7. The negative instability index values are likely an after-effect of the precipitation that occurred close to where the cold pool is detected by 3DVar analysis of the dropsonde

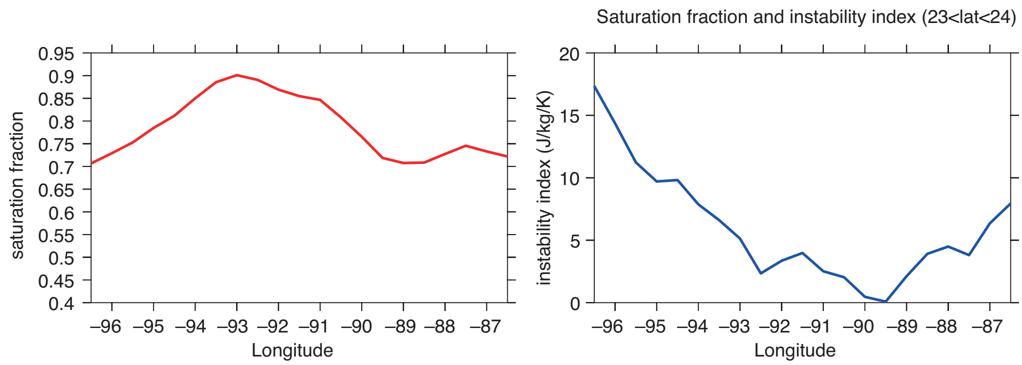

Fig. 8. Saturation fraction (left) and instability index (right) cross sections, based on FNL analysis data.

profiles. The cold pool and localized regions of precipitation are not detected by the FNL, thus, we attribute the same difference between both figures as a consequence of the differences in resolution between both datasets.

As we will discuss in the next sub-section, the results in Figure 7 indicate how the temperature and moisture structure are intricately related to the vorticity.

3.5 Vorticity and divergence cross-sections

The vertical component of absolute vorticity ς_z is

$$\varsigma_z = \left(\frac{\partial v}{\partial x} - \frac{\partial u}{\partial y}\right) + f \qquad (3)$$

where x and y are the respective longitude and latitude coordinates modified implicitly to account for a spherical Earth, u and v are the zonal and meridional components of the wind vector, and f is the latitude-varying Coriolis parameter. Our two traverses are too close together in latitude, and too dispersed in time to trust the derivatives. Therefore, we present a partial evaluation of vorticity considering only x derivatives, such that

$$\varsigma_z \approx \frac{\partial v}{\partial x} + f \qquad (4)$$

To test the assumption of whether the x derivative represents the vorticity within the bounds of the experimental box, we use analysis data from the FNL.

Figure 9 shows a side-to-side comparison of FNL vorticity profiles, in which the left plot represents the vorticity field calculated with both x and y derivatives, and the right plot represents the vorticity associated only with its x derivative. Both plots show a broad region of enhanced mid-level vorticity with a vertically-sheared structure. Thus, for the purpose of this case study, we can rely on the vorticity field calculation that only considers x derivatives.

Figure 10 shows estimates of absolute vorticity based on dropsonde data, assuming that the meridional directions can be neglected. The vorticity profile calculated using only x derivatives is noticeably weaker than that shown in Figure 9. This strongly indicates that y derivatives have a significant impact on the calculated value of vorticity using 3DVar analysis in the experimental domain.

A comparison between the vorticity cross-sections of Figure 9 and the temperature anomalies shown in Figure 5 suggests that these temperature anomalies, observed in the experimental box, are related to the vertically-sheared vorticity structure.

In a similar way to how we estimate the vorticity, we can express divergence in a simplified form as

$$\nabla \cdot \vec{u} = \frac{\partial v}{\partial y} + \frac{\partial u}{\partial x} \qquad (5)$$

We see the same issues with the y derivatives, so we present a partial evaluation of divergence considering only x derivatives, such that

$$\nabla \cdot \vec{u} \approx \frac{\partial u}{\partial x} \qquad (6)$$

We also use analysis data from the FNL to test how representative is the above approximation.

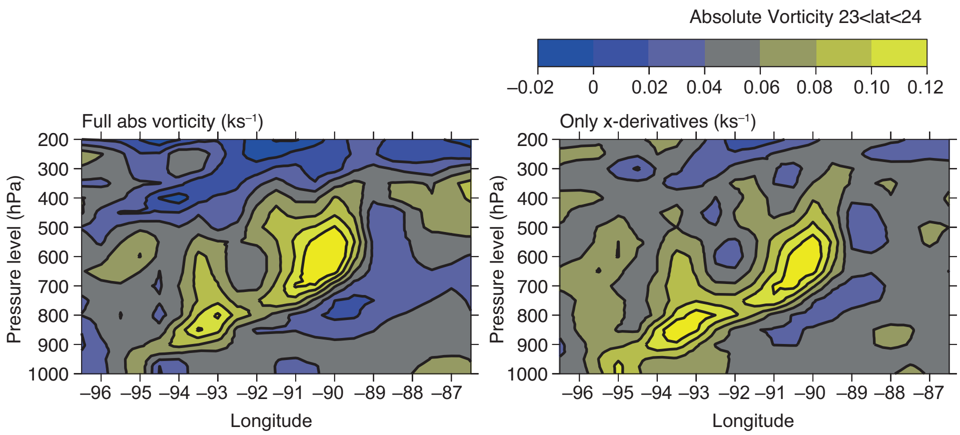

Fig. 9. Side-to-side comparison of absolute vorticity profiles, based on FNL analysis data.

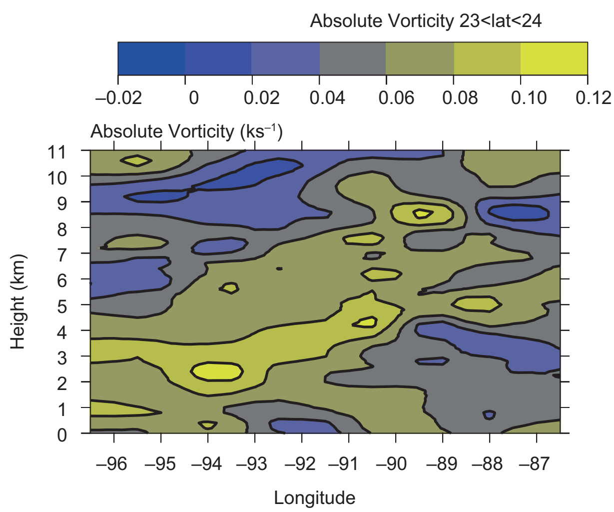

Fig. 10. Absolute vorticity vertical cross-sections, based on dropsonde data.

We show a side-to-side comparison of FNL divergence profiles in Figure 11. In contrast to the vorticity profiles, no prominent feature is clear from either plot, except the presence of low-level convergence with a vertically-sheared structure at 95ºW, west of the observed cold pool. We show the partial divergence profile corresponding to dropsonde data (Figure 12), only considering *x* derivatives, for the sake of consistency, but we admit limited confidence in the validity of these profiles. Figure 12 shows a sheared divergence structure, with some low-level convergence and a significantly sheared mid-level divergence, consistent with the dominant stratiform cloudiness observed during the experiment.

Based on the sheared-structure seen in all plots based on dropsonde data within the experimental box, we explore the large-scale conditions at the Gulf

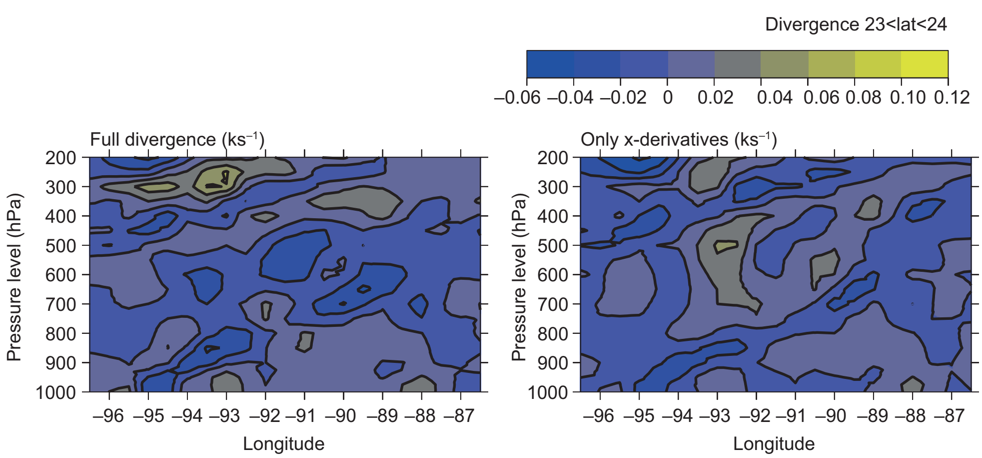

Figure 11. Side-to-side comparison of divergence profiles, based on FNL analysis data.

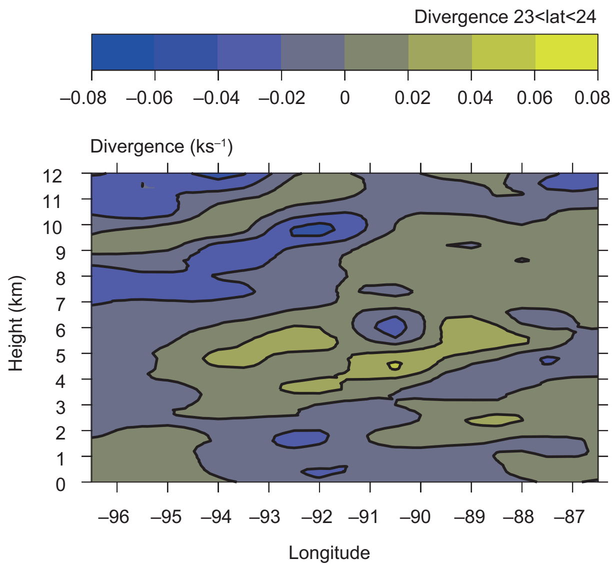

Figure 12. Divergence vertical cross-sections, based on dropsonde data.

of Mexico and Western Atlantic not just within the temporal bounds of our experiment, but also within a few days of the mission flight.

3.6 Large-scale conditions

To visualize analysis data variables relevant to our case study over the Gulf of Mexico, we relied on the FNL analysis data. We are mainly interested in diagnosing rather than forecasting; thus, we use FNL to show the large-scale conditions within the experimental box and its vicinity.

We investigate the large-scale conditions in two separate steps. First, we illustrate vertical wind profiles, similar to the ones shown in Figure 4, for various latitudes in the Gulf of Mexico and Western Atlantic, to evaluate the overall moisture transport from the tropics into mid-latitudes, occurring around the time of the mission flight. Second, we show large-scale plan views of the tropical ocean over the Gulf of Mexico, the Caribbean, and portions of the Western Atlantic.

Figure 13 shows wind cross-sections with respect to longitude for 4 different latitudes, 3 of which were chosen to illustrate the wind field at different levels in regions of the Gulf of Mexico, which is under the influence of the large cloud system, defined in Figures 1 and 4. The fourth cross-section shown in Figure 13, corresponding to latitude 29º N, visualizes the large-scale conditions near the southwest portion of the Western Atlantic, also under the influence of the same cloud system. The first three cross-sections indicate that there is strong low-level cross-flow into the jet, as the predominant direction of low-level winds is across the defined system. The fourth cross section, at 29º N, indicates weak cross-flow into the jet, and a predominance of along-system winds at all vertical levels, consistent with the definition of AR transport mentioned in the introduction. Based on Figure 13, the geographical extent of the AR does not include the Gulf of Mexico. In the next two figures, we explain why this is not the case.

Figures 14 and 15 show large-scale plan views for the Gulf of Mexico, Western Atlantic and Caribbean, at mid-levels and low-levels, respectively. Filled contours in Figure 14 indicate absolute vorticity distributions during the mission flight, averaged over the 500-700 *mb* pressure interval. Figure 15 shows the same information as Figure 14, but with vorticity averaged over the 700-900 *mb* pressure intervals. As an auxiliary analysis tool, contour plots of high saturation fraction (greater than 0.7) and low instability index (between –5 and 5 (*J*/*Kg*/*K*)), solid blue and green dashes, are respectively included.

Strong mid-level winds, shown in Figure 14 are associated with a weak high pressure ridge over the Western Atlantic and a low pressure trough over the continental United States. Conversely, strong low-level northwestward winds over the Gulf of Mexico shown in Figure 15 are driven by strong surface easterlies in the central Caribbean, which brought slightly drier air into the region of interest. The contrast in wind direction between low-levels and mid-levels over the Gulf of Mexico suggests that the AR transport over the Gulf of Mexico is very weak.

Blue dashed contours in Figures 14 and 15 corresponding to high saturation fraction, show a river-like structure in the Western Atlantic that becomes more narrow with increasing latitude, and widens in the tropics. In addition, the strength of the winds increases with latitude within this poleward channel. Figure 14 indicates that the mid-level vorticity structure in the Gulf of Mexico is being deformed due to the influence of strong vertical shear. Low instability index values, extending from mid-latitudes into the Gulf of Mexico, precisely where the mid-level vorticity is

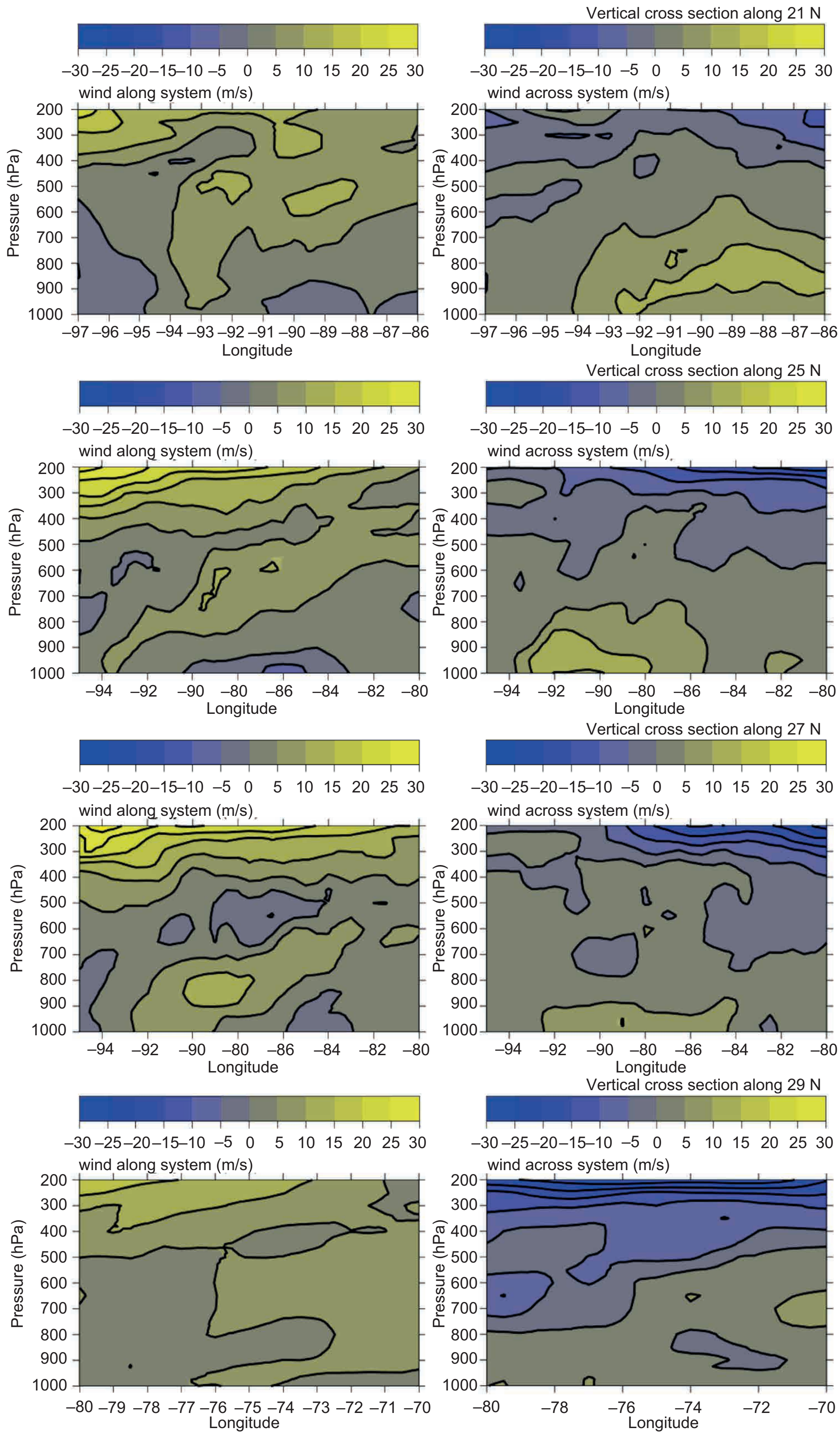

Fig. 13. Northeastward (along system) and northwestward (across system) winds with respect to longitude, based on FNL analysis output for June 2, 2017 (18:00 Z) at 4 different latitudes. The system is defined in the same way as in Figure 4.

positive, suggests that the mid-level vorticity is being advected into mid-latitudes. Thus, by virtue of MQE and how the vorticity governs the instability index, the atmospheric river can extend from the tropics into mid-latitudes, both by vorticity-induced moisture convergence in the tropics, and the combined effect of moisture transport and moisture convergence in mid-latitudes. We present our conclusions in section 4.

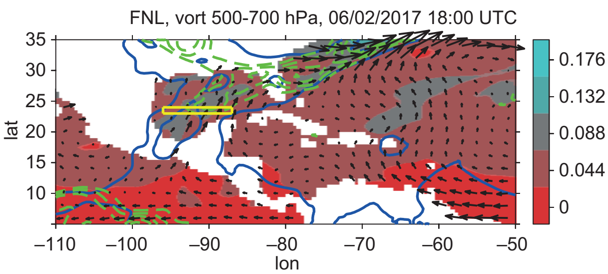

Fig. 14. Mid-level (700-500 *mb*) winds and vorticity (ks^{-1}) FNL analysis output for June 2, 2017 (18:00 Z) at the Gulf of Mexico. Solid-blue contours correspond to high saturation fraction (≥ 0.7). Green-dashed contours correspond to low instability index $-5 < ii < 5$ (*J/Kg/K*).

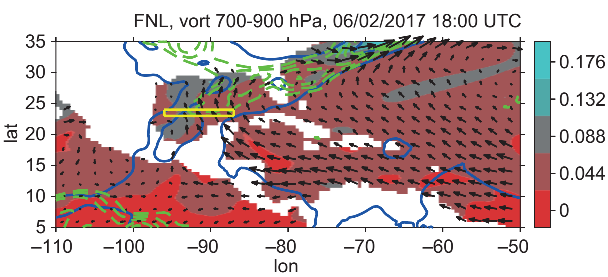

Fig. 15. Low-level (900-700 *mb*) winds and vorticity (ks^{-1}) FNL analysis output for June 2, 2017 (18:00Z) at the Gulf of Mexico. Solid-blue contours correspond to high saturation fraction (≥ 0.7). Green-dashed contours correspond to low instability index $-5 < ii < 5$ (*J/Kg/K*).

4. Conclusions

We observed a situation in which vorticity in the Gulf of Mexico was being advected to the northeast into the Western Atlantic and also being sheared. This sheared vorticity structure is most noticeable at mid-levels. The temperature perturbations associated with this vorticity structure are consistent with a balanced thermal response to it. This is evidenced particularly in the observed regions of reduced convective instability, as measured by the instability index. Moreover, the observed saturation fraction varies inversely with this instability, in agreement with the previously discussed MQE principle.

We did not observe any ongoing strong convection in the traverse; however, we saw the remnants of previous convection, in the form of extensive stratiform regions with leftover precipitation, and a strong cold pool which occurred precisely where the instability index is minimum and the saturation fraction is maximum.

We obtained a broader perspective with the FNL analysis, from which it appears that this region is under the influence of what is conventionally called an atmospheric river. However, the flow structure near the tropics is in disagreement with some of the requirements of what an atmospheric river looks like, particularly due to the absence of a low-level moisture flow along the system in this region. We present an alternative mechanism to characterize the atmospheric river, which is not constrained on the preconceived notion of horizontal moisture flux, and which relates the well-known mid-latitude river structure to the low-level cross-flow in the tropics. This picture is consistent with the notion that this is a different type of moisture (atmospheric) river, perhaps a vorticity river. By the processes we have outlined, this vorticity is ultimately responsible for the convection, which is associated with the observed moisture convergence. Finally, the alternative mechanism we have presented is meant to include the upward forcing of moisture leading to precipitation as part of the AR system.

Acknowledgments

We wish to thank Charles Jensen for processing the APR-2 radar data, and producing the radar plots in this paper. We also extend our gratitude to two anonymous reviewers, who provided valuable comments that helped make this a significantly better paper. This work was sponsored by NASA grant NNX12AJ80G.

References

Bao J, Michelson S, Neiman P, Ralph F, Wilczak J. 2006. Interpretation of enhanced integrated water vapor bands associated with extratropical cyclones: Their formation and connection to tropical moisture. Monthly Weather Review 134(4), 1063–1080. https://doi.org/10.1175/MWR3123.1

Bretherton CS, Peters ME, Back LE. 2004. Relationships between water vapor path and precipitation over the tropical oceans. Journal of Climate 17(7), 1517–1528. https:// doi.org/10.1175/1520-0442(2004)017<1517:RBWVPA>2.0.CO;2

Charney JG. 1963. A note on large-scale motions in the tropics. Journal of the Atmospheric Sciences 20(6), 607-609.

Cordeira JM, Ralph FM, Moore BJ. 2013. The development and evolution of two atmospheric rivers in proximity to western north pacific tropical cyclones in October 2010. Monthly Weather Review 141(12), 4234–4255. https://doi.org/10.1175/MWR-D-13-00019.1

Dacre HF, Clark PA, Martinez-Alvarado O, Stringer MA, Lavers DA. 2015. How do atmospheric rivers form? Bulletin of the American Meteorological Society 96(8), 1243–1255. https://doi.org/10.1175/BAMS-D-14-00031.1

Dettinger MD, Ralph FM, Das T, Neiman PJ, Cayan DR. 2011. Atmospheric rivers, floods and the water resources of California. Water 3(2), 445–478. https://doi.org/10.3390/w3020445

Gjorgjievska S, Raymond D. 2014. Interaction between dynamics and thermodynamics during tropical cyclogenesis. Atmospheric Chemistry and Physics 14(6), 3065–3082. https://doi.org/10.5194/acp-14-3065-2014

Hoskins BJ, McIntyre ME, Robertson AW. 1985. On the use and significance of isentropic potential vorticity maps. Quarterly Journal of the Royal Meteorological Society 111(470), 877–946. https://doi.org/10.1002/qj.49711147002

Houze RA. 1997. Stratiform precipitation in regions of convection: A meteorological paradox? Bulletin of the American Meteorological Society 78(10), 2179–2196. https://doi.org/10.1175/1520-0477(1997)078<2179:SPIROC>2.0.CO;2

Lavers DA, Allan RP, Wood EF, Villarini G, Brayshaw DJ, Wade AJ. 2011. Winter floods in Britain are connected to atmospheric rivers. Geophysical Research Letters 38(23). https://doi.org/10.1029/2011GL049783

López Carrillo C, Raymond DJ. 2011. Retrieval of three-dimensional wind fields from doppler radar data using an efficient two-step approach. Atmospheric Measurement Techniques 4(12), 2717–2733. https://doi.org/10.5194/amt-4-2717-2011

Neiman PJ, Ralph FM, Wick GA, Lundquist JD, Dettinger MD. 2008. Meteorological characteristics and overland precipitation impacts of atmospheric rivers affecting the west coast of north America based on eight years of SSM/I satellite observations. Journal of Hydrometeorology 9(1), 22–47. https://doi.org/10.1175/2007JHM855.1

Ralph F, Dettinger MD, Cairns MM, Galarneau TJ, Eylander J. 2018. Defining "Atmospheric River": How the Glossary of Meteorology helped resolve a debate. Bulletin of the American Meteorological Society 99(4), 837–839. https://doi.org/10.1175/BAMS-D-17-0157.1

Ralph F, Iacobellis S, Neiman P, Cordeira J, Spackman J, Waliser D, Waliser DE, Wick GA, White AB, Fairall C. 2017. Dropsonde observations of total integrated water vapor transport within north pacific atmospheric rivers. Journal of Hydrometeorology 18(9), 2577–2596. https://doi.org/10.1175/JHM-D-17-0036.1

Ralph F, Neiman P, Wick G, Rotunno R, GN Kiladis KW, Reynolds D. 2011. A multiscale observational case study of a Pacific atmospheric river exhibiting tropical-extratropical connections and a mesoscale frontal wave. Monthly Weather Review 139, 1169-1189. https://doi.org/10.1175/2010MWR3596.1

Ralph F, Neiman PJ, Rotunno R. 2005. Dropsonde observations in low-level jets over the northeastern pacific ocean from CALJET-1998 and PACJET-2001: Mean vertical-profile and atmospheric-river characteristics. Monthly Weather Review 133(4), 889–910. https://doi.org/10.1175/MWR2896.1

Ralph F, Neiman PJ, Wick GA. 2004. Satellite and CALJET aircraft observations of atmospheric rivers over the eastern north Pacific Ocean during the winter of 1997/98. Monthly Weather Review 132(7), 1721–1745. https://doi.org/10.1175/1520-0493(2004)132%3C1721:SACAOO%3E2.0.CO;2

Ralph F, Neiman PJ, Wick GA, Gutman SI, Dettinger MD, Cayan DR, White AB. 2006. Flooding on California's Russian River: Role of atmospheric rivers. Geophysical Research Letters 33(13). https://doi.org/10.1029/2006GL026689

Ralph F, Rutz JJ, Cordeira JM, Dettinger M, Anderson M, Reynolds D, Schick L, Smallcomb C 2019. A scale to characterize the strength and impacts of atmospheric rivers. Bulletin of the American Meteorological Society 100(2), 269–289. https://doi.org/10.1175/BAMS-D-18-0023.1

Raymond DJ. 1992. Nonlinear balance and potential-vorticity thinking at large Rossby number. Quarterly Journal of the Royal Meteorological Society 118, 987–1015. https://doi.org/10.1002/qj.49711850708

Raymond DJ. 2000. Thermodynamic control of tropical rainfall. Quarterly Journal of the Royal Meteorological Society 126, 889–898. https://doi.org/10.1002/qj.49712656406

Raymond DJ. 2013. Sources and sinks of entropy in the atmosphere. Journal of Advances in Modeling Earth Systems 5(4), 755–763. https://doi.org/10.1002/jame.20050

Raymond DJ, Flores MM. 2016. Predicting convective rainfall over tropical oceans from environmental conditions. Journal of Advances in Modeling Earth Systems 8(2), 703–718. https://doi.org/10.1002/2015MS000595

Raymond DJ, Gjorgjievska S, Sessions S, Fuchs Z. 2014. Tropical cyclogenesis and midlevel vorticity. Australian Meteorological and Oceanographic Journal 64, 11–25. Retrieved from https://pdfs.semanticscholar.org/78c5/c95e0f2fda2d1f9db320324764dc051302dc.pdf

Raymond DJ, Kilroy G. 2019. Control of convection in high-resolution simulations of tropical cyclogenesis. Journal of Advances in Modeling Earth Systems 11(6), 1582–1599. https://doi.org/10.1029/2018MS001576

Raymond DJ, Sessions S, López Carrillo C. 2011. Thermodynamics of tropical cyclogenesis in the northwest Pacific. Journal of Geophysical Research: Atmospheres 116(D18). https://doi.org/10.1029/2011JD015624

Raymond DJ, Sessions SL. 2007. Evolution of convection during tropical cyclogenesis. Geophysical Research Letters 34(6). https://doi.org/10.1029/2006GL028607

Sessions SL, Herman MJ, Sentic S. 2015. Convective response to changes in the thermodynamic environment in idealized weak temperature gradient simulations. Journal of Advances in Modeling Earth Systems 7(2), 712–738. https://doi.org/10.1002/2015MS000446

Sessions SL, Sentic S, Herman MJ. 2016. The role of radiation in organizing convection in weak temperature gradient simulations. Journal of Advances in Modeling Earth Systems 8(1), 244–271. https://doi.org/10.1002/2015MS000587

Sessions SL, Sentic S, Raymond DJ. 2019. Balanced dynamics and moisture quasi equilibrium in DYNAMO convection. Journal of the Atmospheric Sciences 76(9), 2781–2799. https://doi.org/10.1175/JAS-D-18-0173.1

Singh MS, O'Gorman PA. 2013. Influence of entrainment on the thermal stratification in simulations of radiative-convective equilibrium. Geophysical Research Letters 40(16), 4398–4403. https://doi.org/10.1002/grl.50796

Sobel AH, Bretherton CS. 2000. Modeling tropical precipitation in a single column. Journal of Climate 13(24), 4378–4392. https://doi.org/10.1175/1520-0442(2000)013<4378:MTPIAS>2.0.CO;2

Sodemann H, Stohl A. 2013. Moisture origin and meridional transport in atmospheric rivers and their association with multiple cyclones. Monthly Weather Review 141(8), 2850–2868. https://doi.org/10.1175/MWR-D-12-00256.1

Stohl A, Forster C, Sodemann H. 2008. Remote sources of water vapor forming precipitation on the Norwegian west coast at 60 N–a tale of hurricanes and an atmospheric river. Journal of Geophysical Research: Atmospheres 113(D5). https://doi.org/10.1029/2007JD009006

Warner MD, Mass CF, Salathé Jr EP. 2012. Wintertime extreme precipitation events along the Pacific northwest coast: Climatology and synoptic evolution. Monthly Weather Review 140(7), 2021–2043. https://doi.org/10.1175/MWR-D-11-00197.1

Wick GA, Neiman PJ, Ralph FM. 2013. Description and validation of an automated objective technique for identification and characterization of the integrated water vapor signature of atmospheric rivers. IEEE Transactions on Geoscience and Remote Sensing 51(4), 2166–2176. https://doi.org/10.1109/TGRS.2012.2211024

Zhu Y, Newell RE. 1998. A proposed algorithm for moisture fluxes from atmospheric rivers. Monthly Weather Review 126(3), 725–735. https://doi.org/10.1175/1520-0493(1998)126<0725:APAFMF>2.0.CO;2

Atmósfera 35(2), 287-305 (2022)
https://doi.org/10.20937/ATM.52942

CONTENTS

Synoptic patterns of South Atlantic Convergence Zone episodes associated with heavy rainfall events in the city of Rio de Janeiro, Brazil

Gustavo Carlos Juan ESCOBAR[1]*, Ana Clara DE ALMEIDA MARQUES[2] and Claudine Pereira DERECZYNSKI[2]

[1] *Coordenação-Geral de Ciências da Terra (CGT), Instituto Nacional de Pesquisas Espaciais (INPE), Rodovia Dutra km 39, 12630-000, Cachoeira Paulista, SP, Brazil.*
[2] *Universidade Federal do Rio de Janeiro, Centro de Ciências Matemáticas e da Natureza Instituto de Geociências, Departamento de Meteorologia, Avenida Athos da Silveira Ramos 274, Bloco G, 21941-916, Cidade Universitária, Ilha do Fundão, Rio de Janeiro, RJ, Brazil.*
*Corresponding author: gustavo.escobar@inpe.br

Received: July 06, 2020; accepted: November 06, 2020

RESUMEN

El presente estudio presenta una caracterización sinóptica de los episodios de la Zona de Convergencia del Atlántico Sur (ZCAS) que causaron eventos de lluvia fuerte (ELF) en la ciudad de Río de Janeiro (CRJ) entre 2006 y 2016. Se identificaron 77 episodios de ZCAS en la CRJ (ZCRJ), que representaron el 81% del total de eventos de ZCAS en Brasil. Se encontró un total de 37 episodios de ZCRJ con al menos un día de ELF durante el período que duró el evento (ZELF), representando casi la mitad (48%) de los eventos de ZCAS en la CRJ. En el 68.6% de estos casos, los ELF ocurrieron en los dos primeros días del evento de ZELF. El patrón sinóptico medio asociado con ZELF mostró un frente frío en el Océano Atlántico conectado con un sistema de baja presión ubicado cerca de la costa del estado de Río de Janeiro (RJ). La humedad específica en 850 hPa mostró un patrón de dipolo con anomalías positivas en el sureste de Brasil y anomalías negativas en el sur de Brasil, desde el día anterior a la ocurrencia del ZELF. La presencia de una cresta anómala en niveles superiores en el sureste de Brasil fue determinante para intensificar las fuertes lluvias en la CRJ. La clasificación sinóptica mostró cuatro patrones de superficie principales asociados con ZELF. Los dos patrones más frecuentes se asociaron con un frente frío cerca de la costa del estado de RJ y los otros dos se relacionaron con la presencia de un anticiclón con características de bloqueo y con la presencia de un ciclón extratropical débil cerca de la costa del estado de RJ, respectivamente.

ABSTRACT

The present study provides a synoptic characterization of South Atlantic Convergence Zone (SACZ) episodes that caused heavy rainfall events (HRE) in the city of Rio de Janeiro (CRJ) between 2006 and 2016. A total of 77 SACZ episodes were identified in the CRJ (SCRJ), which represented 81% of the total SACZ events in Brazil. At least one day of HRE during the SACZ period (SHRE) was found in 37 SCRJ episodes, representing almost half (48%) of the SACZ events in the CRJ. In 68.6% of these cases, the heavy rainfall occurred on the first two days of the SHRE period. The mean synoptic pattern of SHRE showed a cold front in the Atlantic Ocean connected with a low-pressure system located near the coast of Rio de Janeiro state (RJ). The 850 hPa specific humidity showed a dipole pattern with positive anomalies in southeastern Brazil and negative anomalies in southern Brazil since the day before the occurrence of SHRE. An anomalous upper-level ridge in southeastern Brazil was relevant to intensifying the heavy rainfall in the CRJ. The synoptic classification showed four main surface synoptic patterns associated with SHRE. The two most frequent patterns were associated with a cold front close to the coast of RJ, and the other two were related to the presence of an anti-cyclone with blocking characteristics and to the presence of a weak extratropical cyclone near the coast of RJ.

Keywords: SACZ, synoptic climatology, composite analysis, principal pattern sequence analysis.

1. Introduction

The city of Rio de Janeiro (CRJ) is located in the Southeast region of Brazil and is the capital of Rio de Janeiro state (RJ), which is an important economic, cultural, and tourist center in the country. The city is considered a World Heritage Site by the United Nations Educational, Scientific, and Cultural Organization (UNESCO) and is the second-largest Brazilian metropolis, responsible for the second-largest Gross Domestic Product (GDP) in the country. The presence of three massifs (Tijuca, Pedra Branca and Gericinó), the proximity of the Atlantic Ocean, the Guanabara Bay and the Sepetiba Bay (Fig. 1), produce a great spatial variability of precipitation in the region, which according to Pristo et al. (2018) varies between 912 mm of total annual rainfall in the north of the city and 2546 mm over the Tijuca massif.

During the rainy season (from October to April), much of the Southeast region of Brazil is affected by the occurrence of heavy rainfall events (HRE) that cause natural disasters such as landslides and floods, which have strong impacts on the population (Seluchi and Chou, 2009; Dereczynski et al. 2017; Nery and Malvestio, 2017; Reboita et al., 2017).

Several of these extreme events are caused by the South Atlantic Convergence Zone (SACZ), known as one of the main systems modulating the weather and climate in Brazil during the rainy season. The SACZ is characterized by a persistent cloud-band oriented northwest-southeast from the Amazon Basin to the South Atlantic Ocean, affecting the North, Central-West and Southeast regions of Brazil, north of Paraná state and southern part of Bahia state (Kousky, 1988; Kodama, 1992; Quadro, 1994; Carvalho et al., 2004).

The SACZ is associated with 13% of the HRE that occur in the CRJ, while frontal systems are responsible for 77% of the cases since these occur throughout the year (Dereczynski et al., 2009). Dolif and Nobre (2012) identified 32 HRE in the CRJ between January 2000 and December 2010, and of these 37% were caused by SACZ and 47% by cold fronts. Considering only the rainy season in the Southeast region of Brazil, Lima et al. (2010) found a total of 157 HRE, of which 74 cases (47%) were associated with SACZ and 83 cases (53%) with frontal systems. Despite the lower frequency of SACZ episodes associated with HRE in the CRJ, even during the rainy season, SACZ has the potential to produce higher rainfall totals compared to frontal system events, as SACZ remains stationary for several days over the same region, causing rainfall intensification (Marchioro et al., 2016), mainly in late spring and summer months (Grimm, 2011).

Between 11 and 20 January 2011, a SACZ event caused extreme rain in large parts of the RJ becoming

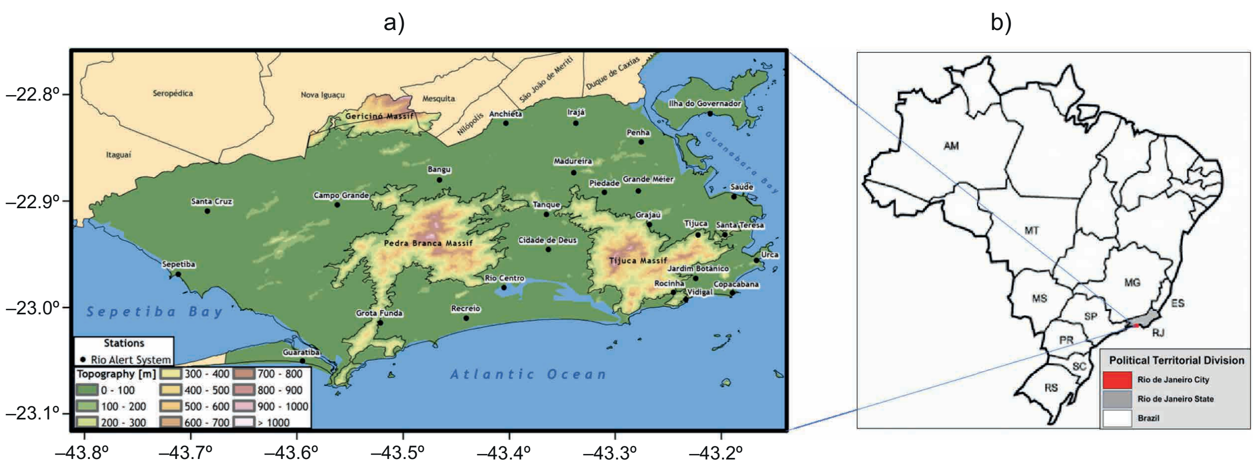

Fig. 1. a) Topography (m) of the city of Rio de Janeiro (RJ). Black circles show the rain gauge stations of the Rio Alert System used in this work; b) Brazilian map, showing the Rio de Janeiro State (RJ) in gray and the city of Rio de Janeiro (CRJ) in red. The location of the other states cited in this article are also shown: Amazon (AM), Espírito Santo (ES), Minas Gerais (MG), Mato Grosso do Sul (MS), Mato Grosso (MT), Paraná (PR), Rio Grande do Sul (RS), Santa Catarina (SC) and São Paulo (SP).

the largest climatic catastrophe in Brazil's history. On 12 January the intense and voluminous rain affected the CRJ and especially the cities in the mountainous areas of RJ, with successive episodes of mass landslides (Dourado et al., 2012) that caused the death of 905 people and more than 200 disappeared (Dereczynski et al., 2017; Nery and Malvestio, 2017). This episode culminated with the creation of the Brazilian National Centre for Monitoring and Early Warnings of Natural Disasters (CEMADEN - http://www.cemaden.gov.br/).

Cold fronts, baroclinic troughs (Escobar et al., 2019) and extratropical and subtropical cyclones (Kousky, 1979; Reboita et al., 2010; Gozzo et al., 2014; Rocha et al., 2019) are the main surface meteorological systems identified by weather forecasters in the synoptic charts related to SACZ episodes during the rainy season in Brazil. The atmospheric circulation pattern associated with these meteorological systems, when positioned on the coast of southeastern Brazil, maintains the moisture convergence at low levels and, consequently, contributes to the intensification of precipitation.

The Bolivian High (Lenters and Cook, 1997) and the trough of the Northeast region of Brazil (Kousky and Gan, 1981) are the main upper-level meteorological systems observed during the Brazilian rainy season having important contribution in the SACZ episodes. The mean atmospheric circulation pattern associated with both systems (Bolivian High and the trough of the Northeast region of Brazil) promotes strong divergence at high levels and, consequently, maintains the convective precipitation observed in much of the Central-West, Southeast and North regions of Brazil.

Escobar (2019) performed a synoptic classification at the surface and mid-troposphere during the rainy season in Brazil (November to March), using the Principal Component Analysis (PCA) methodology. The study identified four main synoptic patterns during the rainy season, and the most frequent was related to SACZ events, with the presence of a stationary front close to the coast of São Paulo state and RJ and with the South Atlantic Subtropical Anticyclone (SASA) positioned to the south of its climatological position. A similar synoptic pattern of SACZ was found by Weide-Moura et al. (2013) in their synoptic classification related to the occurrence of HRE in the CRJ. With such a surface circulation pattern, the maritime winds from the southeast persist for several days on the coast of São Paulo state and RJ, favoring the intensification of rain.

Considering that the HRE that occur in the CRJ under the influence of SACZ episodes trigger events with strong impacts on the population, the knowledge of the behavior of these episodes is very important for city planners to mitigate their impacts. Therefore, taking into account the importance that the SACZ events represent in the modulation of precipitation in this region during the rainy season, the objective of this study is to describe the dynamic and thermodynamic characteristics associated with such events through the development of a synoptic climatology.

This paper is organized as follows: section 2 details the data and the methodology used in this study, section 3 analyzes the synoptic features and identifies the principal surface weather patterns associated with SHRE in the CRJ, and section 4 presents the conclusions.

2. Data and Methodology

2.1. Data

The studied period comprises 10 rainy seasons, considered here as the months between October and April of 2006-2016. So, the first rainy season or the "2007 rainy season" extends from October 1, 2006, to April 30, 2007, and the last one or the "2016 rainy season" extends from October 1, 2015, to April 30, 2016. This studied period is referred to as "October-April/2006-2016".

The SACZ episodes were identified by analyzing the surface and upper levels (850 hPa, 700 hPa, 500 hPa, and 250 hPa) synoptic charts at 1200 UTC October-April/2006-2016, using the methodology described in Escobar and Matoso (2018). Those charts were prepared by the weather forecasters from the Brazilian Center for Weather Forecasts and Climate Studies (CPTEC) - National Institute for Space Research (INPE).

Brightness temperature (K) images from the Geostationary Operational Environmental Satellite (GOES; 10, 12, and 13) from CPTEC-INPE were also used to identify the cloudiness associated with the SACZ meteorological situations.

To identify the SACZ episodes that caused rain in the CRJ (SCRJ), daily precipitation maps were built using the MERGE product (Rozante et al., 2010), with a spatial resolution of 0.2º latitude x 0.2º longitude. These daily precipitation maps were constructed for each SACZ episode to verify if the rain band was established over CRJ. MERGE results from the combination of surface observations over the South American continent with Tropical Rainfall Measuring Mission (TRMM) satellite precipitation estimates.

The HRE detection criterion in the CRJ was defined through the use of precipitation data observed every 15 minutes at the Rio Alert System from the Municipality of Rio de Janeiro. Twenty six rain gauge stations in the CRJ were used for this work (Fig. 1).

In order to study the synoptic characteristics associated with SACZ episodes related to the occurrence of HRE in the CRJ (SHRE), daily (1200 UTC) gridded reanalysis meteorological data from the National Centers for Environmental Prediction (NCEP) Climate Forecast System Reanalysis (CFSR) were used. The CFSR version 1 (CFS-v1 – Saha et al., 2010) covers the period from January 1979 to March 2011. The CFSR version 2 (CFSv2 – Saha et al., 2014) was released in March 2011, and it has been running operationally since then. Both (CFSv1 and CFSv2) have a horizontal native resolution of T382 (~38 km). Their horizontal resolution is 0.25º × 0.25ºlatitude/longitude between 10ºS and 10ºN, reducing gradually towards the poles, reaching 0.5º between 30ºN and 30ºS. The CFSR meteorological variables used were: i) mean sea-level pressure (hPa); ii) 850 hPa specific humidity (gkg^{-1}); 850 hPa wind components (ms^{-1}), and iii) 850, 500 and 250 hPa geopotential height (gpm) from October-April/2006-2016.

2.2. Detection of SHRE

The SACZ episodes were identified by analyzing the surface and upper synoptic charts at 1200 UTC from October-April/2006-2016. The dates of the SACZ events were selected using the methodology presented by Escobar and Matoso (2018) in which the following characteristics should appear simultaneously in the synoptic charts:

(a) a cold front or a baroclinic trough located over the ocean, near the coast between São Paulo and Espírito Santo states,
(b) a trough at mid- (500 hPa) and upper troposphere (250 hPa) located over the Southeast region of Brazil or the southern part of the Northeast region of Brazil,
(c) a polar jet stream (250 hPa) coupled with a subtropical jet stream associated with the surface cold front at the surface,
(d) a subtropical jet stream associated with the baroclinic trough at the surface,
(e) a horizontal equivalent potential temperature gradient at 850 hPa pointing from the Atlantic Ocean to the continent,
(f) a northwesterly flow at 850 hPa extending from the Amazon Basin to the Atlantic Ocean and through the Central-West and Southeast regions of Brazil,
(g) a homogeneous region where the upward motion at 500 hPa is in phase with the convergent flow at 850 hPa and the precipitable water values are greater than 45 mm

and

(h) a low-level convergence zone and the pre-sence of a band of cloudiness persisting for at least 3 consecutive days.

After identifying SACZ cases by applying the above criterion, daily precipitation maps were constructed using MERGE data, to identify the SACZ cases that caused rain on the CRJ (SCRJ). The Dereczynski et al. (2009) criterion was used to select the SACZ cases that produced HRE in the CRJ (SHRE), which considers an HRE when the 24 h accumulated rainfall reaches the threshold of 30 mm in at least 4 of the 26 meteorological stations considered in this study. The 24 h accumulated rainfall was computed using the rainfall data observed every 15 minutes, from 1215 UTC on the previous day until 1200 UTC on the day in question.

Because a SACZ event lasts at least 3 days, in several episodes the criterion for HRE in the CRJ was verified in more than one day. The frequency of SHRE was caculated if at least one day of heavy rainfall during the SACZ event ocurred. Moreover, to compute the monthly frequency of SHRE, the SACZ month is considered regarding the first SACZ day. For example, if one episode begins on February 29 and lasts for 5 days, this event will be considered a February case.

2.3. Composite fields

After the selection of the SHRE, average composite fields and anomaly composite fields of atmospheric variables mentioned in section 2.1 for two days before the initial day (D–2), one day before the initial day (D–1), and at the initial SHRE day (D0) were calculated, to identify the synoptic features associated with such episodes. For example, for the first SHRE (29 November 2006 -12 December 2006), D–2 is 27 November, D–1 is 28 November and D0 is 29 November 2006. It is important to emphasize that the D0 is always taken as the first day of the SACZ episode, regardless of when the HRE was observed. Composite fields were constructed in the spatial domain of 10ºN-55ºS and 80º-20ºW for all variables. Climatology fields are constructed for the whole period comprising the 10 rainy seasons, from "2007 rainy season" to "2016 rainy season". Average and anomaly composites were calculated considering the October-April/2006-2016 climatology. The composite fields for D–2, D–1, and D0 were useful for tracking the evolution of the synoptic systems responsible for the SHRE.

2.4. Synoptic classification

After identifying the mean synoptic characteristics associated with SHRE, a synoptic classification at the surface was performed through the Principal Pattern Sequence Analysis (PPSA; Compagnucci et al., 2001; Escobar et al., 2004; Huth et al., 2008). According to Compagnucci et al. (2001), the PPSA is considered an extension of the traditional Principal Component Analysis (PCA), with a correlation matrix in T-Mode (Green and Carrol, 1978; Richman, 1986; Escobar et al., 2016), whose main objective is to obtain the evolution of the principal dominant modes of atmospheric circulation for specific meteorological situations. Thus, in this application, each variable is a sequence of the consecutive spatial mean sea level pressure patterns, and the correlation matrix represents the correlation between sequences.

In order to explore the synoptic variability where the surface baroclinic systems are more associated with SHRE, a smaller domain (5ºS-40ºS, 30ºW-80ºW) was used for the calculation of the composites fields. The matrices are composed by mean sea level pressure data of the 37 SHRE x 7171 grid points for 3 days: D–2, D–1, and D0. With such an objective methodology, it is possible to identify subgroups or types of fields with the same spatial structure.

After the application of the PPSA, the Varimax rotation (Richman, 1986) was performed. This methodology is useful to redistribute the total variance of the data among the components in order to emphasize the physical meaning of the Principal Pattern Sequence (PPS) that is generated (Richman,1986). The optimum number of rotated PPSs was determined by the eigenvalue 1.0 rule (Richman et al., 1992).

The real meteorological fields correlated significantly with the Principal Pattern Sequences (PPSs) were determined through temporal series of factor loadings that represent the correlations between the variable used (real meteorological field) and each PPS (Richman, 1986).

The analysis of the component loadings allows the evaluation of the representative patterns (obtained from PPSA) as real atmospheric circulation fields (registered in the reanalyses). Values of component loadings closer to 1 represent sequences of atmospheric circulation fields similar to the obtained pattern sequence (Harman, 1976; Cattell, 1978).

The spatial field of the PPSs can be interpreted in both their positive and negative phases (Compagnucci and Salles, 1997). PPSs are related to two different synoptic patterns that have the same shape. For positive values of component loadings (direct mode), PPSs have the same sign as the meteorological variable under study. For example, positive (negative) values of sea level pressure, represent high (low) pressures in the PPSs. Conversely, for negative values of component loadings (indirect mode), PPSs have the opposite sign as the real meteorological fields. Therefore, positive (negative) values represent low (high) pressures. In this study, the values of component loadings (figures not shown) were positive, meaning that the PPSs have the same sign as the meteorological fields (weather type).

3. Results

3.1 SACZ Climatology

The dates of the 95 SACZ episodes (9.5 events per year) identified in the 10-year (October-April/2006-2016) are listed in Table I. The longest SACZ event took place in December 2013 and lasted for 15 days (12/Dec/2013 - 26/Dec/2013). The other three longest

Table I. Start and end dates (month/date/year) of the 95 SACZ episodes that occurred over Brazil in the 10-year period (October-April/2006-2016).

Start Date	End Date	Start Date	End Date	Start Date	End Date
17/10/2006	**20/10/2006**	28/10/2009	01/11/2009	09/01/2013	17/01/2013
10/11/2006	12/11/2006	04/12/2009	09/12/2009	26/01/2013	30/01/2013
29/11/2006	01/12/2006	13/12/2009	15/12/2009	04/02/2013	10/02/2013
08/12/2006	16/12/2006	21/01/2010	23/01/2010	27/02/2013	04/03/2013
27/12/2006	29/12/2006	01/03/2010	12/03/2010	27/03/2013	30/03/2013
21/01/2007	25/01/2007	28/03/2010	31/03/2010	18/10/2013	20/10/2013
30/01/2007	05/02/2007	27/10/2010	29/10/2010	05/11/2013	09/11/2013
12/02/2007	16/02/2007	01/11/2010	04/11/2010	12/12/2013	26/12/2013
19/03/2007	**22/03/2007**	01/12/2010	04/12/2010	17/01/2014	20/01/2014
23/10/2007	25/10/2007	14/12/2010	18/12/2010	15/02/2014	19/02/2014
04/11/2007	06/11/2007	27/12/2010	07/01/2011	**28/02/2014**	**02/03/2014**
27/11/2007	02/12/2007	11/01/2011	20/01/2011	06/03/2014	10/03/2014
12/12/2007	15/12/2007	15/02/2011	17/02/2011	22/03/2014	24/03/2014
19/12/2007	23/12/2007	28/02/2011	10/03/2011	26/10/2014	29/10/2014
06/01/2008	11/01/2008	04/04/2011	07/04/2011	15/11/2014	19/11/2014
20/01/2008	**23/01/2008**	02/10/2011	07/10/2011	**27/11/2014**	**30/11/2014**
30/01/2008	02/02/2008	16/10/2011	20/10/2011	14/12/2014	17/12/2014
03/02/2008	**08/02/2008**	01/11/2011	04/11/2011	**24/12/2014**	**26/12/2014**
24/02/2008	08/03/2008	23/11/2011	05/12/2011	05/02/2015	09/02/2015
13/03/2008	18/03/2008	09/12/2011	12/12/2011	16/02/2015	19/02/2015
13/11/2008	24/11/2008	15/12/2011	22/12/2011	27/02/2015	01/03/2015
03/12/2008	**06/12/2008**	26/12/2011	30/12/2011	09/03/2015	14/03/2015
12/12/2008	21/12/2008	01/01/2012	09/01/2012	17/03/2015	20/03/2015
25/12/2008	31/12/2008	15/01/2012	21/01/2012	**22/03/2015**	**25/03/2015**
04/01/2009	09/01/2009	26/01/2012	31/01/2012	06/04/2015	08/04/2015
21/01/2009	23/01/2009	11/02/2012	13/02/2012	28/10/2015	30/10/2015
29/01/2009	31/01/2009	16/03/2012	21/03/2012	14/01/2016	19/01/2016
12/02/2009	15/02/2009	24/03/2012	26/03/2012	20/01/2016	23/01/2016
13/03/2009	**17/03/2009**	04/11/2012	08/11/2012	29/02/2016	05/03/2016
25/03/2009	02/04/2009	14/11/2012	22/11/2012	**10/03/2016**	**14/03/2016**
08/04/2009	11/04/2009	26/11/2012	28/11/2012	24/03/2016	27/03/2016
08/10/2009	12/10/2009	15/12/2012	17/12/2012		

The dates of the 77 SCRJ and 37 SHRE events are highlighted in bold and gray, respectively. The rest of the dates correspond to SACZ episodes outside the CRJ.

SACZ events (all lasting 12 days) took place in the periods 13/Nov/2008-24/Nov/2008, 01/Mar/2010-12/Mar/2010, and 27/Dec2010-07/Jan/2011.

In the CRJ, 77 episodes of SACZ (SCRJ) were configured (highlighted in bold in Table I), representing 81% of the total SACZ events in Brazil. As was mentioned in Section 2.2, in several episodes of SACZ, the criterion for HRE in the CRJ was reached in more than one day during the entire period of the event. Considering the episodes of SCRJ with at least one day of HRE (SHRE), 37 cases were identified (highlighted in gray in Table I). This indicates that almost half (48%) of the total SACZ events configured in the CRJ cause heavy rainfall in the city.

During the 37 SHRE episodes, the rainfall reached the HRE threshold in 51 days. A total of 22 of these 51 days (43.1%) occurred on the first day of the SHRE episode, and in 13 of these 51 days (25.5%), the rainfall reached the HRE threshold on the second day, totalizing 68.6% of the heavy rainfall days occurring in the first two SHRE days. This result indicates that the beginning of an SHRE, which in general is associated with the arrival of a frontal system, is more likely to cause heavy rainfall in the CRJ compared to the other days of the event. The other HRE occurred in the third (11.8%), fourth (3.9%), fifth (7.8%), sixth (5.9%) and eighth (2.0%) SHRE days. No HRE occurred in the seventh day.

The mean daily precipitation in the 51 heavy rainfall days during the 37 SHRE episodes is presented in Figure 2. The SACZ rainfall band, extending in the NW-SE direction from the Amazon region through de Atlantic Ocean, is evident in Figure 2. Although the daily precipitation varies from 10 to 15 mm/day over RJ, it is in the Atlantic Ocean, around 27ºS/40ºW, where it achieves its maximum intensity (35 mm/day). Figure 3 presents the frequency of the 95 SACZ, 77 SCRJ, and 37 SHRE episodes organized by their duration, lasting just 3 days, only 4 days, and so on, until 15 days. It is clear from Figure 3 that most of the episodes lasted between 3 and 6 days. The higher frequency of the SACZ and SCRJ events was 4 days, and the higher frequency of the SHRE was 5 days.

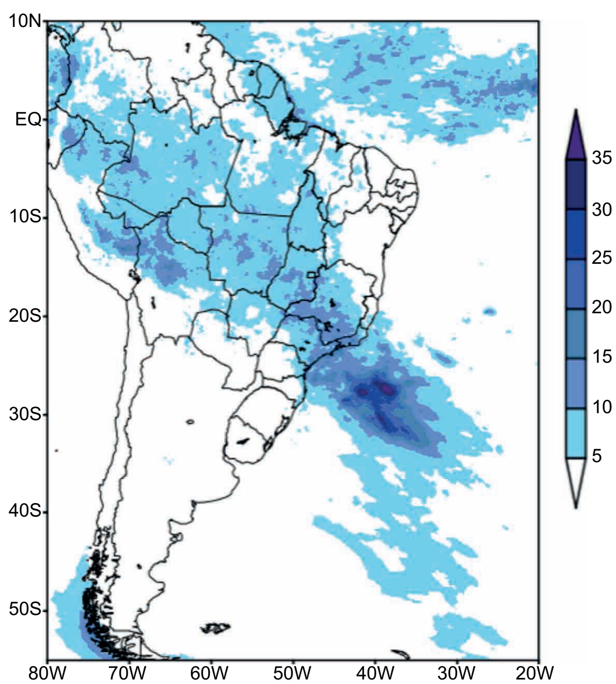

Fig. 2. Mean precipitation (mm/day) accumulated in 51 heavy rainfall days during the 37 SHRE. (Source: MERGE - Rozante et al., 2010).

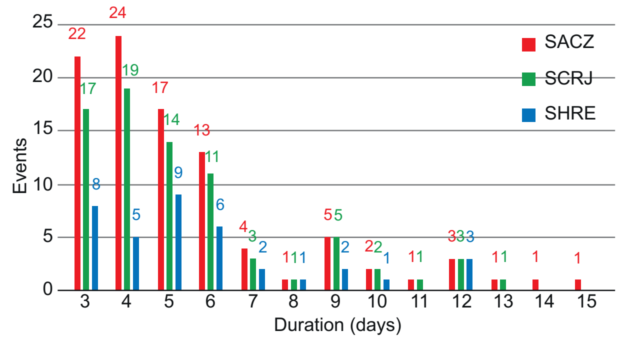

Fig. 3. Total number of the 95 SACZ, 77 SCRJ and 37 SHRE distributed by their duration (in days) during the studied period (October-April/2006-2016).

The monthly distribution of the 95 SACZ, 77 SCRJ, and 37 SHRE (Fig. 4) shows an increase in their frequency from October through January, which peaks in the middle of the rainy season. A small rise in the frequency from February to March is also seen, which can be explained by two reasons: First, the month of February is shorter than the others, reducing the chance of a SACZ occurrence during that month. And, second, temperature and humidity are still high in March, but coincide with the first stronger cold fronts that begin their journey inside the continent, promoting the formation of more SACZ events. As mentioned before, Figure 4 also shows that most of the SACZ events that occurred in Brazil reached the CRJ (SCRJ). It is noteworthy that during March, all 16 SACZ events reached the CRJ (SCRJ), and during April, none of the 2 SCRJ produced HRE.

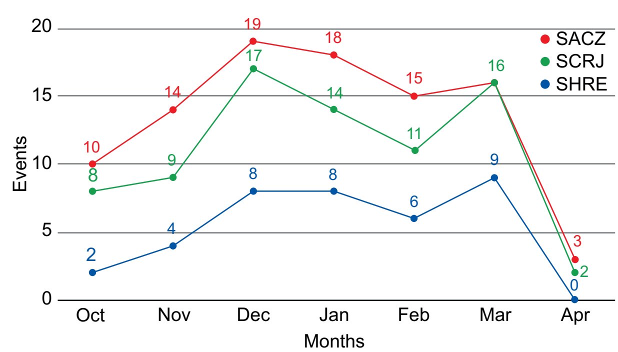

Fig. 4. Monthly distribution of the 95 SACZ, 77 SCRJ and 37 SHRE events during the studied period (October-April/2006-2016).

3.2 Synoptic climatology associated with SHRE

3.2.1 Composites of average and anomalies

In order to identify the main synoptic features associated with SHRE as well as their differences in relation to climatology, composites of average and anomalies were calculated of the variables described in section 2.1. Thirty seven SHRE are considered, which correspond to the total cases identified during the studied period (October-April/2006-2016).

The composites of average and anomalies of the 500 hPa geopotential height and mean sea level pressure, associated with SHRE for D–2, D–1 and D0 are shown in Figure 5. The fields of 500 hPa geopotential height average composites (Fig. 5a) show a slightly amplified frontal trough located near Buenos Aires Province (Argentina) on D–2 that intensifies and amplifies as it moves northeastward and reaches the eastern part of Santa Catarina state on D0. There is another weak trough positioned between northern Argentina and southern Bolivia on D–2, which in the following days connects with the previously mentioned trough. Note that there is a strong geopotential height gradient located to the south of 40ºS, and in this intense baroclinic flow, there are several cyclonic disturbances with a slight amplification that move rapidly eastwards.

The mean sea level pressure average composites (Fig. 5a) show a weak cold front located between the

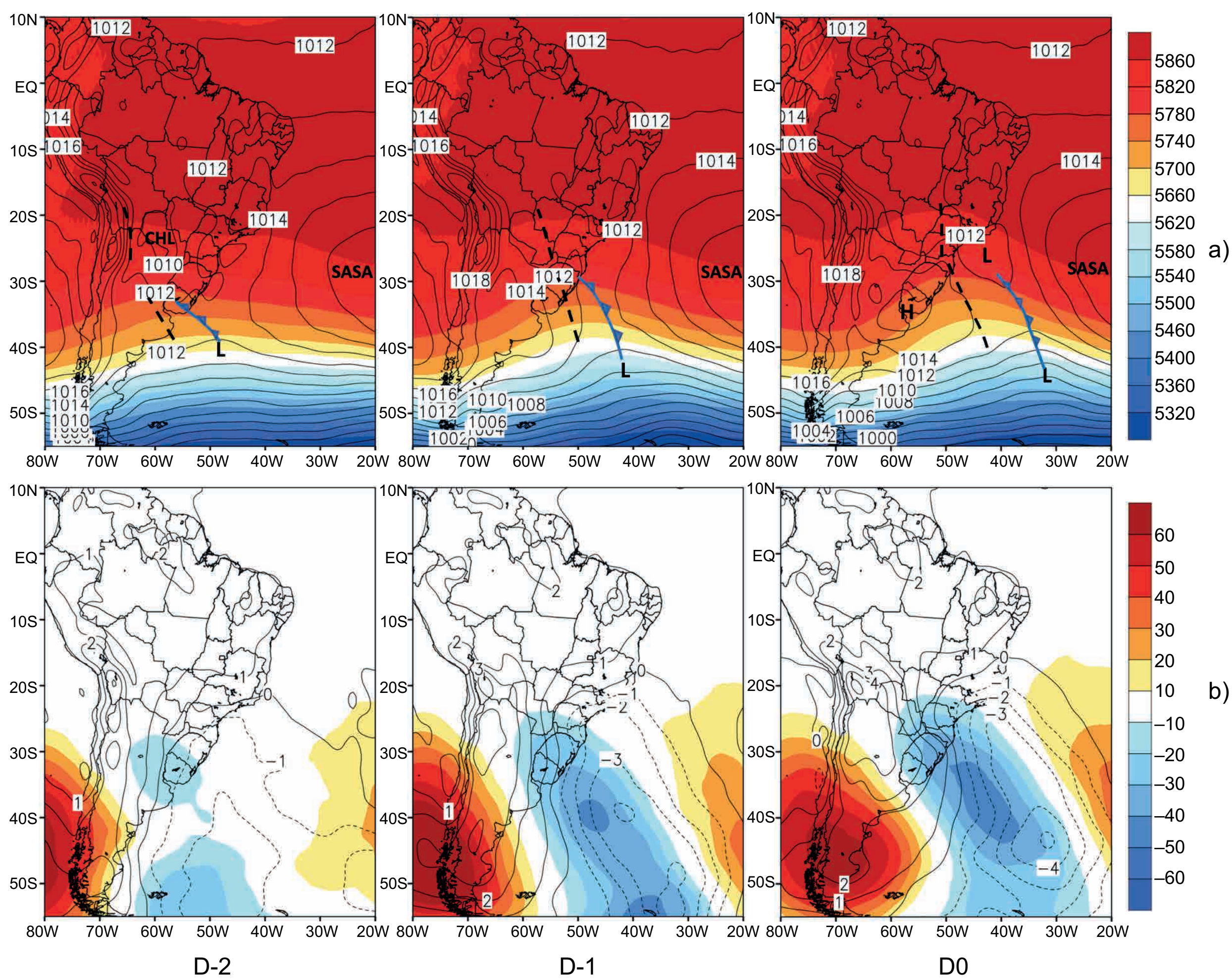

Fig. 5. 500 hPa geopotential height (gpm in shaded) and mean sea level pressure (hPa in lines) SHRE composites: a) average and b) anomalies. From left to right: D–2, D–1, and D0. CHL= Chaco Low; H=High; L=Low; SASA=South Atlantic Subtropical Anticyclone.

Atlantic Ocean and southern Rio Grande do Sul state on D–2, which moves northeastwards in the subsequent days. On this day (D–2), there is a low-pressure system of 1010 hPa related to the Chaco Low, which is located over Paraguay. On D–1, this frontal system is located approximately to the southeast of the Santa Catarina state without reaching the coast of southeastern Brazil on D0. A similar pattern was observed by Andrade and Cavalcanti (2018) during heavy rainfall summer fronts over southeastern Brazil. Note also that the SASA is located around 30ºS, 20ºW, and slowly moves eastwards over the entire analyzed period. The 500 hPa trough that advances from northern Argentina and southern Bolivia contributes to the formation of a wide low-pressure system of 1012 hPa over the Atlantic Ocean, to the south of RJ during D0. On this day, this cyclone is connected to the cold front and both of these systems contribute to the intensification of the moist air mass convergence over the coast of RJ, including the CRJ.

The composite anomalies of 500 hPa geopotential height and sea level pressure are shown in Figure 5b. This combination of levels shows the displacement of a typical baroclinic system, with the 500 hPa wave positioned to the west of the surface wave.

Negative anomalies of mean sea level pressure and geopotential height observed respectively at the surface and the 500 hPa level, allow the identification of the mid-troposphere trough and the cold front at the surface. On the other hand, the positive anomalies at both of the levels identify the ridge and the post-frontal anticyclone, respectively at mid- level and at surface. On D–2, there are negative height anomalies with a minimum of -10 gpm at 500 hPa located over northeastern Argentina and Uruguay. This pattern is related to the frontal trough at mid-level that moves northeastwards during the following days. In the South Atlantic Ocean, to the southeast of the Malvinas Islands, there is a minimum of –20 gpm at the 500 hPa level on D–2, associated with a cyclonic disturbance that exhibits a rapid zonal displacement during the analyzed period. The minimum related to the frontal trough intensifies during the subsequent days reaching a minimum value of –40 gpm near 37ºS, 40ºW on D0. Similar behavior is observed at the surface, with slight negative anomalies over RJ of the order of –1 hPa to –2.5 hPa on D–1 and D0, respectively. On SACZ day (D0), a minimum of –5 hPa is observed over the Atlantic Ocean around 42ºS, 30ºW, associated with the low-pressure system related to the cold front mentioned in Figure 5a.

The composites of average and anomalies of streamlines and 850 hPa specific humidity associated with SHRE are shown in Figure 6. The composite of streamlines at 850 hPa (Fig. 6a) show the typical mean circulation pattern over South America during the rainy season in Brazil. There is a clear northerly/northwesterly flow over continental areas during the analyzed period. This circulation pattern at low levels is determined by the trade winds that penetrate to the north of the continent and deviate by the action of the Andes Cordillera, and by the winds coming from the Atlantic Ocean related to the presence of the SASA. On D–2, there is northerly wind over the RJ, determined by the western edge of the SASA since the flow from the Amazon region is directed to the northern part of southern Brazil. On D–1, the flow caused by the SASA persists over the RJ, and the influence of the Amazonian flow is beginning to be observed. During D0, there is a large influence of the Amazonian flow over RJ and a smaller contribution from the wind from the Atlantic Ocean. This change in the atmospheric circulation at the 850 hPa level is related to the advance of a frontal trough that on D–2 is observed approximately in the farther south of Rio Grande do Sul state and on D0 is identified over the Atlantic Ocean, close to São Paulo state. On D–2 the Chaco Low can also be observed in southern Bolivia and western Paraguay, which is connected with the frontal trough mentioned above. On D–1, the frontal trough is near the coast of Santa Catarina state and, simultaneously, another trough can be observed further to the north with its axis extending between southern Bolivia and the far west of Santa Catarina state. On D0, this trough advances northeastwards, extending between southern Mato Grosso state and northern Paraná state, where a low-pressure system forms. With such low-level atmospheric circulation, the RJ is affected by warm and moist air transported from the Amazon Basin.

The composites of 850 hPa specific humidity (Fig. 6a) show high values over most of the North, Central-West and Southeast regions of Brazil, of the order of 12 to 14 gkg^{-1}, typical of the rainy season in Brazil. The specific humidity shows an increase over RJ from approximately 10 to 13 gkg^{-1} between

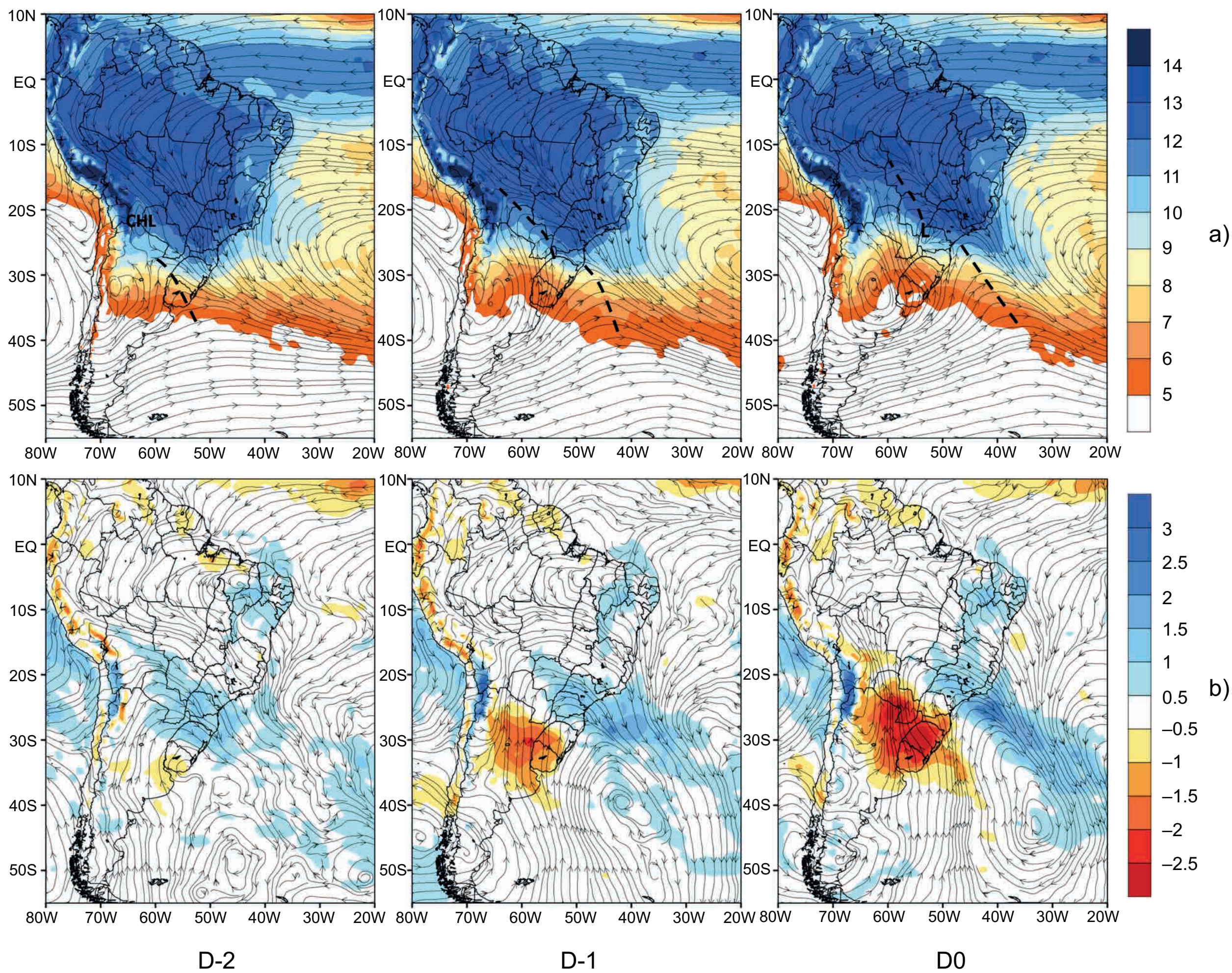

Fig. 6. 850 hPa streamlines and 850 hPa specific humidity (gkg^{-1} in shaded) SHRE composites: a) average and b) anomalies. From left to right: D–2, D–1, and D0. CHL= Chaco Low.

D–1 and D0. This increase is related to the change in the wind direction from northerly to northwesterly, as previously described. Also, as noted by Moraes et al. (2020), when studying mesoscale convective complexes forming in subtropical South America, the moisture increase results from the enhanced convergence between the flows coming from the Amazon Basin and the Atlantic Ocean. It is noteworthy that during the rainy season the specific humidity over the southeast region is very high due to the combination of high temperatures and the persistent northerly flow from the Atlantic Ocean and from the northern Brazil.

The 850 hPa streamline composite anomaly fields (Fig. 6b) show the zonal displacement of cyclonic anomalies that on D–2 are centered over Uruguay and in the following days move over the Atlantic Ocean, approximately south of 40ºS and between 40ºW and 30ºW. This anomalous pattern is mainly associated with the displacement of the cold front described previously (Fig. 6a). The anomalous trough associated with these cyclonic anomalies extends from the southern Amazon Basin to the South Atlantic Ocean, determining a band of negative anomalies that affects much of southeastern Brazil, especially since D–1. A similar configuration was found by Doss-Gollin et al. (2018) when they analyzed 850 hPa anomaly fields associated with the occurrence of heavy rainfall in the central-southern Paraguay. The authors identified a circulation pattern with cyclonic anomalies over the

Atlantic Ocean, southeast of southern Brazil, one day after the occurrence of heavy rainfall in Paraguay.

The specific humidity composite anomaly fields (Fig. 6b) are consistent with the anomalous atmospheric circulation pattern described above. There is a large area of positive anomalies of specific humidity located over northeastern Argentina, Paraguay, southern Brazil, most of Mato Grosso do Sul state and the western and southwestern part of São Paulo state during D–2, showing small values (~1 gkg^{-1}-1.5 gkg^{-1}). On D–1, these positive anomalies are located to the east of the anomalous trough, affecting most of the states of Paraná, Mato Grosso do Sul, and São Paulo, and the adjacent Atlantic Ocean. Moreover, negative anomalies of specific humidity varying between –1 and –2 gkg^{-1} are also observed over Uruguay, northeastern Argentina and central-western Rio Grande do Sul state, related to the advection of dry air produced by the advance of the post-frontal anticyclone (Fig. 4a). On D0, the positive anomalies are located over the São Paulo and RJ states, western and southern Minas Gerais state and in the adjacent Atlantic Ocean. In addition, the negative anomalies are more intense comparing to D–1, affecting Uruguay, northeastern Argentina, most of Paraguay, Rio Grande do Sul state and most of Santa Catarina state.

An interesting feature to mention is the establishment of a "dipole" configuration in the specific humidity anomalies fields during D0. This dipole, also called the seesaw pattern, is determined by the presence of positive anomalies in southeastern Brazil and by the presence of negative anomalies in the South, in agreement with Nogués-Paegle and Mo (1997).

The composites of average and anomalies of 200 hPa streamlines and geopotential heights associated with SHRE are shown in Figure 7. Average composites (Fig. 7a) allow identifying a typical upper-level atmospheric circulation pattern of the rainy season in Brazil, with the presence of the Bolivian High and the trough in the Northeast region of Brazil. This pattern is observed in climatology during the rainy season regardless of the occurence of SACZ events because it is associated with strong convective activity in the Amazon Basin (Lenters and Cook, 1997). On D–2, there is a trough with its axis extending from central Argentina to the Atlantic Ocean that intensifies as it propagates eastwards over the following days. On D–1, the axis of this trough is positioned approximately between northeastern Argentina and the Atlantic Ocean and on D0 it reaches southern Brazil, extending between Paraná state and the Atlantic Ocean.

This upper-tropospheric trough shows an intense horizontal geopotential height gradient that is associated with the cold front identified at the surface and at the 850-hPa level. On D0, this upper-level trough increases the divergent flow over RJ and southern Minas Gerais state, contributing to the intensification of the convergence flow at the surface. Therefore, with such upper-level atmospheric circulation pattern, the precipitation will intensify over the study area during the SHRE.

The Bolivian High appears practically stationary over Bolivia during the analyzed period; however, its associated ridge changes position particularly from D–1. On D–2, the axis of the ridge extends southward from Bolivia to the northeastern part of Southern Brazil. The ridge moves towards southeastern Brazil on the following days and on D0 it appears approximately over RJ, southern Espírito Santo state and central-southern Minas Gerais state. Simultaneously, the trough in the Northeast region of Brazil moves slightly to the west as the ridge intensifies towards the Southeast region of Brazil. The change in the upper-level atmospheric circulation associated with both of the systems (the ridge and the trough of the Northeast region of Brazil) is related to the advance of the frontal trough from mid-latitudes.

The 200 hPa streamline and geopotential height anomaly fields (Fig. 7b) reveal a well-defined wave train that propagates northeastward, with an anomalous ridge over the South Pacific Ocean and southern South America and an anomalous trough over most southern Brazil. There are positive geopotential height anomalies on D–2 over most southern Brazil and Paraguay and part of Mato Grosso do Sul and São Paulo states, with values varying between 10 and 20 gpm. These positive anomalies increase the intensity and propagates eastwards on D–1, reaching the RJ and the southern part of MG and Espírito Santo states. Anticyclonic anomalies are located over the Atlantic Ocean on D0, centered to the southeast of RJ but nevertheless affecting most of RJ, MG and Espírito Santo states. On this day, the highest anomalies are of the order of 20 to 30 gpm over RJ, southern part of

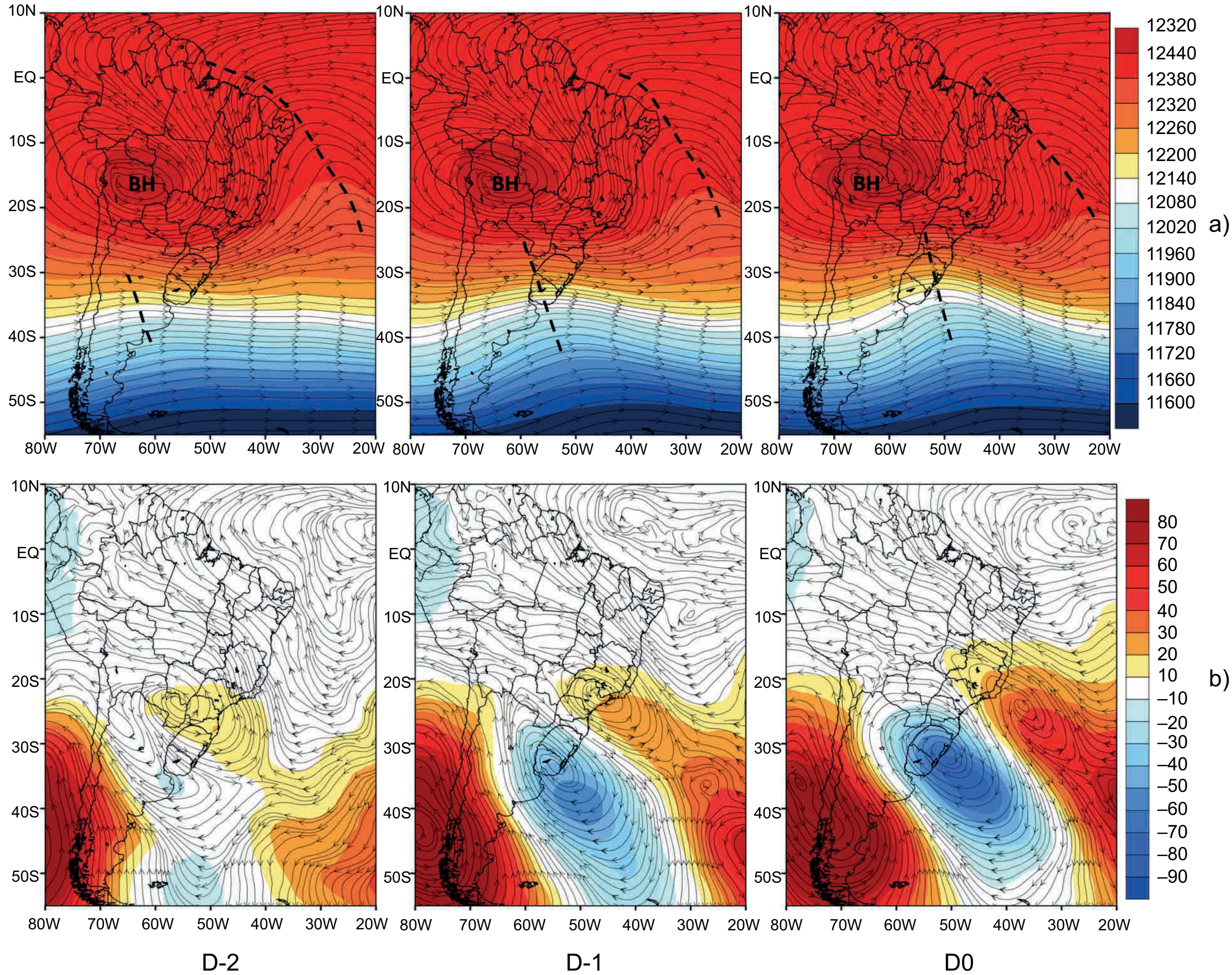

Fig. 7. 200 hPa streamlines and 200 hPa geopotential height (gpm in shaded) SHRE composites: a) average and b) anomalies. From left to right: D–2, D–1, and D0. BH=Bolivian High.

Espírito Santo state and the south of Minas Gerais state. These positive anomalies are associated with the intensification of the ridge described in Figure 6a, indicating strong divergence at upper levels and, consequently mantaining moisture convergence at low levels. Thus, such an anomalous upper-level atmospheric circulation pattern is related to the mean position of the band of cloudiness associated with SHRE that contributes to precipitation intensification in the CRJ.

The negative anomalies show a pattern similar to that observed at the 500 hPa level (Fig. 4b). On D–2, there is a band of a cyclonic anomaly of streamline oriented northwest-to-southeast, from northern Argentina to the South Atlantic Ocean. The highest values of the negative geopotential height anomalies are of the order of –10 gpm to –20 gpm, located approximately to the east of the Buenos Aires Province (Argentina) and the adjacent Atlantic Ocean. On D–1, these negative anomalies intensify as they move eastwards and cover northeastern Argentina, most of Uruguay and the Rio Grande do Sul state. On D0, the negative anomalies continue increasing in intensity, showing values of approimately –60 gpm in southeastern Rio Grande do Sul state and the adjacent Atlantic Ocean. On this day, the cyclonic streamline anomalies extend from southern Bolivia to the South Atlantic Ocean. A similar configuration at high levels was found by Nielsen et al. (2019) when they studied the SACZ episodes during the South American Monsoon period. The authors identified the presence of cyclonic anomalies between southern Brazil and the adjacent Atlantic Ocean associated with the presence of SACZ located in different positions.

In the Tropical Atlantic Ocean east of the Northeast region of Brazil, there are cyclonic streamline anomalies affecting the area where the trough of the Northeast region of Brazil acts during the rainy season. This result is in agreement with Carvalho (1989) who suggests that the most intense SACZ events are associated with more intense trough of the Northeast region of Brazil.

3.2.2. Synoptic patterns associated with SHRE

The synoptic classification at the surface associated with SHRE, identified seven PPSs that explain 83.8% of the total variance, with the first four PPSs representing 69.8% of that total (Table II). The remaining PPSs were not considered in the analysis because their series of component loadings presented values lower than 0.5. The four PPSs associated with SHRE are shown in Figure 8.

Table II. Percentages of explained variance (P. Var) and the cumulative percentages (P. C.Var) explained by the different PPSs.

PPS	P. Var (%)	P. C. Var (%)
1	21.4	21.4
2	20.0	41.4
3	19.0	60.4
4	9.4	69.8
5	5.9	75.7
6	4.6	80.3
7	3.5	83.8

PPS1 (Fig. 8a) and PPS2 (Fig. 8b) show a sequence pattern associated with the displacement of a cold front that arrives on the coast of RJ on D0. PPS1 explains 21.4% of the total variance and is associated with a shorter and more oceanic baroclinic system than PPS2. It is noted that the cold front is unable to reach the continent because on D0 the frontal system appears connected with a low-pressure system located over the Atlantic Ocean, close to the coast of RJ. PPS1 also shows the Chaco Low, located between northern Argentina, central-western Paraguay, and southern Bolivia. This synoptic pattern at the surface is similar to the average of the mean sea level pressure associated with SHRE, obtained through the composite method (Fig. 5a). This result was expected due to the fact that the PPSs that explain the higher percentage of the total variance is related to the most frequent synoptic pattern, which coincides frequently with the average field. The PPS2 sequence pattern (Fig. 8b) explains 20.0% of the total variance and shows on D0 the cold front over RJ with a more intense and wider post-frontal anticyclone compared to PPS1.

PPS3 (19.0%) (Fig. 8c) also shows an intense and wide post-frontal anticyclone with a slow displacement during the analyzed period. On D–2, the frontal system is already over São Paulo state, reaching RJ during D–1. On D–1 and D0, the post-frontal anticyclone is practically stationary over the Atlantic Ocean around 35ºS, 45ºW, and acquiring blocking characteristics. With such surface atmospheric circulation pattern, the RJ is affected by persistent southeast winds which favor increased moisture convergence and, consequently, heavy rain intensification in the CRJ.

The patterns PPS2 and PPS3 are similar to those identified by Escobar (2019) related to a synoptic climatology during the Brazilian rainy season. The last sequence pattern (PPS4) (Fig. 8d) explains 9.4% of the total variance and reveals the presence of a low-pressure system located over the Atlantic Ocean to the south of RJ, which remains practically stationary during the analyzed period. This low-pressure system on D–2 is observed connected with a cold front located over the South Atlantic Ocean, close to 40ºS, 35ºW. On D–1 and D0, the cold front moves eastwards quickly whilst the low-pressure system remains practically in the same position, approximately at 25ºS, 45ºW. In general, these cyclones have a weak baroclinic structure whose associated cold fronts affect the coasts of the São Paulo and RJ states. On several occasions, these cyclones are not frontal and show subtropical features (Evans and Braun, 2012; Escobar, 2014; Gozzo et al., 2014; Brasiliense et al., 2018; Silva et al. 2019). In both cases (extratropical or subtropical cyclones), this cyclone contributes to increase moist and warm air convergence towards southeastern Brazil. Moreover, surface southerly and

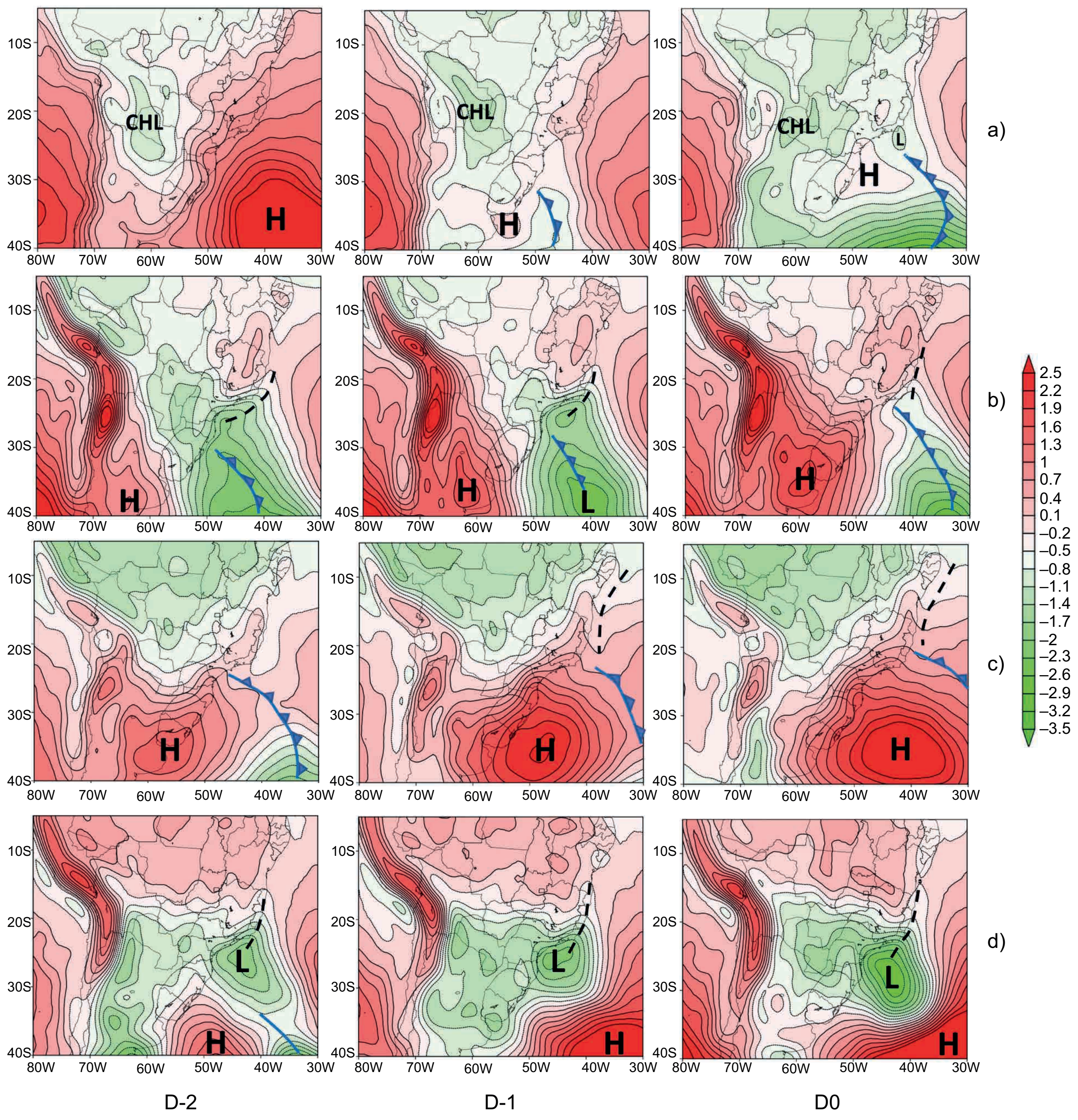

Fig. 8. Principal Pattern Sequences (PPSs) obtained at surface level. a) PPS1, b) PPS2, c) PPS3, d) PPS4. From left to right: D–2, D–1, and D0. CHL= Chaco Low; H=High; L=Low.

southeasterly winds also favor rainfall intensification over the coastal areas of RJ.

While the low sample size (37 cases) is a statistical limitation, pattern PPS3 related to a blocking configuration, was the synoptic pattern of SHRE that showed the longest duration. The rest of the patterns did not show significant differences associated with the duration of SHRE events.

Similar results were obtained asking how these four primary patterns varied throughout the October

April rainy season. There were no significant differences associated with the intraseasonal variability of the four PPS of SHRE.

Despite the small number of cases, pattern PPS2 associated with the incursion of cold fronts, was more common in spring (November) and autumn (March) than in summer. This result is similar to Escobar (2019) of the synoptic climatology during the Brasilian rainy season.

Differences in the accumulated precipitation were evaluated for each of the four patterns associated with SHRE. Despite the few cases of SHRE events, the synoptic composite maps (figures not shown) did not show significant differences between the patterns (PPSs).

Figure 9 shows the synoptic surface charts highly correlated with the four PPSs associated with SHRE. The synoptic surface charts associated with the patterns PPS1 (Fig. 9a) and PPS2 (Fig. 9b) show a cold front over the Atlantic Ocean, favoring mass and moisture convergence towards the continent. The synoptic surface chart related to the pattern PPS3

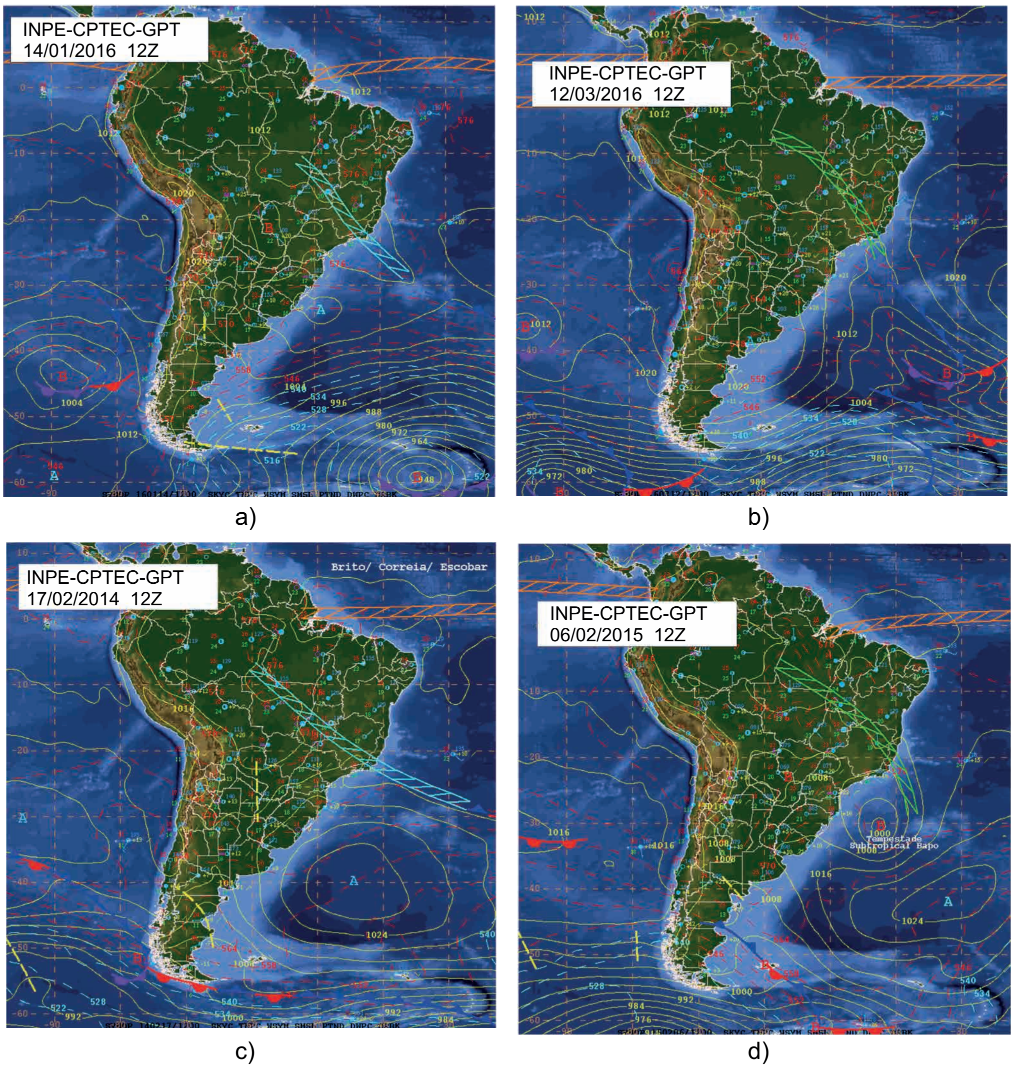

Fig. 9. Surface synoptic charts elaborated by CPTEC/INPE at 1200 UTC associated with SHRE in the CRJ. a) January 14, 2016. b) March 12, 2016. c) February 17, 2014. d) February 6, 2015. Sea level pressure (hPa) in continuous yellow lines and 1000-500 hPa thickness in red dashed lines. Synoptic symbols as in conventional mode.

(Fig. 9c) is associated with a wide high-pressure system located over the Atlantic Ocean and the stationary front close to the coast of RJ state. Such surface atmospheric circulation is similar to a blocking configuration pattern, with southeasterlies over the São Paulo and RJ state's coast and favoring the intensification of heavy rain in the CRJ. The surface synoptic chart associated with PPS4 (Fig. 9d) shows the presence of the subtropical cyclone "Bapo" located in the Atlantic Ocean, approximately to the southeast of Santa Catarina state. This low-pressure system can persist for several days maintaining the convergence of a warm and moist air mass from the Amazon region to the Southeast region of Brazil and, consequently contributing to the intensification of the rain in the CRJ.

4. Conclusions

A synoptic climatology of SACZ episodes associated with HRE in the CRJ during the period October-April/2006-2016 was developed in this study to identify the main synoptic characteristics and the modes of variation of the surface atmospheric circulation related to this extreme meteorological situation.

Over the 10 rainy seasons analyzed, 95 SACZ episodes were identified over Brazil, 77 (81%) of which reached the CRJ (SCRJ). Considering the SCRJ episodes with at least one day of HRE in the CRJ (SHRE), 37 cases were identified from the 77 cases of SCRJ. This means that almost half (48%) of the SCRJ events caused HRE in the city.

A total of 43.1% of SHRE reached the heavy rainfall threshold on the first day and in 68.6% of the cases the rain reached this threshold on the first two days. This result indicates that the heavy rainfall in the CRJ caused by SACZ episodes occurs mainly during the beginning of the episode.

December, January, and March were the months with the highest frequency of episodes of SACZ, SCRJ, and SHRE and most of these episodes last between 3 and 6 days.

The mean synoptic pattern associated with SHRE shows the advance of a typical cold front from Argentina that is connected with a mid-tropospheric trough at lower latitudes and both of them contribute to the intensification of moist air mass convergence in the CRJ. Two days before the SHRE (D–2),the Chaco Low is observed over Paraguay and a weak mid-tropospheric trough is located on the lee side of the Andes Cordillera, over northern Argentina.

On D0, the 500 hPa cyclonic disturbance is located over São Paulo state and favors the formation of a wide area of low pressure over the Atlantic Ocean, to the south of RJ. The anomaly fields clearly show the propagation of a typical baroclinic system, with the 500 hPa wave positioned to the west of the surface wave. The negative anomalies at both levels are more intense over the South Atlantic Ocean and significantly decrease their intensities as they extend towards the RJ, including the CRJ.

The atmospheric circulation at 850 hPa shows the typical configuration observed during rainy season in Brazil, with a predominant northerly flow. On D–2, the RJ shows a northerly flow from the Atlantic Ocean through the influence of the SASA, and on following days the flow rotates to the northwest from the Amazon region. Simultaneously, there is a frontal trough associated with the displacement of the cold front identified at the surface.

The 850 hPa anomaly fields show negative anomalies over a wide area in the South Atlantic Ocean with a pronounced anomalous trough that favors the establishment of a continental flow in a northwestern direction over much of the Southeast region of Brazil. This type of anomaly pattern at 850 hPa level induces the intensification of moisture transport from the Amazon region over the CRJ. This behavior is confirmed by the specific humidity anomalies at 850-hPa, where an increase of approximately $2gkg^{-1}$ is observed over part of the Southeast region of Brazil during D0. On this day, a "dipole" or seesaw pattern configuration is established, determined by positive anomalies in southeastern Brazil and negative anomalies in the South region of Brazil.

The atmospheric circulation at upper level (200 hPa) shows, between D–1 and D0, the presence of cyclonic anomalies in southern Brazil, Uruguay, and the adjacent Atlantic Ocean and anticyclonic anomalies over part of southeastern Brazil. The cyclonic anomalies are associated with the frontal trough, and the trough of the lower latitudes and the anticyclonic anomalies indicates strong divergence at high levels contributing to the precipitation intensification in the CRJ.

The synoptic classification at the surface associated with SHRE, allowed the identification of four main synoptic patterns that represented approximately 70% of the total variance. Two of the patterns (PPS1 and PPS2) are related to the displacement of a cold front that arrives on the coast of RJ on D0. PPS1 does not directly reach the continent and is associated with a shorter and more oceanic baroclinic system compared to PPS2, and they accounted for 21.4% and 20.0% of the total variance, respectively.

Pattern PPS3 represented 19.0% of the total variance and is associated with an intense post-frontal anticyclone that remains practically stationary over the Atlantic Ocean, acquiring blocking characteristics. The constant flow from the southeast determined by this synoptic pattern favors increased moisture convergence and, consequently, the precipitation intensification in the CRJ. Pattern PPS4 explained 9.4% of the total variance and it is related to the presence of a cyclone over the Atlantic Ocean to the south of RJ, which reveals a weak baroclinic structure. The cold front associated with this cyclone usually affects the coasts of the São Paulo and RJ states. Frequently this type of cyclone is not frontal and has subtropical characteristics, remaining stationary for several days and favouring rainfall intensification in the CRJ.

Finally, note that the results of this study are useful for weather forecasters who work in operational meteorological centers and need to forecast the heavy rainfall that occurs in the CRJ during the the Brazilian rainy season.

Acknowledgments

The authors thank the Brazilian Research Council (CNPq) for the financial support (“Edital Universal” Grant number 424157/2016-0). We also express our gratitude to the National Institute for Space Research (INPE) of Brazil for the synoptic charts and satellite images; the Rio Alert System from the Municipality of Rio de Janeiro for the precipitation data and to the National Center for Environmental Prediction (NCEP) for the reanalysis data.

References

Andrade KM, Cavalcanti IFA. 2018. Atmospheric characteristics that induce extreme precipitation in frontal systems over Southeastern Brazil during summer: Observations and atmospheric model simulation. International Journal of Climatology 38: 1–18. https://doi.org/10.1002/joc.5744

Brasiliense CS, Dereczynski CP, Satyamurty P, Chou SC, Silva Santos VR, Calado RN. 2018. Synoptic analysis of an intense rainfall event in Paraíba do Sul river basin in southeast Brazil. Meteorological Application 25: 66–77. https://doi.org/10.1002/met.1670

Carvalho AMG. 1989. Conexões entre a circulação em altitude e a convecção sobre a América do Sul. Master´s thesis, Instituto Nacional de Pesquisas Espaciais.

Carvalho LMV, Jones C, Liebmann B. 2004. The South Atlantic convergence zone: Intensity, form, persistence, and relationships with intraseasonal to interannual activity and extreme rainfall. Journal of Climate 17: 88–108. https://doi.org/10.1175/1520-0442(2004)017<0088:T-SACZI>2.0.CO;2

Cattell R.1978. The Scientific use of factor analysis in behavioral and life sciences. New York and London, Plenum Press.

Compagnucci R, Salles MA. 1997. Surface Pressure Patterns during the year over Southern South America. International Journal of Climatology 17: 635-653. https://doi.org/10.1002/(SICI)1097-0088(199705)17:6<635::AID-JOC81>3.0.CO;2-B

Compagnucci R, Araneo D, Canziani P. 2001. Principal sequence pattern analysis: A new approach to classifying the evolution of atmospheric systems. International Journal of Climatology 21: 197-217. https://doi.org/10.1002/joc.601

Dereczynski CP, Oliveira JS, Machado CO. 2009. Climatologia da precipitação no município do Rio de Janeiro. Revista Brasileira de Meteorologia 24: 24-38. https://doi.org/10.1590/S0102-77862009000100003

Dereczynski CP, Calado RN, Barros AB. 2017. Chuvas extremas no Município do Rio de Janeiro: Histórico a partir do Século XIX. Anuário do Instituto de Geociências 40: 17-30. https://doi.org/10.11137/2017_2_17_30

Dolif G, Nobre CA. 2012. Improving extreme precipitation forecasts in Rio de Janeiro, Brazil: are synoptic patterns efficient for distinguishing ordinary from heavy rainfall episodes? Atmospheric Science Letters 13(3): 216-222. https://doi.org/10.1002/asl.385

Dourado F, Arraes TC, Silva MF. 2012. O Megadesastre da Região Serrana do Rio de Janeiro – as Causas do Evento, os Mecanismos dos Movimentos de Massa e a Distribuição Espacial dos Investimentos de Reconstrução no Pós-Desastre. Anuário do Instituto de Geociências 35: 43-54. https://doi.org/10.11137/2012_2_43_54

Doss-Gollin J, Muñoz AG, Mason SJ, Pastén M. 2018. Heavy rainfall in Paraguay during the 2015/16 austral summer: Causes and subseasonal-to-seasonal predictive skill. Journal of Climate 31: 6669–6685. https://doi.org/10.1175/JCLI-D-17-0805.1

Escobar GCJ, Compagnucci RH, Bischoff SA. 2004. Sequence patterns of 1000 hPa and 500 hPa geopotential height fields associated with cold surges in Buenos Aires. Atmósfera 12: 69-89.

Escobar GCJ. 2014. Padrões de circulação em superfície e em 500 hPa na América do Sul e eventos de anomalias positivas de precipitação no Estado de Minas Gerais durante o mês de dezembro de 2011. Revista Brasileira de Meteorologia 29:105-124. https://doi.org/10.1590/S0102-77862014000100011

Escobar GCJ, Seluchi ME, Andrade K. 2016. Classificação sinótica de frentes frias associadas a chuvas extremas no leste de Santa Catarina (SC). Revista Brasileira de Meteorologia 31: 649-661. https://doi.org/10.1590/0102-7786312314b20150156

Escobar GCJ, Matoso V. 2018. Zona de Convergência do Atlântico Sul (ZCAS): Definição prática segundo uma visão operacional. In: XX Congresso Brasileiro de Meteorologia. Maceió. Anais do XX Congresso Brasileiro de Meteorologia.

Escobar GCJ, Reboita MS, Souza A. 2019. Climatology of surface baroclinic zones in the coast of Brazil. Atmósfera 32: 129-141. https://doi.org/10.20937/ATM.2019.32.02.04

Escobar GCJ. 2019. Classificação sinótica durante a estação chuvosa do Brasil. Anuário do Instituto de Geociências – UFRJ 42: 421-436. https://doi.org/10.11137/2019_2_421_436

Evans JL, Braun A. 2012. A climatology of subtropical cyclones in the South Atlantic. Journal of Climate 25: 7328–7340. https://doi.org/10.1175/JCLI-D-11-00212.1

Gozzo LF, Rocha RP, Reboita MS, Sugahara S. 2014: Subtropical cyclones over the southwestern South Atlantic: Climatological aspects and case study. Journal of Climate 27: 8543–8562. https://doi.org/10.1175/JCLI-D-14-00149.1

Green PE, Carroll JD. 1978. Analyzing Multivariate Data. The Dryden Press. Illinois.

Grimm AM. 2011. Interannual climate variability in South America: impacts on seasonal precipitation, extreme events, and possible effects of climate change. Stochastic Environmental Research and Risk Assessment 25: 537-554. https://doi.org/10.1007/s00477-010-0420-1

Harman H.1976. Modern Factor Analysis. The University of Chicago Press Chicago. IL.

Huth R, Beck C, Philipp A, Demuzere M, Ustrnul Z, Cahynová M, Kyselý J, Tveito OT. 2008. Classications of atmosfheric ciculation patterns. Recent advances and applications. Trends and Directions in Climate Research. Annals of the New York Academy of Sciences 1146: 105-152. https://doi.org/10.1196/annals.1446.019

Kodama Y. 1992. Large-scale common features of subtropical precipitation zones (the Baiu frontal zone. the SPCZ and the SACZ) Part I: Characteristics of subtropical frontal zones. Journal of the Meteorological Society of Japan. Ser. II. 70: 813-835. https://doi.org/10.2151/jmsj1965.70.4_813

Kousky VE. 1979. Frontal influences on northeast Brazil. Monthly Weather Review 107: 1140-1153. https://doi.org/10.1175/1520-0493(1979)107<1140:FIONB>2.0.CO;2

Kousky VE, Gan M. 1981. Upper tropospheric cyclonic vortices in the tropical South Atlantic. Tellus 33: 538-551. https://doi.org/10.3402/tellusa.v33i6.10775

Kousky VE. 1988. Pentad outgoing longwave radiation climatology for the South American sector. Revista Brasileira de Meteorologia 3: 217-231.

Lenters JD, Cook KH. 1997. Summertime precipitation variability over South America: Role of the large-scale circulation. Monthly Weather Review 127: 409-431. https://doi.org/10.1175/1520-0493(1999)127%3C0409:SPVOSA%3E2.0.CO;2

Lima KC, Satyamurty P, Fernández JP. 2010. Large-scale atmospheric conditions associated with heavy rainfall episodes in Southeast Brazil. Theoretical and Applied Climatology 101: 121-135. https://doi.org/10.1007/s00704-009-0207-9

Marchioro E, Silva GM, Correa W. 2016. A Zona de Convergência do Atlântico Sul e a precipitação pluvial do município de Vila Velha (ES): repercussões sobre as inundações. Revista do Departamento de Geografia 31: 101-117. https://doi.org/10.11606/rdg.v31i0.108447

Moraes FDS, Aquino FE, Mote TL, Durkee JD, Mattingly KS. 2020. Atmospheric characteristics favorable for the development of mesoscale convective complexes in Southern Brazil. Climate Research 80: 43-58. https://doi.org/10.3354/cr01595

Nogués-Paegle J and Mo KC. 1997. Alternating wet and dry conditions over South America during summer. Monthly Weather Review 125:279– 291. https://doi.org/10.1175/1520-0493(1997)125%3C0279:AWADCO%3E2.0.CO;2

Nery JT, Malvestio L. 2017. Natural Disasters in Southeastern Brazil Associated with the South Atlantic Convergence Zone. Natural Hazards and Earth System Sciences Discussions 1-24. https://doi.org/10.5194/nhess-2015-33

Nielsen DM, Belém AL, Marton E, Cataldi M. 2019. Dynamics-based regression models for the South Atlantic Convergence Zone. Climate Dynamics 52: 5527–5553. https://doi.org/10.1007/s00382-018-4460-4

Pristo MV, Dereczynki CP, Souza PRD, Menezes WF. 2018. Climatologia de Chuvas Intensas no Município do Rio de Janeiro. Revista Brasileira de Meteorologia 33: 615-630. https://doi.org/10.1590/0102-7786334005

Quadro MFL. 1994. Estudo de episódios de Zona de Convergência do Atlântico Sul (ZCAS) sobre a América do Sul. 1994. Master´s thesis, Instituto Nacional de Pesquisas Espaciais.

Reboita MS, Gan MA, Rocha RP, Ambrizzi T. 2010. Regimes de precipitação na América do Sul: uma revisão bibliográfica. Revista Brasileira de Meteorologia 25: 185-204. https://doi.org/10.1590/S0102-77862010000200004

Reboita MS, Marietto DMG, Souza A, Barbosa M. 2017. Caracterização atmosférica quando da ocorrência de eventos extremos de chuva na região sul de Minas Gerais. Revista Brasileira de Climatologia 21: 20-37. https://doi.org/10.5380/abclima.v21i0.47577

Richman M. 1986. Rotation of Principal Components. Journal of Climatology 6: 293-335.

Richman M, Angel J, Gong X. 1992. Determination of Dimensionality in Eingenanalysis. In: Proceedings of the 5th International meeting on statistical climatology, Toronto, Canadá.

Rocha RP, Reboita MS, Gozzo LF, Dutra LMM, Jesus EM. 2019. Subtropical cyclones over the oceanic basins: a review. Annals of the New York Academy of Sciences 1436: 138-156. https://doi.org/10.1111/nyas.13927

Rozante JR, Moreira DS, Gonçalves LGG, Vila DA. 2010. Combining TRMM and surface observations of precipitation: technique and validation over South America. Weather and forecasting 25: 885-894. https://doi.org/10.1175/2010WAF2222325.1

Saha S, Moorthi S, Pan H, Wu X, Wang J, Nadiga S, Tripp P, Kistler R, Woollen J, Behringer D, Liu H, Stokes D, Grumbine R, Gayno G, Wang J, Hou Y, Chuang H, Juang HH, Sela J, Iredell M, Treadon R, Kleist D, Delst PV, Keyser D, Derber J, Ek M, Meng J, Wei H, Yang R, Lord S, van den Dool H, Kumar A, Wang W, Long C, Chelliah M, Xue Y, Huang B, Schemm J, Ebisuzaki W, Lin R, Xie P, Chen M, Zhou S, Higgins W, Zou C, Liu Q, Chen Y, Han Y, Cucurull L, Reynolds RW, Rutledge G, Goldberg M. 2010. The NCEP Climate Forecast System Reanalysis. Bulletin of the American Meteorological Society 91: 1015-1057. https://doi.org/10.1175/2010BAMS3001.1

Saha S, Moorthi S, Wu X, Wang J, Nadiga S, Tripp P, Behringer D, Hou Y, Chuang H, Iredell M, Ek M, Meng J, Yang R, Mendez MP, van den Dool H, Zhang Q, Wang W, Chen M, Becker E. 2014. The NCEP Cimate Forecast System Version 2. Journal of Climate 27: 2185-2208. https://doi.org/10.1175/JCLI-D-12-00823.1

Seluchi ME, Chou SC. 2009. Synoptic patterns associated with landslide events in the Serra do Mar, Brazil. Theoretical and Applied Climatology, 98: 67-77. https://doi.org/10.1007/s00704-008-0101-x

Silva JP, Reboita MS, Escobar GCJ. 2019. Caracterização da zona de convergência do Atlântico Sul em campos atmosféricos recentes. Revista Brasileira de Climatologia 15: 355-377. http://doi.org/10.5380/abclima.v25i0.64101

Weide-Moura CR, Escobar GCJ, Andrade KM. 2013. Padrões de circulação em superfície e altitude associados a eventos de chuva intense na região metropolitana do Rio de Janeiro. Revista Brasileira de Meteorologia 28: 267-280. https://doi.org/10.1590/S0102-77862013000300004

Atmósfera 35(2), 307-330 (2022)
https://doi.org/10.20937/ATM.52832

CONTENTS

Atmospheric thermodynamics and dynamics during convective, stratiform and nonprecipitating clouds over the metropolitan area of Rio de Janeiro – Brazil

Fabricio Polifke DA SILVA[1]*, Otto Corrêa ROTUNNO FILHO[2], Maria Gertrudes ALVAREZ JUSTI DA SILVA[3], Rafael João SAMPAIO[2], Gisele Dornelles PIRES[2,4] and Afonso Augusto MAGALHÃES DE ARAÚJO[5]

[1] *Department of Meteorology, Institute of Geosciences, Universidade Federal do Rio de Janeiro - UFRJ, CCMN - Cidade Universitária - Ilha do Fundão, Avenida Athos da Silveira Ramos, 274, Rio de Janeiro, RJ, 21941-916, Brazil.*
[2] *Civil Engineering Program, Alberto Luiz Coimbra Institute for Postgraduate Studies and Research in Engineering – COPPE, Universidade Federal do Rio de Janeiro – UFRJ, Avenida Horácio Macedo, 2020 – Cidade Universitária, Rio de Janeiro, RJ 21945-970, Brazil.*
[3] *Meteorology Laboratory, Science and Technology Center, Universidade Estadual do Norte Fluminense Darcy Ribeiro – UENF, Avenida Brenand, s.n., Imboassica, 27925–535, Macaé – RJ, Brazil.*
[4] *Engineering and Society Group, Exact Sciences and Technologies School, Universidade Iguaçu – UNIG, Av. Abílio Augusto Távora, 2134 – Jardim Nova Era, 26275-580, Nova Iguaçu – RJ, Brazil.*
[5] *Department of Water Resources and Environment, Polytechnic School, Universidade Federal do Rio de Janeiro – UFRJ. Av. Athos da Silveira Ramos, CT, Cidade Universitária – 21941–590, Rio de Janeiro–RJ.*
*Corresponding author; fabriciopolifke@igeo.ufrj.br

Received February 10, 2020, accepted: July 29, 2020

RESUMEN

Los mecanismos físicos involucrados en el desarrollo y pronóstico de nubes y precipitación son bastante complejos y dependen del ambiente atmosférico local, especialmente cuando condiciones severas son inminentes. Investigaciones destinadas a comprender los mecanismos favorables para los diferentes escenarios atmosféricos pueden ayudar a los meteorólogos operativos a emitir alertas. Este trabajo proporciona contribuciones cualitativas y cuantitativas a partir de datos de radiosondas y radar y simulaciones numéricas para evaluar la formación de nubes convectivas, estratiformes y no precipitantes sobre el área metropolitana de Río de Janeiro, Brasil. La energía potencial disponible para convección (CAPE) y el índice Liftex (LI) mostraron valores más altos en los días convectivos (CAPE = 2600 J Kg^{-1} y LI = –4 ºC), seguidos de los días sin precipitación (CAPE = 1500 J Kg^{-1} y LI = –2 ºC) y días nublados estratiformes (CAPE = 1400 J Kg^{-1} y LI = –1.5 ºC). Se observó una alta convergencia del viento a niveles bajos (1000–850 hPa) y medios (850–700 hPa) en días convectivos (–16.5 s^{-1} y –9.6 s^{-1}, respectivamente). En contraste, se observó divergencia del viento a los mismos niveles en días estratiformes (6.4 s^{-1} y 6.9 s^{-1}) y sin precipitación (9.7 s^{-1} y 7.3 s^{-1}). Se observó una mayor divergencia del viento (8.3 s^{-1}) en los días convectivos en los niveles superiores (300–200 hPa) en comparación con los días estratiformes (3.2 s^{-1}) y sin precipitación (2.8 s^{-1}). Los resultados muestran un acoplamiento de la convergencia del viento, la humedad y la energía en la troposfera inferior y la divergencia en los niveles superiores en los días convectivos. A pesar de la disponibilidad de humedad en los días estratiformes y de energía termodinámica en los días sin precipitación, no se observó el acoplamiento respectivo entre estas condiciones y los forzantes dinámicos.

ABSTRACT

Physical mechanisms involved in the development and forecast of clouds and precipitation are both quite complex and dependent on the local atmospheric environment, especially when severe weather conditions are imminent. Research aimed at understanding the environmental mechanisms favorable to the different atmospheric scenarios can help operational weather forecasters to issue warnings. This paper provides qualitative and quantitative contributions from radiosondes, radar, and numerical simulations to evaluate the formation of convective, stratiform, and nonprecipitating clouds over the metropolitan area of Rio de Janeiro, Brazil. The convective available potential energy (CAPE) and lifted index (LI), showed higher values on convective days (CAPE = 2600 J.Kg^{-1} and LI = –4 ºC), followed by nonprecipitating (CAPE = 1500 J.Kg^{-1} and LI = –2 ºC) and stratiform cloud days (CAPE = 1400 J.Kg^{-1} and LI = –1.5 ºC). High wind convergence was observed at low- (1000–850 hPa) and mid- (850–700 hPa) levels on convective days ($^{-1}$6.5 s^{-1} and –9.6 s^{-1}, respectively). In contrast, wind divergence at the same levels was observed on stratiform (6.4 s^{-1} and 6.9 s^{-1}) and nonprecipitating (9.7 s^{-1} and 7.3 s^{-1}) days. Higher wind divergence (8.3 s^{-1}) was observed on convective days at upper levels (300–200 hPa) compared with stratiform (3.2 s^{-1}) and nonprecipitating (2.8 s^{-1}) days. Results show a coupling of wind convergence, moisture and energy in the lower troposphere and divergence at upper levels on convective days. Despite moisture availability on stratiform days and thermodynamic energy on nonprecipitating days, the respective coupling between these conditions and dynamic triggers was not observed.

Keywords: Clouds, Rainfall, Reflectivity, Radiosonde.

1. Introduction

Clouds play an important role in the climate, since they significantly affect hydrological, geochemical and energy cycles. Clouds generally present large variability in time and space and their development is related to moisture and dynamic and thermodynamic atmospheric processes (Collier, 2006; Meerkotter and Bugliaro, 2009). The atmospheric dynamic motions required to lift air and trigger cloud development are found at various scales, such as tropical cyclones, midlatitude fronts and cyclones, mesoscale systems, breezes and local surface wind convergence (Collier, 2006). Complementarily, the physical mechanisms related to cloud development are quite complex and also depend on the local thermodynamic environment (Silva et al., 2017; Silva et al., 2019). Clouds have different characteristics based on their shape and height in the atmosphere. From those, two main cloud types, namely convective and stratiform, can be further categorized and evaluated (Penide et al., 2013; Powell et al., 2015).

Convective clouds present a deeper vertical structure, strong updrafts and downdrafts and heavy rains (Hong et al., 1999). In contrast, stratiform clouds are characterized for being shallow and presenting greater horizontal homogeneity, possibly extending for hundreds of kilometers. Stratiform clouds present weak vertical air motion and generate light rains (Hong et al., 1999; Deng et al., 2014). Different microphysical cloud processes are related to drop size growth. Cloud droplets in a convective structure grow chiefly by riming or accretion, which subsequently develops into large and dense hydrometeors. In stratiform clouds, vapor deposition and aggregation mechanisms dominate; consequently, ice hydrometeors tend to be smaller and less dense, and, once melted, tend to favor the formation of smaller raindrops (Penide et al., 2013).

The thermodynamic and dynamic atmospheric environments related to convective and stratiform cloud vertical structures are also characterized through distinct patterns. Convective clouds are characterized by the presence of low-level convergence transitioning to divergence at upper atmospheric levels (Mapes and Houze, 1993), which transfers energy (sensible and latent heat) along the entire troposphere. Stratiform clouds are characterized by lower-level divergence, convergence in the middle of the troposphere and divergence at atmospheric upper levels. This pattern of vertical divergence in stratiform clouds indicates the occurrence of cooling in the lower troposphere and heating throughout the atmospheric levels above it (Homeyer et al., 2014). In general, upward vertical motion throughout the troposphere is associated with convective clouds, while downward motion at lower atmospheric levels capped with an opposite (upward) motion above characterize stratiform clouds (Mapes, 1993, 2000). Due to the great variability in convective and stratiform cloud development, we must also understand the evolution of atmospheric characteristics between these cloud types, especially at the local scale (Yang and Smith, 1999).

Many authors have explored the dynamic and thermodynamic variables related to convective clouds, such as Silva et al. (2016) and Silva et al. (2017). However, few publications address these variables in order to characterize the atmospheric environment of stratiform clouds (Alfieri et al., 2007; Silva et al., 2019). Findell and Eltahir (2003) used sounding data to separate convective from stratiform events based on thermodynamic indices. They find that the main thermodynamic distinction mechanism between these types of clouds is the existence of significant potential energy to drive air parcels up more than five kilometers above midlatitude continental regimes.

In light of the above, this study endeavored to intercompare the performances of thermodynamic parameters and investigate the dynamic triggering conditions over different atmospheric scenarios, classified as convective, stratiform, and nonprecipitating events, in the metropolitan area of Rio de Janeiro on selected days between November to March 2018. Before further discussion, it is important to point out that the results could have some implicit bias due to the short study period adopted. As such, the main goal of these analyses is not to establish thresholds, but rather to evaluate qualitative and quantitative differences regarding the cloud types categorized. Finally, this work attempted to support surveys that could be used by operational forecasters and also didactical local trainings.

2. Methodology and Dataset

2.1 Site description

Atmospheric phenomena over the metropolitan area of Rio de Janeiro (Figure 1) are mainly related to the presence of the South Atlantic Convergence Zone (SACZ) (Ferreira et al., 2004; Seluchi and Chou, 2009), frontal systems (Seluchi and Chou, 2009; Dereczynski et al., 2009) or isolated convective systems (Britto et al., 2016). Figure 1S shows land use (top) and digital elevation model (bottom) of the metropolitan area of Rio de Janeiro (MARJ). Especially during the warm season, the proximity of Atlantic Ocean and different types of land use creates low-level atmospheric instability as a consequence of solar heating and evapotranspiration. The mountainous area of MARJ acts as a dynamic trigger for cloud development, which may lead to the occurrence of high rainfall accumulations, and local natural hazards such as floods and landslides (Roe et al., 2003; Barros et al., 2004; Boers et al., 2015; Oakley et al., 2017, Silva et al., 2016; Dereczynski et al., 2017).

To explore the local vertical profiles over different atmospheric scenarios in Rio de Janeiro a set of radiosondes RS92-SGP (http://www.vaisala.com)

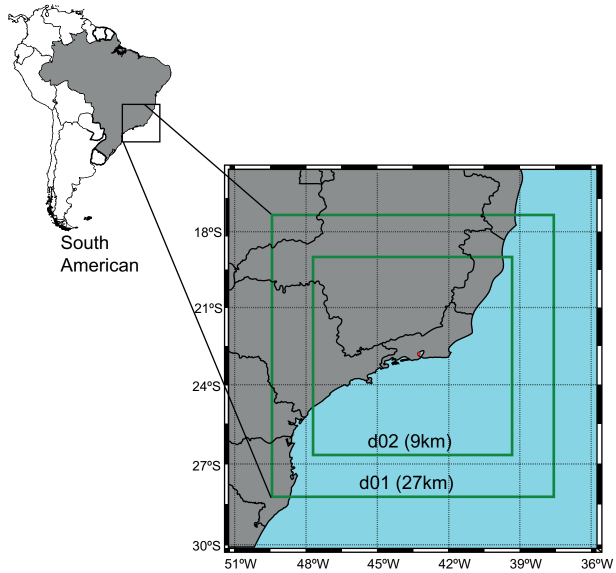

Fig. 1. Experimental site (red point) used in the study.

was used as a part of infrastructure provided by the Water Resources and Environmental Studies Laboratory (LABH2O/COPPE) of the Federal University of Rio de Janeiro (UFRJ). The atmospheric profiling data were collected outside of standard hours at 00:00 UTC and 12:00 UTC, between 11-November-2016 and 03-March-2018, corresponding to the warm and rainy season over the region (Dereczynski et al., 2009; Silva et al., 2017).

The methodology followed Silva et al. (2017), with additional radiosondes launched from the experimental site whenever a rainfall forecast was issued for the metropolitan area of Rio de Janeiro, for a total of thirty days and seventy radiosondes. Figure 2S shows the location of the site at the UFRJ campus. Radiosonde calibration followed the user's guide manual available at the Vaisala website. Addition information on the accuracy of the measured parameters by Vaisala radiosonde sensors can be found in publications of the World Meteorological Organization (https://www.wmo.int/pages/prog/www/IMOP/publications/).

2.2 Cloud classification criteria

Radar reflectivity was used to diagnose and classify cloud types (Hagen et al., 2000; Punkka and Bister, 2005; Goudenhoofdt and Delobbe, 2013; Yang et al., 2013). Convective clouds are characterized by reflectivity echoes greater than 40 dBZ, while

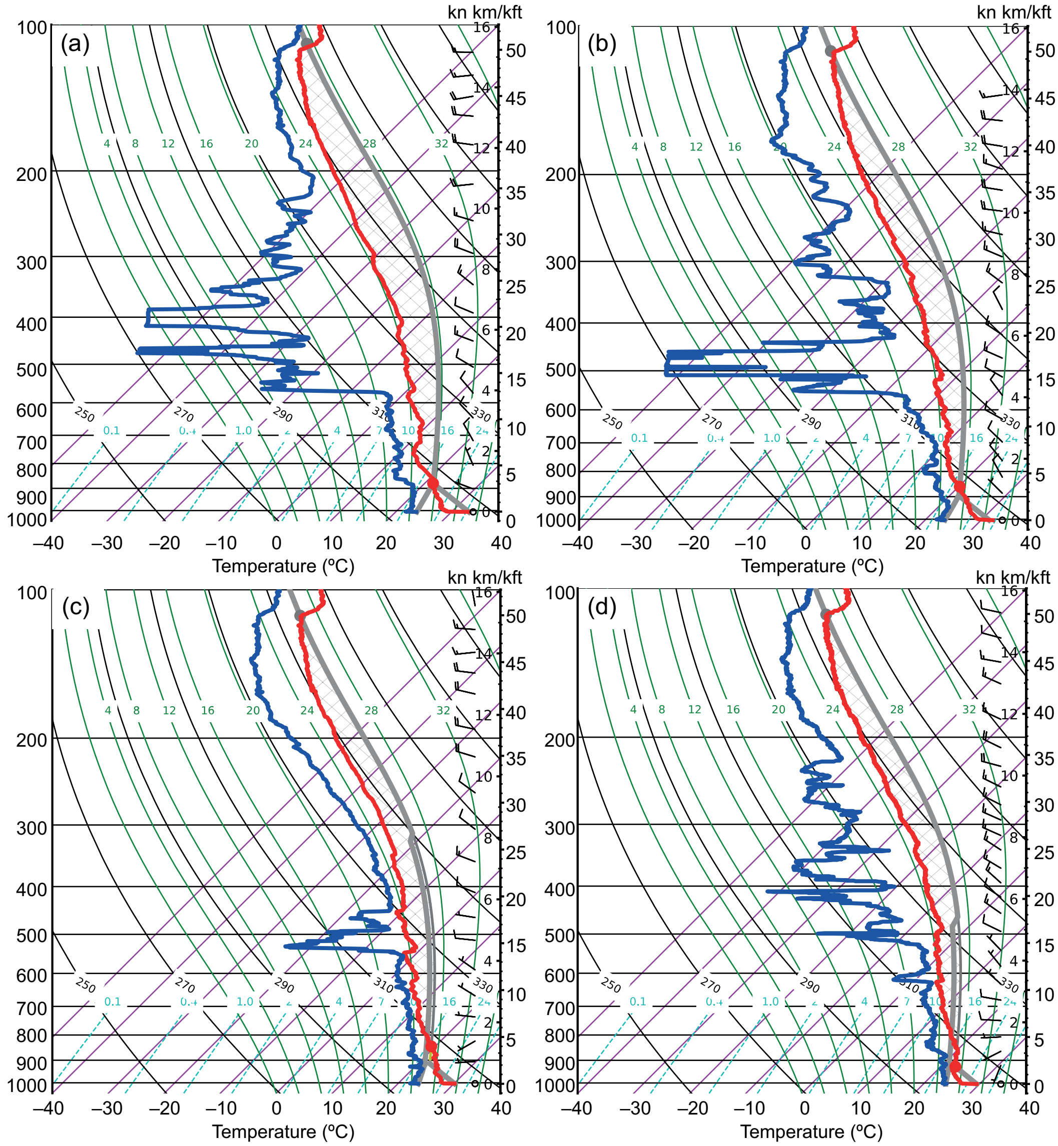

Fig. 2. SkewT/LogP diagram at: (a) 15 UTC, (b) 17 UTC, (c) 19 UTC and (d) 21 UTC on February 22, 2018.

stratiform clouds present reflectivity between 20 dBZ and 40 dBZ and so-called nonprecipitating clouds present values lower than 20 dBZ (Hagen et al., 2000; Goudenhoofdt and Delobbe, 2013; Yang et al., 2013). According to these criteria, reflectivity data from the Sumaré weather radar (provided by the Alerta Rio system, http://alertario.rio.rj.gov.br/) was used to classify the days of the experiments. Table I shows the selected days according to the radar reflectivity criteria of clouds classification.

We selected three days for initial discussion during which these cloud types were observed over the study region: 02/22/2018, characterized by convective clouds (Figure 3S); 03/08/2018, characterized by stratiform clouds (Figure 4S); and 03/15/2018, characterized by nonprecipitating clouds. These days were also selected since they had the same number of radiosondes launched at the same hours, i.e., 15 UTC (12 Local Time (LT)), 17 UTC (14 LT), 19 UTC (16 LT) and 21 UTC (18 LT).

Table I. Radiosonde experiments and cloud type classification

Days with Radiosonde launches	Cloud type classification
11/17/2016, 12/12/2016, 01/02/2017, 01/03/2017, 01/06/2017, 01/12/2017, 01/19/2017, 03/06/2017, 03/13/2017, 03/24/2017, 01/03/2018, 01/11/2018, 01/12/2018, 01/22/2018, 01/25/2018, 02/22/2018, 03/01/2018, 03/02/2018, 03/03/2018	Convective
11/18/2016, 01/13/2018, 01/15/2018, 03/08/2018	Stratiform
11/29/2016, 02/13/2017, 01/16/2018, 01/17/2018, 01/23/2018, 03/15/2018, 03/16/2018	Nonprecipitating

Subsequently, the results considering all the selected days presented in Table I are also discussed.

2.3 Thermodynamic parameters and numerical modeling

Thermodynamic variables are utilized to evaluate atmospheric thermal parameters (temperature and moisture), especially as those relate to the convective cloud environment (Teixeira and Satyamurty, 2007; Busuioc et al., 2015). Dynamic variables characterize atmospheric motions (both wind speed and direction) and are generally dependent on large-scale and local circulation patterns (Rudolph and Friedrich, 2014). Simultaneous presence of these thermodynamic and dynamic parameters on a given time of day, cloud formation is expected to take place within the expected horizon (Wetzel and Martin, 2000; Nascimento, 2005; Silva et al., 2017).

Given the days selected according to the criteria of clouds classification, this work sought to analyze and compare the behavior of thermodynamic and dynamic variables for days categorized as having convective, stratiform and nonprecipitating clouds. Table II presents the thermodynamic and dynamic parameters chosen for this study: convective available potential energy (CAPE), convective inhibition (CIN), lifted index (LI), K index (K), Total Totals (TT) index, environmental lapse-rate (LR), velocity convergence (CONV), velocity divergence (DIV), wind shear (WS) and vertical movement (MV). Variables related to the state of the atmosphere were also chosen. Those include surface air temperature (TEMP), surface dewpoint temperature (DEWT), surface air depression (DEP) and precipitable water (PW).

In the formulas of the variables presented in Table II, T and Td represent air and dewpoint temperatures (measured in degrees centigrade (ºC)), respectively, while the subscripts refer to surface (SFC) or isobaric levels (hPa). T*p* expresses the temperature of a lifted parcel (using the parcel method) at 500 hPa; T*vp* and T*v* (also in ºC) characterize the virtual temperature of a lifted parcel and the surrounding environment temperature, respectively. LFC represents the level of free convection (i.e. lifted parcel is warmer than surrounding environment), while LNB represents the neutral buoyancy level. The physical interpretations of the variables in Table II are briefly described below.

Surface air depression represents the difference between air temperature (T_{SFC}) and dewpoint temperature (Td_{SFC}), an indicator of moisture availability in the atmosphere. Convective available potential energy (CAPE) represents the energy of an air parcel calculated as the difference between parcel virtual temperature (T_{vp} (z)) and environment virtual temperature (T_v(z)) from LFC until LNB (Blanchard, 1988). Conversely, convective inhibition (CIN) is related to the energy (work) required to lift the air parcel from surface (SFC) to the LFC. Graphically, CAPE represents a "positive area" and CIN a "negative area" in the Skew T log P diagrams. The lifted index (LI), measured by the difference between the T of a lifted parcel (T_{v500}) and the surrounding air (T_{v500}) at 500 hPa (Galway, 1956), graphically expresses the "width" measurement of CAPE.

The lapse-rate (LR) represents temperature variation for an atmospheric layer. Typically, the layer between 700 hPa and 500 hPa is also a measurement of CAPE "width" (Nascimento, 2005), which we will adopt in this study. The K index represents the sum of air and dew point temperatures measured at 850 hPa subtracted from air depression at 700 hPa and air

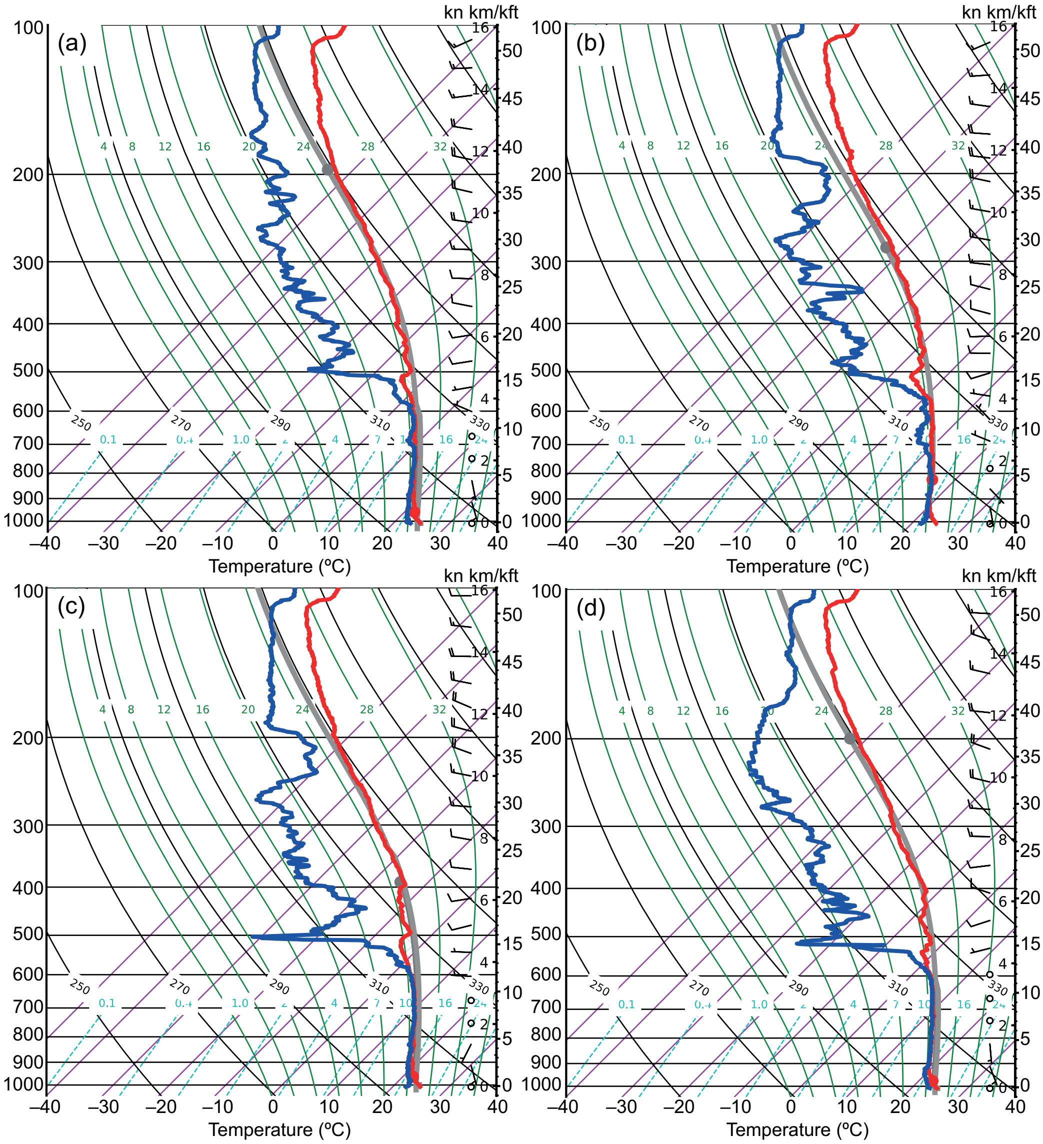

Fig. 3. SkewT/LogP diagram at: (a) 15 UTC, (b) 17 UTC, (c) 19 UTC and (d) 21 UTC on March 8, 2018.

temperature at 500 hPa (George, 1960). The Total Totals index (TT) is quite similar to the K index, with the main difference being that air depression at 700 hPa is not considered in the calculation of TT (Miller, 1972). If the atmosphere is vertically warm and wet, K and TT present similar behavior. In contrast, in case a dry layer is present at 700 hPa, TT is not affected and can better represent atmospheric instability (Silva Dias, 1987; Henry, 1999; Nascimento, 2005). Precipitable water (PW) represents the available rain water if all water vapor integrated over an atmospheric column (this study integrated from surface to 100 hPa) precipitated (Silva et al.,2018).

To analyze the behavior of thermodynamic parameters during the classified days (Table I), upper air sounding data was plotted in SkewT/LogP diagrams using the SkewT 1.1.0 Python software package (https://pypi.python.org/pypi/SkewT) and the MetPy Python package (https://pypi.org/project/met/) was used to calculate the thermodynamic parameters.

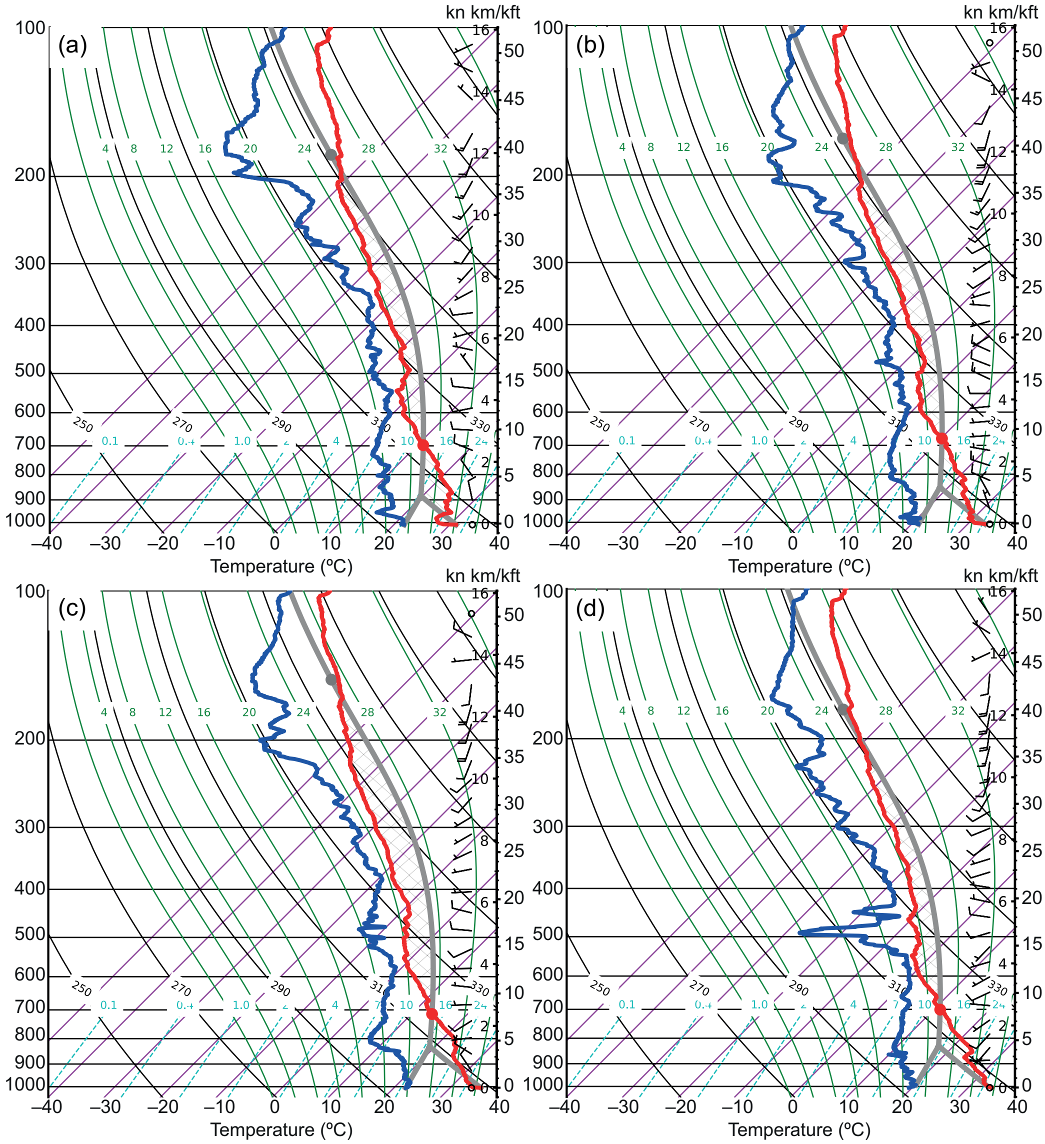

Fig. 4. SkewT/LogP diagram at: (a) 15 UTC, (b) 17 UTC, (c) 19 UTC and (d) 21 UTC on March 15, 2018.

The dynamic parameters were calculated using Weather Research and Forecasting (WRF) model (Skamarock et al., 2008) version 3.8. The model was configured with two nested domains, with horizontal spatial domain resolutions for coarse grid (d01) and fine grid (d02) of 27 km and 9 km, respectively, 27 vertical levels with the highest level at 50 hPa, and 4 vertical levels of soil. The green squares in the Figure 1 show the horizontal domains used. The physical parameterizations selected were: the WRF single-moment 3-class microphysics scheme (Hong et al., 2004), the Kain-Fritsch cumulus parameterization scheme (Kain 2004), the Rapid Radiative Transfer Model for longwave radiation (Mlawer et al., 1997), the Dudhia shortwave radiation scheme (Dudhia, 1989), the Unified Noah land surface model (Tewari et al., 2004), the Revised MM5 Monin-Obukov (Jiménez et al., 2012) for surface layer, and the Yon-Sei University Planetary Boundary Layer parameterization scheme (Hong et al., 2006). Initial

Table II. Thermodynamic and dynamic parameters

Variable	Formula
Air depression	$DEP = T_{SFC} - Td_{SFC}$
Convective potential available energy	$CAPE = g\int_{LFC}^{LNB} \frac{T_{vp}(z) - T_v(z)}{T_v(z)} dz$
Convective inhibition	$CIN = g\int_{SFC}^{LFC} \frac{T_{vp}(z) - T_v(z)}{T_v(z)} dz$
Lifted index	$LI = T_{500} - T_{p_{500}}$
Lapse-rate	$LR = -\frac{\partial T}{\partial Z}$
K index	$K = (T_{850} + Td_{850}) - (T_{700} - Td_{700}) - T_{500}$
TT index	$TT = (T_{850} + Td_{850}) - 2 * T_{500}$
Precipitable water	$PW = \frac{1}{\rho g}\int_{SFC}^{100} wdp$
Velocity convergence	$CONV = \left(\frac{\partial u}{\partial x} + \frac{\partial v}{\partial y}\right) < 0$
Velocity divergence	$DIV = \left(\frac{\partial u}{\partial x} + \frac{\partial v}{\partial y}\right) > 0$
Wind shear	$WS = \frac{V_{500_{hPa}} - V_{10_m}}{Z_{500_{hPa}} - Z_{10_m}}$
Vertical motion	$MV = \frac{\partial Z}{\partial t}$

and lateral boundary conditions were obtained from the Global Forecast System (GFS, http://www.emc.ncep.noaa.gov/GFS/doc.php) at six-hour intervals and horizontal resolution of 0.50º x 0.50º and provided to the WRF model.

Horizontal negative velocity convergence (CONV) and divergence (DIV) are essential dynamic and trigger mechanisms to promote air motions throughout the atmosphere (Doswell, 1987; Tajbakhsh et al., 2012; Silva et al., 2019). Given these distinct mechanisms related to convective and stratiform clouds (Homeyer et al., 2014), this study considered the atmospheric levels between 1000 hPa and 850 hPa to characterize convergence (CLL) and divergence (DLL) in the lower troposphere, the layer between 700 hPa and 500 hPa to characterize CONV (CML) and DIV (DML) in the middle of the atmosphere, and the atmospheric level from 300 hPa to 200 hPa to characterize upper CONV (CUL) and DIV (DUL). Wind shear (WS) was calculated as the difference between wind speed and direction in two atmospheric levels (at 10 meters and 500 hPa). Vertical motion (MV) at 500 hPa is also a dynamic trigger for cloud development, where positive values characterize upward motion (Houze,1993; Banacos and Schultz, 2005; Chen et al., 2006; Baba, 2016).

3. Results and Discussion

3.1 Case studies

Analysis of upper air sounding data and the SkewT/LogP diagrams made it possible to verify the atmospheric vertical profile through measurements of air temperature (red line) and dew point temperature (blue line) for 15 UTC (12 LT), 17 UTC (14 LT), 19 UTC (16 LT), 21 UTC (18 LT) on February 22 (Figure 1), March 8 (Figure 2) and March 15 (Figure 3), 2018. The circles filled in red and gray represents the LFC and LNB, respectively. For all days, small rates (~5.7 ºC km^{-1}) of air temperature decrease throughout the troposphere are observed. This vertical profile is related to coastal regions, in this case to the proximity of the study region to the Atlantic Ocean, which tends to exhibit lower vertical air temperature profile rates compared to interior continental regions (Holton et al., 2002).

On February 22 late morning (Figure 2a), a near-saturated (moisture availability) unstable-temperature atmospheric layer is observed from surface to 600 hPa; a dry layer is observed from 600 hPa to the upper atmospheric levels. In early afternoon (Figure 2b) and mid-afternoon (Figure 2c), a progressive increase of moisture is observed from surface to upper levels. Large potential energy (gray shaded area on SkewT/logP diagram) is observed in all soundings on this day, driving an air parcel ascending vertically from the LFC to the LNB (Figure 2) with CAPE values reaching above 3000 J.kg^{-1} (Houze, 1993; Schultz et al., 2000). This potential energy was mainly related to the presence of the South American Convergence Zone (SACZ), which configures the northwest flow and brings warmer and moister air from the Amazon region towards the metropolitan area of Rio de Janeiro (Ferreira et al., 2004; Quadro et al., 2012), where lower atmospheric levels show local instability from solar heating and evapotranspiration near the surface during warm season (Doswell, 2001). Figures 5S and 6S show the corresponding satellite image and surface charts provided by the Center for Weather Forecasting and Climate Studies (http://satelite.cptec.inpe.br/home/index.jsp), indicating the SACZ configuration over South America. In addition, the SACZ also provides a dynamic environment favorable for upward air motion, reinforcing the deep convection observed in Figure 3S (Mota and Nobre, 2006; Tavares and Mota, 2012; Gille and Mota, 2014).

A similar vertical profile of moisture is observed on March 03, 2018 compared to February 22. However, for all sub-daily soundings launched on March 03, a more saturated atmospheric layer is observed from surface to 550 hPa (Figure 3). We observed no significant potential energy (gray shaded area) during this day. Such condition indicates the importance of a dynamic mechanism in the development of stratiform clouds (Figure 4S) within a moisture content local cloud scale environment in the absence of significant CAPE (Doswell, 2001; Itterly et al., 2018).

On March 15, the SkewT/logP diagrams (Figure 4) show CAPE and an unstable temperature profile, which corroborates the warm season daily cycle of solar heating warming the troposphere by conduction of atmospheric layer closest to the surface and subsequent convection (Seidel et al., 2005). However, in contrast to February 22 and March 03, significan CIN (beige area in the SkewT/Log P diagrams) is observed, requiring the need for dynamic forcing in order to develop clouds (Doswell, 2001).

CAPE, CIN, Lapse-Rate (LR), and LI, K and TT indices were calculated from the upper air sounding data to evaluate and intercompare sub-daily (15 UTC, 17 UTC, 19 UTC and 21 UTC) thermodynamic variations related to the three cloud types categorized, i.e., convective on February 22 (Figure 3S), stratiform on March 8 (Figure 4S) and nonprecipitating on March 15, 2018. The results are shown in Figure 5, where the convective day is represented by “Conv”, stratiform day is represented by “Strat” and nonprecipitating day is represented by “NoRain”.

Significant CAPE (above 2500 J.kg^{-1}) values are observed for the convective day (Figure 4a), while non-significant CAPE values are observed for the stratiform day (Figure 4b), as seen in the Skew T Log P diagrams (Figure 3). Despite the intermediary CAPE values on March 15, it is possible to observe the presence of CIN (Figure 5b) with values between –100 J.kg^{-1} and -300 J.kg^{-1}, which were not observed on February 22 (Figure 5b) and March 8 (Figure 5b). The LI index (Figure 5c) also shows its largest values (below -5 ºC) only on the convective day, characterized by the larger broad area observed in the SkewT/logP diagrams (Figure 2), corroborating the presence of atmospheric thermodynamic potential energy driving development of the convective clouds observed on this day (Nascimento, 2005; DeRubertis, 2006). In the opposite direction of CAPE behavior, LR sub-daily variations (Figure 5d) present significant values (above 6.5 ºC km^{-1}) only during the nonprecipitating day (Figure 5d). This suggests that smaller moisture availability in the atmospheric lower levels could be

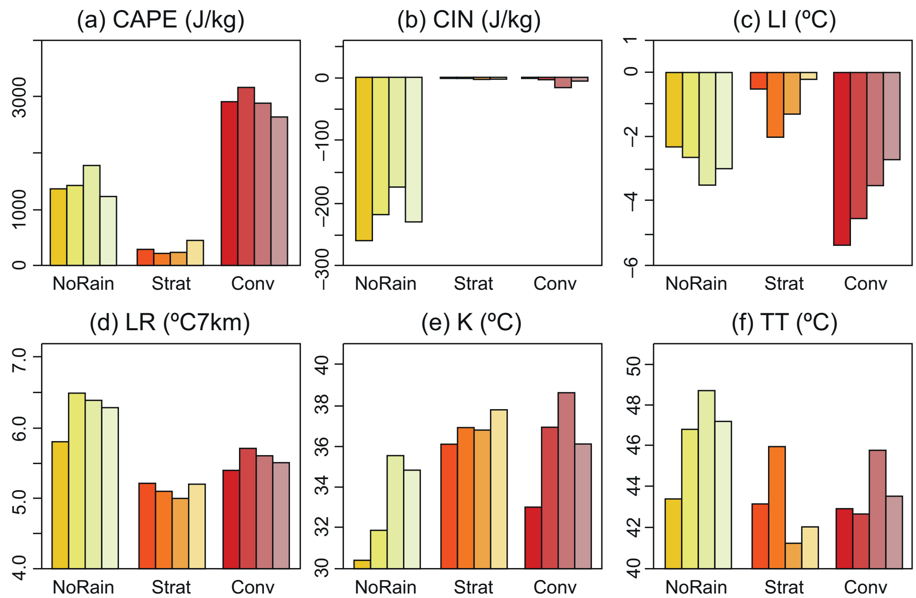

Fig. 5. Sub-daily (15 UTC, 17 UTC, 19 UTC and 21 UTC) variations of thermodynamic indices: (a) – CAPE; (b) – CIN; (c) – LI; (d) – K ; (e) – TT and (f) – LR on March 15 ("NoRain"), March 8 ("Strat") and February 22 ("Conv") 2018.

producing warm air lifting following the adiabatic curve in the SkewT/logP diagrams (Figure 4) and, consequently, higher levels of air saturation (higher CIN). K (Figure 5e) and TT (Figure 5f) presented values above 30 ºC, as well as 40 ºC, for the three days analyzed, which indicate high storm potential with likely intense rainfall (Nascimento, 2005). This behavior was observed because these two indices are not able to represent atmospheric instability if it occurs below the 850 hPa threshold, suggesting that the main thermodynamic characteristics over the analyzed region are observed in the atmospheric layer closest to the surface (DeRubertis, 2006; Silva et al., 2017).

Figures 6 and 7 present WRF simulations for: on the left column, air temperature at 2 m and wind circulation at 850 hPa (T2M+WD); on the middle column, wind convergence (negative shaded area) and divergence (positive shaded area) at 1000 hPa and wind convergence (negative lines) and divergence (positive lines) at 850 hPa (CV+DV); and on the right column, wind shear between 500 hPa and 10 meters and wind convergence (negative lines) and divergence (positive lines) at 250 hPa (WSH + DVM) for 15 UTC (Figure 6) and 17 UTC (Figure 7) on February 22 (top row), March 8 (middle row) and March 15 (bottom row), respectively.

On February 22, wind circulation at 850 hPa shows a northwest flow advecting moist and warm air from the Amazon region towards the metropolitan area of Rio de Janeiro (Figure 6a) and the adjacent Atlantic Ocean (Figure 7a) at 15 UTC and 17 UTC. Such atmospheric pattern is related to the configuration of SACZ (Teixeira and Satyamurty, 2007). It is possible to observe a coupling between convergence (negative lines over negative areas) in the lower atmospheric levels (Figure 6b and 7b) and divergence at the upper levels (Figures 6c and 7c). This behavior shows an atmospheric vertical structure promoting a dynamic mechanism to lift air parcels and develop convective clouds (Doswell, 1987; Tajbakhsh et al., 2012). Weak wind shear is also observed, which can create an atmospheric environment to develop heavy rainfall (Silva et al., 2017).

A different pattern is observed on March 8 at 15 UTC (Figure 6, middle row) and 17 UTC (Figure 7, middle row), with 850 hPa wind circulations indicating a southeast flow advecting moist air from the Atlantic Ocean (Figure 6d). This atmospheric circulation was related to a high-pressure system which

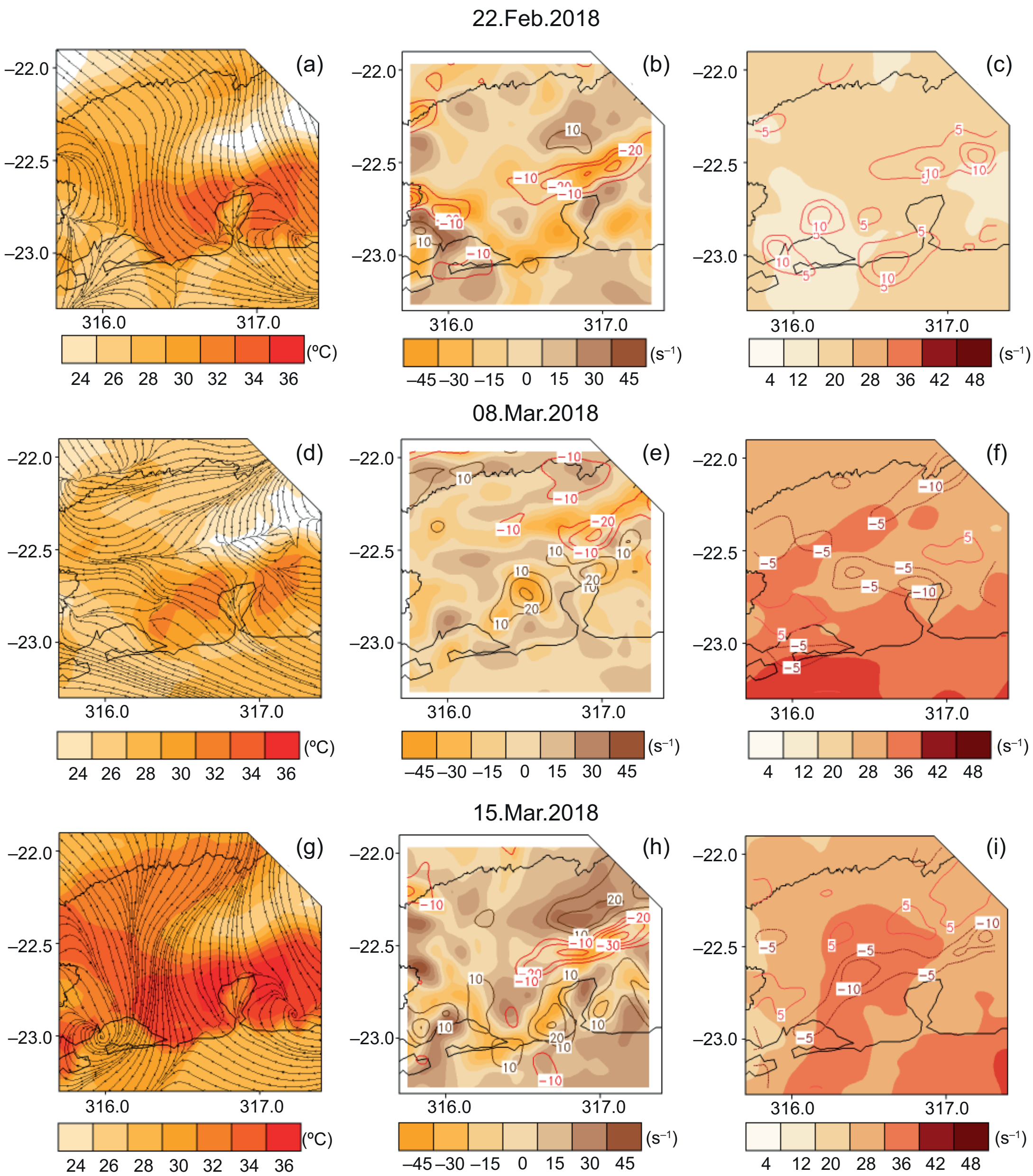

Fig. 6. WRF simulations for: on the left column, air temperature at 2 m and wind circulation at 850 hPa (left); on the middle column, wind convergence (negative shaded area) and divergence (positive shaded area) at 1000 hPa; convergence (negative lines) and divergence (positive lines) at 850 hPa (middle); and on the right column, wind shear between winds at 500 hPa and 10 meters; and convergence (negative lines) and divergence (positive lines) at 250 hPa at 15 UTC on February 22 (top row), March 8 (middle row) and March 15 (bottom row).

brought cold air from higher latitudes towards the metropolitan area of Rio de Janeiro (Bonnet et al., 2018). Wind convergence at 1000 hPa (Figure 6e) was aligned under a wind divergence at 850 hPa (Figure 6e); suggesting upward vertical motion confined within this layer. At upper levels, wind convergence (Figure 6f and 7f) can also be observed. These occurrences of simultaneous wind convergence and

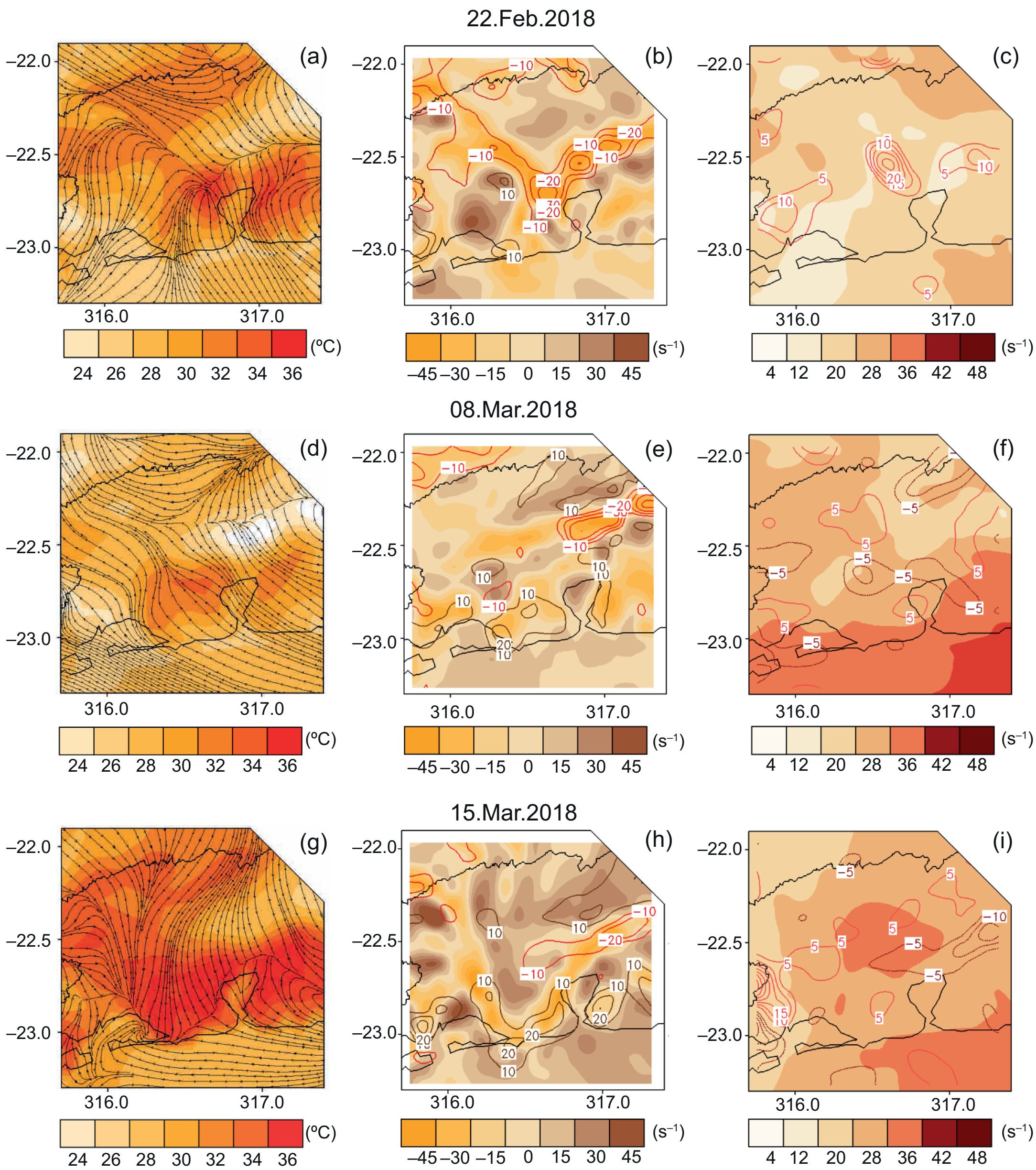

Fig. 7. Same as Fig. 6 but for 17 UTC.

divergence throughout lower and upper levels characterize the physical structure of stratiform clouds, i.e. a shallow and layered configuration, consistent with the results found by Collier (2006).

On March 15, the pattern of convergence and divergence at lower (Figures 6h and 7h) and upper layers (Figures 6i and 7i) is similar to March 8. The main difference was observed for wind circulation at 850 hPa, which showed a northeast component over Rio de Janeiro city. As a consequence, this scenario promoted a decrease of moisture and thermodynamic availability favoring cloud formation but without the potential for droplet growth and precipitation (Moraes et al., 2005; Moura et al., 2013).

The simultaneous presence of atmospheric instability and moisture is an important condition for convective clouds, observed by the high values of CAPE, LI, K and TT convective days (Figure 5).

Vertical dynamic coupling is seen by means of the wind convergence at low level and divergence at upper levels. Over the metropolitan area of Rio de Janeiro, stratiform days are observed mainly after the passage of cold fronts and the presence of the migratory high pressure system with advection of cold air and moisture at low levels (Bonnet et al., 2018). This local pattern corroborated the lower LR values (Figure 5d) and the divergence behavior analyzed (Figures 6 and 7). On days with non-precipitating clouds, despite the presence of thermodynamic instability, higher CIN values (Figure 5b) and wind divergence at low levels were observed, suggesting the absence of dynamic triggers for ascent and clouds with precipitation development. These initial results indicate that analyses associated with the behavior of dynamic and thermodynamic variables under different atmospheric scenarios can provide qualitative tools for local predictors and warning systems, especially in the face of severe weather events.

3.2 Statistical overview

In order to describe qualitative and quantitative analyses related to the atmospheric environment of convective, stratiform and nonprecipitating clouds during the experiments made by LABH2O between 11-November-2016 and 03-March-2018, statistical analyses were conducted of vertical atmospheric profiles, wind, and thermodynamic and dynamic parameters. It is important to note that results may have some implicit biases due to the short period considered. As such, the main goal of these analyses is not to establish quantitative thresholds, but rather to characterize differences regarding the cloud types categorized.

Figures 8-10 illustrate the mean profile for the selected days presented in Table I. Qualitatively, a greater average CAPE (gray hatched area) can be observed on convective cloud days (Figure 8), possibly related to the simultaneous presence of warming and moisture content at low (1000-850 hPa) level. The mean profile for stratiform (Figure 9) and nonprecipitating (Figure 10) cloud days presented less CAPE than convective days (Figure 8). The stratiform days (Figure 9) presented more moisture availability, between 1000-600 hPa. However, there is a lower surface mean temperature (~27 ºC) compared to convective days (~31 ºC) suggesting the

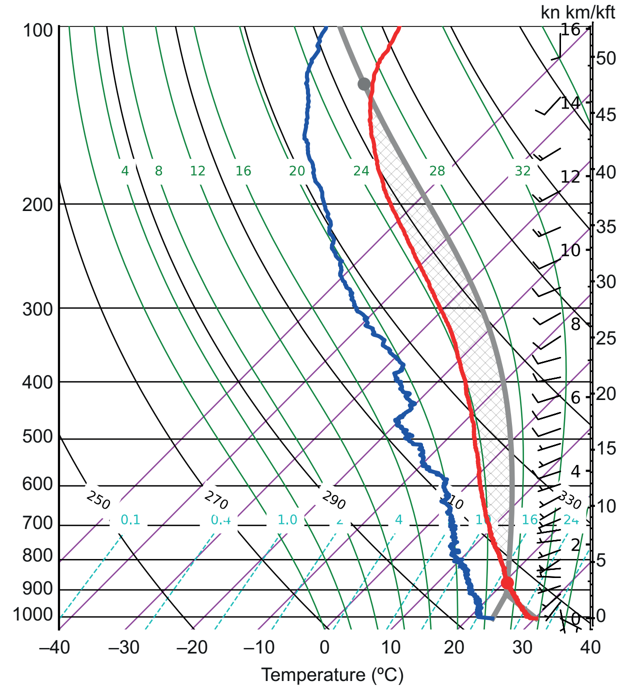

Fig. 8. SkewT/LogP mean diagram for the convective cloud days between November 2016 and March 2018.

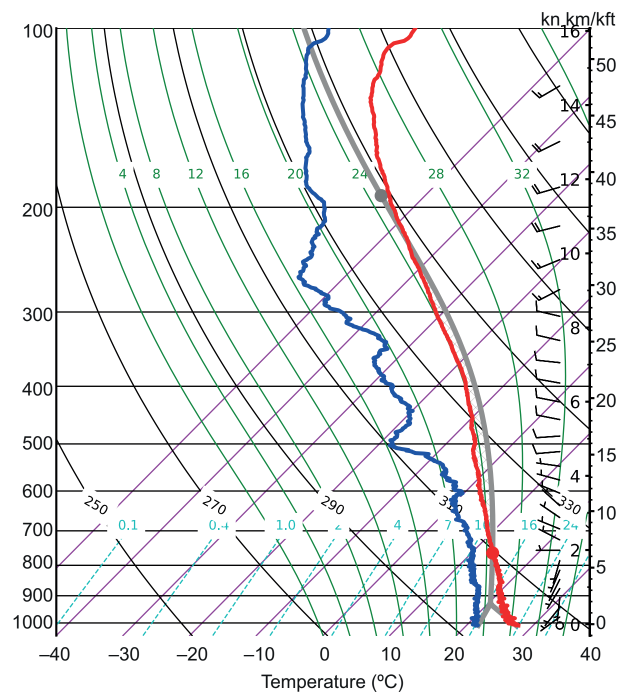

Fig. 9. SkewT/LogP mean diagram for the stratiform cloud days between November 2016 and March 2018.

importance surface warming for convective development. Nonprecipitating days (Figure 10) presented the highest surface mean temperature (~33 ºC), but also the largest CIN area (yellow hatched area) and a dry layer between1000-900 hPa.

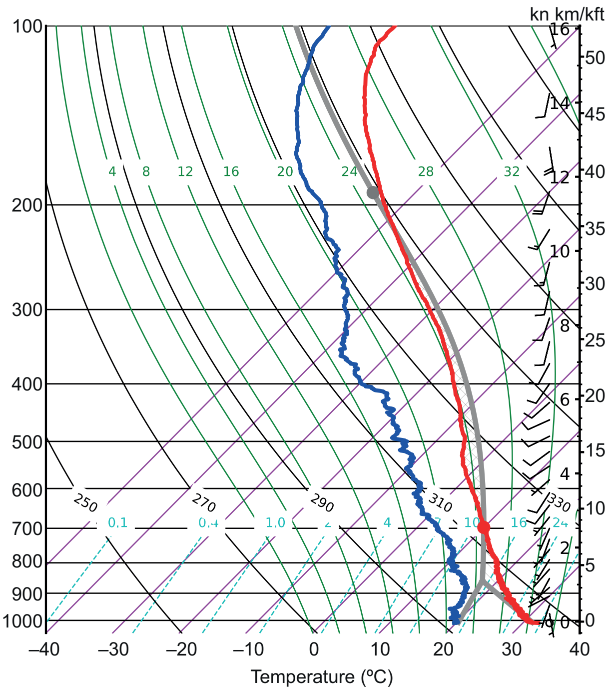

Fig. 10. SkewT/LogP mean diagram for the nonprecipitating cloud days between November 2016 and March 2018.

Figure 11 shows thermodynamic variables and dynamic variable boxplots for convective (red), stratiform (orange) and nonprecipitating (yellow) cloud days. The thermodynamic parameters (Figure 11a to 11l) were calculated using the upper air sounding data collected during the experiments. The dynamic parameters were calculated using the results of the WRF numerical model. Given the spatial diversity of wind convergence and wind divergence, a region surrounding the campus of Federal University of Rio de Janeiro (UFRJ) was used to evaluate the local effects of this trigger during the thirty days (Table I).

The higher temperature (~33 ºC) and lower dew point temperature (~21 ºC) (Figure 11a and Figure 11b) were observed for the nonprecipitating cloud days. The stratiform cloud days presented the lower temperature (27 ºC) and dew point depression (2 ºC) (Figure 11a and 11c). The higher dew point temperature (23.5 ºC) was observed for the convective days (Figure 11b), since moisture is an important ingredient for convective cloud development (Doswell, 2010; Pucik et al., 2015). The combined presence of low-level higher moisture (Figures 11b and 11c) and diurnal warming (Figure 11a and Figure 11e) resulted in the highest CAPE (around 2600 J kg^{-1}) and low CIN (~–15 J kg^{-1}) on convective days (Figure 11d). Analyzing severe and nonsevere storms, Pucik et al. (2015) verified that CAPE values diminish for decreasing severe weather intensity, corroborating the results between the three categorized clouds.

LFC was highest (860 hPa, corresponding to lower altitude) on stratiform cloud days, followed by convective (820 hPa) and nonprecipitating (740 hPa) days (Figure 11f). The nonprecipitating cloud days presented high LFC (740 hPa) and LNB (165 hPa) values, indicative of the small layer with thermodynamic available energy. Convective days were also characterized by the most negative LI values (-4 ºC) compared to the other days (Figure 11h), suggesting that besides the larger vertical extension of thermodynamic energy (Figures 11f and 11g), the atmosphere also tended to present a "greater width" with respect to this distribution of energy along the analyzed period (Nascimento, 2005; Tajbakhsh et al., 2012; Pucik et al., 2015).

The LR (Figure 11i) presented the highest values (6 ºC/km) for the nonprecipitating cloud days. As previously discussed, this could be a result of the higher temperatures values (Figure 11a) and the lowest moisture availability (Figure 11c), causing air parcels to ascend dry adiabatically and resulting in higher cooling rate through the vertical profile (Tajbakhsh et al., 2012). Convective and stratiform days, however, presented lower LR values (Figures 11b and 11c), which could be related to liberation of heat latent in the atmosphere due to higher moisture availability. On convective cloud days the results agree with the evaluation conducted by Taszarek et al. (2017) of sounding-derived parameters associated with convective hazards in Europe, in which the authors verified that convective cloud development occurred in environments with lower lapse rates, high CAPE and high low-level moisture. The K (Figure 11j) and TT (Figure 11k) indices presented significant K values (above 30 ºC) and TT above 40 ºC (Silva Dias,

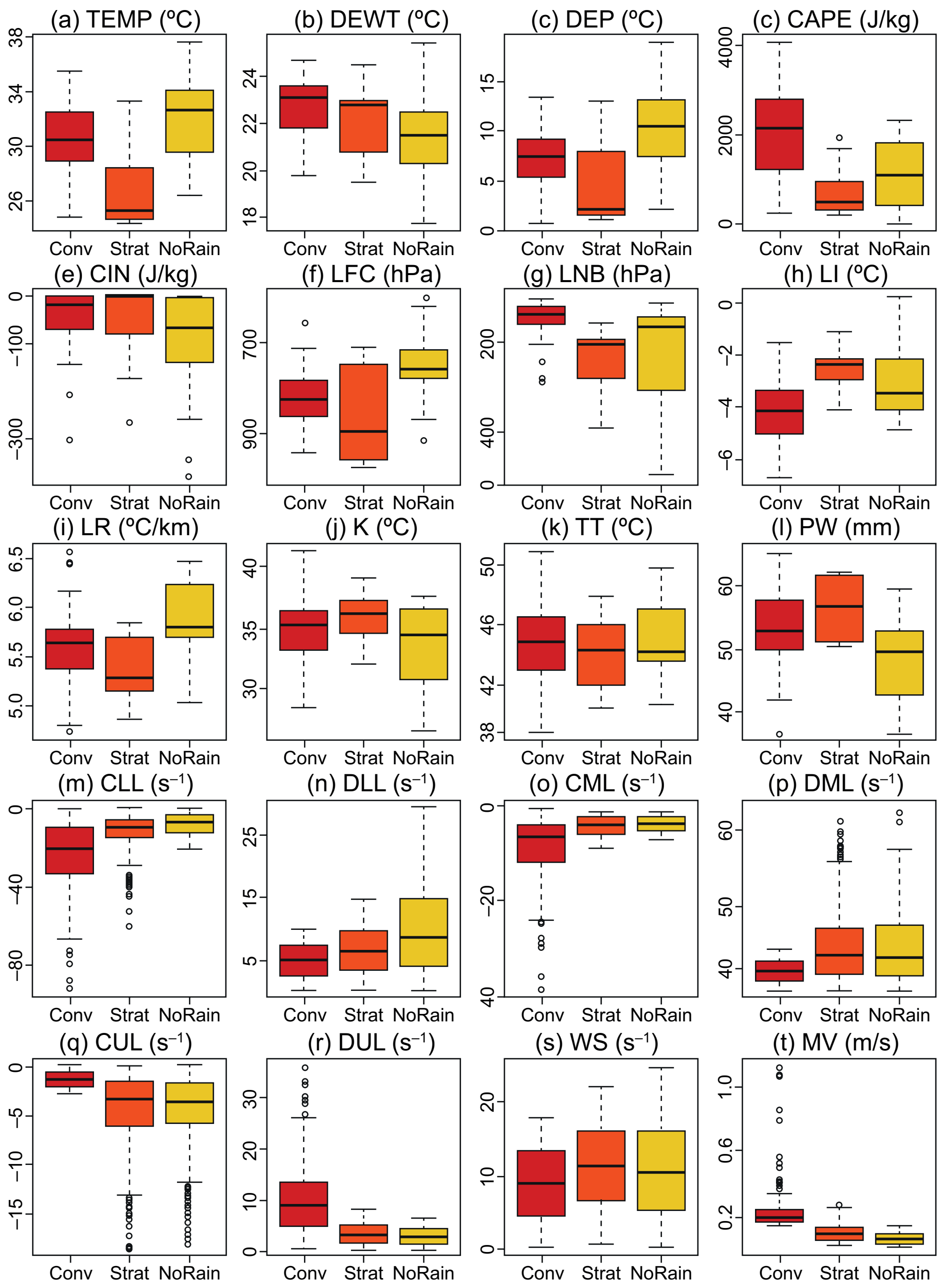

Fig. 11. Boxplots of thermodynamic and dynamic variables for the convective (red), stratiform (orange) and nonprecipitating cloud days (yellow) between November 2016 and March 2018.

2000) for the three cloud types, confirming the previous discussion presented in Figure 6 and the results found in DeRubertis (2006) and Silva et al. (2017). Higher PW values were observed for the convective (53 mm) and stratiform (56 mm) days, also agreeing with the results found for other moisture variables (Figures 11b and 11c).

Among the dynamic triggers, the CLL layer (Figure 11m) presented the most expressive convergence (negative) values in the convective days (–16.5 s^{-1}).

This characteristic, associated to the low-level moisture (Figures 11b and 11c) and thermodynamic instability (Figure 11d), could have created the atmospheric environment on convective days observed (Boer et al., 2013). An opposite behavior was observed for the DLL (Figure 11n) and DML (Figure 11p) layers with the highest (positive) values for the nonprecipitating days (9.7 s^{-1} and 7.3 s^{-1}, respectively). CLL values (–11.7 s^{-1}) in the stratiform days also could characterize the effects of air friction by changing surface wind flow from ocean to continent over the analyzed period (Bonnet et al., 2018). However, DLL (Figure 11n) and DML (Figure 11p) values (6.4 s^{-1} and 6.9 s^{-1}, respectively) were observed on stratiform days. An opposite mechanism for CLL (Figure 11m) and DML (Figure 11p) suggested that air confinement between these layers was occurring on stratiform days. Consequently, cloud development under this atmospheric environment tended to present the shallow and layered development characteristic of stratiform clouds (Collier, 2006).

At upper levels, higher CUL values (Figure 11q) and lower DUL values (Figure 11r) were observed on stratiform (-4.5 s^{-1} and 3.2 s^{-1}, respectively) and nonprecipitating (-4.4 s^{-1} and 2.8 s^{-1}, respectively) days, corroborating the dynamic mechanism observed in the middle atmospheric levels for this type of clouds (Tajbakhsh et al.,2012). On convective days, however, we observed higher (negative) CLL and CML values (Figures 11m and 11o) (–16.5 s^{-1} and -9.6 s^{-1}, respectively) under higher (positive) DUL values (Figures 11r) (8.3 s^{-1}), which agrees with the mass conservation principle and suggests a dynamic vertical structure configuration for convective development (Clark et al., 2009; Silva et al., 2017). The highest wind shear (11.5 s^{-1}) was observed during stratiform events (Figure 11s), while the largest vertical motion (0.3 m/s) was observed during convective events (Figure 11t). This is consistent with the results found by Silva et al. (2017), whereby weak wind shear and vertical motion could act as a dynamic trigger for convective clouds.

4. Conclusions

This study evaluated the thermodynamic and dynamic atmospheric conditions relying on upper air sounding data and numerical simulations as they relate to the formation of convective, stratiform, and nonprecipitating clouds over the metropolitan area of Rio de Janeiro (MARJ), Brazil. A radar echo reflectivity criterion was used to classify such cloud types. Three days (February 22, March 03 and March 15, 2018) were initially chosen as representative of each of the three cloud types to qualitatively analyze the dynamic and thermodynamic characteristics associated with them.

Significant potential energy (CAPE > 2500 Jkg^{-1}) was driving air parcels and vertical ascent on convective cloud day (February 22, 2018). The stratiform day (March 03, 2018) presented a similar vertical moisture profile, but no significant CAPE was available, suggesting the importance of dynamic mechanisms for stratiform clouds development within a moist local scale environment. The nonprecipitating day (March 15, 2018) showed potential energy and an unstable temperature profile. That being said, in contrast to convective and stratiform days, there is a need for external work for air parcel ascent on this day given CIN values between –100 J kg^{-1} and –300 J kg^{-1}, requiring dynamic forcing to develop clouds.

The statistical overall evaluation and metrics calculated considered all the experimental days between November 2016 and March 2018. The results showed that the mean values of higher moisture (Td ~23.5 ºC) combined with the diurnal warming (31 ºC) would have resulted in the highest CAPE (~ 2600 $J.kg^{-1}$) and lowest CIN (around –15 $J.kg^{-1}$) observed on convective days. Nonprecipitating cloud days showed the highest temperature (~33 ºC) and lower moisture (Td ~ 21 ºC). Stratiform days presented the lowest temperature (27 ºC) and intermediate moisture (Td ~23 ºC).

Furthermore, convective days also presented the greatest negative LI values (–4 ºC), suggesting that besides the larger vertical extension of thermodynamic energy, the atmosphere also tended to present a "greater width" of the referred energy distribution in the atmosphere. The lapse rate was highest values (6 ºC/km) on nonprecipitating cloud days, a result of the higher temperature and the lower moisture availability, causing air parcels to ascend dry adiabatically and presenting a higher cooling rate through the vertical profile. K and TT presented significant values (> 30 ºC and 40 ºC) for the three cloud types, possibly as a result that these two indices are not able to represent atmospheric instability if it occurs below the 850 hPa level. Convective and stratiform days presented higher PW values (53 and 56 mm) suggesting the relevance of moisture availability for cloud development.

Regarding the dynamic triggers, convective days presented the most relevant low-level convergence and upper-level divergence ($-16.5\ s^{-1}$ and $8.3\ s^{-1}$, respectively), which associated with low-level moisture and thermodynamic instability could have created the atmospheric environment for this cloud type. Indeed, such pattern agrees with mass conservation and characterizes the dynamic vertical structure and increased potential for convective development.

Stratiform days showed a different dynamic mechanism, with low-level convergence occurring under a mid-level divergence layer. In this case, such profile suggests vertical air confinement between those layers and horizontal spread creating an atmospheric environment favorable for shallow and layered clouds. Nonprecipitating days presented a similar behavior, but with a small moisture and thermodynamic availability. In general, results show a coupling of wind convergence, moisture and energy in the lower atmospheric levels and divergence in the upper atmospheric levels on convective days. Despite the moisture availability observed on stratiform days and the thermodynamic energy on nonprecipitating days, the respective coupling between these conditions and dynamic triggers was not observed.

Acknowledgements

The authors would like to express their gratitude to the Civil Engineering Program of the Alberto Luiz Coimbra Institute of Postgraduate Studies and Research in Engineering (COPPE), which is part of the Federal University of Rio de Janeiro (UFRJ), for the support offered, particularly through availability of the Water Resources and Environmental Studies Laboratory (LABH2O). The study was financed in part by the Coordenação de Aperfeiçoamento de Pessoal de Nível Superior (CAPES) – Finance Code 001, which also helped support this work through CAPES Call 27/2013 - Pró-Equipamentos Institucional and CAPES/MEC Call No. 03/2015 – BRICS. The authors are thankful to the National Council for Scientific and Technological Development (CNPq), which helped fund this work through CNPq Universal Calls No. 14/2013 – Proceeding No. 485136/2013-9; No. 28 /2018 – Proceeding No. 435714/2018-0; and and also by CNPq Call No. 12/2016 – Proceeding No. 306944/2016-2 and CNPq Call No. 06/2019 – Proceeding No. 303846/2019-4 . The authors are also grateful to the Fundação de Amparo à Pesquisa do Estado do Rio de Janeiro (FAPERJ), which helped to fund this work through Project FAPERJ – Pensa Rio – Call 34/2014 (2014-2021).

References

Alfieri L, Thielen J, Pappenberger F. 2012. Ensemble hydrometeorological simulation for flash flood early detection in southern Switzerland. Journal of Hydrology 424–425, 143–153. https://doi.org/10.1016/j.jhydrol.2011.12.038

Baba Y. 2016. Response of rainfall to land surface properties under weak wind shear conditions. Atmospheric Research 182, 335–345. https://doi.org/10.1016/j.atmosres.2016.08.010

Banacos PC, Schultz DM. 2005. The use of moisture flux convergence in forecasting convective initiation: Historical and operational perspectives. Weather Forecasting 20, 351–366. https://doi.org/10.1175/WAF858.1

Barros AP, Kim G, Williams E, Nesbitt SW. 2004. Probing orographic controls in the Himalayas during the monsoon using satellite imagery. Natural Hazards and Earth System Sciences 4(1), 29–51. https://doi.org/10.5194/nhess-4-29-2004

Blanchard DO. 1998. Mesoscale convective patterns of the Southern High Plains. Bulletin of the American Meteorological Society 71, 994-1005. https://doi.org/10.1175/1520-0477(1990)071<0994:MCPOTS>2.0.CO;2

Boer AM, Collier AB, Caballero R. 2013. Processes driving thunderstorms over the Agulhas Current. Journal of Geophysical Research: Atmospheres. 118, 2220–2228. https://doi.org/10.1002/jgrd.50238

Boers N, Bookhagen B, Marwan N, Kurths J. 2015. Spatiotemporal characteristics and synchronization of extreme rainfall in South America with focus on the Andes Mountain range. Climate Dynamics 46, 601–617. https://doi.org/10.1007/s00382-015-2601-6

Bonnet SM, Dereczynski CP, Nunes AMB. 2018. Caracterização Sinótica e Climatológica de Eventos de Chuva Pós-Frontal no Rio de Janeiro. Revista Brasileira de Meteorologia 33, 547-557. https://doi.org/10.1590/0102-7786333013

Britto TT, Oliveira-Júnior JF, Lyra GB, Gois G, Zeri M. 2016. Multivariate analysis applied to monthly rainfall over Rio de Janeiro state, Brazil. Meteorology and Atmospheric Physics 129, 469–478. https://doi.org/10.1007/s00703-016-0481-x

Busuioc A, Birsan MV, Carbunaru D, Baciu M, Orzan A. 2015. Changes in the large scale thermodynamic instability and connection with rain shower frequency over Romania: verification of the Clausius–Clapeyron scaling. International Journal of Climatology 36, 2015–2034. https://doi.org/10.1002/joc.4477

Chen SS, Knaff JA, Markes Jr FD. 2006. Effects of vertical wind shear and storm motion on tropical cyclone rainfall asymmetries deduced from TRMM. Monthly Weather Review 134, 3190–3208. https://doi.org/10.1175/MWR3245.1

Clark AJ, Schaffer CJ, Gallus Jr. WA, Johnson-'Mara K. 2009. Climatology of storm reports relative to upper-level jet streaks. Weather Forecasting 24, 1032–1051. https://doi.org/10.1175/2009WAF2222216.1

Collier CG. 2006. On the formation of stratiform and convective cloud. Weather 58, 62–68. https://doi.org/10.1256/wea.239.02

Deng M, Kollias P, Feng Z, Zhang C, Long CN, Kalesse H, Chandra A, Kumar VV, Protat A. 2014. Stratiform and convective precipitation observed by multiple radars during the DYNAMO/AMIE experiment. Journal of Applied Meteorology and Climatology 53, 2503–2523. https://doi.org/10.1175/JAMC-D-13-0311.1

Dereczynski CP, Calado RN, Barros AB. 2017. Extreme Rainfall in The City of Rio de Janeiro: History from the 19th Century. Anuário do Instituto de Geociências 40, 17-30. http://dx.doi.org/10.11137/2017_2_17_30

Dereczynski CP, Oliveira JSd, Machado CO. 2009. Climatologia da precipitação no município do Rio de Janeiro. Revista Brasileira de Meteorologia 24(1), 24–38. https://doi.org/10.1590/S0102-77862009000100003

DeRubertis D. 2006. Recent trends in four common stability indices derived from U.S radiosonde observations. Journal of Climate 19, 309-323. https://doi.org/10.1175/JCLI3626.1

Doswell CA. 2001. Severe convective storms–an overview. In: Doswell C (ed) Severe convective storms, Meteorological Monograph, 28(50), 1–26. American Meteorological Society. https://doi.org/10.1007/978-1-935704-06-5_1

Doswell III CA. 1987. The distinction between large-scale and mesoscale contribution to severe convection: A case study example. Weather Forecasting 2, 3-16. https://doi.org/10.1175/1520-0434(1987)002<0003:TDBLSA>2.0.CO;2

Dudhia J. 1989. Numerical study of convection observed during the winter monsoon experiment using a mesoscale two-dimensional model. Journal of the Atmospheric Sciences 46, 3077-3107. https://doi.org/10.1175/1520-0469(1989)046<3077:NSOCOD>2.0.CO;2

Ferreira NJ, Correia AA, Ramirez MCV. 2004. Synoptic scale features of the tropospheric circulation over tropical South America during the WETAMC TRMM/LBA experiment. Atmósfera 17(1), 13–30.

Findell KL, Eltahir EAB. 2003. Atmospheric controls on soil moisture–boundary layer interactions. Part I: Framework development. Journal of Hydrometeorology 4, 552–569. https://doi.org/10.1175/1525-7541(2003)004<0552:ACOSML>2.0.CO;2

Galway J. 1956. The lifted index as a predictor of latent instability. Bulletin of the American Meteorological Society 37, 528-529. https://doi.org/10.1175/1520-0477-37.10.528

George JJ. 1960. Weather Forecasting for Aeronautics. Academic Press, USA. https://doi.org/10.1016/C2013-0-12567-6

Gille FSS, Mota MAS. 2014. Importância das condições termodinâmicas nos eventos extremos de precipitação na cidade de Belém e região metropolitana. Revista Brasileira de Meteorologia 29, 73-82. https://doi.org/10.1590/0102-778620130066

Goudenhoofdt E, Delobbe L. 2013. Statistical characteristics of convective storms in Belgium derived from volumetric weather radar observations. Journal of Applied Meteorology and Climatology 52, 918–934. https://doi.org/10.1175/JAMC-D-12-079.1

Hagen M, Schiesser HH, Dorninger M. 2000. Monitoring of mesoscale precipitation systems in the Alps and the northern Alpine foreland by radar and rain gauges. Meteorology and Atmospheric Physics 72, 87–100. https://doi.org/10.1007/s007030050008

Henry NL. 1999. A Static Stability Index for Low-Topped Convection. Weather and Forecasting 15, 246-265. https://doi.org/10.1175/1520-0434(2000)015<0246:ASSIFL>2.0.CO;2

Holton JR, Pyle J, Curry CA. 2002. Encyclopedia of Atmospheric Sciences. Academic Press, New York.

Homeyer CR, Schumacher C, Hoppe Jr. LJ. 2014. Assessing the Applicability of the Tropical Convective–

Stratiform Paradigm in the Extratropics Using Radar Divergence Profiles. Journal of Climate 27, 6673–6686. https://doi.org/10.1175/JCLI-D-13-00561.1

Hong Y, Kummerow C, Oslon WS. 1999. Separation of convective/stratiform precipitation using microwave brightness temperature. Journal of Applied Meteorology and Climatology 38, 1195–1213. https://doi.org/10.1175/1520-0450(1999)038<1195:SOCASP>2.0.CO;2

Hong SY, Dudhia J, Chen SH. 2004. A revised approach to ice microphysical processes for the bulk parameterization of clouds and precipitation. Monthly Weather Review 132, 103-120. https://doi.org/10.1175/1520-0493(2004)132<0103:ARATIM>2.0.CO;2

Hong SY, Noh, Y, Dudhia J. 2006. A new vertical diffusion package with an explicit treatment of entrainment processes. Monthly Weather Review 134, 2318-2341. https://doi.org/10.1175/MWR3199.1

Houze RA. 1993. Cloud Dynamics. International Geophysics Series, 53, Academic Press, Waltham.

Itterly KF, Taylor PC, Dodson JB. 2018. Sensitivity of the Amazonian Convective Diurnal Cycle to Its Environment in Observations and Reanalysis, Journal of Geophysical Research: Atmospheres 23, 12621–12646. https://doi.org/10.1029/2018JD029251

Jiménez PA, Dudhia J, González-Rouco JF. 2012. A revised scheme for the WRF surface layer formulation. Monthly Weather Review 140, 898-918. https://doi.org/10.1175/MWR-D-11-00056.1

Kain J. 2004. The Kain–Fritsch convective parameterization: an update. Journal of Applied Meteorology 43, 170-181. https://doi.org/10.1175/1520-0450(2004)043<0170:TKCPAU>2.0.CO;2

Mapes BE, Houze Jr. RA. 1993. Cloud clusters and superclusters over the oceanic warm pool. Monthly Weather Review 12, 1398-1416. https://doi.org/10.1175/1520-0493(1993)121<1398:CCASOT>2.0.CO;2

Mapes BE. 1993. Gregarious tropical convection. Journal of the Atmospheric Sciences 50, 2026–2037. https://doi.org/10.1175/1520-0469(1993)050<2026:GTC>2.0.CO;2

Mapes BE. 2000. Convective inhibition, subgrid-scale triggering energy, and stratiform instability in a toy tropical wave model. Journal of the Atmospheric Sciences 57, 1515–1535. https://doi.org/10.1175/1520-0469(2000)057<1515:CISSTE>2.0.CO;2

Meerkotter R, Bugliaro L. 2009. Diurnal evolution of cloud base heights in convective cloud fields from MSG/SEVIRI data. Atmospheric Chemistry and Physics 9, 1767–1778. https://doi.org/10.5194/acp-9-1767-2009

Miller R. 1972. Notes on analysis and severe storm forecasting procedures of the Air Force Global Weather Central. IOP Publishing https://apps.dtic.mil/sti/citations/AD0744042 Accesed 22 July 2019.

Mlawer EJ, Taubman SJ, Brown PD. 1997. Radiative transfer for inhomogeneous atmosphere: RRTM, a validated correlated-k model for the longwave. Journal of Geophysical Research: Atmospheres 102, 16663-16682. https://doi.org/10.1029/97JD00237

Moraes NO, Marton E, Pimentel LCG. 2005. Simulações Numéricas da Formação de Ilha de Calor na Região Metropolitana do Rio de Janeiro. Anuário do Instituto de Geociências 28, 116-138.

Mota MAS, Nobre CA. 2006. Relação da variabilidade da energia potencial convectiva diponível (CAPE) com a precipitação e a alta da Bolívia durante a campanha WETAMC LBA. Revista Brasileira de Meteorologia 21, 344-355.

Moura CRW, Escobar GCJ, Andrade KM. 2013. Surface and altitude circulation patterns associated to intense rainfall events over the metropolitan region of Rio de Janeiro. Revista Brasileira de Meteorologia 28, 267–280. https://doi.org/10.1590/S0102-77862013000300004

Nascimento EL. 2005. Previsão de tempestades severas utilizando-se parâmetros convectivos e modelos de mesoescala: uma estratégia operacional adotável no Brasil? Revista Brasileira de Meteorologia 20, 113-122

Oakley NS, Lancaster JT, Kaplan ML, Ralph FM. 2017. Synoptic conditions associated with cool season post-fire debris flows in the Transverse Ranges of southern California. Natural Hazards 88, 327–354. https://doi.org/10.1007/s11069-017-2867-6

Penide G, Protat A, Kumar VV, May PT. 2013. Comparison of two convective/stratiform precipitation classification techniques: Radar reflectivity texture versus drop size distribution–based approach. Journal of Atmospheric and Oceanic Technology 30, 2788–2797. https://doi.org/10.1175/JTECH-D-13-00019.1

Powell SW, Houze Jr. RA. 2015. The effect of dry large-scale vertical motions on initial MJO convective onset. Journal of Geophysical Research: Atmospheres 120, 4783–4805. doi:https://doi.org/10.1002/2014JD022961

Pucik T, Groenemeijer P, Ryva D, Kolar M. 2015. Proximity soundings of severe and nonsevere thunderstorms in central Europe. Monthly Weather Review 143, 4805–4821. https:// doi.org/10.1175/MWR-D-15-0104.1

Punkka AJ, Bister M. 2005. Occurrence of summertime convective precipitation and mesoscale convective systems in Finland 2000–01. Monthly Weather Review 133, 362–373. https://doi.org/10.1175/ MWR-2854.1

Quadro MFL, Dias MAFS, Hersies DL. 2012. Análise climatológica da precipitação e do transporte de umidade na região da ZCAS através da nova geração de reanálises. Revista Brasileira de Meteorologia 27, 152-162. https://doi.org/10.1590/S0102-77862012000200004

Roe GH, Montgomery DR, Hallet B. 2003. Orographic precipitation and the relief of mountain ranges. Journal of Geophysical Research: Solid Earth 108, 2315. https://doi.org/10.1029/2001JB001521

Rudolph JV, Friedrich K. 2014. Dynamic and thermodynamic predictors of vertical structure in radar-observed regional precipitation. Journal of Climate 27, 2143–2158. https://doi.org/10.1175/JCLI-D-13-00239.1

Schultz DM, Schumacher PN, Doswell CA. 2000. The intricacies of instabilities. Monthly Weather Review 128, 4143–4148. https://doi.org/10.1175/1520-0493(2000)129<4143:TIOI>2.0.CO;2

Seidel DJ, Free M, Wang J. 2005. Diurnal cycle of upper-air temperature estimated from radiosondes. Journal of Geophysical Research: Atmospheres 110, D09102. https://doi.org/10.1029/2004JD005526

Seluchi ME, Chou ESC. 2009. Synoptic patterns associated with landslide events in the Serra do Mar, Brazil. Theoretical and Applied Climatology 98, 67-77. https://doi.org/10.1007/s00704-008-0101-x

Silva Dias MAF. 1987. Sistemas de mesoescala e previsão de tempo a curto prazo. Revista Brasileira de Meteorologia 2, 133-150.

Silva Dias MAF. 2000. Índices de instabilidade para previsão de chuva e tempestades severas. Departamento de Ciências Atmosféricas.

Silva FP, Justi da Silva MGA, Menezes WF, Almeida VA. 2016. Avaliação de indicadores atmosféricos utilizando o modelo numérico WRF em eventos de chuva na cidade do Rio de Janeiro. Anuário do Instituto de Geociências 38, 81-90. https://doi.org/10.11137/2015_2_81_90

Silva FP, Rotunno Filho OC, Sampaio RJ, Dragaud ICV, Magalhães AAA, Justi da Silva MGA, Pires GD. 2017. Evaluation of atmospheric thermodynamics and dynamics during heavy-rainfall and no-rainfall events in the metropolitan area of Rio de Janeiro, Brazil. Meteorology and Atmospheric Physics 131, 299–311. https://doi.org/10.1007/s00703-017-0570-5

Silva FP, Justi da Silva MGA, Rotunno Filho OC, Pires GD, Sampaio RJ, Magalhães AAA. 2019. Synoptic thermodynamic and dynamic patterns associated with Quitandinha River flooding events in Petropolis, Rio de Janeiro (Brazil). Meteorology and Atmospheric Physics 131, 845–862. https://doi.org/10.1007/s00703-018-0609-2

Skamarock WC, Klemp JB, Dudhia J, Gill DO, Barker DM, Duda M, Huang XY, Wang W, Powers JG. 2008. A description of the advanced research WRF version 3. Tech. Rep. TN-475+STR, NCAR.

Tajbakhsh S, Ghafarian P, Sahraian F. 2012. Instability indices and forecasting thunderstorms: the case of 30 April 2009. Natural Hazards and Earth System Sciences 12, 1-11. https://doi.org/10.5194/nhess–12-403-2012

Taszarek M, Brooks HE, Czernecki B. 2017. Sounding-derived parameters associated with convective hazards in Europe. Monthly Weather Review 145, 1511–1528. https://doi.org/10.1175/MWR-D-16-0384.1

Tavares JPN, Mota MAS. 2012. Condições termodinâmicas de eventos de precipitação extrema em Belém-PA durante a estação chuvosa. Revista Brasileira de Meteorologia 27, 207-2018. https://doi.org/10.1590/S0102-77862012000200007

Teixeira MS, Satyamurty P. 2007. Dynamical and synoptic characteristics of heavy rainfall episodes in southern Brazil. Monthly Weather Review 135, 598-617. https://doi.org/10.1175/MWR3302.1

Tewari M, Chen F, Wang W, Dudhia J, LeMone M, Mitchell EK, Gayno MG, Weigel J, Cuenca R. 2004. Implementation and verification of the unified Noah land surface model in the WRF model. Proceedings of the 20th Conference on weather analysis and forecasting/16th Conference on numerical weather prediction. https://ams.confex.com/ams/84Annual/webprogram/Paper69061.html

Wetzel SW, Martin JE. 2001. An Operational Ingredients-Based Methodology For Forecasting Midlatitude Winter Season Precipitation. Weather and Forecasting 16, 156-167. https://doi.org/10.1175/1520-0434(2001)016<0156:AOIBMF>2.0.CO;2

Yang Y, Chen X, Qi Y. 2013. Classification of convective/stratiform echoes in radar reflectivity observations using a fuzzy logic algorithm. Journal of Geophysical

Research: Atmospheres 118, 1896–1905. https://doi.org/10.1002/jgrd.50214
Yang S, Smith EA. 1999. Moisture budget analysis of TOGA COARE area using SSM/I-retrieved latent heating and large-scale Q2 estimates. Journal of Atmospheric and Oceanic Technology 16, 633–655. https://doi.org/10.1175/1520-0426(1999)016<0633:MBAOTC>2.0.CO;2

Supplementary material

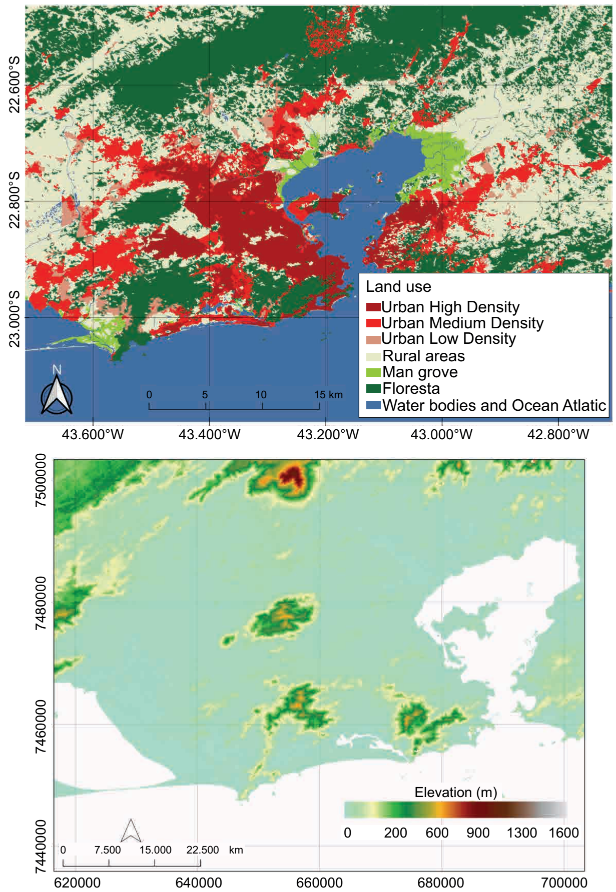

Fig. 1S. Soil land use (top) e digital elevation (bottom) in the metropolitan area of Rio de Janeiro

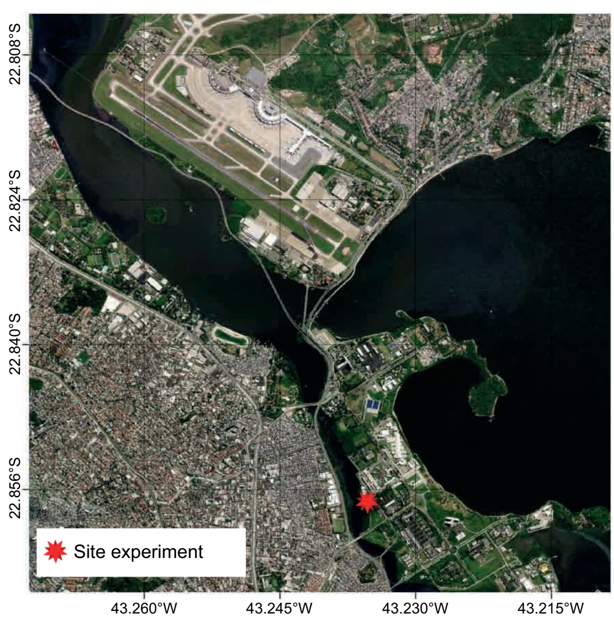

Fig. 2S. Site from which the radiosondes were launched, i. e., from the Federal University of Rio de Janeiro (“UFRJ”).

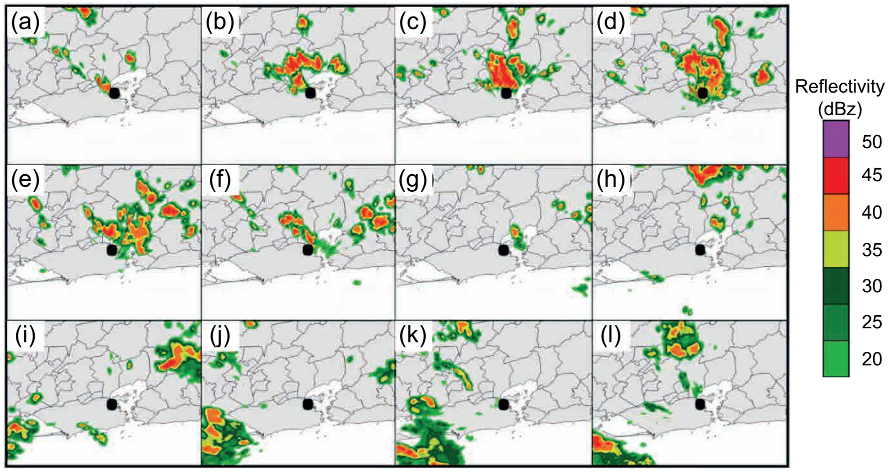

Fig. 3S. Sumaré weather radar images at (a) 13:30 UTC, (b) 14:30 UTC, (c) 15:30 UTC, (d) 16:30 UTC, (e) 17:30 UTC, (f) 18:30 UTC, (g) 19:30 UTC, (h) 20:30 UTC, (i) 21: 30 UTC, (j) 22:30 UTC, (k) 23:30 UTC on February 22, 2018 and (l) 00:30 UTC on February 23, 2018. The black point shows the sampling site of the study.

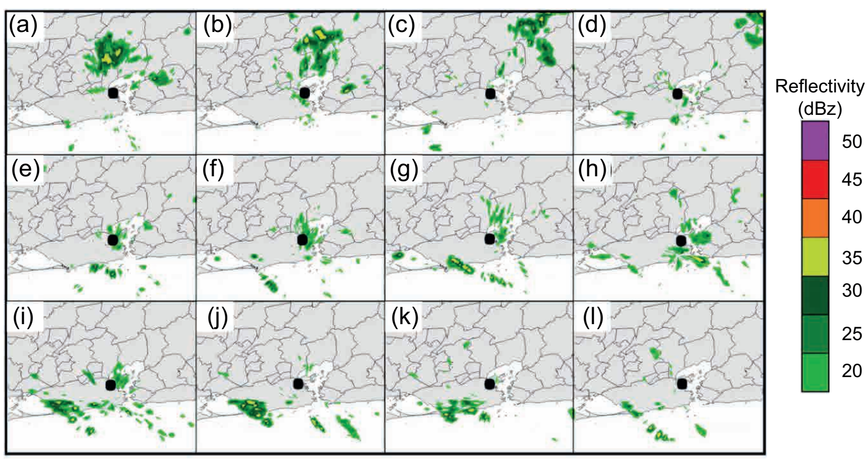

Fig. 4S. Sumaré weather radar images at (a) 13:30 UTC, (b) 14:30 UTC, (c) 15:30 UTC, (d) 16:30 UTC, (e) 17:30 UTC, (f) 18:30 UTC, (g) 19:30 UTC, (h) 20:30 UTC, (i) 21: 30 UTC, (j) 22:30 UTC, (k) 23:30 UTC on March 8, 2018 and (l) 00:30 UTC on March 09, 2018. The black point shows the sampling site of the study

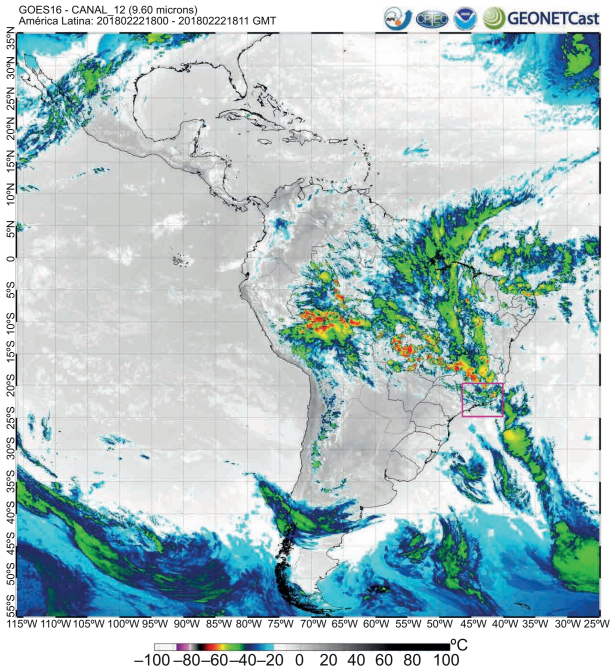

Fig. 5S. Satellite image provided by the Center for Weather Forecasting and Climate Studies. The pink square delimits the Rio de Janeiro state.

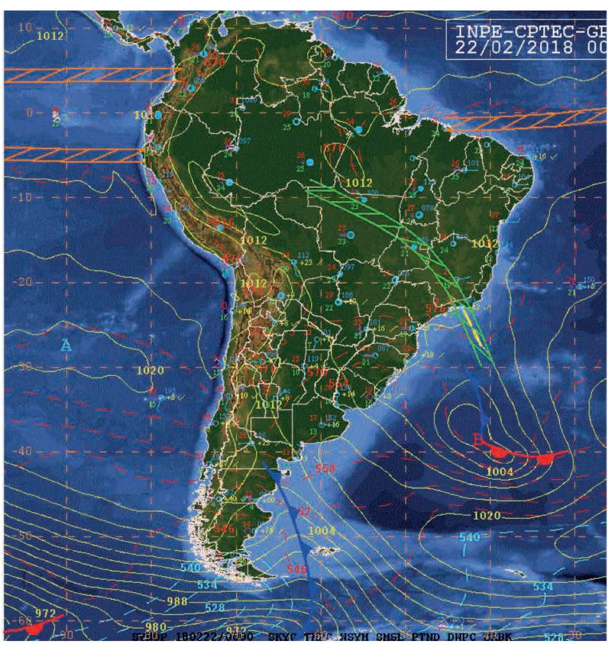

Fig. 6S. Surface chart provided by the Center for Weather Forecasting and Climate Studies. The green symbol is the standard symbol for the SACZ system.

Atmósfera 35(2), 331-355 (2022)
https://doi.org/10.20937/ATM.52934

CONTENTS

Thermodynamic analysis of convective events that occurred in Belém-PA city

Ludmila MONTEIRO DA SILVA[1]* and Maria Aurora SANTOS DA MOTA[1]

[1] *Faculdade de Meteorologia/Instituto de Geociências-Universidade Federal do Pará (UFPA), Belém, PA, Brazil.*
*Corresponding author: ludmila@ufpa.br

Received: June 22, 2020; acepted: November 20, 2020

RESUMEN

La cuenca del Amazonas está dominada por lluvias convectivas con gran variabilidad espacial y diurna. Las distribuciones diurnas y estacionales de eventos convectivos se determinaron a partir de la lluvia y la temperatura máxima del tope de nubes (CTT) entre enero de 2008 y diciembre de 2010 en la ciudad de Belém-PA. La técnica decis se utilizó para seleccionar los eventos más intensos (tasa de lluvia $\geq$ 15 mm h^{-1}), que posteriormente fueron subclasificados en eventos de convección profunda (DCE) y eventos de convección somera (SCE). Se encontraron 94 casos intensos, la mayoría entre 12 y 19 LT (hora local), con el 55% durante la época de lluvias. Se analizó también un conjunto de eventos DCE y SCE con tasa de lluvia $\geq$ 1 mm h^{-1}, encontrándose 42 casos también entre 12 y 19 LT, con un máximo a las 16 LT. Los perfiles de temperatura difirieron entre las temporadas lluviosa y menos lluviosa, asociados con la intensificación de convección somera y profunda. Los perfiles de humedad mostraron mayor variabilidad entre 850 y 500 hPa, indicativo de su papel en la actividad convectiva; durante la temporada de lluvias, la atmósfera era más húmeda antes de la ocurrencia de eventos DCE. Las componentes del viento mostraron una cizalladura significativa entre la superficie y ~ 850 hPa, con mayor componente zonal en los casos de DCE. Los valores más altos de CAPE se observaron de 2 a 3 horas antes de DCE y SCE, con valores máximos antes de DCE en la temporada de lluvias. Los resultados presentados aquí son relevantes para mejorar los pronósticos a corto plazo y la simulación de eventos convectivos con modelos numéricos meteorológicos y climáticos.

ABSTRACT

The Amazon Basin is dominated by convective rainfall with significant spatial and diurnal variability. Diurnal and seasonal distributions of convective events were determined from rainfall and Cloud Top Temperature (CTT) between January 2008 and December 2010 in city Belém-PA. The decis technique was used to select the most intense events (rainfall rate $\geq$ 15 mm h^{-1}), which were subsequently, subclassified into deep convection events (DCE) and shallow convection events (SCE). Ninety four cases were found, mostly occurring between 12 and 19 LT, and 55% in the rainy season. Another set of DCE and SCE with rainfall rate $\geq$ 1 mm h^{-1} was selected to analyze the effect of seasonality. Of these, 42 cases were found also between 12 and 19 LT, with a maximum at 16 LT. Temperature profiles differed between the rainy and less rainy seasons, in the intensification of shallow and deep convection. Moisture profiles showed greater variability between 850 and 500 hPa, indicative of their role in convective activity; during the rainy season the atmosphere was more humid (less humid) before (at the time) of the occurrence of DCE. Wind components showed significant shear between surface and ~850 hPa, with stronger zonal component in the cases of DCE. The highest values of CAPE were observed about 2 to 3 hours before DCE and SCE, with maximum values before DCE in the rainy season. Results presented here are relevant to improve short-term forecasts and convective event simulations with numerical weather and climate models.

Keywords: Deep convection, Shallow convection, Instability, Eastern Amazonia.

1. Introduction

Among the various characteristics of the Amazon region, are the high rainfall levels that occur in this area - which exceed 2000 mm per year (Figueroa and Nobre, 1990; Rao and Hada, 1990) - and its potential to function as a great source of heat and moisture for South America and for the energy balance of the global atmosphere. Evaporation is the main source of water vapor in most of the tropical troposphere (Folkins and Martin, 2005), and deep convection is the main mechanism for vertically distributing moisture and heat, via mostly Cumulonimbus (Cb) extending to the tropopause and producing intense rain. Therefore, variations in intensity, diurnal distribution and location of deep convection plays an important role in weather and climate of this region. The rainfall regime, among other factors, varies depending on the topography and proximity to rivers, as has been shown by many authors (Greco at al., 1990; Marengo, 1992; Cutrim et al., 2000; Angelis et al., 2004; Machado et al., 2004; Fitzjarrald et al., 2008; Santos e Silva, 2013; Tanaka et al., 2014; Ahmed and Schumacher, 2015; Baba, 2016; Ahmed and Schumacher, 2017; Machado et al., 2018).

Weather and climate of the Amazon basin are affected by, among other factors, the position of the Intertropical Convergence Zone (ITCZ) which modulates the rainy and less rainy seasons in the region. (Uvo and Nobre, 1989; Cavalcanti et al., 2009). In addition to isolated deep convection, Squall Lines (SLs) (Kousky, 1980; Cohen et al.,1995; Alcântara et al., 2011; Germano et al., 2017; Germano and Oyama, 2020) predominate through Amazonia and challenge numerical weather forecasting models. The presence of diferent convective regimes and the complex interactions betweenthe surface and the atmosphere have hindered testing convective parameterizations in this region (Betts and Jakob, 2002; Betts, 2003; Sherwood et al., 2004; Grabowski et al., 2006; Allan and Soden, 2007; Neelin, Peters and Hales, 2009; Sherwood et al., 2010; Bengtsson et al., 2011; Del Genio and Wu, 2012; Lee et al., 2013; Santos e Silva, 2013 ; Hottovy and Stechmann, 2015; Santos e Silva and Freitas, 2015; Schiro et al., 2016; Lintner et al., 2017; Freitas et al., 2018; Schiro and Neelin, 2019).

One of the main difficulties in numerical prediction is to associate atmospheric moisture with precipitation, which can vary in linear or non-linear ways, depending on the degree of organization of convection and the time interval analyzed (Bengtsson et al., 2011; Masunaga, 2012; Back et al., 2017). It has already been shown that strong and organized convection with large areas of stratiform clouds, has a greater contribution to rainfall in humid tropical atmospheres (Tan et al., 2013; Deng et al., 2014). Other research suggests that convection models are producing excess moisture in the boundary layer, perhaps because the parameterization schemes for this layer are too mixed (Sherwood et al., 2010; Itterly et al., 2018; Kuo et al., 2020), which probably leads to early precipitation. And the simulation of insufficient moisture transport can lead to less active convection, which can make it difficult to trigger deep convection (Vilà-Guerau de Arellano et al., 2020). On the other hand, modeling successfully captures the interannual variability of precipitation in relation to large-scale phenomena such as ITCZ, representing well the migration of convective activity throughout the year, especially over the continent (Sousa et al., 2018).

Several studies (Adams et al., 2009; Ahmed and Schumacher, 2015; Wolding et al., 2020) indicate that the way in which convective parameterizations deal with the relationship between thermodynamic stability, convective initiation and intensity, determines the nature of simulated precipitation in deep convective regimes, such as in the Amazon. In other words, the thermodynamic conditions of the atmosphere are extremely important for convective initiation, cloud formation and precipitation development in tropical regions (Gille and Mota, 2014). So, the daytime convection cycle, its sensitivity to atmospheric conditions and its representation in numerical models is of fundamental importance to understand its role in the climate system (Adams et al., 2015; Itterly et al., 2018). And in addition to thermodynamic instability, the wind shear could play a fundamental role in initiation and suppression of convection (Adams et al., 2009; Rudolph and Friedrich, 2014).

Therefore, given the importance of the behavior of moist convection, this study presents an analysis of diurnal and seasonal distributions of shallow and deep convective events, combined with the analysis of thermodynamic profiles before and during the occurrence of selected events. The results may be useful in improving the forecast of events of intense moist convection, mainly in the short term.

This paper is organized as follows: Section 2 describes the data and methodology; Section 3 shows the results and discussions of diurnal and seasonal analysis of the convectives events, the termodinamic analysis of the some events selected and their atmospheric stability. Conclusions are presented in Section 4.

2. Methodology and Dataset

The study area in centered in the city of Belém-PA (01º 27' 18" S; 48º 27' 09" W) (Fig. 1), which is located in eastern Amazonia and has an average annual rainfall above 3000 mm. The rainy season spans from December to May, while the less rainy season occurs from June to November (Figueroa and Nobre, 1990).

Hourly rainfall data from January 2008 to December 2010 were obtained from the Instituto Nacional de Meteorologia (INMET) and data from radiosondes launched at 00 and 12 UTC (21 and 00 Local Time (LT), respectively, from the Destacamento de Controle do Espaço Aéreo de Belém (DTCEA-BE) were used for the thermodynamic analysis of the atmosphere. Additional radiosondes obtained during the Balanço Atmosférico Regional do Carbono na Amazônia (Mini-BARCA) experimental campaign from 9 to 30 June 2008 were also used, launched at 06 and 18 UTC at the Universidade Federal do Pará (UFPA).

Cloud Top Temperature (CTT) data were obtained every 15 minutes from the in the infrared channel 4 (11 µm) of the Geostationary Operational Environmental Satellite (GOES 12), pixel resolution of 4 x 4 km.

The decis technique was used to select the events with intense rain, which divide a data set into ten equal parts (decis). The ninth decil was used to determine the top 10% of the most extreme values from the series. This technique was applied to the hourly rainfall data, and an average value of 15 mm h^{-1}

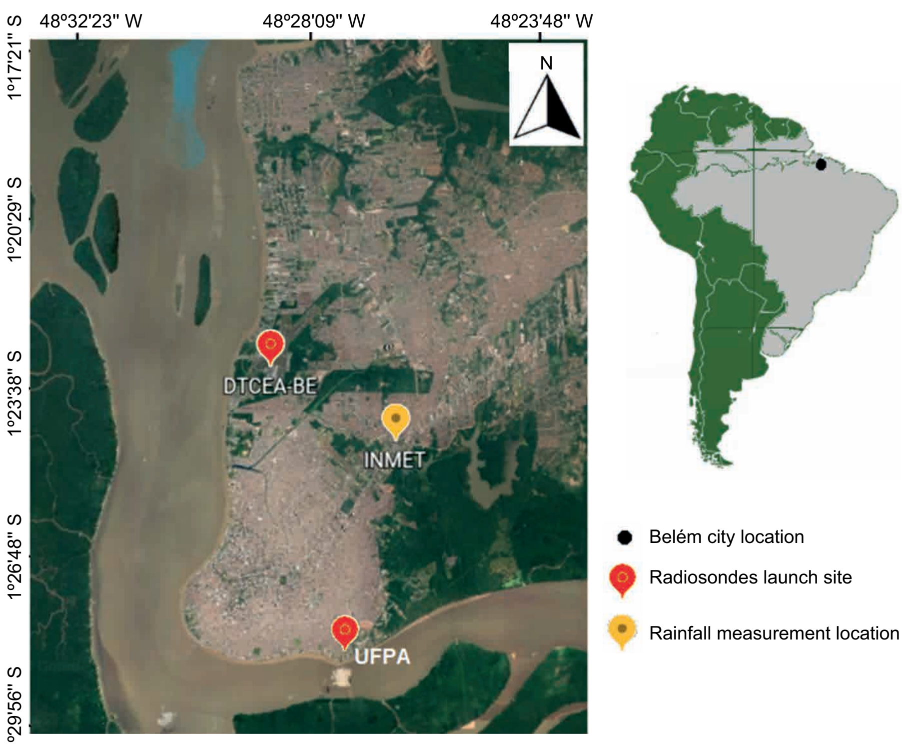

Fig. 1. Location of the study area and rainfall data collection points (INMET) and launch of radiosondes (DTCEA-BE and UFPA). Since, the distance in a straight line from INMET to DTCEA-BE is 5 km; INMET to UFPA is 7 km and DTCEA-BE to UFPA is 10 km.

was obtained as the minimum threshold for an intense rain event. Thus, all rainfall events with values equal to or greater than 15 mm h^{-1} were classified as convective events.

A second method was used to subclassify the events into Deep Convective Events (DCE) and Shallow Convective Events (SCE), according to cloud vertical extent. The CTT data was used since the lower the absolute value of CTT, the greater the cloud vertical development (Houze, 1993). Spatial averages were estimated from the point closest to the location of the raingauge site (INMET), which was assumed as the center of the study area. The nine CTT values surrounding the raingauge site were averaged into a single value every 15 minutes, corresponding to an area of 144 km^2. Considering that the horizontal scale of a single storm varies from 10 to 30 km, it was possible to represent, at least, a local convective event using average CTT values.

Only spatially-averaged 15-min CTT values corresponding to full hours were used to match the rainfall data frequency. In the absence of CTT data for the full hour, the average CTT values for the prior 15 minutes were considered. This was performed in about 20% of the data.

Studies for different regions of South America have used different CTT values to define deep convective clouds associated with moist convection ranging from 230 K to 2060K (Silva Dias et al. (2002): 230 K; Vila et al. (2008) and Ribeiro et al. (2019): 235 K; Greco et al. (1990): 240 K; Machado et al. (2004): 260 K). In this work, events with CTT $\leq$ 235 K were assumed to be DCE. The threshold CTT for SCE was taken to be 271K based on Tanaka (2014).

To ensure that CCT values indeed corresponded to clouds, a maximum CTT value corresponding to warm cloud base temperature, was estimated as 289K for a 1500 m cloud base height. Thus, CTT values of up to 289 K could represent the presence of clouds. Then, for all convective events with rainfall $\geq$ 15 mm h^{-1}, those with CTT $\leq$ 235 K were classified as DCE, while events with 235 < CTT > 289 K were classified as SCE.

Radiosondes that took place up to three hours before the time of occurrence of maximum rain caused by each DCE or SCE were considered to determine the vertical atmospheric profile. However, since radiosondes were launched at 00 and 12 UTC, hindered the analysis. It was possible to select only three events in which radiosonde data was available before the time of maximum rain, and another five events in which the radiosonde was launched during the rain (Table I).

Table I. Events selected for the analysis of the thermodynamic profile and stability of the atmosphere. Five events are SCE and three are DCE. On 01/20/2008 and 05/06/2010 the radiosonde took place three hours before the rain; on 05/12/2010 two hours before and on the other days, the radiosonde coincided with the time of the rain.

Event date	Time of rain $\geq$ 15 mm h^{-1} (UTC)	Radiosonde time (UTC)	Event type
01/20/2008	15	12	SCE
*06/13/2008	18	18	SCE
07/07/2009	00	00	DCE
08/04/2009	00	00	DCE
05/06/2010	15	12	SCE
05/12/2010	02	00	SCE
05/28/2010	00	00	SCE
11/14/2010	00	00	DCE

*Only selected event with rain greater than 15 mm h^{-1}, in which radiosonde was launched at UFPA during the Mini-BARCA experiment.

In an attempt to obtain a larger sample to analyze the atmospheric thermodynamic conditions for DCE and SCE, an alternative classification was made including all rainfall events $\geq$ 1 mm h^{-1}, maintaining the same cloud-based criteria. Under these conditions, it was possible to consider 42 events (Table II). These events were selected in such a way that we tried to obtain two cases for situations in which radiosondes were launched at the hour, one hour, two hours and three hours before the occurrence of DCE and SCE. Also, the separation was made by season.

The analyzes of the events shown in Table II were performed separately from those shown in Table I, since the criterion of rain intensity used for the two sets is different. And to perform averages for a given time interval, between the radiosonde and the convective event, 00 and 12 UTC were considered. For example: to obtain the average profile representative

Table II - Events selected for the analysis of the thermodynamic profile and stability of the atmosphere, considering rainfall equal to or greater than 1 mm h^{-1}, CTT ≤ 235 K for DCE and 235 <CTT> 289 K for SCE.

Event type	Time between radiosonde and rain ≥ 1 mm h^{-1}				Radiosonde time (UTC)	Season
	0 hour	1 hours	2 hours	3 hours		
DCE	01/21/2010 04/23/2010	04/10/2009 04/29/2010	12/26/2008 04/13/2010	01/14/2010 04/25/2010	0	Rainy
	01/25/2010 04/08/2010	02/21/2009 *	04/02/2009 05/02/2009	01/15/2008 *	12	
	06/11/2009 06/16/2010	06/16/2009 06/24/2010	06/17/2010 06/30/2010	08/14/2009 *	0	Less rainy
	06/02/2008 *	* *	* *	* *	12	
SCE	05/15/2008 02/04/2009	05/05/2008 *	04/24/2009 05/21/2010	* *	0	Rainy
	01/27/2008 04/04/2009	02/18/2010 03/22/2010	02/26/2009 01/08/2010	01/30/2008 02/16/2009	12	
	06/19/2010 08/07/2010	06/14/2010 08/15/2010	* *	06/15/2009 *	0	Less rainy
	06/08/2009 *	* *	* *	06/01/2009 *	12	

* There is no information.

of one hour before the occurrence of DCE, profiles measured at 00 and 12 UTC were used to represent the DCE that occurred at 01 and 13 UTC. And as for each interval (same time, one, two or three hours before the convective event occurs) a maximum of two profiles was selected, so each average profile represents the average of a maximum of four profiles. And even if using these criteria, it was not possible to obtain an average profile to represent the conditions of the atmosphere two hours before the occurrence of an SCE, during the less rainy season, as it was not possible to select any radiosonde for these conditions. Therefore, in the analysis of the average temperature profiles, mixing ratio and wind components, the average profile, two hours before the occurrence of SCE, during the less rainy season, will not be analyzed.

From the average temperature and humidity profiles, graphs were also made to analyze the differences (anomalies) between the DCE and SCE profiles, for the two seasons, specified.

Vertical profiles of air temperature and humidity, wind speed and direction were analyzed for the selected events. The stability of the atmosphere was estimated from the Convective Available Potential Energy (CAPE), representing the kinetic energy that the parcel gains from the environment to ascend in the atmosphere. CAPE was calculated from Equation (1), suggested by Emanuel et al. (1994):

$$\mathrm{CAPE} = \int_{LFC}^{EL} g\left(\frac{T_{vp} - T_{ve}}{T_{ve}}\right)dz \qquad (1)$$

where: LFC is the Level of Free Convection, the level at which the parcel would become positively buoyant by ascent; EL is the Equilibrium Level, where the parcel would be neutrally buoyant; T_{vp} is the virtual temperature of the parcel; T_{ve} is the virtual temperature of the environment, in the interval between the base (LFC) and the top of the cloud (EL); g is the acceleration due to gravity (equal to 9.8 m s^{-2}) and dz represents the thickness of the layer.

Table III shows the CAPE values and the conditions of the atmosphere associated with them, according to Bluestein (1993), and these intervals will be used for comparison purposes with the results found in this study.

Table III. CAPE values and associated instability conditions. Adapted from: Bluestein (1993)

CAPE (J kg^{-1})	Atmospheric conditions.
0 < CAPE < 1000	Limit for deep convection formation.
1000 < CAPE < 2500	Moderate deep convection.
2500 < CAPE < 4000	Strong deep convection.
CAPE > 4000	Extreme deep convection.

3. Results and Discussions

3.1 Diurnal and seasonal distribution

Following the methodology described in the previous section, 94 events were identified for the entire study period, of which 60 are DCE and 34 are SCE. From the 60 DCE events, 34 occurred in the rainy season (December to May) and 26 in the less rainy season (June to November), while the SCE events were distributed in 25 in the rainy season and 9 in the less rainy season. The hourly distribution of the rain intensity of these events, by season, is shown in Figure 2, where it can be seen that most events occurred between 15 and 22 UTC (12 and 19 LT, respectively), corresponding to approximately 86% of the total events, of which 55% occurred in the rainy season. This distribution shows a diurnal cycle of the events associated with the expected solar radiation forcing at the surface and local convection in the absence of dynamic forcings. In addition, there is a tendency for DCE to occur at times closer to 00 UTC (21 LT), during the less rainy period and, proportionally, the reduction in the number of SCE between the two periods was more significant. In other words, during the less rainy period, the DCE tended to be more frequent than the SCE, and because the DCE depend more on daytime heating for their formation (because at this time of the year the local convective activity predominates), they caused more "late" rains in relation to the rainy season.

Another explanation for the higher frequency of heavy rains in the afternoon/night in the city of Belém is the influence of sea breeze circulation, when there is a greater thermal contrast between the continent and the ocean (Kousky, 1980; Germano et al., 2017; Germano and Oyama, 2020). This sea breeze circulation is responsible for most of the rainfall that occurs in the region in the less rainy season, and it is important in the organization of SL close to Foz do Amazonas, as SL are often formed along the convergence zone of the sea; they enter the continent and reach the city of Belém in the late afternoon (Cohen et al., 1995). In addition, in the study area, the presence of a river breeze occurs between 12 and 00 UTC in the northwest quadrant, and it can be observed throughout the year (Germano et al., 2017). So, the breeze circulation process could also justify the "delay" in the occurrence of DCE between the rainy and dry seasons.

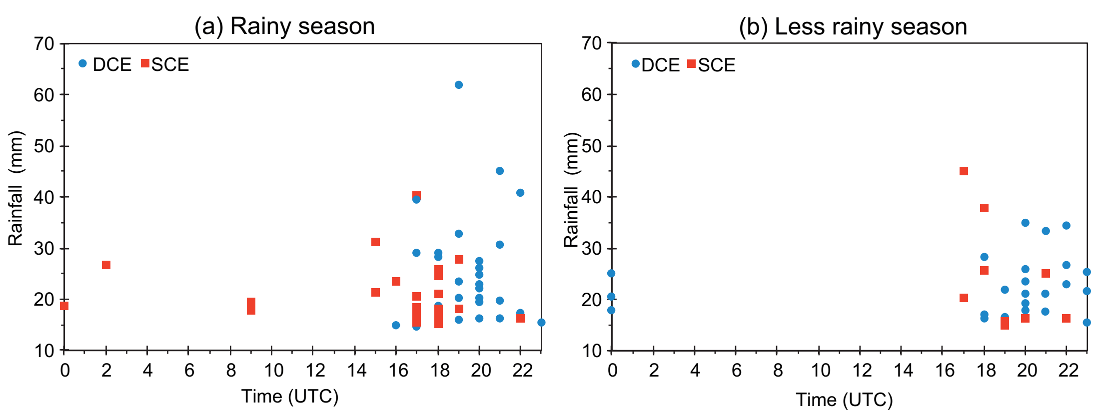

Fig. 2. Hourly distribution of DCE (blue circles) and SCE (red squares) in Belém, in the rainy (a) and less rainy (b) seasons, from January 2008 to December 2010.

As shown by Santos et al. (2012), for the years 2005 and 2006, the maximum rainfall values observed in Belém - at 17 UTC (2005) and at 19 UTC (2006) - occurred when the local horizontal wind showed a rotation, varying from northeast to southwest, due to the effects of sea and river breeze circulations, in both seasons. Angelis et al. (2004) also found similar results for the same study area from 1998 to 2000, when a higher frequency of rainfall events was observed in the afternoon, with a peak of 39 events at 18 UTC (15 LT). However, these authors defined any value above 0 mm h^{-1} as a rain event.

On the other hand, Tanaka et al. (2014), analyzing six years of hourly rainfall data for Central Amazonia (Manaus and surroundings), found a higher occurrence of rain events ≥ 1 mm h^{-1} in the morning and afternoon. The frequency of events was higher in the forest areas, with peaks between 12 and 16 LT, while in urban areas the peaks occur between 10 and 14 LT. However, the localities representative of the urban area of Manaus are located closer to the Rio Negro, when compared to the representative forest areas, and, according to the authors, this condition allows these areas closer to the river to suffer the effect of river breeze in the modulation of the diurnal rainfall cycle, which justifies the higher frequency of rain events in the early morning hours in the urban area. Therefore, this indicates that the behavior of the diurnal rainfall variation is different between the urban areas of Belém and Manaus. On the other hand, analyzing the occurrence of rain events in Belém, according to the conditions in Manaus (rain ≥ 1 mm h^{-1}), Figure 3 shows that the highest frequency of events occurs between 17 and 22 UTC (14 and 19 LT), a little later than that observed in the urban area of Manaus. Therefore, this indicates that the behavior of the daytime rainfall variation is different between the urban areas of Belém and Manaus. But the diurnal cycle of rainfall in these urban areas seems to be modulated by the process of breeze circulation, even at different times.

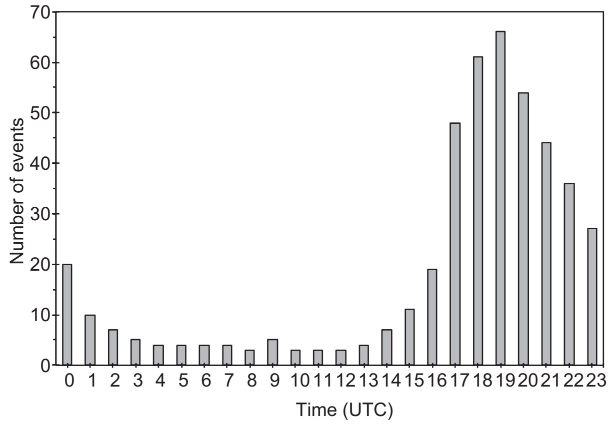

Fig. 3. Mean diurnal cycle of rain events with rainfall rate ≥ 1 mm h^{-1} in Belém, for the period 2008-2010.

3.2 Thermodynamic analysis

3.2.1 Events with rainfall equal to or greater than 15 mm h^{-1}

In order to facilitate the thermodynamic analysis, the events that presented rain and observation of the atmosphere profile at 00 UTC (07/07/09, 08/04/09, 05/28/10 and 11/14/10) were analyzed together, while events that occurred at different times (01/20/09, 06/13/08, 05/06/10 and 05/12/10) were analyzed separately.

Figure 4 shows the vertical temperature profiles for 01/20/2008, 06/13/2008, 05/06/2010 and 05/12/2010, when cases of SCE occurred. These temperature profiles were measured three hours before (01/20/2008 and 05/06/2010), two hours before (12/05/2010) and at the time of intense rain (06/13/2008). Figure 4a indicates a small temperature difference between the analyzed profiles. At most levels, over the depth of the atmosphere, air temperature tended to be higher on 05/12/2010 at 00 UTC (21 LT), when the observation occurred two hours before the rain event (green line), showing a warming trend of the atmosphere before shallow convection. On 06/13/2008, the temperature profile variation was slightly more accentuated than in the other cases, perhaps due to the fact that the measurements took place during the rain and were carried out at 18 UTC (15 LT), time when the atmosphere tends to be more unstable than at 00 or 12 UTC. The lower temperature values from the surface to 850 hPa for the days 01/20/2008 and 05/06/2010 may be related to the fact that the measurements were taken at 12 UTC (09 LT), before solar heating is fully effective. Figure 4b shows the corresponding diferences in profiles for SCE cases that occurred two hours before and at the time of the rain (green line) and three hours

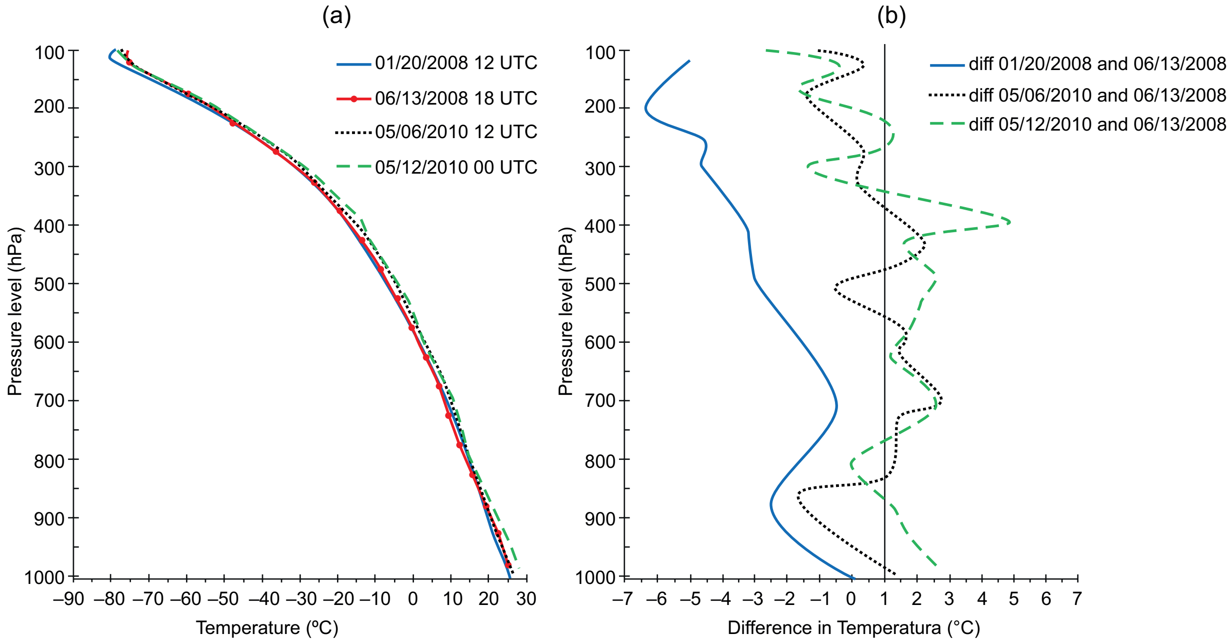

Fig. 4. (a) Vertical air temperature profiles: three hours before (01/20/2008 and 05/06/2010), two hours before (05/12/2010) and at the time of rain (06/13/2008), for cases of SCE in Belém-PA. And (b) Differences vertical air temperature profiles between cases that ocorred two hours before e in the at the time of rain (green line) and three hours before e in the at the time of rain (blue and black lines).

before and during the rain (blue and black lines). It is clear that in practically all the low and medium troposphere, the temperature was higher two hours before the occurrence of the SCE, than at the time of occurrence of an event in this category. And there was a tendency for temperature to be lower for the cases that occurred 3 hours before the rain, which is more evident on 01/20/2008.

Figure 5 shows the air temperature profile for cases of convective events, in which the rain coincided with the 00 UTC radiosonde launch. The DCE events that occurred on 07/07/2009, 08/04/2009 and 11/14/2010, and the SCE event on 05/28/2010.

From surface up to 589 hPa, on 05/28/2010, the temperature is almost always higher than in other events. To the pressure levels lower that 589 hPa (higher altitudes) there is no data available for that day 05/28, but for the other days it is observed that, above 589 hPa, there was a tendency for the temperature to be higher on 08/04/2009, up to ~270 hPa. For 07/07 and 08/04/2009, temperatures were lower from the surface to 925 hPa, probably because it had already rained before the most intense rain events (25 mm on 07/07 and 20.6 mm on 08/04/2009) recorded at the time of launching the radiosonde (00 UTC). For

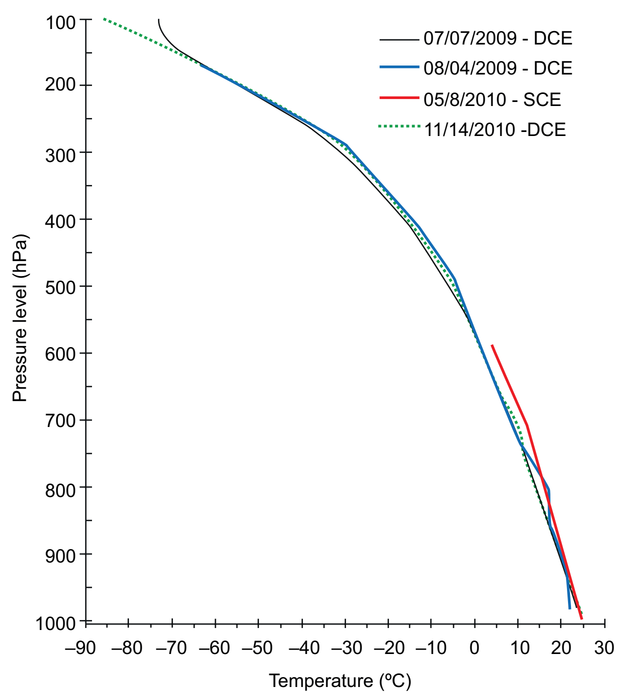

Fig. 5. Vertical air temperature profiles measured at the time of the occurrence of intense rain events, for cases of DCE (blue lines) and SCE (red line) that occurred in Belém-PA, at 00 UTC, on 07/07/2009, 08/04/2009, 05/28/2010 and 11/14/2010.

07/07 rain of 1.6 mm was observed at 23 UTC on 07/06, while on 08/04 two rain values were observed, one of 2.2 mm at 22 UTC, and another 0.6 mm at 23 UTC on 08/03, and this may have caused the greatest variation in the temperature profile (in the sup-500 hPa layer), in relation to the other three cases. Therefore, these less intense rainfall events, which occurred before the time of the radiosonde, started a cooling process at low levels of the atmosphere in these two days. On 05/28 and 11/14/2010 rain was recorded only at 00 UTC but due to the fact that it precipitated only during the radiosonde time, the low-level cooling (surface to 900 hPa) was not detected as it was observed on other days. In addition, rains were slightly less intense, with values of 18.6 and 18 mm, on 05/28 and 11/14/2010, respectively.

As observed through the air temperature profiles, this variable presents small variations between the cases analyzed, but the most important thing to mention is the fact that there is a tendency for the temperature to be higher at low levels when SCE occurs, as in figure 4, in which all cases are SCE, the air temperature close to the surface was higher than 25 ºC, while in figure 5, the temperatures close to the surface were up to 25 ºC, with higher values observed throughout the profile of day 05/28/2010, which was the only case of SCE analyzed in the figure. So, in order to obtain a better visualization of the tendency of increasing air temperature in the lower atmosphere, when SCE occurs, figure 6 was created, in it are the air temperature profiles of all the events analyzed up to the level of 589 hPa (last level that has measures of 05/28/2010). Again, it is possible to notice that the temperature tended to be higher when SCE occurred, mainly from the surface up to approximately 850 hPa. And when the temperature was measured two hours before the rain (dashed red line) it was higher than all other cases.

Even if a comparison is made between the SCE profiles that occurred at the same time of rain observation (06/13/2008 and 05/28/2010) with all the DCE (07/07/2009, 04/08/2009 and 11/14/2010) - which were also measured at the same time of the rain - the temperature is observed to be higher during the SCE. This result indicates that when there is more intense convection, a more pronounced atmosphere stabilization occurs. And this decrease in temperature can be caused by downdrafts, which bring cold, dry air

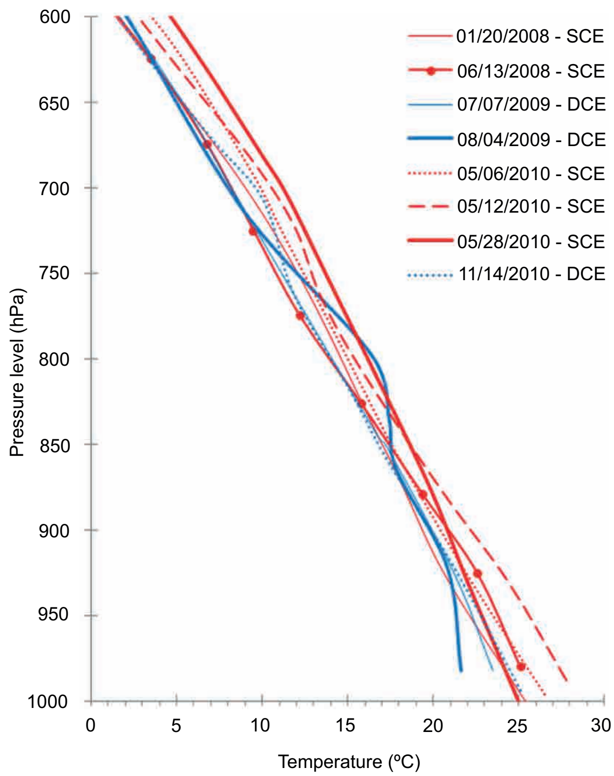

Fig. 6. Vertical air temperature profiles for all DCE (blue lines) and SCE (red lines) selected in the studied period, in Belém-PA.

from inside to outside the cloud. This can be seen mainly through the DCE profiles of 07/07 (thin continuous blue line) and 08/04/2009 (thick continuous blue line), when the rain started before the most intense rain observation time. That is, the cooling of the atmosphere started before the time of temperature measurements and the most intense rain.

Figure 7 shows the vertical profiles of the mixing ratio for the events that occurred at different times. The highest humidity values occurred in the boundary layer and, from the surface to 720 hPa, the atmosphere was more humid on 05/12/2010, and less humid on 06/13/2008. Above 550 hPa, the atmosphere was more humid on 01/20 and 06/13/2008.

On 06/13/2008 the radiosonde was started at 17:34 UTC, and the rain of 38 mm observed at 18 UTC is equivalent to all rain that fell between 17:01 and 18 UTC, that is, the measurement of the profile of that day's humidity occurred during the rain, when the humidity of the atmosphere was decreasing,

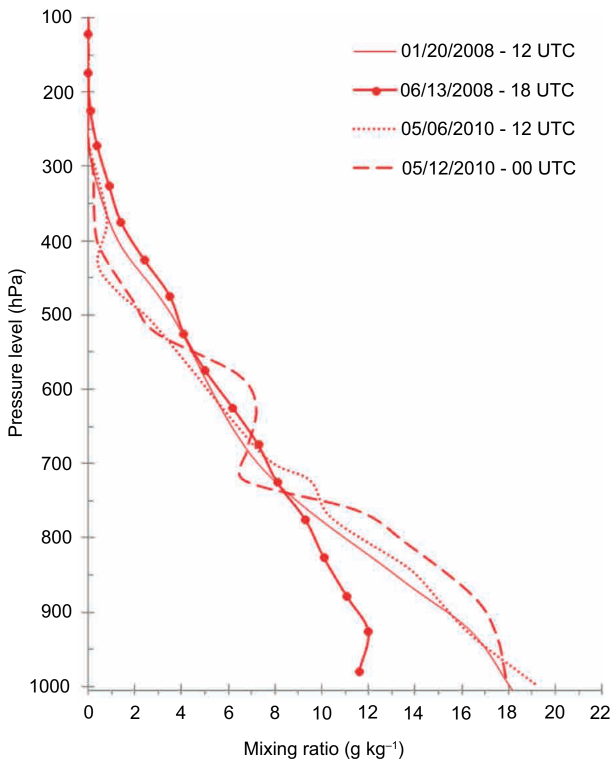

Fig. 7. Vertical profiles of the mixing ratio: three hours before (01/20/2008 and 05/06/2010), two hours before (05/12/2010) and at the time of rain (06/13/2008), for cases of SCE in Belém-PA.

which justifies a drier atmosphere than the other cases. In addition, this event occurred in June, when the atmosphere tends to be less humid.

As already mentioned, on 05/12/2010 the measurement of the humidity profile occurred two hours before the 26.6 mm rainfall event, showing that the atmosphere was more humid before the rainfall. Likewise, on 01/20/2008 and 05/06/2010, when measurements were taken three hours before the rain, the atmosphere was less humid than two hours before, and more humid than the case when the measurement was performed during the rainy season (06/13/2008). This result suggests humidity increases as the time of intense rain approached, and t tended to dry the atmosphere during its occurrence.

These results are similar to those found in Central Amazonia, where it was observed that an increase in humidity in the lower troposphere occurred at the beginning of deep convection (Schiro et al. 2016). However, in Central Amazonia the intense data collection carried out during the GoAmazon experimental campaign gave the opportunity to analyze how the variability in the vertical structure of humidity and the conditional instability of the environment control the beginning of deep convection, both for smaller scale convection and in mesoscale (Schiro and Neelin, 2019). But despite the low sampling of events analyzed in this research, it is possible to observe similar patterns.

It has been observed that even for mid-latitude regions, the humidity at 850 hPa is a good indicator of severe rain events (Silva et al., 2015). The behavior in the vertical humidity profile observed in Belém is similar to that found by Rocha (2010) in Manaus, where the humidity between 850 and 700 hPa exerts a certain control in convective events. Schiro et al. (2016) found that humidity was higher at the time of rainfall and slightly lower before and after. They also showed that at levels below 800 hPa, mainly below 900 hPa, before and during rainfall it was more humid than after, possibly because of the cold pools. And in the upper troposphere (above 400 hPa), the humidity was higher during and after the rains. And this behavior of the highest humidity during rain at upper levels, can also be seen in Figure 7, on 06/13/2008, when the humidity was higher than in the other cases, above the level of 500 hPa.

Figure 8 shows the behavior of humidity during the occurrence of rainfall at 00 UTC for cases of DCE and SCE. Up to the level of 925 hPa the humidity was higher for the case of DCE that occurred on 11/14/2010, with a maximum value of 20 g kg^{-1} at the surface. On 05/28/2010 it was more humid above 925 hPa, while on 07/07/2009, in the surface-820 hPa layer the atmosphere was less humid, just as on 08/04/2009 lower humidity is observed in the surface-600 hPa layer. The behavior of humidity in the last two days is consistent with that found in the temperature profiles, when a cooling of the atmosphere was observed, due to rain having started before the launch time of the radiosonde. The idea that the decrease in temperature could have been caused by downward currents of cold and dry air is reinforced by the decrease in humidity.

In general, the moisture profiles show significant differences between the different cases analyzed (Fig. 9), and the most interesting thing is that during the SCE that occurred on 05/28/2010 the layer of 925-589 hPa

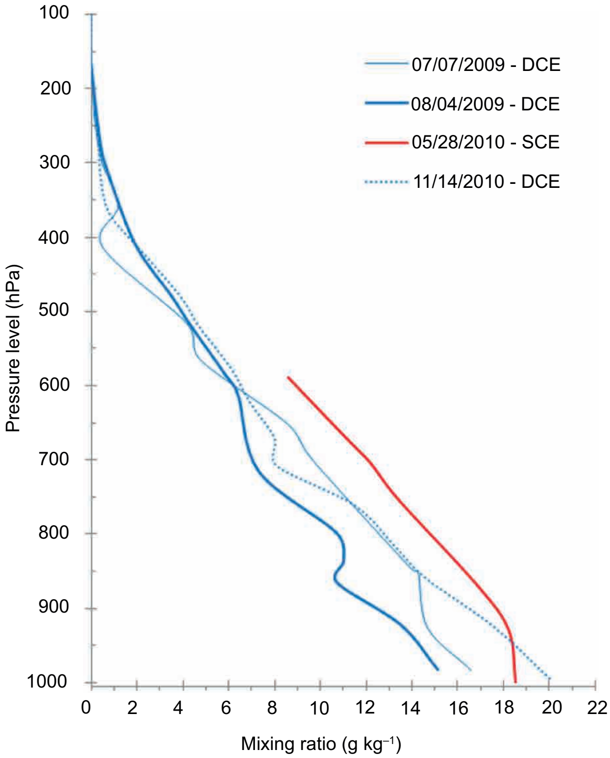

Fig. 8. Vertical profiles of the mixing ratio measured at the time of the occurrence of intense rain events, for cases of DCE (blue lines) and SCE (red line) that occurred in Belém-PA, at 00 UTC, on 07/07/2009, 08/04/2009, 05/28/2010 and 11/14/2010.

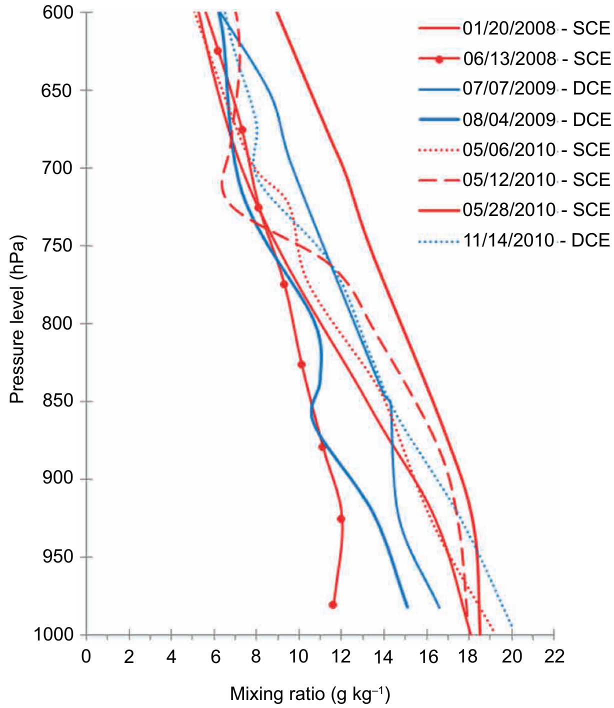

Fig. 9. Vertical profiles of the mixing ratio for all DCE (blue lines) and SCE (red lines) selected in the studied period, in Belém-PA.

in the atmosphere was more humid than on the other days analyzed, and the DCE of 11/14/2010 showed the highest humidity from the surface to 925 hPa. Two more SCE occurred, one on 6 May 2010, when the humidity was relatively high in the lower atmosphere and the other on 12 May, when the humidity also showed significant values in the 925-760 hPa layer. This shows that in that month the atmosphere was quite humid, which may have favored the occurrence of three SCE with rainfall rates above 15 mm h^{-1}. On 6 May the humidity values are not as high as on 12 May and 28 May, may be due to the rain that fell on 5 May, between 19 and 23 UTC, which possibly kept the atmosphere less humid (above the level of 930 hPa) until the radiosonde launch time at 12 UTC on 6 May.

Meteorological observations in May 2010 (Climanálise, 2010a) indicate that the formation of SL and the northernmost position of the ITCZ contributed to the highest accumulated rainfall observed in the far north of the Amapá, in the northwest and north of Pará and in the northeast of Roraima. Rainfall in these areas exceeded monthly climatology by more than 100 mm, while the monthly anomaly was 85.1 mm in Belém resulting in na accumulated total of 390.6 mm. These results confirm that the atmosphere was more humid in May 2010.

Figure 10 shows the variation of the wind components for the analyzed cases. The event on 06/13/08 has no wind information. In general, the zonal component (Fig. 10a) is easterly in almost the entire troposphere, advecting moisture from the Atlantic Ocean to the continent.

The vertical wind shear in the lower troposphere was larger on 05/06/2010, while on 05/12/2010 it was larger in the 930-760 hPa layer, indicating that the shear was more intense at the time of occurrence of the rainfall. This variation of the wind with height in the atmospheric boundary layer favors the instability of the layer.

The meridional component (Fig. 10b) was weaker than the zonal component and presented irregular

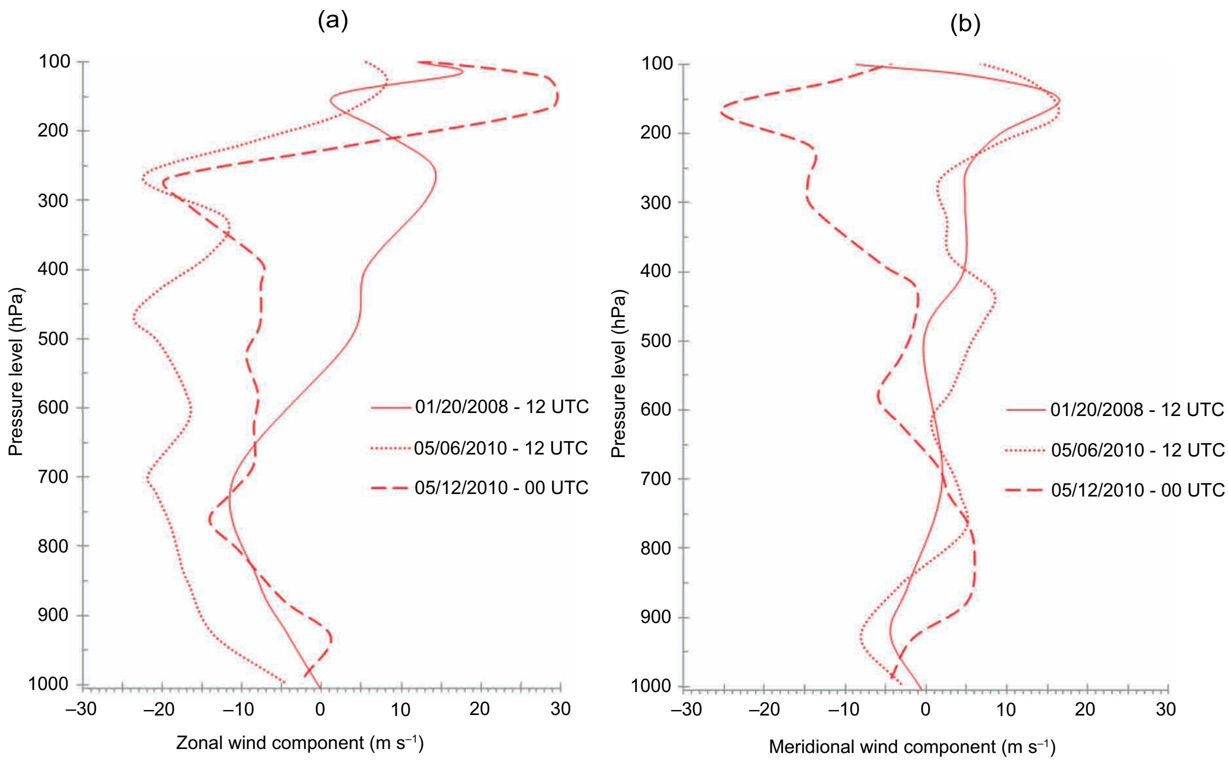

Fig. 10. Vertical profiles of the zonal (a) and meridional (b) components of the wind: three hours before (01/20/2008 and 05/06/2010) and two hours before (05/12/2010) heavy rain, for cases of SCE in Belém-PA.

profiles. On 01/20/2008 and 05/06/2010, from the surface up to ~750 hPa, the predominant wind was northerly, and with southerlies above that level. On May 12, 2010, the meridional component was almost reversed: southerly in the 880-625 hPa layer and northerly above. The most important point of the meridional component is the greatest shear that occurred in the surface-925 hPa layer in the three cases analyzed.

The vertical profile of the wind components at the time of the occurrence of SCE and DCE, at 00 UTC, are shown in Figure 11. As can be seen, at the time of rain, on average, the zonal component was more intense than at times before the rain (Fig. 10) and predominantly easterly, from the surface to the upper troposphere. The wind shear was also strong at low levels in all four cases, mainly on 08/04/2009. From the surface to ~600 hPa, the northerly winds predominated on 05/28 and 11/14/2010, and southerly winds predominated on 07/07 and 08/04/2009. Strong shear was observed at low levels on 05/28 and 11/14/2010.

By comparing the wind components between all SCE and DCE (Fig. 12), it is possible to notice that there is really a predominance of easterly winds at low and mid-levels even reaching the upper troposphere, except for the 01/20/2008 in which the wind becomes westerly at 500 hPa. On average, wind shear is large from the surface up to 850 hPa, proving to be stronger in the three cases of DCE, confirming that wind shear plays an important role in deep convection (Adams et al., 2009; Baba 2016). Regarding the meridional component, only larger low-level shear is observed between SCE and DCE and no difference above.

3.2.2 Events with rainfall equal to or greater than 1mm h^{-1}

The following analyzes correspond to DCE and SCE associated rainfall ≥ 1 mm h^{-1}, evaluating average profiles measured at the same time, one, two and three hours before the occurrence of DCE and SCE, for the rainy and less rainy periods.

Figure 13 indicates that the temperature profiles do not show significant variations between them,

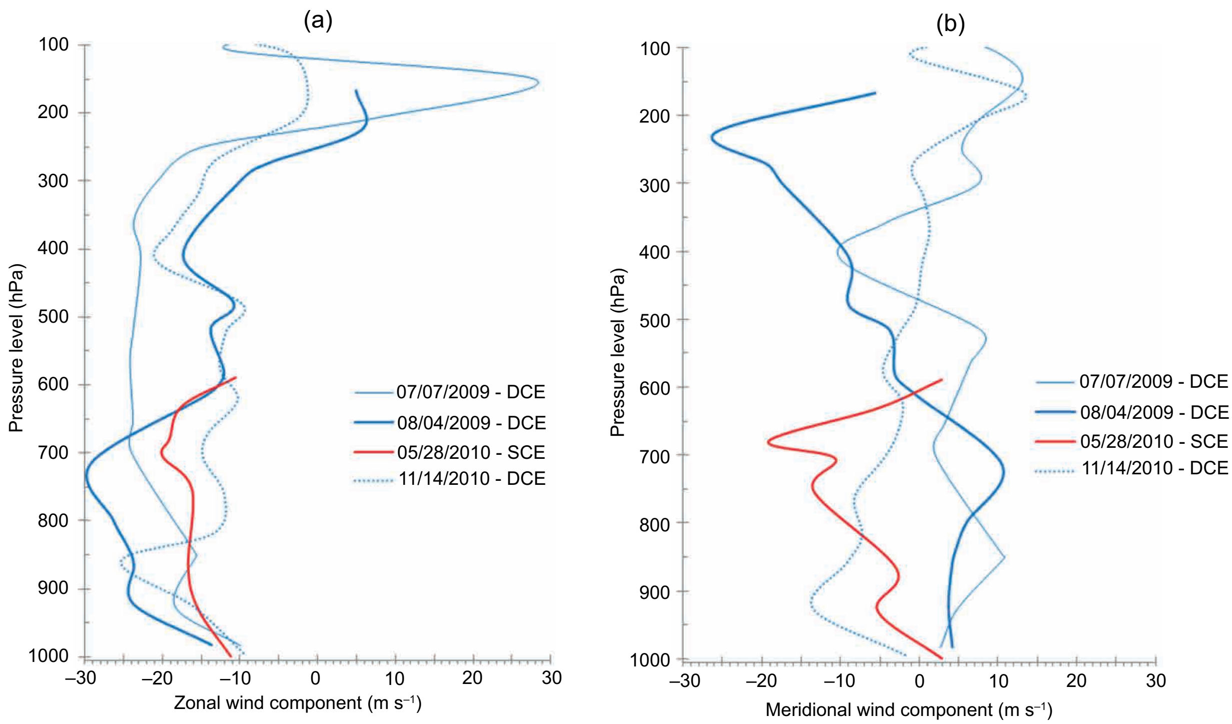

Fig. 11. Vertical profiles of the zonal (a) and meridional (b) components of the wind, measured at the time of the occurrence of intense rain events, for cases of DCE (blue lines) and SCE (red lines) that occurred in Belém-PA, at 00 UTC, on 07/07/2009, 08/04/2009, 05/28/2010 and 11/14/2010.

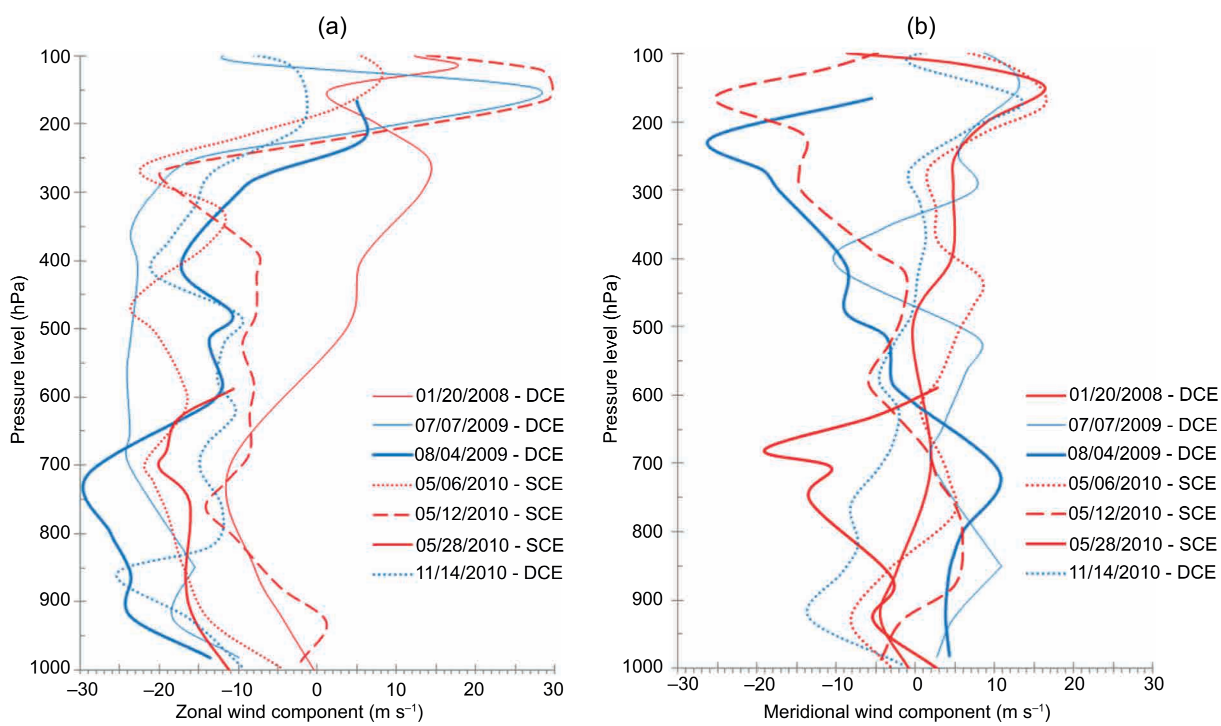

Fig. 12. Vertical profiles of the zonal (a) and meridional (b) components of the wind for all DCE (blue lines) and SCE (red lines) selected in the studied period, in Belém-PA.

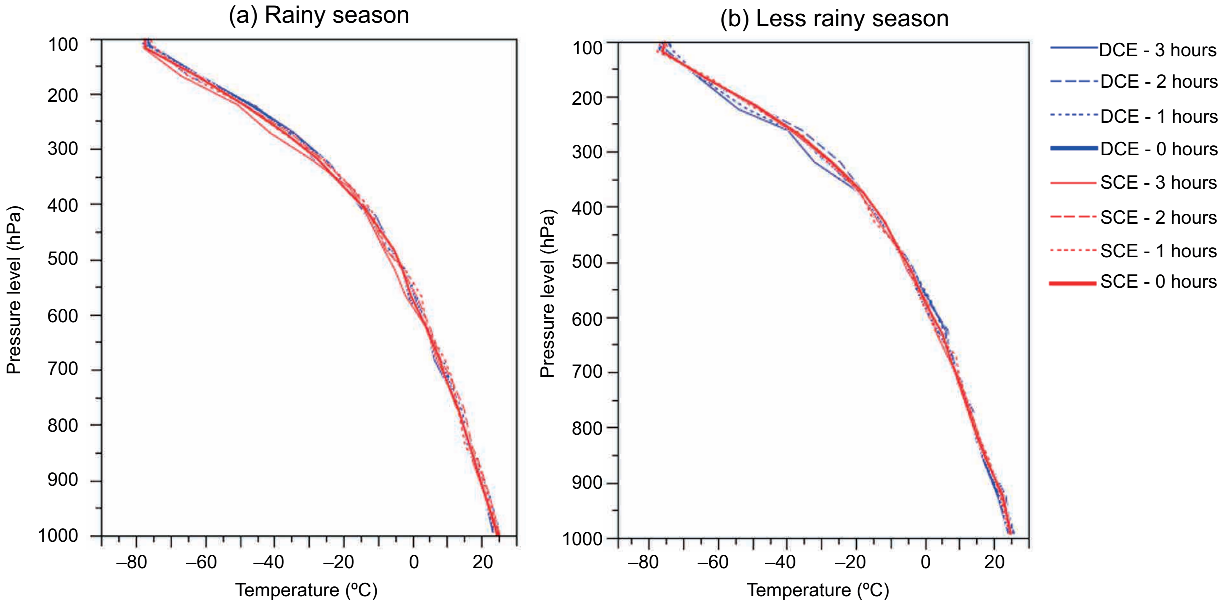

Fig. 13. Vertical air temperature profiles during, one, two and three hours before the occurrence of DCE (blue lines) and SCE (red lines), for the seasons: (a) rainy and (b) less rainy, in Belém-PA.

but note that during the rainy season (Fig. 7a) there is a slight tendency for higher temperature from the surface to 700 hPa, two hours before the occurrence of SCE, similar behavior observed in Figures 4 and 6.

At pressure levels below 400 hPa, higher temperature is observed during both seasons and for both types of events, indicating an increase in temperature as the time of convective events approaches, consistent with the release of latent heat of condensation. In addition, lower temperature values are observed three hours before the rain for SCE (DCE) in the rainy season (less rainy).

In order to better visualize the small temperature differences between the DCE and SCE profiles, Figure 14 shows variations at all levels for both seasons. On average, smaller variations (around 1 ºC) are observed between the surface and approximately 700 hPa, with larger variations (up to 5 ºC) above. It is possible to better visualize the highest temperature values for SCE two hours before the rain, in the rainy season (Fig. 14a), as the temperature differences between DCE and SCE are negative, from the surface to approximately 500 hPa. Unfortunately, it is not possible to see if the same occurs for the less rainy season, due to the lack of data.

Once again, it can be seen that at low levels, in both seasons, and during the rainy season, the temperature is lower for cases of DCE (negative anomalies), indicating that the presence of downward currents, which bring dry and cold air from higher levels, are more intense in the presence of deep convection. In addition, during convective events the solar radiation absorbed by the surface is less than the total energy supplied to the atmosphere (Machado, 2000).

Interestingly, at altitudes above 500 hPa, temperature anomalies are on average positive (negative) during the rainy season (less rainy), before and during the rainfall events. This suggests that the air temperature plays different roles in the intensification of shallow and deep convection in the rainy and less rainy seasons.

Figure 15 shows the average vertical profiles of the mixing ratio, for the rainy and less rainy seasons. Between ~975 to 850 hPa in the reainy season (Fig. 15a), humidity was higher two hours before the occurrence of SCE (similar to that observed in figure 7, for the event of 05/12/2010). It is not possible to observe the behavior of the average humidity profile, two hours before the occurrence of SCE, in the less rainy season, because no event was found in this category. In contrast, between surface and 850 hPa during the rainy season (Fig. 15b), the atmosphere was less humid for both DCE and SCE (similar to the case

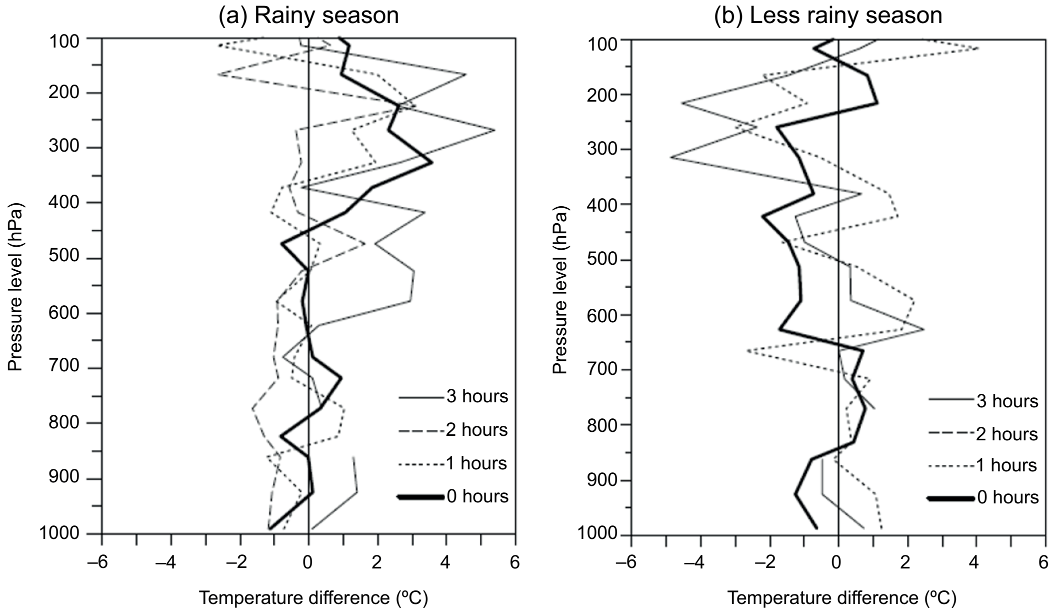

Fig. 14. Differences in the average vertical air temperature profiles between DCE and SCE, during, one, two and three hours before the occurrence of these events, for the seasons: (a) rainy and (b) less rainy, in Belém- PA.

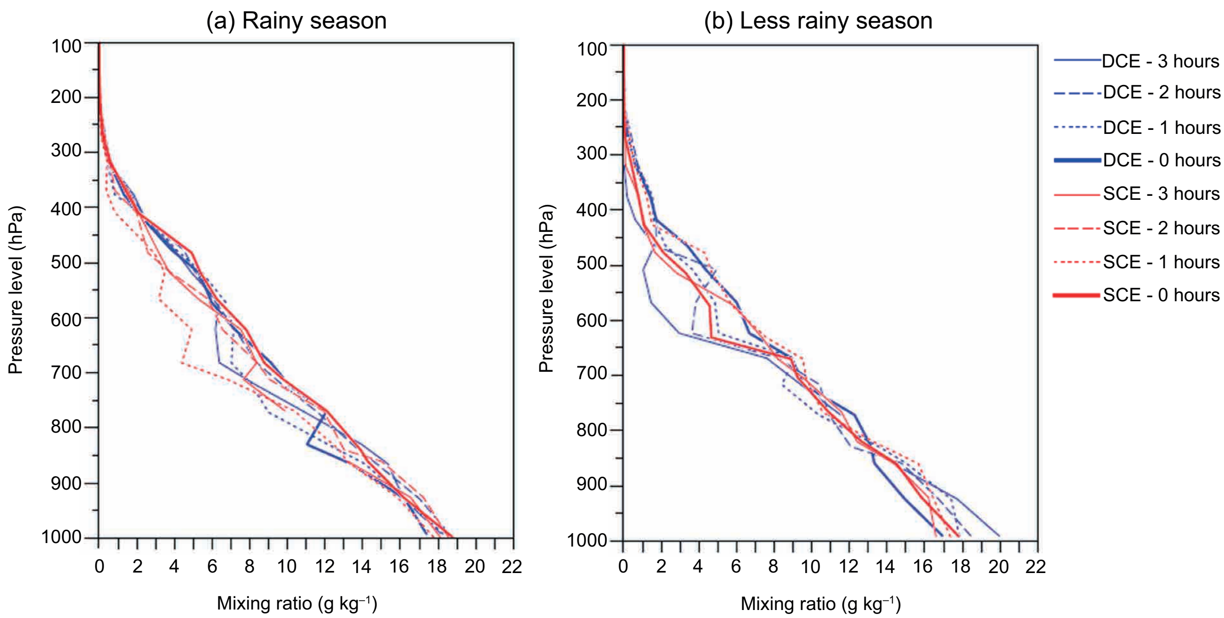

Fig. 15. Vertical profiles of the mixing ratio during, one, two and three hours before the occurrence of DCE (blue lines) and SCE (red lines), for the seasons: (a) rainy and (b) less rainy, in Belém-PA.

of day 06/13/2008, shown in Figure 7). On average, the humidity was higher during the rainy season, at pressure levels above 825 hPa, being more evident for SCE (DCE) in the rainy season (less rainy), a behavior consistente with Schiro et al. (2016).

Note that from the surface up to 850 hPa profiles in the rainy season are not too different from those in the less rainy season. In the rainy season low humidity near the surface is observed closer to the time of occurrence of DCE; the opposite is observed for cases of SCE; and before the rain, humidity is always higher for DCE. In contrast, at mid-levels (between 675 and 450 hPa), humidity increases as the DCE occurrence time approaches (Fig. 15b). In summary, these results were expected, since before precipitation, more humid air parcels ascend in the atmosphere to form convective clouds, and after precipitation initiates, humidity tends to be higher at mid- and upper-levels, and lower at low-levels mainly associated with downdrafts which bring cold, dry air towards the surface. Further, results indicate that these downdrafts are more intense for DCE.

Figure 16 shows the differences in the average humidity profiles between DCE and SCE. Note that in the rainy (Fig. 16a) and less rainy (Fig. 16b) seasons, the maximum variations occurred in the 850 to 500 hPa layer, indicating that humidity in this layer is important for convective activity. The maximum differences (about 4 g kg^{-1}) are observed ~600 hPa in the two seasons; positive (negative) humidity anomalies are also observed before the occurrence of DCE in the rainy (less rainy) season. The large differences observed around 600 hPa indicate the presence of a slightly “drier layer”, more evident in the less rainy season, which suggests the existence of less humid air outside the convective region. Thus, the entrainment of ambient air is important for shallow and deep convection.

In the rainy season there is a predominance of positive anomalies before the rain and negative anomalies during the rain event, from the surface to approximately 350 hPa. Similarly in the less rainy season, but only from the surface up to 850 hPa. Negative anomalies before the rain and positive anomalies during the rain are observed above, reinforcing observations in Figures 7, 8 and 9.

In summary, during the rainy season the atmosphere is more humid (less humid) before (at the time) the occurrence of DCE. Similarly in the less rainy season, but only at low levels (up to 850 hPa), since at mid- and upper levels the atmosphere is more humid before (during) the occurrence of SCE (DCE).

Figure 17 shows the average vertical profiles of the zonal and meridional components of the wind, for the same temporal conditions shown in Figures 13 and 15. The largest variability in the average profiles of the two wind components is observed as the time of occurrence of convective events approaches. The zonal component is predominantly easterly east the entire atmosphere, mainly during the less rainy season (Fig. 17b) associates with the southeast trade winds. The meridional component oscillates between

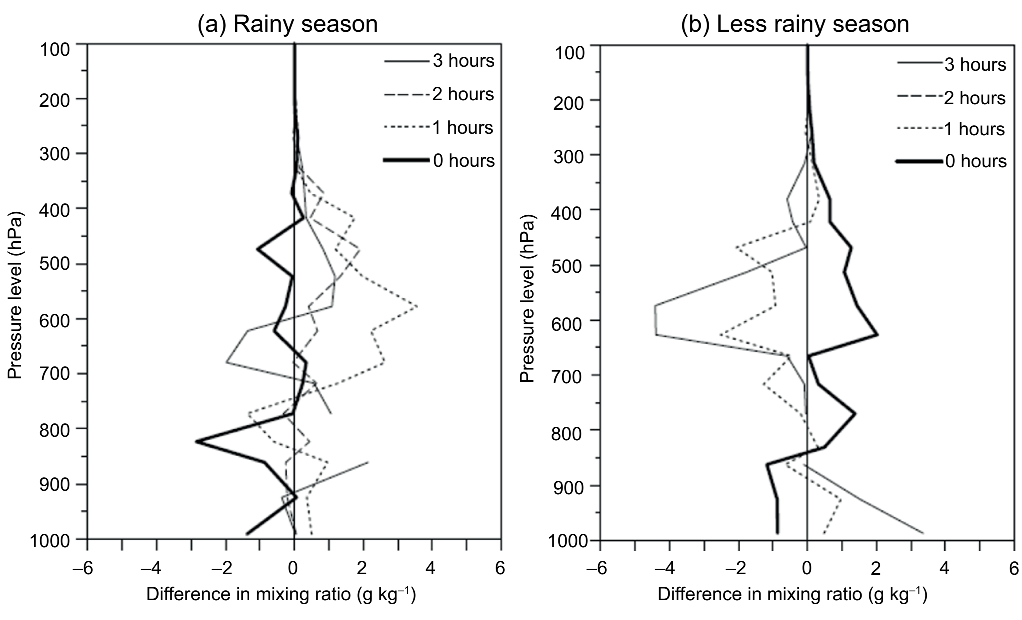

Fig. 16. Differences in the average vertical profiles of the mixing ratio between DCE and SCE during, one, two and three hours before the occurrence of these events, for the seasons: (a) rainy and (b) less rainy, in Belém- PA.

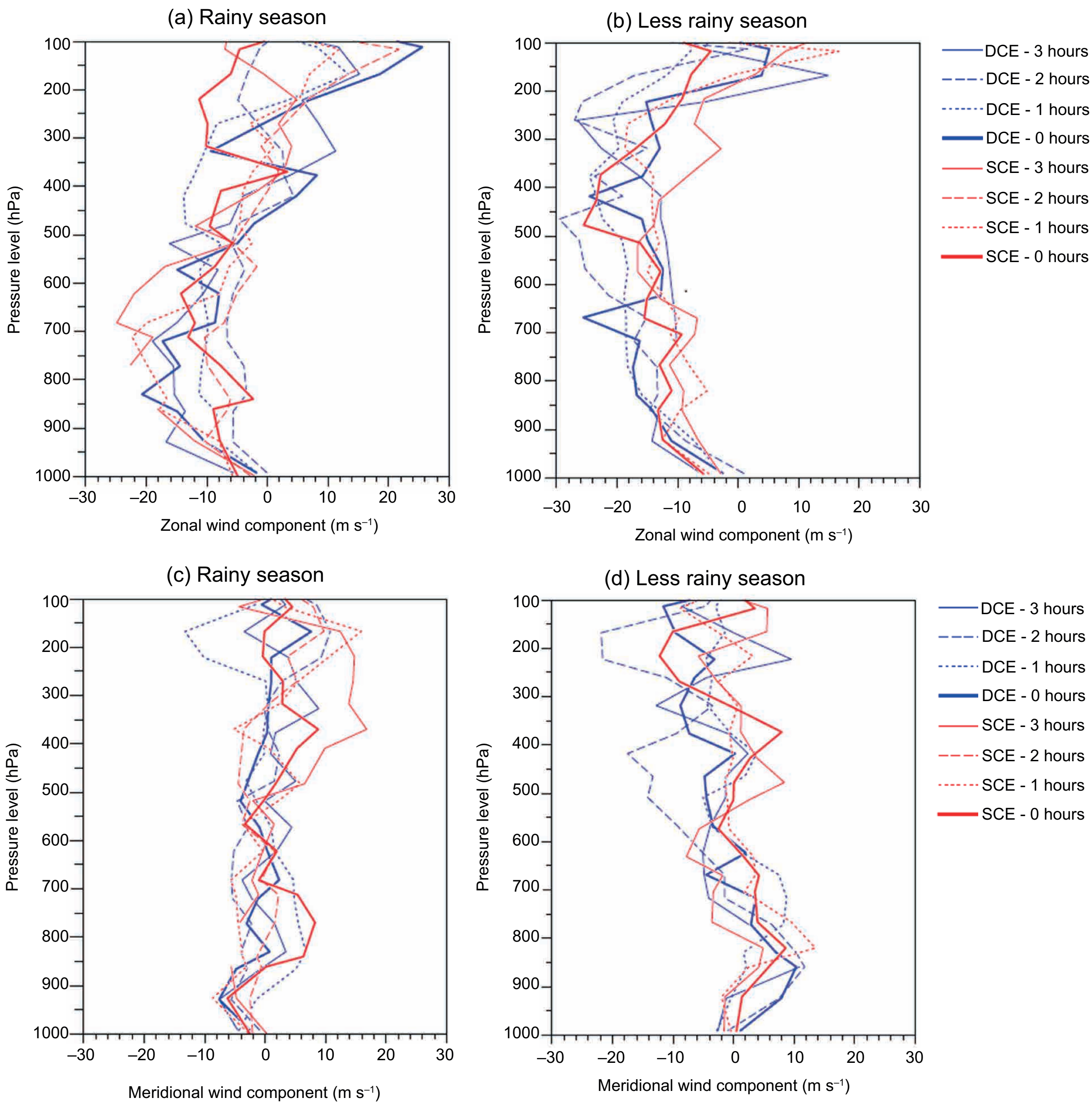

Fig. 17. Vertical profiles of the zonal (a and b) and meridional (c and d) components of the wind during, one, two and three hours before the occurrence of DCE (blue lines) and SCE (red lines), for the rainy and lesser seasons rainy season, in Belém-PA.

northerly and southerly throughout the troposphere, with more significant variations during the less rainy season (Fig. 17d).

The shear in the two wind components is quite significant between the surface and ~850 hPa in both rainy seasons for all events, but mainly for cases of DCE that occurred during the rainy season. Thus, the wind shear plays a significant role in deep convection, as also seen in Figure 12.

3.3 Atmospheric stability analysis

Table IV facilitates the analysis and discussion of the stability of the atmosphere, displaying CAPE, maximum rainfall observed for all the convective events

Table IV. CAPE values, rainfall, duration of rainfall, time of launching of the radiosonde and number of hours that the radiosonde before the time of occurrence of rain events.

Date	Event type	CAPE ($J\ kg^{-1}$)	Rainfall ($mm\ h^{-1}$)	Rain duration (hour)	Radiosonde time (UTC)	Time between radiosonde and rain (hour)
01/20/2008	SCE	3850	21,4	15	12	3
06/13/2008	SCE	409	38,0	*	18	0
07/07/2009	DCE	1187	25,0	6	00	0
08/04/2009	DCE	600	20,6	4	00	0
05/06/2010	SCE	3433	31,2	9	12	3
05/12/2010	SCE	2867	26,6	1	00	2
05/28/2010	SCE	19	18,6	2	00	0
11/14/2010	DCE	5624	18,0	8	00	0

analyzed, time corresponding to the CAPE value (launch of the radiosonde), as well as, the number of hours between radiosonde and observation of the maximum rainfall.

CAPE values greater than zero are observed in all events analyzed, which is the limit for deep convection formation (Bluestein, 1993), with both the lowest (19 J kg^{-1}) and the highest (5624 J kg^{-1}) observed at the time of rain on 28 May and 14 November 2010, respectively. In both cases the rain started at the same time as the radiosonde launch. On 28 May 18.6 mm were recorded in two hours. On 14 November the atmosphere was quite unstable (classified as extreme deep convection) when the rain started, which lasted for 7 hours accumulating 30.8 mm. The release of latent heat during the rain together with the evaporation of the rain itself may have contributed to the instability. Even though CAPE was depleted during the rain event, at 12 UTC CAPE was still 2828 J kg^{-1}, a condition of strong deep convection.

The rain of the 28 May 2010 was not associated with any larger-scalr meteorological system, and the small cluster of clouds over the study area, suggests the development of CAPE due to daytime heating (thermodynamic forcing). On the other hand, on 14 November 2010, areas of instability were associated with increased heat and humidity in the interior of the continent, especially in the north of the North and Northeast regions. There was widespread cloudiness, from 13 to 18 November 2010, which may have masked the formation of cumulonimbus cloud lines which form along the North and Northeast coast of Brazil (Climanálise, 2010b). So, the high CAPE value found for 14 November can be justified by the strong instability of the local atmosphere and the possible presence of SL. And it is important to highlight that this intense instability was associated with an DCE, which presented the highest humidity values, from the surface to 925 hPa (Fig. 9), among all the analyzed events.

The second highest CAPE value (3850 J kg^{-1}) occurred on 20 January 2008, associated with an SCE, but characterized as strong deep convection, according to Table III. On that day, the rain started at 15 UTC, three hours after the radiosonde launch, and lasted until 05 UTC of the following day, accumulating 35.2 mm. And between 08 UTC on 21 January and 12 UTC on 22 January, slight rain was observed (0.2 - 1.4 mm). This shows that although the rain lasted 15 hours, it was intermitente and likely associated with a larger-scale meteorological system. This was confirmed by Climanálise (2008a) showing the presence of SL and organized convection associated with the ITCZ closer to the coast of the North and Northeast regions of Brazil between 16 and 20 January.

The third and fourth highest CAPE values were for SCE and occurred on 6 May 2010, (3433 J kg^{-1}) and 12 May (2867 J kg^{-1}), about three and two hours before the maximum rain events rain, respectively. Table III indicates strong deep convection conditions on both days, possibly favored by the combination of dynamic and thermodynamic forcing, but convective trigger dominated by dynamics (Gille and Mota, 2014). As discussed in relation to Figure 7, high rainfall values observed in northern Pará in May were associated with SL and the location of the ITCZ. On 7 May, the day following the SCE, 101.6 mm were recorded in 24hrs, the highest observed in May 2010.

The second and third lowest CAPE values were 409 and 600 J kg^{-1}, which occurred, respectively, on 13 June 2008 (SCE) and 4 August 2009 (DCE), at the same time of the rain. CAPE remained below the limit for deep convection formation (1000 J kg^{-1}). Rain started after 17 UTC on 13 June, and until 21 UTC 48.4 mm were recorded. It is not possible to inform the duration of the rain, as the data has flaws from 22 UTC until 11 UTC the next day. No SL event was observed on the 13 June and the ITCZ had moved further to the north (Climanálise, 2008b). Thus, CAPE was only due to thermodynamics forcing. Likewise, the event of 4 August 2009 also depended more on thermodynamics forcing, since the rain was caused by a cluster of convective clouds (Fig. 18).

Figure 18 shows enhanced images of the cloud top temperature, from the GOES 10 satellite, and where the study area is identified by white arrows. The images are from 3 August at 18 UTC (Figure 18a), showing intense convective activity (15 LT); at 21 UTC of the same day (Figure 18b), time of rain onset and where (in relation to Figure 18a) an intensification and displacement of the cloud cluster in the ocean-continent direction is perceived. At 00 UTC on 4 August (Figure 18c) low CAPE (32 J kg^{-1}) and warmer CTT indicate that the system was weakening and dissipating at 04 UTC (Figure 18d).

On 7 July 2009 there was also the occurrence of an DCE, when the CAPE was 1187 J kg^{-1} (moderate deep convection, Table III). The radiosonde launch coincided with the time of the rain event, which started after 22 UTC on 6 July and ended before 05 UTC on 7 July. Unfortunately, there are no Climanálise publications for July 2009, but through satellite images (not shown) some isolated cloud clusters are observed above the study area, indicating that CAPE was favored by daytime heating.

Considering the dissipative losses, the CAPE required in tropical regions to support deep convection

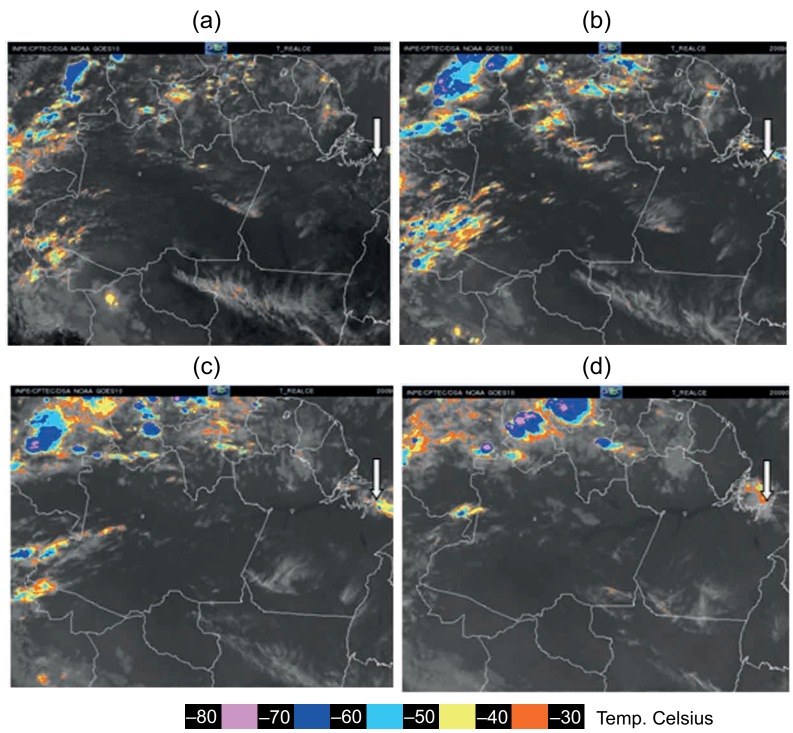

Fig. 18. Enhanced images of cloud top temperature, from the GOES 10 satellite, (a) at 18 UTC and (b) at 21 UTC on 08/03/2009; (c) at 00 UTC and (d) at 04 UTC on 08/04/2009. The region shown is the northern region of Brazil, where the study area is indicated with a white arrow.

must be at least 1000 J kg^{-1} (Williams and Renno, 1993). Therefore, the cases reported here in which heavy rainfall occurred with low CAPE values are noteworthy. In addition to the fact that thermodynamic observations were made at the time of the rain (which reduces the CAPE), the rains from these events may have been caused by some meteorological system (playing the role of the dynamic force), because CAPE is essential for the development of storms only in the absence of larger scale forcers (Mota and Nobre, 2006). As previously discussed, the analysis of Climanálise and the satellite images indicate the presence of a medium-to large scale meteorological system only on 13 June 2008 (considering only days with CAPE below 1000 J kg^{-1}). In the other two cases (4 August 2009 and 28 May 2010), the low CAPE values were the result of rains coinciding with radiosonde launches.

It is important to also note that almost all the SCE (except the event of 28 May 2010) occurred in the presence of a meteorological system (Table V), which may force air parcel ascent (Mota et al., 2007) resulting in deep convection even for low CAPE values. In this study, the only SCE that presented a low CAPE in the presence of a meteorological system, was 13 June 2008.

The three cases of DCE, on the other hand, occurred when there was a predominance of local convection but only the event on 14 November 2010 had a high CAPE value. However, despite the fact that in these three cases the maximum rainfall was observed at the time of radiosonde launch, in the cases of 7 July and 4 August 2009 the rain started two hours before, suggesting that CAPE may have increased before rain initiation.

Table V. CAPE values and meteorological systems active during the events analyzed.

Date	Event type	CAPE (J kg^{-1})	Meteorological system active
01/20/2008	SCE	3850	ITCZ
06/13/2008	SCE	409	ITCZ and SL
07/07/2009	DCE	1187	Local convection
08/04/2009	DCE	600	Local convection
05/06/2010	SCE	3433	ITCZ and SL
05/12/2010	SCE	2867	ITCZ and SL
05/28/2010	SCE	19	Local convection
11/14/2010	DCE	5624	Local convection and SL

However, when analyzing mean CAPE values (Table VI) of the events described in Table II, note that CAPE tends to be greater before the occurrence of convective events in both seasons, with the highest values observed in the rainy season, mainly two and three hours before the occurrence of DCE. And although there is no CAPE information two hours before SCE occur in the less rainy season, CAPE values are higher.

Therefore, from Table VI, in the rainy and less rainy periods there was a greater availability of potential convective energy in the study area when DCE occurred, being greater in the rainy season. While for SCE cases, CAPE was higher during the less rainy period.

In summary, the conditions of atmospheric stability when analyzed case by case for DCE and SCE events with precipitation ≥ mm 15 mm h^{-1}, indicate an important role of dynamics for both the occurrence of DCE and SCE, in agreement with previous

Table VI. Average CAPE values, at the same time, one, two and three hours before the occurrence of DCE and SCE, and for the rainy and less rainy seasons.

Event type	Time between radiosonde and rain ≥ 1 mm h^{-1}				Season	Average per season
	0 hour	1 hours	2 hours	3 hours		
DCE	777	42T2	2916	2211	Rainy	1582
	1726	1200	1082	1859	Less rainy	1467
SCE	1188	997	897	1491	Rainy	1144
	1261	1452	*	1419	Less rainy	1377

*There is no information.

studies (Mota and Nobre, 2006; Tavares and Mota, 2012; Gille and Mota, 2014; Santos, Mota and Rocha, 2014). And for events with precipitation ≥ 1 mm h^{-1}, CAPE was larger during the rainy season with DCE, and that SCE need higher CAPE during the less rainy season.

4. Conclusions

This study analysed convective events that occurred in the city of Belém-PA, from January 2008 to December 2010, classifying them in DCE and SCE. For events that caused rain equal to or greater than 15 mm h^{-1}, it was observed that 86% of them occurred between 15 and 22 UTC (12 and 19 LT, respectively), and 55% occurred during the rainy season. On the other hand, considering events that caused rainfall equal to or greater than 1 mm h^{-1}, it was observed that the highest frequency occurred in the same interval, approximately, with a maximum at 19 UTC (16 LT). That is, lower and higher intensity rains are directly related to greater convective activity, which occurs in the region during the afternoon and early evening.

The variation in the vertical profile of the air temperature was small, but there was a tendency for it to be greater when SCE occurred, mainly on the surface up to approximately 800 hPa. And the average values of this variable indicate different behaviors, between the rainy and less rainy seasons, in the intensification of shallow and deep convection.

The average humidity profiles showed behaviors similar to those analyzed on a case-by-case basis. It was observed that the maximum variations, in the DCE and SCE profiles, occurred in the 850 to 500 hPa layer, indicating that the humidity in this layer has great importance for the convective activity. It was also seen that during the rainy season the atmosphere was more humid (less humid) before (at the time) the occurrence of DCE. And the same occurred in the less rainy season, between the surface and 850 hPa, because in the medium and high troposphere the humidity was higher before the (on the hour) occurrence of SCE (DCE).

For all the cases analyzed, the zonal component of the wind showed a predominance of easterly winds throughout the entire troposphere, mainly during the less rainy season, when the study area receives greater influence from the southeast trade winds. The southern component was weaker and had irregular profiles, with more significant variations during the less rainy season. In both components, on average, strong shear from the surface to 850 hPa was observed, in both seasons, for all events, but mainly for cases of DCE, showing that the wind shear has a significant role in deep convection.

On the other hand, the analysis of the stability of the atmosphere, carried out through CAPE, showed that it was greater than zero in all the analyzed events, agreeing with the limit condition for the formation of convection. Case-by-case analyzes show that dynamic forcing plays an important role in the formation of intense convection, from the shallowest to the deepest. While, the average values showed that the highest values of CAPE were observed about 2 to 3 hours before DCE and SCE, while the lowest values occurred in the hour of rain, since the rain reduces the CAPE. In addition, the highest mean values of CAPE were observed when DCE occurred during the rainy season, and in the cases of SCE the CAPE was higher during the less rainy season.

Although some results are similar to those already found by other authors, it is important to emphasize that in this research it was prioritized to use precipitation events equal to or greater than 15 mm h^{-1}, and precipitation events equal to or greater than 1 mm h^{-1} were used with the objective of obtaining more events to differentiate the behavior of DCE and SCE between the rainy and less rainy seasons, since, in the first classification, the number of events was low. And even if using different precipitation intensity criteria, it was possible to observe similar results between the two data sets. Therefore, the results presented in this article may be relevant for numerical modeling studies and to be used as indicators of convective events in the short-term forecast. However, it is of fundamental importance to use a larger sample of events to analyze, mainly, the effect of seasonality.

Acknowledgments

We thank a Pró-Reitoria de Pesquisa e Pós-Graduação da UFPA supports research (Projeto PRO3220-2016) through the Support Program for Doctor Researcher UFPA (Edital 02/2016).

References

Adams DK, Souza EP, Costa AA. 2009. Convecção úmida na Amazônia: implicações para modelagem numérica. Revista Brasileira de Meteorologia 24: 168-178. https://doi.org/10.1590/S0102-77862009000200006

Adams DK, Fernandes RM, Holub KL, Gutman SI, Barbosa HM, Machado LA, Calheiros AJ, Bennett RA, Kursinski ER, Sapucci LF, DeMets C, Chagas GF, Arellano A, Filizola N, Rocha AA, Silva RA, Assunção LM, Cirino GG, Pauliquevis T, Portela BT, Sá A, de Sousa JM, Tanaka LM. 2015. The Amazon dense GNSS meteorological network: a new approach for examining water vapor and deep convection interactions in the tropics. Bulletin of the American Meteorological Society 96: 2151-2165. https://doi.org/10.1175/BAMS-D-13-00171.1

Ahmed F, Schumacher C. 2015. Convective and stratiform components of the precipitation-moisture relationship. Geophysical Research Letters 10: 453-462. https://doi.org/10.1002/2015GL066957

Ahmed F, Schumacher C. 2017. Geographical differences in the tropical precipitation-moisture relationship and rain intensity onset. Geophysical Research Letters 44: 1114-1122. https://doi.org/10.1002/2016GL071980

Alcântara CR, Silva Dias MAF, Souza EP, Cohen JCP. 2011. Verification of the role of the low level jets in Amazon squall lines, Atmospheric Research 100: 36-44. https://doi.org/10.1016/j.atmosres.2010.12.023

Allan RP, Soden BJ. 2007. Large discrepancy between observed and simulated precipitation trends in the ascending and descending branches of the tropical circulation. Geophysics Research Letters 34: 1-6. https://doi.org/10.1029/2007GL031460

Angelis CF, McGregor GR, Kidd C. 2004. Diurnal cycle of rainfall over the Brazilian Amazon. Climate Research 26: 139-149. https://doi.org/10.3354/cr026139

Baba Y. 2016. Response of rainfall to land surface properties under weak wind shear conditions. Atmospheric Research 182: 335-345. https://doi.org/10.1016/j.atmosres.2016.08.010

Back LE, Hansen ZR, Handlos ZJ. 2017. Estimating vertical motion profile top-heaviness: Reanalysis compared to satellite-based observations and stratiform rain fraction. Journal of the Atmospheric Sciences 74: 855-864. https://doi.org/10.1175/JAS-D-16-0062.1

Bengtsson L, Körnich H, Källén E, Svensson G. 2011. Large-scale dynamical response to subgrid-scale organization provided by cellular automata. Journal Atmospheric Science 68: 3132-3144. https://doi.org/10.1175/JAS-D-10-05028.1

Betts AK, Jakob C. 2002. Evaluation of the diurnal cycle of precipitation, surface thermodynamics, and surface fluxes in the ECMWF model using lba data. Journal of Geophysics Research. 107(D20): LBA 12–1–LBA 12–8. https://doi.org/10.1029/2001JD000427

Betts AK. 2003. The diurnal cycle over land. In Forests at the land-atmosphere interface. Mencuccini M, Grace J, Moncrieff J, McNaughton KG, eds. pp. 73–93, CABI Publ.,Wallingford, UK.

Bluestein HB. 1993. Synoptic – dynamic meteorology in midlatitudes. Oxford University Press, UK.

Cavalcanti IFA, Ferreira NJ, Silva Dias MAF, Justi MGA. 2009. Tempo e Clima no Brasil. São Paulo: Oficina de Textos.

Climanálise, 2008a. Boletim de Monitoramento e Análise Climática 23. Available online at: http://climanalise.cptec.inpe.br/~rclimanl/boletim/pdf/pdf08/jan08.pdf. Accessed 05/05/2020.

Climanálise, 2008b. Boletim de Monitoramento e Análise Climática 23 Available online at: http://climanalise.cptec.inpe.br/~rclimanl/boletim/pdf/pdf08/jun08.pdf. Accessed 05/05/2020.

Climanálise, 2010a. Boletim de Monitoramento e Análise Climática 25 Available online at: http://climanalise.cptec.inpe.br/~rclimanl/boletim/pdf/pdf10/mai10.pdf. Accessed 28/04/2020.

Climanálise, 2010a. Boletim de Monitoramento e Análise Climática 25. Available online at: http://climanalise.cptec.inpe.br/~rclimanl/boletim/pdf/pdf10/nov10.pdf. Accessed 04/05/2020.

Cohen JCP, Silva Dias MAF, Nobre CA. 1995. Environmental conditions associated with Amazonian squall lines: a case study. Monthly Weather Review 123: 3163-3174. https://doi.org/10.1175/1520-0493(1995)123<3163:ECAWAS>2.0.CO;2

Cutrim EMC, Martin DW, Butzow DG, Silva IM, Yulaeva E. 2000. Pilot analysis of hourly rainfall in Central and Eastern Amazonia. Journal of Climate 13: 1326-1334. https://doi.org/10.1175/1520-0442(2000)013<1326:PAOHRI>2.0.CO;2

Del Genio AD, Wu J. 2012. Representing the sensitivity of convective cloud systems to tropospheric humidity in general circulation models. Surveys in Geophysics 33: 637-656.

Deng M, Kollias P, Feng Z, Zhang C, Long CN, Kalesse H, Chandra A, Kumar VV, Protat A. 2014. Stratiform and convective precipitation observed by multiple radars during the DYNAMO/AMIE Experiment. Journal Applied Meteorology and Climatology 53: 2503-2523. https://doi.org/10.1175/JAMC-D-13-0311.1

Emanuel KA, Neelin JD, Bretherton CS. 1994. On large-scale circulations in convecting atmospheres. Quarterly Journal of the Royal Meteorological Society 120: 1111-1143. https://doi.org/10.1002/qj.49712051902

Figueroa SN, Nobre CA. 1990. Precipitations distribution over Central and Western Tropical South America. Climanálise 5: 36-45.

Fitzjarrald DR, Sakai RK, Moraes OLL, Oliveira RC, Acevedo OC, Czikowsky MJ, Beldini T. 2008. Spatial and temporal rainfall variability near the Amazon Tapajós confluence. Journal of Geophysics Research. 113: 1-17. https://doi.org/10.1029/2007JG000596

Folkins I, Martin RV. 2005. The vertical structure of tropical convection and its impact on the budgets of water vapor and ozone. Journal of the Atmospheric Sciences 62: 1560-1573. https://doi.org/10.1175/JAS3407.1

Freitas SR, Grell GA, Molod A, Thompson MA, Putman WM, Santos e Silva CM, Souza EP. 2018. Assessing the Grell-Freitas Convection Parameterization in the NASA GEOS Modeling System. Journal of Advances in Modeling Earth Systems 10: 1-24. https://doi.org/10.1029/2017MS001251

Germano MF, Vitorino MI, Cohen JCP, Costa GB, Souto JIO, Rebelo MTC, De Sousa AML. 2017. Analysis of the breeze circulations in Eastern Amazon: an observational study. Atmospheric Science Letter 18: 67-75. https://doi.org/10.1002/asl.726

Germano MF, Oyama MD. 2020. Local circulations features in the eastern Amazon: high-resolution simulation. Journal of Aerospace Technology and Management 12: e0820. https://doi.org/10.5028/jatm.v12.1100

Grabowski WW, Bechtold P, Cheng A, Forbes R, Halliwell C, Khairoutdinov M, Lang S. Nasuno T, Petch J, Tao W-K, Wong R, Wu X, Xu K-M. 2006. Daytime convective development over land: a model intercomparison based on LBA observations. Quarterly Journal of the Royal Meteorological Society 132: 317-344. https://doi.org/10.1256/qj.04.147

Greco S, Swap R, Garstang M, Ulanski S, Shipham M, Harris RC, Talbot R, Andreae MO, Artaxo P. 1990. Rainfall and surface kinematics conditions over central Amazona during ABLE-2B. Journal Of Geophysics Research 95: 17001-17014. https://doi.org/10.1029/JD095iD10p17001

Gille FSS and Mota MAS. 2014. Importância das condições termodinâmicas nos eventos extremos de precipitação na cidade de Belém e região metropolitana. Revista Brasileira de Meteorologia 29: 73-82. https://doi.org/10.1590/0102-778620130066

Hottovy S and Stechmann SN. 2015. Threshold models for rainfall and convection: Deterministic versus stochastic triggers, SIAM Journal on Applied Mathematics 75: 861–884. https://doi.org/10.1137/140980788

Houze Jr. RA. 1993. Cloud dynamics. University of Washington, USA.

Itterly KF, Taylor PC, Dodson JB. 2018. Sensitivity of the Amazonian convective diurnal cycle to its environment in observations and reanalysis. Journal of Geophysical Research: Atmosphere 23: 12621-12646. https://doi.org/10.1029/2018JD029251

Kousky VE. 1980. Diurnal rainfall variation in Northeast Brazil. Monthly Weather Review 108: 488-498. https://doi.org/10.1175/1520-0493(1980)108<0488:DRVINB>2.0.CO;2

Kuo YH, Neelin JD, Chen CC, Chen WT, Donner LJ, Gettelman A, Jiang X, Kuo KT, Maloney E, Mechoso CR, Ming Y, Schiro KA, Seman CJ, Wu CM, Zhao M, 2020. Convective transition statistics over tropical oceans for climate model diagnostics: GCM evaluation. Journal of the Atmospheric Sciences 77: 379-403. https://doi.org/10.1175/JAS-D-19-0132.1

Lee D, Oreopoulos L, Huffman GJ, Rossow WB, Kang I. 2013. The precipitation characteristics of ISCCP tropical weather states. Journal of Climate 26: 772-788. https://doi.org/10.1175/JCLI-D-11-00718.1

Lintner BR, Adams DK, Schiro KA, Stansfield AM, Amorim Rocha AA, Neelin DN. 2017. Relationships among climatological vertical moisture structure, column water vapor, and precipitation over the central Amazon in observations and CMIP5 models. Geophysical Research Letters 44: 1981-1989. https://doi.org/10.1002/2016GL071923

Machado LAT. 2000. The Amazon energy budget using the ABLE-2B and FluAmazon data. Journal of the Atmospheric Sciences 57: 3131–3144. https://doi.org/10.1175/1520-0469(2000)057<3131:TAEBUT>2.0.CO;2

Machado LAT, Laurent H, Dessay N, Miranda I. 2004. Seasonal and diurnal variability of convection over the Amazonia: A comparison of different vegetation types and large scale forcing. Theoretical Applied Climatology 78: 61-77. https://doi.org/10.1007/s00704-004-0044-9

Machado LAT, Calheiros AJP, Biscaro T, Giangrande S, Silva Dias MAF, Cecchini MA, Albrecht R, Andreae M, Araujo WF, Artaxo P, Borrmann S, Braga R, Burleyson C, Eeichholz CW, Fan J, Feng Z, Fisch GF, Jensen MP, Martin ST, Pöschl U, Pöhlker C, Pöhlker ML, Ribaud J-F, Rosenfeld D, Saraiva JMB, Schumacher C, Thalman R, Walter D, Wendisch M. 2018. Overview: Precipitation characteristics and sensitivities to environmental conditions during GoAmazon2014/5 and ACRIDICON-CHUVA. Atmospheric Chemistry and Physics 18: 6461-6482. https://doi.org/10.5194/acp-18-6461-2018

Marengo JA. 1992. Interannual variability of surface climate in the Amazon basin. International Journal of Climatology 12: 853-863. https://doi.org/10.1002/joc.3370120808

Masunaga H. 2012. Short-term versus climatological relationship between precipitation and tropospheric humidity. Journal of Climate 25: 7983-7990. https://doi.org/10.1175/JCLI-D-12-00037.1

Mota MAS, Nobre CA. 2006. Relação da variabilidade da energia potencial convectiva diponível (CAPE) com a precipitação e a alta da Bolívia durante a campanha WETAMC LBA. Revista Brasileira de Meteorologia 21: 344-355.

Mota MAS, Silva LM da, Sá LDA. 2007. Variabilidade da altura da camada de mistura (CM) e da energia potencial convectiva disponível (CAPE) durante o WetAMC/LBA. Ciência e Natura, v. especial: 419-421.

Neelin JD, Peters O, Hales K. 2009. The transition to strong convection. Journal Atmospheric Sciences 66: 2367-2384. https://doi.org/10.1175/2009JAS2962.1

Rao VB and Hada K. 1990. Characteristics of rainfall over Brazil: annual variations and connections with the southern oscillation. Theoretical and Applied Climatology 42: 81-91. http://dx.doi.org/10.1007/BF00868215

Ribeiro BZ, Machado LAT, Huamán Ch JH, Biscaro TS, Freitas ED, Mozer KW, Goodman SJ. 2019. An evaluation of the GOES-16 rapid scan for nowcasting in southeastern Brazil: analysis of a severe hailstorm case. Weather and Forecasting 34: 1-18. https://doi.org/10.1175/WAF-D-19-0070.1

Rocha AAA. 2010. A relação do perfil vertical do vapor d'água com a convecção profunda na Amazônia. Dissertação de Mestrado, Instituto Nacional de Pesquisas da Amazônia.

Rudolph JV, Friedrich K. 2014. Dynamic and thermodynamic predictors of vertical structure in radar-observed regional precipitation. Journal of Climate 27: 2143–2158. https://doi.org/10.1175/JCLI-D-13-00239.1

Santos e Silva CM. 2013. Ciclo diário e semidiário de precipitação na costa norte do Brasil. Revista Brasileira Meteorologia 28: 34-42.

Santos e Silva CM, Freitas SR. 2015. Impacto de um mecanismo de disparo da convecção na precipitação simulada com o modelo regional BRAMS sobre a Bacia Amazônica durante a estação chuvosa de 1999. Revista Brasileira de Meteorologia 30: 145-157. https://doi.org/10.1590/0102-778620140039

Santos SRQ, Vitorino MI, Braga CC, Campos TLOB, Santos APP. 2012. O efeito de brisas marítimas na cidade de Belém-PA: utilizando análise em multivariada. Revista Brasileira de Geografia Física 5: 1110-1120.

Santos JS, Mota MAS, Rocha EJP. 2014. Classificação climatológica da Energia Potencial Disponível para a Convecção na cidade de Belém-PA. Revista Brasileira Meteorologia 29: 60-72. http://dx.doi.org/10.1590/0102-778620130040.

Schiro KA, Neelin JD, Adams DK, Lintner BR. 2016. Deep convection and column water vapor over tropical land versus tropical ocean: a comparison between the Amazon and the tropical western pacific. Journal of the Atmospheric Sciences 73: 4043-4063. https://doi.org/10.1175/JAS-D-16-0119.1

Schiro KA and Neelin JD. 2019. Deep convective organization, moisture vertical structure, and convective transition using deep-inflow mixing. Journal of the Atmospheric Sciences 76: 965-987. https://doi.org/10.1175/JAS-D-18-0122.1

Sherwood SC, Chae JH, Minnis P, McGill M. 2004. Underestimation of deep convective cloud tops by thermal imagery. Geophysical Research Letters 31: 1-4. https://doi.org/10.1029/2004GL019699

Sherwood SC, Roca R, Weckwerth TM, Andronova NG. 2010. Tropospheric water vapor, convection and climate. Revista of Geophysics 48: 1-29. https://doi.org/10.1029/2009RG000301

Silva Dias MAF, Rutledge S, Kabat P, Silva Dias PL, Nobre C, Fisch G, Dolman AJ, Zipser E, Garstang M, Manzi AO, Fuentes JD, Rocha HR, Marengo

J, Plana-Fattori A, Sá LDA, Alvalá RCS, Andreae MO, Artaxo P, Gielow R, Gatti L. 2002. Cloud and rain processes in a biosphere-atmosphere interaction context in the Amazon region. Journal of Geophysical Research: Atmospheres, 107(D20): 8072. https://doi.org/10.1029/2001JD000335

Silva FP, Justi da Silva MGA, Menezes WF, Almeida VA. 2015. Avaliação de indicadores atmosféricos utilizando o modelo numérico WRF em eventos de chuva na cidade do Rio de Janeiro. Anuário do Instituto de Geociências – UFRJ 38: 81-90.

Sousa AC, Candido LA, Andreoli RV. 2018. Variabilidade interanual da precipitação e fluxo de umidade sobre a Amazônia usando o QTCM. Revista Brasileira de Meteorologia 33: 41-56. https://doi.org/10.1590/0102-7786331015

Tanaka LMS. 2014. Convecção profunda na Amazônia Central. Tese de doutorado, Instituto Nacional de Pesquisas da Amazônia.

Tanaka LMS, Satyamurty P, Machado LAT. 2014. Diurnal variation of precipitation in central Amazon Basin. International Journal of Climatology 34: 3481-3640. https://doi.org/10.1002/joc.3929

Tavares JPN, Mota MAS. 2012. Condições termodinâmicas de eventos de precipitação extrema em Belém-PA durante a estação chuvosa. Revista Brasileira de Meteorologia 27: 207-2018.

Tan J, Jakob C, Lane TP. 2013. On the identification of the large-scale properties of tropical convection using cloud regimes. Journal of Climate 26: 6618-6632. https://doi.org/10.1175/JCLI-D-12-00624.1

Uvo CB, Nobre CA. 1989. A Zona de Convergência Intertropical (ZCIT) e a precipitação no norte do Nordeste do Brasil. Parte I: A posição da ZCIT no Atlântico equatorial. Climanálise 4: 34-42.

Vilà-Guerau de Arellano J, Wang X, Pedruzo-Bagazgoitia X, Sikma M, Agusti-Panareda A, Boussetta S, Balsamo G, Machado LAT, Biscaro T, Gentine P, Martin ST, Fuentes JD, Gerken T. 2020. Interactions between the Amazonian rainforest and cumuli clouds: A large-eddy simulation, high-resolution ECMWF and observational intercomparison study. Journal of Advances in Modeling Earth Systems 12: 1-34. https://doi.org/10.1029/2019MS001828

Vila DA, Machado LAT, Laurent H, Velasco I. 2008. Forecast and tracking the evolution of cloud clusters (ForTraCC) using satellite infrared imagery: methodology and validation. Weather and Forecasting 23: 233-245. https://doi.org/10.1175/2007WAF2006121.1

Williams E and Rennó N. 1993. An analysis of the conditional instability of the tropical atmosphere. Monthly Weather Review 121: 21-36. https://doi.org/10.1175/1520-0493(1993)121<0021:AAOTCI>2.0.CO;2

Wolding B, Dias J, Kiladis G, Ahmed F, Powell SW, Maloney E, Branson M. 2020: Interactions between moisture and tropical convection. part I: the coevolution of moisture and convection. Journal of the Atmospheric Sciences 77: 1783–1799. https://doi.org/10.1175/JAS-D-19-0225.1

Atmósfera 35(2), 357-376 (2022)
https://doi.org/10.20937/ATM.52916

CONTENTS

Evaluating the Global Forecast System (GFS) for energy management over Minas Gerais State (Brazil) against in-situ observations

Rafael Arcanjo DE OLIVEIRA FILHO[1]*, Vanessa Silveira BARRETO CARVALHO[1] and Michelle Simões REBOITA[1]

[1] *Av. B.P.S., 1303. Pinheirinho, Itajubá - MG - Brazil. Institute of Natural Resources - Federal University of Itajubá.*
*Corresponding author: rafaarcanjoflho@gmail.com

Received: May 29, 2020; accepted: December 7, 2020

RESUMEN

Varias regiones de Brasil han experimentado períodos de intensa sequía en las últimas décadas. Las centrales hidroeléctricas producen la mayor parte de la energía del país y una reducción en el caudal de los embalses puede comprometer al sector energético. Por lo tanto, el gobierno brasileño ha buscado la diversificación de la producción de energía con otras fuentes renovables. La introducción de nuevas fuentes renovables, como energía eólica y solar, requiere estudios detallados de las condiciones climáticas locales, generalmente a través del análisis de datos históricos. Sin embargo, varias áreas de Brasil no tienen buena densidad de estaciones meteorológicas. En dicho contexto, este estudio tiene como objetivo evaluar la capacidad del producto de reanálisis del Sistema de Pronóstico Global (GFS) para representar el viento en el estado de Minas Gerais (MG), que produce el 79.5% de la energía de recursos hídricos. Si bien el estudio considera una región específica, presenta una metodología que se puede replicar en regiones donde no hay datos disponibles. En la mayoría de las áreas los valores de velocidad del viento a 10 m de GFS fueron similares a los registrados por las estaciones meteorológicas. Los resultados a 10 y 100 m de altitud muestran altos valores de velocidad del viento en el norte del estado, región donde también se registran las mayores densidades de potencia (~150 W m^{-2} durante invierno y primavera). En conclusión, el producto de reanálisis GFS, aunque con los sesgos aquí reportados, puede ser utilizado en regiones con datos meteorológicos insuficientes para estimar el potencial de producción de energía eólica como fuente complementaria de hidroelectricidad.

ABSTRACT

Several regions of Brazil have experienced periods of intense drought in the last decades. Hydropower plants produce most of the country's energy and a reduction in reservoir flow can compromise the energy sector. Therefore, the Brazilian government has sought the diversification of energy production with other renewable sources. The introduction of new renewable sources, such as wind and solar, requires detailed studies of the local weather conditions usually through historical data analysis. However, several areas in Brazil lack weather stations. In this context, this study aims to assess the ability of the Global Forecast System (GFS) reanalysis product to represent wind, in the state of Minas Gerais (MG) which has 79.5% of energy production associated with water resources. Although the study considers a specific region, it presents a methodology that can be replicated in regions where data is not available. Over most areas, 10 m wind speed values of the GFS reanalysis were similar to those registered by weather stations. Results at 10 and 100 m of altitude show high wind speed values in the north of the state, a region where the highest power densities are also recorded (approximately 150 W m^{-2} during winter and spring). In conclusion, the GFS reanalysis product, albeit with the biases reported here, can be used in regions with scarce meteorological data to estimate the potential for wind energy production as a complementary source of hydroelectricity.

Key words: Renewable energy, Wind power density, GFS reanalysis.

1. Introduction

Energy production depends on different local factors, such as climate and terrain (Tan and Zhi, 2016). The large availability of water resources in Brazil is used for human consumption, industry, agriculture, and energy production. According to the Energy Research Company (EPE, 2019), renewable resources in Brazil generated 495.290 GWh of electricity in 2018, and almost 80% by hydropower plants.

Adami et al. (2017) estimated the wind energy generated worldwide from 2006 to 2016, indicating an average growth of 23%, and currently representing 3% of the total energy generated worldwide. This growth can be associated with public policies which encourage wind power generation (Adami et al., 2017; Raimundo et al., 2018; Rego and Ribeiro, 2018). Brazil created, through Law Nº 10.438 of April 26 of 2002, the Alternative Energy Sources Incentive Program (PROINFRA) to increase the use of alternative renewable resources to produce energy, especially encouraging wind farms, small hydroelectric power plants, and biomass sources in order to reach 10% of country's annual electricity consumption by 2022 (Brasil, 2002). In 2018, wind and solar power plants were responsible for, respectively, 9.78% and 0.70% of the total energy production (EPE, 2019).

Minas Gerais (MG) located in southeastern Brazil is the fourth largest state in territorial extension, with an area of ~ 587000 km², a population of ~21 million people and a Human Development Index (HDI) of 0.731. Its main economic activities are: agriculture, livestock, industry, services, power generation, and mining (IBGE, 2018). MG is the fourth state in terms of power generation in Brazil. However, due to the high demand, the production is still insufficient, and for example in 2017, the state generated only 54.3% of its energy demand. A decrease in production in 2014 and 2015 due to an intense drought period (Coelho et al., 2016) contributed an increase on external energy dependence (3.4% per year). Energy production in MG corresponds to 7.35% of the total national production from basically three sources: hydro (79.0%), thermal (19.2%), and solar (1.8%). No energy is produced by wind sources in MG, despite the existence of a wind power plant in the city of Gouveia (Jequitinhonha Valley), but not in operation due to financial reasons (CEMIG, 2019; EPE, 2019). The large seasonal and interannual variability in rainfall rates hinders energy production and, according to the AR5 Synthesis Report from Intergovernmental Panel on Climate Change (IPCC, 2014), climate projections indicate the intensification of weather extremes, placing the hydroelectric system at risk. Due to the severe droughts during 2014 and 2015 in the southeastern region of the country, where 42.13% of the Brazilian population lives (IBGE, 2018), local governments were forced to implement energy rationing and to reduce water distribution for human consumption (Ribeiro, 2017).

Natividade et al. (2017) through the analysis of observations and projections data, identified an increase in the number of dry days in the northern region of MG; meanwhile, Reboita et al. (2018b) revealed an increase of dry consecutive days and a decrease of wet consecutive days in most MG from precipitation projections. Potential Evapotranspiration also shows positive trends directly proportional to temperature trends in MG (Salviano et al. 2016). With higher availability of moisture in the atmosphere, the number of rainfall extreme events can increase. Reboita et al. (2018b) analyzed climate projections for MG and indicated an increase of extreme events mainly in the austral summer. All these climate factors directly affect water level in reservoirs.

Towers for wind energy generation need to be at least 100 m tall, to avoid the drag effect of the wind at the surface. Moreover, wind intensity projections at 100 m using the RegCM4 regional climate model for MG (RCP8.5 scenario) showed only slight differences between the near future (2020 to 2050) and the present (1979-2005) of ~ 0.5 m s^{-1} depending on the season and state region. Differences between the present and the far future, however, presented variations of around 1 m s^{-1} (Reboita et al., 2018a). These results may indicate that wind patterns are less vulnerable to climate change when compared with other weather variables and it could be a promising source of electricity production in the state, complementing the hydroelectric source (Reboita et al., 2018a).

The wind resource assessment and characterization of a given region needs to consider information about the availability and variability of local winds. The Wind Power (2019) highlights that minimum extreme intensity values (less than 4 m s^{-1}) may not move the turbines; speeds between 13 and 25 m s^{-1} do not generate increases in power density; and maximum extremes (higher than 25 m s^{-1}) can cause severe structural damage to the towers. Moreover, small variations in wind intensity generate significant variations in energy production since the power density is proportional to the cube of the wind speed (Emeksiz and Cetin, 2019).

The approval and installation of wind power projects require initial studies with at least five years of data from weather stations at 50, 70, and 100 m which, in general, are scarce in Brazil (Cancino-Solorzano and Xiberta-Bernat, 2009). The Wind Atlas of the MG Energy Company used the Mesomap system, complemented by data from anemometric measurement stations, to assess wind energy potential throughout the state. The Mesomap system is a set of atmospheric simulation models that consists of the Mesoscale Atmospheric Simulation System (MASS) with a horizontal resolution of 3.6 km x 3.6 km (CEMIG, 2010). The results show wind in MG reaches values above 8 m s^{-1} during the winter and mainly in the northern region. However, in the absence of observations, the use of Numerical Weather Forecast (NWF) models can help in the decision-making process. Its results also can help to identify possible new viable sources of renewable energy and contribute to the diversification of state production. Therefore, this study aims to assess the ability of the Global Forecasting System (GFS) reanalysis product to estimate the potential for wind power generation, using the state of MG - Brazil from 2013 to 2017 as an example. The GFS model results data are available through the National Oceanic and Atmospheric Administration (NOAA, 2018) since 1980; therefore, the methodology presented in this study can be applied to other regions where observations are scarce or unavailable.

2. Methodology

2.1 Data

The GFS is a global weather forecasting model (NOAA, 2018), developed and operated by the National Centers for Environmental Prediction (NCEP), which uses the Gridpoint Statistical Interpolation (GSI) as a global analysis scheme (Rajagopal et al., 2007; Prasad et al., 2011). The GSI is included in the Global Data Assimilation and Forecasting (GDAF) system at National Centre for Medium Range Weather Forecasting (NCMRWF) and the assimilation runs are performed using the six-hour intermittent method (the system has access to a database observed four times a day), where three main interactions are carried out (between predictions and observations) and the analyses are used as initial conditions for subsequent predictions (Prasad et al., 2011; 2017). The results of the GFS analyses (meteorological term applied to indicate a model result that is not a forecast) were used with horizontal resolution of 0.5 degrees, 64 vertical levels, and six-hour frequency (0, 6, 12 and 18 UTC). The period considered was from 2013 to 2017 for the entire state of MG. From the zonal (UGRD) and meridional (VGRD) components, the intensities (m s^{-1}) and directions (º) of the wind were obtained every six hours. Daily and monthly averages were also calculated.

To verify how the GFS analyses represent the weather conditions in the state, observations at 10 m from twelve weather stations between 2013 and 2017 were used (Table I). These weather stations belong to the National Institute of Meteorology (INMET) and were chosen according to the mesoregions of the State of MG. These regions were defined, based on economic and social similarities, by the Brazilian Institute of Geography and Statistics (Brazilian Institute of Geography and Statistics - IBGE, 2018). For comparison, GFS data were extracted from the nearest grid points of the weather stations. Figure 1 shows the location of the stations and terrain elevation through the state. In the south, the altitude is higher, characterized by the Mantiqueira Mountains (Serra da Mantiqueira). In the north the altitude is more heterogeneous, with the Espinhaço Mountains (Serra do Espinhaço) and the São Francisco River Depression, for example (CEMIG, 2010).

2.2 Statistical Analyses

The evaluation of the wind speed and direction from GFS results was made through graphs and wind roses. Data obtained by weather stations were also compared with model results (at 10 m). Seasonal, monthly, and diurnal variability analyses of wind speed data were also performed. The diurnal cycle variability is important, as it allows the identification of the time when the wind reaches its highest intensity in a given location; in general, efficient production of wind energy will occur when the highest wind speed is recorded. The average 6-hour and monthly wind

Table I. List of weather stations.

Region	Code	Station	Latitude	Longitude
Campo das Vertentes	A514	São João Del Rei	21.10ºS	44.25ºW
Central Mineira	A538	Curvelo	18.74ºS	44.45ºW
West	A524	Formiga	20.45ºS	45.45ºW
Northwest	A553	João Pinheiro	17.78ºS	46.11ºW
North	A506	Montes Claros	16.68ºS	43.84ºW
Metropolitan Region	F501	Belo Horizonte	19.98ºS	43.95ºW
South	A515	Varginha	21.56ºS	45.40ºW
Triângulo Mineiro	A507	Uberlândia	18.91ºS	48.25ºW
Jequitinhonha Valley	A537	Diamantina	18.23ºS	43.64ºW
Zona da Mata	A518	Juiz de Fora	21.76ºS	43.36ºW
Mucuri Valley	A527	Teófilo Otoni	17.89ºS	41.51ºW
Doce River Valley	A511	Timóteo	19.56ºS	42.56ºW

the acronym was explained in the text): Source: Adapted from INMET (2018)

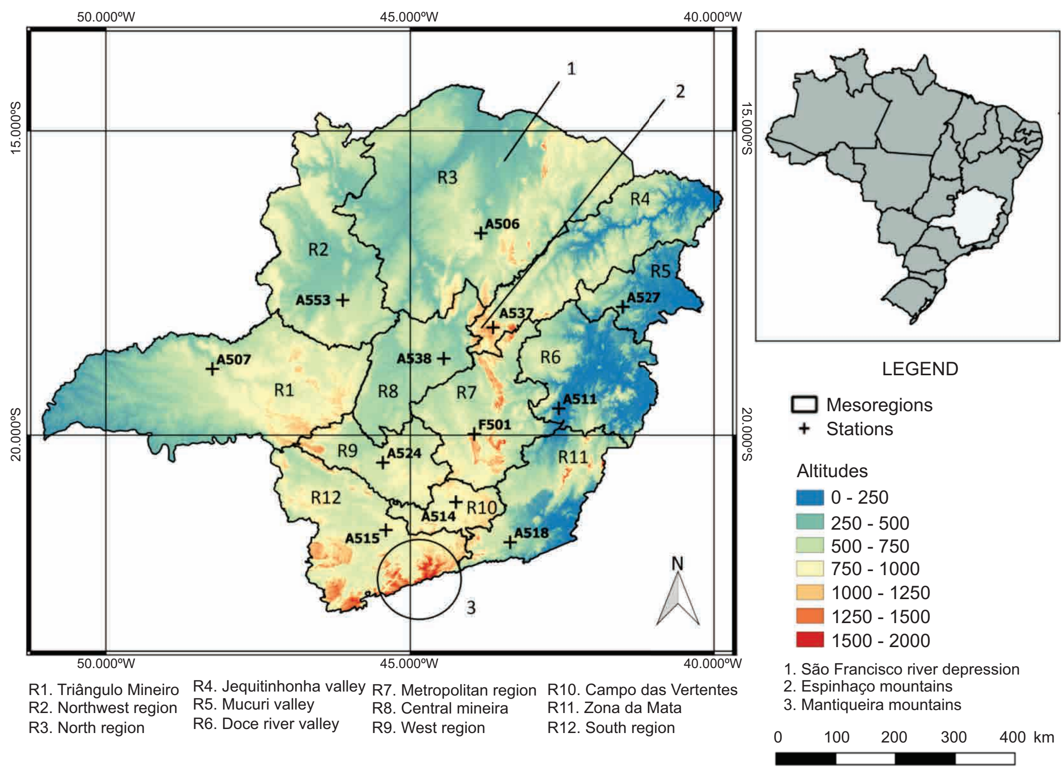

Fig 1. Location of MG state in relation to Brazil, spatial distribution of meteorological stations (+) and topography (m) of MG. Different regions within the state are denoted as R1, R2, …R12.

profiles from observational data and GFS results were also compared.

The frequency distribution of wind intensity can be represented by the Weibull distribution. This distribution has been adjusted to the GFS analysis and observational data to identify the constancy of wind intensity around an average value. Note that the Weibull distribution depends only on two parameters: the "k" shape and the "c" scale (Chandel et al., 2014; Wais, 2017). These parameters were obtained through Equations 1 and 2 respectively, where σ is the standard deviation, $\bar{v}$ is the average velocity and the gamma function (Γ). The parameter "k" is related to the shape of the wind speed distribution (dimensionless), and it is strictly related to the standard deviation of wind speed data while the parameter "c" is directly related to the average wind speed (ms^{-1}) (Wais, 2017; Katinas et al., 2018). The parameters of the Weibull distribution are a simple way to compare different datasets.

$$k = \left(\frac{\sigma}{\bar{v}}\right)^{-1.086} \tag{1}$$

$$c = \frac{\bar{v}}{\left[\Gamma\left(1 + \frac{1}{k}\right)\right]} \tag{2}$$

2.3 Wind Power Density (WPD)

Kalmikov (2017) indicates that seasonal mean power density (WPD) values are more advantageous than wind speed values, especially when comparing locations with asymmetric frequency characteristics, given the sensitivity of WPD to wind variations. WPD (W m^{-2}) was calculated from the GFS using Equation 3, widely used nowadays. This methodology was also applied by Hennessey Jr. (1977), Patel (2006), Silva et al. (2016), Reboita et al. (2018a), and Emeksiz et al. (2019), and considers the air density (ρ = 1.225 kg m^{-3}) and the wind speed (v):

$$WPD = cp\,\frac{1}{2}\,\rho\, v^3 \tag{3}$$

Calculating WPD per unit area (W m^{-2}) and considering the maximum power coefficient (cp) imposed by the Betz Law. The Betz Limit shows the maximum efficiency can be obtained from a wind turbine is 59.3%, which means the ratio between the input and output of the wind turbine is one third (Manwell et al., 2009; Burton et al., 2011). Thus, cp = 0.593.

Elliotti et al. (1991) previously used WPD = 0.955 ρv^3 to calculate tables of wind power density classification for winds measured at 10 and 50 m. Table II is a modified version of the one presented in Elliotti et al. (1991), comparing original WPD estimates with those calculated from Eqn. 3 and including data at 100 m.

3. Results and Discussion

3.1 Wind Spatial Distribution

Wind seasonal averages at 10 and 100 m are shown in Figures 2 and 3, respectively. Wind averages vary over the seasons due to intensification or weakening of atmospheric systems, mainly associated with the South Atlantic Subtropical Anticyclone (SASA), South Atlantic Convergence Zone (SACZ), and Frontal Systems (Reboita et al., 2010; Reboita et al., 2015; Reboita et al., 2019).

GFS indicates that, in general, the wind at 10 m (Fig. 2) has low intensity, not exceeding 2 m s^{-1} in

Table II - Classification of wind power density, where v is the wind speed (ms^{-1}) and WPD is the wind power density (W.m^{-2}). The WPD 1 correspond to values for 10 and 50 m calculated in the original study based on the Rayleigh distribution (Elliotti et al., 1991). WPD 2 values were calculated using Equation 3.*Values calculated for 100 m, maintaining the calculation standard of the original publication.

Classes	10 m			50 m			100 m		
	v	WPD 1	WPD 2	v	WPD 1	WPD 2	v*	WPD 1*	WPD 2*
1. Poor	0-4.4	0-100	0-52.2	0-5.6	0-200	0-107.6	0-6.2	0-280.6	0-146.9
2. Marginal	4.4-5.1	100-150	52.2-81.3	5.6-6.4	200-300	107.6-160.6	6.2-7.2	280.6-436.9	146.9-228.7
3. Moderate	5.1-5.6	150-200	81.3-107.6	6.4-7.0	300-400	160.6-210.1	7.2-7.9	436.9-578.4	228.7-302.8
4. Good	5.6-6.0	200-250	107.6-132.3	7.0-7.5	400-500	210.1-258.4	7.9-8.5	578.4-711.4	302.8-372.5
5. Excellent	6.0-6.4	250-300	132.3-160.6	7.5-8.0	500-600	258.4-313.6	8.5-9.0	711.4-863.4	372.5-452.0
6. Excellent	6.4-7.0	300-400	160.6-210.1	8.0-8.8	600-800	313.6-417.4	8.0-9.9	863.4-1129.7	452.0-591.5
7. Excellent	>7.0	>400	>210.1	>8.8	>800	>417.4	>9.9	>1129.7	>591.5

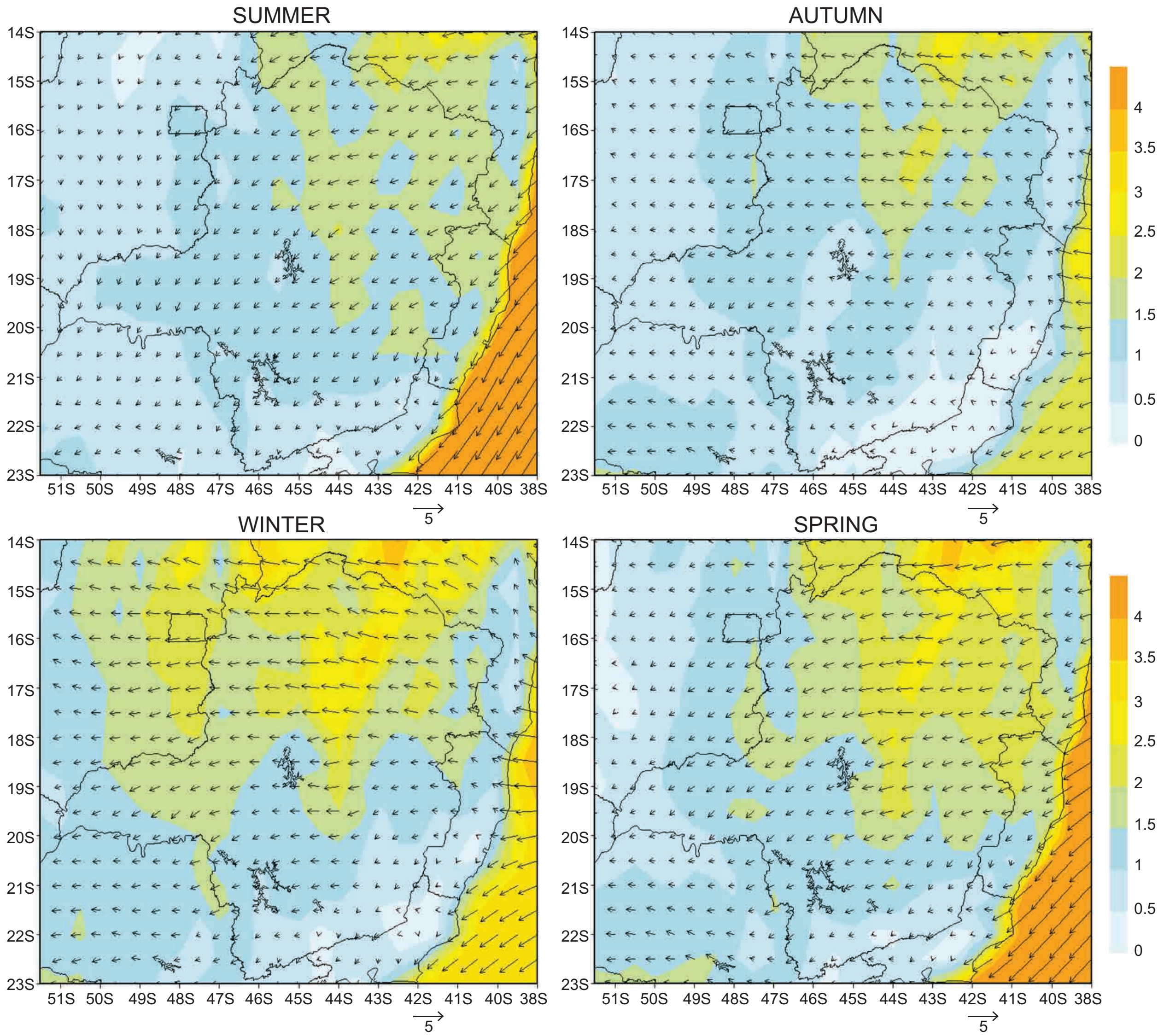

Fig 2. Wind seasonal average at 10 m from 2013 to 2017. Intensity (ms^{-1}) is shaded and vectors indicate wind direction (º).

the south and 3.5 m s^{-1} upstate. However, the wind speed at 100 m (Fig. 3) shows higher values due to surface roughness which tends to decrease with height. The northern portion of the State shows wind speed average at 10 m between 1 and 2.5 m s^{-1} during austral summer and autumn; at 100 m, average values between 3.5 and 4.5 m s^{-1} were found, respectively. During winter and spring, wind-speed values increase from 2.5 to 3.5 m s^{-1} (at 10 m) and from 4 to 6 m s^{-1} (at 100 m). A similar pattern is seen throughout the state. The wind speed at 100 m is equal to the minimum threshold for energy generation during winter and spring (dry season), which is 4 m s^{-1} (for small electric wind turbines) and wind turbines on a scale of public utility and 6 m s^{-1} (wind farms on larger scales), according to Culture Change (2017) and The Wind Power (2019). The North (R3, see map in Fig. 1) and Jequitinhonha Valley (R4) regions have the highest wind intensities, agreeing with CEMIG (2010). Higher wind speed values during winter and spring indicates a possible anti-correlation between wind and precipitation which presents minimum values in these seasons (Silva and Reboita, 2013; Reboita et al., 2015; Reboita et al., 2017; Reis et al.

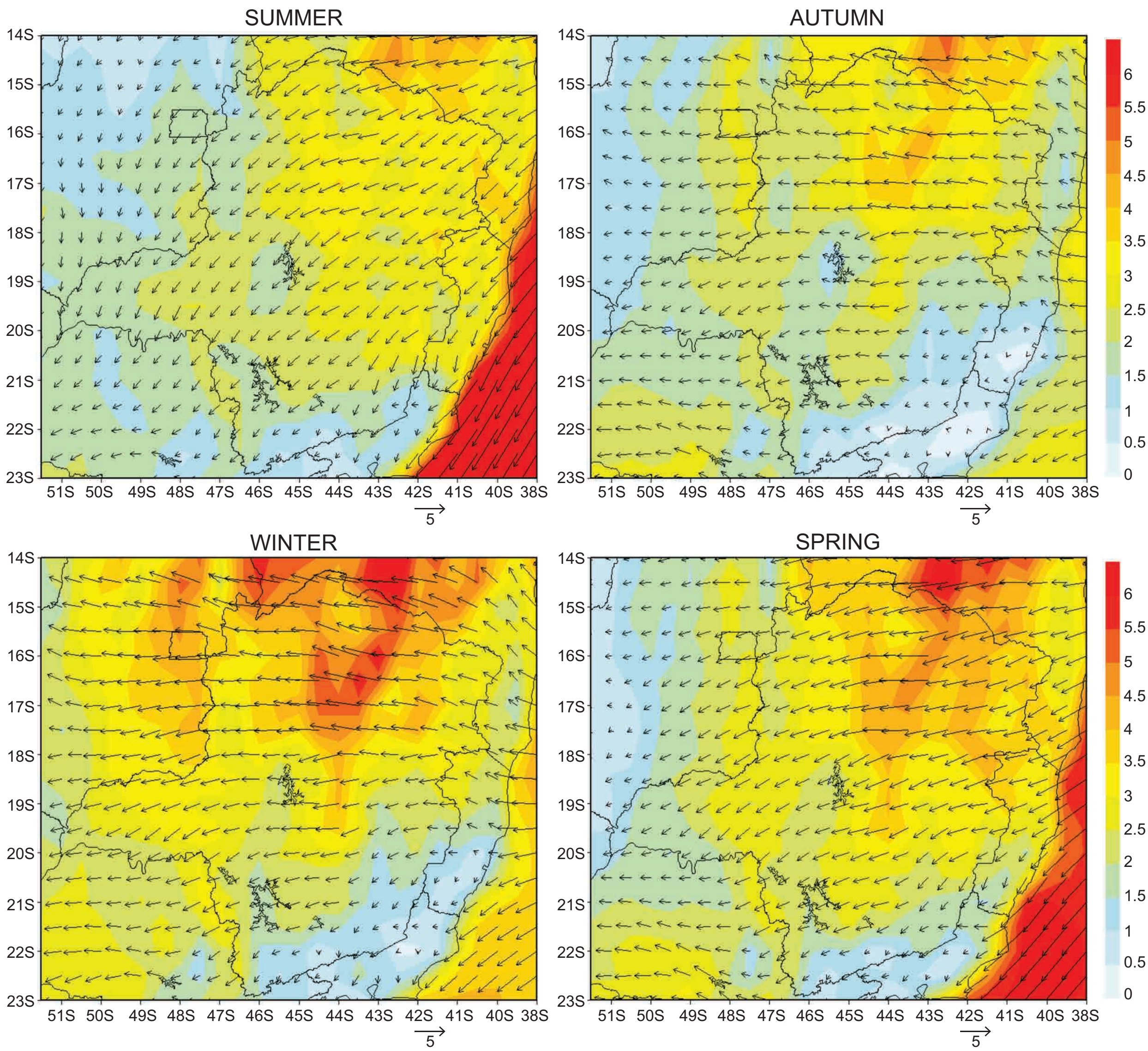

fig. 3. Wind speed seasonal averages at 100 m (ms^{-1}) from 2013 to 2017. Intensity (ms^{-1}) is shaded and vectors indicate wind direction (º)

2018) and reinforces a positive factor for the expansion of wind power in the state energy matrix. Wind farms would have greater production in months with low operation of the hydroelectric power plants and thus, energy production would be complementary between the two sources.

In agreement with ERA-Interim reanalysis data and RegCM4 model results by Reboita et al. (2018a), wind density values show significant differences between northern (R3) and southern (R12) regions of MG and higher wind speed values during winter and springtime. However, ERA-Interim data presented a higher contrast between those regions; while the northern region showed wind intensity lower than 6 m s^{-1}, the southern region presented values lower than 3 m s^{-1}, matching those of the GFS analysis.

Another important factor is that the average wind speed is less than the maximum limit, favouring eolic energy generation throughout the day and seasons, minimizing possible structural problems. Results in Figure 4 do not differ significantly from those reported by Paula et al. (2017): wind speeds varying

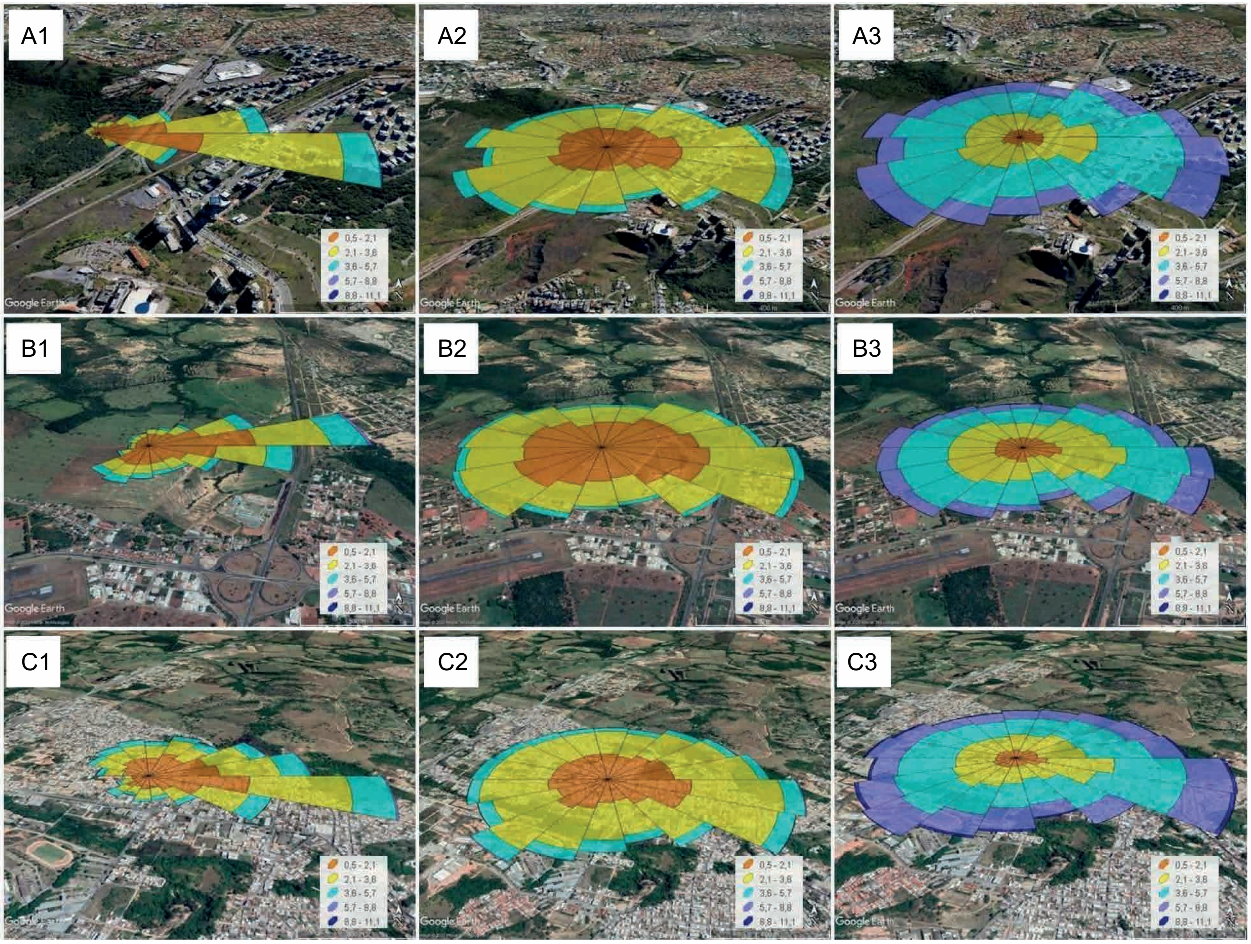

Fig. 4. Wind roses determined for the period 2013-2017 in stations: (A) Belo Horizonte, (B) Curvelo and (C) Formiga, representing: (1) observed data, (2) GFS data (10 m) and (3) GFS data (100 m). The legend is in ms^{-1}.

from 0.8 to 5.5 m s^{-1}, more intense in winter and in northern MG. It is worth mentioning that Paula et al. (2017) used only data from meteorological stations, and, in addition, authors performed vertical extrapolation of wind speed data to estimate values at 100m.

The wind direction pattern at 10 m and 100 m is mainly influenced by SASA, which plays an important role in the climate of South America. Moreover, as reported by Reboita et al. (2019), the SASA area expands to south and west in climate projections compared to its current climate position. This expansion of SASA may affect weather conditions, modifying the frequency of dry periods, and directly impacting the energy sector in southeastern Brazil. The SASA gains strength in winter and extends to the western Atlantic Ocean, hampering convective movements and cold fronts in southeastern Brazil and, consequently, reducing precipitation rates (Reboita et al., 2015; Reboita et al., 2017). Therefore, there is a possible complementarity between wind and hydroelectric power plants mainly during the winter (dry season) when hydroelectric power plants operate at low capacity.

3.2 Analysis of predominant wind direction

Wind direction from GFS results at 10 m was compared with observed wind direction data at twelve sites. Wind roses are presented for the predominant wind direction from GFS at 100 m. Emeksiz et al. (2019) indicate the wind direction analysis can provide information to support the decision of where to install the wind turbines in order to maximize its efficiency. Table III shows that observational data at 10 m from stations presented variable directions. In contrast, the GFS data at both 10 and 100 m, presented predominant northeast-southeast direction, while showing differences in wind speed, and not satisfactorily simulating the observed direction at 10 m.

Table III. Predominant wind direction.

Station	Observed (10 m)	Simulated (10 m)	Simulated (100 m)
Belo Horizonte	NE - SE	NE - SE	NE - SE
Curvelo	NE - SE	NE - SE	NE - SE
Diamantina	E - S	NE - SE	NE - SE
Formiga	NE - SE	NE - SE	NE - SE
Juiz de Fora	N - E	NE - SE	NE - SE
João Pinheiro	E - S	NE - SE	NE - SE
Montes Claros	N - E	NE - SE	NE - SE
São João Del Rei	E - S	NE - SE	NE - SE
Timóteo	NW - NE	NE - SE	NE - SE
Teófilo Otoni	NE - E	NE - SE	NE - SE
Uberlândia	N - E	NE - SE	NE - SE
Varginha	E - S	NE - SE	NE - SE

As an example, Figure 4 shows that Belo Horizonte (A), Curvelo (B) and Formiga (C) stations have a similar predominant wind direction at 10 and 100 m. In contrast, wind direction from GFS are more homogenously distributed. In general, the wind turbines would be better positioned in the NE-SE direction, where they would experience the highest frequency of winds.

Moreover, Figure 4 indicates that wind direction patterns from GFS do not show significant differences between 10 and 100 m. This absence of changes in the wind direction with height over cities (most of the stations analyzed are located in or close to urban centers) suggests little or no influence of urbanization. However, it is well known that urbanization increases energy loss at the surface, affecting both the intensity and the prevailing wind direction. Large urban centers, which expand as population grows, undergo processes that involve changes in land use and occupancy which, in turn, modify surface roughness conditions. GFS is unable to represent terrain conditions adequately well in the interpolation process of wind direction in these regions.

3.2 Wind variability patterns

In terms of seasonal variability, wind speed averages in MG are lower during austral summer and fall, coinciding with higher rainfall rates which guarantee that hydroelectric plants can operate at maximum efficiency. Wind speed averages are higher between July and October (austral winter) reinforcing potential complementarity between higher wind and lower precipitation. Thus, during the dry season, stronger winds can help meet the state's energy demand. At 100 m, cities as Uberlândia, Montes Claros, and Teófilo Otoni (located in the Triângulo Mineiro (R1), North region (R3), and Mucuri Valley (R5), respectively) presented wind speed averages close to 6 m s^{-1}. Observations and results from GFS at 10 m show values between 1.5 and 3 m s^{-1}. The lowest wind speed averages were registered between February and May.

The comparison between observed and GFS profiles showed similar patterns in most sites (Fig. 5). Best results were found for Belo Horizonte, São João del Rei and Varginha (municipalities where the stations are located in areas with few obstacles, in general, with undergrowth or agricultural plantations), while greater differences can be observed in Diamantina, Montes Claros and Juiz de Fora where stations are located in areas with larger obstacles (such as high rocks in the case of Diamantina) or residential areas (in Montes Claros and Juiz de Fora). In general, the GFS model overestimated values at 10 m when compared to the observations, except in Diamantina, Juiz de Fora and São João Del Rei (also shown by the percentage changes).

As for diurnal wind speed variability, at 10 m the highest speed was recorded at 12 h and the lowest between 0 h and 6 h, in agreement with the diurnal cycle of the Earth's surface temperature. At 100 m, the highest speed occurred between 0 h and 6 h (night and dawn) and decreased throughout the day. Observed and GFS profiles show similar patterns at most sites (Fig. 6). The GFS model also overestimated values at 10 m when compared to the observed values, except in Diamantina and Juiz de Fora.

3.4 Weibull Distribution

Statistics are used in wind studies to represent wind variability and evaluate its evolution, with respect to average values and the probability of occurrence

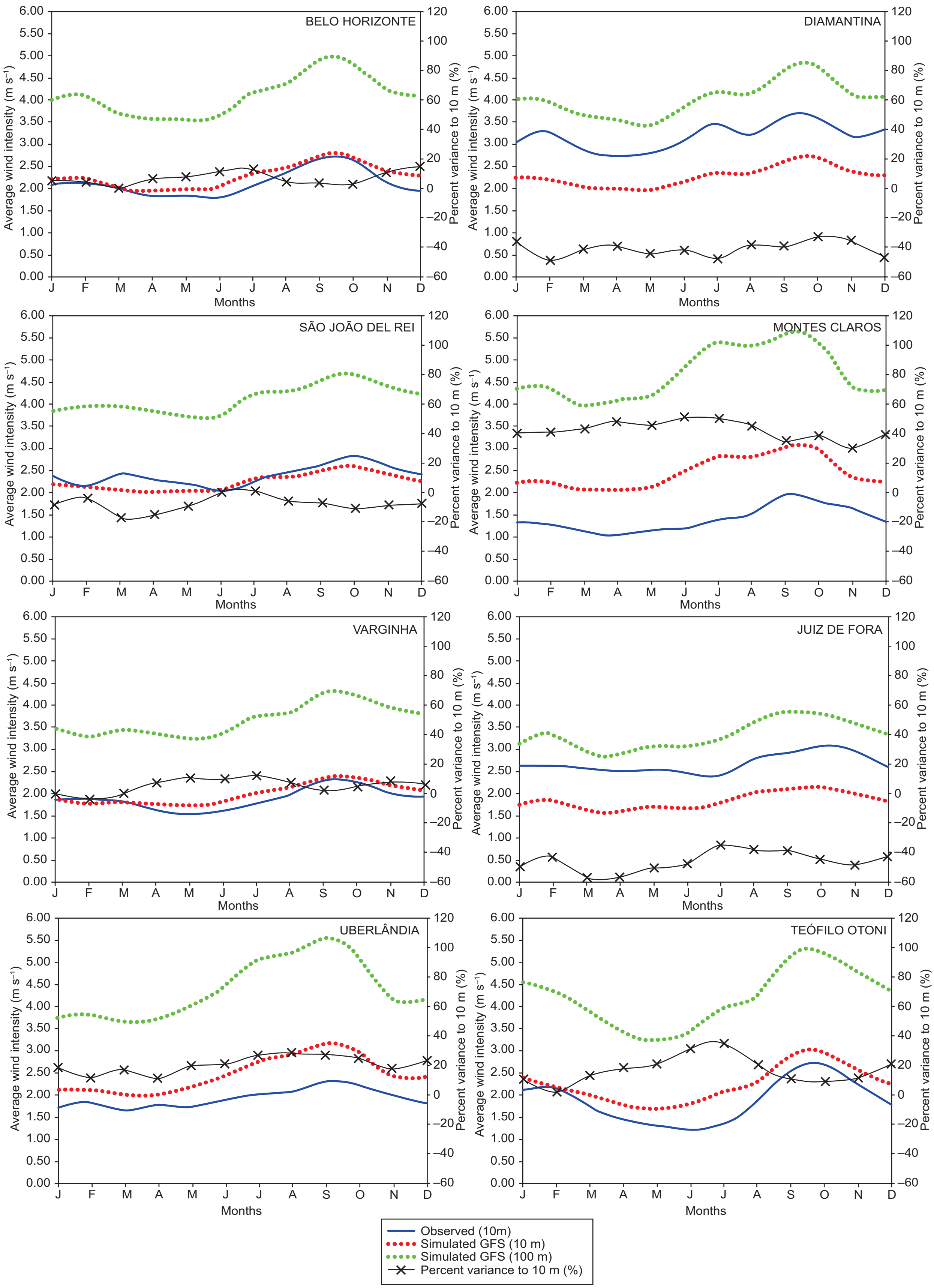

Fig. 5. Average monthly wind profile (ms^{-1}) observed at 8 selected sites (at 10 m, blue line) compared with derived GFS values at 10 m (red dots) and at 100 m (green dots). The black line corresponds to the variance of the observed wind at 10m.

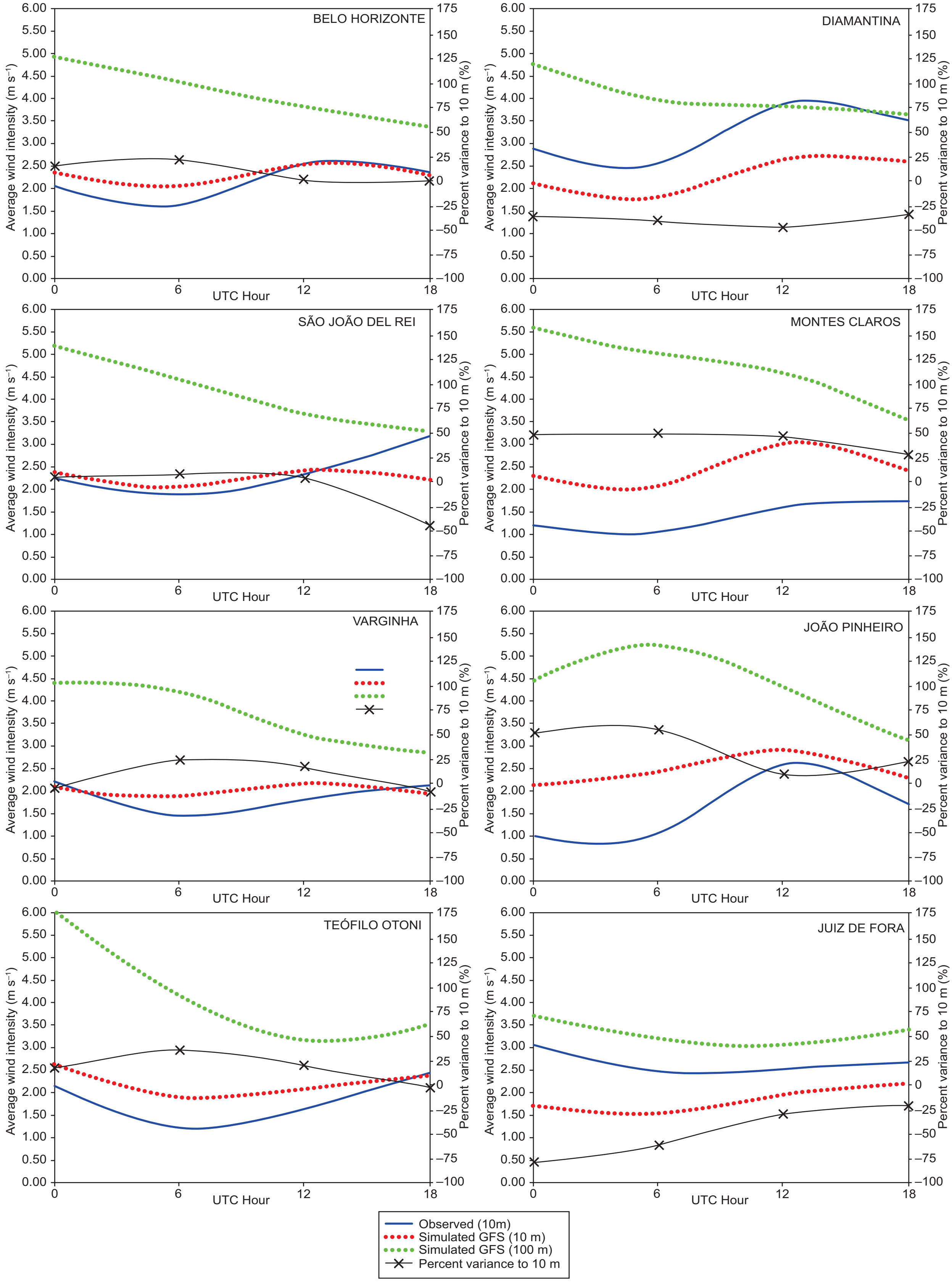

Fig. 6. Diurnal average wind profile (ms^{-1}) observed at 8 selected sites (at 10 m, blue line) compared with derived GFS values at 10 m (red dots) and at 100 m (green dots). The black line corresponds to the variance of the observed wind at 10m.

of extreme values, and facilitate the comparison between data sets. When the Weibull shape parameter *k* presents high values, it indicates little variability of the wind speed around an average value, whereas the parameter c indicates the average value of the data. For observations at 10 m at all sites, *k* values ranged between 1 and 2.16. The values of *c* presented greater variability, as can be seen in Table IV. According to Patel (2006), when *k* is equal or close to 1 the Weibull distribution approaches an exponential distribution, as in the case of Montes Claros (top-right panel in Fig. 8, blue line), and it indicates that most days registered calm or very weak winds. When *k* values equal to or close to 2 (Rayleigh distribution), such as in Belo Horizonte, Diamantina, Juiz de Fora and Uberlândia, present standard distributions of wind speeds (found in most places), and in these cases most days have speeds below the average speed.

All observational datasets showed positive asymmetries, where the modal value < median of the values < average speed value (Pishgar-Komleh et al., 2015). Similar calculations with the GFS datasets at 10 m and 100 m, result in values of *k* between 2 and 3 (Fig. 7 and 8). Also according to Patel (2006), distributions with $k = 3$ (as in Diamantina and Belo Horizonte) are similar to a normal distribution, where the number of strong winds is equal to the number of light winds (symmetric with respect to the mean). The parameter *c*, in general, was close to 3 ms^{-1} (10 m) and 4 ms^{-1} (100 m). Analyses carried out by Ramos et al. (2018) show distribution patterns as positive examples for eolic energy generation, as they detect only minor problems with the change of the wind (winds with less variability).

Results from observations and GFS show that the frequency of occurrence of extreme events greater than 8 ms^{-1} is less than 1%. The analysis show that the winds have acceptable annual values of *k* but are lower than those found in regions with high wind potential, such as the Brazilian Northeast (with *k* values equal to or greater than 6) (CRESESB, 2001).

An accurate and reliable assessment of wind resources plays an important role in the effective use of wind energy (Shamshirband et al., 2016). Given the variety of studies carried out that confirm the efficiency of the Weibull distribution (Shoaib et al., 2017; Katinas et al., 2018; Souza et al., 2019) in wind studies, it can be concluded that the results presented show that wind intensity data, provide relevant general information on wind variability.

3.5 Wind Power Density (WPD)

Values of WPD depend on the wind turbine model with different power coefficients (*cp*), as expressed in Eqn. 3. Figure 9 presents the seasonal average of WPD at 100m, considering the air density equal to 1,225 kg m^{-3}. The left column in Fig. 9 disregards the maximum power conversion estimated by the Betz Law, which shows maximum yield from a wind turbine to be 59.3% (Manwell et al., 2009). WPD

Table IV. Parameter values *k* (distribution format, Eqn. 1) and *c* (average speed, Eqn. 2).

Station	Observed (10 m)		Simulated (10 m)		Simulated (100 m)	
	k	c (m s^{-1})	k	c (m s^{-1})	k	c (m s^{-1})
Belo Horizonte	2.05	2.42	2.86	2.57	2.59	4.62
Curvelo	1.44	2.15	2.42	2.21	2.16	3.98
Diamantina	2.16	3.67	2.73	2.59	2.79	4.57
Formiga	1.50	2.25	2.52	2.58	2.24	4.62
João Pinheiro	1.53	2.87	2.67	2.78	2.34	4.86
Juiz de Fora	2.08	3.18	2.31	2.09	2.29	3.77
Montes Claros	1.39	1.73	2.58	2.78	2.64	5.30
S. João Del Rei	1.65	2.74	2.57	2.56	2.29	4.65
Teófilo Otoni	1.54	2.20	2.81	2.53	2.39	4.72
Timóteo	1.70	1.37	2.50	1.94	2.31	3.54
Uberlândia	1.90	2.24	2.22	2.78	2.27	4.97
Varginha	1.81	2.22	2.39	2.26	2.09	4.10

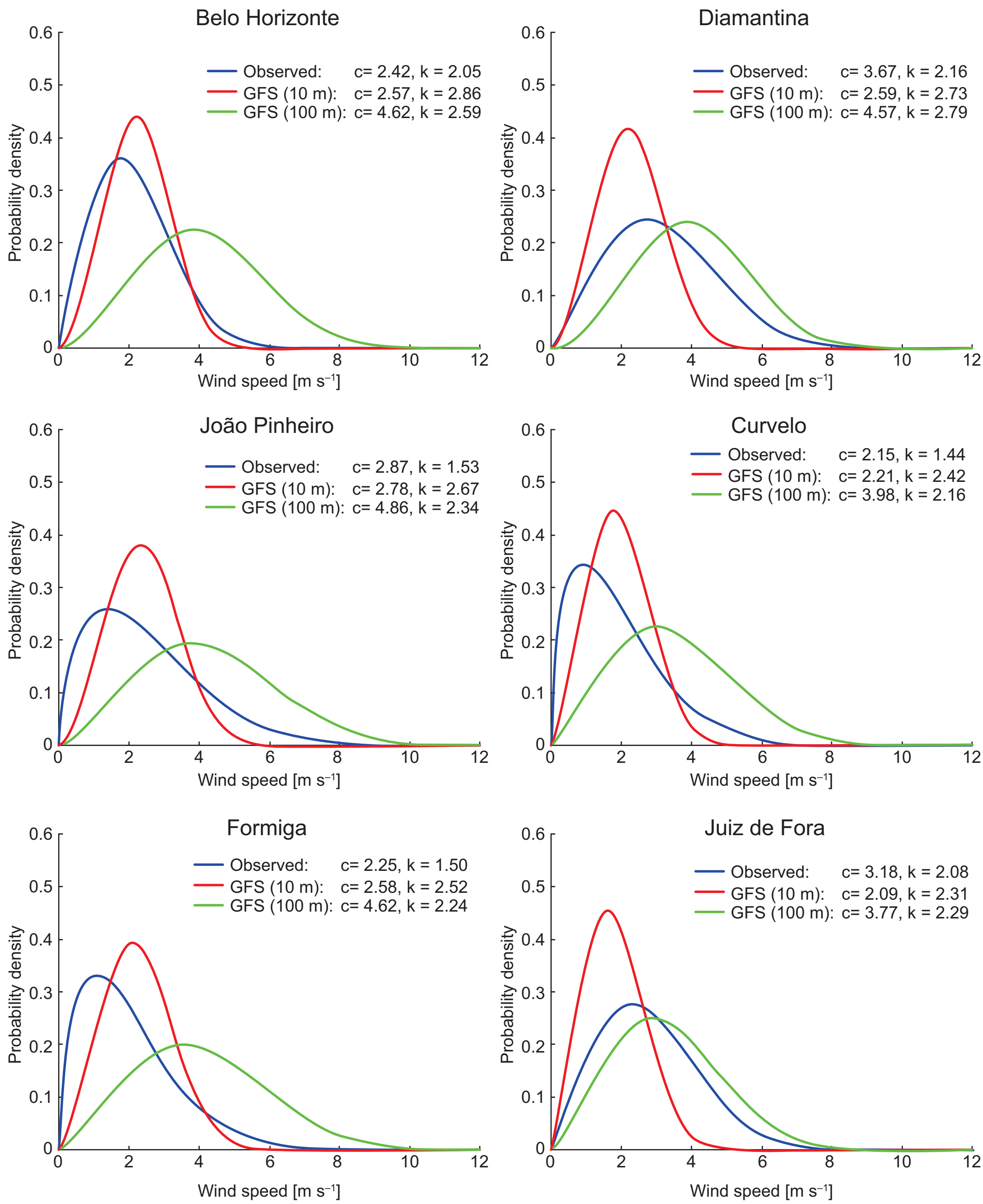

Fig. 7. Weibull distributions calculated for observed wind speed at 10 m (blue line) at selected 6 sites for the period (2013 - 2017) and GFS values at 10m (red line) and 100m (green line).

results show lowest values during summer and fall, below 70 W m^{-2} with higher values in the north and lower values in the south of MG. During winter and spring values are higher, reaching 150 Wm^{-2} in the north region. The right column (Fig. 9) shows WPD seasonal average at 100 m, considering the maximum power conversion estimated by the Betz Law, resulting in an approximate 60% reduction compared to the right column. As *cp* values depend on the wind turbine chosen, such reduction is variable,

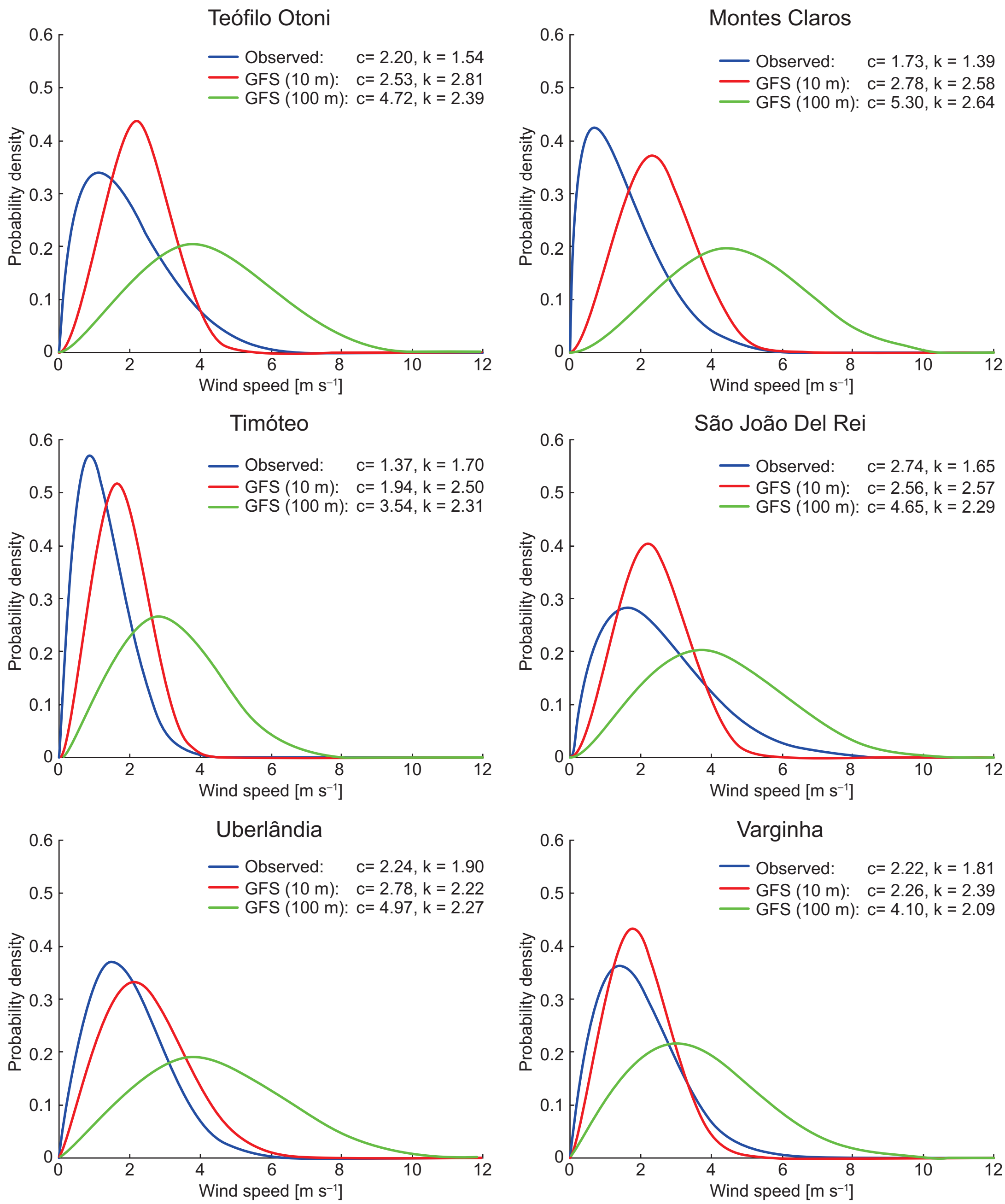

Fig. 8. Same as Figure 7 for the remaining 6 sites.

and it should be taken into account in the calculations as it influences the relationship between wind speed and generated power density.

WPD results have a high sensitivity to wind speed; therefore, its values are higher when wind speed values are higher. Regions with wind speed above 4.5 ms^{-1} at 100 m have higher wind energy generation potential. However, the values are low when compared to results for the Northeast region of Brazil. Ramos et al. (2018) found sites in the Northeast (Alagoas State) during the dry season with WPD values around 700 W m^{-2}, and even during the rainy season, 400 Wm^{-2}. However, it is important to highlight that the Northeast has wind speeds higher than 8 ms^{-1},

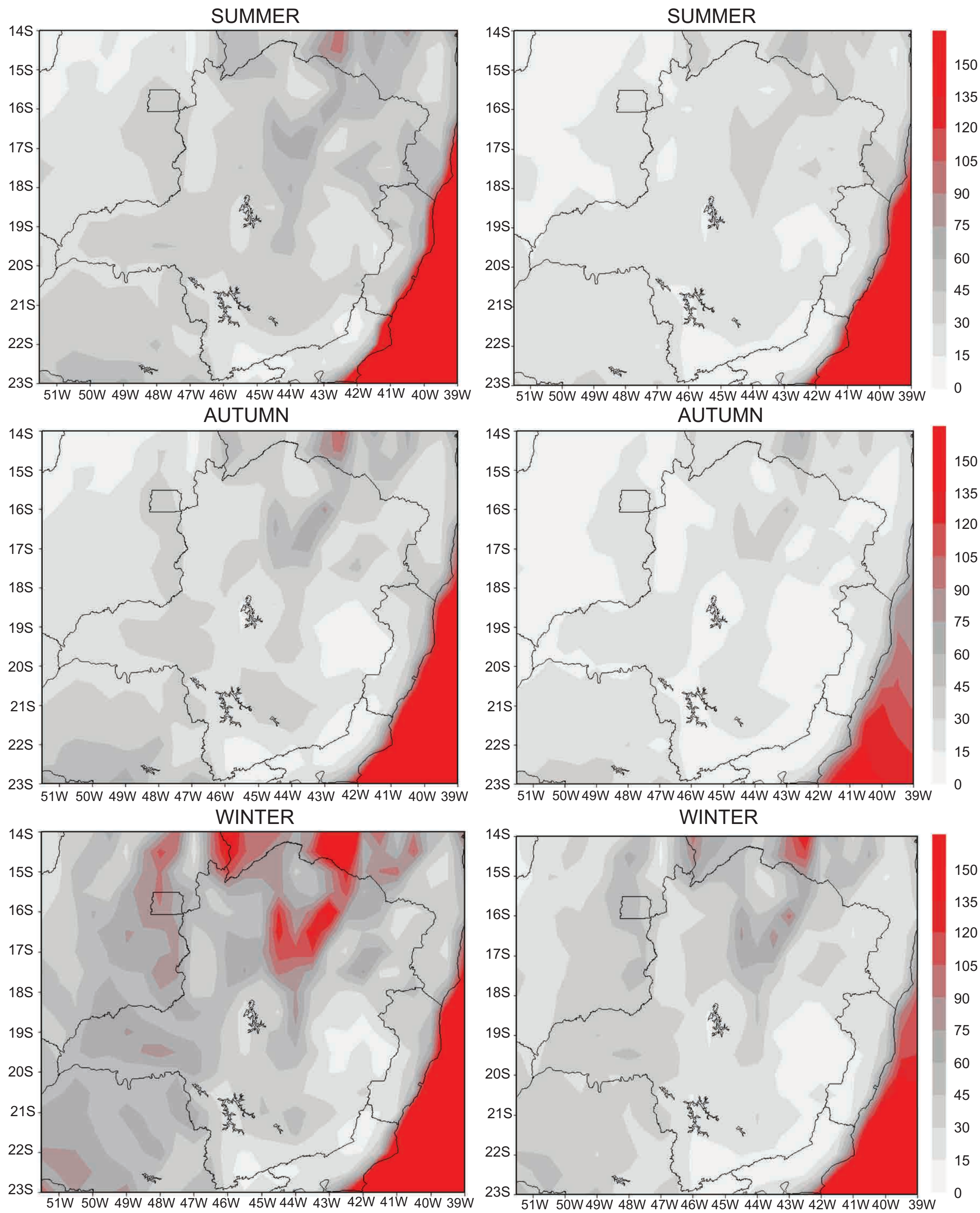

Fig. 9. WPD (Wm^{-2}) at 100 m, from 2013 to 2017. Left column: WPD without considering cp. Right column: WPD considering the maximum *cp* value (59.3%) of the Betz Limit (Manwell et al., 2009).

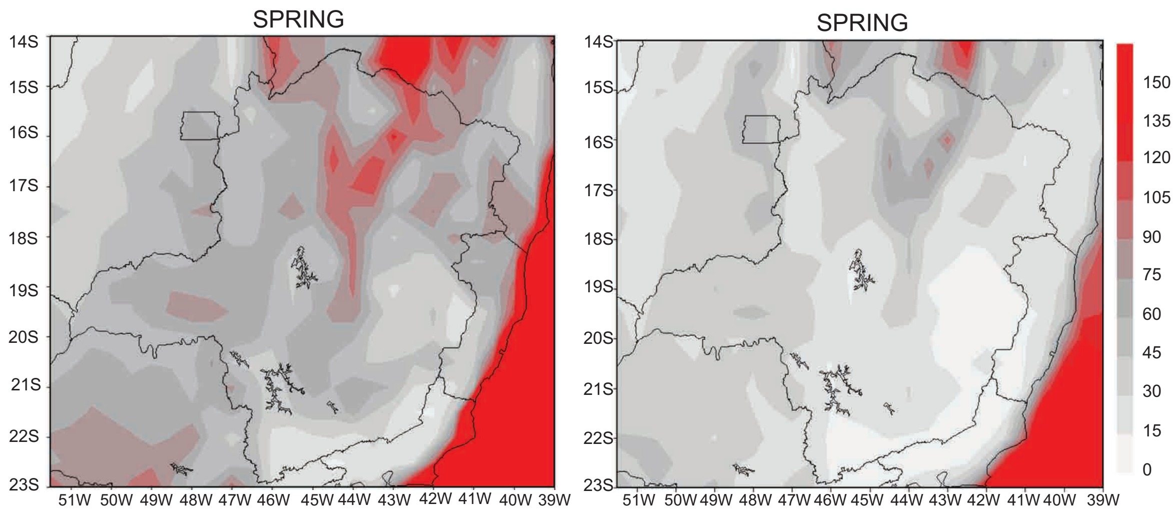

Fig. 9. WPD (Wm^{-2}) at 100 m, from 2013 to 2017. Left column: WPD without considering cp. Right column: WPD considering the maximum *cp* value (59.3%) of the Betz Limit (Manwell et al., 2009).

besides high k values. Other regions with high WPD are located south of Bahia (Northeast region) where several wind farms already operate.

In terms of areas in the State of MG with the highest wind potential, the results confirm areas highlighted by ANEEL (2003) and CEMIG (2010), but with lower wind intensity and WPD values. However, it is important to highlight that the study conducted by CEMIG (2010) used atmospheric modeling at a higher resolution (3.6 km x 3.6 km) than the GFS data. Thus, considering a spatial scale of 50 km adapted in this work, one can classify the wind potential of MG in Class 1 (Table II).

4. Conclusions

The results of the GFS analysis compared with observational data show the seasonal and spatial distribution of the wind potential of the State of MG. Both at 10 m and 100 m, the lowest wind intensity was recorded during summer and autumn, and the highest during winter and spring (reaching 4 m s^{-1} at 10 m and 6 m s^{-1} at 100 m). The interaction between the wind and the surface influenced the speed values (being greater than 100 m). The average hourly wind profile indicates greater intensities of the wind at 12 UTC (at 10 m) and during the night and dawn (at 100 m). The spatial distribution analysis shows higher wind speed in the Northern Region of MG. In comparison with the observed wind speed data, in general, the GFS model presents similar patterns to those observed, overestimating values in most sites, except in Diamantina and Juiz de Fora. As for the predominant wind direction, there is a greater discrepancy between observed and GFS results; in addition, the model creates a similar pattern of data at 10 and 100 m, suggesting that the GFS does not represent well the surface conditions.

Analysis in terms of Weibull distributions showed that most of the sites had a k parameter between 2 and 3, indicating that, most of the time, the recorded speeds are below average values. The parameter c showed a greater variability with values close to 3 m s^{-1} (at 10 m) and 4 ms^{-1} (at 100 m). In addition, the frequency of occurrence of extreme events greater than 8 ms^{-1} was less than 1%. As for the WPD at 100 m, values are higher during winter and spring, reaching a seasonal average value equal to 150 Wm^{-2}. In this sense, it can be concluded that the North region of MG can be characterized as in Class 1, presenting low potential and reduced use for electricity generation. However, more specific studies with higher spatial resolution data are necessary in order to assess the areas of hotspots and to verify the economic, social and environmental feasibility of implementation of wind farms.

Estimates of regions appropriate for the installation of wind energy projects require observational data at least at 2 vertical levels. Despite of the reported limitation of the GFS reanalysis product in this study, the methodology applied here can be recommended for locations with limited or no observational data. The GFS output may need to be modified to take into account local terrain features that affect both wind speed and direction, such as in urban areas. In summary, usage of output from atmospheric models (e.g. GFS) and the methodology applied in this study can provide accurate information for the decision-making process.

Acknowledgments

This research was carried out with the support of the Institute of Natural Resources of the Federal University of Itajubá and financed by the Coordination for the Improvement of Higher Education Personnel (Capes) - Financing Code 001. The authors would like to thank the National Oceanic and Atmospheric Administration (NOAA) for the availability of the Global Forecast System (GFS) model and the INMET for providing the station data used. The third author also thanks CNPq and FAPEMIG for financial support.

References

Adami VS, Antunes Júnior JAV, Sellitto MA. 2017. Regional industrial policy in the wind energy sector: The case of the State of Rio Grande do Sul, Brazil. Energy Policy 111: 18-27. https://doi.org/10.1016/j.enpol.2017.08.050

ANEEL. 2003. Banco de Informações de Geração BIG. Available at http://bit.ly/39LK90S (accessed 2020 January 29)

BRASIL. Lei nº 10.438, de 26 de abril de 2002. Dispõe sobre a expansão da oferta de energia elétrica emergencial, recomposição tarifária extraordinária e cria o Programa de Incentivo às Fontes Alternativas de Energia Elétrica (Proinfa). Presidência da República, Casa Civil, Brasília, DF, 26 abr. 2002. 181º da Independência e 114ºda República.

Burton T, Jenkins N, Sharpe D, Bossanyi E. 2011. Wind Energy Handbook. New York: John Wiley & Sons.

Cancino-Solorzano Y, Xiberta-Bernat J. 2009. Statistical analysis of wind power in the region of Veracruz (Mexico). Renewable Energy 34: 1628-1634. https://doi.org/10.1016/j.renene.2008.11.018

Cresesb. 2001. Atlas do potencial eólico brasileiro. Available at http://www.cresesb.cepel.br/index.php?-section=publicacoes&task=livro&cid=1; (accessed 2019 October 02)

Chandel SS, Ramasamy P, Murthy KSR. 2014. Wind power potential assessment of 12 locations in western Himalayan region of India. Renewable and Sustainable Energy Reviews 39: 530–545. https://doi.org/10.1016/j.rser.2014.07.050

Coelho CAS, Oliveira C, Ambrizzi T, Reboita MS, Carpenedo CB, Campos JLPS, Tomaziello ACN, Pampuch LA, Custódio MS, Dutra LMM, Rocha RP, Rehbein A. 2016. The 2014 southeast Brazil austral summer drought: regional scale mechanisms and teleconnections. Clim. Dynamics 46: 3737-3752. https://doi.org/10.1007/s00382-015-2800-1

Cemig. 2019. 33º Balanço Energético do Estado de Minas Gerais – BEEMG. Minas Gerais: CEMIG.

Cemig. 2010. Atlas Eólico de Minas Gerais. Minas Gerais: CEMIG.

Culture Change. 2017. The most frequently asked questions about wind energy (circa 2001-2004). Available at http://www.culturechange.org/wind.htm (accessed 2018 September 10)

Elliotti DL, Wendel LL, Gower GL. 1991. An assessment of the available wind energy potential in the contiguous United States. Springfield: Battelle.

Emeksiz C, Cetin T. 2019. In case study: Investigation of tower shadow disturbance and wind shear variations effects on energy production, wind speed and power characteristics. Sustainable Energy Technologies and Assessments 35: 148-159. https://doi.org/10.1016/j.seta.2019.07.004

EPE. 2019. Balanço Energético Nacional 2019: Ano Base 2018. São Paulo: EPE.

Hennessey Junior JP. 1977. Some Aspects of Wind Power Statistics. Journal of Applied Meteorology 16: 119-128.

IBGE. 2018. Panorama. Available at https://cidades.ibge.gov.br/brasil/mg/panorama (accessed 2018 October 07)

INMET. 2018. Estações Automáticas. Available at http://www.inmet.gov.br/portal/index .php?r =estacoes/estacoesAutomaticas (accessed 2018 October 10)

IPCC, 2014: Climate Change 2014: Synthesis Report. Contribution of Working Groups I, II and III to the Fifth

Assessment Report of the Intergovernmental Panel on Climate Change [Core Writing Team, R.K. Pachauri and L.A. Meyer (eds.)]. IPCC, Geneva, Switzerland, 151 pp.

Kalmikov A. 2017. Wind Power Fundamentals", Atmospheric and Planetary Sciences Massachusetts Institute of Technology. Available at https://www.researchgate.net/publication/317119352_Wind_Power_Fundamentals (accessed 2020 March 16)

Katinas V, Gecevicius G, Marciukaitis M. 2018. An investigation of wind power density distribution at location with low and high wind speeds using statistical model. Applied Energy 218: 442–451. https://doi.org/10.1016/j.apenergy.2018.02.163

Manwell JF, Mcgowan JG, Rogers AL. 2009. Wind Energy Explained: Theory, Design and Application. New York: John Wiley & Sons.

NOAA. 2018. Global Forecast System (GFS) [0.5 Deg.]. Available at https://www.ncei.noaa. gov/access/metadata/landing-page/bin/iso?id=gov.noaa.ncdc:C00634 (accessed 2018 October 08)

Natividade UA, Garcia SR, Torres RR. 2017. Tendência dos Índices de Extremos Climáticos Observados e Projetado no Estado de Minas Gerais. Revista Brasileira de Meteorologia 32: 600-614. https://doi.org/10.1590/0102-7786324008

Patel MR. 2006. Wind and Solar Power Systems: Design, analysis and operation. New York: Taylor & Francis Group.

Paula DLP, Cardoso FAC, Cardoso GPQ, Vieira EM. 2017. Modelagem espacial da velocidade do vento a 50, 75 e 100 metros de altura para o estado de Minas Gerais, Brasil, empregando geoestatística. Revista Brasileira de Geografia Física 10: 1281-1295. https://doi.org/10.26848/rbgf.v10.4.p1281-1295

Pishgar-Komleh SH, Keyhani A, Sefeedpari P. 2015. Wind speed and power density analysis based on Weibull and Rayleigh distributions (a case study: Firouzkooh county of Iran). Renewable and Sustainable Energy Reviews 42: 313–322. https://doi.org/10.1016/j.rser.2014.10.028

Prasad VS, Johny CJ, Malo P, Singh SK, Rajagopal EN. 2017. Global retrospective analysis using NGFS for the period 2000-2011. Current Science 112-2: 370-377. https://www.jstor.org/stable/24912364

Prasad VS, Mohandas S, Gupta MD, Rajagopal EN, Dutta SK. 2011. Implementation of Upgraded Global Forecasting Systems (T382L64 and T574L64) at NCMRW". Available at https://www.researchgate.net/publication/327727886_Implementation_of_Upgraded_Global_Forecasting_Systems_T382L64_and_T574L64_at_NCMRWF (accessed 2020 March 14)

Raimundo DR, Santos IFS, Tiago Filho GL, Barros RM. 2018. Evaluation of greenhouse gas emissions avoided by wind generation in the Brazilian energetic matrix: A retroactive analysis and future potential. Resources, Conservation & Recycling 137: 270–280. https://doi.org/10.1016/j.resconrec.2018.06.020

Rajagopal EN, Gupta MD, Mohandas S, Prasad VS, George JP, Iyengar GR, Kumar DP. 2007. Implementation of T254L64 Global Forecast System at NCMRWF. NCMRWF Technical Report: 1-42.

Ramos DNS, Lyra RFF, Silva Junior RSS, Cavalcante Segundo GH, Lopes GEV. 2018. Wind Power in Girau do Ponciano, Alagoas, Brazil Using Anemometric Data and Microscale Modeling. Revista Brasileira de Meteorologia 33: 279-288. https://doi.org/10.1590/0102-7786332007

Reboita MS, Amaro TR, Souza MR. 2018a. Winds: intensity and power density simulated by RegCM4 over South America in present and future climate. Climate Dynamics 51: 187–205. https://doi.org/10.1007/s00382-017-3913-5

Reboita MR, Ambrizzi T, Silva BA, Pinheiro RF, Rocha RP. 2019. The South Atlantic Subtropical Anticyclone: Present and Future Climate. Frontiers in Earth Science 7: 1-15. https://doi.org/10.3389/feart.2019.00008

Reboita MS, Gan MA, Rocha RP, Ambrizzi T. 2010. Regimes de precipitação na América do Sul: Uma revisão bibliográfica. Revista Brasileira de Meteorologia 25: 185-204. http://dx.doi.org/10.1590/S0102-77862010000200004

Reboita MS, Marietto DMG, Souza A, Barbosa M. 2017. Caracterização atmosférica quando da ocorrência de eventos extremos de chuva na região sul de Minas Gerais. Revista Brasileira de Climatologia 21: 20-37. http://dx.doi.org/10.5380/abclima.v21i0.47577

Reboita MS, Marrafon VH, Llopart M, Rocha RP. 2018b. Cenários de mudanças climáticas projetados para o estado de Minas Gerais. Revista Brasileira de Climatologia Ano 14: 110-128. http://dx.doi.org/10.5380/abclima.v1i0.60524

Reboita MS, Rodrigues M, Silva LF, Alves MA. 2015. Aspectos climáticos do estado de Minas Gerais. Revista Brasileira de Climatologia 17: 206-226. http://dx.doi.org/10.5380/abclima.v17i0.41493

Rego EE, Ribeiro CO. 2018. Successful Brazilian experience for promoting wind energy generation. The Electricity Journal 31: 13–17. https://doi.org/10.1016/j.tej.2018.02.003

Reis AL, Silva MS, Regis MV, Silveira WW, Souza AC, Reboita MS, Carvalho VSB. 2018. Climatologia e eventos extremos de precipitação no estado de Minas Gerais. Revista Brasileira de Geografia Física 11: 652-660. https://doi.org/10.26848/rbgf.v11.2.p652-660

Ribeiro L. 2017. Mapa da crise hídrica bate recorde e já abrange 265 municípios de Minas Gerais. Available at https://www.em.com.br/app/noticia/gerais/2017/11/20/interna_gerais,917953/mapa-da-crise-hidrica-bate-recorde-e-ja-abrange-265-municipios-de-mg.shtml (accessed 2018 June 01)

Salviano MF, Groppo JD, Pellegrino GQ. 2016. Análise de Tendências em Dados de Precipitação e Temperatura no Brasil. Revista Brasileira de Meteorologia 31: 64-73. https://doi.org/10.1590/0102-778620150003

Shamshirband S, Keivani A, Mohammadi K, Lee M, Hamid SHA, Petkovic D. 2016. Assessing the proficiency of adaptive neuro-fuzzy system to estimate wind power density: Case study of Aligoodarz, Iran. Renewable and Sustainable Energy Reviews 59: 429–435. https://doi.org/10.1016/j.rser.2015.12.269

Shoaib M, Siddiqui I, Amir YM, Rehman SU. 2017. Evaluation of wind power potential in Baburband (Pakistan) using Weibull distribution function. Renewable and Sustainable Energy Reviews 70: 1343–1351. https://doi.org/10.1016/j.rser.2016.12.037

Silva AR, Pimenta FM, Assireu AT, Spyrides MHC. 2016. Complementarity of Brazil's hydro and offshore wind power. Renewable and Sustainable Energy Reviews 56: 413–427. https://doi.org/10.1016/j.rser.2015.11.045

Silva ED, Reboita MS. 2013. Estudo da precipitação no estado de Minas Gerais – MG. Revista Brasileira de Climatologia 13: 120-136. http://dx.doi.org/10.5380/abclima.v13i0.33345

Souza A, Bouzahir H, Tizgui I, Guezar F, Ozonur D. 2019. Probability distributions of Wind speed in the Campo Grande, MS, Brazil. Revista Brasileira de Climatologia 25: 138-160. http://dx.doi.org/10.5380/abclima.v25i0.64110

Tan C, Zhi Q. 2016. The Energy-Water Nexus: A literature Review of the Dependence of Energy on Water. Energy Procedia 88: 277-284. https://doi.org/10.1016/j.egypro.2016.06.154

The Wind Power. 2019. Wind Energy Market Intelligence: V90/2000. Available at https://www.thewindpower.net/turbine_en_32_vestas_v90-2000.php (accessed 2019 December 02)

Wais P. 2017. A review of Weibull functions in wind sector. Renewable and Sustainable Energy Reviews 70: 1099-1107. https://doi.org/10.1016/j.rser.2016.12.014

Supplementary Material

The intensity of the wind is characterized by two functions in the Weibull distribution, a density function and a cumulative one, which explain the probabilities of occurrence of certain velocity values by means of equations and coefficients, where one of the factors *k* (shape) assumes values that explain the variability of the wind. Higher values of *k* indicate greater constancy of winds, with less occurrence of extreme values. Statistical analysis was performed for each selected weather station. The data observed at the stations (10 m) and those simulated by the GFS data for the nearest grid points (10 and 100 m) were considered. The calculation of the Weibull distribution was performed following the following stages:

1. Calculation of the standard deviation of speeds and average speed in each data set.
2. Calculation of the shape parameter *k* from Equation 1, which is dimensionless.
3. Using the average speeds and the *k* values found, the values of the scale factor c were calculated in ms^{-1}. The Gamma function Γ has a certain complexity, which is why it was implemented using MATLAB® software.
4. Construction of frequency hydrographs, that is, the distribution of wind intensities over time and their respective probability densities (using the MATLAB® software).
5. Adjustment of the Weibull curve following the shape and scale factors found. The graphics were made using the MATLAB® software.

The values of *c* and *k* for each meteorological station and for each data set are shown in Table IV and Figures 7 and 8.

Atmósfera 35(2), 377-393 (2022)
https://doi.org/10.20937/ATM.52956

CONTENTS

CO_2 variability in the Mexico City region from *in situ* measurements at an urban and a background site

Eugenia GONZÁLEZ DEL CASTILLO[1], Noémie TAQUET[1], Alejandro BEZANILLA[1], Wolfgang STREMME[1], Michel RAMONET[2], Olivier LAURENT[2], Yang XU[2], Marc DELMOTTE[2] and Michel GRUTTER[1]*

[1] *Instituto de Ciencias de la Atmósfera y Cambio Climático, Universidad Nacional Autónoma de México, Circuito de la Investigación Científica s/n, Ciudad Universitaria, 04510 Ciudad de México, México.*
[2] *Université Paris-Saclay, Commissariat à l'énergie atomique et aux énergies alternatives, Centre national de la recherche scientifique, Université de Versailles Saint-Quentin-en-Yvelines, Laboratoire des Sciences du Climat et de l'Environnement/ Institut Pierre-Simon Laplace, Bât. 12, avenue de la Terrasse, F-91191 Gif-sur-Yvette CEDEX, France.*
*Corresponding author: grutter@unam.mx

Received: August 8, 2020; Accepted: December 07, 2020

RESUMEN

Las áreas urbanas son importantes contribuyentes al aumento de los niveles globales de CO_2 debido a las actividades humanas, pero los registros continuos de concentración de CO_2 en las ciudades son escasos, especialmente en el mundo en vías de desarrollo. En este estudio presentamos cinco años de mediciones simultáneas *in situ* en un campus universitario en el sur de la Ciudad de México (UNAM) y en una estación a gran altura, el observatorio atmosférico Altzomoni (ALTZ), a 60 km de distancia del primer sitio. Las características de los ciclos diarios, la estacionalidad y las tendencias a largo plazo se extrajeron de ambas series de tiempo. El ciclo diario y estacional en la UNAM están dominados por la dinámica del crecimiento de la capa límite, mientras que la estacionalidad en Altzomoni está determinada tanto por la meteorología local como por la actividad fotosintética de la vegetación. Se estimaron tasas de crecimiento anual de CO_2 de 2.4 y 2.6 ppm año^{-1} para UNAM y ALTZ, respectivamente, en estrecha concordancia con las tasas de crecimiento global reportadas y con estimaciones previas de las tendencias de la fracción molar seca de CO_2 en columna. El monitoreo simultáneo en los sitios urbano y de montaña reveló un intercambio regular de masas de aire entre la ciudad y sus alrededores. El ciclo anual en la UNAM muestra un máximo de CO_2 secundario al final de la estación seca cuya fuente aún no se ha determinado, pero que probablemente esté asociado con el arribo de parcelas de aire enriquecidas con emisiones de quemas agrícolas. Asimismo, el ciclo diario de CO_2 en ALTZ durante la estación seca muestra evidencia de una llegada vespertina de masas de aire contaminado de las áreas urbanas vecinas. Este estudio sienta las bases de una próxima expansión en los sitios y capacidades de medición de CO_2 en el área metropolitana de la Ciudad de México.

ABSTRACT

Urban areas are important contributors to the increase of global CO_2 levels due to human activities, but continuous records of CO_2 concentration in cities are scarce, especially in the developing world. In this study we present five years of simultaneous, in-situ measurements at a university campus in the south of Mexico City (UNAM) and at a high-altitude station, the Altzomoni atmospheric observatory (ALTZ), 60 km apart from the first site. The characteristics of the daily cycles, seasonality, and long-term trends were extracted from both time series. The features of the daily and seasonal cycles at UNAM are dominated by the dynamics of the boundary layer growth, while the seasonality at Altzomoni is determined by both the local meteorology and the photosynthetic activity of the vegetation. Annual CO_2 growth rates of 2.4 and 2.6 ppm yr^{-1} were estimated for UNAM and Altzomoni, respectively, in close agreement with reported global growth rates and with previous estimates of total column CO_2 trends. The simultaneous monitoring at the urban and the mountain sites revealed a regular exchange of air masses between the city and its vicinities. The annual cycle at UNAM shows a secondary CO_2 maximum at the end of the dry season, the source of which is yet to be determined, but likely due to incoming air parcels enriched with emissions from agricultural burnings. Likewise, the daily CO_2 cycle at ALTZ during the dry season shows evidence of a daily afternoon arrival of polluted air masses from the neighboring urban areas. This study lays the foundation of an upcoming expansion in the CO_2 measurement sites and capabilities in the metropolitan area of Mexico City.

Keywords: Carbon dioxide, Mexico City, Natural variability, Urban pollution, Long-term trends.

1. Introduction

An interest in determining the natural and anthropogenic trends of carbon dioxide (CO_2) began in the 1950s after C.D. Keeling performed the first continuous measurements to establish a global atmospheric record (Keeling, 1960). The amount of CO_2 in the atmosphere is regulated by a balanced exchange with the Earth's oceans, biosphere, and geosphere. However, recent human activities related mostly to fossil fuel combustion and land-use changes have resulted in a 47% increase in the global average CO_2 concentration, from 277 ppm at the beginning of the pre-industrial era (i.e. 1750) to 407 ppm in 2018 (Friedlingstein et al., 2019).

It has been estimated that people living in urban areas use up 78% of the world's consumed energy and are responsible for emitting more than 60% of the anthropogenic CO_2, which implies that mitigation strategies adopted by city and local governments could be the most effective to slow the current growth in ambient Greenhouse Gas (GHG) concentrations (World Bank, 2010; Bazaz et al., 2018). Efficient mitigation policies hinge on having realistic estimates of the intensity and distribution of sinks and sources of CO_2 in the landscape. However, emissions from urban environments are commonly estimated from inventories of fixed and mobile sources, emission factors and usage data, a type of bottom-up methodology associated with considerable uncertainty (Marland et al., 2009) and updated infrequently. Recent studies have shown that in addition to thorough inventories, a combination of continuous monitoring of CO_2 dry mole fraction at surface stations and atmospheric transport modelling are required for a verifiable quantification of the emissions landscape in a complex urban environment (Lauvaux et al. 2013; Bréon et al., 2015; Turnbull et al., 2014; Leip et al., 2017; Wu et al., 2018). By incorporating the movement of air masses within and outside urban boundaries, an integral top-down approach can also address the influence of non-local sources and sinks that might not be contemplated in an urban inventory but nonetheless contribute to the urban GHG concentrations. Such a comprehensive appraisal of emissions is still infrequent, particularly in cities in the developing world.

The most recent emissions inventory for Mexico City Metropolitan Area (22 million inhabitants) (SEDEMA, 2018) reports that 52.5 Mt of CO_2 were emitted in 2016 (10% of the national emissions), contributing 62.3 Mt of CO_2-equivalent when the other main GHGs are considered. The transportation sector is responsible for about 65% of the CO_2 emissions, while point and area sources contribute up to 17-18% each. This inventory reports an estimated 7% uncertainty for CO_2 emissions (SEDEMA, 2018), calculated from published uncertainties for emission factors and activity data, as well as expert opinions, as recommended by the Good Practice Guidance of the IPCC (IPCC, 2000). There has not, however, been an independent verification of either the anthropogenic emission values nor their stated uncertainties. Regarding monitoring efforts, there are only a few studies in Mexico documenting regional CO_2 variability. Continuous CO_2 concentrations were measured at the Universidad Nacional Autónoma de México (UNAM) campus in southern Mexico City during 20 days in September 2001 with an infrared spectrometer (Grutter, 2003), and reported an average concentration of 374 ppm. Since 2013, CO_2 total column measurements have been carried out both at UNAM and at Altzomoni (Baylon, 2017), a high-altitude rural station 60 km ESE from the UNAM campus (Fig. 1). Using Fourier Transform Infrared (FTIR) spectroscopy in solar absorption mode, this study found annual increases of 2.4 ppm yr^{-1} for 2016 at UNAM, and 2.6 ppm yr^{-1} at Altzomoni during the 2013-2017 period. Since 2009, NOAA also performs weekly flask samplings at the High-Altitude Global Climate Observation Center (MEX station, 4,469 m.a.s.l.) near Pico de Orizaba, in the state of Veracruz, 140 km east of Altzomoni, as part of the Global Greenhouse Gas Reference Network sites.

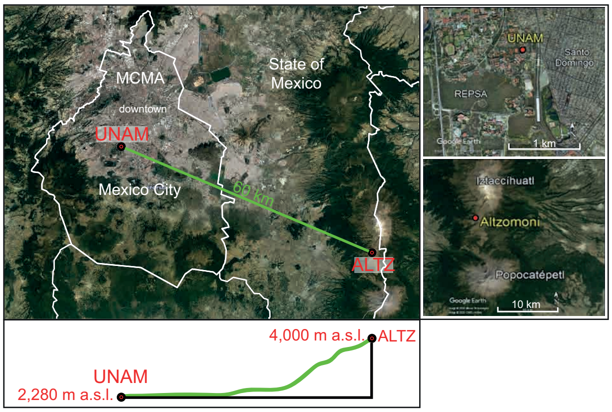

Fig. 1. Location of UNAM station within the Mexico City Metropolitan Area (MCMA) and ALTZ mountain site (top, left), separated by a line-of-sight distance of 60 km (green line); political boundaries of Mexico City and the State of Mexico are shown in white and the altimetry is shown in the lower panel. Right panels show details of the neighboring terrain for UNAM (top) and ALTZ (bottom).

In the top-down approach that combines *in situ* observations of CO_2 concentrations with atmospheric transport models in cities, a critical consideration is the ability of the sampling scheme to discriminate between the regional background level and the local enhancements of CO_2 due to fossil fuel usage in the urban area (Turnbull et al., 2014). Coastal locations and remote sites have been traditionally selected for background measurements, since they are representative of the global, well-mixed, marine boundary layer, free from the influence of local sources or sinks of CO_2. For a continental city, however, mountain stations at nearby locations may be a better option. Under the adequate meteorological conditions, these sites capture a free-troposphere, regional background signal better suited to interpret patterns of regional exchange (Zhang et al., 2013; Turnbull et al., 2014; Conil et al., 2019). However, city sources and sinks may still influence the background sites (Zellweger et al., 2009; Zhang et al., 2013; Yuan et al., 2019), thus a screening procedure is needed to assure the regional background estimation is free from the signal of the adjacent urban environment.

In this contribution, we present a 5-year time series showing the variability of surface CO_2 in central Mexico using high-precision *in situ* analyzers at two stations, UNAM and Altzomoni, representing urban and background environments. Our main objective is to describe the measurement systems at both sites, examine their performance, and characterize the trend, seasonality and daily cycles on each record. We aim to examine the suitability of the mountain station to monitor regional background conditions, and to evaluate the usefulness of this record to discriminate between the signals of the biogenic exchanges and the anthropogenic enhancement at the urban station.

2. Site description

2.1. The RUOA network

The University Network of Atmospheric Observatories (RUOA, https://ruoa.unam.mx) is comprised of 16 measurement stations within the Mexican territory that provide high-quality data for research and teaching. Six of these stations in both urban and natural settings include high precision GHG analyzers and all of the RUOA stations are fully instrumented to routinely monitor ancillary meteorological variables such as air temperature and relative humidity, wind speed and direction, global solar radiation and barometric pressure, among other atmospheric parameters. The two stations featured in this study, located in central Mexico, are part of this network.

2.2. The urban station

The UNAM atmospheric observatory (19.3262 N, 99.1761 W, 2280 m.a.s.l.) is situated atop of a three-story building on the eastern edge of the UNAM main campus (730 ha), in southwestern Mexico City, 13 km from the city center (Fig. 1). North and west of the observatory, the campus includes low-rise buildings interspersed with lawns and patches of native shrub. To the east, there is a major public transportation hub and a compact, low-rise, highly populated area flanking the campus (Santo Domingo). An urban natural reserve with an area of 237 ha, called Reserva Ecológica del Pedregal de San Ángel

(REPSA), spreads to the south and southwest of the observatory and covers a third of the campus area. This reserve represents a relict of the vegetation that covered this portion of the city before its explosive urbanization during the 20th century (Lot and Camarena, 2009). The dominant vegetation type in the REPSA is xerophilous scrub with few interspersed trees, growing on shallow and low-nutrient soil over a basaltic substrate (Rzedowski, 1954). The climate is temperate sub-humid (García, 1988), with summer rains. Daily records of temperature and precipitation are kept by the Meteorological Observatory of the College of Geography of UNAM since 1963 (http://observatoriometeorologico.filos.unam.mx/2016/10/metadatos-historicos). In a period of 57 years, the annual temperature averages 15.6 ºC (min/max range from 14.3 ºC to 17.4 ºC), the temperature peaks at 26.7 ºC on average in May, the warmest month of the year (range 23.2 ºC to 30.9 ºC), and the daily minimum temperature is 3.9 ºC on average in January, the coldest month (range 1.5 ºC to 6.8 ºC). Mean annual precipitation is 870 mm (ranging from 624 mm in 1982 to 1201 mm in 2006), 90% of which falls between May and October. The annual maximum occurs in August and September (~180 mm/month) and the minimum in January, when only 5 mm of total precipitation fall on average. From RUOA hourly records, at a daily scale, wind speed peaks around 17-18 h and the minimum occurs at 5-7 h. Annually, the windiest months are March and April, with daily peak wind speeds of 3.0 ± 1.1 m/s on average, while the daily minimum peak occurs in December, with only 1.9 ± 0.9 m/s on average. The diurnal cycle of wind direction will be discussed in terms of its influence on CO_2 mole fraction in subsequent sections.

2.3. The high-altitude station

The Altzomoni (ALTZ) atmospheric observatory (19.1187 N, 98.6552 W, 3985 m.a.s.l.) is located 60 km ESE in a straight line from the UNAM site (Fig. 1), and 48 km at 280º from the city of Puebla (1.5 million inhabitants). The observatory lies in a mountainous pass between the active Popocatépetl volcano to its south, and the dormant Iztaccíhuatl volcano to its north, inside the Izta-Popo-Zoquiapan National Park and Biosphere Reserve (Fig. 1), far from immediate sources of anthropogenic emissions. The immediate surroundings of the observatory are just above the timberline (3,700-3,800 m.a.s.l.) (Beaman, 1962); the vegetation cover consists of subalpine grassland dominated by dense tussock grasses and some scattered individuals of *Pinus hartwegii* Lindl. Pine trees become more abundant at slightly lower altitudes, and along other conifer species form dense forests in the hillsides of the volcanic ridge. From hourly meteorological records kept by RUOA since 2011, the mean annual temperature is 4.9 ºC (ranging from 4.7 ºC to 5.3 ºC); the warmest month is April, with a daily maximum temperature of 9.7 ºC on average (range from 3.9 ºC to 14.8 ºC), and the coldest month is January, with a daily minimum temperature of –0.1 ºC on average (range from –6.5 ºC to 4.8 ºC). Throughout the year, the diurnal temperature oscillation is moderate (6.1 ± 1.9 ºC). Annual precipitation averages 780 mm (from 573 mm in 2016 to 1052 mm in 2013); on an annual basis, 85% of the rain falls between May and October. June and August are the wettest months of the year (~170 mm/month) while December is the driest, with only 5 mm of average cumulative rain. Daily wind speed peaks at 10 h from October to mid-March at an average of 4.7 ± 2.7 m/s; the maximum shifts to a broader peak around 16 h during March to May, at 4.1 ± 1.7 mean wind speed, and it is displaced to the late evening (20-21 h) for the whole summer (June to September), when the it reaches 5.6 ± 2.7 m/s on average, the highest daily maxima year-round. The weather is also characterized by high levels of global horizontal irradiation (5.0 kWh m^{-2}), and an average of 32 frost events per year. Climate is temperate, semi-cold, sub-humid, with a mild summer (García, 1988).

3. Sampling protocols and instrument calibration

Sampling at the UNAM site of atmospheric mole fractions of CO_2, CH_4, CO and H_2O started on July of 2014, with a Cavity Ring-Down Spectrometer (CRDS) model G2401 from Picarro Inc. Since the beginning of its operation and until July 2019, the air inlet was located on the rooftop of the observatory, at 16 m.a.g.l. The sampling line length from the inlet to the analyzer was under 5 m; air was drawn to the analyzer with an external low-leak diaphragm pump (A0702, Picarro Inc.) and no filtering or air drying system was installed. A calibration system was set up in December 2018, when three 29-liter gas tanks (see Table I), traceable to the WMO X2007 scale for CO_2, were acquired from the National Oceanic and Atmospheric Administration Earth System Research Laboratory (NOAA ESRL). Each gas cylinder was equipped with a Scott Q1-14B nickel-plated brass regulator (Air Liquide) and connected to a programmable 8-port rotary valve (EMTSD8MWE, VICI) that selects between gas streams. The sampling line was replaced by a dedicated tubing of ¼" OD (Synflex 1300, Eaton); air drawn from the inlet passes through a 2 µm ceramic filter (FS-2K, M&C TechGroup), a 2 µm sintered filter (SS-2F-2, Swagelok), and then to the rotary valve. Before reaching the analyzer, the air is dried using a Nafion membrane (MD-070-144S-4, PermaPure) in 'reflux mode': the stream of dried air from the low-pressure exhaust of the analyzer as a purge gas in counter-flow.

Prior to installing the Nafion dryer, a single calibration was performed on December 2018 without drying the sample, and the resulting coefficients were retroactively applied to correct all past measurements. Additionally, the sensitivity of the Picarro analyzer to varying levels of humidity in the incoming air stream was tested through the water droplet method (Rella et al., 2013). A 0.2 ml droplet of ultra-pure water (Milli-Q, Millipore) was injected with a syringe directly into the inlet of the CRDS instrument, upstream of the hydrophobic internal filter, in order to humidify the dry gas stream from a gas tank. The wetted internal filter is progressively dried by evaporation with the dry air stream applied, which results in a gas stream with a stable GHG dry mole fraction and a decreasing water vapor content. The procedure was repeated three times and the results used to assess the Picarro built-in correction and to derive analyzer-specific coefficients to correct for the effects of H_2O on the GHG dry mole fraction measurement, mainly dilution and spectral line broadening. After these initial tests, a monthly calibration was established.

In March 2019 a second and longer dedicated sample tube was installed at a nearby tower so that the inlet reached 24 m.a.g.l., in order to reduce high-frequency variations from local sources. During a period of about 5 months, the incoming air stream to the analyzer was alternated between the low and high inlet every 15 min; the first 5 min of each period were discarded, and the molar fraction of CO_2 was compared between heights. On 23 August 2019 the lower inlet was cancelled; however, given that the measurements done at 24 m comprise a minor portion of the dataset all analysis presented here are based solely on the roof-level data.

In August 2019 the set of NOAA cylinders was replaced by three calibration tanks and one short-term target tank (40 l) provided by LSCE, and calibrated against their NOAA secondary scale (Table I). This set of standards encompass a higher range of molar fractions of CO_2 (and CH_4) that are better suited for the higher values expected in the urban atmosphere of Mexico City. A target tank which does not participate in the calibration corrections, is measured routinely as a quality control (Laurent, 2017). A final measuring protocol with the target tank alternating with the sampling line and one calibration per month was established (Table II).

A CRDS analyzer (Picarro G2401) was installed at ALTZ on August 2014. On December 2018, a single calibration using the NOAA standards was performed on the analyzer and the resulting coefficients applied

Table I. Characteristics and site of deployment of calibration standards and target gas cylinders.

Tank ID	Lab	CO_2 (μmol mol^{-1})	CH_4 (nmol mol^{-1})	CO (µmol mol –1)	Deployment[a]	
					Dec 2018-Aug 2019	Aug 2019-ongoing
CC506424	NOAA	391.16	1827.25	unknown	UNA.Cal1	ALZ.Cal1
CB11619	NOAA	405.21	1896.25	unknown	UNA.Cal2	ALZ.Cal2
CC506485	NOAA	420.22	1961.20	unknown	UNA.Cal3	ALZ.Cal3
D856136	LSCE	366.69	1721.43	222.43	--	ALZ.TGT

[a] Cal: calibration tank; TGT: target tank.

to past measurements. The water droplet test described above was also carried out. Initially the gas sampling tube was connected to a glass manifold that extended above the roof of the enclosure and reached a height of aprox. 4 m.a.g.l. The inlet was replaced by a dedicated sampling line of ¼” OD (Synflex 1300, Eaton) at the same height on January 2019; air is drawn by the external diaphragm pump of the CRDS analyzer and passes through a 2 µm ceramic filter (FS-2K, M&C TechGroup) before reaching the analyzer.

On August 2019, a calibration system was set up at ALTZ using the three NOAA calibration standards previously deployed at UNAM (Table I), with an identical valve and filters, and an identical measuring and calibration sequence (Table II). A Nafion dryer is yet to be installed. At this date the UNAM calibration scale was changed with a set of tanks (traceable to WMO-X2007 reference scale) provided by LSCE. Since the measurements made after this change are not used in this study, we do not describe this new scale further.

4. Data processing

4.1 Record filtering, seasonality extraction and trend retrieval

The spectrometers at both locations collect raw data at ~0.3 Hz. The data were averaged and their standard deviation calculated per minute, then per hour. Calibration periods and times affected by any operator’s interference with the instrument were flagged out, which amounted to 4.6% of hours at UNAM and 15.8% at ALTZ. Daily averages were calculated on the filtered datasets. Hourly data were detrended by subtracting the daily mean from each hourly average in order to estimate diurnal cycles for each station, free of the influence of the seasonal cycle and long-term trend.

To extract the trend and the seasonal features of the evolution of CO_2 at each station, the hourly data were filtered to include only nighttime periods representative of background conditions at ALTZ and those under well-developed turbulence conditions at UNAM. We looked for correlations between dry-air CO_2 mole fractions and local meteorological conditions (e.g. wind direction, wind speed, temperature), but no clear patterns emerged. The filtering criteria were thus based only on time-of-day and statistical variability.

Seasonal features, peak-to-trough amplitudes, and long-term trends were estimated for each station using the curve fitting described in Thoning et al. (1989) and the Python code made available by NOAA (Thoning, 2018). This fitting procedure finds a function with a number of polynomial terms and a number of harmonics that approximate the long-term trend of the data and the annual cycle, respectively. We used two polynomial terms and four harmonic terms in our function fitting. The residuals were then filtered through two low-pass filters, one short-term (80 days) to smooth the data, and one long-term (667 days) to capture interannual variations not determined by the fitted function. The polynomial portion of the fitted function plus the residuals of the long-term cutoff filter give a trend series that represents the de-seasonalized upward growth of the CO_2 concentration. The first derivative of this trend series constitutes a continuous growth rate series, i.e. the rate of change of the upward trend. The trend was also used to compute a discrete annual growth rate of CO_2, defined as the difference between the average CO_2 mole fraction for the month of December of any given year and January of the following year, and

Table II. Final measurement and calibration scheme for Picarro analyzers on UNAM and ALTZ stations.

	Injection duration (min)	Cycles	Frequency
Calibration standard 1	20	4	Monthly
Calibration standard 2	20	4	Monthly
Calibration standard 3	20	4	Monthly
Short-term target	20	1	Every 6 h
Atmospheric air	1200		

the average mole fraction recorded during the same pair of months of the preceding year (Dlugokencky and Tans, 2019).

4.2. Uncertainties

The two analyzers installed at UNAM and ALTZ were purchased on 2014 and they were both manufactured by Picarro Inc. at the same period (S/N CFKADS2141 and CFKADS2142). The precision of the two instruments, calculated as the standard deviation of raw data over 1-minute intervals when measuring calibration gases, are equal to 0.03 ppm and 0.024 ppm respectively for UNAM and ALTZ. This is compatible with the precisions calculated for similar instruments deployed at ICOS sites in Europe (Yver Kwok et al., 2021). Unfortunately, the instruments were operated without reference measurements from summer 2014 to December 2018, so we cannot fully characterize the repeatability and drift for this period. Regular measurements of a target gas at UNAM, performed once per day since December 2018, show a very stable repeatability of 0.02 ppm. Monthly calibrations done at UNAM since December 2018 do not indicate a significant drift. We assume that the calibration coefficients established in December 2018 in the two stations had not changed since the summer of 2014. This assumption leads to an increasing uncertainty the further we go back in time. Most G2401 analyzers have a low CO_2 drift, but a drift up to 0.1 ppm yr^{-1} cannot be excluded (Yver Kwok et al., 2015).

It is important to point out that the calibration scale used at UNAM does not cover the full range of measurements, especially the high concentrations observed at night. Indeed, at UNAM, 8% of the daytime observations and 22% of the night time hourly means are above 450 ppm. However, the Picarro G2401 has been evaluated at different laboratories and has exhibited remarkable linearity. Yver Kwok et al. (2015) have tested the same instrument for CO_2 concentrations up to 500 ppm, and the NOAA central laboratory uses an earlier version of the same CRDS analyzer (Picarro G2301) to certify calibration material up to 600 ppm (Tans et al., 2017). Both studies show the response of the CRDS instrument to be linear. The results of the linear fit to our sequences of three calibration tanks indicate that the reduced scale does not have an impact on the linearity of the instruments' response. The residuals of the linear regressions are within a min/max range of –0.02 to +0.04 ppm and –0.02 to +0.03 ppm for UNAM and ALTZ, respectively. The mean RMSE for all instances of the calibrations are 0.01 ppm for UNAM, and 0.02 ppm for ALTZ.

The humidifying technique of the water droplet performed on site allows the evaluation of the built-in factory water vapor correction, and the determination of a new correction, specific to the tested analyzers, with an uncertainty typically around 0.03 ppm for CO_2 (Laurent et al., 2019). The built-in factory correction assessment showed an unusual CO_2 response to H_2O with a residual correction error of –0.22 ± 0.02 ppm and –0.03 ± 0.02 ppm for UNAM and ALTZ respectively, over their site-specific H_2O atmospheric range. The residual error of the specific H_2O correction determined on site was estimated to be between –0.05 ppm and +0.05 ppm for CO_2, depending on the H_2O content. Even though the new specific correction seems to improve the performance, it has not been implemented on the database yet, due to our low confidence on the unusual CO_2 response to H_2O. Indeed, the droplet test must be performed again on site in order to increase this level of confidence. Moreover, the H_2O correction residual error may drift over time for CO_2. The drift magnitude depends on the H_2O content: below +0.01 ppm CO_2 per year for H_2O lower than 10 000 ppm and up to +0.03 ppm CO_2 per year for H_2O between 20 000 and 25 000 ppm (Laurent et al., 2019). In consequence, with a H_2O content typically below 15 000 ppm at UNAM and 10,000 ppm at ALTZ during the dry season (November to April), the H_2O correction drift is not significant (below 0.05 ppm CO_2) for either station over the 4-year period preceding the water droplet test (December 2018). During the wet season (May to October), with a H_2O content up to 25,000 and 20,000 ppm respectively for UNAM and ALTZ, the H_2O correction drift may induce a residual error up to –0.14 and –0.11 ppm of CO_2 at these locations, respectively, on the oldest data and highest H_2O content. However, based on experience collected by testing more than 50 CRDS analyzers at LSCE (Laurent et al., 2019), the factory water vapor correction assessed on UNAM and ALTZ analyzers does not show a typical drifted response to H_2O. At this stage, the overall uncertainty related to the water vapor correction for UNAM and ALTZ is estimated at ±0.2 ppm and ±0.05 ppm CO_2, respectively, over the whole period.

5. Results and Discussion

5.1. Daily cycles

The average daily course of CO_2 molar fractions at UNAM is presented in Figure 2A, for both weekdays (Monday to Friday) and weekends/holidays. Irrespective of the day of the week, the overall pattern is consistent with a dominant effect of the boundary layer height on the CO_2 concentration. A maximum CO_2 level is reached daily between 6 and 7 h (all times are LST), then as sun rises and warms the surface, the boundary layer grows and turbulent mixing of the atmosphere increases, as described by

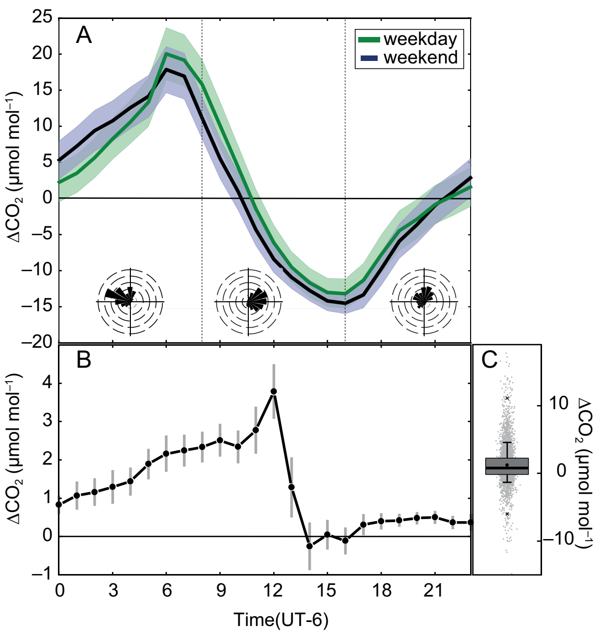

Fig. 2. A) Diurnal cycle of hourly, detrended CO_2 measurements at UNAM for weekdays (green) and weekends/holidays (blue). The polar plots inserted show the frequency distribution of wind directions for the periods 0-8 h, 8-16 h, and 16-24 h. B) Mean diurnal difference in CO_2 molar fraction sampled at 16 m and 24 m.a.g.l between March 8th and August 23rd, 2019. Error bars are 95% CI. C) Box and whiskers plot of difference in molar fraction between heights. Percentiles shown are the 1st and 99th (crosses), 10th and 90th (cap of whiskers), 25th, 50th and 75th (box). The central black dot indicates the mean.

García-Franco et al. (2018). The CO_2 is diluted over a larger air volume, so its concentration decreases steadily, down to its minimum at 16 h. After sunset, the increase in atmospheric stability reduces the depth of the boundary layer and produces a steady buildup of CO_2 during the night in this shallower layer.

A further inspection of the prevalent wind direction at different times of the day confirms that the boundary layer dynamics is the main controller of the observed CO_2 cycle and offers some insight into the influence of the underlying urban surface. The polar histograms inserted into Figure 2A show a rapid change in the predominant wind direction from the NW quadrant at night (23 - 8 h) to NE-SE sector for most of the day (8 - 15 h), while from 16 h to 23 h the wind directions are more evenly distributed over the NE to WNW sector. The location of the UNAM station is such that the wind coming from the west should carry the signal of the more vegetated surface that releases CO_2 at night, while larger emissions could be expected from the more urbanized and almost devoid of vegetation eastern sector during the day. However, the observed daily pattern does not show an association between the relative position of the station and the wind direction, as the concentration falls steadily during the times of the day when the predominant wind comes from the heavily populated sector. The nighttime buildup might include the CO_2 respired by the vegetation on the campus side, but the observed enhancement occurs year long and even intensifies in winter, when the vegetation is less active.

In megacities where large anthropogenic emissions dominate, CO_2 molar ratio may differ between weekdays and weekends since traffic and other human activities in general diminish noticeably during non-working days. Analyses of surface CO_2 records in Melbourne (Coutts et al., 2007), Lecce (Italy) (Contini et al., 2012), Mexico City (Velasco et al., 2014), Helsinki (Kilkki et al., 2015), Sakai (Ueyama and Ando, 2016) Beijing (Cheng et al., 2018) and Chennai (Kumar and Nagendra, 2015), have found perceptible influences of traffic volume on daily concentration and flux patterns. Even in remote marine stations and continental mountain measurements, the weekly periodicity of the anthropogenic activity of nearby cities has been detected and used to unravel the biogenic and anthropogenic contributions to atmospheric CO_2 (Cerveny and Coakley, 2002; Yuan et al., 2019). However, it is also common for the daily to seasonal variability of urban environments to be driven by the dynamics of the boundary layer depth, concealing the signal of the human activity, as has been shown in locations like Basel (Schmutz et al., 2016), and in suburban and central London (Hernández-Paniagua et al., 2015; Helfter et al., 2011). At UNAM, we found similar daily cycles of CO_2 molar ratio for weekdays and weekends/holidays (Fig. 2A). On non-working days, a peak anomaly of ~17 ± 3 ppm with respect to the daily average occurs between 6 and 7 h, while during the weekdays the peak reaches 20 ± 4 ppm. The only noticeable but transient difference between days of the week occurs in this early morning maxima for April and May (not shown), when it reaches 32.6 ± 4.0 ppm above the daily average from Monday to Friday, in contrast to 23 ± 3 ppm during weekends and holidays. On the year-round average, the mean daily amplitude (peak to trough) during weekdays is 45 ± 17 ppm, and 43 ± 18 ppm during non-working days. Weekday and weekend daily courses show considerable overlap, and there are no evident features associated to diurnal changes in traffic volume.

Our analysis indicates that there is a significant positive difference between the roof level measurements and those made 8 m above, for the period between March and August 2019 (mean difference 1.23 ppm, [1.15, 1.37] 95% CI) (Fig. 2B, 2C). This gradient reaches a maximum of 4 ppm at 6 h, coinciding with the largest CO_2 accumulation in the stable surface layer before dawn (Fig. 2B). The difference decreases rapidly as the turbulent mixing takes up in the early morning, remains stable until 17 h, and begins to gradually grow again as the sun goes down. On average, between 9 h and 17 h the difference between the two sampling levels is equal to 0.31 ± 0.20 ppm.

At ALTZ, four diurnal cycles in the de-trended CO_2 mole fraction can be distinguished as the year progresses (Fig. 3). The periods roughly correspond to dry wintertime (Jan-Mar), dry springtime (Apr-May), rainy season (Jun-Oct) and late fall (Nov-Dec),

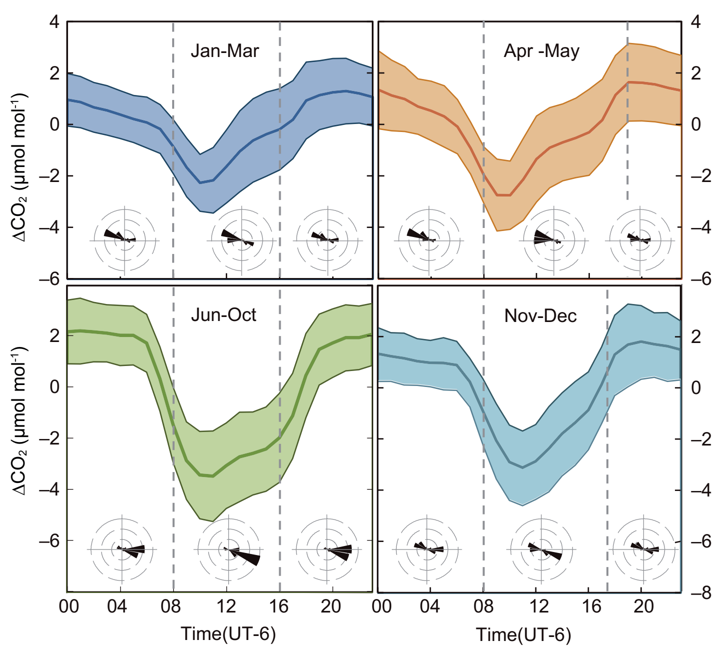

Fig. 3. Diurnal cycles from hourly, detrended CO_2 measurements at Altzomoni (ALTZ) for different periods of the year. Inserts are circular histograms of the wind direction for the periods delimited by the light gray vertical lines.

when some precipitation may still occur. The overall average daily amplitude is 7.2 ± 2.5 ppm; it goes from a minimum of 5.7 ± 2.1 ppm in the dry winter period to a maximum of 8.3 ± 2.3 ppm in the rainy season. From November to May, the daily maximum occurs in the evening, between 18 and 21 h, and the mean concentration continues to decrease the rest of the night. During the rainy season the maximum is displaced to a later period (0-5 h) and the CO_2 mole fraction is mostly constant throughout the night. A sharp decrease ensues sunrise, and the minimum is reached from 9 -11 h; slightly earlier in Apr-May (~9 h) and slightly later from June to Dec (~11 h). From June to October the afternoon increase from the minimum CO_2 mole fraction is slow up to 16 h, and then increases quickly back to nighttime values.

In general, the seasonal changes in daily patterns of surface CO_2 at the ALTZ mountain site are consistent with a combination of the aforementioned regional boundary layer dynamics and the local effect of vegetation activity. The tussock grasses in the immediate vicinity of the station and the conifers covering the hillsides of the mountainous range capture and release carbon more actively during the warm, wet season. After the onset of the rains in May, we observe a larger daily amplitude of the CO_2 cycle, a more prolonged afternoon minimum, and a larger accumulation at night from June to October, all consistent with increased photosynthetic uptake during the day and increased respiration by vegetation at night. However, a stronger vegetation sink and a more effective vertical mixing of the surface layer are correlated on daily, seasonal and annual basis, so their relative contributions to the daily patterns along the seasons are not easily unraveled.

One interesting feature of the daily cycle of the dry season, is a small but consistent enhancement from midday to the late afternoon (11-16 h). It is more prominent in April and May, and although present during the rainy season, it is considerably shortened (12-15 h). This afternoon enhancement could be the result of a change in local biogenic emissions, the transport of air parcels enriched with anthropogenic CO_2 from adjacent cities, or a mixture of these situations. It has been documented that the convective boundary layer starts to develop over Mexico City one hour after sunrise and reaches 2000 m above UNAM's elevation around midday (Shaw et al., 2007, García-Franco et al. 2018). From January to May, wind from the WNW sector dominate from 0 to 16 h (Fig. 3), consistent with an upslope flow of polluted air masses from the MCMA arriving to ALTZ at midday. In contrast, wind from the E-ESE prevails from June to October; if no recirculation occurs, the smaller increase in CO_2 from 12 to 15 h in the rainy season could be the result of lower emissions from Puebla reaching ALTZ, having being partially offset by the photosynthetic uptake of crops and forests as air traversed over the valley and the mountain slope. Granted, the anemometer used in this analysis is situated only at 5 m.a.g.l. at the station, therefore its measurements are likely influenced by the local topography and might not reflect regional circulation. However, the detection of an enhancement of other combustion-related tracers such as CO and NO_x at the Altzomoni station during the afternoon is consistent with polluted air parcels being transported from the major neighboring cities (Whiteman et al., 2000; Baumgardner et al., 2009). Preliminary analyses of FTIR solar absorption measurements at Altzomoni show larger CO total columns from January to June, and transient elevated values around 15 h and 18 h in April and May only (N. Taquet, unpublished data).

At the end of the dry season, a contribution from biomass burning to CO_2 levels can also be expected from both forest fires and prescribed agricultural burnings, a common practice in the region. However, this alone would not explain the persistence of the daily enrichment well into July and August, in the middle of the rainy season, because most natural and manmade fires take place in March and April, are less frequent in May, and stop after the rains start (Gutiérrez Martínez et al., 2015).

5.2. Seasonal variation and long-term trend

The hourly measurements obtained at UNAM from July 2014 to August 2019 present a large variability (Fig. 4, gray). Once the invalid data -previously defined as calibration periods and times when operator interference occurred- are discarded, the hourly average of CO_2 mole fraction ranges from 392 to 577 ppm. The overall mean (± SD) of the original (not de-trended) series is 427.7 ± 16.5 ppm. Values in excess of 450 ppm constitute 17% of the dataset. The average mole fraction are in reasonable agreement with a previous study of flux measurements over a densely populated neighborhood in Mexico City, in which Velasco et al. (2005) found a mixing ratio range of 398 to 444 ppm, and an average of 421 ppm. The slightly higher mean concentration reported here could be attributed to a combination of the CO_2 added to the atmosphere between 2003 and 2018 globally (35 ppm) (Dlugokencky and Tans, 2019) and the increase in CO_2 emissions that the city has experienced in the years since the Velasco et al. (2005) study took place. The official CO_2 annual emissions in 2004 were 35.8 Mt (SEDEMA, 2008) and 52.5 Mt for the year 2016 (SEDEMA, 2018). Additionally, sampling in the earlier study took place during a short, three-week campaign in spring which included Easter week, a holiday period for schools in Mexico (Velasco et al., 2005). Our CO_2 levels are comparable to those reported for other megacities like Beijing (Song and Wang, 2012) where monthly averages range from 400 to 440 ppm. Similar concentrations are also observed in Paris, Cité des Sciences, where the CO_2 average observed over the same period (2015-2019) equals 426 ppm, with a higher variability in the hourly concentrations, ranging from 388 to 754 ppm (Lian et al., 2019), probably due to a more dynamic atmospheric boundary layer (Pal and Haeffelin, 2015). On the other hand, the short term variability (calculated as the hourly standard deviation of minute averages) is higher at UNAM site (3.6 ppm) compared to Cité des Sciences in Paris (2.0 ppm), which probably reflects a higher exposure to local sources of CO_2.

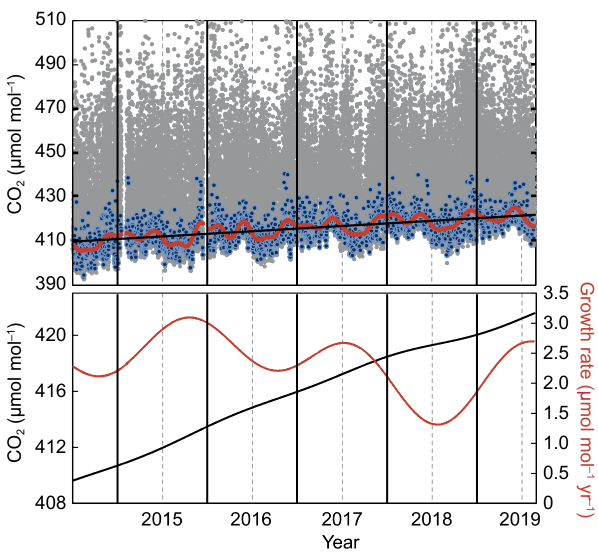

Fig. 4. Above: Hourly (gray) and daily (blue) average of daytime (13-17 h) CO_2 mole fractions at UNAM, smoothed fitted function (red) and polynomial component of fitted function (black). Below: trend (black) and growth rate (red) for 2014-2019.

In order to estimate the five-year trend in the UNAM series, we selected only daytime periods from 13 to 17 h, with hourly standard deviations SD < 6 ppm. These filters simultaneously exclude hours when transient and very local effects were recorded (e.g. people working close to the gas intake), and periods when hour-to-hour means differ by more than 3 ppm. Point-like local disturbances are less common at night, but CO_2 concentrations steadily rise all night long as the boundary layer stability increases; additionally, nocturnal CO_2 exhibits larger effects of seasonality compared to daytime (not shown). We excluded also the observations made at a higher level above ground starting on August 2019. Therefore, the trend, seasonal amplitude, and growth rate were computed for the period between July 2014 and August 2019 only.

The results of fitting NOAA's CCGCRV function (Thoning et al., 1989) to the filtered dataset at UNAM are also depicted in Figure 4. We estimated an annual growth rate of 2.4 ppm yr^{-1} for 2014-2019, slightly lower than the global growth rate and the rate reported for Mauna Loa (both 2.6 ppm yr^{-1}) over the same period (Dlugokencky and Tans, 2019; Tans and Keeling, 2019). The continuous growth rate shows a maximum at the end of October 2015 and a minimum at the end of July 2018 (Fig. 4). Our time series is too short to attempt a correlation between the observations and inter-annual climate drivers, but it is worth mentioning that from March 2015 and March 2016, one of the strongest ENSO events on record took place (Chen et al., 2017). In Mexico, the El Niño phase of ENSO is associated with negative precipitation anomalies in the northern and central parts of the country, which can reach deficits of up to 250 mm in the southwestern area of Mexico City, causing increased drought and a higher occurrence of forest fires (Bravo-Cabrera et al., 2018).

A measurement of the evolution of the concentration of CO_2 in the atmosphere that is closely related to the annual growth rate is the slope of the polynomial component of the fitted CCGCRV function

(Thoning et al., 1989), which we estimated also as 2.4 ± 0.5 ppm yr^{-1}. This value is directly comparable and identical with the yearly gain estimated by Baylon (2017) for total column CO_2 at the same site for the year 2016.

The seasonality of data at UNAM is presented in Figure 5. Annual averages were subtracted from daily data to remove the long-term trend from the seasonal change. There is an annual maximum in mid-December, likely due to the shallower boundary layer that prevails during winter (García-Franco et al., 2018), as previously explained. The summer-autumn minimum occurs in mid-September, when both the dilution of trace gases in a deeper convective boundary layer and more active urban vegetation draw down of CO_2 occurs. A secondary maximum occurs consistently right before the onset of the rains; we suggest that it is likely not thermally-driven but reflects 1) a significant contribution of transported CO_2 from agricultural burnings and forest fires outside the city, which peak at this time of year, and whose effects on air quality in the city's metropolitan area have been documented elsewhere (i.e. Yokelson et al., 2007; Tzompa-Sosa et al., 2016), and 2) the lack of photosynthetic uptake by vegetation and the dominance of respiration at the end of the dry period. A simultaneous increase in the concentration of other gases and biomass burning tracers in the particulate matter added to the atmosphere during the spring months would lend support to the biogenic origin of these enhancements. Indeed, a preliminary analysis of the CH_4 data from the Picarro in our study suggests that minor enrichments do occur in April and May for three out of five years of observations at UNAM (2015-2019). However, in general, the concentration of CH_4 in the city is highly variable and it shows large events likely of local origin throughout the year (Bezanilla et al., 2014). A more comprehensive analysis of wind trajectories of the spring enhancements and a concurrent measurement of other biomass burning products is warranted for a more conclusive attribution of emissions to a specific source.

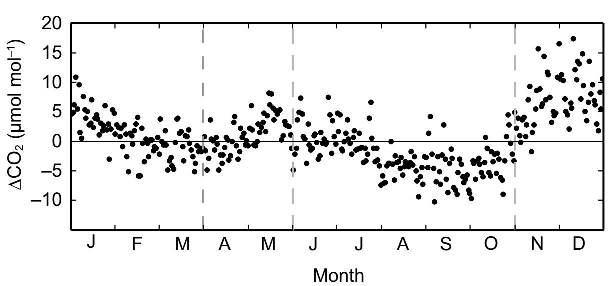

Fig. 5. Average annual course of de-trended daily means of CO_2 mole fraction at UNAM for the period 2014-2019.

The daily amplitude shows little seasonality, with a maximum in late fall (50.5 ± 18.9 ppm; Nov-Dec) and a minimum in the dry winter (42.2 ± 14.9 ppm; Jan-Mar), the latter is not significantly different from the rainy season (43.0 ± 18.3 ppm; Jun-Oct) or the dry season average (45.5 ± 14.8 ppm, Apr-May). The average seasonal amplitude was 8.9 ppm, with little interannual variation (8.2 ppm in 2018 to 10.2 ppm in 2015). In the only other long-term CO_2 monitoring study in a tropical city that we are aware of, Roth et al. (2017) showed a larger seasonal amplitude of ~14 ppm for Singapore.

Seasonality and trend for ALTZ were computed using only nighttime data (19 to 5 h) and hourly averages with standard deviations lower than 2.0 ppm. The selected daily period is the most appropriate to avoid the influence of either local vegetation activity or polluted air masses from urban areas, and therefore suitable to monitor conditions representative of the free troposphere. The overall mean CO_2 mole fraction is 406.2 ± 5.6 ppm, slightly higher than NOAA's global average for the same period (404.9 ppm). We found an annual average growth rate of 2.6 ppm yr^{-1} from 2015 to 2019, and again, like at UNAM, the continuous growth rate shows a maximum during the second half of 2015 (Fig. 6). The annual growth rate at ALTZ is in agreement with NOAA's global rate and Mauna Loa's (2.6 ppm yr^{-1}), but is slightly higher than the annual growth rate we obtain from NOAA's data taken at the MEX station in Veracruz (2.4 ppm yr^{-1}) over the same period, at almost the same latitude but further away from the influence of large cities and at a higher altitude. In short times series, however, trend estimates and computations of growth rates are very sensitive to high or low years, so meaningful comparisons are difficult to establish at this point. The slope of the first-degree polynomial of the CCG-CRV adjusted curve is 2.7 ± 0.0 ppm yr^{-1}, close to the comparable annual increment derived from the total column measurements for the period 2013-2017 (2.6 ppm yr^{-1}) (Baylon, 2018).

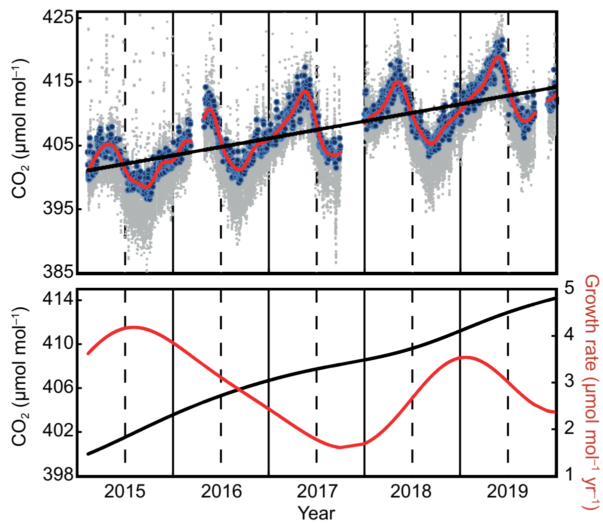

Fig. 6. Above: Hourly (gray) and daily (blue) average of nocturnal (19-5 h) CO_2 mole fractions at ALTZ, smoothed fitted function (red) and polynomial component of fitted function (black). Below: trend (black) and growth rate (red) for 2015-2019.

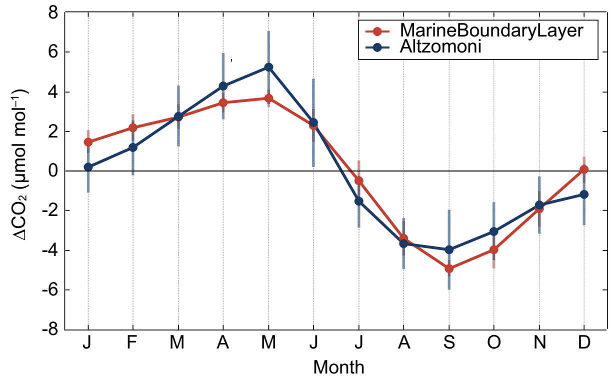

Fig. 7. De-trended, monthly CO_2 mole fraction at ALTZ (blue) and from NOAA's Marine Boundary Layer product for a latitude of 19º N (red), averaged over 2015-2019.

A marked seasonal cycle is discernible with a maximum between the last week of April and the first half of May, and a minimum in the last days of August and the first week of September. The cycle presents an average amplitude of 10.0 ppm, ranging from 8.4 ppm in 2015 to 10.6 ppm in 2018. In order to highlight local contributions to the seasonality of the CO_2 annual cycle, we extracted the de-trended monthly means and compared them to the typical seasonal cycle estimated from the reference Marine Boundary Layer (MBL) time series at a latitude of 19º N, for the period 2015-2019 (Fig. 7). The reference MBL record is computed from averages of weekly measurements of several long-lived atmospheric trace gases from the Cooperative Global Air Sampling Network (Conway et al., 1994). A subset of the sites is selected for the CO_2 MBL reference; only remote, sea level marine sites that sample well-mixed air from onshore prevailing wind directions are considered. The time series is therefore representative of background conditions of CO_2 in the atmosphere.

Times of seasonal maximum and minimum concentrations are coincident in both datasets, and in general both curves exhibit considerable overlap, although peak-to-trough seasonal amplitude is lower for the MBL (8.8 ppm), as data from ALTZ shows a slightly higher annual maximum in May probably due to the influence of polluted air masses. From December to February, the atmosphere at ALTZ shows a lower CO_2 mole fraction compared to the MBL. Although no systematic observations of photosynthesis by individual species have been carried out at ALTZ, casual observations indicate that the mixture of alpine grassland and conifer forests that surround the station stays more active in late fall and winter than most broad-leaved forests in mid latitudes. The evergreen vegetation would tend to prolong the carbon uptake season compared to species that shed the leaves in the cold season and become dormant, so the differences observed between the MBL signal and ALTZ are likely reflecting the influence of the regional vegetation acting as a sink for atmospheric CO_2 during winter.

6. Conclusions

We examined five years of continuous surface CO_2 measurements at an urban station in southern Mexico City and at a high-altitude station 60 km away from the first. The daily and weekly variability of the urban site is dominated by the dynamics of the boundary layer depth, with no discernible association to traffic volume patterns or the degree of urbanization of the source area of incoming air. At Altzomoni, the high-altitude station, the daily cycle shows also the influence of the thermally-driven growth of the regional boundary layer, but the effect of the photosynthetic activity of the vegetation controls the features of the cycle throughout seasons, in a pattern consistent with other vegetated surfaces in the northern hemisphere.

The filters applied to the urban record effectively screened out local influences in the immediate vicinity of the air intake, and left only periods of maximum vertical mixing every day. At Altzomoni, the exclusion of daytime values was effective to ensure that trend and seasonality of CO_2 concentration were examined under conditions representative of the free troposphere. This background record thus constitutes a suitable baseline to evaluate the evolution of the emissions in the city, as well as the efficacy of mitigation policies. In fact, several features of the regional atmospheric CO_2 exchange can only be evaluated as a result of the monitoring of urban and rural sites simultaneously. For example, a daily afternoon CO_2 enhancement in Altzomoni's daily cycle during the dry season signals the effect of polluted air parcels likely coming from Mexico City. Likewise, at UNAM, the CO_2 mole fraction of the filtered time series shows an expected maximum in winter but also a secondary peak at the end of the dry season, probably due to incoming emissions from biomass burnings in the agricultural landscape that surrounds the city.

The experimental setup and measurements described here lay the groundwork to the deployment of a network of low-cost CO_2 sensors in fifteen stations around the MCMA in the incoming months, in the framework of the Mexico City Regional Carbon Impacts (MERCI-CO_2) project. The installation of this network will help in the characterization of the distribution and interplay of sources and sinks of CO_2 within the city. It will be complemented by a high-resolution transport model, and by total column CO_2 measurements in urban and peri-urban sites. The combined approach will allow the assessment of spatial gradients within, upwind, and downwind the city, and will allow the refinement and verification of current emission inventories.

Acknowledgments

We thank the financial and operational assistance of the University Network of Atmospheric Observatories (RUOA), coordinated by the Center of Atmospheric Sciences of UNAM, with technical support from Delibes Flores, Omar López and Ángel Bautista. Financial support also came from the CONACyT-ANR project 290589 'Mexico City's Regional Carbon Impacts' (ANR-17-CE04-0013-01). We thank the Parque Nacional Izta-Popo for providing access and facilitating the operation of the Altzomoni station. We acknowledge the invaluable access to data and products from the Global Greenhouse Reference Network stations, maintained by the US National Oceanic and Atmospheric Administration (NOAA).

References

Baumgardner D, Grutter M, Allan J, Ochoa C, Rappenglueck B, Russell LM, Arnott P. 2009. Physical and chemical properties of the regional mixed layer of Mexico's Megalopolis. Atmospheric Chemistry and Physics 9: 5711-5727. https://doi.org/10.5194/acp-9-5711-2009

Baylon CJL. 2017. CO_2 en el Centro de México por Espectroscopía Infrarroja de Absorción Solar. Doctoral Thesis. Universidad Nacional Autónoma de México.

Bazaz A, Bertoldi P, Cartwright A, de Coninck H, Engelbrecht F, Jacob D, Hourcade JC, Klaus I, de Kleijne K, Lwasa S, et al. 2018. Summary for Urban Policymakers: What the IPCC Special Report on 1.5 ºC Means for Cities. Geneva: Intergovernmental Panel on Climate Change. https://www.ipcc.ch/site/assets/uploads/sites/2/2018/12/SPM-for-cities.pdf

Beaman JH. 1962. The Timberlines of Iztaccihuatl and Popocatepetl, Mexico. Ecology 43: 377-385.

Bezanilla A, Krüger A, Stremme W, Grutter M. 2014. Solar absorption infrared spectroscopic measurements over Mexico City: Methane enhancements. Atmósfera 27: 173-183.

Bravo-Cabrera JL, Azpra-Romero E, Rodríguez-González FJ, Rodríguez-López O. 2018. Effects of ENSO on precipitation in Mexico City. Investigaciones Geográficas 97: 1-12. https://doi.org/10.14350/rig.59679

Bréon FM, Broquet G, Puygrenier V, Chevallier F, Xueref-Remy I, Ramonet M, Dieudonné E, Lopez M, Schmidt M, Perrussel O, Ciais, P. 2015. An attempt at estimating Paris area CO_2 emissions from atmospheric concentration measurements. Atmospheric Chemistry and Physics 15: 1707-1724. https://doi.org/10.5194/acp-15-1707-2015

Cerveny RS, Coakley KJ. 2002. A weekly cycle in atmospheric carbon dioxide. Geophysical Research Letters 29: 15-1-15-4. https://doi.org/10.1029/2001GL013952

Chen L, Li T, Wang B, Wang L. 2017. Formation mechanism for 2015/16 Super El Niño. Scientific Reports 7: 2975. https://doi.org/10.1038/s41598-017-02926-3

Cheng XL, Liu XM, Liu YJ, Hu F. 2018. Characteristics of CO_2 concentration and flux in the Beijing urban area. Journal of Geophysical Research: Atmospheres 123: 1785–1801. https://doi.org/10.1002/2017JD027409

Conil S, Helle S, Langrene L, Laurent O, Delmotte M, Ramonet M. 2019. Continuous atmospheric CO_2, CH_4 and CO measurements at the OPE station in France from 2011 to 2018. Atmospheric Measurement Techniques 12: 6361-6383. https://doi.org/10.5194/amt-12-6361-2019

Contini D, Donateo A, Elefante C, Grasso FM. 2012. Analysis of particles and carbon dioxide concentrations and fluxes in an urban area: Correlation with traffic rate and local micrometeorology. Atmospheric Environment 46: 25-35. https://doi.org/10.1016/j.atmosenv.2011.10.039

Conway TJ, Tans PP, Waterman LS, Thoning KW, Kitzis DR, Masarie KA, Zhang N. 1994. Evidence for interannual variability of the carbon cycle from the NOAA/CMDL global air sampling network. Journal of Geophysical Research 99: 22831-22855.

Coutts AM, Beringer J, Tapper NJ. 2007. Characteristics influencing the variability of urban CO_2 fluxes in Melbourne, Australia. Atmospheric Environment 41: 51-62. https://doi.org/10.1016/j.atmosenv.2006.08.030

Dlugokencky E, Tans P. 2019. NOAA/ESRL. Trends in atmospheric carbon dioxide. Available at www.esrl.noaa.gov/gmd/ccgg/trends/global.html (accessed 2020 January 15)

Friedlingstein P, Jones MW, O'Sullivan M et al. 2019. Global Carbon Budget 2019. Earth Systems Science Data 11: 1783-1838. https://doi.org/10.5194/essd-11-1783-2019

Garcia E. 1988. Modificaciones al Sistema de Clasificación Climática de Köppen (para adaptarlo a las condiciones de la República Mexicana). Mexico City: UNAM, Instituto de Geografía.

García-Franco JL, Stremme W, Bezanilla A, Ruiz-Angulo A, Grutter M. 2018. Variability of the Mixed-Layer Height Over Mexico City. Boundary Layer Meteorology 167: 493-507. https://doi.org/10.1007/s10546-018-0334-x

Grutter M. 2003. Multi-gas analysis of ambient air using FTIR spectroscopy over Mexico City. Atmósfera 16: 1-13.

Gutiérrez Martínez G, Orozco Hernández ME, Ordóñez Díaz JAB, Camacho Sanabria JM. 2015. Régimen y distribución de los incendios forestales en el Estado de México (2000 a 2011). Revista Mexicana de Ciencias Forestales 6: 92-107.

Helfter C, Famulari D, Phillips GJ, Barlow JF, Wood CR, Grimmond CSB, Nemitz E. 2011. Controls of carbon dioxide concentrations and fluxes above central London. Atmospheric Chemistry and Physics 11: 1913-1928. https://doi.org/10.5194/acp-11-1913-2011

Hernández-Paniagua IY, Lowry D, Clemitshaw KC, Fisher RE, France JL, Lanoisell M, Ramonet M, Nisbet EG. 2015. Diurnal, seasonal, and annual trends in atmospheric CO_2 at southwest London during 2000-2012: Wind sector analysis and comparison with Mace Head, Ireland. Atmospheric Environment 105: 138-147. https://doi.org/10.1016/j.atmosenv.2015.01.021

IPCC. 2000. Good practice guidance and uncertainty management in national greenhouse gas inventories. Geneva: Intergovernmental Panel on Climate Change.

Keeling CD. 1960. The concentration and isotopic abundances of carbon dioxide in the atmosphere. Tellus 12: 200-203.

Kilkki J, Aalto T, Hatakka J, Portin H, Laurila T. 2015. Atmospheric CO_2 observations at Finnish urban and rural sites. Boreal Environment Research 20: 227-242.

Kumar NK, Nagendra SMS. 2015. Characteristics of ground level CO_2 concentrations over contrasting land uses in a tropical urban environment. Atmospheric Environment 115: 286-294. https://doi.org/10.1016/j.atmosenv.2015.05.044

Laurent O. 2017. ICOS Atmospheric Station Specifications, ICOS technical report. Available at Available at https://www.icos-cp.eu/sites/default/files/cmis/ICOS Atmospheric Station specifications Version 1.3 - November 2017.pdf (accessed 2018 November 4)

Laurent O, Philippon C, Yver Kwok C, Rivier L, Ramonet M. 2019. How to deal with water vapor for Greenhouse gas dry mole fraction measurement with Cavity Enhanced Spectrometer: water vapor correction vs Nafion dryer. Poster (P12) at the 20th WMO/IAEA Meeting on Carbon Dioxide, Other Greenhouse Gases, and Related Measurement Techniques (GGMT-2019).

Lauvaux T, Miles NL, Richards SJ, Deng A, Stauffer DR, Davis KJ, Jacobson G, Rella C, Calonder GP, DeCola PL. 2013. Urban Emissions of CO_2 from Davos, Switzerland: The First Real-Time Monitoring System

Using an Atmospheric Inversion Technique, Journal of Applied Meteorology and Climatology 52: 2654–2668. https://doi.org/10.1175/JAMC-D-13-038.1

Leip A, Skiba U, Vermeulen A, Thompson RL. 2017. A complete rethink is needed on how greenhouse gas emissions are quantified for national reporting. Atmospheric Environment 174:237-240. https://doi.org/10.1016/j.atmosenv.2017.12.006

Lian J, Bréon F-M, Broquet G, Scott Zaccheo T, Dobler J, Ramonet M, Staufer J, Santaren D, Xueref-Remy I, Ciais P. 2019. Analysis of temporal and spatial variability of atmospheric CO_2 concentration within Paris from the GreenLITETM laser imaging experiment. Atmospheric Chemistry and Physics 19:13809–13825. https://doi.org/10.5194/acp-19-13809-2019

Lot A, Camarena P. 2009. El Pedregal de San Ángel de la ciudad de Mexico: reserva ecológica urbana de la Universidad Nacional. In: Lot A, Cano-Santana Z, eds. Biodiversidad del ecosistema del Pedregal de San Ángel. Mexico City: UNAM, 19-25.

Marland G, Hamal K, Jonas M. 2009. How uncertain are estimates of CO_2 emissions? Journal of Industrial Ecology 13: 4-7.

Pal S, Haeffelin M. 2015. Forcing mechanisms governing diurnal, seasonal, and interannual variability in the boundary layer depths: Five years of continuous lidar observations over a suburban site near Paris. Journal of Geophysical Research - Atmospheres 120: 11936-11956. https://doi.org/10.1002/2015JD023268

Rella CW, Chen H, Andrews AE, Filges A, Gerbig C, Hatakka J, Karion A, Miles NL, Richardson SJ, Steinbacher M, Sweeney C, Wastine B, Zellweger C. 2013. High accuracy measurements of dry mole fractions of carbon dioxide and methane in humid air. Atmospheric Measurements Techniques 6:837-860. https://doi.org/10.5194/amt-6-837-2013

Rzedowskyi J. 1954.Vegetación del Pedregal de San Ángel (Distrito Federal, México). Anales de la Escuela Nacional de Ciencias Biológicas 8:59-129.

Roth M, Jansson C, Velasco E. 2017. Multi-year energy balance and carbon dioxide fluxes over a residential neighbourhood in a tropical city. International Journal of Climatology 37: 2679-2698. https://doi.org/10.1002/joc.4873

Schmutz M, Vogt R, Feigenwinter C, Parlow E. 2016. Ten years of eddy covariance measurements in Basel, Switzerland: Seasonal and interannual variabilities of urban CO_2 mole fraction and flux. Journal of Geophysical Research Atmospheres, 121: 8649–8667. https://doi.org/10.1002/2016JD025063

SEDEMA. 2008. Inventario de Emisiones. Gases de Efecto Invernadero. Zona Metropolitana del Valle de México 2006. Mexico City: Secretaría del Medio Ambiente, Gobierno del Distrito Federal.

SEDEMA. 2018. Inventario de Emisiones de la Ciudad de México 2016. Mexico City: Dirección General de Gestión de la Calidad del Aire, Dirección de Programas de Calidad del Aire e Inventario de Emisiones.

Shaw WJ, Pekour MS, Coulter RL, Martin TJ, Walters JT. 20087. The daytime mixing layer observed by radiosonde, profiler and lidar during MILAGRO. Atmospheric Chemistry and Physics Discussions 7: 15025-15065. https://doi.org/10.5194/acpd-7-15025-2007

Song T, Wang YS. 2012. Carbon dioxide fluxes from an urban area in Beijing. Atmospheric Research 106: 139-149. https://doi.org/10.1016/j.atmosres.2011.12.001

The World Bank. 2010. Cities and climate change: an urgent agenda. Urban development series knowledge papers 10.Washington, DC: World Bank.

Tans PP, Keeling R. 2019. NOAA/ESRL. Trends in atmospheric carbon dioxide. Available at www.esrl.noaa.gov/gmd/ccgg/trends/mlo.html (accessed 2020 January 15)

Tans PP, Crotwell AM, Thoning KW. 2017. Abundances of isotopologues and calibration of CO_2 greenhouse gas measurements. Atmospheric Measurements Techniques 10: 2669-2685. https://doi.org/10.5194/amt-10-2669-2017

Thoning KW. 2018. Python class for curve fitting time series in NOAA/ESRL/GMD. Available at ftp://ftp.cmdl.noaa.gov/user/thoning/ccgcrv (accessed 2018 August 1st).

Thoning KW, Tans PP, Komhyr WD. 1989. Atmospheric carbon dioxide at Mauna Loa Observatory 2. Analysis of the NOAA GMCC data, 1974-1985. Journal of Geophysical Research 94: 8549-8565.

Turnbull J, Sweeney C, Karion A, Newberger T, Tans P, Lehman S, Davis KJ, Miles NL, Richardson SJ, Lauvaux T, Cambaliza MO, Shepson P, Gurney K, Patarasuk R, Zondervan A. 2014. Towards quantification and source sector identification of fossil fuel CO_2 emissions from an urban area: Results from the INFLUX experiment. Journal of Geophysical Research Atmospheres 120: 292-312. https://doi.org/10.1002/2014JD022555

Tzompa-Sosa ZA, Sullivan AP, Retama A, Kreidenweis SM. 2016. Contribution of Biomass Burning to Carbonaceous Aerosols in Mexico City during May 2013. Aerosol and Air Quality Research 16: 114-124. https://doi.org/10.4209/aaqr.2015.01.0030

Ueyama M, Ando T. 2016. Diurnal, weekly, seasonal, and spatial variabilities in carbon dioxide flux in different urban landscapes in Sakai, Japan. Atmospheric Chemistry and Physics 16: 14727–14740. https://doi.org/10.5194/acp-16-14727-2016

Velasco E, Pressley S, Allwine E, Westberg H, Lamb B. 2005. Measurements of CO_2 fluxes from the Mexico City urban landscape. Atmospheric Environment 39: 7433-7446. https://doi.org/10.1016/j.atmosenv.2005.08.038

Velasco E, Perrusquia R, Jiménez E, Hernández F, Camacho P, Rodríguez S, Retama A, Molina LT. 2014. Sources and sinks of carbon dioxide in a neighborhood of Mexico City. Atmospheric Environment 97: 226-238. https://doi.org/10.1016/j.atmosenv.2014.08.018

Whiteman CD, Zhong S, Bian X, Fast JD, Doran JC. 2000. Boundary layer evolution and regional-scale diurnal circulations over the Mexico Basin and Mexican plateau. Journal of Geophysical Research 105: 10081-10102.

Wu K, Lauvaux T, Davis KJ, Deng A, Lopez Coto I, Gurney KR, Patarasuk R. 2018. Joint inverse estimation of fossil fuel and biogenic CO_2 fluxes in an urban environment: An observing system simulation experiment to assess the impact of multiple uncertainties. Elementa Science of the Anthropocene 6: 17. https://doi.org/10.1525/elementa.138

Yokelson RJ, Urbanski SP, Atlas EL, Toohey DW, Alvarado EC, Crounse JD, Wennberg PO, Fisher ME, Wold CE, Campos TL, Adachi K, Buseck PR, Hao WM. 2007. Emissions from forest fires near Mexico City. Atmospheric Chemistry and Physics 7: 5569-5584. https://doi.org/10.5194/acp-7-5569-2007

Yuan Y, Ries L, Petermeier H, Trickl T, Leuchner M, Couret C, Sohmer R, Meinhardt F, Menzel A. 2019. On the diurnal, weekly, and seasonal cycles and annual trends in atmospheric CO_2 at Mount Zugspitze, Germany, during 1981–2016. Atmospheric Chemistry and Physics 19: 999-1012. https://doi.org/10.5194/acp-19-999-2019

Yver Kwok C, Laurent O, Guemri A, Philippon C, Wastine B, Rella C, Vuillemin C, Truong F, Delmotte M, Kazan V, Darding M, Lebugue B, Kaiser C, Ramonet M. 2015. Comprehensive laboratory and field testing of cavity ring-down spectroscopy analyzers measuring H_2O, CO_2, CH_4 and CO. Atmospheric Measurement Techniques Discussions. 8: 4219-4272. https://doi.org/10.5194/amtd-8-4219-2015

Yver-Kwok C, Philippon C, Bergamaschi P, Biermann T, Calzolari F, Chen H, Conil S, Cristofanelli P, Delmotte M, Hatakka J, Heliasz M, Hermansen O, Komínková K, Kubistin D, Kumps N, Laurent O, Laurila T, Lehner I, Levula J, Lindauer M, Lopez M, Mammarella I, Manca G, Marklund P, Metzger J-M., Mölder M, Platt SM, Ramonet M, Rivier L, Scheeren B, Sha MK, Smith P, Steinbacher M, Vítková G, Wyss S. 2021. Evaluation and optimization of ICOS atmospheric station data as part of the labeling process, Atmospheric Measurement Techniques 14: 89-116. https://doi.org/10.5194/amt-14-89-2021

Zellweger C, Hüglin C, Klausen J, Steinbacher M, Vollmer M, Buchmann B. 2009. Inter-comparison of four different carbon monoxide measurement techniques and evaluation of the long-term carbon monoxide time series of Jungfraujoch. Atmospheric Chemistry and Physics 9: 3491-3503. https://doi.org/10.5194/acp-9-3491-2009

Zhang F, Zhou L, Conway TJ, Tans PP, Wang Y. 2013. Short-term variations of atmospheric CO_2 and dominant causes in summer and winter: Analysis of 14-year continuous observational data at Waliguan, China. Atmospheric Environment 77: 140-148. https://doi.org/10.1016/j.atmosenv.2013.04.067

Atmósfera 35(2), 395-420 (2022)
https://doi.org/10.20937/ATM.52922

CONTENTS

The Role of Sustainable Technological Innovations in the Relationship between Freight Pricing and Environmental Degradation: Evidence from a Panel of 39 R&D economies

Muhammad Khalid ANSER[1], Sajid ALI[2], Muhammad Azhar KHAN[3], Abdelmohsen A. NASSANI[4], Sameh E. ASKAR[5], Khalid ZAMAN[3]*, Muhammad Moinuddin QAZI ABRO[4] and Ahmad KABBANI[6]

[1] *School of Public Administration, Xi'an University of Architecture and Technology, Xi'an 710000, China.*
[2] *School of Economics, Bahauddin Zakariya University, Multan, Pakistan.*
[3] *Department of Economics, University of Haripur, Khyber Pakhtunkhwa, Haripur, Pakistan*
[4] *Department of Management, College of Business Administration, King Saud University, PO Box 71115, Riyadh, 11587, Saudi Arabia.*
[5] *Department of Statistics and Operations Research, College of Science, King Saud University, PO Box 11451, Riyadh 11587 Saudi Arabia.*
[6] *Department of Management, Aleppo University, Aleppo, Syria.*
*Corresponding author: khalid_zaman786@yahoo.com

Received: June 07, 2020; Accepted: December 08, 2020

RESUMEN

Este estudio está en línea con la Convención Marco de las Naciones Unidas sobre el Cambio Climático (CMNUCC) para evaluar el Acuerdo post-París (COP21) a través de innovaciones tecnológicas y fijación de precios del carbono en un panel de 39 economías de I + D desde 1995 hasta 2018. Los resultados muestran que las innovaciones tecnológicas y las aplicaciones inteligentes de los servicios financieros y de seguros ayudan a reducir las emisiones de GEI en la distribución de cuantiles desde más bajos a más altos. Por el contrario, el transporte aéreo de mercancías, los precios del transporte aéreo y el flujo de inversión extranjera directa (IED) aumentan las emisiones de gases de efecto invernadero debido a actividades logísticas no sostenibles, precios de transporte ineficientes y producción sucia, confirmando la hipótesis del 'paraíso de contaminación' en todos los países. Los ingresos por flete aéreo tienen un impacto diferencial en las emisiones de GEI en la distribución de cuantiles, ya que en los cuantiles más bajos ($\tau_{0.2}$ a $\tau_{0.4}$) los ingresos por flete aéreo aumentan emisiones de GEI, mientras que en los cuantiles más altos ($\tau_{0.9}$), las disminuyen. Por lo tanto, la viabilidad de los ingresos por transporte aéreo se evalúa a mayor profundidad utilizando la matriz de innovación de panel y causalidad de Panel Granger. Los resultados muestran causalidad bidireccional entre i) los precios del flete aéreo y las emisiones de gases de efecto invernadero, ii) el flete del transporte aéreo (y el precio del flete, los ingresos por flete, la IED) y las innovaciones tecnológicas, iii) la IED y los ingresos del flete aéreo, mientras que existe una causalidad unidireccional desde i) seguros y servicios financieros a emisiones de GEI, ii) emisiones de GEI a innovaciones tecnológicas y flujos de IED, y iii) fletes de transporte aéreo a flujos de IED.

ABSTRACT

This study is in line with the United Nations Framework Convention on Climate Change (UNFCCC) to evaluate the post-Paris Agreement (COP21) through technological innovations and carbon pricing in a panel of 39 R&D economies from 1995 to 2018. The results show that sustainable technological innovations and smart applications of insurance and financial services help decrease GHG emissions in the lowest to highest quantile distribution. In contrast, air transportation freight, air freight pricing, and foreign direct investment (FDI) inflows escalate GHG emissions due to unsustainable logistics activities, inefficient freight pricing, and dirty production, which confirmed the 'pollution haven' hypothesis across countries. The impact of air freight revenues has a differential impact on GHG emissions in the different quantiles' distribution, as in the lowest quantiles (i.e., $\tau_{0.2}$ to $\tau_{0.4}$), air freight revenues increase GHG, whereas, at the highest quantiles' distribution (i.e., $\tau_{0.9}$) emissions decrease. Thus, the viability of air freight revenues is further assessed using Panel Granger causality and panel innovation matrix. The results show the bidirectional causality between i) air freight pricing and GHG emissions, ii) air transportation freight (and freight pricing, freight revenues, FDI) and technology innovations, iii) FDI and air freight revenues, while there is a unidirectional causality running from i) insurance and financial services to GHG emissions, ii) GHG emissions to technological innovations and FDI inflows, and iii) air transportation freight to FDI inflows.

Keywords: Technological innovation, Air freight; Freight revenue, GHG emissions, Inbound FDI, Panel regression.

1. Introduction

The UNFCCC (2017) report on technological innovation and climate-resilient action plan is highly embarked on the post-Paris agreement, previously agreed among the United Nation (UN) member countries to combat climate change and mitigate GHG emissions within a global partnership and cooperation in the Paris Conference of the Parties (COP21) in 2015. The COP21 agenda set out a vision of low carbon and climate-resilient technologies to maintain the global temperature of less than 1.5ºC. Climate change effects threaten the 2030 agenda of international sustainable development, which would be handled by national adaptation plans and mutual coordinated action plans. Given this scenario, the role of technological innovation is to enhance efforts to implement global climate actions with integrated economic and environmental national policies towards green development. The latest IPCC (2018) report informed that global warming continues to increase, negatively impacting goal to keep global average temperature below 1.5ºC. The need for a reduction in carbon emissions by almost half by 2030 and reaching net-zero carbon emission by 2050 is required to achieve the COP21climate goals. Countries require an integrated set of national and mutually coordinated action policies, including science, technology and innovation policies, that would help cut GHG emissions globally. The CIGI (2017) report presented four alternative ways to achieve the environmental sustainability agenda of low carbon emissions, i.e., the establishment of innovative carbon emissions' mitigation global fund, sustainable contract programs related to financial performance, international environmental regulatory programs, and the formation of a green infrastructure development program. These programs would be highly decarbonizing and advance climate mitigation action reforms. Table I shows current facts and figures about computer technology progression, freight pricing and GHG emissions in a panel of 39 R & D economies used in this study for more robust policy inferences.

The study seeks answers to three research questions to devise sustainable environmental policies. The first question is: *Does technology innovation help limit GHG emissions to maintain global average temperature below 1.5ºC?* This research question would be helpful to assess efficient green Information and Communication Technology (ICTs) policies in a panel of selected R&D economies in line with the Kyoto Protocol and Paris Agreement (COP21) (Dogan & Ozturk, 2017). The transportation sector is highly responsible for escalating GHG emissions due to its unsustainable logistics activities; thus, freight pricing would be an optimal solution to cut GHG emissions through a carbon tax and emissions -cap trading (Salahuddin et al. 2016).

The second research question is: *To what extent air freight pricing could reduce GHG emissions through managing air freight revenue for reinvesting in cleaner sustainable options?* This question supports innovative technology mechanisms and synergy with the sustainable policy agenda through a freight tax, which provides more investment opportunities in cleaner options to protect the natural environment and comply with the Kyoto protocol (Usman et al. 2020).

Finally, the 'pollution haven' hypothesis is evaluated across a panel of selected countries, which we assume to be true due to un-green financial policies; thus, the third question is: *Does foreign direct investment (FDI) inflows increase GHG emissions due to lax environmental regulations and financial*

Table I. Current Facts for Information Technology, Freight Pricing, and GHG Emissions

Countries	Computer communication (% of commercial service exports)	Freight Pricing (%)	GHG emissions (kt of CO2 equivalent)	Countries	Computer communication (% of commercial service exports)	Freight Pricing (%)	GHG emissions (kt of CO2 equivalent)
United States	45.685	2.442	6343841	Finland	72.538	1.083	69072.94
China	60.764	2.074	12064260	Czech Republic	49.036	2.149	138957.4
Japan	55.001	0.979	1478859	Egypt	9.971	29.501	295499.7
Germany	55.219	1.732	951716.7	South Africa	20.576	4.504	502130.3
India	72.227	4.860	3002895	Portugal	25.116	0.993	72524.22
France	54.538	1.850	499146.6	Thailand	14.537	1.063	440411.7
UK	46.525	2.292	585779.8	Ukraine	51.570	10.951	404900.3
Russian Federation	44.169	2.878	2803398	Greece	10.298	0.625	100571.2
Brazil	60.546	3.664	2989418	Pakistan	65.177	5.078	369734.6
Italy	39.980	1.137	482634	Indonesia	31.191	3.198	780550.8
Canada	50.321	2.268	1027064	New Zealand	17.779	1.598	78130.98
Australia	19.698	1.911	761686.3	Saudi Arabia	2.526	2.465	514967.3
Spain	34.301	1.675	3482.57.3	Colombia	18.940	3.240	173411.8
Turkey	6.974	16.332	445640.1	Chile	31.976	2.434	120687.9
Switzerland	51.566	0.936	54108.1	Slovenia	34.113	1.738	21074.75
Belgium	58.787	2.053	133373.7	Morocco	35.848	1.912	80436.72
Austria	40.645	1.998	90460.21	Romania	58.407	4.625	121762.2
Poland	49.831	1.812	414606.9	Belarus	45.161	4.872	109647.2
Malaysia	35.933	0.884	279098.4	Singapore	42.227	0.438	55901.28
Mexico	0.507	4.899	663425				

Total Countries: 39
Time Period: 1995-2018
Data Reported Period: 2018

Source: World Bank (2019).

liberalization policies? This question is important to analyze countries' sustainable development efforts that may be influenced by meager environmental policies and unconditional financial agreements, which does not generally favor the UN sustainable development goals (Khan & Ozturk, 2020).

These research questions allow to set clear objectives for this study that would help to devise long-term and broad-based sustainable policies:

i) To investigate the role of technology innovation in mitigating GHG emissions across a panel of selected R&D economies
ii) To analyze the role of air freight pricing and freight revenues on the growth of GHG emissions
and
iii) To assess to what extent financial liberalization policies influenced countries' efforts to mitigate GHG emissions to comply with the Kyoto protocol and COP21 Paris agreement.

2. Literature Review

Earlier literature findings largely work around the environmental sustainability agenda through multi-faceted socio-economic and technological factors, providing a path to understanding sustainability issues in different economic settings. For instance, Zhang et al. (2013) discussed the importance of synthetic nitrogen fertilizer in food production to feed half of the world's population. However, the overuse of nitrogen fertilizer negatively influenced water quality, soil, and the atmosphere. The central question in the environmental agenda remains how to mitigate emissions through sustainable technologies, optimally decreasing excessive fertilizer use across countries. Lybbert and Sumner (2012) found a two-way channel as climate change negatively influenced agricultural production, while conventional agriculture produces GHG emissions through unsustainable practices. Thus, the development of new agricultural technologies and practices helps increase yield and reduce GHG emissions to achieve green agriculture development. Developing countries face severe challenges of low agricultural productivity, high poverty, greater inequality, and food insecurity.

Long et al. (2016) found many potential barriers that restrain the possible way of mitigating GHG emissions through climate-smart agriculture technologies, including the users' constraints from the demand side and technology providers' constraints on the supply side. The supply-side barriers include convincing customers to use new technologies for climate-smart agriculture, high capital requirement, regulatory issues, technology pricing, and end-user delivery. In contrast, the demand side issues include low technology awareness, high cost, uncertainty about technology and its positive impact, less training for technology use, and low consumer demand. These are the factors that diffuse technology innovation across Europe.

Williams et al. (2012) suggested the number of channels through which the global GHG emissions reduction target would be achieved by 2050, including achieving energy efficiency through sustainable energy supply to help generate transportation demand technologies for green development. Nikzad and Sedigh (2017) discussed the viability of green technologies to mitigate GHG emissions in Canada. Advancement in alternative green energy sources, sustainable transportation systems, and energy conservation are a few sustainable options to achieve sustainable development by decreasing GHG emissions countrywide. Lukkarinen et al. (2018) considered Finland as case study and analyzed the role of clean technological policies in reducing emissions and found that the *Cleantech Program* is an effective tool to analyze innovation dynamics based upon market information and experimentation. Thus, the need for clean technologies is imperative for launching successful *cleantech* products that support renewable energy and material sources. Bel and Joseph (2018) suggested the need to critically evaluate carbon pricing policy instruments in the European Union emissions trading that has a crucial impact on technology adaptation in the energy sector. Fernández- Fernández et al. (2018) analyzed the dynamic interaction between technology innovation and carbon emissions in a panel of 15 European countries, the US, and China, for 1990-2013. Their results show that technology innovation positively impacts environmental quality and mitigates carbon emissions across countries. Energy demand is a significant predictor for negative environmental impacts and increased carbon emissions in China and the US but is relatively low in the European region. The results emphasized the need to increase R&D spending in achieving the environmental sustainability agenda to mitigate GHG emissions from the production process. Nunes et al. (2019) analyzed the role of biomass energy in the Portuguese textile industry's sustainable growth that is less competitive due to high energy costs. After a thorough empirical survey, the results show that biomass energy can be used efficiently in the textile industry to become more competitive through up to 35% cost-saving energy compared to steam generation. Thus, R&D spending in biomass energy production may become a viable, sustainable instrument to achieve green energy development. Yusuf et al. (2019) examined the role of technological innovation in reducing carbon emissions in the Indonesian economy over the period 1980-2017 and found the existence of a technology induced environmental Kuznets curve. The study concludes that high-technology exports are important to revitalize economic and environmental policies to lessen high carbon abatement costs across the globe. Liu et al. (2019) found the different drivers of GHG emissions across 40 heterogeneous countries analyzing the period 1995-2009 and show that continued global economic growth is one of the main factors of increased GHG emissions while achieving energy efficiency after surpassed the certain income threshold reduces global GHG emissions. Another important factor is technological innovation that has a certain positive impact on environmental quality. The investment effect shows some evidence of the 'pollution haven' hypothesis that exhibit polluting industries in different countries. The viability of sustainable environmental policies is imperative to mitigate GHG emissions across the globe. Miyamoto and Takeuchi (2019) argued that the Kyoto Protocol has a significant impact on international patenting applications that reduce energy associated emissions by increasing R&D spending on renewable energy technologies. Thus, climate agreements largely concentrated on global patenting technologies. Table II shows the different technology innovation factors that are largely used in previous studies under the environmental sustainability agenda domain.

The study's research objectives have been empirically analyzed at different quantiles distribution by panel quantiles regression estimated at low to high quantiles distribution, further complemented with panel causality test and panel innovation accounting matrix.

3. Data and Methodology

The study utilized four broad measures of technology innovation to construct a single composite technology index, including computer communications as a percentage of commercial service exports (denoted by TINOV_1), fixed telephone subscriptions per 100 people (indicated by TINOV_2), ICT service exports as a percentage of service exports (marked by TINOV_3), and internet users as a percentage of the population (denoted by TINOV_4). The data of

Table II. Recent Literature on Technology Innovation and Environmental Sustainability

Authors	Time Period	Country	Technology Innovation Factors	Environmental / Other Factors	Results
Chen and Lei (2018)	1980-2014	30 countries	Total patent applications	Carbon emissions, renewable energy consumption	Technological innovations support to achieve carbon mitigation agenda through attained energy efficiency level.
Zhang et al. (2018)	2008-2015	31 Chinese provincial data	Number of patent applications	R&D investment and GDP per capita	R&D spending and continued economic growth are considered the main factors to increase technology investment, which support the country's sustainability agenda.
Xue et al. (2018)	Primary / questionnaire research	A qualitative survey from some major cities of China	Technology patents in the process of Information and Communication Technologies (ICTs)	ICTs network size, density, emotional attachment, signal strength, relationship, etc.	ICTs would be able to build new green construction methods through promoting innovation.
Li et al. (2018)	Bibliometric research	Global bibliometric studies count	Disruptive technology and emerging technology	Co-citation and Bibliographic coupling.	It is confirmed the link between disruptive and emerging technology through innovation.
Shubbak (2019)	1995-2017	China	Photovoltaic technology, R&D expenditures, patents, etc.	PV installations, trade disputes, and carbon emissions	The role of government policies assists in PV installation to progress towards environmental sustainability.

Table II. Recent Literature on Technology Innovation and Environmental Sustainability

Authors	Time Period	Country	Technology Innovation Factors	Environmental / Other Factors	Results
Wu et al. (2019)	1992-2010	735 Chinese emerging companies	Total number of patents	Market maturity, cultural distance, and absorptive capability	Market maturity, intellectual property rights of foreign markets protection, cultural space, and absorptive capacity to enter emerging companies increase technology innovation performance.
Aldakhil et al. (2019)	1975-2016	South Asia	ICTs	Carbon-fossil fuel emissions, R&D expenditures, FDI inflows, GDP per capita, etc.	ICTs have a positive impact on environmental quality by limiting carbon-fossil emissions through higher R&D spending.
Batool et al. (2019)	1973-2016	South Korea	ICTs	Carbon emissions, GDP per capita, and energy demand.	ICTs have a positive link to mitigate carbon emissions by the synergetic effect of continued economic growth and level of energy efficiency.
Shahbaz et al. (2018)	1955-2016	France	Energy innovations measured by R&D spending in the energy sector	Carbon emissions, financial development, energy demand, and economic growth	Energy innovation and financial development decrease carbon emissions while FDI inflows increase carbon emissions.
Al Mamun et al. (2018)	1980-2015	25 OECD countries	R&D spending in the energy sector	Financial development, carbon emissions, and renewable energy demand.	Financial development and renewable energy improve innovation across countries.
Ahmed and Ozturk (2018)	1985-2013	China	Total number of patent applications in the energy sector	Carbon emissions and energy intensity.	Technological innovations increase energy intensity to reduce carbon emissions.

technology innovation factors from TINOV_1 to TINOV_4 is obtained from the World Bank (2019) data base, for the period 1995-2018.

Principal Component Analysis (PCA) is used for this purpose, shown in Table SI in the supplementary material. Two factors, out of four elements, have eigenvalues larger than unity, i.e., 1.619 and 1.375, while the remaining two factors have eigenvalues of 0.601 and 0.403, respectively. A modest difference was found between factors one and two, i.e., 0.244, while the greater difference was found between factors two and three, i.e., 0.773. The least difference was found between factors three and four, which is about 0.198. The eigenvalue difference clearly shows that the variation among two and three factors is large. Thus, factors one and two are used to construct the TINDEX in the study. Further, the eigenvectors loading shows the four principal components (PC), and PC1 has a greater sum value, i.e., 1.96, followed by PC4 (0.322), PC2 (0.217), followed by PC3 with minimum additive eigenvalue loading of 0.028. Thus, PC1 is used to construct a single composite index for technology innovation. Finally, the correlation matrix between the technology index shows that TINOV_1 is positively correlated with the rest of the technology innovation factors, i.e., TINOV_2, TINOV_3, and TINOV_4, whereas there is a negative correlation is found between TINOV_2 and TINOV_3. A weak correlation was found between TINOV_3 and TINOV_4. Thus, TINOV_1 has a greater variation among the correlated technology factors, which exhibits a strong basis of TINDEX by utilizing the appropriate technical aspects. Figure 1 shows the eigenvalue plots and orthonormal loadings.

Figure 1 illustrates that orthonormal loadings divided the technology factors into the two sub-components, the first component has a greater percentage variance (40.5%) while the second component exhibits 34.4% variance of the composite technology index. The remaining 25.1% variance is due to unseen components of other possible factors. Followed by orthonormal loadings, the scree plots also indicate the

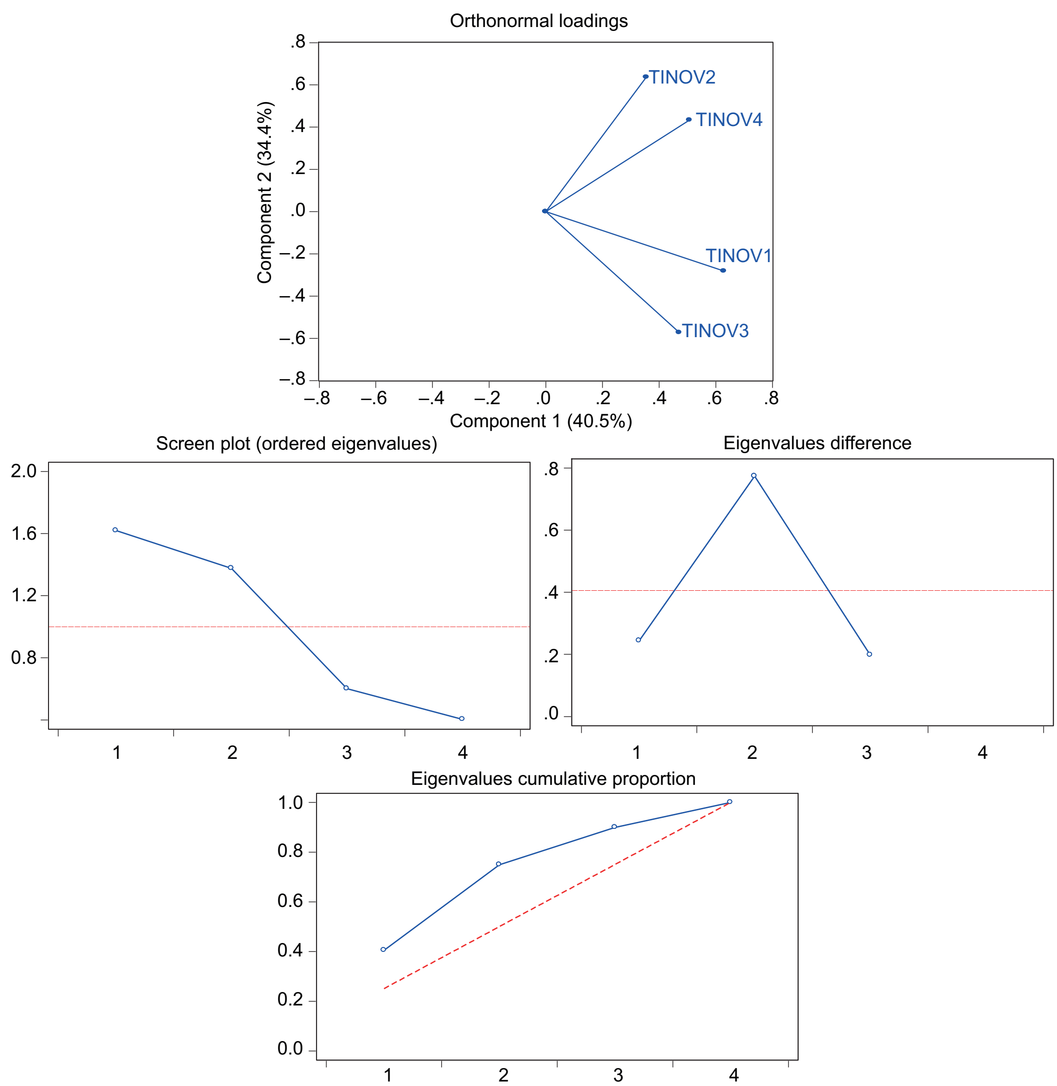

Fig. 1. Eigenvalue Plots and Orthonormal Loadings.

two main factors with eigenvalues larger than unit, and the substantial peak visible in the eigenvalue difference shows that the difference of variation is quite high in the second and third technology factors. Finally, the cumulative eigenvalue proportion shows the consistent trend towards one. This exercise gives a sound composite technology index (TINDEX) with a minimum value of –4.692 and a maximum value of 1.611 with a median value of 0.128.

The study used additional variables such as, air transport freight in million ton-km (denoted by ATF), freight pricing as CPI percentage (denoted by FPRICE), freight revenue per million ton-km in US$ (denoted by FREV) [estimated by the authors as (ATF×FPRICE/100)× Quantity of cargo/shipment], foreign direct investment inflows in current US$ (denoted by FDI), insurance and financial services as percentage of commercial service exports (denoted by IFS), and greenhouse gas emissions in kt of CO2 equivalent (denoted by GHG). All of the data is taken from the World Bank (2019) database from 1995 through 2018. Missing information is filled by subsequent and preceding values of the respective variables where required.

The study followed the scholarly work of Ahmed and Ozturk (2018), Hishan et al. (2019), and Al Mamun et al. (2018) to estimate the dynamic interaction among technology innovation, freight pricing, and GHG emissions in a panel of 39 R&D economies. Ahmed and Ozturk (2018) concluded that technology innovation is desirable to set up renewable energy projects to assess the clean energy reforms, while Hishan et al. (2019) argued that access to technologies would be achieved environmental sustainability agenda via limiting the carbon emissions. Al Mamun et al. (2018) found that synergies in financial development and innovations would help improve the cleaner energy resources to enhance environmental quality. The following linear model is proposed based on the cited studies:

$$GHG_{it} = \alpha_0 + \alpha_1 TINDEX_{it} + \alpha_2 ATF_{it} + \alpha_3 FPRICE_{it} + \alpha_4 FREV_{it} + \alpha_5 FDI_{it} + \alpha_6 IFS_{it} + \varepsilon_{it} \quad (1)$$

where GHG corresponds to GHG emissions, TINDEX is the technology innovation index, ATF shows air transport freight, FPRICE shows freight pricing, FREV shows freight revenues, FDI shows FDI inflows, IFS correspond to insurance and financial services. The subscripts 'i' indicate each of the 39 countries and 't' the years from 1995-2018; and, finally, ε corresponds to the error term.

Equation (1) shows that the environmental sustainability agenda (expressed by GHG emissions) is influenced by technology innovation, air transportation freight, air freight pricing, air freight revenues, FDI inflows, and insurance and financial services a panel of 39 R&D economies. The sign of the coefficient relating GHG emissions, and the technology innovation index is expected to be negative ($\alpha_1<0$), since technology will result in decreased emissions. The relationship between air transportation cargo and GHG emissions is expected to be positive ($\alpha_2>0$) since increase air freight increases GHG emissions, resulting in negative impact on climate.

The R&D economies are investing in energy conservation and environmental resources and complement the Paris Agreement through carbon pricing (Sarkodie and Ozturk, 2020). The carbon tax and emissions-cap modeling are used as sustainable policy instruments to mitigate GHG emissions. Given this scenario, this study used air freight pricing to impose a tax on unsustainable cargo activities to raise sufficient freight revenue to reinvest in environmentally sustainable activities. The sign of the coefficients for the interventions of air freight pricing and air freight revenues is expected to be negative with GHG emissions ($\alpha_3<0$ and $\alpha 4<0$). The study used the two broad measures of institutional factors in the form of FDI inflows and insurance and financial services to assess their role in the environmental sustainability agenda across a panel of countries. It is expected that institutional performance would perform better under the technology innovation factor, if and only if the air freight pricing could achieve the desired pollution reduction targets. If this case persists, the impact of FDI inflows and insurance and financial services would be positive (the negative relationship between them), and it would decline GHG emissions ($\alpha 5<0$ and $\alpha 6<0$). On the other hand, if the air freight pricing strategy fails to achieve the assigned pollution targets, it will negatively impact climate change exacerbating GHG emissions across countries. Thus, it will confine the findings of the 'pollution haven' hypothesis. Therefore, differential impacts would be expected between institutional factors and mitigating GHG emissions given the different signs of the coefficients (i.e., α5>0 and α6>0). Figure 2 shows the research framework, coupled with the research hypothesis of the study.

Figure 2 shows that technological innovation, freight pricing, and institutional factors will have a differential impact on GHG emissions. Technology leads to increased economic activity and environmental deterioration. However, after reaching some maturity stage, carbon pricing would help generate sufficient revenues to reinvest in the ecological protection agenda and increased investment in R&D, sustainable logistics freight activities, and responsible consumption and production. Further, it may lead to bidirectional linkages between the technological factors, air transportation freight mechanism, institutional factors, and environmental sustainability agenda. Thus, the study hypothesized the following statements for analysis:

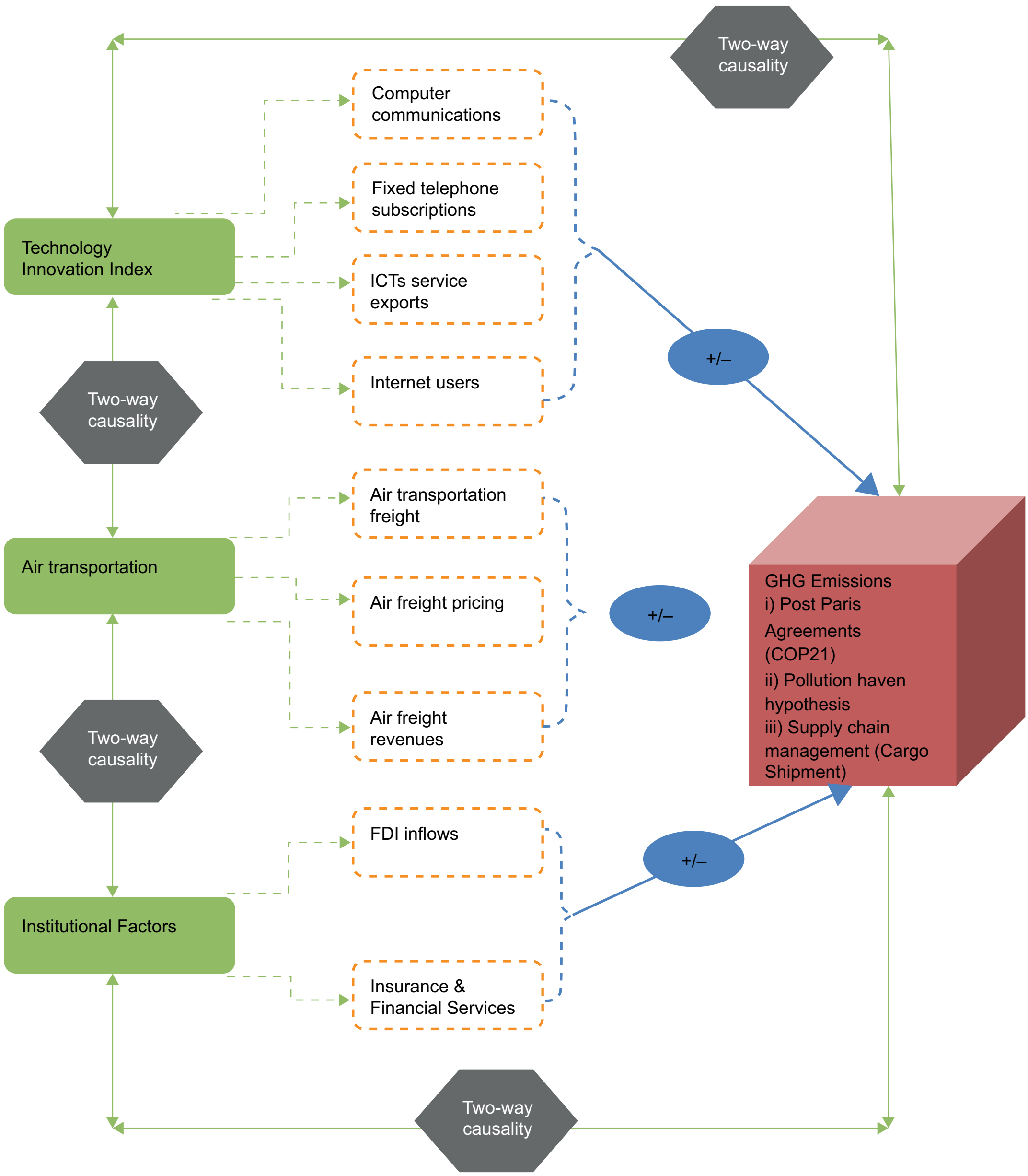

Fig. 2. Research Framework of the Study.

H1: Technological innovations will positively impact environmental quality in the form of a reduction of GHG emissions.
H2: Airfreight pricing and air freight revenues will decrease GHG emissions to support the COP21 Paris agreement, and
H3: Institutional factors will positively work under technological innovations and air freight mechanisms to lessen GHG emissions.

These hypotheses are evaluated using sophisticated panel econometric modeling, including panel quantiles regression, panel Dumitrescu-Hurlin (DH) causality test, and innovation accounting matrix.

Two generations of panel unit root testing are presented, differentiated in Table III for clear understanding.

The first-generation tests assume no cross-sectional dependency (CSD) among the cross-sectional identifiers; thus, this test is based on a homogenous assumption. In contrast, the second-generation tests find the CSD among the selected cross-section identifiers. Therefore, this test is based upon heterogeneous assumptions. The study used the first line testing framework to validate the homogenous assumptions. In contrast, after analyzing the unit root test results, once the candidate variables exhibit stationarity, the study moves to the panel quantile regression that accounts for unobserved heterogeneity and heterogeneous covariate effects. However, on the other hand, if the candidate variables are non-stationary, then first-generation cointegration estimates are used.

The panel quantiles regression works under the distributional pattern in the number of different quantiles from 10% to 90%, which handle the unobserved heterogeneity in the given model (Kato et al. 2012). Let us consider the model:

$$(y)_{i,t} = x_{i,t} + v_i + u_{i,t} \tag{2}$$

where 'y' corresponds to a response variable, 'x' indicates the list of regressors, 'v' corresponds to fixed-effect estimators, and u indicates the white noise term.

The quantile specification of the parameters to minimize quantile function is:

$$Q_{GHG_{i,t}}[\tau \perp \left(TINDEX, ATF, FPRICE, FREV, FDI, IFS\right)_{i,t}] = v_i + x^T{}_{i,t}\beta(\tau), \quad T \subseteq (0,1) \tag{3}$$

Further, the panel DH causality test (Dumitrescu-Hurlin, 2012) is utilized to assess whether the stated variables have some cause-effect relationship between them. Eqn. 4 is formulated at the cross-section 'i' concerning some given period 't', as:

$$y_{it} = c_i + \rho_{i,1}y_{i,t-1} + \rho_{i,2}y_{i,t-2} + \ldots\ldots + \rho_{i,p}y_{i,t-p} + \upsilon_{i,1}x_{i,t-1} + \upsilon_{i,2}x_{i,t-2} + \ldots\ldots + \upsilon_{i,p}x_{i,t-p} + \varepsilon_{i,t} \tag{4}$$

The null and alternative hypotheses are presented below:

$H_0 : \Psi k \geq 1$ and ψi, $\beta_{i,k} = 0$; $x_{i,t}$ does not homogenous cause $y_{i,t}$, ψi where, Ψ shows w-statistics, 'k' shows z-bar statistics, β shows intercept coefficient, x shows

Table III. Generations of Panel Unit Root Testing Framework.

First Generation Panel Testing Framework		Second Generation Panel Testing Framework	
I. Panel Unit Root Tests			
Im, Pesaran, and Shin test	Levin, Lin, and Chu test	Pesaran test	Bai and Ng test
Breitung test	Hadri test	Chang test	Moon and Perron test
Maddala et al. test		Harris et al. test	
II. Panel Cointegration Tests			
Pedroni residual cointegration	Kao residual cointegration	Westerlund cointegration	Westerlund and Edgerton cointegration

Source: Sharif et al. (2019), Jardón et al. (2017) and Yalçınkaya et al. (2017).

explanatory variables, 'i' shows cross-section, and 't' shows time period.

H_A: $\Psi k \geq 1$ and ψi, $\beta_{i,k} \neq 0$; $x_{i,t}$ does homogenous cause $y_{i,t}$, ψi where, Ψ shows w-statistics, 'k' shows z-bar statistics, β shows intercept coefficient, 'y' shows response variable, x shows explanatory variables, 'i' shows cross-section, and 't' shows time period.

The panel DH causality test (Dumitrescu-Hurlin, 2012) test is used in this study based upon semi-asymptotic distributions. The cross-section identifiers are larger than the period; thus, it would help policymaking that further leads to inter-temporal setting over a time horizon. The innovation accounting matrix, including impulse response function (IRF) and variance decomposition analysis (VDA), is further used for forecasting VAR modeling.

4. Results and Discussion

Table IV shows the candidate variables' descriptive statistics and that there are four technology innovation factors, including computer communications (TINOV_1) that have a mean value of 35.327% of commercial service exports with a maximum value of 75.445% and a minimum value of 0.469%. The remaining technology factors, i.e., fixed telephone subscriptions (TINOV_2), ICT service exports (TINOV_3),and internet users (TINOV_4) have a mean value of 30.859 per 100 people, 6778% of service exports, and 38.811% of the population, respectively. The mean value of air transport freight, freight pricing, and freight revenues are 2708 million ton-km, 7.829%, and US$9,26,466.3, respectively. The FDI inflows have a maximum value of 5.09E+11 with a mean value of 2.68E+10 and positively skewed distribution and high kurtosis value. The insurance and financial services and GHG emissions have a mean value of 5.950% of commercial service exports and 909930.1 kt of CO2 equivalent.

Table V shows the summary of panel unit roots and found that except ATF, the remaining variables are level stationary while ATF is differenced stationary as per LLC and PP estimates. In another panel unit root estimates, ATF and TINDEX are first differenced stationary while the remaining variables are level stationary as per IPS estimates. Finally, except TINDEX, the remaining variables are level stationery,

Table V. Panel Unit Roots Estimates.

Variables	LLC	IPS	ADF	PP
ATF	0.349	1.044	98.531***	84.278
FDI	–3.302*	–3.677*	123.951*	200.451*
FPRICE	–7.149*	–10.302*	263.239*	776.950*
FREV	–2.563*	–4.985*	171.835*	496.812*
GHG	–4.383*	–2.845*	115.446*	153.331*
IFS	–2.424*	–2.524*	109.952*	169.807*
TINDEX	–4.459*	–0.652	89.855	130.739*
		First Difference		
ΔATF	–11.038*	–13.040*	319.326*	675.940*
ΔFDI	–15.168*	–18.159*	445.651*	1801.83*
ΔFPRICE	–18.318*	–22.238*	566.270*	2382.85*
ΔFREV	–18.871*	–21.239*	538.602*	1695.67*
ΔGHG	–10.367*	–13.582*	337.058*	1313.58*
ΔIFS	–12.505*	–16.823*	412.168*	1176.31*
ΔTINDEX	–5.922*	–9.230*	228.071*	506.425*

Note: * and *** shows a 1% and 10% level of significance.

Table IV. Descriptive Statistics.

Methods	ATF	FPRICE	FREV	TINOV_1	TINOV_2	TINOV_3	TINOV_4	FDI	IFS	GHG
Mean	2708.269	7.829	926466.3	35.327	30.859	6.778	38.811	2.68E+10	5.950	909930.1
Maximum	41591.55	709.346	59335554	75.445	74.742	52.088	94.620	5.09E+11	41.318	12064260
Minimum	0.418	–1.736	–4379784	0.469	1.247	0.291	0.000123	–6.77E+10	–1.462	18869.70
Std. Dev.	5952.352	31.121	5073669	16.475	18.658	7.475	30.098	5.51E+10	7.120	1795114
Skewness	4.563	15.542	7.754	0.045	0.182	3.520	0.171	4.168	2.641	3.895
Kurtosis	25.933	308.315	68.92	2.455	1.871	17.778	1.594	24.803	10.674	20.030

Note: ATF shows air transport freight; FPRICE shows freight pricing, FREV shows freight revenues, TINOV_1 shows Computer communications, TINOV_2 shows fixed telephone subscriptions, TNOV_3 shows ICT service exports, TINOV_4 shows internet users, FDI shows FDI inflows, IFS show insurance and financial services, and GHG shows GHG emissions.

while TINDEX is first differenced stationary. Hence, we may generally conclude that all variables are level stationary; thus, we proceed towards panel quantile regression.

Table VI shows the panel quantiles estimates and found that technology innovation index has a negative relationship with GHG emissions at different quantiles distribution, which implies that technology innovation is helpful in reducing GHG emissions and promoting a sustainability agenda. Su and Moaniba (2017) concluded that advancements in technology innovation result in mitigating global carbon emissions in high carbon-emitting countries, which need increased public funding to conserve the natural environment through sustainable policy efforts. Huang et al. (2016) found that additive manufacturing technologies help achieve energy efficiency to mitigate GHG emissions. Zhang et al. (2016) suggested that global innovators should increase the market share of energy-intensive commodities to advance in global technologies that would help combat climate change vulnerabilities and achieve energy efficiency through knowledge diffusion across the globe. Atuonwu et al. (2018) argued that the importance of technology innovation in food processing and preservation is highly desirable to achieve energy efficiency leading to the reduction of GHG emissions. Technology advancement improves biological activities and nutritional quality that recover hygiene and public health for sustainable food production. Park (2018) found that eco-environmental policies are imperative to sustained long-term goals that would help mitigate carbon emissions by reconfiguring economic structure. Grubler et al. (2018) concluded that energy transformation and renewable energy restructuring are important to limit global average temperature to less than 2ºC that would escalate economic activity and sustainable development. Nerini et al. (2019) concluded that R&D spending, innovation, governance, and social innovation sustain economic and environmental policies to limit high carbon emissions to combat climate change.

Figure 3 shows the panel quantiles process estimates. There is a positive relationship between air transport freight and GHG emissions at different quantiles distribution, which implies that logistics activities are based upon unsustainable fuel consumption; hence it negatively impacts the natural

Table VI. Panel Quantile Regression Estimates.

Quantiles	0.1	0.2	0.3	0.4	0.5	0.6	0.7	0.8	0.9
Constant	48841.6*	60128.63*	80779.62*	112190.6*	144926.8*	249701*	299640.9*	349150.5*	454583.6*
TINDEX	−18801.8***	−57804.2*	−71614.2*	−108936*	−144802*	−284580*	−346105*	−361872*	−338723*
ATF	61.262**	99.737*	117.401*	135.237*	144.334*	161.680*	186.934*	245.289*	383.620*
FPRICE	109.334	67.847	32.263	100.207	555.009	−329.126	285.980	870.557	9990.594*
FREV	0.078*	0.050*	0.039*	0.024*	0.008	−0.0002	−0.025	−0.105	−0.224*
FDI	1.26E−06	6.47E−07**	1.19E−06***	1.63E−06***	3.02E−06***	6.47E−06*	1.16E−05*	2.38E−05*	2.59E−05*
IFS	−8675.16	−4030.67*	−6499.61*	−7383.07*	−5872.54*	−6349.63*	−8111.77**	−21176.6**	−22021*
					Statistical Tests				
Pseudo R^2	0.126	0.213	0.260	0.295	0.313	0.345	0.402	0.483	0.640
Adjusted R^2	0.120	0.208	0.255	0.290	0.308	0.341	0.398	0,480	0.602

Note: *, ** and *** indicates 1%, 5%, and 10% level of significance.

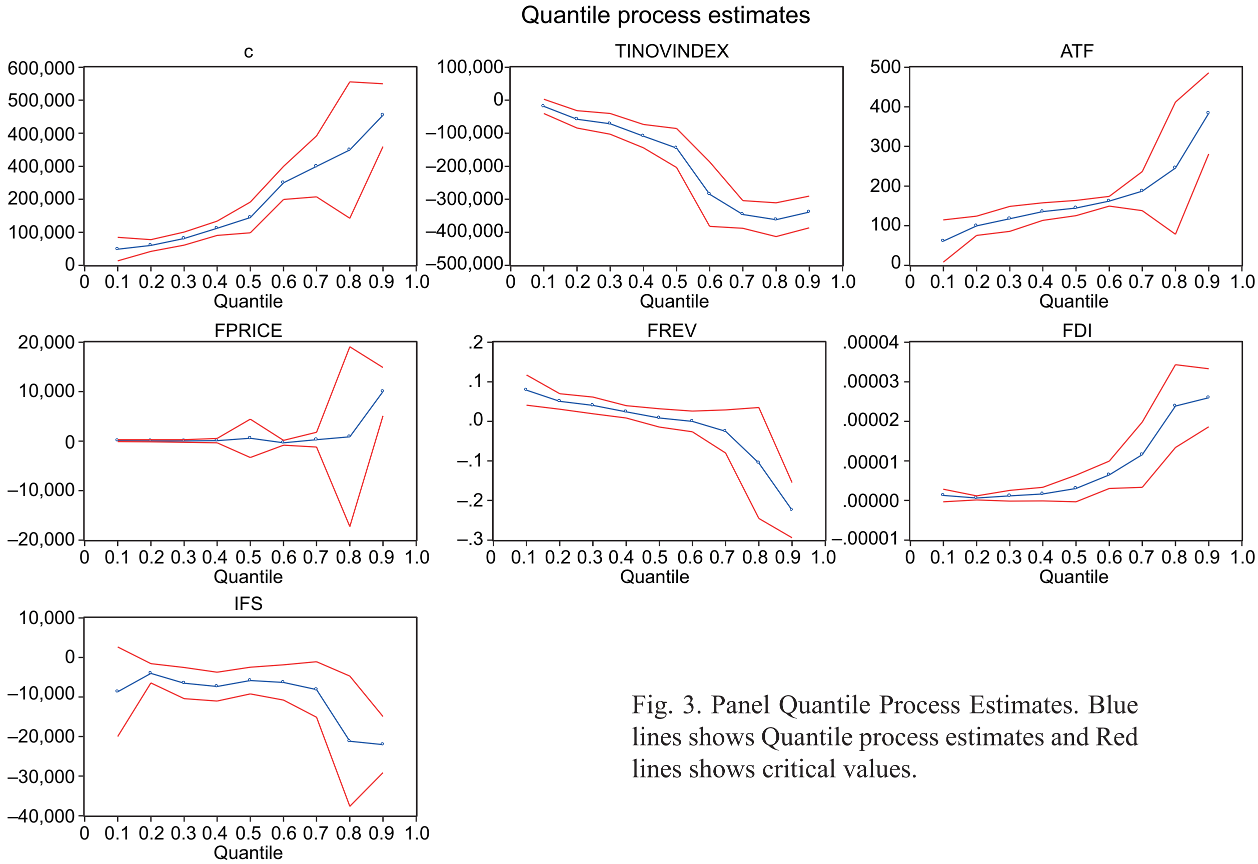

Fig. 3. Panel Quantile Process Estimates. Blue lines shows Quantile process estimates and Red lines shows critical values.

environment in the form of high GHG emissions. The post-Paris agreement (COP21) is highly affected by unsustainable logistics activities, and thus, there is an increased need to use renewable fuels in logistics activities. Hao et al. (2015) argued that air transportation freight has a substantial impact on energy demand, largely responsible for escalating global GHG emissions. Sustainable policy options should be desirable to mitigate environmental problems from logistics activities. According to Van Fan et al. (2018), the transportation industry is to blame for rising GHG emissions, with severe issues arising when products' loaded capacity exceeds its allocated capacity, resulting in emissions. Its a reaction to a logistics service provider's request to track the loaded power of items to reduce air pollution. Goetz and Alexander (2019) suggested several ways through which climate action plans (CAPs) could be executed efficiently by seeking information from freight transportation data and found that GHG emissions could be lowered by reducing the vehicle miles traveled, using city-owned vehicle fleets, electrified transportation and alternatively shift fuels from non-renewable to renewable. Thus, these CAPs would include sustainable policies to decarbonize logistics through smart freight movement. Pizzol (2019) emphasized the need to use intermodal transportation that could prevent emissions through reducing traffic from high to low emissions vehicles. Thus, sea-route freight could be shifted to road routes, while for other intermodal transportation the use of ferries in cargo transportation would help reduce emissions, depending on the size and fuel used. Thus, the transportation shipment could be made in sustainable modes via shifting of goods movement from intermodal transportation.

The relationship between air freight pricing and GHG emissions is less evident as in the 90^{th} quantiles this relationship is positive (Fig. 3), indicating less efficient freight pricing in mitigation of GHG emissions across countries. The results evidence that freight pricing needs more sustainable options to impose optimum freight tariffs to limit GHG emissions.

Gupta (2016) argued that the willingness-to-pay for environmental protection shows a greater concern for mitigating carbon emissions in green development portfolios. For this purpose, carbon pricing in the transportation sector would be a desirable strategy to reduce environmental risks through the contingent valuation method. Santos (2017) suggested the need to impose fuel taxes on the different modes of transportation that reduce negative environmental externalities, and it is desirable to emphasize pay-as-you-drive insurance schemes for safe movement. Avetisyan (2018) found that the transportation sector contributed a maximum share of GHG emissions through ground transportation, air, and water transport. Global carbon pricing is considered a highly sustainable policy instrument that improves transportation exports and lessens global emissions. Zahedi et al. (2019) generalized the field survey findings of willingness-to-pay for environmental protection through carbon tax imposition on the transport sector. They found positive remarks about the imposition of transportation taxes to reduce carbon emissions stock to achieve sustainable development agendas. Gupta et al. (2019) were generally in favor of the imposition of carbon taxes on the transportation sector. They found the different emissions reduction targets by diverse carbon tariffs, thus imposing an appropriate pricing mechanism on getting sustainable payoffs and achieving greater carbon reduction targets.

The relationship between air freight revenues and GHG emissions is positive (negative impact) at 10^{th} percentiles to 40^{th} percentiles; however, at 90^{th} percentiles, air freight revenues have a negative relationship (positive effect) with GHG emissions that confirmed the positivity of air fright revenues to mitigate emissions. There is a positive relationship between FDI inflows and GHG emissions, which established the 'pollution haven' hypothesis across countries. There is a need to regulate environmental policies by limiting GHG emissions, which requires sustainable policy options for achieving green development by advancement in cleaner energy. There is a negative relationship between insurance and financial services and GHG emissions, which implies that green financing improves logistics performance, utilizing renewable fuels to gear economic performance for shipment. Michaelowa (2015) discussed the importance of sustainable insurance policies to reduce the risk of climate change in line with the Paris Agreement and the Kyoto protocol. Naz et al. (2019) presented a long-term policy channel through which carbon emissions stock could be reduced by achieving energy efficiency by cleaner energy production, launching green financial projects to improve air quality, and continued economic growth responsible production and consumption. Thus, the flair of socio-economic and environmental policies is desirable to attain sustainable development agenda with national integrated green systems. Sarkodie and Strezov (2019) emphasized the need to improve global partnerships to delimit high mass carbon emissions by adopting sustainable policy options. The advancement in the cleaner production agenda, utilization of renewable energy projects, fossil fuel storage, and biomass production are the few complementary examples that would be placed in the carbon mitigation agenda for global prosperity. Hassan et al. (2019) generally favor mitigation carbon emissions based on aviation transportation through the reduction of diesel oil and replaced it with renewable fuels. Shouket et al. (2019) designed a green vehicle framework and emphasized the need to adopt some re-corrective measures, including the use of smart applications in travel services, stringent environmental regulations, population control, and improve transportation infrastructure. All these measures would reduce carbon emissions and achieve green development agendas with sustainable modes of transportation.

Table VII shows the slope and symmetric quantiles estimates and confirmed no such heteroskedasticity problem as slope equality and symmetric quantiles estimates fall in the 5% critical region. Thus, the panel quantile estimates are reliable and valid.

Table SII presents the causality estimates as supplementary material. It is found that there is bidirectional causality running between fright price and GHG emissions, while there is a unidirectional causality running from insurance and financial services (IFS) to GHG emissions, from fright price to IFS, and from FDI to IFS. The one-way linkage runs from GHG to the technology innovation index, from GHG emissions to FDI inflows, and from ATF to FDI inflows. Besides, the feedback relationship found between i) ATF to TINOVINDEX, ii) FPRICE to TINOVINDEX, iii) FREV to TINOVINDEX,

Table VII. Slope and Symmetric Quantiles Test Estimates.

Methods	Chi-Square Statistic	Ch-square degree of freedom	Probability value
Quantile Slope Equality – Wald Test	837.109	18	0.000
Symmetric Quantiles – Wald Test	316.800	14	0.000

iv) FDI to TINOVINDEX, v) FREV to ATF, and vi) FDI to FREV.

The following results emerged from this exercise:

i) The need for a technology innovation index is desirable to mitigate GHG emissions.
ii) The imposition of freight prices is desirable to promote sustainable logistics activities.
iii) The reinvestment of freight revenues into cleaner production technologies is desirable to achieve the environmental sustainability agenda.
iv) Transportation freight contributes to the growth of FDI inflows at the expense of increased GHG emissions.
v) Logistic activities based upon green insurance and financial services can reduce GHG emissions.

Table VIII shows the Impulse Response Function (IRF) estimates, indicating that the technology index has a negative relationship with GHG emissions, which implies that technology innovation will largely reduce GHG emissions through advancement in cleaner production technologies in the next ten years. Further, sustainable logistics activities in the form of shipment, air freight prices, freight revenues, FDI inflows, and green insurance will also decrease GHG emissions over this time horizon. The positive determinant of technology innovation will be freight price while the remaining factors, including GHG emissions, air transportation freight, freight revenues, FDI inflows, and IFS, will negatively impact on technology innovation index over this time horizon. Other IRF estimates are presented in Table SIII.

The technology innovation index will positively support air transportation freight, while freight prices and freight revenues will negatively impact air transportation freight. In the next decade, there will be a negative association between freight prices and GHG emissions, technology innovation index, FDI inflows, and insurance and financial services,

Table VIII. IRF Estimates for GHG Emissions.

The response of GHG:							
Period	GHG	TINOVINDEX	ATF	FPRICE	FREV	FDI	IFS
1	234456.2	0	0	0	0	0	0
2	159458.7	-2317.655	9742.038	-9386.730	-15765.52	3211.644	-629.1388
3	190194.1	-2412.029	-5712.869	-12057.68	-20237.34	-3468.127	-1207.644
4	185564.4	-2165.258	-7166.369	-15572.39	-20514.57	-3040.836	-1621.616
5	193377.9	-2197.448	-10832.68	-17684.09	-21771.24	-3417.555	-1678.556
6	196968.5	-2291.145	-13445.17	-19478.11	-21803.09	-3170.008	-1697.907
7	202130.0	-2423.833	-16001.42	-20824.92	-21632.68	-2850.160	-1611.961
8	206807.5	-2606.357	-18356.19	-21937.72	-21241.21	-2417.190	-1473.782
9	211689.9	-2828.593	-20702.31	-22861.67	-20740.73	-1963.985	-1290.380
10	216524.3	-3088.365	-23026.40	-23664.91	-20156.14	-1482.865	-1073.105

Source: Author’s estimation.

but a positive relationship between freight prices and freight revenues. Freight revenues will largely be affected by increased GHG emissions, while FDI inflows will exert positive environmental impacts through advancement in technology innovation across countries. The insurance and financial services will positively impact FDI inflows, air transportation freight, and technology innovation index, leading to a decrease in GHG emissions over this time horizon.

Table IX shows the VDA estimates indicating that GHG emissions are largely affected by freight revenues with a variance proportion of 0.919%, followed by freight price (0.769%), and air transportation freight (0.492%), while the least influenced will be insurance and financial statistics over this time horizon. The innovation shocks to GHG emissions are more significant than the other external shocks, and as a result, the percentage share of freight revenues reached just 0.919 percent. The IRF estimates conclude that technology innovations, air transportation freight, air freight pricing, air freight revenues, FDI inflows, and insurance & financial services will positively limit GHG emissions across this panel of selected 39 countries. Sustainable technological innovations and air freight pricing would be viable policy instruments to implement in the Post Paris Agreement (COP21) and 2030 agenda of sustainable development. Thus, more concentrated economic and environmental regulatory policies are desirable to reap sustainable payoffs through mutual collaborative global partnerships for shared prosperity. Other VDA estimates are presented in Table SIV.

Freight revenue will largely be affected by the technology innovation index, while the technology innovation index least influences freight price over the next ten years. Freight revenue exerts a greater impact on air transportation freight with a magnitude variance of 20.364%, while freight prices will least influence air freight. GHG emissions have a large impact on freight prices with a magnitude of 0.894%, while FDI inflows will least influence freight prices over this time horizon. Air transportation freight is the main predictor of freight revenues with a magnitude value of 40.559% while the technology innovation index will least influence freight revenues over the next 10 years. GHG emissions largely impact FDI inflows, while high FDI inflows largely affect insurance and financial statistics over time. The overall results indicate that technological innovations have an enormous role in promoting a country's economic growth through improved logistics activities, smart applications in finance & insurance services, and technology associated FDI inflows. However, technological innovations need to be sustainable (low-carbon) for compliance with the post-Paris Agreement (COP21) and the 2030 UN agenda on sustainable development.

5. Conclusions and Policy Implications

A worldwide partnership and mutual collaboration to limit GHG emissions and maintain the global average temperature less than 2ºC are highly desirable for sustainable development. Advancements in low-carbon

Table IX. VDA Estimates for GHG Emissions.

Variance Decomposition of GHG:								
Period	SE.	GHG	TINOVINDEX	ATF	FPRICE	FREV	FDI	IFS
1	234456.2	100	0	0	0	0	0	0
2	284331.5	99.44628	0.006644	0.117395	0.108988	0.307444	0.012759	0.000490
3	342965.1	99.10348	0.009513	0.108433	0.198511	0.559491	0.018995	0.001576
4	390884.2	98.83121	0.010392	0.117089	0.311536	0.706162	0.020675	0.002935
5	437160.0	98.58239	0.010835	0.155015	0.412710	0.812592	0.022641	0.003821
6	480582.2	98.37075	0.011238	0.206539	0.505770	0.878212	0.023085	0.004410
7	522484.5	98.19143	0.011660	0.268532	0.586761	0.914423	0.022507	0.004682
8	563066.2	98.03768	0.012183	0.337498	0.657027	0.929674	0.021222	0.004717
9	602703.2	97.90328	0.012835	0.412552	0.717332	0.929839	0.019585	0.004575
10	641594.3	97.78309	0.013644	0.492858	0.769051	0.919223	0.017816	0.004317

Source: Author's estimation.

technological innovations provide an option as climate-resilient strategies. This study examines the role of technological innovations and air freight pricing in mitigating GHG emissions in a panel of 39 R&D economies between 1995 and 2018. For this purpose, the study employed the panel quantile regression technique to obtain parameter estimates at lowest to highest quantile distribution. In addition, the panel Granger causality test and innovation accounting matrix assess the cause-effect relationship and inter-temporal forecast relationship between the variables over the next ten years. The results show that technology innovations and insurance and financial services are the main predictors to reduce GHG emissions whereas, air transportation freight, freight pricing, and FDI inflows increase GHG emissions, evidencing the 'pollution haven' hypothesis across countries. The causality estimates confirmed the feedback relationship between freight pricing and GHG emissions and technology innovations. Furthermore, causality is two-way between technology innovation and air freight, freight revenues and FDI inflows. Air freight revenues and FDI inflows have a unidirectional relationship with insurance and financial services while GHG emissions Granger cause technical innovation and FDI inflows. Air freight and insurance and financial services Granger cause FDI inflows and GHG emissions, respectively. The IRF and VDA estimates confirmed the viability of sustainable technological innovation and air freight pricing in GHG emissions' mitigation over the next 10 years. Thus, based on robust inferences, the following policy implications are proposed to support the post-Paris agreement (COP21) and the 2030 UN agenda on sustainable development:

i) Technological advancement in cleaner production, including upgrading renewable energy projects, electrified vehicles, and hybrid technology, are climate-resilient strategies which would be achieved through higher spending on R&D projects across countries.
ii) Air freight pricing would help improve air freight and logistics activities towards a more sustainable model, i.e., by shifting to renewable fuel-based activities, technology–improved logistics operations, and logistics environmental regulations.
iii) Efficient air freight pricing would result in freight revenues available to support sustainable policy options, i.e., new emerging technological innovation-based markets and enhancing economic activities.
iv) Urgent need to improve insurance and financial activities to support logistics activities and climate-based financing by technological advancement and logistics pricing.
v) Urgent need for strict governmental environment-based reforms to limit polluting industries by advances in cleaner production, renewable energy sources, smart grid energy applications, electrified vehicles, and hybrid technologies. Massive environmental reforms are required across all countries to achieve sustainability.

These five important policy implications may set out environmental sustainability targets as suggested by the Paris Agreement (COP21) and 2030 United Nations sustainable development agenda through technology assisted growth, integrated climate-resilient projects, renewable energy reforms, energy and resource market financing and strict environmental regulatory mechanisms. Thus, it would help maintain the global temperature of less than 1.5ºC through cooperation among the R&D economies for globally shared prosperity.

Acknowledgments
Researchers Supporting Project number (RSP-2022/87), King Saud University, Riyadh, Saudi Arabia.

References

Ahmed K, Ozturk I. 2018. What new technology means for the energy demand in China? A sustainable development perspective. Environmental Science and Pollution Research, 25: 29766-29771. https://doi.org/10.1007/s11356-018-2957-3

Al Mamun M, Sohag K, Shahbaz M, Hammoudeh S. 2018. Financial markets, innovations and cleaner energy production in OECD countries. Energy Economics, 72: 236-254. https://doi.org/10.1016/j.eneco.2018.04.011

Aldakhil AM, Zaheer A, Younas S, Nassani AA, Abro MMQ, Zaman K. 2019. Efficiently managing green information and communication technologies, high-technology exports, and research and development expenditures: A case study. Journal of Cleaner Production, 240: 118164. https://doi.org/10.1016/j.jclepro.2019.118164

Atuonwu JC, Leadley C, Bosman A, Tassou SA, Lopez-Quiroga E, Fryer PJ. 2018. Comparative assessment of innovative and conventional food preservation technologies: Process energy performance and greenhouse gas emissions. Innovative food science & emerging technologies, 50: 174-187. https://doi.org/10.1016/j.ifset.2018.09.008

Avetisyan M. 2018. Impacts of global carbon pricing on international trade, modal choice and emissions from international transport. Energy Economics, 76: 532-548. https://doi.org/10.1016/j.eneco.2018.10.020

Batool R, Sharif A, Islam T, Zaman K, Shoukry AM, Sharkawy MA, Gani S, Aamir A, Hishan SS. 2019. Green is clean: the role of ICT in resource management. Environmental Science and Pollution Research, 26: 25341-25358. https://doi.org/10.1007/s11356-019-05748-0

Bel G, Joseph S. 2018. Policy stringency under the European Union Emission trading system and its impact on technological change in the energy sector. Energy Policy, 117: 434-444. https://doi.org/10.1016/j.enpol.2018.03.041

Chen W, Lei Y. 2018. The impacts of renewable energy and technological innovation on environment-energy-growth nexus: New evidence from a panel quantile regression. Renewable Energy, 123: 1-14. https://doi.org/10.1016/j.renene.2018.02.026

CIGI 2017. Generating Growth from Innovation for the Low-carbon Economy: Exploring Safeguards in Finance and Regulation. Centre for International Governance Innovation (CIGI) Papers No.117, January 2017. Online available at: https://www.cigionline.org/sites/default/files/documents/Paper%20no.117_WEB.pdf (accessed 2019 September 14).

Dogan E, Ozturk I. 2017. The influence of renewable and non-renewable energy consumption and real income on CO2 emissions in the USA: evidence from structural break tests. Environmental Science and Pollution Research, 24: 10846-10854. https://doi.org/10.1007/s11356-017-8786-y

Dumitrescu EI, Hurlin C. 2012. Testing for Granger non-causality in heterogeneous panels. Economic modelling, 29: 1450-1460. https://doi.org/10.1016/j.econmod.2012.02.014

Fernández-Fernández Y, Fernández-López M, Olmedillas-Blanco B. 2018. Innovation for sustainability: the impact of R&D spending on CO2 emissions. Journal of cleaner production, 172: 3459-3467. https://doi.org/10.1016/j.jclepro.2017.11.001

Goetz AR, Alexander S. 2019. Urban Goods Movement and Local Climate Action Plans: Assessing Strategies to Reduce Greenhouse Gas Emissions from Urban Freight Transportation. Mineta Transportation Institute Publications. online available at: https://scholarworks.sjsu.edu/mti_publications/262/ (accessed 2019 September 15).

Grubler A, Wilson C, Bento N, Boza-Kiss B, Krey V, Mc-Collum DL, Rao ND, Riahi K, Rogelj J, De Stercke S, Cullen J, Frank S, Fricko O, Guo F, Gidden M, Havlík P, Huppmann D, Kiesewetter G, Rafaj P, Schoepp W, Valin H. 2018. A low energy demand scenario for meeting the 1.5 C target and sustainable development goals without negative emission technologies. Nature Energy, 3(6): 515-527. https://doi.org/10.1038/s41560-018-0172-6

Gupta M. 2016. Willingness to pay for carbon tax: A study of Indian road passenger transport. Transport Policy, 45: 46-54. https://doi.org/10.1016/j.tranpol.2015.09.001

Gupta M, Bandyopadhyay KR, Singh SK. 2019. Measuring effectiveness of carbon tax on Indian road passenger transport: A system dynamics approach. Energy Economics, 81: 341-354. https://doi.org/10.1016/j.eneco.2019.03.013

Hao H, Geng Y, Li W, Guo B. 2015. Energy consumption and GHG emissions from China's freight transport sector: scenarios through 2050. Energy Policy. 85: 94-101. https://doi.org/10.1016/j.enpol.2015.05.016

Hassan SA, Nosheen M, Rafaz N. 2019. Revealing the environmental pollution in nexus of aviation transportation in SAARC region. Environmental Science and Pollution Research, 26: 25092-25106. https://doi.org/10.1007/s11356-019-05648-3

Hishan SS, Khan A, Ahmad J, Hassan ZB, Zaman K, Qureshi MI. 2019. Access to clean technologies, energy, finance, and food: environmental sustainability agenda and its implications on Sub-Saharan African countries. Environmental Science and Pollution Research, 26: 16503-16518. https://doi.org/10.1007/s11356-019-05056-7

Huang R, Riddle M, Graziano D, Warren J, Das S, Nimbalkar S, Cresko J, Masanet E. 2016. Energy and emissions saving potential of additive manufacturing:

the case of lightweight aircraft components. Journal of Cleaner Production, 135: 1559-1570. https://doi.org/10.1016/j.jclepro.2015.04.109

IPCC 2018. Special Report: Global Warming of 1.5 ºC. The Intergovernmental Panel on Climate Change, online available at: https://www.ipcc.ch/sr15/ (accessed 2019 September 14).

Jardón A, Kuik O, Tol RS. 2017. Economic growth and carbon dioxide emissions: An analysis of Latin America and the Caribbean. Atmósfera, 30(2): 87-100. https://doi.org/10.20937/ATM.2017.30.02.02

Kato K, Galvao Jr, AF, Montes-Rojas GV. 2012. Asymptotics for panel quantile regression models with individual effects. Journal of Econometrics, 170: 76-91. https://doi.org/10.1016/j.jeconom.2012.02.007

Khan MA, Ozturk I. 2020. Examining foreign direct investment and environmental pollution linkage in Asia. Environmental Science and Pollution Research, 27: 7244-7255. https://doi.org/10.1007/s11356-019-07387-x

Li M, Porter AL, Suominen A. 2018. Insights into relationships between disruptive technology/innovation and emerging technology: A bibliometric perspective. Technological Forecasting and Social Change, 129: 285-296. https://doi.org/10.1016/j.techfore.2017.09.032

Liu D, Guo X, Xiao B. 2019. What causes growth of global greenhouse gas emissions? Evidence from 40 countries. Science of The Total Environment, 661: 750-766. https://doi.org/10.1016/j.scitotenv.2019.01.197

Long TB, Blok V, Coninx I. 2016. Barriers to the adoption and diffusion of technological innovations for climate-smart agriculture in Europe: evidence from the Netherlands, France, Switzerland and Italy. Journal of Cleaner Production, 112: 9-21. https://doi.org/10.1016/j.jclepro.2015.06.044

Lukkarinen J, Berg A, Salo M, Tainio P, Alhola K, Antikainen R. 2018. An intermediary approach to technological innovation systems (TIS)—The case of the cleantech sector in Finland. Environmental innovation and societal transitions, 26: 136-146. https://doi.org/10.1016/j.eist.2017.04.003

Lybbert TJ, Sumner DA. 2012. Agricultural technologies for climate change in developing countries: Policy options for innovation and technology diffusion. Food Policy, 37: 114-123. https://doi.org/10.1016/j.foodpol.2011.11.001

Michaelowa A. 2015. Can insurance deal with negative effects arising from climate policy measures? In Climate Change and Insurance (pp. 80-90). Routledge.

Miyamoto M, Takeuchi K. 2019. Climate agreement and technology diffusion: Impact of the Kyoto Protocol on international patent applications for renewable energy technologies. Energy policy, 129: 1331-1338. https://doi.org/10.1016/j.enpol.2019.02.053

Naz S, Sultan R, Zaman K, Aldakhil AM, Nassani AA, Abro MMQ. 2019. Moderating and mediating role of renewable energy consumption, FDI inflows, and economic growth on carbon dioxide emissions: evidence from robust least square estimator. Environmental Science and Pollution Research, 26: 2806-2819. https://doi.org/10.1007/s11356-018-3837-6

Nerini F, Slob A, Engström RE, Trutnevyte E. 2019. A Research and Innovation Agenda for Zero-Emission European Cities. Sustainability, 11(6): 1692. https://doi.org/10.3390/su11061692

Nikzad R, Sedigh G. 2017. Greenhouse gas emissions and green technologies in Canada. Environmental Development, 24: 99-108. https://doi.org/10.1016/j.envdev.2017.01.001

Nunes LJR, Godina R, Matias JCDO. 2019. Technological Innovation in Biomass Energy for the Sustainable Growth of Textile Industry. Sustainability, 11(2): 528. https://doi.org/10.3390/su11020528

Pizzol M. 2019. Deterministic and stochastic carbon footprint of intermodal ferry and truck freight transport across Scandinavian routes. Journal of Cleaner Production, 224: 626-636. https://doi.org/10.1016/j.jclepro.2019.03.270

Salahuddin M, Alam K, Ozturk I. 2016. The effects of Internet usage and economic growth on CO2 emissions in OECD countries: A panel investigation. Renewable and Sustainable Energy Reviews, 62: 1226-1235. https://doi.org/10.1016/j.rser.2016.04.018

Santos G. 2017. Road fuel taxes in Europe: Do they internalize road transport externalities? Transport Policy, 53: 120-134. https://doi.org/10.1016/j.tranpol.2016.09.009

Sarkodie SA, Ozturk I. 2020. Investigating the environmental Kuznets curve hypothesis in Kenya: a multivariate analysis. Renewable and Sustainable Energy Reviews, 117: 109481. https://doi.org/10.1016/j.rser.2019.109481

Sarkodie SA, Strezov V. 2019. Effect of foreign direct investments, economic development and energy consumption on greenhouse gas emissions in developing countries. Science of the Total Environment, 646: 862-871. https://doi.org/10.1016/j.scitotenv.2018.07.365

Shahbaz M, Nasir MA, Roubaud D. 2018. Environmental degradation in France: the effects of FDI, financial development, and energy innovations. Energy Economics, 74: 843-857. https://doi.org/10.1016/j.eneco.2018.07.020

Sharif A, Raza SA, Ozturk I, Afshan S. 2019. The dynamic relationship of renewable and non-renewable energy consumption with carbon emission: a global study with the application of heterogeneous panel estimations. Renewable Energy, 133: 685-691. https://doi.org/10.1016/j.renene.2018.10.052

Shouket B, Zaman K, Nassani AA, Aldakhil AM, Abro MMQ. 2019. Management of green transportation: an evidence-based approach. Environmental Science and Pollution Research, 26: 12574-12589. https://doi.org/10.1007/s11356-019-04748-4

Shubbak MH. 2019. The technological system of production and innovation: The case of photovoltaic technology in China. Research Policy, 48(4): 993-1015. https://doi.org/10.1016/j.respol.2018.10.003

Su HN, Moaniba IM. 2017. Does innovation respond to climate change? Empirical evidence from patents and greenhouse gas emissions. Technological Forecasting and Social Change, 122: 49-62. https://doi.org/10.1016/j.techfore.2017.04.017

UNFCCC 2017. Technological Innovation for the Paris Agreement: Implementing nationally determined contributions, national adaptation plans and mid-century strategies. The United Nations Framework Convention on Climate Change, Bonn, Germany. Online available at: https://unfccc.int/ttclear/misc_/StaticFiles/gnwoerk_static/brief10/8c3ce94c20144fd5a8b0c06fefff6633/57440a5fa1244fd8b8cd13eb4413b4f6.pdf (accessed 2019 September 14).

Usman A, Ullah S, Ozturk I, Chishti MZ, Zafar SM. 2020. Analysis of asymmetries in the nexus among clean energy and environmental quality in Pakistan. Environmental Science and Pollution Research, 27: 20736-20747. https://doi.org/10.1007/s11356-020-08372-5

Van Fan Y, Klemes JJ, Perry S, Lee CT. 2018. An Emissions Analysis for Environmentally Sustainable Freight Transportation Modes: Distance and Capacity. Chemical Engineering Transactions, 70: 505-510. https://doi.org/10.3303/CET1870085

Williams JH, DeBenedictis A, Ghanadan R, Mahone A, Moore J, Morrow III WR, Price S, Torn MS. 2012. The tech- nology path to deep greenhouse gas emissions cuts by 2050: the pivotal role of electricity. Science, 335(6064): 53-59. https://doi.org/10.1126/science.1208365

World Bank 2019. World Development Indicator, World Bank, Washington DC.

Wu J, Ma Z, Liu Z, Lei CK. 2019. A contingent view of institutional environment, firm capability, and innovation performance of emerging multinational enterprises. Industrial Marketing Management, 82: 148-157. https://doi.org/10.1016/j.indmarman.2019.01.018

Xue X, Zhang X, Wang L, Skitmore M, Wang Q. 2018. Analyzing collaborative relationships among industrialized construction technology innovation organizations: A combined SNA and SEM approach. Journal of Cleaner Production, 173: 265-277. https://doi.org/10.1016/j.jclepro.2017.01.009

Yalçınkaya Ö, Hüseyni İ, Çelik AK. 2017. The impact of total factor productivity on economic growth for developed and emerging countries: A second-generation panel data analysis. Margin: The Journal of Applied Economic Research, 11(4): 404-417. https://doi.org/10.1177/0973801017722266

Yusuf M, Sabara Z, Wekke IS. 2019. Role of Innovation in Testing Environment Kuznets Curve: A Case of Indonesian Economy. International Journal of Energy Economics and Policy, 9(1): 276-281. https://doi.org/10.32479/ijeep.7230

Zahedi S, Batista-Foguet JM, van Wunnik L. 2019. Exploring the public's willingness to reduce air pollution and greenhouse gas emissions from private road transport in Catalonia. Science of the Total Environment, 646: 850-861. https://doi.org/10.1016/j.scitotenv.2018.07.361

Zhang N, Wang B, Chen Z. 2016. Carbon emissions reductions and technology gaps in the world's factory, 1990–2012. Energy Policy, 91: 28-37. https://doi.org/10.1016/j.enpol.2015.12.042

Zhang WF, Dou ZX, He P, Ju XT, Powlson D, Chadwick D, Norse D, Lu YL, Zhang Y, Wu L, Chen XP, Cassman KG, Zhang FS. 2013. New technologies reduce greenhouse gas emissions from nitrogenous fertilizer in China. Proceedings of the National Academy of Sciences, 110(21): 8375-8380. https://doi.org/10.1073/pnas.1210447110

Zhang Y, Na S, Niu J, Jiang B. 2018. The influencing factors, regional difference and temporal variation of industrial technology innovation: Evidence with the FOA-GRNN model. Sustainability, 10(1): 187. https://doi.org/10.3390/su10010187

Supplementary Material

Table SI. Principal Component Analysis (PCA) for Technology Innovation Index (TINDEX).

Eigenvalues: (Sum = 4, Average = 1)					
Number	Value	Difference	Proportion	Cumulative Value	Cumulative Proportion
1	1.619	0.244	0.404	1.619	0.404
2	1.375	0.773	0.343	2.994	0.748
3	0.601	0.198	0.150	3.5963	0.899
4	0.403	---	0.100	4	1
Eigenvectors (loadings):					
Variable	PC 1	PC 2	PC 3	PC 4	
TINOV_1	0.628	–0.280	0.448	–0.570	
TINOV_2	0.355	0.636	0.498	0.469	
TINOV_3	0.470	–0.572	–0.205	0.638	
TINOV_4	0.507	0.433	–0.7122	–0.215	
Ordinary correlations:					
	TINOV1	TINOV2	TINOV3	TINOV4	
TINOV_1	1				
TINOV_2	0.141625	1			
TINOV_3	0.497567	–0.171175	1		
TINOV_4	0.205890	0.416831	0.078619	1	

Table S2. Dumitrescu Hurlin Panel Causality Tests.

Null Hypothesis:	W-Stat.	Zbar-Stat.	Prob.
TINOVINDEX ╬ GHG	5.20111	7.06997	2.E-12
GHG ╬ TINOVINDEX	3.67852	3.40158	0.0007
ATF ╬ GHG	5.38831	7.52098	5.E-14
GHG ╬ ATF	4.14349	4.52183	6.E-06
FPRICE ╬ GHG	3.76676	3.61417	0.0003
GHG ╬ FPRICE	8.00943	13.8361	0.0000
FREV ╬ GHG	2.84295	1.38843	0.1650
GHG ╬ FREV	4.80693	6.12027	9.E-10
FDI ╬ GHG	4.26128	4.80564	2.E-06
GHG ╬ FDI	3.32739	2.55560	0.0106
IFS ╬ GHG	3.71429	3.48777	0.0005
GHG ╬ IFS	5.22585	7.12957	1.E-12
ATF ╬ TINOVINDEX	3.12196	2.06066	0.0393
TINOVINDEX ╬ ATF	3.09398	1.99325	0.0462
FPRICE ╬ TINOVINDEX	3.44860	2.84764	0.0044
TINOVINDEX ╬ FPRICE	3.71544	3.49055	0.0005
FREV ╬ TINOVINDEX	3.06784	1.93028	0.0536
TINOVINDEX ╬ FREV	3.55222	3.09728	0.0020
FDI ╬ TINOVINDEX	3.29888	2.48693	0.0129
TINOVINDEX ╬ FDI	3.03813	1.85868	0.0631
IFS ╬e TINOVINDEX	4.75054	5.98441	2.E-09
TINOVINDEX ╬ IFS	4.94154	6.44459	1.E-10
FPRICE ╬ ATF	4.85606	6.23864	4.E-10
ATF ╬ FPRICE	4.90792	6.36359	2.E-10
FREV ╬ ATF	6.24772	9.59156	0.0000
ATF ╬ FREV	7.23952	11.9811	0.0000
FDI ╬ ATF	4.02515	4.23671	2.E-05
ATF ╬ FDI	3.09510	1.99594	0.0459
IFS ╬ ATF	4.74880	5.98021	2.E-09
ATF ╬ IFS	4.89463	6.33156	2.E-10
FREV ╬ FPRICE	4.84142	6.20337	6.E-10
FPRICE ╬ FREV	4.40877	5.16098	2.E-07
FDI ╬ FPRICE	2.68430	1.00620	0.3143
FPRICE ╬ FDI	2.94947	1.64507	0.1000
IFS ╬ FPRICE	4.17232	4.59130	4.E-06
FPRICE ╬ IFS	3.19262	2.23090	0.0257
FDI ╬ FREV	3.46386	2.88441	0.0039
FREV ╬ FDI	3.44165	2.83088	0.0046
IFS ╬ FREV	4.93863	6.43757	1.E-10
FREV ╬ IFS	4.39860	5.13648	3.E-07
IFS ╬ FDI	2.45126	0.44473	0.6565
FDI ╬ IFS	3.84106	3.79321	0.0001

Note: ╬ shows 'does not Granger cause'.

Table S3. Other IRF Estimates.

Response of TINOVINDEX:							
Period	GHG	TINOVINDEX	ATF	FPRICE	FREV	FDI	IFS
1	0.006996	0.143862	0	0	0	0	0
2	0.007779	0.154365	1.44E–05	0.001921	–0.006198	–0.008429	–0.003595
3	0.006053	0.154358	–0.002255	0.002796	–0.008228	–0.008032	–0.004784
4	0.005108	0.153868	–0.003335	0.003328	–0.009922	–0.007133	–0.005408
5	0.003867	0.153326	–0.003981	0.003661	–0.010710	–0.006635	–0.005961
6	0.002743	0.152780	–0.004185	0.003898	–0.011011	–0.006324	–0.006468
7	0.001578	0.152223	–0.004155	0.004080	–0.011113	–0.006146	–0.006945
8	0.000414	0.151661	–0.004021	0.004237	–0.011112	–0.006066	–0.007405
9	–0.000765	0.151100	–0.003827	0.004379	–0.011060	–0.006044	–0.007852
10	–0.001957	0.150541	–0.003599	0.004516	–0.010987	–0.006059	–0.008288
Response of ATF:							
Period	GHG	TINOVINDEX	ATF	FPRICE	FREV	FDI	IFS
1	22.53127	28.02587	474.0766	0	0	0	0
2	42.69527	10.94580	406.5271	0.478103	–153.9177	–51.09418	–5.203977
3	56.95983	15.98292	350.9324	–2.599750	–174.8257	–79.75076	–13.46052
4	81.26306	22.93814	338.5393	–6.353762	–192.9530	–85.60743	–17.94478
5	102.9077	28.19438	327.2605	–10.15455	–206.4116	–89.74252	–21.69883
6	126.3216	33.34876	318.9573	–13.77222	–213.6043	–91.87496	–25.06563
7	150.1104	38.34796	313.1534	–17.21821	–218.4319	–92.74849	–28.07165
8	174.5420	43.18261	308.1302	–20.47783	–221.9690	–93.25879	–30.86308
9	199.4598	47.90528	303.4603	–23.59954	–224.6929	–93.58605	–33.50653
10	224.8829	52.52854	298.8684	–26.62347	–226.9593	–93.82003	–36.03283
Response of FPRICE:							
Period	GHG	TINOVINDEX	ATF	FPRICE	FREV	FDI	IFS
1	–0.583654	0.001513	0.079817	11.03347	0	0	0
2	1.217401	–0.360767	0.159501	7.337689	0.048301	–0.011956	0.473231
3	0.213671	–0.333651	0.249345	4.931379	0.120002	0.040648	0.251233
4	0.324511	–0.303051	0.153418	3.343073	0.129077	–0.005239	0.116981
5	0.126807	–0.281641	0.138641	2.257896	0.128704	–0.005285	0.023147
6	0.085880	–0.267112	0.096954	1.530020	0.108262	–0.014243	–0.038875
7	0.025117	–0.256839	0.069565	1.036608	0.093033	–0.015922	–0.080494
8	–0.005094	–0.249611	0.046538	0.703638	0.078996	–0.016579	–0.107446
9	–0.029856	–0.244589	0.030164	0.478276	0.068507	–0.015714	–0.124585
10	–0.045624	–0.241075	0.018033	0.325901	0.060722	–0.014496	–0.134975
Response of FREV:							
Period	GHG	TINOVINDEX	ATF	FPRICE	FREV	FDI	IFS
1	–43750.29	8254.447	1152528.	61020.13	2306578.	0	0
2	108917.5	–46661.81	1322306.	85724.65	682997.2	140990.1	29035.25
3	–8148.433	–68364.28	642311.3	82764.53	235642.9	–98752.50	–25948.70
4	28956.17	–40777.13	459792.6	67753.64	86959.10	–115140.8	–52998.51
5	29818.73	–29850.49	375391.0	49918.80	–38797.91	–108548.4	–65171.70
6	44669.53	–22961.48	313181.1	34570.53	–100600.1	–105436.4	–73564.14
7	58886.98	–16807.72	282549.3	21517.11	–131305.3	–98240.08	–78708.90
8	75799.72	–11796.70	265254.2	11121.96	–148824.5	–92358.72	–81930.90
9	93263.65	–7379.804	254534.3	2898.216	–158461.6	–88225.32	–84155.74
10	111668.2	–3286.634	247410.4	–3608.250	–164053.3	–85415.35	–85769.03

Table S3. Other IRF Estimates.

Response of FDI:							
Period	GHG	TINOVINDEX	ATF	FPRICE	FREV	FDI	IFS
1	1.66E+09	4.19E+08	2.20E+09	1.56E+08	1.58E+09	2.60E+10	0
2	2.06E+09	4.64E+08	1.29E+09	–2.89E+08	–3.37E+09	1.40E+10	1.39E+09
3	1.91E+09	5.53E+08	6.87E+08	–4.37E+08	–1.14E+09	7.16E+09	1.24E+09
4	2.31E+09	6.00E+08	1.63E+09	–4.72E+08	–9.08E+08	4.01E+09	1.27E+09
5	2.42E+09	5.72E+08	1.69E+09	–4.62E+08	–1.09E+09	2.07E+09	1.25E+09
6	2.60E+09	5.82E+08	1.62E+09	–4.42E+08	–1.16E+09	9.82E+08	1.22E+09
7	2.77E+09	6.02E+08	1.57E+09	–4.28E+08	–1.25E+09	3.90E+08	1.18E+09
8	2.94E+09	6.23E+08	1.50E+09	–4.20E+08	–1.32E+09	58837400	1.14E+09
9	3.11E+09	6.46E+08	1.44E+09	–4.20E+08	–1.38E+09	–1.24E+08	1.10E+09
10	3.29E+09	6.69E+08	1.39E+09	–4.25E+08	–1.41E+09	–2.24E+08	1.07E+09

Response of IFS:							
Period	GHG	TINOVINDEX	ATF	FPRICE	FREV	FDI	IFS
1	–0.013793	0.033542	0.066385	–0.022186	–0.059138	0.051513	1.182659
2	0.000789	0.088794	0.032260	–0.015979	–0.059183	0.081600	1.135451
3	–0.003939	0.096597	0.044148	–0.018128	–0.057201	0.109064	1.113183
4	–0.003405	0.100000	0.050723	–0.019351	–0.061962	0.122594	1.092128
5	–0.004393	0.103254	0.056456	–0.020271	–0.064711	0.127765	1.071426
6	–0.004101	0.106556	0.062746	–0.020825	–0.067534	0.128703	1.051132
7	–0.003618	0.109832	0.068904	–0.021137	–0.070658	0.127176	1.031167
8	–0.002599	0.113121	0.074794	–0.021272	–0.073942	0.124292	1.011506
9	–0.001164	0.116435	0.080475	–0.021303	–0.077348	0.120710	0.992137
10	0.000723	0.119773	0.085942	–0.021275	–0.080839	0.116772	0.973056

Table S4. Other VDA Estimates.

Variance Decomposition of TINOVINDEX:								
Period	S.E.	GHG	TINOVINDEX	ATF	FPRICE	FREV	FDI	IFS
1	0.144032	0.235898	99.76410	0.000000	0.000000	0.000000	0.000000	0.000000
2	0.211566	0.244513	99.47380	4.66E–07	0.008246	0.085837	0.158729	0.028874
3	0.262281	0.212352	99.36014	0.007392	0.016728	0.154265	0.197069	0.052052
4	0.304456	0.185740	99.28039	0.017483	0.024365	0.220697	0.201146	0.070179
5	0.341234	0.160703	99.22235	0.027525	0.030908	0.274199	0.197931	0.086380
6	0.374200	0.139007	99.17958	0.035400	0.036552	0.314598	0.193156	0.101703
7	0.404281	0.120613	99.14667	0.040890	0.041501	0.345083	0.188596	0.116642
8	0.432081	0.105684	99.11936	0.044460	0.045947	0.368243	0.184818	0.131485
9	0.458017	0.094333	99.09476	0.046548	0.050034	0.386027	0.181894	0.146402
10	0.482396	0.086685	99.07080	0.047528	0.053867	0.399866	0.179752	0.161499
Variance Decomposition of ATF:								
Period	S.E.	GHG	TINOVINDEX	ATF	FPRICE	FREV	FDI	IFS
1	475.4384	0.224586	0.347480	99.42793	0.000000	0.000000	0.000000	0.000000
2	647.7478	0.555450	0.215755	92.95377	5.45E–05	5.646316	0.622201	0.006454
3	763.7689	0.955693	0.198976	87.96995	0.001198	9.300653	1.537826	0.035702
4	866.0274	1.623813	0.224915	83.70299	0.006314	12.19802	2.173247	0.070704
5	959.0210	2.475602	0.269842	79.90190	0.016361	14.57956	2.647884	0.108850
6	1045.662	3.541744	0.328690	76.51370	0.031109	16.43648	2.999255	0.149021
7	1128.219	4.812631	0.397878	73.42994	0.050014	17.86743	3.252192	0.189918
8	1208.094	6.284645	0.474771	70.54635	0.072351	18.95872	3.432267	0.230899
9	1286.306	7.948107	0.557491	67.79386	0.097480	19.77463	3.556907	0.271527
10	1363.656	9.791598	0.644422	65.12455	0.124852	20.36497	3.638188	0.311419
Variance Decomposition of FPRICE:								
Period	S.E.	GHG	TINOVINDEX	ATF	FPRICE	FREV	FDI	IFS
1	11.04919	0.279029	1.87E-06	0.005218	99.71575	0.000000	0.000000	0.000000
2	13.33380	1.025207	0.073207	0.017893	98.75634	0.001312	8.04E-05	0.125961
3	14.22699	0.923077	0.119303	0.046433	98.76021	0.008267	0.000887	0.141826
4	14.62308	0.922995	0.155877	0.054959	98.70905	0.015617	0.000852	0.140646
5	14.80082	0.908300	0.188365	0.062421	98.67973	0.022806	0.000845	0.137533
6	14.88310	0.901614	0.218498	0.065977	98.64844	0.027846	0.000927	0.136699
7	14.92207	0.897195	0.246984	0.067806	98.61650	0.031587	0.001036	0.138896
8	14.94141	0.894885	0.274254	0.068601	98.58310	0.034301	0.001156	0.143707
9	14.95181	0.894040	0.300632	0.068912	98.54835	0.036353	0.001265	0.150451
10	14.95812	0.894215	0.326353	0.068999	98.51264	0.037970	0.001358	0.158466
VarianceDecompositionofFREV:								
Period	S.E.	GHG	TINOVINDEX	ATF	FPRICE	FREV	FDI	IFS
1	2579598.	0.028765	0.001024	19.96176	0.055955	79.95250	0.000000	0.000000
2	2985199.	0.154601	0.025198	34.52665	0.124247	64.93678	0.223065	0.009460
3	3066190.	0.147248	0.073596	37.11502	0.190630	62.14221	0.315165	0.016129
4	3105423.	0.152245	0.088990	38.37537	0.233446	60.66038	0.444724	0.044850
5	3131514.	0.158786	0.096600	39.17558	0.254983	59.66914	0.557499	0.087418
6	3151956.	0.176817	0.100658	39.65633	0.263716	58.99953	0.662188	0.140760
7	3170483.	0.209254	0.102295	39.98843	0.265249	58.48354	0.750484	0.200750
8	3188373.	0.263432	0.102520	40.23307	0.263497	58.04695	0.825997	0.264536
9	3206126.	0.345141	0.101917	40.41901	0.260669	57.65016	0.892597	0.330513
10	3224053.	0.461278	0.100891	40.55966	0.257903	57.26976	0.952887	0.397619

Table S4. Other VDA Estimates.

Variance Decomposition of FDI:

Period	S.E.	GHG	TINOVINDEX	ATF	FPRICE	FREV	FDI	IFS
1	2.62E+10	0.402257	0.025522	0.705152	0.003517	0.363134	98.50042	0.000000
2	3.00E+10	0.776554	0.043338	0.720409	0.011936	1.531888	96.70186	0.214011
3	3.10E+10	1.109328	0.072444	0.725464	0.031045	1.572676	96.12904	0.360006
4	3.14E+10	1.618996	0.106813	0.972909	0.052747	1.612842	95.12278	0.512913
5	3.17E+10	2.173851	0.137600	1.239666	0.073173	1.704131	94.01064	0.660940
6	3.19E+10	2.808616	0.168952	1.479595	0.091383	1.813913	92.84014	0.797407
7	3.21E+10	3.511767	0.201760	1.697595	0.107895	1.941293	91.61810	0.921590
8	3.24E+10	4.287142	0.236053	1.889333	0.123269	2.082034	90.34880	1.033368
9	3.26E+10	5.134798	0.271903	2.057103	0.138070	2.229950	89.03502	1.133156
10	3.28E+10	6.056529	0.309231	2.203576	0.152713	2.380553	87.67582	1.221574

Variance Decomposition of IFS:

Period	S.E.	GHG	TINOVINDEX	ATF	FPRICE	FREV	FDI	IFS
1	1.187876	0.013483	0.079734	0.312321	0.034883	0.247851	0.188061	99.12367
2	1.649133	0.007018	0.331274	0.200311	0.027487	0.257386	0.342405	98.83412
3	1.996398	0.005178	0.460167	0.185588	0.027001	0.257726	0.532094	98.53225
4	2.282581	0.004184	0.543944	0.191349	0.027842	0.270840	0.695495	98.26635
5	2.528422	0.003711	0.610079	0.205804	0.029119	0.286235	0.822167	98.04289
6	2.744934	0.003372	0.668324	0.226870	0.030462	0.303392	0.917424	97.85015
7	2.938777	0.003094	0.722742	0.252903	0.031750	0.322497	0.987661	97.67935
8	3.114373	0.002824	0.775471	0.282864	0.032936	0.343525	1.038701	97.52368
9	3.274858	0.002567	0.827738	0.316206	0.034018	0.366465	1.075255	97.37775
10	3.422556	0.002355	0.880305	0.352557	0.035009	0.391307	1.100860	97.23761

ISSN 0187-6236

9 770187 623606

UNIVERSIDAD NACIONAL AUTONOMA DE MEXICO

POR MI RAZA HABLARA EL ESPIRITU

Universidad Nacional
Autónoma de
México